frontiers | Research Topics

Advances and applications of artificial intelligence and numerical simulation in risk emergency management and treatment, volume II

Edited by
Yunhui Zhang, Yihuai Zhang, Long Yan, Lei Xia and Chengyi Pu

Published in
Frontiers in Environmental Science
Frontiers in Earth Science
Frontiers in Ecology and Evolution

ISSN 1664-8714
ISBN 978-2-8325-5425-8
DOI 10.3389/978-2-8325-5425-8

About Frontiers

Frontiers is more than just an open access publisher of scholarly articles: it is a pioneering approach to the world of academia, radically improving the way scholarly research is managed. The grand vision of Frontiers is a world where all people have an equal opportunity to seek, share and generate knowledge. Frontiers provides immediate and permanent online open access to all its publications, but this alone is not enough to realize our grand goals.

Frontiers journal series

The Frontiers journal series is a multi-tier and interdisciplinary set of open-access, online journals, promising a paradigm shift from the current review, selection and dissemination processes in academic publishing. All Frontiers journals are driven by researchers for researchers; therefore, they constitute a service to the scholarly community. At the same time, the *Frontiers journal series* operates on a revolutionary invention, the tiered publishing system, initially addressing specific communities of scholars, and gradually climbing up to broader public understanding, thus serving the interests of the lay society, too.

Dedication to quality

Each Frontiers article is a landmark of the highest quality, thanks to genuinely collaborative interactions between authors and review editors, who include some of the world's best academicians. Research must be certified by peers before entering a stream of knowledge that may eventually reach the public - and shape society; therefore, Frontiers only applies the most rigorous and unbiased reviews. Frontiers revolutionizes research publishing by freely delivering the most outstanding research, evaluated with no bias from both the academic and social point of view. By applying the most advanced information technologies, Frontiers is catapulting scholarly publishing into a new generation.

What are Frontiers Research Topics?

Frontiers Research Topics are very popular trademarks of the *Frontiers journals series*: they are collections of at least ten articles, all centered on a particular subject. With their unique mix of varied contributions from Original Research to Review Articles, Frontiers Research Topics unify the most influential researchers, the latest key findings and historical advances in a hot research area.

Find out more on how to host your own Frontiers Research Topic or contribute to one as an author by contacting the Frontiers editorial office: frontiersin.org/about/contact

Advances and applications of artificial intelligence and numerical simulation in risk emergency management and treatment, volume II

Topic editors

Yunhui Zhang — Southwest Jiaotong University, China
Yihuai Zhang — University of Glasgow, United Kingdom
Long Yan — Central South University, China
Lei Xia — KU Leuven, Belgium
Chengyi Pu — Central University of Finance and Economics, China

Citation

Zhang, Y., Zhang, Y., Yan, L., Xia, L., Pu, C., eds. (2024). *Advances and applications of artificial intelligence and numerical simulation in risk emergency management and treatment, volume II*. Lausanne: Frontiers Media SA.
doi: 10.3389/978-2-8325-5425-8

Table of contents

frontiers | Frontiers in Ecology and Evolution

TYPE Perspective
PUBLISHED 17 April 2023
DOI 10.3389/fevo.2023.1114259

OPEN ACCESS

EDITED BY
Yunhui Zhang,
Southwest Jiaotong University, China

REVIEWED BY
Rui Ma,
Institute of Soil Science,
Chinese Academy of Sciences (CAS), China
Zejun Wang,
Wuhan University, China

*CORRESPONDENCE
Jian Luo
✉ jian.luo@imu.edu.cn

SPECIALTY SECTION
This article was submitted to Environmental Informatics and Remote Sensing, a section of the journal Frontiers in Ecology and Evolution

RECEIVED 02 December 2022
ACCEPTED 03 March 2023
PUBLISHED 17 April 2023

CITATION
Xia C, Zuecco G, Chen K, Liu L, Zhang Z and Luo J (2023) The estimation of young water fraction based on isotopic signals: challenges and recommendations.
Front. Ecol. Evol. 11:1114259.
doi: 10.3389/fevo.2023.1114259

The estimation of young water fraction based on isotopic signals: challenges and recommendations

Chengcheng Xia[1], Giulia Zuecco[2,3], Ke Chen[4,5], Li Liu[6], Zhiliang Zhang[6] and Jian Luo[7,8]*

[1]School of Geography and Tourism, Chongqing Normal University, Chongqing, China, [2]Department of Land, Environment, Agriculture, and Forestry, University of Padova, Legnaro, Italy, [3]Department of Chemical Sciences, University of Padova, Padova, Italy, [4]State Key Laboratory of Hydraulics and Mountain River Engineering, Sichuan University, Chengdu, China, [5]Department of Ecohydrology, Leibniz Institute of Freshwater Ecology and Inland Fisheries, Berlin, Germany, [6]College of Water Conservancy and Hydropower Engineering, Sichuan Agricultural University, Ya'an, China, [7]Inner Mongolia Key Laboratory of River and Lake Ecology, School of Ecology and Environment, Inner Mongolia University, Hohhot, China, [8]Key Laboratory of Mongolian Plateau Ecology and Resource Utilization, Ministry of Education, Hohhot, China

Young water fraction (*Fyw*) is defined as the fraction of water in a stream with a transit time of less than 2–3months. *Fyw* is a metric used to quantify the proportion of precipitation input converted into the runoff in the form of fast flow, which provides new insights for characterizing the mechanisms of water storage and release, understanding the time-scale of ecohydrological processes and indicating water-related risks. However, *Fyw* has been advanced for a relatively short time, and the research on its applicability conditions and main drivers is still ongoing. Studies estimating *Fyw* are still very few and this index has not been reported in many landscapes and climate backgrounds, limiting its further application in hydrological studies. On the basis of summarizing the progresses of *Fyw* in previous studies, this paper provides a preliminary analysis of the potential uncertainties in the *Fyw* estimation, which can be due to temporal trends in the isotopic composition of precipitation, uneven sampling interval of stream water, and complex hydrological systems. Finally, this paper provides some recommendations for the optimization of the sampling design and the methods used for the *Fyw* estimation.

KEYWORDS

young water fraction, isotope tracers, sources of uncertainty, water-related risks, further studies

Introduction

The rate of water transport in catchments regulates processes such as biogeochemical cycling, pollutant transport, and chemical weathering. The time water takes to travel through a catchment, from inputting as precipitation to reaching the outlet, is an important indicator to characterize the catchment hydrology and determine the sensitivity of the catchment to pollutants (Sprenger et al., 2019). Since the migration, transformation, and phase change of water are accompanied by the transport, mixing, and fractionation of hydrogen and oxygen stable isotopes (i.e., ^{18}O and ^{2}H), these isotopes are widely used to perform hydrological and meteorological analyses at different scales, such as the identification of water vapor sources and transport patterns, the quantification of the contribution of end members to runoff, and the evaluation of water interactions and estimation of evaporation losses (e.g., Chen et al., 2015;

Eissa et al., 2016, 2018; Zuecco et al., 2019; Laonamsai et al., 2021, 2022; Wang et al., 2022). During the process of runoff generation in rainfall-dominated catchments, the isotopic signal in precipitation is usually dampened when it is transmitted to river water, due to the buffering effect of the catchment and its mixing with groundwater and soil water with relatively constant isotopic signals. Based on the regularities of isotope fluctuation decay during the conversion from precipitation into river water, mean transit time (*MTT*), mean residence time and damping ratio can be estimated to evaluate the water age and water transport rate (McGuire and McDonnell, 2006; Bansah and Ali, 2019; Sprenger et al., 2019; Benettin et al., 2022). Such metrics have been widely applied to analyze the catchment behaviors in many regions across the world.

Recently, Kirchner (2016) found that the distribution function of water transit time in a catchment is often not static in space, especially for those landscapes characterized by strong spatial heterogeneity, and great uncertainty is likely to exist in the estimation of *MTT*, because of the aggregation bias. Consequently, Kirchner (2016) developed the concept of a substitutive metric, the young water fraction (*Fyw*), which is defined as the runoff component that is younger than 3 months in the water flowing through the catchment outlet. *Fyw* is negligibly affected by the aggregation bias (with an error usually less than 2%, Kirchner (2016)), and thus it can be used to effectively investigate the hydrological processes and the response of a catchment to climate change and human activities (e.g., groundwater abstraction, contaminant transport, or land use changes), and to evaluate hydrogeological and environmental risks related to water storage and release mechanisms in catchments. The estimation of *Fyw* is based on the aggregate parameter model, with precipitation as the input and runoff at the outlet as the output (shown in Figure 1). The isotopic signal of the output water is considered as the convolution of the isotopic fluctuation function (set as a sine function) of the input water and the transit time distribution function (set as a Gamma function). Using the Fourier transform method, the shape and scale coefficients of the Gamma distribution function can be determined, and then *Fyw* can be obtained by integration. Through a numerical simulation experiment, Kirchner (2016) found that *Fyw* can be approximated using the isotopic amplitude ratio between stream water and precipitation obtained by sine function fitting. This simple method is known as "amplitude ratio method" and has become the most commonly used method to estimate the *Fyw*. In the fitting of the sine function, the precipitation amount and the discharge are commonly used as weights for the observed isotopic compositions of precipitation and stream water (e.g., von Freyberg et al., 2018; Gallart et al., 2020a). To estimate *Fyw*, isotopic time series of input and output water, are required to be longer than a year. Typically, higher *Fyw* is associated with shorter flow paths, implying that surface water and groundwater in the catchment are more susceptible to pollutant contamination, while lower *Fyw* is associated with longer flow paths and slower recharge rates. Therefore, this metric could benefit the understanding of water recharge mechanisms, as well as of the exchange and transfer of pollutants, and is thus of practical importance for the management of water-related risks.

Jasechko et al. (2016) collected isotopic data from more than 60,000 precipitation samples from 459 meteorological stations and 10,000 river water samples from 254 rivers worldwide, and they estimated the *Fyw* based on the amplitude ratio method. Jasechko et al. (2016) found that the arithmetic mean value of *Fyw* in rivers worldwide is 26%, the amount weighted mean value is 34% and the median value is 21%, providing a reference for studies on *Fyw* in different geographic regions, at different spatial scales, and under different climatic backgrounds. Since then, the *Fyw* estimation has been determined in different study areas. For example, *Fyw* was found to be positively correlated with vegetation coverage and proportion of swamp, negatively correlated with the watershed area and elevation, but not significantly correlated with average runoff coefficient in Tibetan Plateau catchments (Song et al., 2017). Higher *Fyw* are typically associated with wetter climates, soils with lower permeability, and higher precipitation intensity in Swiss catchments (von Freyberg et al., 2018). Wilusz et al. (2017) reported that an increase in *Fyw* may result from increased precipitation amount in the Plynlimon region of Wales. In the Alpine area, the increase of snowpack duration promotes the emptying of groundwater storage in winter, thus decreasing the *Fyw*, while the snowpack with short duration is generally associated with the increased rapid flow path, resulting in increased *Fyw* (Gentile et al., 2022).

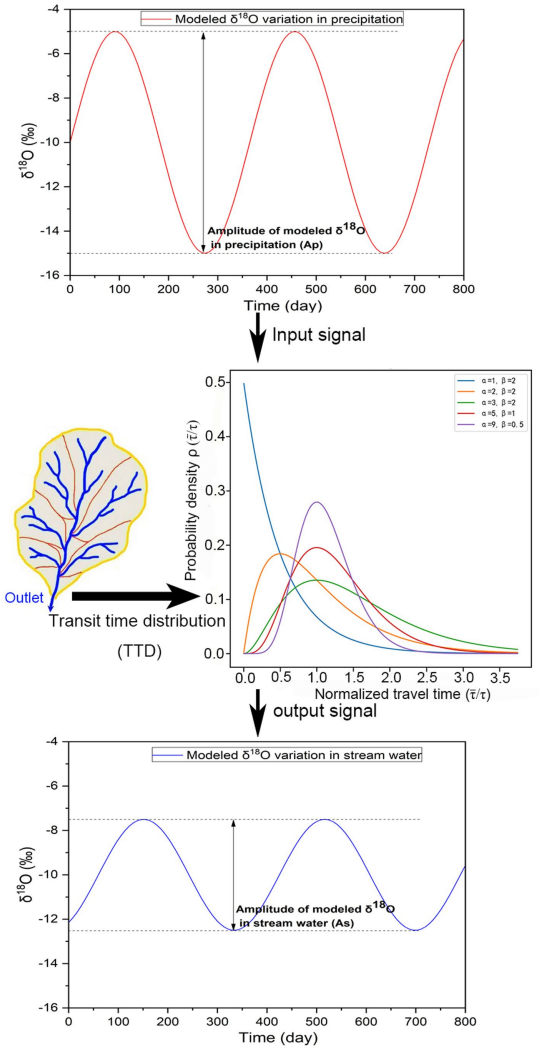

FIGURE 1
Conceptual scheme showing the *Fyw* estimation based on the lumped parameter model.

In previous studies, the interference of environmental and systematic factors, such as sampling frequency, evaporation and snowmelt, on the accuracy of *Fyw* estimates have been preliminarily explored (e.g., Ceperley et al., 2020; Gallart et al., 2020a). However, the source of uncertainties and the extent of application of this metric have not been fully explored, which limits its development as a practical indicator for catchment properties. The goal of this paper is to summarize the potential sources of uncertainty and possible limitations of *Fyw*, in the aspects of both hydro-meteorological conditions and data quality. Furthermore, in this perspective paper we provide some methodological recommendations aimed to reduce the uncertainty in *Fyw* estimation.

Uncertainty in the complexity of isotopic composition of precipitation and stream water

The theoretical basis of the *Fyw* estimation is the attenuation of isotope amplitude during the mixing process between precipitation, with a clear seasonal isotope periodicity, and water sources (e.g., shallow and deep groundwater, soil water), with an isotopic composition less time variable compared to precipitation. In the *Fyw* estimation, the lumped parameter model is based on the premise that precipitation is the only initial water source in the hydrologic system and phase shift in the path of water migration is not considered. Under this hypothesis, the influences of precipitation input in multiple forms (e.g., snowmelt and ice melt) and natural and anthropogenic processes on the composition and periodicity of isotopes in stream water are generally overlooked. For instance, based on data from three Alpine catchments, Ceperley et al. (2020) showed the limitations of isotopic periodicity in snowmelt-dominated catchments, and proposed an optimized method for the *Fyw* estimation in high altitude areas, considering the influence of lag release of water caused by the seasonal snowmelt. However, the uncertainty brought by melt water should be further explored in other mountainous catchments with different size and elevations, as well as with different contributions of melt water to stream runoff. In addition, previous research (i.e., Ceperley et al., 2020; Gentile et al., 2022) showed that there is a lack of studies providing *Fyw*, as well as transit times estimations in glacierized catchments; in these catchments *Fyw* can be larger than *Fyw* determined for snowmelt-dominated catchments due to fast flow paths and a less permeable bedrock (Schmieder et al., 2019; Zuecco et al., 2019).

In precipitation, the isotopic variations caused by sublimation of snow and ice, water-vapor exchange and sub-cloud secondary evaporation may lead to uncertainty in the sine-wave fitting, whose impacts also need to be evaluated in the *Fyw* estimation. Previous studies also showed that processes such as evaporation and scheduling of reservoirs may interfere the isotopic periodicity in stream water inherited from rainfall (Reckerth et al., 2017; Xia et al., 2021). Therefore, in catchments with complex flow systems or those heavily influenced by human activities, the uncertainty of the *Fyw* estimation based on the current estimation methods may be large. Therefore, to estimate *Fyw* is necessary to develop a more flexible approach, considering the isotopic variation associated with phase behavior changes.

Effects of trends in the isotopic composition of precipitation and stream water

Previous studies have confirmed that although *Fyw* is dependent on catchment properties, the accuracy of its estimation results is also confounded by systematic factors such as weighting methods, sampling frequency and selection of calculation periods (von Freyberg et al., 2018; Stockinger et al., 2019; Gallart et al., 2020a). Under the influence of climate change, the global temperature increase is widespread, leading to an enrichment trend in isotopic composition in precipitation at longer time scales. Wang and Chen (2020) reported the trend variations in temperature, precipitation, and $\delta^{18}O$ in precipitation based on data from stations of the global network of isotopes in precipitation (GNIP) with long-term records. Wang and Chen (2020) found that among 98 selected stations around the world, about 2/3 (65 stations) showed a significant upward trend of $\delta^{18}O$ in precipitation. Such a trend may also be transmitted to the isotopes in the river water and cause the amplitudes obtained from the sinusoidal function fit to not reflect the actual seasonal fluctuations of the isotopes in the water. The commonly-used amplitude ratio method for the *Fyw* estimation is based on the assumption that the isotopes in the waters vary seasonally following a fixed sinusoidal curve. However, in actual catchments, the isotope signals do not vary in a constant pattern. Fitting multi-year isotope records using sine waves will oversimplify the shape of the interannual isotope signal. The interannual differences in the amplitudes of isotopic fluctuations and the effects of isotopic trends at longer time scales on the periodicity are not considered, which are possible sources for inaccurate *Fyw* estimates.

Impact of the sampling approach of stream water

As the *Fyw* estimation is based on comparison of periodicity between precipitation and stream water, the extent that the captured isotopic records can reflect the actual variability is important. Gallart et al. (2020a) found that the accuracy of estimated *Fyw* is greatly dependent on the sampling frequency of stream water. Weekly-resolution sampling could not reflect the isotopic variation under high flows, thus resulting in an underestimation of *Fyw* in their catchment. Stockinger et al. (2019) pointed out that a 1-year isotopic time series is not long enough for an accurate *Fyw* estimation, and the selection of the fitting period may lead to a marked uncertainty. However, as the *Fyw* has been proposed for a relatively short time, in many studies, the time series of isotopic data, used to estimate the *Fyw*, was originally collected for the investigation of hydrological processes occurring at short timescales. Furthermore, in isotope-based studies, it is common to increase the sampling frequency of stream water in the rainy season with concentrated precipitation and high flows. Previous studies have shown that flows are positively correlated with *Fyw* (von Freyberg et al., 2018; Gallart et al., 2020b). Therefore, isotopic data collected mainly at the event timescale (i.e., during high flows) may lead to an overestimation of *Fyw*, as the proportion of high-flow condition in the "isotope discharge" (i.e., the observed flow accompanied with isotope collection), which is involved in sine-wave fitting, exceeds that of the low flow records. Additionally, it is difficult to guarantee long-term

and periodic stream water sampling, and the isotope datasets of river water with irregular sampling frequency and data gaps are common in many study areas, due to different research objectives and limitations in logistics conditions (e.g., Ceperley et al., 2020). In previous studies focusing on *Fyw*, the influence of such widespread heterogeneous datasets on the estimation uncertainty has not been determined yet.

Concluding remarks and future perspectives

Although research on *Fyw* based on isotopic signals has received much attention during the past few years and has been continuously promoted, there is still a lack of comparative understanding on *Fyw* under different landscapes and climate conditions. The knowledge about the influencing factors of this metric and the sources of uncertainty in the processes and results of its estimation is still very limited. Factors, such as temporal isotopic trends under changing climate, commonly-used irregular sampling schemes for isotope hydrology, complex recharge sources and evaporation conditions, have potential impacts on the accuracy of *Fyw* estimation. In future studies, more effort to explore the error sources and to develop optimization methods for *Fyw* estimation should be made. For example, future research should conduct *Fyw* estimations in areas with potential isotopic complexity (e.g., where there is a complex isotopic signal of melt waters or enhanced evaporation in the water sources), develop detrending models to reduce (or lower down) the impact of an existing trend on the isotopic periodicity, implement a sampling approach consistent with the full flow record during the observation period (i.e., able to capture all flows, without a bias toward low or high flows). To develop and test better methodological approaches for *Fyw* estimation, researchers should consider using long-term isotopic datasets (> 5–10 years) and datasets collected at very high temporal resolutions (e.g., von Freyberg et al., 2017). Combining *Fyw* estimation and transit times modeling across more catchments should help to better understand the drivers of *Fyw* and its sources of uncertainty, as well as to develop specific recommendations for the application of this metric. By deepening the understanding of *Fyw* and by reducing the uncertainty in its estimation, this metric could be applied more effectively to improve our comprehension of runoff generation and tracer transport in a variety of catchments.

Data availability statement

The original contributions presented in the study are included in the article/supplementary material, further inquiries can be directed to the corresponding author.

Author contributions

CX: formal analysis, methodology, and writing-original draft, GZ, KC, and LL: writing -review & editing and ZZ: writing-original draft. JL: formal analysis and writing -review & editing. All authors contributed to the article and approved the submitted version.

Funding

This work was financially supported by the Start-up Funding from Inner Mongolia University (21800-5223728) and the China Scholarship Council (No. 202006240192).

Conflict of interest

The authors declare that the research was conducted in the absence of any commercial or financial relationships that could be construed as a potential conflict of interest.

Publisher's note

References

Bansah, S., and Ali, G. (2019). Streamwater ages in nested, seasonally cold Canadian watersheds. *Hydrol. Process.* 33, 495–511. doi: 10.1002/hyp.13373

Benettin, P., Rodriguez, N. B., Sprenger, M., Kim, M., Klaus, J., Harman, C. J., et al. (2022). Transit time estimation in catchments: recent developments and future directions. *Water Resour. Res.* 58:e2022WR033096. doi: 10.1029/2022WR033096

Ceperley, N., Zuecco, G., Beria, H., Carturan, L., Michelon, A., Penna, D., et al. (2020). Seasonal snow cover decreases young water fractions in high alpine catchments. *Hydrol. Process.* 34, 4794–4813. doi: 10.1002/hyp.13937

Chen, F., Zhang, M., Wang, S., Ma, Q., Zhu, X., and Dong, L. (2015). Relationship between sub-cloud secondary evaporation and stable isotopes in precipitation of Lanzhou and surrounding area. *Quat. Int.* 380-381, 68–74. doi: 10.1016/J.QUAINT.2014.12.051

Eissa, M. A., Mahmoud, H. H., Shouakar-Stash, O., El-Shiekh, A., and Parker, B. (2016). Geophysical and geochemical studies to delineate seawater intrusion in Bagoush area, northwestern coast, Egypt. *J. African Earth Sci.* 121, 365–381. doi: 10.1016/j.jafrearsci.2016.05.031

Eissa, M., Shawky, H., Samy, A., Khalil, M., and El Malky, M. (2018). Geochemical and isotopic evidence of groundwater salinization processes in El Dabaa area, northwestern coast. *Egypt. Geosci.* 8:392. doi: 10.3390/geosciences8110392

Gallart, F., Valiente, M., Llorens, P., Cayuela, C., Sprenger, M., and Latron, J. (2020a). Investigating young water fractions in a small Mediterranean mountain catchment: both precipitation forcing and sampling frequency matter. *Hydrol. Process.* 34, 3618–3634. doi: 10.1002/hyp.13806

Gallart, F., Von Freyberg, J., Valiente, M., Kirchner, J. W., Llorens, P., and Latron, J. (2020b). Technical note: an improved discharge sensitivity metric for young water fractions. *Hydrol. Earth Syst. Sci.* 24, 1101–1107. doi: 10.5194/hess-24-1101-2020

Gentile, A., Canone, D., Ceperley, N., Gisolo, D., Previati, M., Zuecco, G., et al. (2022). What drives Fyw variations with elevation in alpine catchments? *EGUsphere* 2022, 1–28. doi: 10.5194/egusphere-2022-921

Jasechko, S., Kirchner, J. W., Welker, J. M., and McDonnell, J. J. (2016). Substantial proportion of global streamflow less than three months old. *Nat. Geosci.* 9, 126–129. doi: 10.1038/ngeo2636

Kirchner, J. W. (2016). Aggregation in environmental systems-part 1: seasonal tracer cycles quantify young water fractions, but not mean transit times, in spatially heterogeneous catchments. *Hydrol. Earth Syst. Sci.* 20, 279–297. doi: 10.5194/hess-20-279-2016

Laonamsai, J., Ichiyanagi, K., Kamdee, K., Putthividhya, A., and Tanoue, M. (2021). Spatial and temporal distributions of stable isotopes in precipitation over Thailand. *Hydrol. Process.* 35:e13995. doi: 10.1002/hyp.13995

Laonamsai, J., Ichiyanagi, K., Patsinghasanee, S., Kamdee, K., and Tomun, N. (2022). Application of stable isotopic compositions of rainfall runoff for evaporation estimation in Thailand Mekong River basin. *Water* 14:2803. doi: 10.3390/w14182803

McGuire, K. J., and McDonnell, J. J. (2006). A review and evaluation of catchment transit time modeling. *J. Hydrol.* 330, 543–563. doi: 10.1016/j.jhydrol.2006.04.020

Stockinger, M. P., Reemt Bogena, H., Lücke, A., Stumpp, C., and Vereecken, H. (2019). Time variability and uncertainty in the fraction of young water in a small headwater catchment. *Hydrol. Earth Syst. Sci.* 23, 4333–4347. doi: 10.5194/hess-23-4333-2019

Reckerth, A., Stichler, W., Schmidt, A., and Stumpp, C. (2017). Long-term data set analysis of stable isotopic composition in German rivers. *J. Hydrol.* 552, 718–731. doi: 10.1016/j.jhydrol.2017.07.022

Schmieder, J., Seeger, S., Weiler, M., and Strasser, U. (2019). 'Teflon Basin' or not? A high-elevation catchment transit time modeling approach. *Hydrology* 6:92. doi: 10.3390/hydrology6040092

Song, C., Wang, G., Liu, G., Mao, T., Sun, X., and Chen, X. (2017). Stable isotope variations of precipitation and streamflow reveal the young water fraction of a permafrost watershed. *Hydrol. Process.* 31, 935–947. doi: 10.1002/hyp.11077

Sprenger, M., Stumpp, C., Weiler, M., Aeschbach, W., Allen, S. T., Benettin, P., et al. (2019). The demographics of water: a review of water ages in the critical zone. *Rev. Geophys.* 57, 800–834. doi: 10.1029/2018RG000633

von Freyberg, J., Allen, S. T., Seeger, S., Weiler, M., and Kirchner, J. W. (2018). Sensitivity of young water fractions to hydro-climatic forcing and landscape properties across 22 Swiss catchments. *Hydrol. Earth Syst. Sci.* 22, 3841–3861. doi: 10.5194/hess-22-3841-2018

von Freyberg, J., Studer, B., and Kirchner, J. W. (2017). A lab in the field: high-frequency analysis of water quality and stable isotopes in stream water and precipitation. *Hydrol. Earth Syst. Sci.* 21, 1721–1739. doi: 10.5194/hess-21-1721-2017

Wang, T., and Chen, J. (2020). Long-term trend of precipitation stable isotopic compositions under global warming conditions. *J. Radioanal. Nucl. Chem.* 325, 557–565. doi: 10.1007/s10967-020-07246-x

Wang, Z., Guo, X., Kuang, Y., Chen, Q., Luo, M., and Zhou, H. (2022). Recharge sources and hydrogeochemical evolution of groundwater in a heterogeneous karst water system in Hubei Province, Central China. *Appl. Geochem.* 136:105165. doi: 10.1016/j.apgeochem.2021.105165

Wilusz, D. C., Harman, C. J., and Ball, W. P. (2017). Sensitivity of catchment transit times to rainfall variability under present and future climates. *Water Resour. Res.* 53, 10231–10256. doi: 10.1002/2017WR020894

Xia, C., Liu, G., Zhou, J., Meng, Y., Chen, K., Gu, P., et al. (2021). Revealing the impact of water conservancy projects and urbanization on hydrological cycle based on the distribution of hydrogen and oxygen isotopes in water. *Environ. Sci. Pollut. Res.* 28, 40160–40177. doi: 10.1007/s11356-020-11647-6

Zuecco, G., Carturan, L., De Blasi, F., Seppi, R., Zanoner, T., Penna, D., et al. (2019). Understanding hydrological processes in glacierized catchments: evidence and implications of highly variable isotopic and electrical conductivity data. *Hydrol. Process.* 33, 816–832. doi: 10.1002/hyp.13366

frontiers | Frontiers in Environmental Science

TYPE Methods
PUBLISHED 21 April 2023
DOI 10.3389/fenvs.2023.1177891

OPEN ACCESS

EDITED BY
Long Yan,
Central South University, China

REVIEWED BY
Yahui Guo,
Beijing Normal University, China
Joao Paulo Moura,
University of Trás-os-Montes and Alto Douro, Portugal

*CORRESPONDENCE
Jiping Liu,
liujp@casm.ac.cn

RECEIVED 02 March 2023
ACCEPTED 14 April 2023
PUBLISHED 21 April 2023

CITATION
Liu M, Liu J, Xu S, Chen C, Bao S, Wang Z and Du J (2023), 3DCNN landslide susceptibility considering spatial-factor features.
Front. Environ. Sci. 11:1177891.
doi: 10.3389/fenvs.2023.1177891

3DCNN landslide susceptibility considering spatial-factor features

Mengmeng Liu[1,2], Jiping Liu[1,2]*, Shenghua Xu[1,2], Cai Chen[3], Shuai Bao[1,2], Zhuolu Wang[1,2] and Jun Du[4]

[1]College of Geomatics and Geographic Sciences, Liaoning Technical University, Fuxin, China, [2]Chinese Academy of Surveying and Mapping, Beijing, China, [3]School of Geomatics and Urban Spatial Informatics, Beijing University of Civil Engineering and Architecture, Beijing, China, [4]Key Laboratory of Remote Sensing and Geographic Information System of Henan Province, Institute of Geog-raphy, Henan Academy of Sciences, Zhengzhou, China

Effective landslide disaster risk management contributes to sustainable development. A useful method for emergency management and landslide avoidance is Landslide Susceptibility Mapping (LSM). The statistical landslide susceptibility prediction model based on slope unit ignores the re-lationship between landslide triggering factors and spatial characteristics. It disregards the influence of adjacent image elements around the slope-unit element. Therefore, this paper proposes a hardwired kernels-3DCNN approach to LSMs considering spatial-factor features. This method effectively solved the problem of low dimensionality of 3D convolution in the hazard factor layer by combining Prewitt operators to enhance the generation of multi-level 3D cube input data sets. The susceptibility value of the target area was then calculated using a 3D convolution to extract spatial and multi-factor features between them. A geospatial dataset of 402 landslides in Xiangxi Tujia and Miao Autonomous Prefecture, Hunan Province, China, was created for this study. Nine landslide trigger factors, including topography and geomorphology, stratigraphic lithology, rainfall, and human influences, were employed in the LSM. The research area's pixel points' landslide probabilities were then estimated by the training model, yielding the sensitivity maps. According to the results of this study, the 3DCNN model performs better when spatial information are included and trigger variables are taken into account, as shown by the high values of the area under the receiver operating characteristic curve (AUC) and other quantitative metrics. The proposed model outperforms CNN and SVM in AUC by 4.3% and 5.9%, respectively. Thus, the 3DCNN model, with the addition of spatial attributes, effectively improves the prediction accuracy of LSM. At the same time, this paper found that the model performance of the proposed method is related to the actual space size of the landslide body by comparing the impact of input data of different scales on the proposed method.

KEYWORDS

3DCNN, spatial-factor features, landslide susceptibility, trigger factos, scale comparison

1 Introduction

Geological disasters have constantly threatened human life and properties and caused damage to the ecological environment, which seriously restricts the sustainable development of human society (Xu et al., 2020). In China, 4,772 geological disasters occurred in 2021, with 3.2 billion yuan worth of direct economic damage, including 2,335 landslides, accounting for 49% of all geological disasters (Ministry of Natural Resources of the People's Republic of China, 2021). As a result, the monitoring and early warning of landslide disasters has taken center stage in geological disaster prevention and risk mitigation. Especially in recent years, due to environmental and climate changes, the frequency and intensity of landslide disasters have increased rapidly (Liu., 2020). Therefore, quick and accurate analysis and evaluation of Landslide Susceptibility Mapping (LSM) and identification of high susceptibility areas are critical for effectively preventing and managing geological disasters caused by landslides.

The analysis of landslide susceptibility based on big geospatial data quickly inverts the regional landslide risk level by constructing the relationship between landslide hazard points and trigger factors. There are two main categories of landslide susceptibility models: those based on statistical analysis and those based on machine learning (ML) methods. Statistical analysis methods include the information quantity method (Wang et al., 2017), coefficient of determination method, etc. (LUO et al., 2021; Zhao et al., 2021). ML methods mainly include logistic regression (Sun et al., 2021), artificial neural network (Bragagnolo et al., 2020), random forest (Gao and Ding, 2022) and support vector machine (Nhu et al., 2020; Balogun et al., 2021; Wei et al., 2022a; Sajadi et al., 2022), etc. The ML methods have a higher accuracy in landslide susceptibility evaluation than the statistical analysis method. Furthermore, the ML methods can deal with the non-linear correlation between landslide trigger factors and landslide disaster points and avoid the difficulty of obtaining model parameters (Zhu et al., 2017).

The ML methods require constructing a data format that converts the original data of landslide trigger factors into slope units suitable for input (Xu et al., 2020; Liu and Liang, 2022). According to the first law of geography, there is a correlation between any location, and that correlation gradually decreases with distance (Tobler, 1970). Therefore, as a regional natural disaster closely affected by the surrounding environment, landslide disasters only take points or landslide units as the research object, ignoring the correlation with the surrounding geographical space units (Wu et al., 2015; Zhu et al., 2019). Therefore, it is of practical significance to consider how to combine spatial features with improving the accuracy of landslide risk assessment. Some researchers have noticed the influence characteristics of spatial features on LSM. Hong et al. divided the research focus area into two smaller areas according to the Shannon entropy equation, and the prediction accuracy of the regression model increased by 10% (Hong et al., 2017). Huang et al. found that the landslide susceptibility index (LSI) distribution was affected by different landslide boundary manifestations (Huang et al., 2022). Concurrently, Li et al. significantly increased the value of the Receiver Operating Characteristic (ROC) of the LSM. The slope unit's landslide susceptibility value is determined by combining the estimated likelihood of a landslide occurring (spatial probability) with the anticipated area of the slope units where a landslide may occur (Li and Lan, 2020). The structure of the convolutional neural network (CNN) is inspired by the perception of spatial features in the biological visual system. It can identify objects with specific spatial features by using convolutional and pooling layers (Liu et al., 2022). Wang et al. revealed that by rebuilding the input data and confirming the efficacy of the CNN model for spatial feature extraction, they have turned the landslide trigger factors into 2-dimensional and 3-dimensional data. According to Yang et al., the CNN model performs better than the ML model in predicting LSM, and the suggested model produces the most precise and smooth LSM (Yang et al., 2022). Wei et al. used a depthwise separable convolution to extract spatial features and spatial pyramid pooling to extract features at different scales, fusing them into machine learning classifiers to train LSM (Wei et al., 2022b).

The above research on CNN models verifies the influence of spatial features on LSM. However, these studies are limited by the spatial constraints of the CNN model's two-dimensional convolution, which can only take into account the spatial correlation of a single trigger factor but cannot combine the correlation between trigger factors (Wang et al., 2019). The three-dimensional convolution kernel neural network (3DCNN) model can improve image classification accuracy by extracting deep features in layers and has been effectively employed in action recognition and hyperspectral image classification (Li et al., 2017; Shi and Pun, 2017; Li et al., 2022). The intuitive idea is to use the landslide trigger factors and spatial information to design classifiers, incorporating converting spatial structures into slope-unit classifiers. Spatial information contains valuable distinguishing details pertaining to the shape and size of distinct structures, which, when utilized appropriately, can result in more precise classification maps (Fauvel et al., 2013). Essentially, the spatial dependence is initially derived through a variety of spatial filters, such as directional gradients, morphological profiles, and entropies (Plaza et al., 2004; Ghamisi et al., 2015). To perform pixel-level landslide susceptibility classification, these altered spatial features are paired with landslide triggers and historical landslide spatial locations.

This paper proposed the 3DCNN landslide susceptibility mapping model that integrated the landslide trigger factors and spatial features. First, we reconstruct spatial features and the landslide trigger factors as three-dimensional input data. Next, we apply a 3D convolution to explore the relationship between the spatial features and the trigger factors. Ultimately, the 3DCNN model, once trained, will predict landslide susceptibility. Because the CNN model shows better spatial feature extraction performance in the study of LSM, the three-dimensional convolution kernel can perform the correlation calculation between the landslide trigger factors (Ghorbanzadeh et al., 2019; Liu et al., 2022). A case study in Xiangxi Tujia and Miao Autonomous Prefecture, China was used to exemplify the practicality of the proposed model. For comparison with the suggested method, the CNN and SVM model were utilized as reference models. The various models were evaluated and compared using performance criteria, such as statistical indicators and receiver operating characteristic curves (ROC). At the same time, this paper also examined the impact of input data spatial scale on the calculation of LSM using the 3DCNN model.

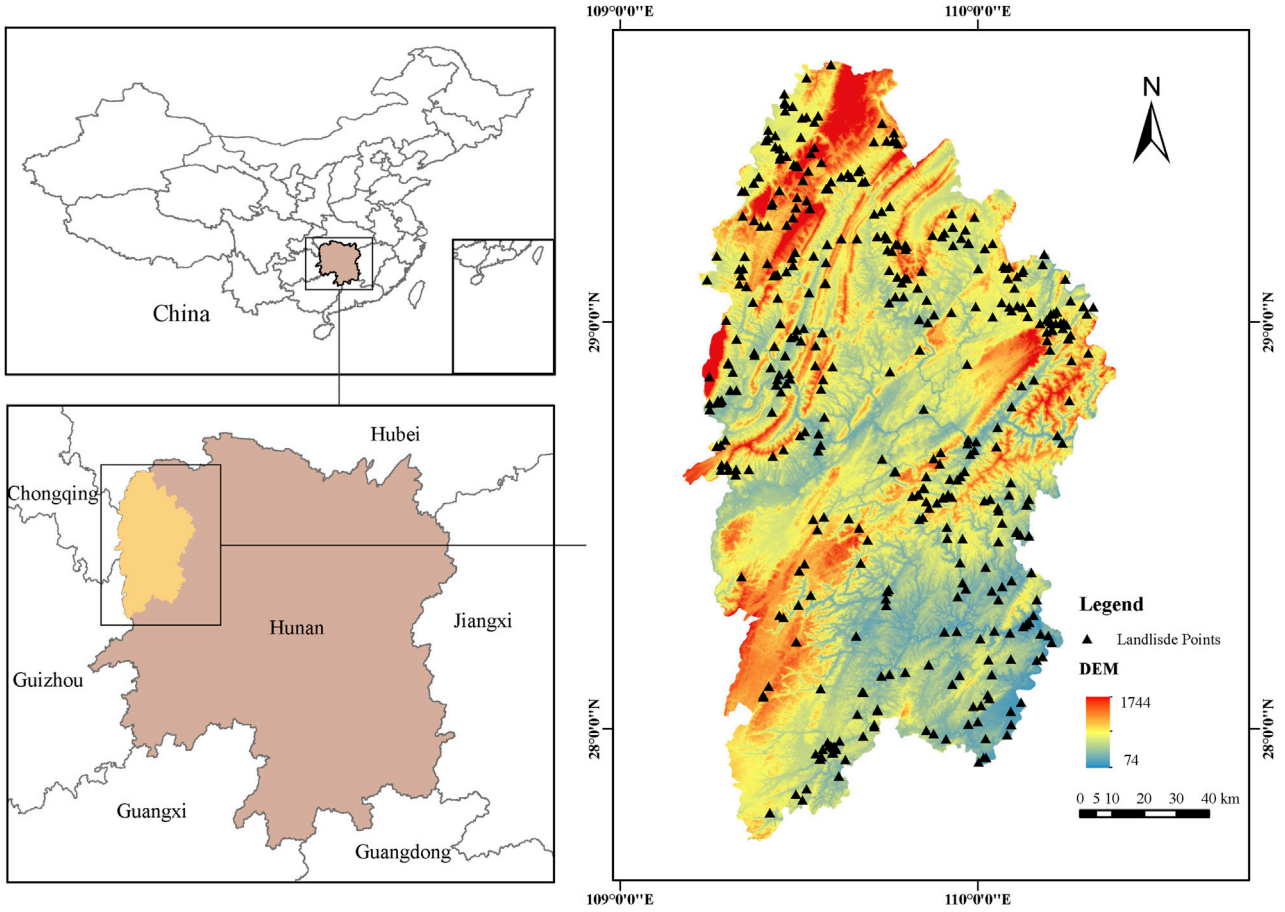

FIGURE 1
The study area and historical landslide hazard points.

2 Study area and data sources

2.1 Study area

The Xiangxi Tujia and Miao Autonomous Prefecture is situated in the northwest of Hunan Province, with coordinates of 109°10′-110°22.5′E and 27°44.5′-29°38′N (Figure 1). It is located in the intermediary region between the Wuling Mountains and the Yunnan-Guizhou Plateau, with small basins and valleys along the rivers between the mountains. The central vein of the Wuling Mountains stretches in the middle, with a northeast-southwest trend. In comparison, the southeastern part belongs to the low hilly area of the Yuan River valley. Wushui and Youshui, tributaries of the Yuan River, are the main rivers. The total area of the state is 15,462 km^2. The terrain slopes from northwest to southeast, with an average altitude of 800–1,200 m. The east and west are mountainous areas of low hills with an average altitude of 200–500 m. Streams and rivers crisscross the area, and there are many alluvial plains on both banks. The general outline of the geomorphological form is dominated by mountain plains, with hills and small plains, and the arc-shaped mountainous landform is prominent to the north and west. The annual precipitation is 1,300–1,500 mm and is concentrated during spring and summer. Xiangxi Prefecture mainly experiences geological hazards such as landslides, followed by mudslides and sinkholes. These are small and medium in scale, mainly distributed in areas with high rainfall intensity and vigorous human engineering activities. During this period of heavy rainfall, a high incidence of geological hazards is eminent .

2.2 Data sources

The information regarding landslide occurrences and geological lithology in Xiangxi Prefecture was collected from the Xiangxi Guoditong integrated spatial and temporal service platform. The data structure is in geographic vector format, including 402 landslide points and 356 geologic lithology units. The Digital Elevation Model (DEM) data were obtained from “ASTERGDEM DEM 30 m resolution digital elevation data” (https://search.earthdata.nasa.gov/search). NDVI data from “Landsat8OLI_TIRS Satellite Digital Product Data at 30 m Spatial Resolution” from the 2018 Geospatial Data Cloud (https://search.earthdata.nasa.gov/search). The annual precipitation data were acquired from “Global Precipitation Measurement Data level 3" (https://pmm.

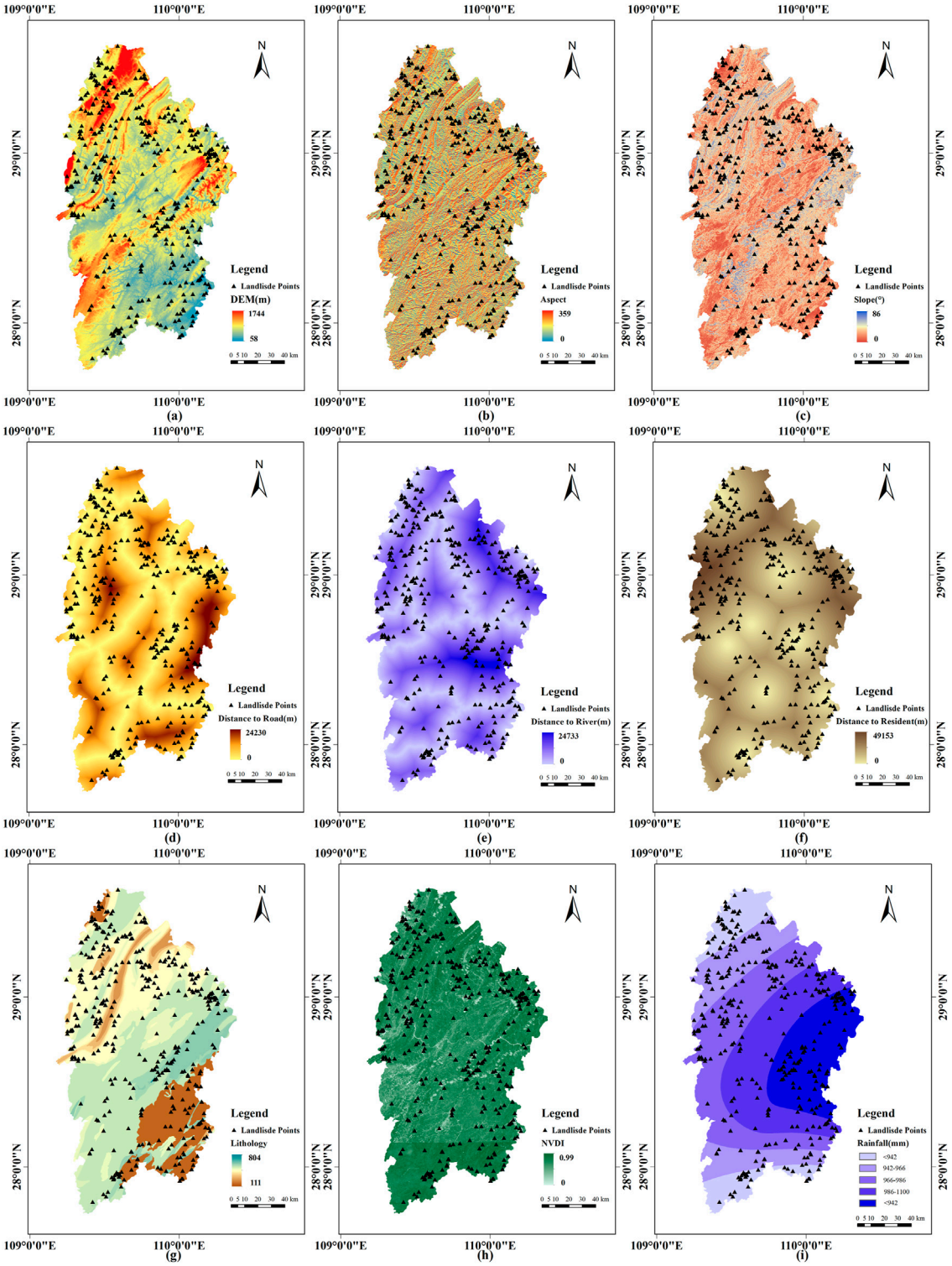

FIGURE 2
Diagrams of the landslide triggering factors.

nasa.gov/precipitation -measurement-missions) of NASA for the year 2018, with annual precipitation. The unit is 1 mm, and the data with road, river and distance data with residential areas are from the first national geographic census re-sults data. For the convenience of statistics and analysis, combined with the resolution of DEM and remote sensing image data, The study area in Xiangxi Prefecture was par-titioned based on a raster resolution of 30 m × 30 m with a total of 31,374,840 raster units.

2.3 Trigger factors

The reasons behind landslide disasters are complex. The influencing factors are mainly divided into two classes: internal pregnancy factor (terrain landform, geological structure, transportation water system, etc.) and external induced factors (rainfall, earthquake, human engineering activities, etc.). LinJeng-Wen et al. analyzed the correlation between the factors, and the study's results proved that the distinguishing factors are independent and can be used as factor variables (Li et al., 2022). This paper chooses 9 factors related to landslide disasters, including DEM, slope, aspect, lithology, distance to faults, distance to roads, rainfall, distance to rivers, and normalized difference vegetation index (NDVI), as illustrated in Supplementary Table S1 and Figure 2. The selection of these factors was based on the reliability of model prediction and the ease of calculating the three-dimensional convolution.

3 Methodology

Figure 3 illustrates the method flowchart used for LSM in this study. First, this paper prepared landslide point data and landslide trigger factors to construct training and validation sets. Second, the SVMmodels were trained using 2D data format while the CNN and 3DCNN was trained using 3D data format. Then, the ROC curves were used for quantitative evaluation of the prediction results obtained by the three methods. Finally, the landslide susceptibility mapping is carried out with three trained models.

3.1 SVM model

The SVM model is a binary classifier based on statistical learning theory that finds the maximum margin hyperplane. This model is effective in addressing various classification problems (Cherkassky and Yunqian, 2004). In the study of LSM, the j-th trigger factor of the i-th position in the layer is expressed as v_{ij}, $i\in\{1,2\ldots,n\}$, $j\in\{1,2\ldots,9\}$. Among them, the variable n represents the total number of samples, while j represents the number of categories of the landslide trigger factors. Then, the SVM model maps the input vector v into u and classifies it, using a non-linear mapping $\phi(v)$, to a high-dimensional feature space. as shown in Eq. 1.

$$\boldsymbol{f}(v) = \boldsymbol{w}\phi(v) + b \tag{1}$$

The regression function of SVM, denoted by $f(v)$, can be expressed as the inner product of a weight vector w and the input vector v, plus a bias term b. Alternatively, the optimization problem can be formulated with Lagrangian transformation and optimality constraints, allowing for the use of Eq. 2 to obtain $f(x)$ (Cremmer et al., 1983).

$$f(v) = \sum_{i=1}^{n}\left(a_i - a_i^*\right) \times K(v, v_i) + b \tag{2}$$

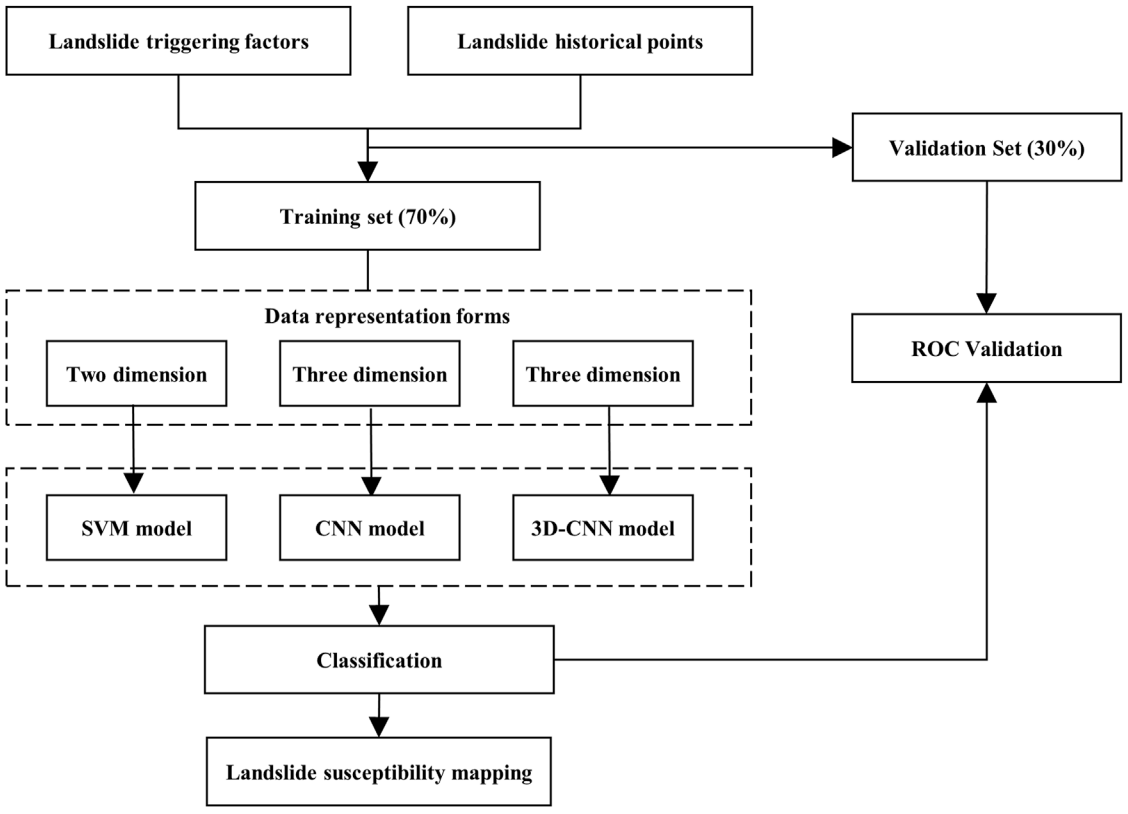

FIGURE 3
Flowchart of the present study.

where α_i and α_i^* are the Lagrange multipliers, K (v, v_i) is a kernel function. This article uses the RBF kernel (Bugmann, 1998).

3.2 CNN model

The CNN model requires two-dimensional images as input, and the slope-unit or landslide unit is not suitable for cooperation as the input of the CNN model (as shown in Figure 4 left part). In order to solve this problem, the original data needs to be reconstructed. As shown in Figure 4 right part, the proposed method expands outward from the centre of the landslide slope unit in each layer of the landslide trigger factors layer to obtain the spatial characteristics of the sample data (Li and Lan, 2020). After that, the multi-layer grid data is brought into the CNN model for training.

In the convolutional layers, the CNN model runs a 2D convolution kernel that collects features from a nearby neighborhood on feature maps from the previous layer. The result is then passed through a sigmoid function with an additive bias. The value of the unit at position (x, y) in the jth feature map in the ith layer is denoted as v_{ij}^{xy} and can be expressed as follows:

$$v_{ij}^{xy} = \tanh\left(b_{ij} + \sum_{m=0}^{P_i-1}\sum_{j=0}^{P_i-1}\sum_{j=0}^{p_i-1} w_j v_i\left(\frac{x+p}{r_i}\right)\right) \quad (3)$$

the expression for v_{ij}^{xy}, the value of the unit at position (x, y) in the jth feature map in the ith layer in the CNN model, is given by the hyperbolic tangent function tanh (), where b_{ij} is the bias for this feature map, m indexes over the set of feature maps in the (i-1)th layer connected to the current feature map, w_{ijk}^{pq} is the value at the position (p, q) of the kernel connected to the kth feature map, and Q_i and P_i are the width and height of the kernel, respectively.

The subsampling layers reduce the feature map resolution by pooling over the local neighbourhood in the previous layer, which increases the invariance to input distortions. To construct the CNN architecture, multiple convolution layers and subsampling are stacked alternately. The CNN parameters, including the bias b_{ij} and the kernel weight w, are typically trained using supervised or unsupervised approaches. The backpropagation algorithm is employed to optimize all parameters in the CNN layer, with the objective of minimizing the loss function (LeCun et al., 1998). The formula is defined as follows:

$$Loss = -\frac{1}{m}\sum_{i=1}^{m}\left[l_i \log\left(l_i'\right) + (1-l_i)\log\left(1-l_i'\right)\right] \quad (4)$$

The CNN model architecture, as shown in Figure 5, involves optimizing all parameters in the CNN layer using the backpropagation algorithm and minimizing the loss function, where the two variables l_i and l_i' represent the actual label and tag of the i-th input sample, respectively. The parameters are updated iteratively until the loss value reaches convergence.

3.3 3DCNN model

The CNN model applies 2D convolution kernels solely to the 2D feature maps, enabling the computation of features solely from the spatial dimensions of the single channel. Convolutional stages of CNNs must perform 3D data augmentation in order to simultaneously capture important features contained in several contiguous layers of 3D feature data. By convolving a 3D kernel into the cube created by stacking several trigger factors together, this method computes features from both the spatial and trigger factor

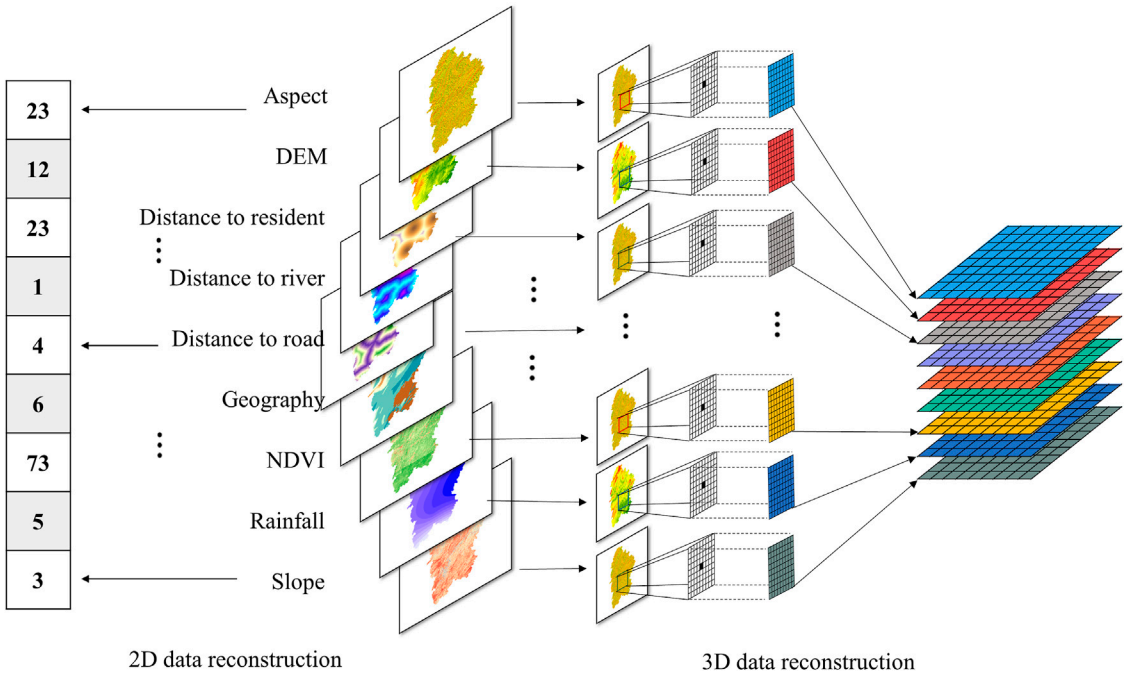

FIGURE 4
Reconstruction of two-dimensional input data.

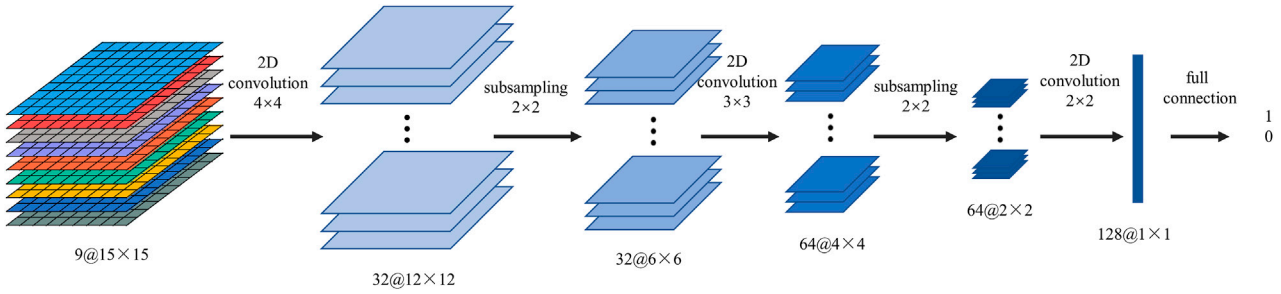

FIGURE 5
The structure of the CNN model.

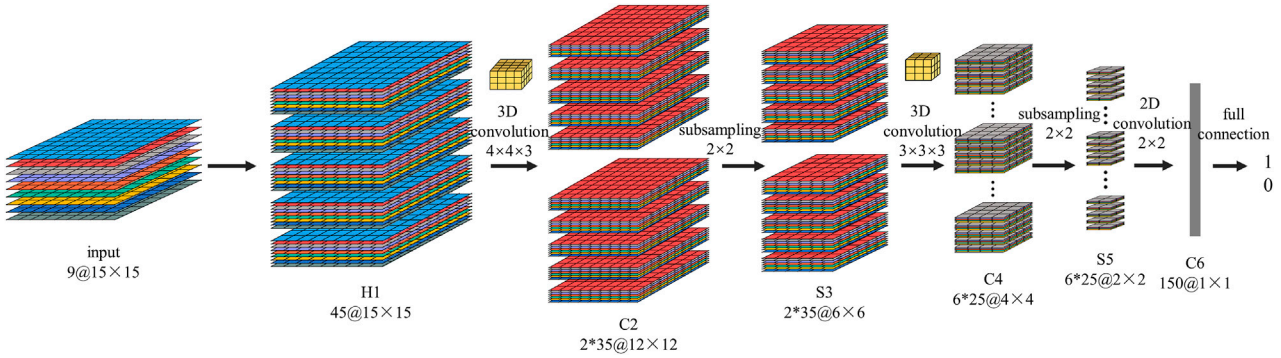

FIGURE 6
The architecture of the 3D augmented convolution kernel neural network.

dimensions. As a result of their connections to various trigger factors in the former layer, the feature maps in the cnn model are able to capture the pertinent features between landslide trigger factors. The value of the unit at position (x, y, z) on the j-th feature map in the i-th layer can be expressed as follows:

$$v_{ij}^{xyz} = tanh\left(b_{ij} + \sum_{m} \sum_{p=0}^{P_i-1} \sum_{q=0}^{Q_i-1} \sum_{r=0}^{R_i-1} w_{ijm}^{pqr} v_{(i-1)m}^{(x+p)(y+q)(z+r)} \right) \quad (5)$$

where R_i is the size of the 3D kernel along the landslide trigger factors dimension $w_{ijm}{}^{pqr}$ and is the (p, q, r)-th value connected to the m-th feature map in the previous layer. Here, the value at position (x, y, z) on the jth feature map in the ith layer is determined by the (p, q, r)-th value connected to the m-th feature map in the previous layer, represented by $w_{ijm}{}^{pqr}$. The size of the 3D kernel along the landslide trigger factors dimension is denoted by R_i. Figure 6 depicts the architecture of the 3D convolutional kernel neural network.

The 3D cube that was recreated using the technique in Figure 4 is also used as input data for the 3DCNN model in the architecture depicted in Figure 6. We initially use a set of hardwired kernels to generate various information channels from the input frame, like H1 in Figure 6, in order to improve the feature amount in the vertical direction. The four directional Prewitt operators used by the feature hardwired kernel provide 45 feature maps in the second layer that are divided into five separate channels known as raw, horizontal gradient, vertical gradient, and two diagonal gradients. The attribute values of the input frames from the nine landslide trigger factors are contained in the original channel. By calculating the gradients along the horizontal, vertical, and two diagonal gradients on the nine landslide hazard factors, respectively, through the Prewitt operator, the feature maps in the horizontal gradient, vertical gradient, and two diagonal gradient channels are generated. Our prior knowledge of the characteristics is encoded in this hardwired layer, and this method typically provides greater performance than random initialization (Ji et al., 2012).

Then, we independently perform 3D convolutions to each of the 5 channels with a kernel size of 4 × 4×3 (3 in the trigger factor dimension, 4 × 4 in the spatial dimension). Using two sets of various solutions at each site, the number of feature maps is increased, yielding two sets of extracted features in the C2 layer, each with 35 feature maps. There are 490 trainable parameters in this layer. Each of the feature maps in the C2 layer is subjected to 2 × 2 subsampling in the subsequent subsampling layer S3, resulting in the same amount of feature maps with lower spatial resolution. This layer contains 140 trainable parameters. Applying 3D convolution with a kernel size of 3 × 3×3 on each of the five channels in the two sets of feature maps individually yields the next convolution layer, C4. We perform three convolutions with various kernels at each position to increase the number of feature layers, resulting in six separate sets of feature maps in the C4 layer, each of which has 25 feature maps. There are 840 trainable parameters in this layer. Each feature map in the C4 layer

is subjected to 2 × 2 subsampling to produce the same amount of feature maps with lower spatial resolution in the subsequent layer S5. This layer contains 300 trainable parameters. We only do convolution in the spatial dimension at this layer because the temporal dimension's size is already quite tiny at this point. The size of the output feature maps is reduced to 1 × 1 due to the convolution kernel size 2 × 2. All of the 150 1×1-sized feature maps in the C6 layer is connected to all 150 feature maps in the S5 layer.

The five input frames have been transformed into a 150D feature vector that captures the motion information in the input frames using many layers of convolution and subsampling. The number of units in the output layer equals the number of actions. The 150 units in the C6 layer are all fully connected to each unit. In this design, the 150D feature vector is subjected to a linear classifier in order to classify actions. The number of trainable parameters at the output layer for an action recognition issue with two classes (one class is a landslide, and the other is non-landslide) is 300.

4 Experimental results

4.1 Factors analysis and models construction

Based on the study area's actual circumstances and an examination of topography, geomorphology, stratigraphic lithology, geological structure, rainfall, surface water, and human variables influencing the occurrence of landslides (Lin et al., 2019), as shown in Supplementary Table S2 the selected landslide trigger factors were tested for multiple covariances by stepwise regression method (Jiping et al., 2022). The correlation between each characteristic factor was tested by tolerance and variance inflation factor (VIF) is shown in Supplementary Table S2 (Kalantar et al., 2019). The findings demonstrate that the identified landslide trigger parameters have a tolerance greater than 0.1, and the variance inflation factor is less than 10, which indicates that each trigger factor has a low degree of co-linearity and good independence.

To create the model's architecture, 804 samples (402 positive and 402 negative) from the entire dataset were used. Using these samples, databases for the Xiangxi Prefecture were created based on the number and distribution of landslide points. Next they were randomly divided into validation groups, which made up 30% of the total, and training groups, which comprised 70% of the total. Finally, each model was tested using both the validation dataset and the complete dataset. The parameters for the CNN and 3DCNN models are randomly initialized, and they are trained via online error backpropagation. The learn-ing rate was set to 0.0005 for the Xiangxi dataset, batch size, dropout rate, and epoch were set to 32, 0.5, and 150 in order to find the ideal hyperparameter.

Also, the weights were updated using SGD as the optimizer, and mean square error (MSE) was chosen as the loss function. The activation function was set to Tanh. The PSO approach is used to identify the ideal parameters for the SVM model by the penalty coefficient C and the RBF kernel function gamma (Fathi and Montazer, 2013). Our tests were run on Windows 10, 64-bit, an Intel i7-10700K processor running at 3.8 GHz with eight cores, 32 GB of RAM, and an NVIDIA GeForce RTX 2060Ti GPU (8 GB).

4.2 Validation and comparison methods

The evaluation of the three models' effects in this paper was undertaken using the "ReceiverOperatingCharacteristic" curve for validation (Park and Kim, 2019). It is the relationship between specificity and sensitivity; it s a g. The logic behind this is that if a test is non-diagnostic, it is just as likely to produce a true positive or a false positive. Specificity, actual positive rate, true positive rate, and false positive rate all rise along with diagnostic competence. The accuracy of the evaluation model is shown by the area under the ROC curve (Area Under Curve, AUC). The evaluation model's prediction effect is stronger the closer the area value is near 1. The area value, on the other hand, has no application value when it equals 0.5. Figure 7 displays the ROC curves and AUC values for the two models.

The 3DCNN model, CNN model, and SVM model all have AUC values of 0.835, 0.816, and 0.794, respectively, as shown in Figure 7. The three models may all have a higher prediction of LSM since the AUC regions of their ROC curves are all greater than 0.5. According to the specifics, the 3DCNN model's ROC curve is situated in the upper-most left corner, which means that its AUC area is the largest and the point in the distance is farther from the reference line, indicating that the 3DCNN model is, in some ways, superior to the other two models. In other words, the 3DCNN of LSM model in Xiangxi Prefecture is more precise and reliable.

4.3 Landslide susceptibility mapping

To create the LSM for Xiangxi Tujia and Miao Autonomous Prefecture, this study used the SVM, CNN, and 3DCNN models

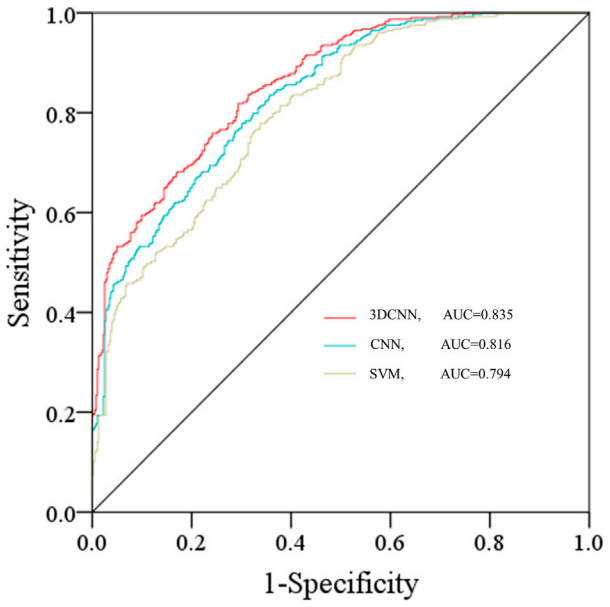

FIGURE 7
The ROC curve of three models with the 15 × 15 size of input data.

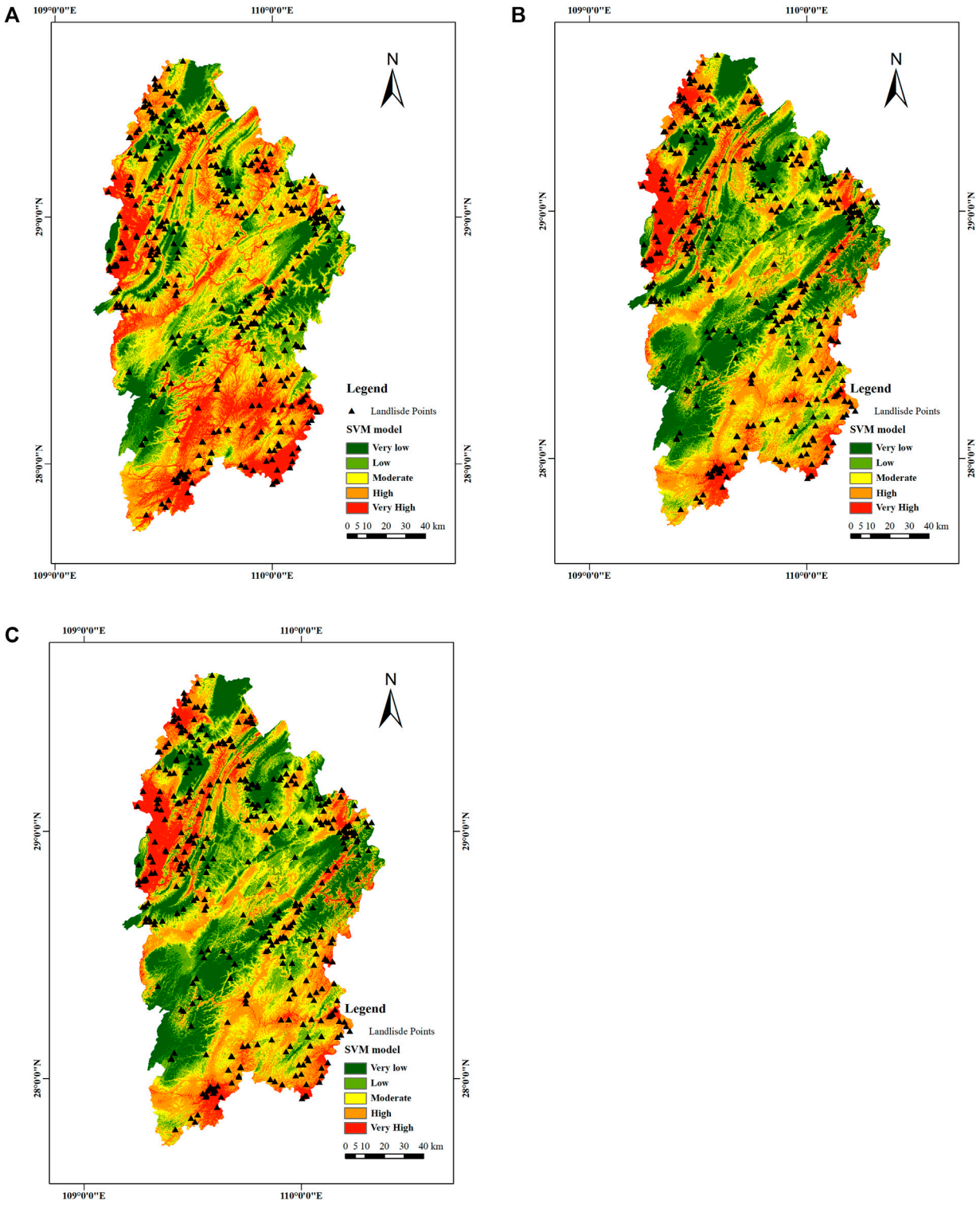

FIGURE 8
Evaluation results of landslide susceptibility mapping. **(A)** LSM of the SVM model; **(B)** LSM of the CNN model; **(C)** LSM of the 3DCNN model.

(Figure 8). For the purpose of computing the landslide susceptibility index, all pixels within the study area were supplied into these trained models (LSI). The LSI was then separated into five susceptibility levels using ArcMap10.6's natural break approach: very low (VLS), low (LS), moderate (MS), high (HS), and very high (VHS). The landslide susceptibility zones, which show the proportion of each susceptibility level to the entire study region, were employed to qualitatively examine the LSM.

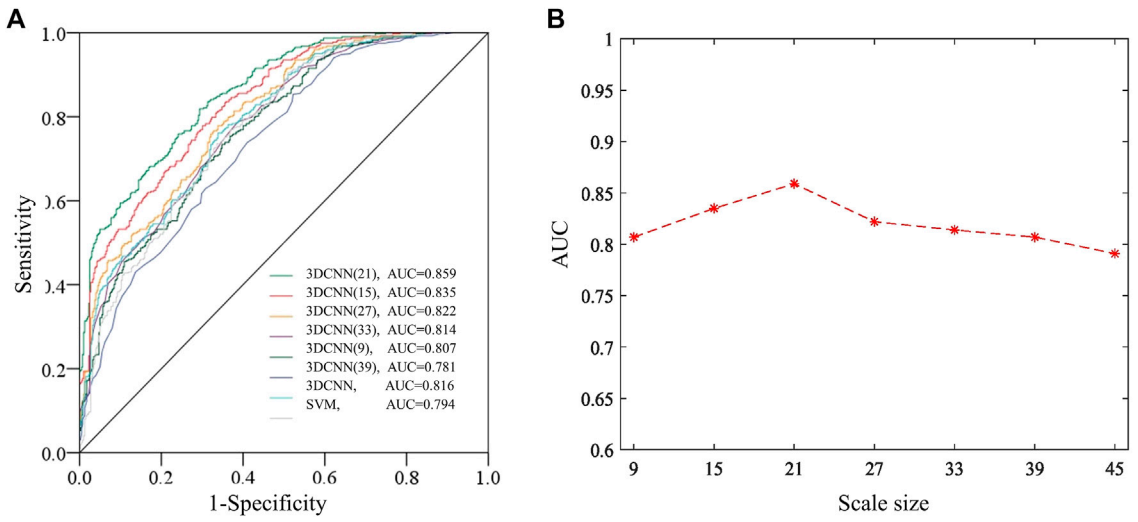

FIGURE 9
The ROC curve. **(A)** The ROC curve with different scale sizes of input data; **(B)** The 3DCNN model's AUC and input data's spatial resolution connection.

As shown in Figure 8, the VHS zones are mostly found in Xiangxi Prefecture's southeast and northwest. Due to the long gullies, steep slopes, complex geological structures, and two major rivers running through the area, coupled with the increasing human engineering activities (such as road projects), the area is highly susceptible to landslide disasters.

The analysis and counting of non-landslide and landslide hazard points in the training samples was done using ArcMap. After that, we determine what percentages of landslide points and non-landslide points are located in each of the five prone zones.

Supplementary Table S3 shows that the majority of landslide hazard spots are anticipated to have high and extremely high susceptibility zones. A relative association between historical landslide events and susceptibility areas is demonstrated by the fact that few landslides occur in places with relatively low susceptibility. Furthermore, more than 80% of historical landslide events for all methods were located in high-sensitivity areas, confirming the plausibility of landslide susceptibility mapping. The percentage of hazard points in each zone likewise gradually grew according to the 3DCNN, CNN, and SVM models. The highest percentages were 47.51%, 39.30%, and 30.85% in the high-prone area. Hence, the proportion of the number of disaster points is more significant than that of other districts, and the proportions are 47.51%, 39.30%, and 35.57%. We found that all three model methods can predict the susceptibility of landslide hazards very well. Compared with the CNN and SVM models, the 3DCNN model has higher accuracy.

4.4 Scale size and model performance

In order to research how the spatial scale of the data input affects the LSM using the 3DCNN model, we compared the input data structures at five different spatial scales of 9 × 9, 15 × 15, 21 × 21, 27 × 27, 33 × 33, and 39 × 39. Furthermore, we compared and analyzed the ROC curve of the corresponding 3DCNN model. In Figure 9, the experimental outcomes are displayed. The 3D CNN model's ROC curve varies depending on the input data scales. As the spatial scale increases, the AUC value of 3DCNN gradually increases. When the sample point range is expanded to 21 × 21, the AUC value reaches the maximum value of 0.859. The AUC value rapidly declines, reaching a minimum of 0.781, which is 0.078 lower than the highest AUC value and even worse than the performance of the CNN model and the SVM model, as the sample space size rises to 39 × 39. The above reasoning proves that scale does affect LSM performance, but this effect varies with size. A further comparative study of the relationship between area and scale in the landslide samples found that the average length and width of the landslide samples in Xiangxi Prefecture used in this paper are 281.5 m and 563.7 m, respectively, projected to a grid of 10 × 20 landslide units (Supplementary Table S4).

5 Discussions

LSM is essential for creating a thematic map that shows where and how likely landslides are to occur. A landslide list made up of landslide points and the association between landslide trigger variables is the basis of LSM. Landslides, as a regional geographic entity, are considered incomplete only in terms of points, with no spatial characteristics or correlation feature between the landslide trigger factors. This research aims to convert point landslide data into three-dimensional data by incorporating spatial and correlation features between landslide trigger factors. To do this, the fundamental module that we deployed was a convolutional neural network. In order to allow for synergy, we suggested a 3DCNN model that incorporates spatial and fators correlation features among landslide trigger components.

By reducing variation and bias in prior related studies, the hybrid model was considered to improve the ability to forecast land slides. In our tests, the proposed 3DCNN model performed better in terms of AUC than the other examined models. These

results met the hybrid model's expectations to some extent and can be considered promising. Meanwhile, the CNN-based models outperformed conventional machine learning models regarding overall performance (SVM). This is because the intricate design of CNN-based models enhances their capacity to collect representations of landslides at deep levels through convolution and pooling procedures.

Aside from that, the suggested 3DCNN technique beat the other two CNN-based models, as shown in Figure 8 and Figure 9. This makes sense because by extracting geographical data and correlation features between landslide trigger components from the land-slide inventory, the 3DCNN model improved landslide prediction accuracy. Using the suggested 3DCNN model, more representations linked to landslides were recovered from the limited datasets.

The contradiction between the complex structure and the scale landslide samples necessitates avoiding overfitting despite CNN's outstanding feature extraction capabilities. We plot ROC curves on training sets with varying scale sizes to further validate the models' fit. According to Figure 9 and Supplementary Table S4, 3DCNN has the maximum AUC value at a scale of 21 × 21, with a value of 0.859. The ROC curves also vary depending on the geographic scale of the data input. The model's predictive performance gradually declines as the spatial scale increases. When the size of the input data unit was compared to the actual length and width of the landslide (Supplementary Table S4), we discovered that the landslide is a regional target with a limited spatial scale. Other noise effects are amplified as the spatial scale is increased indefinitely. As a result, the model's accuracy in predicting landslide risk will decrease after reaching the maximum spatial characteristic gain. To summarise, the CNN landslide susceptibility model combined with spatial features should consider the sample's spatial scale.

The susceptibility maps can also show how plausible and reliable the models are. Figure 8 illustrates how the majority of landslides in the 3DCNN models occurred in the LSM's VH susceptibility zone. This indicates that the constructed models can accurately determine the likelihood of a landslide occurring and provide acceptable hazard mitigation methods to decision-makers, which is good news from the perspective of disaster mitigation. Additionally, scientists evaluate a susceptibility model's dependability using the Specificity and Sensitivity indices. By correctly categorizing non-landslide zones as stable slopes and maximizing land usage, highly accurate models can avoid financial losses. By precisely identifying landslide-prone locations, high-sensitivity value models can also offer safe mitigating advice. The suggested model in the current study outperformed other baseline models in the validation set in terms of specificity and sensitivity, highlighting the dependability of disaster mitigation and land use planning.

6 Conclusion

We conducted our research in the Hunan Province's Xiangxi Prefecture for this paper. Experiments show that the relationship between disaster-causing factors and spatial characteristics affects the LSM prediction model's accuracy. Under the same conditions as the SVM and CNN models, increasing the spatial characteristics of landslide hazard factors can improve LSM prediction accuracy. However, due to the model's complexity, the sample space scale limits this accuracy. The experimental results confirmed this hypothesis as well. The model performs best when the sample point range is expanded to 21 regions, i.e., when the input sample size covers the actual area of the landslide. Because the sample LSM based on points ignores the objective spatial attributes, expanding the factor or expanding the sample area can improve the LSM's prediction accuracy. However, due to data constraints, this paper only considers the impact of a scale change in 30 m resolution sample data on LSM prediction accuracy. It does not consider landslide hazard factors in different resolution scenarios, even if the optimal scale value varies. We intend to investigate this step further in our subsequent paper.

Data availability statement

The original contributions presented in the study are included in the article/Supplementary Material, further inquiries can be directed to the corresponding author.

Author contributions

CC, SB, and JD made a considerable contribution to the writing, design, data gathering, statistical analysis, and experimental planning. JL, SX, and JD all made major contributions to the interpretation of data and the intellectual revision of the text. All writers reviewed and approved the final version. The manuscript has been published with the consent of all authors who have read and approved it.

Funding

This research was funded by the National Key Research and Development Program of China (2022YFC3005705 and 2020YFC1511704).

Conflict of interest

The authors declare that the research was conducted in the absence of any commercial or financial relationships that could be construed as a potential conflict of interest.

Publisher's note

Supplementary material

The Supplementary Material for this article can be found online at: https://www.frontiersin.org/articles/10.3389/fenvs.2023.1177891/full#supplementary-material

References

Balogun, A.-L., Rezaie, F., Pham, Q. B., Gigović, L., Drobnjak, S., Aina, Y. A., et al. (2021). Spatial prediction of landslide susceptibility in western Serbia using hybrid support vector regression (SVR) with GWO, BAT and COA algorithms. *Geosci. Front.* 12 (3), 101104. doi:10.1016/j.gsf.2020.10.009

Bragagnolo, L., da Silva, R. V., and Grzybowski, J. M. V. (2020). Artificial neural network ensembles applied to the mapping of landslide susceptibility. *Catena* 184, 104240. doi:10.1016/j.catena.2019.104240

Bugmann, G. (1998). Normalized Gaussian radial basis function networks. *Neurocomputing* 20 (1–3), 97–110. doi:10.1016/s0925-2312(98)00027-7

Cherkassky, V., and Yunqian, M. (2004). Practical selection of SVM parameters and noise estimation for SVM regression. *Neural Netw.* 17 (1), 113–126. doi:10.1016/S0893-6080(03)00169-2

Cremmer, E., Ferrara, S., Girardello, L., and Van Proeyen, A. (1983). Yang-mills theories with local supersymmetry: Lagrangian, transformation laws and super-Higgs effect. *Nucl. Phys. B* 212 (3), 413–442. doi:10.1016/0550-3213(83)90679-X

Fathi, V., and Montazer, G. A. (2013). An improvement in RBF learning algorithm based on PSO for real time applications. *Neurocomputing* 111, 169–176. doi:10.1016/j.neucom.2012.12.024

Fauvel, M., Tarabalka, Y., Benediktsson, J. A., Chanussot, J., and Tilton, J. C. (2013). Advances in spectral-spatial classification of hyperspectral images. *Proc. IEEE* 101 (3), 652–675. doi:10.1109/jproc.2012.2197589

Gao, Z., and Ding, M. (2022). Application of convolutional neural network fused with machine learning modeling framework for geospatial comparative analysis of landslide susceptibility. *Nat. Hazards* 113, 833–858. doi:10.1007/s11069-022-05326-7

Ghamisi, P., Dalla Mura, M., and Benediktsson, J. A. (2015). A survey on spectral spatial classification techniques based on attribute profiles. *IEEE Trans. Geoscience Remote Sens.* 53 (5), 2335–2353. doi:10.1109/tgrs.2014.2358934

Ghorbanzadeh, O., Blaschke, T., Gholamnia, K., Raj Meena, S., Tiede, D., and Aryal, J. (2019). Evaluation of different machine learning methods and deep-learning convolutional neural networks for landslide detection. *Remote Sens.* 11 (2), 196. doi:10.3390/rs11020196

Hong, H., Pradhan, B., Sameen, M. I., Kalantar, B., Zhu, A., and Chen, W. (2017). Improving the accuracy of landslide susceptibility model using a novel region-partitioning approach. *Landslides* 15 (4), 753–772. doi:10.1007/s10346-017-0906-8

Huang, F., Yan, J., Fan, X., Yao, C., Huang, J., Chen, W., et al. (2022). Uncertainty pattern in landslide susceptibility prediction modelling: Effects of different landslide boundaries and spatial shape expressions. *Geosci. Front.* 13 (2), 101317. doi:10.1016/j.gsf.2021.101317

Ji, S., Xu, W., Yang, M., and Yu, K. (2012). 3D convolutional neural networks for human action recognition. *IEEE Trans. Pattern Analysis Mach. Intell.* 35 (1), 221–231. doi:10.1109/TPAMI.2012.59

Jiping, L., Enjie, L., Shenghua, X. U., Mengmeng, L., Wang, Y., Zhang, F., et al. (2022). Multi-kernel support vector machine considering sample optimization selection for analysis and evaluation of landslide disaster susceptibility. *Acta Geod. Cartogr. Sinica* 51 (10), 2034. doi:10.11947/j.AGCS.2022.20220326

Kalantar, B., Ueda, N., Lay, U. S., Al-Najjar, A. H. H., and Halin, A. A. (2019). "Conditioning factors determination for landslide susceptibility mapping using support vector machine learning," in IGARSS 2019 - 2019 IEEE International Geoscience and Remote Sensing Symposium, Yokohama, Japan, 28 July 2019 - 02 August 2019, 9626–9629. doi:10.1109/IGARSS.2019.8898340

LeCun, Y., Bottou, L., Bengio, Y., and Haffner, P. (1998). Gradient-based learning applied to document recognition. *Proc. IEEE* 86 (11), 2278–2324. doi:10.1109/5.726791

Li, L., and Lan, H. (2020). Integration of spatial probability and size in slope-unit-based landslide susceptibility assessment: A case study. *Int. J. Environ. Res. Public Health* 17 (21), 8055. doi:10.3390/ijerph17218055

Li, W., Chen, H., Liu, Q., Liu, H., Wang, Y., and Gui, G. (2022). Attention mechanism and depthwise separable convolution aided 3DCNN for hyperspectral remote sensing image classification. *Remote Sens.* 14 (9), 2215. doi:10.3390/rs14092215

Li, Y., Zhang, H., and Shen, Q. (2017). Spectral–spatial classification of hyperspectral imagery with 3D convolutional neural network. *Remote Sens.* 9 (1), 67. doi:10.3390/rs9010067

Lin, J.-W., Hsieh, M.-H., and Li, Y.-J. (2019). Factor analysis for the statistical modeling of earthquake-induced landslides. *Front. Struct. Civ. Eng.* 14 (1), 123–126. doi:10.1007/s11709-019-0582-y

Liu, J., and Liang, E. (2022). Evaluation of landslide disaster susceptibility in multi-core SVM based on sample selection strategy. *Geomatics Inf. Sci. Wuhan Univ.* 51 (10), 2034–2045.

Liu, R., Yang, X., Xu, C., Wei, L., and Zeng, X. (2022). Comparative study of convolutional neural network and conventional machine learning methods for landslide susceptibility mapping. *Remote Sens.* 14 (2), 321. doi:10.3390/rs14020321

Liu., K. (2020). *Earthquake-induced failure mechanism and stability evalution of loess slope under rainfall effects*. Lanzhou: Lanzhou University. doi:10.27204/d.cnki.glzhu.2020.001256

Luo, L., Xiangjun, P., Huang, R., Zuan, P., and Ling, Z. (2021). Landslide susceptibility assessment in jiuzhaigou scenic area with GIS based on certainty factor and logistic regression model. *J. Eng. Geol.* 29 (2), 526–535.

Ministry of Natural Resources of the People's Republic of China (2021). *National geological hazard disaster situation in 2021 and geological hazard trend prediction in 2022*. Beijing: Ministry of Natural Resources of the People's Republic of China.

Nhu, V. H., Shirzadi, A., Shahabi, H., Singh, S. K., Al-Ansari, N., Clague, J. J., et al. (2020). Shallow landslide susceptibility mapping: A comparison between logistic model tree, logistic regression, naive bayes tree, artificial neural network, and support vector machine algorithms. *Int. J. Environ. Res. Public Health* 17 (8), 2749. doi:10.3390/ijerph17082749

Park, S., and Kim, J. (2019). Landslide susceptibility mapping based on random forest and boosted regression tree models, and a comparison of their performance. *Appl. Sci.* 9 (5), 942. doi:10.3390/app9050942

Plaza, A., Martinez, P., Perez, R., and Plaza, J. (2004). A new approach to mixed pixel classification of hyperspectral imagery based on extended morphological profiles. *Pattern Recognit.* 37 (6), 1097–1116. doi:10.1016/j.patcog.2004.01.006

Sajadi, P., Sang, Y.-F., Gholamnia, M., Bonafoni, S., and Mukherjee, S. (2022). Evaluation of the landslide susceptibility and its spatial difference in the whole qinghai-Tibetan plateau region by five learning algorithms. *Geosci. Lett.* 9 (1), 9. doi:10.1186/s40562-022-00218-x

Shi, C., and Pun, C. M. (2017). *Superpixel-based 3D deep neural networks for hyperspectral image classification*. S0031320317303515. Chicago, U.S.A.: Pattern Recognition.

Sun, D., Xu, J., Wen, H., and Wang, D. (2021). Assessment of landslide susceptibility mapping based on bayesian hyperparameter optimization: A comparison between logistic regression and random forest. *Eng. Geol.* 281, 105972. doi:10.1016/j.enggeo.2020.105972

Tobler, W. R. (1970). A computer movie simulating urban growth in the detroit region. *Econ. Geogr.* 46, 234–240. doi:10.2307/143141

Wang, Q., Wang, Y., Niu, R., and Peng, L. (2017). Integration of information theory, K-means cluster analysis and the logistic regression model for landslide susceptibility mapping in the three gorges area, China. *Remote Sens.* 9 (9), 938. doi:10.3390/rs9090938

Wang, Y., Fang, Z., and Hong, H. (2019). Comparison of convolutional neural networks for landslide susceptibility mapping in yanshan county, China. *Sci. Total Environ.* 666, 975–993. doi:10.1016/j.scitotenv.2019.02.263

Wei, R., Ye, C., Ge, Y., and Yao, L. (2022a). An attention-constrained neural network with overall cognition for landslide spatial prediction. *Landslides* 19 (5), 1087–1099. doi:10.1007/s10346-021-01841-z

Wei, R., Ye, C., Sui, T., Ge, Y., Yao, L., and Li, J. (2022b). Combining spatial response features and machine learning classifiers for landslide susceptibility mapping. *Int. J. Appl. Earth Observation Geoinformation* 107, 102681. doi:10.1016/j.jag.2022.102681

Wu, X., Chen, X., Benjamin Zhan, F., and Song, H. (2015). Global research trends in landslides during 1991–2014: A bibliometric analysis. *Landslides* 12 (6), 1215–1226. doi:10.1007/s10346-015-0624-z

Xu, S., Liu, J., Wang, X., Zhang, Y., Lin, R., Zhang, M., et al. (2020). Landslide susceptibility assessment method incorporating index of entropy based on support vector machine: A case study of shaanxi Province. *J. Wuhan Univ. Inf. Sci. Ed.* 45 (8), 1214–1222.

Yang, Z., Xu, C., Shao, X., Ma, S., and Li, L. (2022). Landslide susceptibility mapping based on CNN-3D algorithm with attention module embedded. *Bull. Eng. Geol. Environ.* 81 (10), 412. doi:10.1007/s10064-022-02889-4

Zhao, Z., Liu, Z. Y., and Xu, C. (2021). Slope unit-based landslide susceptibility mapping using certainty factor, support vector machine, random forest, CF-SVM and CF-rf models. *Front. Earth Sci.* 9, 589630. doi:10.3389/feart.2021.589630

Zhu, A.-X., Miao, Y., Liu, J., Bai, S., Zeng, C., Ma, T., et al. (2019). A similarity-based approach to sampling absence data for landslide susceptibility mapping using data-driven methods. *Catena* 183, 104188. doi:10.1016/j.catena.2019.104188

Zhu, X. X., Tuia, D., Mou, L., Xia, G.-S., Zhang, L., Xu, F., et al. (2017). Deep learning in remote sensing: A comprehensive review and list of Resources. *IEEE Geoscience Remote Sens. Mag.* 5 (4), 8–36. doi:10.1109/mgrs.2017.2762307

frontiers | Frontiers in Earth Science

TYPE Original Research
PUBLISHED 31 August 2023
DOI 10.3389/feart.2023.1220142

OPEN ACCESS

EDITED BY
Chengyi Pu,
Central University of Finance and Economics, China

REVIEWED BY
Liangchao Zou,
Royal Institute of Technology, Sweden
Min Lee Lee,
University of Nottingham Malaysia Campus, Malaysia

*CORRESPONDENCE
Meng Zhao,
zhaomeng@cdu.edu.cn

†These authors have contributed equally to this work

RECEIVED 10 May 2023
ACCEPTED 15 August 2023
PUBLISHED 31 August 2023

CITATION
Wei Z-X, Dong J-H, Zhao M, Xie F-H, Li Y-J and Feng L (2023), Transient electromagnetic detection and numerical simulation analysis of the deformation characteristics of an old goaf in an alpine coal mine area.
Front. Earth Sci. 11:1220142.
doi: 10.3389/feart.2023.1220142

Transient electromagnetic detection and numerical simulation analysis of the deformation characteristics of an old goaf in an alpine coal mine area

Zhan-Xi Wei[1†], Jian-Hui Dong[2,3], Meng Zhao[3*†], Fei-Hong Xie[3], Ying-Jun Li[1,4,5] and Lin Feng[6]

[1]Qinghai Bureau of Environmental Geological Exploration, Xining, China, [2]Engineering Research Center of Catastrophic Prophylaxis and Treatment of Road and Traffic Safety of Ministry of Education, Changsha University of Science and Technology, Changsha, Hunan, China, [3]Sichuan Engineering Research Center for Mechanical Properties and Engineering Technology of Unsaturated Soils, Chengdu University, Chengdu, China, [4]Qinghai 906 Project Survey and Design Institute, Xining, China, [5]Qinghai Geological Environmental Protection and Disaster Prevention Engineering Technology Research Center, Xining, China, [6]State Key Laboratory of Geological Disaster Prevention and Geological Environment Protection, Chengdu University of Technology, Chengdu, China

In this paper, Qinghai alpine mining area is taken as the research object to explore the deformation characteristics of overlying strata in alpine mining area, so as to prevent geological disasters caused by over-exploitation in alpine mining area. The location of old goaf in coal mine is detected by transient electromagnetic method, and the results are used for numerical simulation. The numerical simulation results show that after coal seam mining, the stress gradually increases from the surface to the bottom, and the stress concentration occurs at both ends and the middle of the mining area. The displacement change area is highly coincident with the stress concentration area, and the displacement monitoring map is consistent with the horizontal displacement cloud map analysis, showing a "U" type distribution. The research results have certain reference value for the future study of surface mining subsidence in inclined coal seams.

KEYWORDS

alpine coal mining area, transient electromagnetic, overburden deformation, discrete element numerical simulation, coal seam

1 Introduction

The mining of underground mineral resources led to the destruction of the overlying strata, which, in turn, led to the subsidence of the surface. In the subsidence area, the surface will produce ground fissures and unstable slopes (Liu et al., 2010; Diao 2011; Ji et al., 2022). The long-term, large-scale, and high-intensity development of mineral resources had caused severe damage to the geological environment. Therefore, it is essential for geological disaster prevention and control engineering to predict the stress and strain characteristics of the overburdened rock in the alpine mining area in time and accurately.

First of all, in the field of geological disaster prevention and control, a large number of scholars have carried out relevant research. Huang et al. (2020) determined the correlation between 13 landslide condition factors (elevation slope, plane curvature, profile distribution, topographic relief amplitude, total surface radiation, population density, river normalized vegetation index, topographic wetness index, and rock type) and landslide location through frequency ratio analysis. They were used to compare heuristic models, general statistical models, and mechanical models, and a machine learning model with high accuracy and reasonable LS distribution characteristics was obtained. Chang et al. (2020) compared the advantages and disadvantages of simple machine learning (SML) and unsupervised machine learning (USML) on the LSP model and finally concluded that USMLModelScan Aso was used for LSP implementation due to its efficient modeling process, dimension reduction, and strong scalability. The results had essential guiding significance for the analysis of landslide stability. Jiang et al. (2018) proposed a simplified approach for generating conditional random feds of soil undrained shear strength. This method can detect the strength of soil to calculate the stability of the slope (Zhao et al., 2020; Zhao et al., 2022), used comparative tests, prices analysis, X-ray diffraction (XRD), and scanning electron microscopy (SEM) analysis to clarify the relationship between loess particle composition, micro structures, and macro mechanics, and analyzes the causes of subgrade settlement in alpine areas. It provided a reference for geological engineering practice. Zhao et al. (2018) and Zhao et al. (2019) used gypsum (MPG) and MPE-cement to reinforce roadbed loess and carried out an unconfined compressive strength test, permeability test, and freeze–thaw test, which improved the strength of modified loess and prevented the settlement of ground roadbed. Zhang et al. (2023) used the finite-element groundwater flow system software to simulate and predict the development of natural seepage field and the dredging construction conditions of seepage field in the West Qinling 1 # tunnel area and studied the change of seepage field in a tunnel engineering aquifer. Zhang et al. (2023) investigated the hydrochemistry, clarifying groundwater quality and assessing human health risks, using various computed techniques of geomodeling, EWQI, GIS mapping, and the USEPA mathematical model.

With the in-depth research of many scholars on the stress distribution of overlying rock mass caused by underground mining, physical models and numerical simulation experiments have been widely used (Li et al., 2019). Geophysical exploration was the main detection method for goaf. Abhay et al. (2019) adopted the resistivity method to conduct tomography detection for the old stope in the Jharia coal field in India, which was helpful to identify the abandoned slope and porous and permeable stratum conditions. The vector finite-element method was used to simulate the TEM response in homogeneous media in three dimensions. It had a good effect on obtaining the HFIL diagram of the real position of the thin layer formation logging instrument (Epov et al., 2007). Shi et al. (2010) carried out terrain correction by combining the high-density resistivity method with the total station instrument. They determined the distribution location of the goaf and verified that the high-density electrical method had a good effect on the detection of goaf.

In addition, researchers have carried out various studies on the deformation characteristics of overburdened rock in near-horizontal and gently dipping coal seam goaf. Boris (1997), on the basis of considering the underground geological characteristics of the slope, used FLAC 2D and UDEC to comprehensively analyze the influence of various factors such as excavation depth, excavation method, and excavation site on slope changes during mining. He found that slope instability is closely related to slope rock inclination conditions.

The abovementioned research showed that the transient electromagnetic method and high-density resistivity method can detect the approximate range, location, and occurrence state of the goaf when studying the underground coal seam goaf and draw the goaf plan accordingly. The plan can provide theoretical practice for the numerical simulation of goaf deformation characteristics. However, no scholars have combined the two methods to study the deformation characteristics of overlying strata in alpine mining areas.

This paper took the mined-out area of Xiaomeidong mine in Datong Coal Mine of Qinghai province as the research object, combined with the geological and hydrological data of the study area, the transient electromagnetic method was used to detect the mined-out area, and the section map of the mined-out area was drawn. The numerical simulation method was used to analyze the surface deformation law under the stress of the original rock in the goaf from the perspective of theoretical analysis and explore the deformation characteristics of the overlying rock in the goaf. It revealed the deformation and failure mechanical characteristics and fracture evolution process of mined-out overburdened rock under the stress of original rock. The research results provided effective theoretical support for surface deformation monitoring and disaster prevention of the mined-out area in Xiaomeidong mine, which had essential theoretical significance.

2 Engineering geology background

2.1 Meteorological and hydrological conditions

The Xiaomeidong mine field was located in the southeast of Datong Hui-Tu Autonomous County, Xining City, Qinghai province. The critical research area belonged to plateau continental climate. The mean annual temperature was 2.8–3.9°C. The temperature difference was 25.3°C, average daily temperature difference was 13.2°C ~ 13.8°C, and average annual precipitation was between 508.7 and 532.6 mm. Summer and autumn had more southeast wind, and the wind speed was small; winter and spring had more northwest wind, with average wind speed 2 m/s, maximum wind speed 17 m/s, and an average frost-free period of 96.3 days.

2.2 Geological condition

The study area was located in the southern margin of the Xining–Datong Basin, which was composed of eroded low hills and eroded valley plains. The erosion and denudation hills in the area were mainly composed of Cretaceous, Paleogene mud,

FIGURE 1
Panoramic view of the subsidence area of the Xiaomeidong coal mine.

sandstone, and Quaternary loess. The altitude was 2,450–2,750 m, the relative height difference was 300 m, the mountain was high and the slope was steep, the ravines were cross, the terrain was undulating, the topography was complex, the vegetation was scarce, and soil erosion was serious. It was the strongest area of modern water erosion. Some villagers in the area built houses according to the mountains, and human engineering activities have caused serious damage to the geological environment.

The coal seam was thick at the top and thin at the bottom, and its structure was complex. The overall distribution characteristics of the overlying strata in the goaf were stratified and crisscrossed. The scale of the mined-out mine was basically the same as the scale of the ore body. The old mined-out area under the surface of the exploration area was covered with tunnels. The distance between the mined-out area and the surface was increased from south to north except the wellhead, and the thickness of the mined-out area was mainly sand mud stone and waste rock, which had low mechanical strength and were easily weathered. Between the layers (between the upper and lower roadway) were mostly sand and mud stone.

The mined-out subsidence area of the Xiaomeidong mine was approximately rectangular in shape, with a length of about 1,600 m and a width of about 650 m. The direction of its long axis was 46°. Figure 1 shows the overall picture. The subsidence area was in the deformation development period. With the extension of time, the surface collapsed will develop from southwest to northeast, and the goaf will lead to the surface movement, which will lead to the continuous increase of the scale of the collapsed, the aggravation of the damage, and further aggravation of the damage to the geomorphic landscape. From the field investigation, it can be concluded that the landslide (such as oil depot landslide) and unstable slope around the Xiaomeidong mine were all induced by the ground collapsed of the goaf, as shown in Figure 2.

Based on the field situation of the study area, this paper intended to use the transient electromagnetic method to conduct geophysical exploration of the hydrogeology of the coal mine site, constructed a numerical analysis model of the subsidence area, studied and inverted the characteristics of the subsidence area, and analyzed its genesis mechanism and influence range.

3 Analysis of geophysical results

The transient electromagnetic method was a method to detect the resistivity of the medium by using an ungrounded loop or ground line source to emit a primary pulse magnetic field to the ground and using coil or ground electrode to observe the secondary-induced eddy current field caused by the underground medium during the intermittent period of primary pulse magnetic field. This method can judge the possible coal mine goaf by detecting the resistivity below the surface, which provides a reliable theoretical basis for the subsequent numerical simulation. It had the advantages of automatically eliminating the main noise source, no terrain influence, combined observation at the same point, best coupling with the detection target, strong abnormal response, simple shape, and strong resolution. Three transient electromagnetic profile lines were set up in the Datong coal mine to detect and identify water-bearing geology in the area, such as karst caves and roadways, coal mine goaves, and deep irregular water bodies, and to establish geological models. The study area was the EH2-2′ survey line area. The geophysical arrangement is shown in Figure 3.

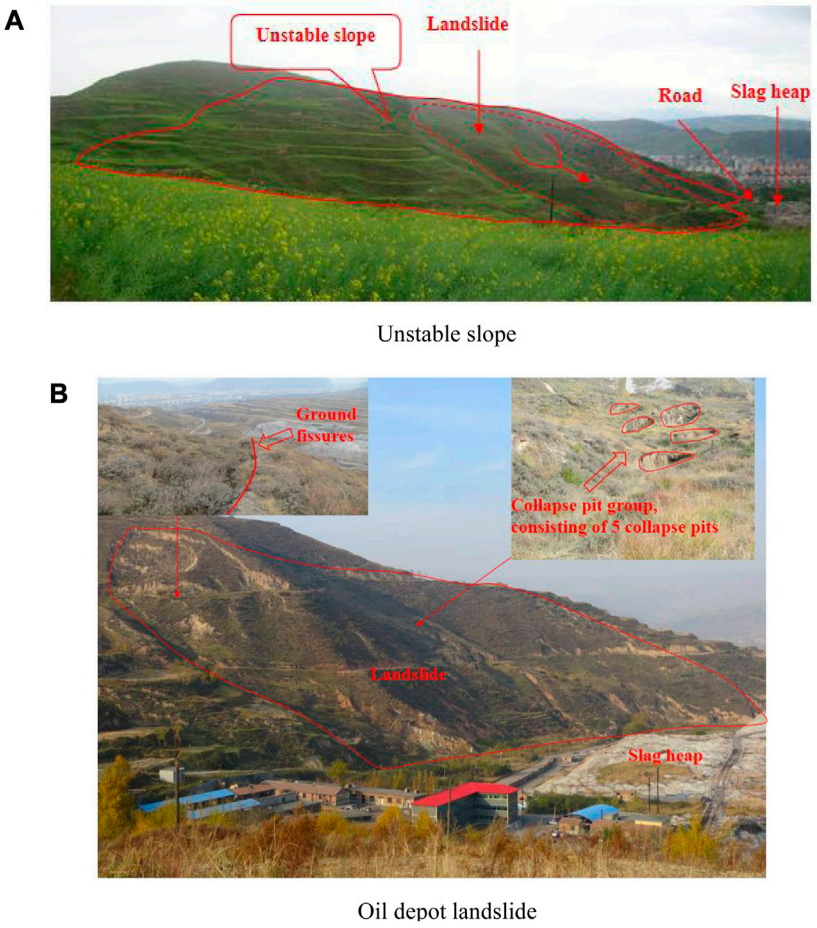

FIGURE 2
Geological disaster of the Xiaomeidong coal mine. **(A)** Unstable slope and **(B)** oil depot landslide.

The original resistivity data were obtained by line detection, and then, the topographic data were added for apparent resistivity model inversion. The error value was obtained by comparing the model data calculated by forward modeling with the original data. When the data error was less than 15%, the model was considered as a qualified inversion model. Section directions are shown in the geophysical survey layout. The horizontal axis of each profile was the horizontal distance (unit m), and the vertical axis was the elevation (unit m). This interpretation work was based on the inversion profile and combined with the geological data and the actual situation to explain each profile. The resistivity profile of the measured line and its detailed interpretation are as follows.

The terrain of the EH2-2′ survey line was relatively flat, and the surface layer was mainly covered with silt, which was relatively thick. From the transient electromagnetic inversion results, it can be seen that there was an obvious low-resistance area between 0 m and 28 m down from the surface at a distance of 300–880 m, and the apparent resistivity was less than 30 Ω m, which was presumed to be a coal mine goaf and subsidence water-rich area. There was an obvious low-resistance area between 0 and 125 m down from the surface at a mileage of 1,400–1,600 m, and the apparent resistivity was less than 30 Ω m, which was presumed to be a coal mine goaf and water-rich area. The apparent resistivity of the entire survey line section was greater than 30 Ω m and less than 50 Ω m, which was presumed to be a weak water-rich area of the coal mine goaf. Figures 4, 5 show the details.

It could be seen that there were obvious low-resistance areas at 300–880 m from the surface, between 0 and 28 m from the surface, between 1,400 and 1,600 m from the surface, and between 0 and 125 m from the surface. It was speculated that these two areas were coal seam goaves. Therefore, these two areas were set as numerical simulation research areas for subsequent coal seamstress and displacement analysis.

4 Analysis of the deformation characteristics of the overlying strata at different working faces

Numerical calculation and analysis of coal and rock stability was one of the essential methods for scientific research, which can reveal the deformation and failure law of rock strata in site engineering. It can solve problems such as the movement and deformation law of surface overburden under various geological conditions and different mining modes (Lei et al., 2018). At present, numerical simulation methods have been widely used in the field of overburden

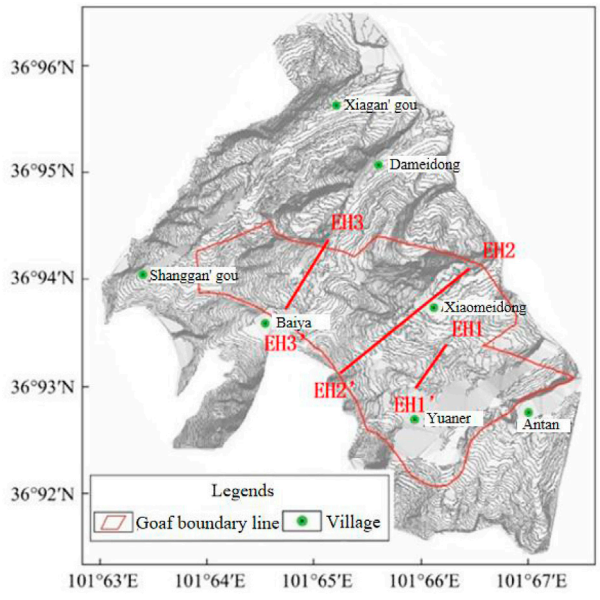

FIGURE 3
Layout plan of geophysical prospecting.

migration and surface deformation. The most commonly used numerical simulation methods mainly include finite-element method, finite-difference method, and discrete-element method. In this study, two-dimensional discrete element numerical simulation technology was used to simulate the mechanical behavior of the overlying strata and mining subsidence, and the numerical simulation results obtained can be used to guide mine safety production (Wang et al., 2021). This numerical simulation method regards the rock mass as a collection of two basic elements of rock and structural plane and continuously judges and updates the contact state of the block during the calculation process. According to these contact states, the load transfer mode between the blocks was judged, the corresponding mechanical laws were selected for contact, and the stress and deformation behavior of these basic elements were defined.

4.1 Model establishment and survey line setting

Due to the complex stratigraphic structure of the study area, in the process of establishing the numerical model, the rock and soil bodies with similar physical and mechanical properties were appropriately simplified and the coal seam was simplified into two layers of coal. The two groups of coal were mined simultaneously.

The model was basically assumed to be an isotropic continuous homogeneous medium, and the Mohr–Coulomb elastic–plastic model was adopted as the mechanical model. The top surface of the model was free, the bottom was a fixed constraint, and the periphery was a horizontal displacement constraint. The initial stress in the mining area was mainly self-weight stress, and the acceleration of gravity was set at 9.81 m/s^2, with a vertical downward direction. Table 1 shows the physical and mechanical parameters of rock strata.

As for the parameters of joints, their values should be relatively smaller than those of rocks, so the tangential stiffness of joints jks=5 GPa. The joint normal stiffness jkn=2.5 GPa. The values of friction angle of joints and cohesion should be less than those of rocks, and the friction angle of joints should be 15; cohesion was 0.2 MPa.

For the constitutive model, the elastic–plastic model was used in modeling, and the block obeyed CONS = 2 in UEDC. The constitutive model of joints obeyed jcons=3 in UDEC.

The established numerical calculation showed that the strike length was 1,600 m, the vertical height was between 270 m and 470 m, the average vertical height was 370 m, the simulated mining

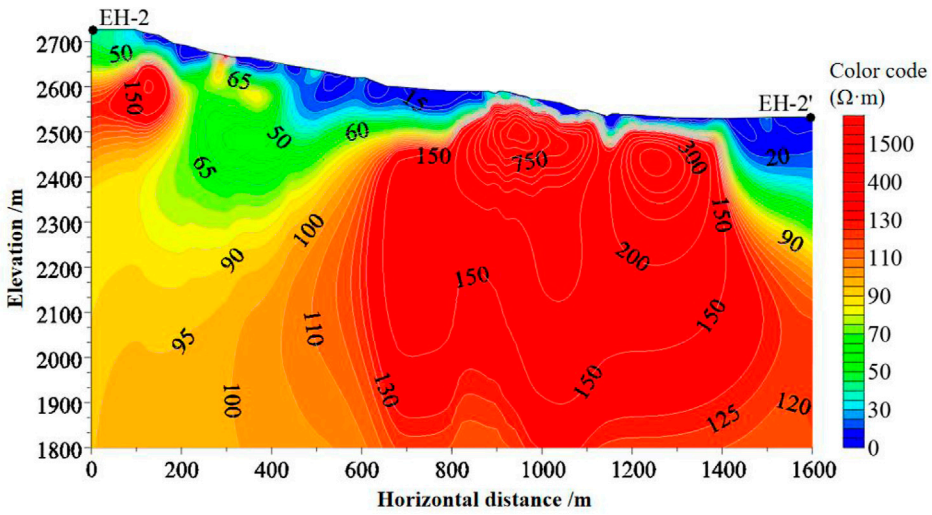

FIGURE 4
Inversion results of the transient electromagnetic method.

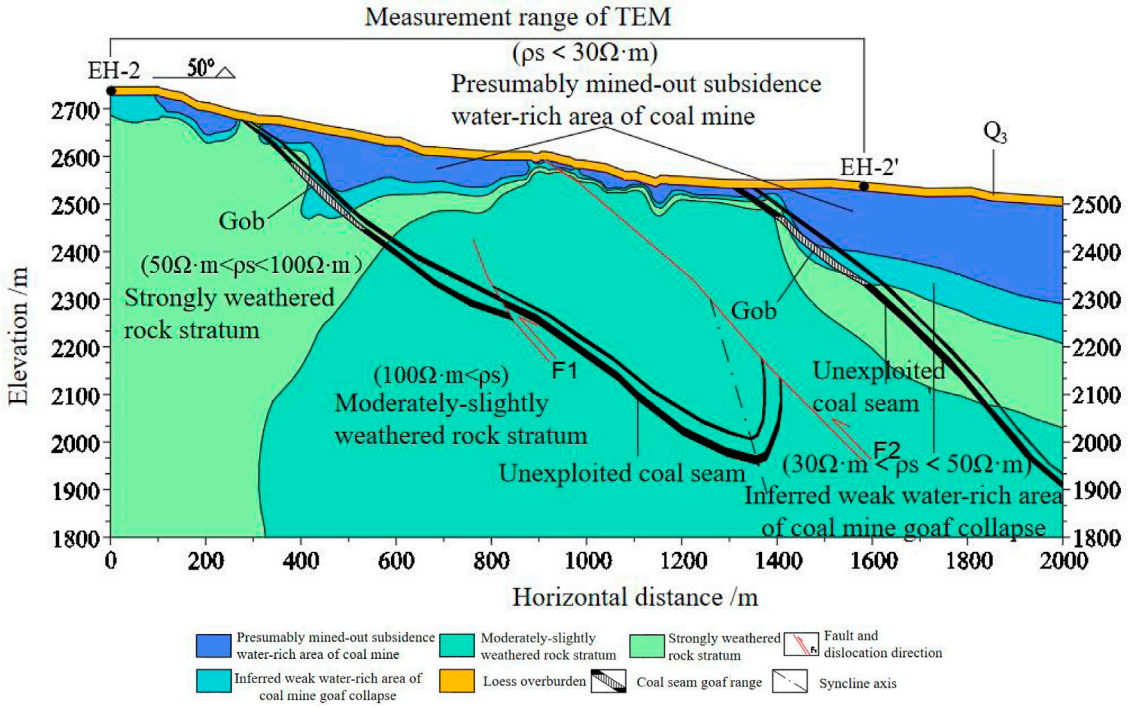

FIGURE 5
Interpretation of inversion results of the transient electromagnetic method.

TABLE 1 Physical and mechanical parameters of overburden.

Rock character	Density	Bulk modulus	Shear modulus	Cohesive strength	Internal friction angle	Tensile strength
	/kN·m^{-3}	/GPa	/GPa	/MPa	/°	/MPa
Malmstone	2,400	6	2.3	0.7	30	0.6
Coal bed	1,400	3.9	1.1	0.5	30	1.04

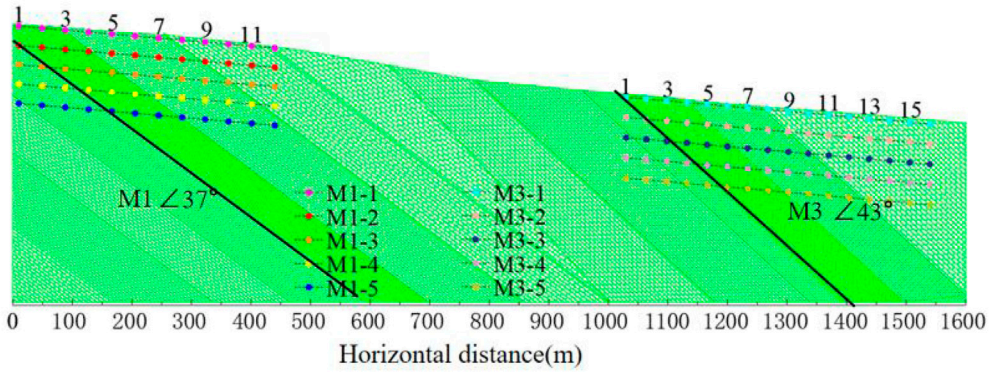

FIGURE 6
Model grid division and survey line layout.

thickness was 2.4 m, and the simulated coal seams were all inclined coal seams, with the dip angle of M1 being 37 and the dip angle of M3 being 43. The model is shown in Figure 7. Above the numerical model coal seam, five monitoring lines were set for M1 and M3, one monitoring line was set near the surface, and four monitoring lines were set down at an equal distance. Figure 6 shows the layout of survey lines.

4.2 Analysis of numerical calculation results

The movement and deformation of the overlying strata and surface caused by coal mining was a complicated mechanical process. In order to explore the movement law of the overlying strata and surface caused by mining and to deeply analyze the influencing factors of movement law under deep mining conditions, taking coal mining in the Xiaomeidong mine as the research background, based on the abovementioned numerical model considering the dynamic response of the overlying strata mining, a numerical simulation scheme was designed to analyze the deformation characteristics and laws of the overlying strata and surface after coal mining (Weng, 2019).

In the actual process of coal mining, there were many multi-layer coal seams in many coal mines. Therefore, taking the actual mining conditions of the Xiaomeidong mine as a prototype, taking into account the rock mass structure conditions actually investigated on the spot, and considering the mining schemes of single-layer mining and multi-layer mining, this paper compared their influences on ground deformation and destruction and provided some theoretical basis for coal mining (Yan, 2019).

Prior to excavation, the model under the original stress needed to be iteratively calculated to reach the equilibrium state. In this working condition, after iterative calculation prior to excavation, when the maximum node unbalanced force reached step 7,647, compared with the initial total force, it was considered that the equilibrium was reached and the dynamic simulation of later excavation could be continued.

After balancing of the original model was completed, it was necessary to start the simulation of coal seam excavation. In UDEC, the delete range region command was used to delete the blocks that needed to be excavated within a certain boundary. At this time, only four corners of the excavation area needed to be determined, and the coordinates (x and y) of each point could be input counterclockwise to delete the blocks in the area to simulate the excavation work. After excavation, iterative calculation was continued to balance. After the solution was completed, the corresponding graphs were output to provide calculation results for further explanation and analysis. The graphs involved included a model graph, horizontal stress graph, vertical stress graph, horizontal displacement graph, vertical displacement graph, combined displacement graph, and monitoring line graph. In this section, the simulation scheme of single-layer excavation and multi-layer excavation would be adopted to analyze the working conditions of the abovementioned graphs.

Coal seam mining characteristics are shown in Table 2.

4.2.1 Analysis of stress field

After the calculation of the model was balanced, the stress distribution was mainly analyzed by the stress cloud chart because the cloud chart had more intuitive advantages than the contour chart.

Figures 7A, B show the horizontal (x-direction) stress nephogram after coal seam mining had reached equilibrium. The nephogram took 4.0 MPa as the equivalent interval, with the minimum value of 0 Mpa and the maximum value of −16.0 MPa (representing compressive stress). The nephogram was in a layered state, and the layered stress was increasing from top to bottom. During single-layer mining, the stress was 0–8.0 MPa in a large area, and the stress changes mainly occurred in the coal seam roof. The stress increased in the central part of the mining area roof, and the stress concentration was obvious in the horizontal direction near the two ends of the mining subsidence area, with the stress value in the range of 4.0–6.0 MPa, as shown in Figure 7A. During multi-layer mining, the stress was 0–8.0 MPa in a large area. After coal mining, there was stress concentration at both ends of the mined-out area of coal seam M1 and obvious compressive stress concentration at the lower end of the mined-out area of coal seam M3, as shown in Figure 7B.

Figures 7C, D show the vertical (y-direction) stress nephogram after coal seam mining was balanced. The nephogram took 4.0 MPa as the equivalent interval, with the minimum value of 0 MPa and the maximum value of −16.0 MPa (expressed as compressive stress), and the large area was in the range of 0–12.0 MPa. During single-layer mining, the stress changes mainly occurred in the coal seam roof, and the stress increased in the central part of the roof in the mining area and showed obvious stress concentration in the horizontal direction near both ends of the mining subsidence area, with the stress value in the range of 4.0–8.0 MPa, as shown in Figure 7C. During multi-layer mining, stress concentration occurred at both ends of M1 and M3 mining areas to a certain extent, especially at the lower end of M3 mined-out area, and the stress concentration area was distributed within 8.0–12.0 MPa, as shown in Figure 7D.

Figures 7E, F show the distribution of shear stress after coal seam mining reaches equilibrium. It could be seen from the figure that there were positive and negative shear stresses in the rock strata near the coal seam mining area. The positive shear stress indicates that it was consistent with the moving direction along the inclined layer, and the shear stress in the mined-out subsidence area was mostly positive, reaching 0–2.0 Mpa. It could be seen from Figure 7E that during single-layer mining, the direction of shear stress in the center of the roof of the mining area was opposite to the movement direction of the strata, and there were negative shear stresses on both sides of the caving area. Shear stress concentration occurred at both ends and the middle of the mining area, and the shear stress was negative, reaching 1.0–2.0 Mpa. It could be seen from Figure 7F that during multi-layer mining, the shear stress of the deformation at the center and both sides of the roof and floor in the mining area was negative, ranging from 0 to 0–2.0 MPa, and the stress concentration occurred at the lower end of the M3 mining area in coal seam.

Figures 7G, H show the cloud pictures of minimum principal stress after coal seam excavation was balanced. Through the analysis of the simulated cloud picture of principal stress, it could be further judged whether there was tensile stress in the goaf of coal seam. It could be seen from Figure 7G that after the single-layer excavation reached a new balance, the minimum principal stress of the roof in

TABLE 2 Coal seam mining characteristics.

Mining area	Mining thickness	Coal seam dip angle	Mining length	Elevation of the mining upper end	Elevation of the mining lower end
	/m	/Degree	/m	/m	/m
M1	2.4	37	225	+2,585	+2,450
M3	2.4	43	273	+2,475	+2,287

the M1 mining area of coal seam was 0–4.0 MPa, which showed compressive stress, and the stress concentration occurred on both sides and the center of the excavation area with the minimum principal stress peak value of -8.0 MPa. It could be seen from Figure 7H that during multi-layer excavation, the minimum principal stress of the roof in the coal seam mining area was 0–4.0 MPa and the stress change of the floor was small.

Figures 7I, J, show the nephogram of the maximum principal stress after coal seam excavation was balanced. For the single-layer excavation scheme, at the top of the M1 mining area of coal seam, there was an obvious tensile stress area, and the overlying strata delaminated and collapsed, forming a caving area. The maximum principal stress in the caving area was 0–2.0 MPa and the angle was 60, as shown in Figure 7I. For the multi-layer excavation scheme, the collapsed shape of overburden in mining area could be clearly shown in the normal tensile stress area, as shown in Figure 7J.

From the abovementioned results, it could be seen that when the coal seam is mined, the stress change mainly occurred in the roof of the coal seam. The stress in the middle of the roof increases, and the horizontal stress concentration near the two ends of the mining subsidence area was obvious.

4.2.2 Analysis of the displacement field

After the coal seam was mined, the original stress balance around the mined-out area was destroyed, which caused the redistribution of stress, thus causing the deformation, destruction, and movement of the rock stratum, which developed from the bottom up to the surface and caused the movement of the surface. Through the displacement nephogram obtained by numerical simulation, the deformation shape and movement angle of overlying strata in goaf could be observed intuitively. This section comprehensively analyzes the horizontal displacement, vertical displacement, and combined displacement of the overlying strata in the mining area after coal seam mining.

The deformation form of the overlying strata could be seen from the figure. With the advancing of the working face, the main roof had vertical and horizontal displacement, and the deformation (horizontal and vertical) was also increasing. Figures 8A, B show the horizontal (x-direction) displacement nephogram after coal seam excavation was balanced. From the numerical simulation results, it could be seen that after coal seam excavation, the horizontal displacement of the roof in the middle of coal seam mining area was the maximum, with the maximum displacement of 1.6 m. The horizontal displacement of the strata near the mined-out area of coal mine changed greatly, and the strata in the excavated area showed obvious bending and collapsed, and the deformation area was 0.8–1.6 m in the large area.

Figures 8C, D show the vertical (Y-direction) displacement nephogram after coal seam excavation was balanced. From the numerical simulation results, it could be seen that after coal seam excavation, the Y-direction displacement showed a certain rule: the deformation of the overlying strata in goaf was concentrated in the main collapsed area, and the vertical displacement after excavation was distributed in layers. The displacement gradually decreased with the increase in the range, and the displacement peak appeared at the roof of goaf, with M1 vertical displacement exceeding 2.0 m in a large range and M3 vertical displacement ranging from 1.5 to 2.0 m in a large area (the negative sign in the figure indicates the vertical downward movement of the strata).

Figures 8E, F show the combined displacement cloud pictures after coal seam excavation was balanced. From the numerical simulation results, it could be seen that after coal seam excavation, the peak value of combined displacement of the roof was concentrated at the top of goaf, and the maximum value of combined displacement after mining appeared in the center of the roof of the mining area. The more the distance from the center of the mining area, the smaller the subsidence displacement. Under the condition of full mining, the rock strata movement angle of the surrounding rock above the M1 goaf was 59°, and that of the surrounding rock above the M1 goaf was 53°.

From the results of numerical simulation displacement, it could be seen that after coal seam excavation, the peak value of coal seam roof displacement was concentrated on the top of goaf and the maximum value of combined displacement after mining appeared in the center of the roof in the mining area. The more the distance from the center of the mining area, the smaller the settlement displacement, which was consistent with the analysis of the stress cloud map.

4.3 Analysis of displacement monitoring data

The cloud map of displacement was a balanced overburden movement pattern after coal seam excavation in order to verify whether the results of this numerical simulation were reliable. In order to analyze the displacement change of coal seam M3 more clearly and intuitively, we set up five monitoring lines parallel to the surface in the overlying strata of coal seam M1 and M3 mining areas, namely, M1-1, M1-2, M1-3, M1-4, M1-5, M3-1, M3-2, M3-3, M3-4, and M3-5, among which in M1, the distance between the measured points was roughly equal. Figure 6 shows the layout of the monitoring line.

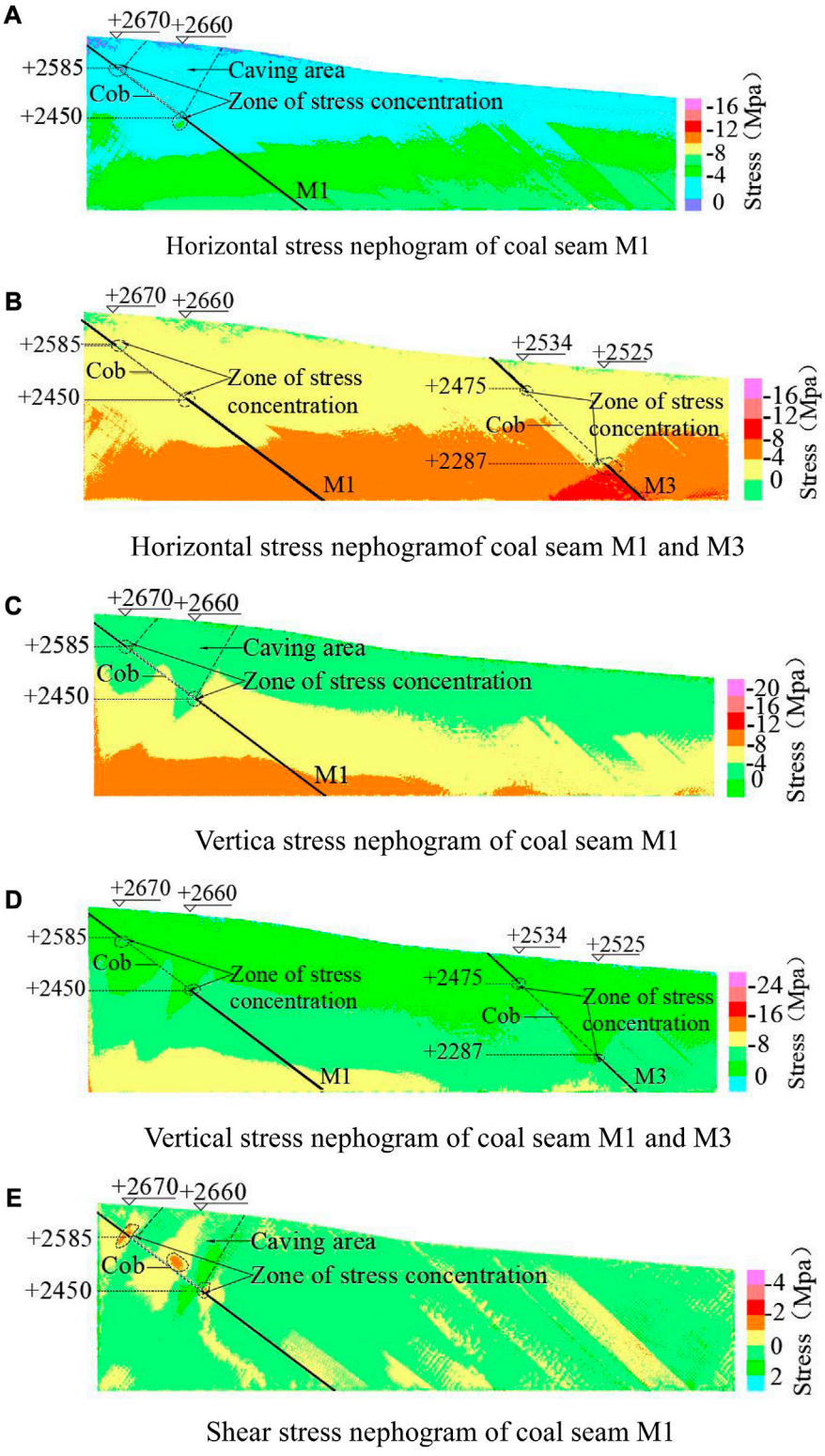

FIGURE 7
(Continued).

As can be seen from Figure 9, the horizontal displacement had positive and negative values at the horizontal distance of the survey line, and coal seam M1 had a large displacement between the horizontal distance of 100–300 m, and the peak value at the monitoring point M1-108 was 1.34 m. The horizontal displacement of the M3 coal seam after mining was generally

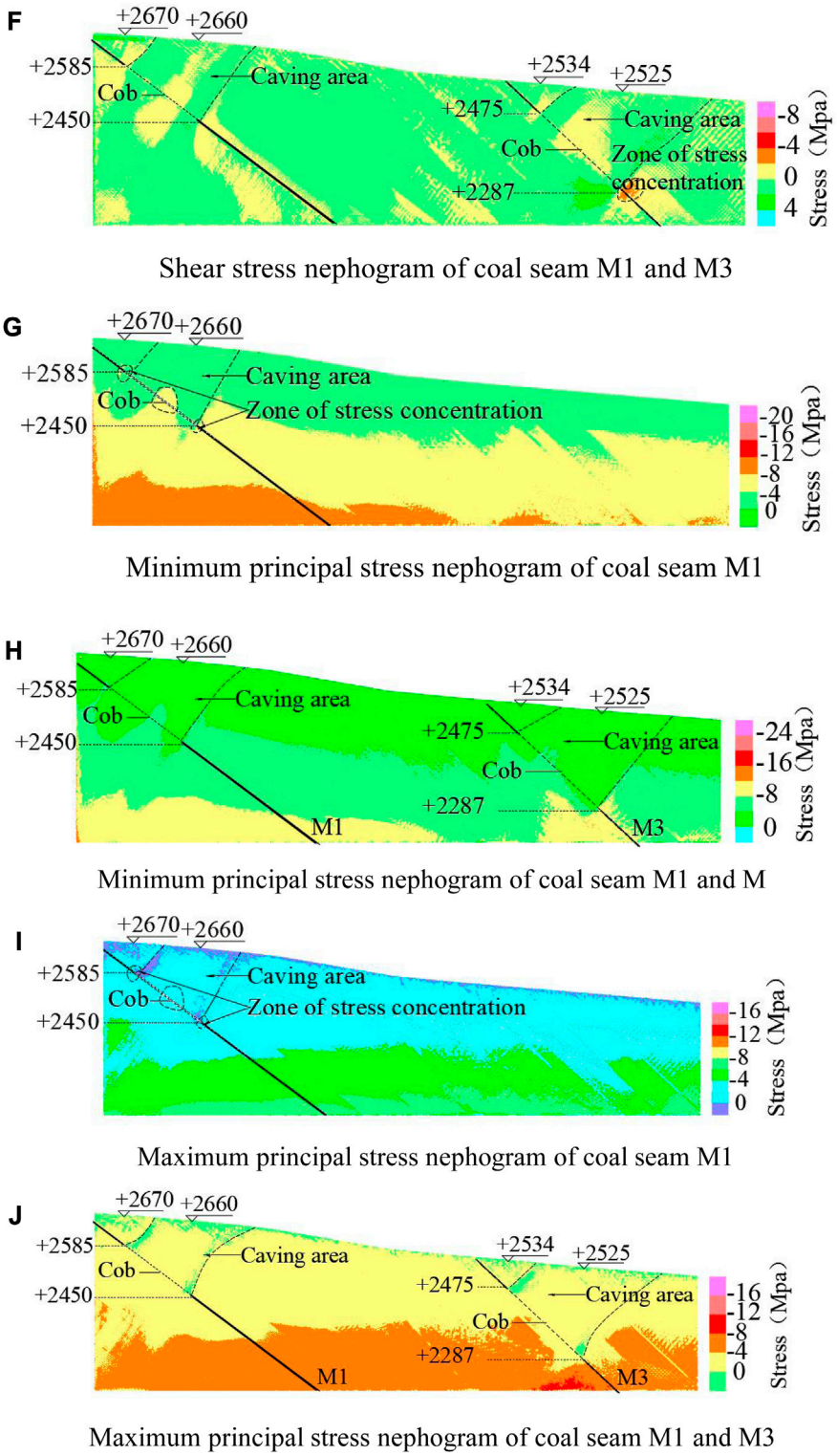

FIGURE 7
(Continued). Stress nephogram of coal seam after excavation. **(A)** Horizontal stress nephogram of coal seam M1, **(B)** horizontal stress nephogram of coal seam M1 and M3, and **(C)**vertical stress nephogram of coal seam M1. **(D)** Vertical stress nephogram of coal seam M1 and M3, **(E)** shear stress nephogram of coal seam M1, **(F)** shear stress nephogram of coal seam M1 and M3, **(G)** minimum principal stress nephogram of coal seam M1, **(H)** minimum principal stress nephogram of coal seam M1 and M, **(I)** maximum principal stress nephogram of coal seam M1, and **(J)** maximum principal stress nephogram of coal seam M1 and M3 .

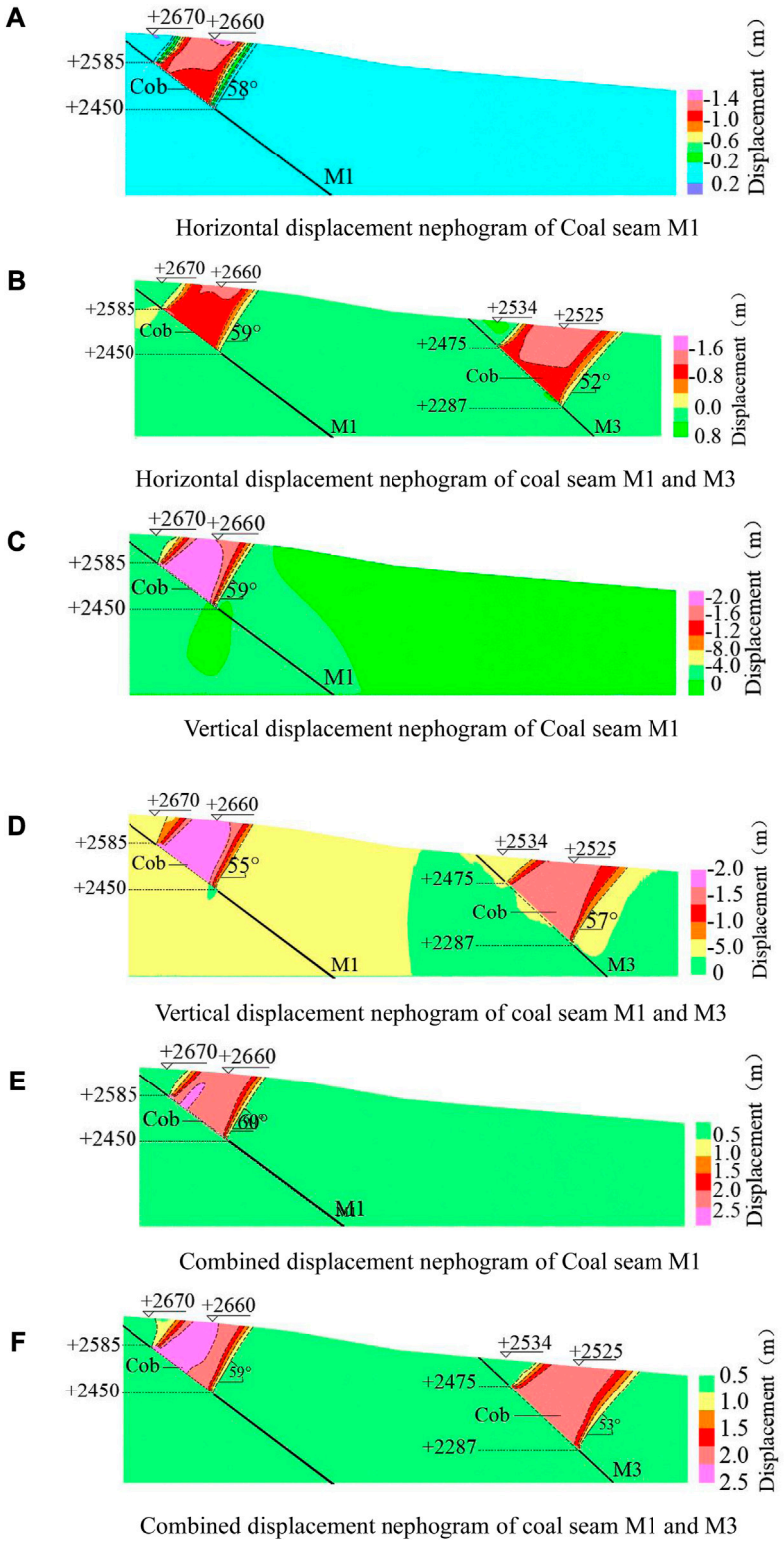

FIGURE 8
Displacement nephogram after coal seam excavation. **(A)** Horizontal displacement nephogram of coal seam M1, **(B)** horizontal displacement nephogram of coal seam M1 and M3, **(C)** vertical displacement nephogram of coal seam M1, **(D)** vertical displacement nephogram of coal seam M1 and M3, **(E)** combined displacement nephogram of coal seam M1, and **(F)** combined displacement nephogram of coal seam M1 and M3.

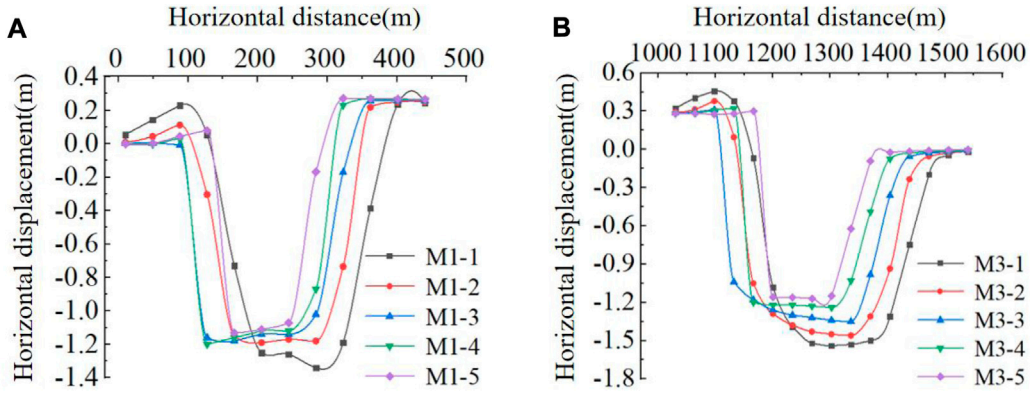

FIGURE 9
Horizontal displacement curve of the coal seam after mining stability. **(A)** Horizontal displacement curve of M1 coal seam. **(B)** Horizontal displacement curve of M3 coal seam.

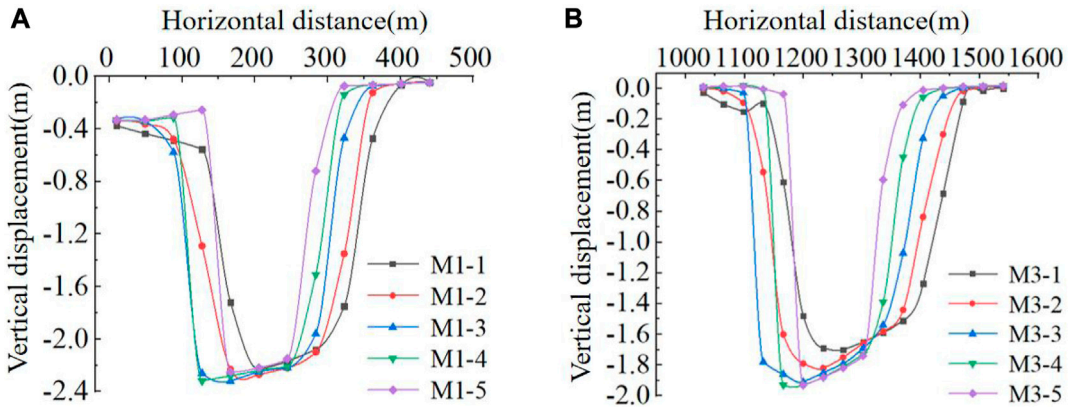

FIGURE 10
Vertical displacement curve of coal seam after mining stability. **(A)** Vertical displacement curve of M1 coal seam. **(B)** Vertical displacement curve of M3 coal seam.

U-shaped, with a large horizontal displacement between 1,150–1,350 m. The maximum horizontal displacement occurred at M3-109, and the maximum displacement was −1.537 m.

As can be seen from Figure 10, the vertical displacement of the monitoring point was negative, which was downward displacement, and the maximum displacement of coal seam M1 was M1-404, with a maximum displacement of 2.32 m. As can be seen from Figure 10A, M1 had a large deformation in the goaf subsidence area with a horizontal distance of 100–200 m, with a relatively uniform change and a large vertical displacement. The subsidence deformation was within the range of 2.0–2.4 m, while the overlying strata outside this range had a small deformation, and the subsidence deformation was within the range of 0–0.6 m. It could be seen from Figure 10B that M3 had a large deformation in the mined-out subsidence area with a horizontal distance of 1,100–1,350 m, with a relatively uniform change and a large vertical displacement. The subsidence deformation was within the range of 1.6–2.0 m, while the overlying strata outside this range had a small deformation, and the subsidence deformation was within the range of 0–0.2 m.

The combined displacement curve of Figure 11 could be obtained from the data in the table.

As can be seen from Figure 11A, M1 had a large deformation within the horizontal distance of 100–300 m. At this time, the roof in the mining subsidence area collapsed and bent, and the settlement deformation developed from above the mined-out area to the surface. The maximum value of combined displacement occurred at M1-404, and the maximum displacement value was 2.611 m. It could be seen from Figure 11B that M3 had a large deformation within the horizontal distance of 1,200–1,300 m. At this time, the roof of the mining subsidence area collapsed and bent, and the settlement deformation developed from above the mined-out area to the surface. The maximum combined displacement occurred at M3-306, and the maximum displacement was 2.291 m.

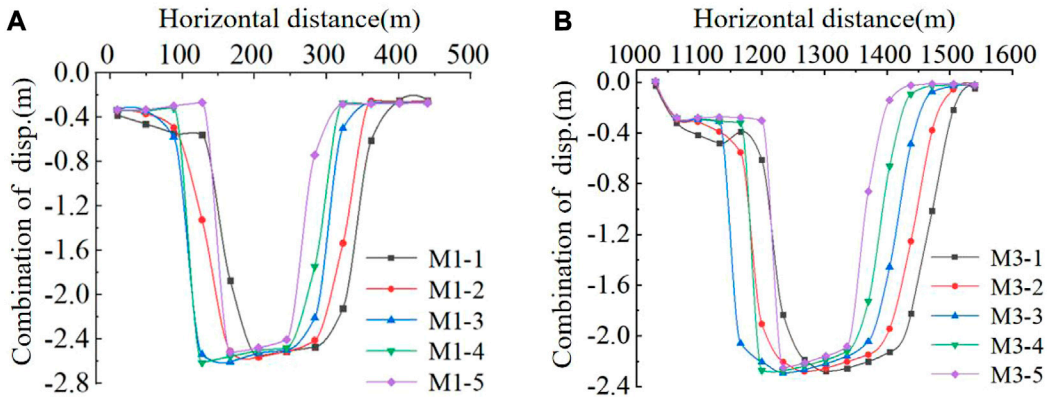

FIGURE 11
Combined displacement curve after coal seam mining is stable. **(A)** Combined displacement curve of M1 coal seam. **(B)** Combined displacement curve of M3 coal seam.

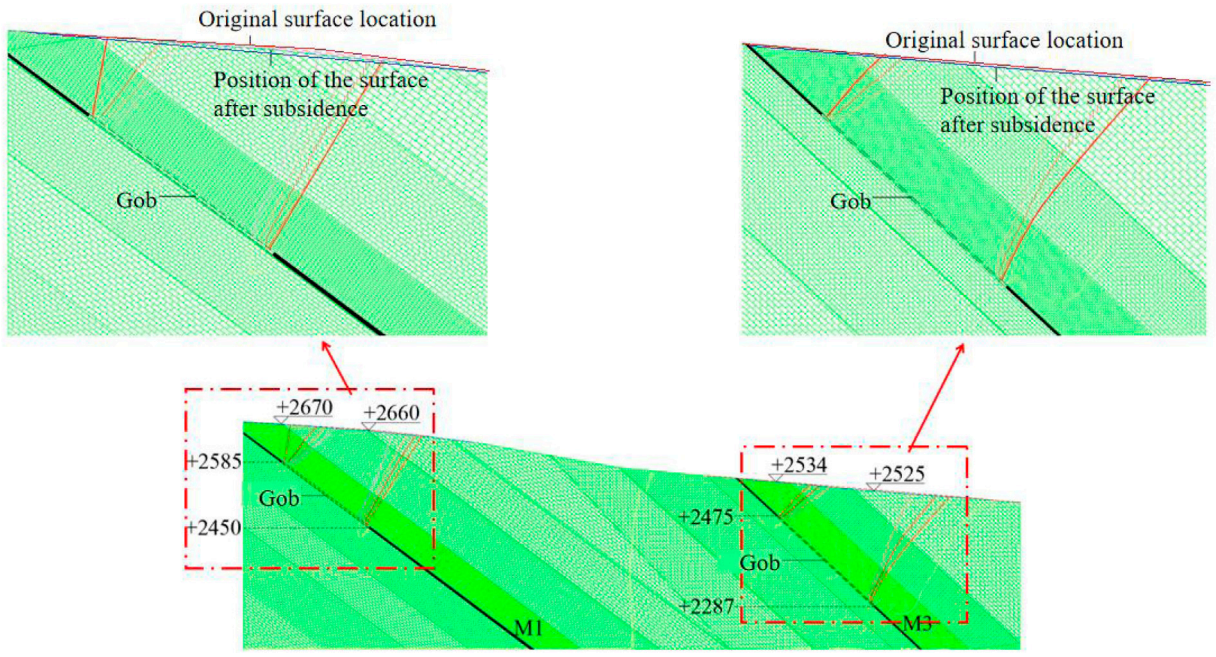

FIGURE 12
Contour map of coal seam excavation subsidence.

The analysis showed that the stress concentration area and the displacement change area were highly coincident, and the displacement monitoring map was consistent with the horizontal displacement cloud analysis, showing a ' U′-type distribution. Under different rock depths, the closer to the coal seam mining area, the greater the displacement change, and the farther away from the main subsidence area, the smaller the overburden displacement change. It was proved that the numerical simulation results do have theoretical guidance for mining subsidence control.

4.4 Analysis of surface movement

In the process of numerical simulation, the overlying strata of the coal seam bent and sunk, and the strata close to the mined-out area of the coal seam bent more. Correspondingly, the strata far from the mining area were less affected by mining and the subsidence was less. Combined with displacement monitoring data and numerical simulation results, it can be seen that the mined-out area made the overlying strata collapse, and the deformation continuously developed from the roof to the surface, and the original surface sunk, as shown in

TABLE 3 Predicted boundary angle, movement angle, and fracture angle under sufficient conditions (unit: °).

Coal seam mining and direction	Boundary angle/°	Moving angle/°	Fissure angle/°
M1 uphill direction	64	79	101
M1 downhill direction	43	49	58
M3 uphill direction	80	105	133
M3 downhill direction	40	46	61

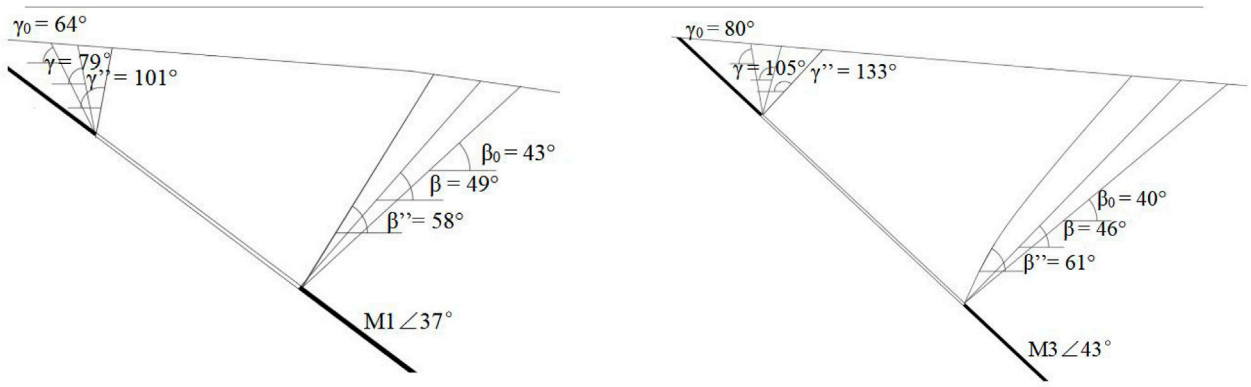

FIGURE 13
Schematic diagram of the boundary angle, movement angle, and fracture angle.

Figure 12, in which the red dotted line is the original surface position and the blue dotted line is the surface position after subsidence.

Table 3 shows the predicted boundary angle, moving angle, and crack values under sufficient conditions. Combined with the boundary angle, movement angle, and fissure angle of M1 and M3 in Table 3, the schematic diagram of boundary angle, movement angle, and fissure angle of M1 and M3 could be obtained, as shown in Figure 13.

Among them, under the condition of full mining or near full mining, the angle formed by the boundary crack and the horizontal line on the side of the coal pillar was called the fissure angle. Under the condition of full mining or close to full mining, the measured subsidence curved on the main section of the surface movement basin was used, and the point with a subsidence value of 10 mm was taken as the boundary point. The angle between the line connecting the boundary point to the goaf boundary and the horizontal line on the side of the coal pillar was called the boundary angle. The moving angle was the angle between the horizontal line and the line connecting the critical deformation point and the goaf boundary at the edge of the subsidence area. These three together determined the safety status of the mine and the surrounding buildings at this time.

From the analysis of Table 3 and Figure 13, it was inferred that the subsidence of the coal seam would not threaten the safety of the surrounding buildings and residents' lives and properties.

5 Conclusion

Based on special geological conditions, mining conditions, and abundant measured data in the Xiaomeidong mining area, the research idea of 'transient electromagnetic detection-numerical simulation' was put forward to explore its role in the prevention and control of geological disasters (Huang et al., 2020, Huang et al., 2020, Zhang et al., 2021).

1. Through the geophysical analysis of the old mined-out area of the Xiaomeidong mine, the predicted water-rich area of coal mine goaf subsidence obtained from the results was basically consistent with the weak water-rich area and the historical coal seam mining area of the Xiaomeidong coal mine, and it was used as the basis of numerical simulation.
2. The results of numerical simulation showed that under the action of *in situ* stress, there was an obvious tensile stress zone at the top of the mined-out area in the old mined-out area, and the overlying strata were separated and collapsed, forming a caving zone. The peak displacement of the coal seam roof was concentrated at the top of the goaf. The more the distance from the center of the mining area, the smaller the subsidence displacement.
3. Through the analysis of the subsidence change of the coal seam goaf, it was known that the boundary angle, moving angle, and fissure angle of M1 and M3 coal seams were within the safe range after mining, so they would not pose a threat to the life and property safety of Xiaomeidong village and nearby residents. In addition, it was necessary to further compare the simulation results with the real-time monitoring results to further improve the evaluation results.

Data availability statement

The original contributions presented in the study are included in the article/Supplementary Material. Further inquiries can be directed to the corresponding author.

Author contributions

Z-XW was responsible for field investigation and data curation. J-HD was responsible for the method. MZ was responsible for the method and writing. F-HX was responsible for the method. Y-JL was responsible for field investigation. LF was responsible for data curation. All authors contributed to the article and approved the submitted version.

Funding

This project was supported by the Open Fund of Engineering Research Center of Catastrophic Prophylaxis and Treatment of Road and Traffic Safety of Ministry of Education (Changsha University of Science and Technology) (kfj180404).

Conflict of interest

The authors declare that the research was conducted in the absence of any commercial or financial relationships that could be construed as a potential conflict of interest.

Publisher's note

All claims expressed in this article are solely those of the authors and do not necessarily represent those of their affiliated organizations, or those of the publisher, the editors, and the reviewers. Any product that may be evaluated in this article, or claim that may be made by its manufacturer, is not guaranteed or endorsed by the publisher.

References

Abhay Kumar, B. H. A. R. T. I., Pal, S. K., Saurabh, S., Singh, K. K. K., Singh, P. K., Prakash, A., et al. (2019). Groundwater prospecting by the inversion of cumulative data of wenner–schlumberger and dipole–dipole arrays: A case study at turamdih, Jharkhand, India. *Earth Syst. Sci.* 128, 107. doi:10.1007/s12040-019-1137-2

Boris, B. (1997). *Numerical modeling of complex slope deformations*. Canada Dissertation of Department of Geological Science,University of Saskatchewan.

Chang, Z., Du, Z., Zhang, F., Huang, F., Chen, J., Li, W., et al. (2020). Landslide susceptibility prediction based on remote sensing images and gis: comparisons of supervised and unsupervised machine learning models. *Remote Sens.* 12, 502. doi:10.3390/rs12030502

Diao, C. C. (2011). Development characteristics of ground fissures in Fushun urban area. *J. Liaoning Univ. Eng. Technol. Nat. Sci. Ed.* 30 (3), 420–422.

Epov, M. I., Shurina, E. P., and Nechaev, O. V. (2007). 3D forward modeling of vector field for induction logging problems. *Russ. Geol. Geophys. s* 48 (9), 770–774. doi:10.1016/j.rgg.2006.05.003

Huang, F. M., Cao, Z. S., Guo, J. F., Jiang, S. H., and Guo, Z. Z. (2020). Comparisons of heuristic, general statistical and machine learning models for landslide susceptibility prediction and mapping. *CATENA* 191, 104580. doi:10.1016/j.catena.2020.104580

Huang, F. M., Cao, Z. S., Jiang, S. H., Zhou, C. B., Huang, J. S., and Guo, Z. Z., (2020). Landslide susceptibility prediction based on a semi-supervised multiple-layer perceptron model. *Landslides* 17, 2919–2930. doi:10.1007/s10346-020-01473-9

Huang, F. M., Jing, Z., Wang, Y., Huang, J., and Zhu, L. (2020). A deep learning algorithm using a fully connected sparse autoencoder neural network for landslide susceptibility prediction. *Landslides* 17 (01), 217-229. doi:10.1007/s10346-019-01274-9

Ji, L., Zhao, J. J., Wan, X., Li, Q. M., and Wu, S. G., (2022). Study on the influence of goaf location on the deformation of high and steep hard rock slopes. *People's Pearl River* 43 (3), 66–76. doi:10.3969/j.issn.1001-9235.2022.03.009

Jiang, S. H., Huang, J. S., Huang, F. M., Yang, J. H., Yao, C., and Zhou, C. B. (2018). Modelling of spatial variability of soil undrained shear strength by conditional random fields for slope reliability analysis. *Appl. Math. Model.* 63, 374–389. doi:10.1016/j.apm.2018.06.030

Lei, Z. Y. (2018). *Study on roof instability law and control of fully mechanized top coal caving face in steeply inclined coal seam*. Xi'an, China Xi'an University of Science and Technology.

Li, X. L., Hu, C. Y., Sun, Q. F., and Zhang, Z., (2019). UDEC software is used to study the stress distribution in the collapsed process of mine goaf. *Guizhou Geol.* 36 (3), 254–260.

Liu, T. G., Li, G. J., Ma, X. Y., Yu, C. L., and Wang, C. J., (2010). Genesis analysis and risk prediction of ground fissures in Jingyu County, Jilin Province. *Chin. J. Geol. Hazards Prev.* 21 (1), 136–139. doi:10.16031/j.cnki.issn.1003-8035.2010.01.031

Shi, L. K., and Liu, H. Y. (2010). Application of high density resistivity method in goaf detection. *J. North China Inst. Water Resour. Hydro Power* 31 (5), 122–123. doi:10.19760/j.ncwu.zk.2010.05.035

Wang, L., Wang, S. M., Chen, X., Zhai, H., and Zhang, P., (2021). UDEC numerical simulation study on dynamic development characteristics of coal seam roof separation in wenjiapo mine. *Min. Technol.* 21 (05), 109–112. doi:10.13828/j.cnki.ckjs.2021.05.031

Weng, L. Y. (2019). *Study on the law of overburden and surface deformation in Deep Strip Mining considering the dynamic response of overburden mining*. Qingdao, China Shandong University of Science and Technology.

Yan, H. Y. (2019). *Study on the formation mechanism of jianshanying deformation body in faer coal mine, Guizhou Province*. Chengdu, China Chengdu University of Technology.

Zhang, Y. H., Dai, Y. S., Wang, Y., Huang, X., Xiao, Y., and Pei, Q. M., (2021). Hydrochemistry, quality and potential health risk appraisal of nitrate enriched groundwater in the Nanchong area, southwestern China. *Sci. Total Environ.* 784, 147186. doi:10.1016/j.scitotenv.2021.147186

Zhang, Y. H., Hu, X. B., Luo, H., Liu, Y., Yao, R. W., Ji, D., et al. (2023). Identifying the change of seepage field in karst aquifer under tunnel engineering: insight from feflow modelling. *Lithosphere* 2021, 6044574. doi:10.2113/2021/6044574

Zhao, M., Chen, L. Y., Wu, H. G., Guo, W., and Ye, C. W, (2018). Computer microscopic test study on the suitability of modified polyimide grease used to improve collapsible loess railway subgrade. *CONCURRENCY COMPUTATION-PRACTICE Exp.* 24, 30. doi:10.1002/cpe.4900

Zhao, M., Chen, L. Y., Wang, S. Y., and Wu, H. G., (2020). Experimental study of the microstructure of loess on its macroscopic geotechnical properties of the Baozhong railway subgrade in Ningxia, China. *Bull. Eng. Geol. Environ.* 9 (79), 4829–4840. doi:10.1007/s10064-020-01816-9

Zhao, M., Guo, W., Chen, L. Y., and Wang, S. Y., (2019). Experiment on the frost resistance of modified phospho gypsum: A case used to improve baozhong railway subgrade loess. *J. Mt. Sci.* 12 (16), 2920–2930. doi:10.1007/s11629-018-5014-2

Zhao, M., Wu, H. G., Guo, W., Tan, B. R., Hu, C., Deng, R., et al. (2022). Experimental study of the particle agglomeration on its mechanical properties of collapsible loess. *Front. EARTH Sci.* 10. 943383 doi:10.3389/feart.2022.943383

frontiers | Frontiers in Earth Science

TYPE Original Research
PUBLISHED 12 September 2023
DOI 10.3389/feart.2023.1194446

OPEN ACCESS

EDITED BY
Yunhui Zhang,
Southwest Jiaotong University, China

REVIEWED BY
Danqing Song,
South China University of Technology, China
Chun Zhu,
Hohai University, China
Rui Yong,
Ningbo University, China

*CORRESPONDENCE
Zhao Zihao,
hua1sheng23@126.com

RECEIVED 27 March 2023
ACCEPTED 28 August 2023
PUBLISHED 12 September 2023

CITATION
Sen K and Zihao Z (2023), Detection and evolution of disaster sources in high slopes of open-pit mines based on time-lapse high-density electricity method. *Front. Earth Sci.* 11:1194446. doi: 10.3389/feart.2023.1194446

Detection and evolution of disaster sources in high slopes of open-pit mines based on time-lapse high-density electricity method

Kang Sen and Zhao Zihao*

School of Mining and Coal, Inner Mongolia University of Science and Technology, Baotou, China

High and steep slopes in open pit mines used for ore production require careful monitoring to ensure stability and safeguard lives, property, and social welfare. Understanding the evolutionary characteristics of hazard sources within these slopes is crucial for effective slope management. This article presents a novel approach to identify the evolution of hazard sources within slopes by utilizing the derivative of normalized inversion data versus time as a characteristic feature. To analyze the evolution of hazard sources, raw apparent resistivity data collected at different times are processed using smoothing and wavelet denoising algorithms to reduce noise. Geological constraints are then applied to the collected data through the parametric region method. The least squares method is employed for independent inversion, and the inversion results are standardized. Subsequently, the standardized inversion results are used to derive the derivative of resistivity versus time equation, which reveals the evolution of hazard sources within the slope. A case study is conducted on a large open pit rocky slope to analyze the effectiveness of the proposed approach. The results demonstrate the successful reduction of noise through the smoothing and wavelet threshold denoising algorithms, effectively suppressing interference caused by acquisition equipment and environmental electromagnetic noise. The application of the parametric region method with geological constraints highlights the spatial and temporal evolution characteristics of hazard sources within the slope. The findings indicate varying degrees of evolution of hazard sources within the slope, with significant changes observed mainly in the shallow part influenced by water erosion and blasting vibration. Areas with lithological stability show minimal changes, while original hazard source areas have evolved to different extents, distinguishable based on the size and sparsity of contour values. By combining inversion data analysis, noise reduction techniques, and geological constraints, the proposed approach provides valuable insights into the evolution of hazard sources within slopes. This information can aid in the development of effective slope management strategies in open pit mines, contributing to enhanced safety and protection of valuable assets.

KEYWORDS

slope of open-pit mine, time-lapse high-density electricity method, apparent resistivity, evolution of disaster sources, geophysical inversion

1 Introduction

China's annual demand for ore is substantial, with a significant portion being sourced from open-pit mines. Open-pit mining represents a widespread method for mineral and resource extraction from the Earth's surface, and its implementation demands meticulous management of unique hazards and risks. These operations entail the excavation of extensive amounts of earth and rock, engendering steep slopes and towering walls. The slopes associated with open-pit mining pose significant dangers of instability, resulting in slope failures, landslides, and rockfalls. Through the identification and assessment of hazard sources, such as unstable geological formations, weak rock layers, and excessive slope angles, mining engineers can adopt appropriate slope stabilization measures, design secure access roads, and establish monitoring systems to detect incipient signs of instability. Such measures ensure the safety of workers and forestall accidents and injuries relating to slope failures. However, the occurrence of landslide accidents in these mines poses a major challenge to the expansion of their production. Addressing slope safety concerns is crucial for mitigating this issue. Given that safety primarily relies on preventive measures, effective control of the dynamic changes in the slope's medium becomes paramount.

The conventional high-density resistivity method is a geophysical technique used to investigate the subsurface properties of the Earth. It involves measuring the electrical resistivity of the ground at multiple locations to create a resistivity image or model. In this method, a series of electrodes are placed at regular intervals along a survey line or grid. Typically, the electrodes are inserted into the ground, and an electrical current is injected into the Earth through one pair of electrodes. The resulting potential difference is measured using another pair of electrodes. By varying the electrode configurations and measuring the potential differences at different locations, a resistivity profile of the subsurface can be obtained. The resistivity of the subsurface materials plays a crucial role in this method. Different geological formations and structures, such as bedrock, clay, water-bearing zones, or mineral deposits, have varying resistivity values. By analyzing the resistivity data, geophysicists can infer the subsurface lithology, identify potential groundwater resources, locate mineral deposits, and map geological structures (Dupis, 1980; Loke and Barker, 1996; Loke et al., 2013).

In the field of engineering practice and research, ensuring mine safety and accurately predicting the timing of slope damage occurrence often involves the establishment of a numerical model for the slope's geotechnical body. This approach allows for the simulation of the progressive collapse process of the slope, aiding in the enhancement of safety measures (Du and Song, 2022; Bao et al., 2023; Du et al., 2023; Ren et al., 2023; Song and Du, 2023). Simultaneously, to preserve slope stability, the placement of anchors within the slope body is frequently implemented, thereby reinforcing slope stability through the enhancement of anchor performance (Wang Q. et al., 2022; Li et al., 2023).

The high-density electrical method collects more data and has a good application effect in detecting slope damage sources. The high-density electrical method offers a comprehensive approach for assessing and analyzing slope safety by detecting faults, fracture zones, and water-conducting fissure zones within a slope. This geophysical technique enables a thorough evaluation of potential hazards and provides valuable insights into slope stability. (Dong and Wang, 2003; Hojat et al., 2019; Lin et al., 2019). The high-density electrical method can also be employed to measure the water content within the slope. This capability allows for a comprehensive assessment of the slope's hydrological conditions, providing important information for evaluating slope stability and potential water-related risks (Lu et al., 2023).

However, the conventional resistivity method can only identify the underground fault sources and cannot reflect the dynamic changes of the fault sources. However, the time-lapse high-density resistivity method can not only show the electrical properties of underground media but also obtain the changes in underground electrical structures by analyzing multiple detection data of the same section at different times (Doetsch et al., 2010; Boyd et al., 2021). The time-lapse high-density resistivity method excels in providing high-resolution imaging of subsurface variations over time. It facilitates in-depth insights into spatial and temporal changes in resistivity, enabling a comprehensive understanding of dynamic subsurface processes. This level of resolution is particularly advantageous for detecting and evaluating disaster sources in the high slopes of open-pit mines, where even small-scale changes can significantly impact slope stability. In comparison with invasive techniques such as drilling or excavation, the time-lapse high-density resistivity method is non-invasive. It eliminates the need for physical disturbance of the site, making it a cost-effective and environmentally friendly option. This advantage holds particular importance when assessing large areas or conducting long-term monitoring campaigns. The time-lapse high-density resistivity method surpasses other geophysical techniques with its high resolution, real-time monitoring capabilities, sensitivity to fluid migration, non-invasive nature, cost-effectiveness, and potential for integration with complementary methods. These advantages make it an invaluable tool for disaster detection and evaluation, particularly in high slopes of open-pit mines, where proactive risk management and effective mitigation strategies are crucial.

At present, it has achieved good application results in dynamic detection of oil and gas reservoirs, groundwater pollution, leak detection of dams, and leak detection of hazardous substances in landfills (Johnson et al., 2021; Norooz et al., 2021; Zhang et al., 2022). In the process of open pit mining, the rock and soil mass of the slope is always in a state of deformation, and its internal electrical structure also changes in real time. It is of great significance for slope safety to master the evolution law of disaster sources in the slope. Therefore, the study of hazard source evolution has also become a current research hotspot (Loke et al., 2013; Lapenna and Perrone, 2022). The study area is located on the northwest border of Baotou City. After 60 years of mining, a large mine has formed a high and steep slope of more than 200 m. In recent years, several cave-ins have occurred. The rock mass of the open pit slope is mainly dolomite and schist and contains a small amount of macular dyke and mica schist. However, the main rock of the slope, dolomite, is different in different regions due to various complex geological processes such as alteration, weathering, and erosion. At the same time, there are 108 geologically identifiable slope faults, mainly in an east-west direction, due to geological formations. The stable dolomite body contains a variety of lithologies such as iron-rich oxidized dolomite, mica, and sodalite (Zhongxin et al., 1992;

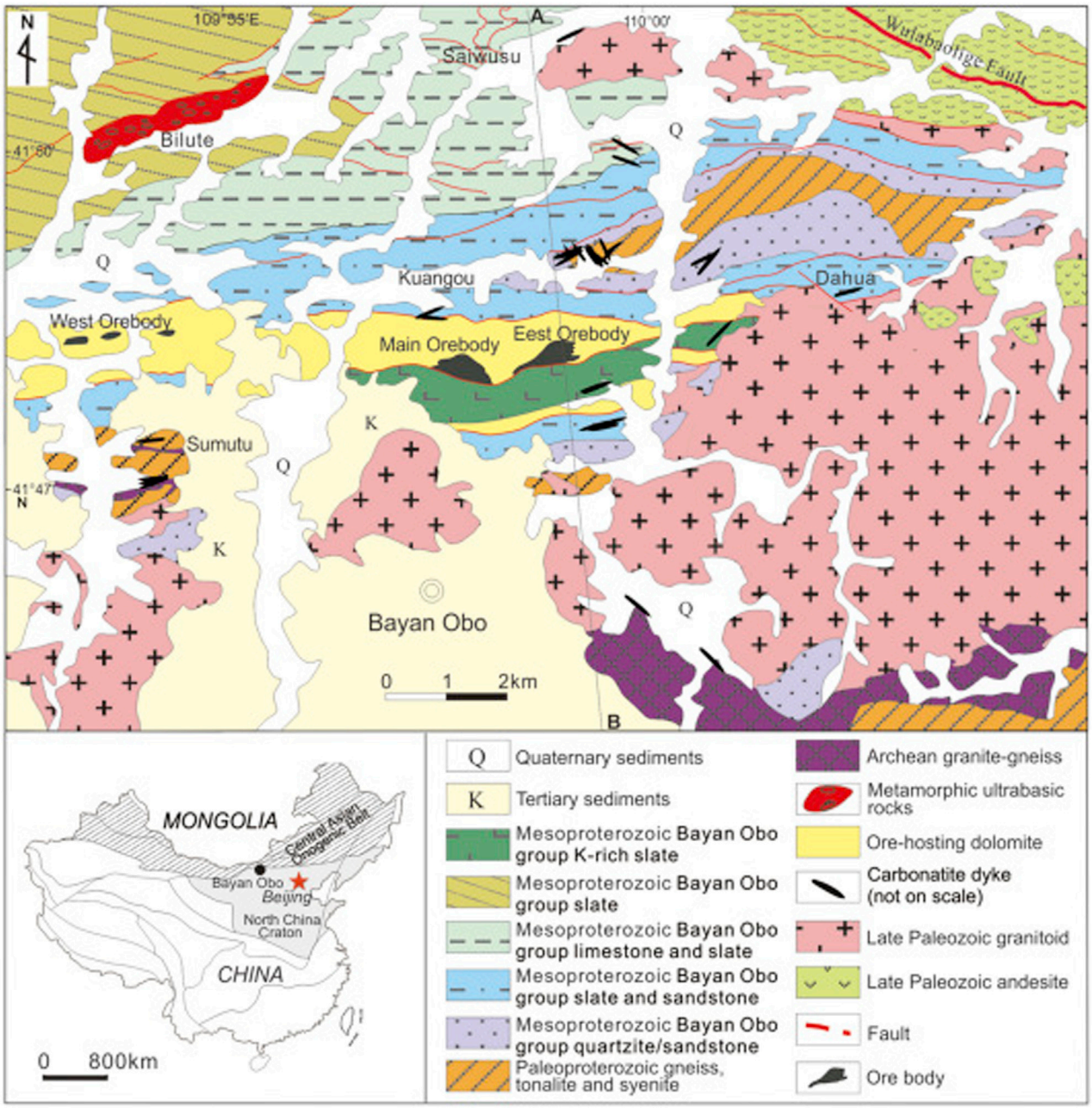

FIGURE 1
Geological sketch map of the Bayan Obo area, northern China. Cited after (Fan et al., 2016).

Fan et al., 2016; Wang et al., 2019). In this study, the rock slope of a large open pit mine was taken as the research object. In 2016, the high-density electrical method was used to explore the slope, and the geophysical data body of the slope was established according to factors such as weak structure fracture zone, lithology, and groundwater extracted from the geophysical data. The slope stability and rock mass characteristics at different depths were analyzed in detail, and the distribution of fault sources was finally determined. In 2020, the mine slope landslide occurred.

The landslide-affected region falls within the designated key geological disaster prevention and control area, as established in 2016. Building upon this designation, the mine successfully predicted slope collapses by integrating slope deformation warning radar data. Analysis of the exposed geological formations following the landslides validated the efficacy of the high-density electrical method in detecting disaster sources within the mine slope. To gain insight into the status of disaster sources in non-landslide areas, understand their evolutionary patterns within the mine slope, and enhance slope disaster prevention and control measures, repeated high-density electrical explorations were conducted in the non-landslide section of the mine slope in 2022. The derivative order and isoline distribution of high-density electrical data over time were employed to visualize the dynamic evolution of the disaster sources within the slope.

2 Overview of the open pit mine slope

2.1 Geology

The mine is situated in a town within Baotou City, located in the Inner Mongolia Autonomous Region. The region is characterized by expansive grasslands and plateau hills and falls within the inland dry climate zone. It experiences the influence of cold air masses originating from Siberia, Lake Baikal, and Wendur Khan, resulting in low temperatures, minimal precipitation, dry and windy conditions, and significant temperature fluctuations. During the summer, there is a concentration of short-term rainfall, and in recent years, there has been an increase in summer rainfall compared to historical records, likely due to warming trends (Wang X. et al., 2022).

The Bayan Obo REE-Nb-Fe deposit is located in the Bayan Obo continental margin rift in the north of the NCC. The ore-hosting dolomites, covered by K-rich slate (H9 term) and extending 18 km from east to west with approximately 2 km width (Figure 1), were once considered as a component of Bayan Obo Group, called H8 term. The origin of the dolomites is still disputed, and it has been proposed to be either sedimentary (Yang et al., 2009; Lai et al., 2012), or carbonatite rel (Yang et al., 2011; Zhu et al., 2015). Basement rocks at Bayan Obo are composed of Neoarchean mylonitic granite-gneiss (2,588 ± 15 Ma), Paleoproterozoic syenite and granodiorite (2018 ± 15 Ma), and biotite granite-gneiss and garnet-bearing granite-gneiss (−1890 Ma). Dioritic-granitic plutons, composed of gabbro, gabbroic diorite, granitic diorite, adamellite, and biotite granite, are distributed within a large area in the south and east Bayan Obo mine (Figure 1). These plutons were once regarded as intruding from Devonian to Jurassic. New geochronology data reveal that these plutons were formed in a post-collisional tectonic regime at convergent margins in the late Paleozoic at a narrow time from 263 to 281 Ma with a peak age of 269 Ma.

FIGURE 2
Extent of lateral slope collapse and the affected area.

2.2 Geological hazards

Based on the site investigation and regional information, it has been determined that the southwest side of the quarry primarily consists of the Quaternary rock group, comprising layers of powder clay and gravel, among others. The main rock groups present in the slope include the slate rock group, dolomite rock group, mica schist rock group, and pyroxene veins. Notably, there is no distinct boundary between the slate rock group and the dolomite rock group, resulting in a complex geological structure. The area is characterized by extensive fault development, with numerous fault fragmentation zones. These fragmentation zones exhibit high water content, and evidence of groundwater erosion can be observed, particularly in the weathering zone of the upper part of the slope and in association with fault influences. Among the identified geological features, certain disaster sources such as cis-layer fracture zones, pyroclastic veins, and mica rocks are known to induce slope collapse occurrences. These factors play a significant role in the stability and potential hazards of the slope.

The slope collapse posed a direct threat to the safety of production personnel and had significant implications for the haul road and ecological restoration of the slope. Furthermore, it resulted in the generation of substantial amounts of rock dust and contributed to an increase in sandstorms within the surrounding residential areas. As a consequence of the slope collapse, approximately 800 m of the haul road were destroyed, exacerbating the instability of the slope.

The slope collapse has presented a significant challenge in terms of slope management. Currently, the No. 1 sweeping platform area has suffered complete destruction, and ongoing rockfall poses a persistent hazard. The No. 2 production and transportation area has experienced significant accumulation due to the collapse, with the impact continuing to expand. Additionally, there is a potential for further collapse in the No. 3 area (Figure 2). Previous minor collapses in area 4 have been reinforced, while the soft rock formations in area 5 of the sweeping platform have accumulated due to weathering and blasting vibrations (Figure 3).

3 Exploration method of the disaster sources in the high slopes of open-pit mines

3.1 Principle of the time-lapse high-density resistivity method forward calculation

In the actual measurement of the high-density electrical method, all electrodes are simultaneously placed on the measurement points,

FIGURE 3
Reinforcement area for side slope.

maintaining a specific interval between them. The reflected apparent resistivity profile is then processed and analyzed to extract information regarding the distribution of stratigraphy. This information can be utilized to delineate different geological layers, identify anomalous areas, and determine the locations of potential hazards. (Figure 4).

Open pit mining disrupts the original mechanical balance of slope rock layers. The rock and soil bodies in the slope are influenced by various factors such as gravity, freeze-thaw weathering, continuous rainfall, groundwater movement, and periodic blasting. As a result, they undergo continuous dynamic changes in order to regain mechanical equilibrium, albeit on a macroscopic scale these changes may be minute. Traditional high-density electrical methods only provide information on the distribution of hazard sources at the time of exploration through the detection of subsurface electric fields. They fail to capture the evolving nature of hazard sources within the slope. Various factors contribute to the evolution of potential hazard sources, including faults, fractures, and weak inclusions within the original rock. When an originally stable rock layer fractures to form a fracture zone, the apparent resistivity increases when the water content of the rock layer is low and decreases when the fracture zone is water-filled. The apparent resistivity also increases as faults develop and expand, particularly in areas of higher resistivity, and decreases when faults are filled. Weak inclusions undergo increased fracturing due to weathering, resulting in a decrease in apparent resistivity when water content is high, and an increase when porosity increases under external forces.

In summary, as hazard sources evolve, the resistivity of the corresponding area undergoes changes. These electrical variations serve as the basis for time-shifted high-density electrical exploration. The time-shifted high-density electrical method introduces a time dimension to the conventional approach. By conducting multiple high-density electrical surveys over time on the same section, it becomes possible to obtain resistivity distribution data for different time periods. These resistivity distribution characteristics can then be utilized to study the evolution of underground fault sources over time, influenced by external forces. (Lesparre et al., 2017; Liu et al., 2017).

In a homogeneous isotropic medium, the current field obeys the following laws (Purcell and Morin, 2013):

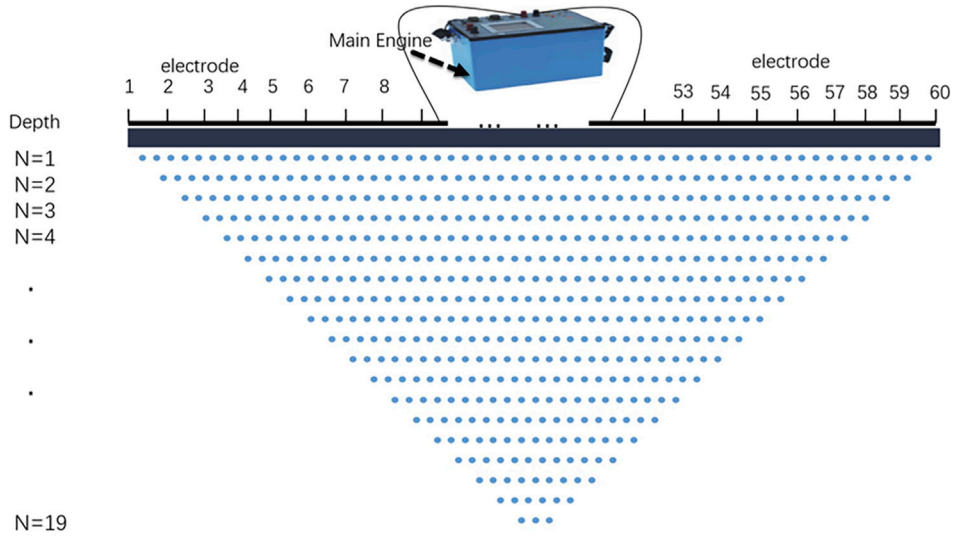

FIGURE 4
Schematic diagram of high-density electrical detection.

$$\boldsymbol{j} = \boldsymbol{\sigma E} \tag{1}$$

Where j is the current density, σ is the conductance, and E is the electric field strength. U represents the electric potential (also known as voltage) at a point in an electric field relative to infinity. According to the nature of the stable current field as a potential field, the relationship between the electric field strength and the potential is satisfied as follows (Purcell and Morin, 2013):

$$\boldsymbol{E} = -\nabla \boldsymbol{U} \tag{2}$$

Assuming that a point source of current magnitude I is placed at point A (x_A, y_A, z_A) underground, the underground current field satisfies the following differential equation (Purcell and Morin, 2013):

$$\frac{\partial}{\partial \boldsymbol{x}}\left(\boldsymbol{\sigma}\frac{\partial \boldsymbol{U}}{\partial \boldsymbol{x}}\right) + \frac{\partial}{\partial \boldsymbol{y}}\left(\boldsymbol{\sigma}\frac{\partial \boldsymbol{U}}{\partial \boldsymbol{y}}\right) + \frac{\partial}{\partial \boldsymbol{z}}\left(\boldsymbol{\sigma}\frac{\partial \boldsymbol{U}}{\partial \boldsymbol{z}}\right) = -\boldsymbol{I}\boldsymbol{\delta}(\boldsymbol{x}-\boldsymbol{x}_A)\boldsymbol{\delta}(\boldsymbol{y}-\boldsymbol{y}_A)\boldsymbol{\delta}(\boldsymbol{z}-\boldsymbol{z}_A) \tag{3}$$

where σ is σ(x, y, z) and δ is the Dirac function.

The time-shifted resistivity method is employed to study the spatial and temporal evolution of slope hazard sources by conducting multiple surveys along the same profile while keeping the coordinates of the excitation source and receiving electrode unchanged. The resistivity values obtained represent the relative resistivity of the surveyed area. Under the theoretical assumption that only the changes in slope hazard sources under external forces are considered, the evolution of these hazard sources leads to variations in the relative resistivity of the surveyed area. By monitoring the resistivity of the area and analyzing the changes in resistivity over time, we can discern the evolutionary patterns of hazard sources in response to external forces.

To simplify the analysis, we assume that the electrical properties of the subsurface medium do not change along the direction perpendicular to the measurement profile (i.e., no changes in the *y*-axis direction). Consequently, the four-dimensional problem is reduced to a three-dimensional problem, specifically the changes in resistivity of the two-dimensional profile in the time dimension. By employing the cosine Fourier transform, we eliminate the *y*-axis and obtain a time-shifted partial differential equation in the wave number domain, which describes the stable current field.

$$\frac{\partial}{\partial \boldsymbol{x}}\left(\boldsymbol{\sigma}(\boldsymbol{x},\boldsymbol{z},\boldsymbol{t})\frac{\partial \boldsymbol{V}}{\partial \boldsymbol{x}}\right) + \frac{\partial}{\partial \boldsymbol{z}}\left(\boldsymbol{\sigma}(\boldsymbol{x},\boldsymbol{z},\boldsymbol{t})\frac{\partial \boldsymbol{V}}{\partial \boldsymbol{z}}\right) - \boldsymbol{\lambda}^2\boldsymbol{\sigma V} = -\boldsymbol{f} \tag{4}$$

where $V(\lambda, x, z)$ is the spatial domain potential, $U(x, y, z)$ is the wavenumber domain potential after cosine Fourier transform, t is time, and λ is called the wavenumber or Fourier transform variable, $\sigma = \sigma(x, z), V = V(\lambda, x, z), and\ f = \frac{1}{2} I\delta(x - x_A)\delta(z - z_A)$.

The resistivity measured during high-density electrical logging represents the resistivity of a specific region within the subsurface medium. When considering the measurement area as a whole, the change in resistivity over time can be represented by a resistivity curve. The first-order derivative of this curve indicates the rate of resistivity change within the subsurface medium, while the second-order derivative reflects the sharpness of resistivity changes in the area. The resistivity derivative for a point on the curve can be approximated theoretically using a Taylor series expansion, which allows us to analyze and understand the variations in resistivity.

$$\boldsymbol{\rho}(\boldsymbol{t}_{i+1}) = \boldsymbol{\rho}(\boldsymbol{t}_i) + \boldsymbol{\rho}'(\boldsymbol{t}_i)\boldsymbol{h} + \frac{\boldsymbol{\rho}''(\boldsymbol{t}_i)}{\boldsymbol{2}}\boldsymbol{h}^2 + \cdots \tag{5}$$

ρ(t) is the resistivity as a function of time, $\rho(t_i)$ is the resistivity of the region at time i, $\rho'(t)$ is the rate of change of resistivity with respect to time, $\rho'(t_i)$ is the rate of change of resistivity at time t_i , $\rho(t_{i+1})$ is the resistivity of the region at time $i + 1$, and t_{i+1} differs from time t_i by h time.

After deformation, it can be written in the following form:

$$\boldsymbol{\rho}'(\boldsymbol{t}_i) = \frac{\boldsymbol{\rho}(\boldsymbol{t}_{i+1}) - \boldsymbol{\rho}(\boldsymbol{t}_i)}{\boldsymbol{h}} - \frac{\boldsymbol{\rho}''(\boldsymbol{t}_i)}{\boldsymbol{2}}\boldsymbol{h} + \boldsymbol{O}(\boldsymbol{h}^2) \tag{6}$$

where $\rho''(t_i)$ is the second-order derivative of the resistivity at time t_i and $O(h^2)$ is the second error residual term.

In the process of development of the fault zone, the larger the absolute value of $\rho'(t_i)$, the area where the resistivity changes drastically, the more the fault zone can be expanded; the more the fault zone remains stable and the rock layer is not destroyed, the smaller the absolute value of $\rho'(t_i)$, the area where the resistivity does not change basically.

Eq. 4 represents a partial differential equation that describes the electrical properties of the subsurface medium. It considers changes in resistivity along the x and z directions and introduces the wavenumber variable λ. By incorporating the cosine Fourier transform, the equation simplifies the problem from four dimensions to three dimensions by eliminating the *y*-axis. This equation is essential for modeling the stable current field and understanding the temporal changes in resistivity within the subsurface medium. Eq. 5 characterizes the temporal variations in resistivity within the subsurface medium. It utilizes a Taylor series expansion to approximate the resistivity derivative at a specific point on the resistivity curve. The equation highlights the relationship between the first-order derivative (rate of resistivity change) and the second-order derivative (sharpness of resistivity changes). This equation provides a theoretical basis for analyzing and interpreting resistivity variations, which are crucial for understanding subsurface geological features and phenomena. Eq. 6 further refines the description of the resistivity derivative by providing a more explicit formulation. It demonstrates that the rate of resistivity change at a given time point can be approximated by the difference in resistivity between consecutive time points divided by the time interval (h), subtracting the second-order derivative term, and incorporating an error residual term. This equation enables a quantitative assessment of resistivity changes and offers insights into the deformation and stability of fault zones within the subsurface.

In summary, Eqs 4–6 play a significant role in this study by mathematically representing the electrical properties, resistivity changes, and behavior of fault zones within the subsurface medium. They contribute to the methodology by establishing the necessary theoretical framework and mathematical models for analyzing and interpreting data obtained through high-density electrical logging. These equations facilitate a deeper understanding of resistivity variations and their implications for subsurface geological structures and processes.

3.2 Principle of the time-lapse high-density resistivity method inversion

The least squares method is widely employed in high-density electrical inversion and serves as the basis for the inversion algorithm utilized in this study (Loke et al., 2014). In our approach, apparent resistivity data from the same profile obtained through high-density electrical sounding at different times are utilized. Anomalies are detected using a consistent threshold, and the same interpolation method is employed. Additionally, a common wavelet threshold is chosen for denoising the apparent resistivity data, thereby minimizing errors arising from the measurement system and environmental currents. Subsequently, the multi-period detection data are independently inferred, and the resulting inversion results are further processed to quantify the resistivity changes over time. This approach enables us to investigate the variations in resistivity within the time dimension (Camporese et al., 2015).

$$(\boldsymbol{J}^{\boldsymbol{T}}\boldsymbol{J} + \boldsymbol{\lambda F})\Delta \boldsymbol{q}_{\boldsymbol{k}} = \boldsymbol{J}^{\boldsymbol{T}}\boldsymbol{g} - \boldsymbol{\lambda F}\boldsymbol{q}_{\boldsymbol{k}} \tag{7}$$

Where: $F = \alpha_x C_x^T C_x + \alpha_y C_y^T C_y + \alpha_z C_z^T C_z$, C_x is the horizontal roughness filter, C_z is the vertical roughness filter, J is the Jacobi matrix of partial derivatives, J^T is the transpose of J, λ is the damping factor, q is the model change vector, g is the column vector of the difference between the apparent resistivity and the inverse model resistivity, and J is the matrix of order m by n of the measured apparent resistivity and the number of measurements.

4 Data processing

During the measurement process of the high-density electrical method, various sources of noise such as electrode grounding, undulating terrain, earth electric field, stray current from underground cables, and system noise from the measurement system can introduce artifacts and reduce the authenticity and clarity of the inverse image. In this study, we have employed the mean threshold filtering method to eliminate outliers and applied conformal interpolation to segment the outliers. Additionally, wavelet decomposition has been utilized to mitigate the influence of instrument system noise and environmental noise. The same threshold filtering and interpolation methods have been consistently applied to ensure the validity of the data obtained from different periods of the apparent resistivity data for the same profile (Fritsch and Carlson, 1980; Ferahtia et al., 2012). A comparison of the denoised third layer data from an exploration profile at the mine is as follows (Figure 5).

To highlight the spatial and temporal progression of the disaster source and mitigate the influence of potential coupling factors, we incorporate the fundamental concept of the reference region approach from the section linkage. This approach involves employing group-ordered clustering, relative coordinate transformation, and weighted averaging techniques to geologically constrain the profiles at the same location. In this approach, we identify a geologically stable region within the same location profile and assume it remains in a constant state throughout the monitoring period. This stable region serves as a reference point against which we can assess the impact of other factors on the disaster source region over time. By comparing the variations in the disaster source region with the reference region, we can better understand the spatial and temporal dynamics of the hazard. This approach helps to isolate the effects of other factors and provides a clearer picture of the evolution of the disaster source.

Data normalization plays a crucial role in highlighting the inherent trends of the data, reducing random noise and systematic errors, and providing a foundation for subsequent data denoising and analysis. There are primarily two common methods for data normalization: standardization and normalization.

Standardization involves transforming the data in such a way that it has a mean of zero and a standard deviation of one. This method ensures that the data distribution is centered around zero and has a consistent scale. Standardization is useful when the absolute values of the data are not as important as their relative differences or when the data have varying scales or units. Normalization, on the other hand, involves scaling the data to a specific range, typically between 0 and 1. This method maintains the relative proportions of the data and allows for easier interpretation and comparison across different variables. Normalization is particularly useful when the absolute values and the relationships between them are important. Both standardization and normalization methods have their advantages and can be applied depending on the specific requirements and characteristics of the data. The choice of method should be made based on the nature of the data and the goals of the analysis. Assuming that a total of 100 periods of high-density electrical exploration have been conducted and 100 sets of apparent resistivity data have been obtained, i =1–100 in $\rho(t_i)$, the common data normalization formula is as follows (Wilkinson et al., 2022):

$$\boldsymbol{\rho}_{\boldsymbol{si}} = \frac{\boldsymbol{\rho}_{\boldsymbol{i}}}{\sum \boldsymbol{\rho}_{\boldsymbol{i}}} \boldsymbol{i} = \mathbf{1}, \mathbf{2}, \cdots, \mathbf{100} \tag{8}$$

Where ρ_{si} is the normalized apparent resistivity data, ρ_i is the apparent resistivity measured at time i, and $\sum \rho_i$ is the sum of the apparent resistivity data at these one hundred times.

In this article, we use the normalization method, which can reduce the influence of large and small values during the measurement process. Assuming that the apparent resistivity data consists of two sets of data, the equation for the amount of resistivity change in the time dimension is as follows (Figure 6).

$$W = \frac{\left|\rho_0 - \rho_i\right|}{(\rho_0 + \rho_i)\Delta t} \tag{9}$$

Where W is the derivative of resistivity *versus* time (taking the absolute value to highlight the change in data); Δt is the interval between two high-density electrical probes; ρ_0 is the resistivity of the probe inversion in 2016; and ρ_i is the apparent resistivity of the probe inversion in 2022.

5 Fieldwork methods

The resistivity statistics provided in Table 1 illustrate the typical resistivity ranges of various rock types within the study area. Mica rocks exhibit the highest resistivity, usually exceeding 10,000 Ω m.

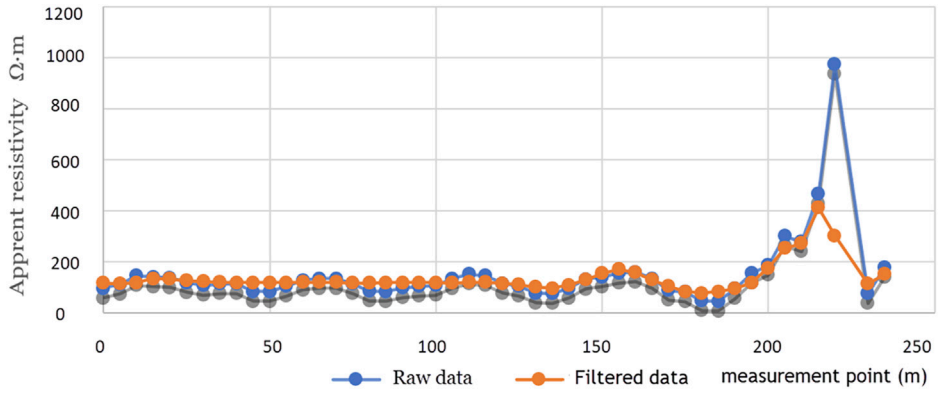

FIGURE 5
Comparison of before and after denoising of the third layer of apparent resistivity data.

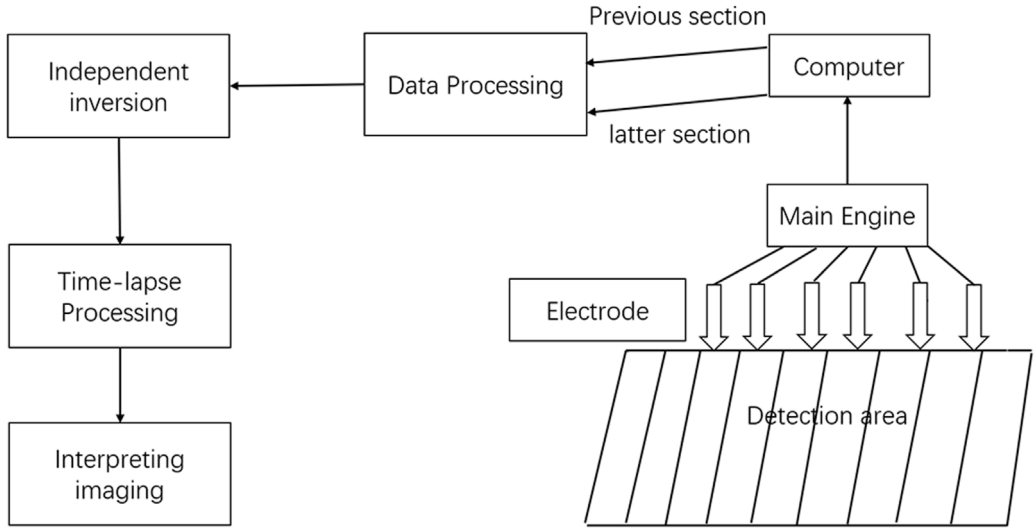

FIGURE 6
Working block diagram of the time-lapse high-density resistivity method.

TABLE 1 Resistivity characteristics of different strata in the study area.

Lithology	Range of resistivity values (Ω · m)
Quaternary Holocene series gravel layer, silty clay	12.5–50
Dolomite	6,000–50,000
Altered dolomite	200–3,000
Slate	30–300
Altered slate	10–60

Micaceous dolomites possess relatively high resistivity values, typically greater than 5,000 Ω m. Altered dolomites with high iron content exhibit lower resistivity, generally below 3,000 Ω m. Weak rock layers, such as sodium amphibolite dikes, display lower resistivity values, typically below 50 Ω m, due to their high water-bearing capacity. Fracture zones, characterized by the presence of natural surface water infiltration channels, exhibit low resistivity. These resistivity parameters serve as valuable indicators for determining the distribution of hazard sources within the slope. By analyzing the resistivity values of different

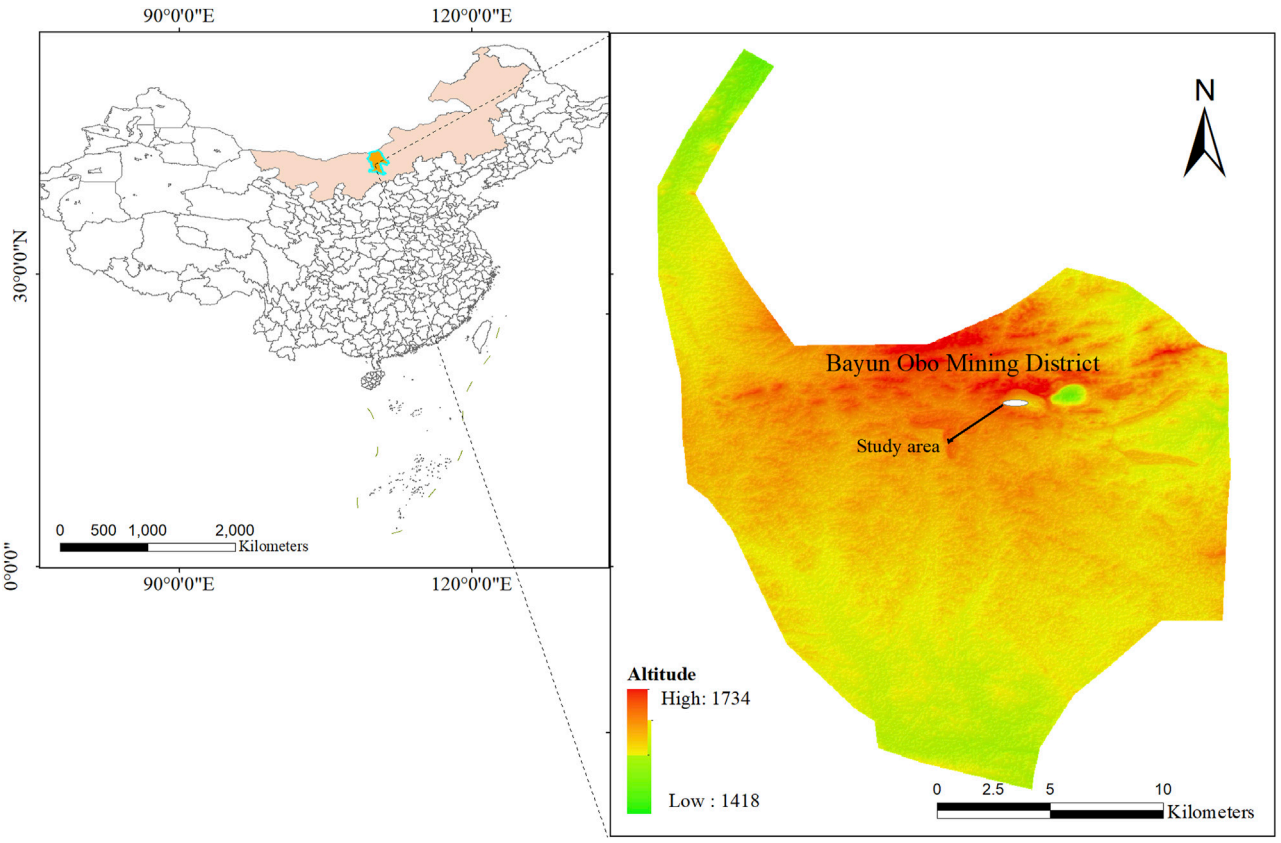

FIGURE 7
Location of the study area of the open mine, Inner Mongolia, China.

rock types, it becomes possible to infer the presence and characteristics of hazard sources, thereby contributing to the understanding and assessment of slope stability.

In 2016, we conducted an exploration of the slope using the high-density electrical method. Based on the physical exploration data, which included factors such as fault fracture zones, lithology, and groundwater, we established a comprehensive dataset of the slope. Detailed analysis of the slope stability and rock characteristics at different depths was performed, leading to the determination of the distribution of disaster sources within the slope. In 2020, a landslide occurred on the slope of the mine, and the affected area fell within the designated key geological disaster prevention and control area established in 2016. Utilizing the data obtained from the slope deformation early warning radar, we were able to successfully predict the occurrence of the landslide. Furthermore, the analysis of the exposed geological features after the landslide confirmed the effectiveness of the high-density electrical method in detecting the disaster sources within the slope.

To further investigate the situation of intra-slope hazard sources in areas where no landslide had occurred and to understand the evolutionary patterns of these hazard sources within the mine, a repeated high-density electrical exploration was conducted in 2022. The primary objective of this exploration was to demonstrate the dynamic evolution of intra-slope hazard sources by utilizing the derivative magnitudes and contour distribution of the high-density electrical method data with respect to time. By analyzing the changes in the high-density electrical data over time and observing the derivative magnitudes and contour distributions, we aim to gain insights into the temporal evolution of hazard sources within the slope. By employing the high-density electrical method and analyzing the resulting data, we aimed to provide valuable information for the prevention and control of slope hazards in the mine (Figures 7, 8).

In order to maintain consistency and comparability with the previous measurements conducted in 2016, the measurement lines were arranged in areas unaffected by the landslide that occurred in 2020. To ensure the position of the measuring lines remained unchanged, a GPS coordinate positioning device was used to select the same electrode points as in 2016. The electrodes were then placed at the same points, and the same measuring direction on the slope steps was maintained for arranging the high-density electrical measuring lines. For the measurements, the same high-density electrical measuring instrument, such as the DUK-2B high-density electrical measuring instrument, was selected. The instrument type, electrode spacing, working voltage, insulation coefficient, and other measuring parameters were also kept consistent with the previous measurements to ensure the comparability of the data obtained. By maintaining these consistent measurement conditions, the study aimed to accurately compare and analyze the changes in the slope hazard sources over time (Table 2).

FIGURE 8
Schematic diagram of the survey line layout and geological survey map.

TABLE 2 List of measurement parameters.

Arrangement	Electrode distance/m	Electrode number	Load Voltage/V	Layer number
Winner α AM=MN=NB	5	60	75	19
Winner γ				
AM=MB=BN				

According to the geological conditions and geophysical characteristics of the area, a total of 2 survey lines were laid in the high slopes of open-pit mines.

6 Results of detective areas and explanation

In this article, we have selected two groups of profiles for analysis: one group consists of profiles showing more pronounced changes in the slope hazard sources, while the other group comprises profiles without significant changes. Prior to the analysis, a preliminary geological survey was conducted, and relevant geological data were collected. Using two high-density electrical methods, we examined the underground structure and inferred the characteristics and locations of the slope hazard sources. By analyzing the resistivity changes observed in the physical inversion maps, we identified areas exhibiting low resistivity anomalies. These areas were determined to be fault fragmentation zones, water-bearing soft rock layers, water-conducting fracture zones, and other potential hazard sources based on their resistivity variations.

Furthermore, by studying the resistivity changes over time in the physical inversion, we observed minor variations in the slope hazard sources. Areas demonstrating significant changes were identified as regions with a higher potential for slope collapse hazards. Through these analyses, we aim to provide valuable insights into the dynamics of slope hazard sources and their potential impact on slope stability.

In the analysis of Section 1, the raw data obtained from the high-density electrical method in both 2016 and 2022 underwent mean-filtering and wavelet denoising. Following the mean-filtering and wavelet denoising, the data underwent further refinement through geological correction using the parametric area method. This correction method incorporates the geological information and characteristics specific to the study area, aiming to enhance the accuracy of the inversion results.

Through the application of the parametric area method for geological correction, a more comprehensive consideration of the subsurface geological structures and properties can be achieved. Consequently, this approach enables more precise

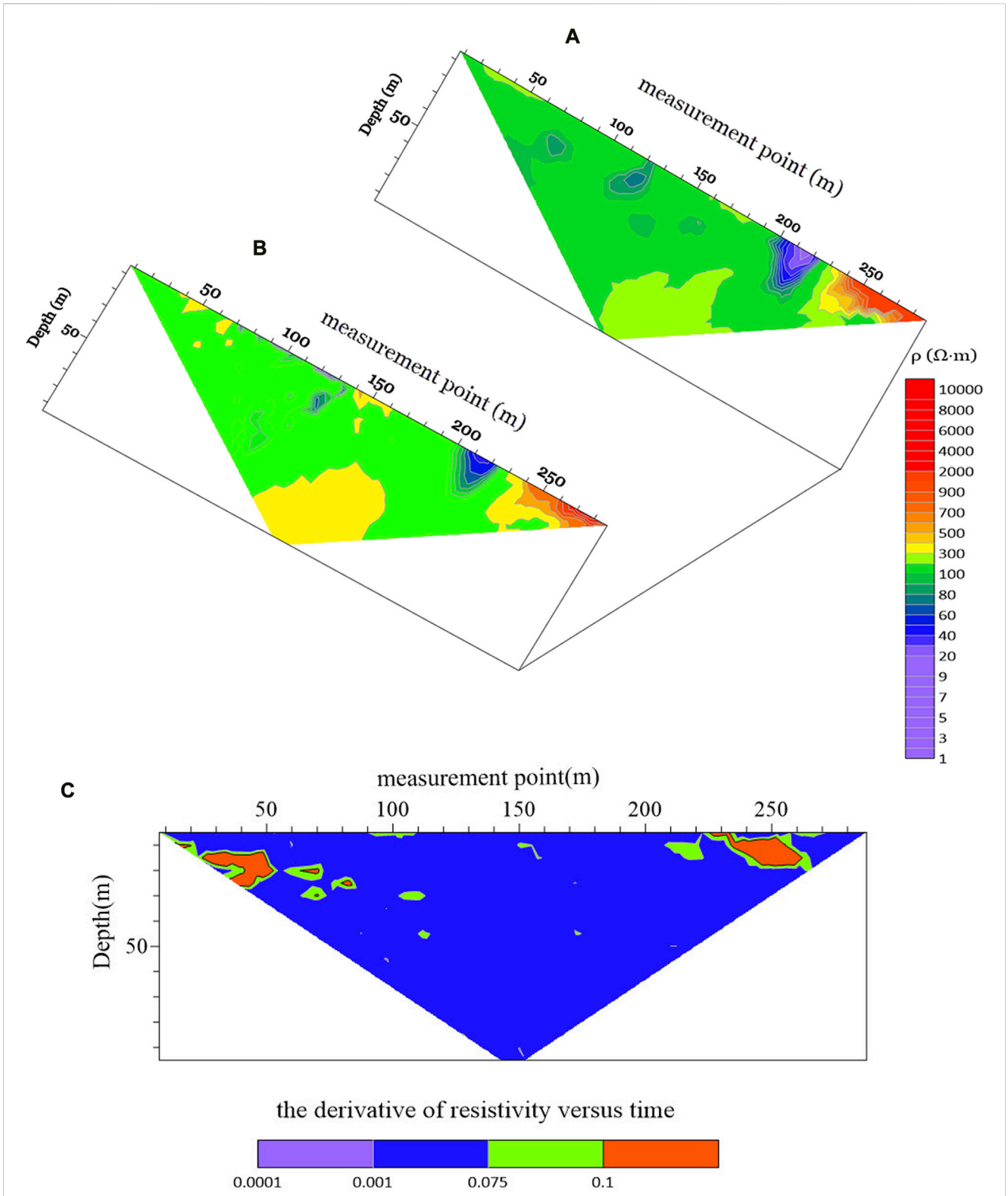

FIGURE 9
Geophysical inversion section Section 1, **(A, B)**; Section 2, **(D, E)** of the high-density resistivity method. The inversion section of the derivative of resistivity changes with time **(C, F)**.

interpretations and representations of the resistivity distribution in Section 1 for both the 2016 and 2022 datasets.

In 2016, the inversion was conducted using the least squares method with smoothing constraints, resulting in the generation of Figure 9A. The resistivity values across the entire section

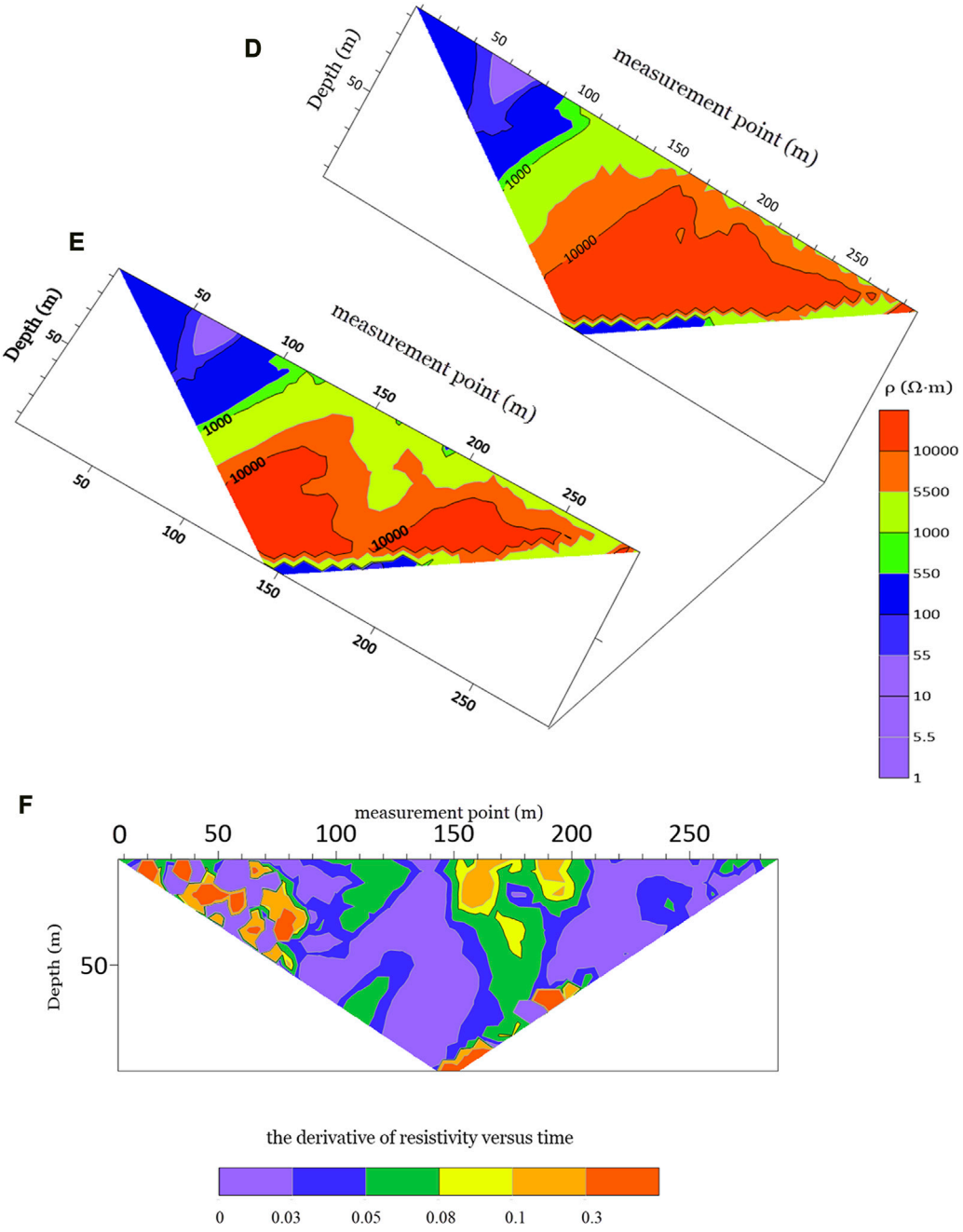

FIGURE 9
Continued.

predominantly ranged between 100 Ω m and 300 Ω m. However, there was a notable decrease in resistivity between measurement points 200 and 220, typically falling below 20 Ω m. Beyond point 250, the resistivity values increased significantly, generally exceeding 10,000 Ω m. Additionally, localized anomalies with low resistivity were observed at survey points 70 and 120, forming closed patterns. By considering the findings from surface surveys, it can be inferred that the majority of the slope rock layers consist of weathered dolomite. Moreover, a fault fracture zone is present between survey points 200 and 220, while mica rocks are observed in the layers beyond point 250. The distinct resistivity variation between deep and shallow dolomite layers can be attributed to various geological factors, as suggested by previous studies. It is worth noting that survey points 70 and 120 might represent pseudo-anomalies or indicate minor fractures and the resistivity of deep dolomite differs from that of the shallow portion.

In 2022, the inversion was also performed using the least squares method with smoothing constraints, resulting in the generation of Figure 9B. When compared with the 2016 results, the resistivity distribution across the entire section remained largely consistent. Notably, there were no localized anomalies with closed patterns observed at measurement points 70 and 120 in 2022. This absence of

anomalies at those points may be attributed to false anomalies generated during the inversion process in 2016 (Figures 9A,B).

Based on the analysis of the resistivity change relationship over time, it can be observed that the majority of the area in profile 1 exhibits a resistivity change rate below 0.09, indicating that the subsurface structure remains relatively unchanged. However, there are specific regions within the profile where the resistivity change rate exceeds 0.12, indicating significant changes in the disaster source in those areas. In the 30–50 m region, which did not initially show the presence of disaster sources in 2016, the derivative inversion diagram of normalized resistivity *versus* time indicates values above 0.12. This evolution is likely due to the combined effects of external freezing and thawing and water erosion on the original geological fractures, leading to weathering and fragmentation of the slate. Field surveys confirm the presence of fault fragmentation zones in the side slope step, with broken geotechnical bodies indicating the evolution of the disaster source in this area. In the 120 m region, the derivative value is below 0.09, suggesting that the disaster source has not significantly evolved compared to the surrounding dolomite area. This implies that the geotechnical body in the fault fragmentation zone remains relatively stable, with a stronger water-supply capacity than the surrounding rock. The measurement line in the 240–260 m area consists of mica-containing dolomite, mica rock, and weathered dolomite. The derivative of resistivity *versus* time in this region exceeds 0.15, indicating the presence of exposed mica rock that has undergone fragmentation due to the influence of atmospheric precipitation and groundwater. Further fragmentation of weathered dolomite occurs under external forces. Site investigations confirm the abundance of mica rocks in this area, which are susceptible to destruction by water erosion, leading to decreased resistivity (Figure 9C).

In summary, for profile 1, the majority of the area exhibits a resistivity change rate below 0.09, suggesting limited evolution. However, the disaster sources in this profile have evolved to varying degrees. The 120 m region shows minimal evolution, while the area of 200–220 m exhibits further internal evolutionary damage. The 30–50 m region, originally considered more stable, experienced significant changes due to the nature of the slate, rainwater erosion, and periodic blasting vibrations. The evolution of slope hazard sources is non-uniform and asynchronous, influenced by geological conditions, structural characteristics, and external factors such as precipitation and blasting vibrations. The derivative of resistivity *versus* time, with values above 0.12, indicates significant evolution in the respective regions.

Figure 9D presents the inversion map of mine profile 2, obtained by denoising the high-density electrical exploration data in 2016. The map clearly illustrates a region with very low resistivity, ranging from points 0 to 80 with values between 0 and 50 Ω m. Based on the known resistivity characteristics of different rock types and previous geological studies, this area is interpreted as fractured dolomite and shale. Notably, the resistivity remains low in the range from measurement point 80 to 120, and an evident boundary is observed between low resistivity on the left and high resistivity on the right. This observation suggests the presence of a fault fracture zone, which is further confirmed by the field geological survey, and it corresponds to the boundary line between dolomite and shale. The resistivity values beyond point 120, extending to 300 m, exceed 6,000 Ω m, indicating the presence of intact dolomite.

Figure 8E depicts the high-density electrical inversion map of Profile 2 in 2022, employing the same parameters for data acquisition and processing. Upon comparison with the 2016 results, the resistivity distribution in most areas remains relatively stable, with no significant changes observed. However, a noticeable alteration is evident between survey points 150 and 200. In conjunction with field surveys, this variation suggests the occurrence of mica-bearing dolomite breakage in that region (Figures 9D,E).

In the 0–80 m area, the majority of derivatives exceed 0.1, indicating that the disaster source has undergone some degree of evolution compared to the surrounding rock. It is presumed that the slate and weak rock layers in this area have experienced fragmentation and an increase in rock voids due to water erosion. Field surveys have provided verification of this evolution, as the weak interlayer in the area was found to be filled with rock debris, and the previously intact slate appeared broken. These observations further support the occurrence of evolution in the area. In the 150–220 m area, the derivative of shallow resistivity *versus* time interval is above 0.1, while in the downward extension area, the derivative value ranges between 0.05 and 0.1. These values differ noticeably from the surrounding area, suggesting the presence of two small fracture zones at approximately 160m and 190 m. However, due to their limited influence area, these zones were not detected during the exploration process. Weathering and mechanical action have contributed to the expansion and downward extension of these zones. Field surveys have revealed fault zone outcroppings at 165 m and 187 m, providing further evidence of the evolution of the disaster source in this area. In the 100–150 m area, both the shallow and deep resistivity derivatives *versus* time interval range between 0.05 and 0.1. This area consists of weathered dolomite, which is prone to weathering when exposed to water. The upper part of the area may be affected by precipitation, surface water, and blasting vibrations, leading to further weathering damage. The lower part, on the other hand, may experience erosion from underground bedrock water, resulting in the breakage of weathered dolomite. The presence of groundwater seepage in the lower part of the terrace during field surveys suggests some level of evolution in this area, as it acts as a transitional zone between slate and dolomite.

In summary, for profile 2, the disaster source originally identified within the 0–80 m range undergoes noticeable evolution, with further damage occurring due to water erosion. The 150–220 m area, not initially identified as a disaster source, experiences significant expansion and evolution of an unidentified small fault at the junction of slate and dolomite. This evolution is attributed to the high degree of rock weathering and periodic blasting vibrations. The single high-density electrical method inversion map alone may not easily identify these changes. However, by utilizing the derivative of the inversion resistivity *versus* time interval as a characteristic parameter in the time-shifted high-density electrical method, the evolution of the disaster source can be effectively highlighted (Figure 8F).

7 Conclusion

The mine is in production, and due to the complex geological genesis, periodic blasting, and short-term heavy rainfall in the

summer in the mining area caused by climate warming, the slope has collapsed several times, which greatly affects the life and property safety of the mine operators. Time-shifted high-density electrical method is a very effective method for slope exploration, which can obtain information about the nature and distribution of underground materials by observing the change of underground resistivity with time. We have investigated and analyzed the slopes in the area where no collapse has occurred and have reached the following conclusions.

1 The time-lapse high-density electrical method can show the evolution of fault sources within the slope, and the use of the derivative of resistivity *versus* time can effectively identify the stratigraphic structure within the slope. During our exploration, the time-shifted high-density electrical method accurately identified faults and weak rock layers, and can clearly reflect the interface between dolomite and fault fracture zones.
2 We found that the geological structure of most areas of the slope did not change significantly, but obvious changes were produced in the original fault fracture zone, soft rock layer, and other hazard source areas, and the potential collapse hazard areas can be classified according to the magnitude of values and sparseness of contours.
3 The time-shifted high-density resistivity method is applicable to slope hazard source monitoring, which can effectively identify the morphological characteristics of the distribution and evolution of hazard sources, on the basis of which the dynamic monitoring of hazard sources within the slope can be realized. It can provide an important basis for future slope safety management and a theoretical basis for monitoring similar geological hazards.

In future research, it is important to conduct a comparative analysis of this method with other approaches for detecting slope hazard sources. Additionally, the implementation of intelligent procedures for automated data collection and processing should be considered. These advancements will contribute to enhancing the effectiveness and efficiency of slope hazard detection and analysis.

Data availability statement

The original contributions presented in the study are included in the article/Supplementary material, further inquiries can be directed to the corresponding author.

Author contributions

KS wrote the manuscript, prepared the graphs, and analyzed the data; ZZ provided guidance in data processing and results interpretation and supervised the fieldwork. All authors contributed to the article and approved the submitted version.

Funding

The project was funded by the Natural Science Foundation of Inner Mongolia Autonomous Region (2019MS04016).

Conflict of interest

The authors declare that the research was conducted in the absence of any commercial or financial relationships that could be construed as a potential conflict of interest.

Publisher's note

References

Bao, Y., Chen, J., Su, L., Zhang, W., and Zhan, J. (2023). A novel numerical approach for rock slide blocking river based on the CEFDEM model: A case study from the samaoding paleolandslide blocking river event. *Eng. Geol.* 312, 106949. doi:10.1016/j.enggeo.2022.106949

Boyd, J., Chambers, J., Wilkinson, P., Peppa, M. V., Watlet, A., Kirkham, M., et al. (2021). A linked geomorphological and geophysical modelling methodology applied to an active landslide. *Landslides* 18, 2689–2704. doi:10.1007/s10346-021-01666-w

Camporese, M., Cassiani, G., Deiana, R., Salandin, P., and Binley, A. (2015). Coupled and uncoupled hydrogeophysical inversions using ensemble Kalman filter assimilation of ERT-monitored tracer test data. *Water Resour. Res.* 51, 3277–3291. doi:10.1002/2014wr016017

Doetsch, J., Linde, N., and Binley, A. (2010). Structural joint inversion of time-lapse crosshole ERT and GPR traveltime data. *Geophys. Res. Lett.* 37. doi:10.1029/2010gl045482

Dong, H.-B., and Wang, C.-L. (2003). Development and application of 2D resistivity imaging surveys. *Earth Sci. Front.* 10, 171–176. doi:10.3321/j.issn:1005-2321.2003.01.020

Du, H., and Song, D. (2022). Investigation of failure prediction of open-pit coal mine landslides containing complex geological structures using the inverse velocity method. *Nat. Hazards* 111, 2819–2854. doi:10.1007/s11069-021-05159-w

Du, H., Song, D., Liu, G., Guo, W., Wang, X., and Bai, R. (2023). Influence of the extra-thick coal seam exploitation on the deformation characteristics of the overlying rock mass in an open-pit mine slope. *Geomatics, Nat. Hazards Risk* 14, 1–23. doi:10.1080/19475705.2022.2161952

Dupis, A. (1980). "Geosounding principles, 1. Resistivity sounding measurements: O. Koefoed," in *Methods in geochemistry and geophysics. Physics of the earth and planetary interiors* (Amsterdam: Elsevier), 23, 160. ISBN 0-444-41704-4. xiv + 276 pp. + 11 pp. encl., Dfl. 130.00., approx. US $ 66.50.

Fan, H.-R., Yang, K.-F., Hu, F.-F., Liu, S., and Wang, K.-Y. (2016). The giant Bayan Obo REE-Nb-Fe deposit,China:Controversy and ore genesis. *Geosci. Front.* 7, 335–344. doi:10.1016/j.gsf.2015.11.005

Ferahtia, J., Djarfour, N., Baddari, K., and Kheldoun, A. (2012). A fuzzy logic-based filter for the removal of spike noise from 2D electrical resistivity data. *J. Appl. Geophys.* 87, 19–27. doi:10.1016/j.jappgeo.2012.08.007

Fritsch, F. N., and Carlson, R. E. (1980). Monotone piecewise cubic interpolation. *SIAM J. Numer. Analysis* 17, 238–246. doi:10.1137/0717021

Hojat, A., Arosio, D., Ivanov, V. I., Longoni, L., Papini, M., Scaioni, M., et al. (2019). Geoelectrical characterization and monitoring of slopes on a rainfall-triggered landslide simulator. *J. Appl. Geophys.* 170, 103844. doi:10.1016/j.jappgeo.2019.103844

Johnson, T. C., Burghardt, J., Strickland, C., Knox, H., Vermeul, V., White, M., et al. (2021). 4D proxy imaging of fracture dilation and stress shadowing using electrical resistivity tomography during high pressure injections into a dense rock formation. *J. Geophys. Research-Solid Earth* 126. doi:10.1029/2021jb022298

Lai, X., Yang, X., and Sun, W. (2012). Geochemical constraints on genesis of dolomite marble in the bayan Obo REE–Nb–Fe deposit, inner Mongolia:

implications for REE mineralization. *J. Asian Earth Sci.* 57, 90–102. doi:10.1016/j.jseaes.2012.06.008

Lapenna, V., and Perrone, A. (2022). Time-lapse electrical resistivity tomography (TL-ERT) for landslide monitoring: recent advances and future directions. *Appl. Sciences-Basel* 12, 1425. doi:10.3390/app12031425

Lesparre, N., Nguyen, F., Kemna, A., Robert, T., Hermans, T., Daoudi, M., et al. (2017). A new approach for time-lapse data weighting in electrical resistivity tomography. *Geophysics* 82, E325–E333. doi:10.1190/geo2017-0024.1

Li, G., Zhu, C., He, M., Zuo, Y., Gong, F., Xue, Y., et al. (2023). Intelligent method for parameters optimization of cable in soft rock tunnel base on longitudinal wave velocity. *Tunn. Undergr. Space Technol.* 133, 104905. doi:10.1016/j.tust.2022.104905

Lin, S., Wang, W., Deng, X., Zha, Y., Zhou, H., and Cheng, M. (2019). Geophysical observation of typical landslides in three gorges reservoir area and its significance: A case study of sifangbei landslide in wanzhou district. *Earth Sci.* 44, 3135–3146. doi:10.3799/dqkx.2019.074

Liu, B., Liu, Z., Li, S., Fan, K., Nie, L., and Zhang, X. (2017). An improved Time-Lapse resistivity tomography to monitor and estimate the impact on the groundwater system induced by tunnel excavation. *Tunn. Undergr. Space Technol.* 66, 107–120. doi:10.1016/j.tust.2017.04.008

Loke, M. H., and Barker, R. D. (1996). Rapid least-squares inversion of apparent resistivity pseudosections by a quasi-Newton method1. *Geophys. Prospect.* 44, 131–152. doi:10.1111/j.1365-2478.1996.tb00142.x

Loke, M. H., Chambers, J. E., Rucker, D. F., Kuras, O., and Wilkinson, P. B. (2013). Recent developments in the direct-current geoelectrical imaging method. *J. Appl. Geophys.* 95, 135–156. doi:10.1016/j.jappgeo.2013.02.017

Loke, M. H., Dahlin, T., and Rucker, D. F. (2014). Smoothness-constrained time-lapse inversion of data from 3D resistivity surveys. *Near Surf. Geophys.* 12, 5–24. doi:10.3997/1873-0604.2013025

Lu, X. C., Liu, X., Xiong, B. B., Cui, X., Tian, B., Cai, Z. L., et al. (2023). Water distribution characteristics of slopes based on the high-density electrical method. *Water* 15, 895. doi:10.3390/w15050895

Norooz, R., Olsson, P. I., Dahlin, T., Gunther, T., and Bernstone, C. (2021). A geoelectrical pre-study of alvkarleby test embankment dam: 3D forward modelling and effects of structural constraints on the 3D inversion model of zoned embankment dams. *J. Appl. Geophys.* 191, 104355. doi:10.1016/j.jappgeo.2021.104355

Purcell, E. M., and Morin, D. J. (2013). *Electricity and magnetism*. Cambridge: Cambridge University Press.

Ren, F., Zhu, C., He, M., Shang, J., Feng, G., and Bai, J. (2023). Characteristics and precursor of static and dynamic triggered rockburst: insight from multifractal. *Rock Mech. Rock Eng.* 56, 1945–1967. doi:10.1007/s00603-022-03173-3

Song, D., and Du, H. (2023). Numerical investigation of the evolution process of an open-pit mine landslide using discrete-element method. *Int. J. Geomechanics* 23, 04023054. doi:10.1061/ijgnai.gmeng-7568

Wang, K., Fang, A., Zhang, J., Yu, L., Dong, C., Zan, J., et al. (2019). Genetic relationship between fenitized ores and hosting dolomite carbonatite of the Bayan Obo REE deposit, Inner Mongolia, China. *J. Asian Earth Sci.* 174, 189–204. doi:10.1016/j.jseaes.2018.12.007

Wang, Q., Xu, S., Xin, Z., He, M., Wei, H., and Jiang, B. (2022a). Mechanical properties and field application of constant resistance energy-absorbing anchor cable. *Tunn. Undergr. Space Technol.* 125, 104526. doi:10.1016/j.tust.2022.104526

Wang, X., Wang, Y., Lin, Q., Li, N., Zhang, X., and Zhou, X. (2022b). Projection of China landslide disasters population risk under climate change. *Progress. Inquisitiones Mutat. Clim.* 18, 166–176. doi:10.12006/j.issn.1673-1719.2021.154

Wilkinson, P. B., Chambers, J. E., Meldrum, P. I., Kuras, O., Inauen, C. M., Swift, R. T., et al. (2022). Windowed 4D inversion for near real-time geoelectrical monitoring applications. *Front. Earth Sci.* 10. doi:10.3389/feart.2022.983603

Yang, K.-F., Fan, H.-R., Santosh, M., Hu, F.-F., and Wang, K.-Y. (2011). Mesoproterozoic mafic and carbonatitic dykes from the northern margin of the north China craton: implications for the final breakup of columbia supercontinent. *Tectonophysics* 498, 1–10. doi:10.1016/j.tecto.2010.11.015

Yang, X.-Y., Sun, W.-D., Zhang, Y.-X., and Zheng, Y.-F. (2009). Geochemical constraints on the genesis of the bayan Obo Fe–Nb–REE deposit in inner Mongolia, China. *Geochimica Cosmochimica Acta* 73, 1417–1435. doi:10.1016/j.gca.2008.12.003

Zhang, H. R., Zhao, B., Dong, S. Q., Wang, X. X., and Jing, P. F. (2022). A method for the inversion of reservoir effective permeability based on time-lapse resistivity logging data and its application. *Geofluids* 2022, 1–13. doi:10.1155/2022/8704344

Zhongxin, Y., Ge, B., Chenyu, W., Zhongqin, Z., and Xianjiang, Y. (1992). Geological features and genesis of the Bayan Obo REE ore deposit, Inner Mongolia, China. *Appl. Geochem.* 7, 429–442. doi:10.1016/0883-2927(92)90004-m

Zhu, X.-k., Sun, J., and Pan, C. (2015). Sm–Nd isotopic constraints on rare-earth mineralization in the Bayan Obo ore deposit, Inner Mongolia, China. *Ore Geol. Rev.* 64, 543–553. doi:10.1016/j.oregeorev.2014.05.015

frontiers | Frontiers in Environmental Science

TYPE Original Research
PUBLISHED 19 December 2023
DOI 10.3389/fenvs.2023.1308808

OPEN ACCESS

EDITED BY
Yunhui Zhang,
Southwest Jiaotong University, China

REVIEWED BY
Lichun Zhang,
Stanford University, United States
Ge Gao,
McGill University, Canada
Qi Zhou,
GFZ German Research Centre for Geosciences Potsdam, Germany

*CORRESPONDENCE
Weiqi Yang,
yangweiqi@scac.edu.com

RECEIVED 07 October 2023
ACCEPTED 06 December 2023
PUBLISHED 19 December 2023

CITATION
Feng Y, Yang W, Wan J and Li H (2023), Granular risk assessment of earthquake induced landslide via latent representations of stacked autoencoder. *Front. Environ. Sci.* 11:1308808. doi: 10.3389/fenvs.2023.1308808

Granular risk assessment of earthquake induced landslide via latent representations of stacked autoencoder

Yuran Feng[1], Weiqi Yang[1]*, Jian Wan[1] and Huajin Li[2,3]

[1]Department of Civil Engineering, SIchuan College of Architectural Technology, Deyang, China, [2]School of Architecture and Civil Engineering, Chengdu University, Chengdu, China, [3]Sichuan Engineering Research Center for Mechanical Properties and Engineering Technology of Unsaturated Soils, Chengdu University, Chengdu, China

Earthquake-induced landslides are ubiquitous on slopes in terrestrial environments, which can pose a serious threat to local communities and infrastructures. Data-driven landslide assessments play a crucial role in preventing future landslide occurrences and recurrences. We present a novel granular computing approach that assesses landslide risk by combining fuzzy information granulation and a stacked autoencoder algorithm. The stacked autoencoder is trained using an end-to-end learning strategy to obtain a central latent vector with reduced dimensionality. The multivariate landslide dataset was used as both the input and output to train the stacked autoencoder algorithm. Subsequently, in the central latent vector of the stacked autoencoder, the Fuzzy C-means clustering algorithm was applied to cluster the landslides into various groups with different risk levels, and the intervals for each group were computed using the granular computing approach. An empirical case study in Wenchuan County, Sichuan, China, was conducted. A comparative analysis with other state-of-the-art approaches including Density-based spatial clustering of applications with noise (DBSCAN), K-means clustering, and Principal Component Analysis (PCA), is provided and discussed. The experimental results demonstrate that the proposed approach using a stacked autoencoder integrated with fuzzy information granulation provides superior performance compared to those by other state-of-the-art approaches, and is capable of studying deep patterns in earthquake-induced landslide datasets and provides sufficient interpretation for field engineers.

KEYWORDS

earthquake-induced landslides, risk assessment, stacked autoencoder, information granule, prototype selection

1 Introduction

Landslides are a major type of natural geohazard and are defined as the movement of a mass of rock, debris, or Earth down a slope (Cruden, 1991; Gao and Meguid, 2018a; 2018b). This can cause numerous casualties and economic losses in mountainous regions (Li et al., 2023). Multiple factors can trigger landslides, including rainfall, earthquake shaking, water level changes, storm waves, rapid stream erosion, and human factors. Among them, earthquake-induced landslides are the most hazardous due to the rapid occurrence and large size of slope failures (Shi et al., 2021).

In practice, landslide risk assessment plays a crucial role in field engineering (Rajabi et al., 2022). The general process involves estimating the level of risk, deciding its appropriateness, and exercising control measures to reduce risk by observing an elevation in risk levels (Dai et al., 2002; Gao et al., 2020; Zhou J. et al., 2021; Chowdhuri et al., 2022). Such procedures are typically followed for landslide assessment and mitigation at regional or catchment scales (Pokharel et al., 2021). The Geographic Information System (GIS) environment in landslide susceptibility map preparation is an effective method for identifying and delineating landslide-prone areas to create a geospatial database of landslide occurrence or 'landslide inventory' (Merghadi et al., 2020). The geospatial properties of landslides can be compiled into a comprehensive database using GIS (Karakas et al., 2021). These properties include slope angle, slope aspect, soil type, precipitation, lithology type, and geometric parameters (Gao et al., 2021; Kasama et al., 2021; Zhou et al., 2022). All the properties in the database are valuable for assessing slope stability and modeling the responses of other slopes in the study area to predict future landslide occurrences (Van Westen et al., 2006).

In recent years, data-driven models and frameworks have achieved great success in landslide risk assessment using GIS-based databases. For example, volumetric estimation, spatial geometric computation, and maximum displacement prediction are all considered part of the assessment tasks in engineering practice (Zhou Q. et al., 2021). Althuwaynee et al. (2014) integrated decision trees and logistic regression models to predict the overall landslide risk using multivariate analysis. Huang et al. (2018) applied a support vector machine (SVM) to forecast landslide susceptibility using a GIS-based dataset. Xu et al. (2019) performed a comparative analysis of seven benchmark data mining algorithms and predicted the maximum landslide displacement in loess landslides in Heifangtai, China. Gorsevski et al. (2016) introduced an artificial neural network (ANN) to predict landslide risks simultaneously using GIS-data and Lidar data. The experimental results demonstrated that the ANN offered superior prediction performance and was capable of learning the relationship between geospatial properties and overall landslide risk.

For the time being, advanced analytical tools such as artificial intelligence (AI) and deep-learning (DL) are also playing an increasingly important role in evaluating landside risks in practice. Zhao and Du (2016) initially proposed using convolutional neural network (CNN) to analyze landslide risk using remote sensing images. Paoletti et al. (2018) developed a 3-D CNN to extract both spectral and spatial information in Lidar images for risk assessment tasks. Yi et al. (2020) proposed a novel landslide susceptibility mapping and risk assessment model using multi-scale convolutional neural network (MCNN) in the image-related tasks. Various levels of geological features from low to high are studied by the algorithm to assess landslide risks. All above work provided advanced insights in terms of landslide mapping and risk assessment tasks.

Summarily, the majority of data-driven approaches that perform landslide risk assessment adopt a supervised learning strategy to train data mining or machine learning algorithms and then predict risk labels for new instances (He and Kusiak, 2017; Li, 2022a). The success of these approaches significantly depends on the availability of high-quality datasets. To generate this type of dataset, time and labor cost for field experts is inevitable. If the required dataset is relatively small, the computational and labor costs can be controlled at a reasonable level. However, some case studies may contain excessive numbers of instances within the dataset, which is challenging in practice. For instance, a single field expert may require several weeks to offer risk labels for tens of thousands of landslide instances. Therefore, it is important to develop a more efficient approach to address this challenge.

Granular computing (GC) has recently become a popular data science research direction, with considerable attention in both industry and academia. The granular computing approach adopts fuzzy rule-based modeling to derive granular descriptors for interpreting a dataset that follows an unsupervised learning strategy. Generally, two major advantages of using a granular computing approach in practice exist. First, high flexibility in coping with datasets with diverse geometries and enhancing the representation of the information granules. Thus, the constructed granules are more interpretable for understanding the essential characteristics of the dataset. Second, information granules are often constructed in a refined representation of the original data structure, which intuitively reduces computation overhead. (Ouyang and Zhang, 2022). In typical landslide risk assessment tasks, conventional machine-learning approaches usually adopt supervised-learning strategy which requires labeling the ground-truth to guide the algorithm to learn data patterns. This step becomes the foundation of a supervised-learning approach which ensures the learning quality. Granular computing can be an effective alternative option which utilizes an unsupervised-learning approach to derive the patterns within the same dataset. In comparison, the information granules can largely increase the efficiency of overall computation cost while only sacrificing a limited amount of information.

Based on the above discussion, this study proposes a combinatory data-driven framework to perform landslide risk assessment based on a stacked autoencoder (SAE) and fuzzy information granules. First, the SAE was employed as an information compressor that removed redundant information but preserved valuable patterns within the landslide dataset. The standard mean square error (MSE) loss was proposed as the loss function for training the SAE algorithm. Second, when the loss function of the SAE converged, the central latent representations of the SAE were extracted for information granule construction. Three training strategies are used to explore the optimal design of the SAE architecture. The Fuzzy-C-means (FCM) algorithm was then employed to select the prototypes for each subcluster. Finally, fuzzy-rule-based information granules were constructed using two risk measures, namely, Value-at-Risk (*VaR*) and Conditional-Value-at-Risk (*CVaR*). The risk boundaries indicating that the ranges for various levels of landslide risk were computed, and interpretation with respect to each attribute was provided. To evaluate the performance of the proposed framework, comprehensive experiments were conducted using an actual earthquake-induced landslide dataset collected from Wenchuan County, Sichuan Province, China.

The main contributions of this study are summarized as follows:

1) This research introduced SAE to compress the landslide dataset and reduced dimensionality effectively.

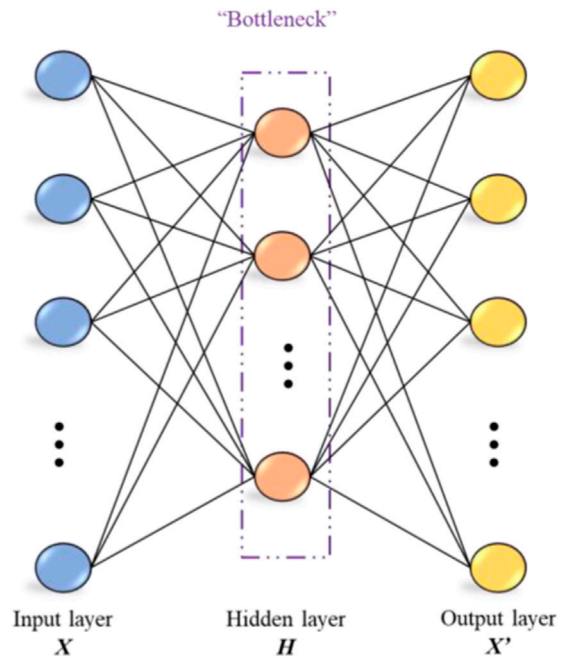

FIGURE 1
Schematic diagram of an autoencoder.

2) Fuzzy information granules were computed over the latent representations of the SAE and risk boundaries were computed for various levels of landslide risk based on the constructed granules.

The remainder of this article is organized as follows. The methodology for the SAE algorithm and granular computation process is introduced in Section 2. An overview of the case study area and earthquake-induced landslide dataset is presented in Section 3. The computational results and comparative analyses are presented in Section 4. Discussions are presented in Section 5, and conclusions are presented in Section 6.

2 Methodology

2.1 Stacked autoencoder

An autoencoder (AE) is a popular deep-learning architecture that effectively compresses information. In a typical AE algorithm, the input is a vector or signal, and the output reconstructs the input via an intermediate layer with a reduced number of hidden nodes. AE algorithms attempt to learn higher-level feature representations in the reduced hidden nodes, which can make the reconstruction of the original input feasible (Zabalza et al., 2016; Li, 2022b). The basic scheme of the AE algorithm is shown in Figure 1.

As shown in Figure 1, the autoencoder has a symmetric structure consisting of two components: an encoder and a decoder (Adem et al., 2019). The encoder contracts a nonlinear mapping between the input vector and central hidden layer nodes. For a given input data vector $\boldsymbol{X}'$, a compressed hidden layer representation $\boldsymbol{H}$ can be computed using Eq. 1.

$$\boldsymbol{H} = f_E(\boldsymbol{W_E} * \boldsymbol{X} + \boldsymbol{b_E}) \tag{1}$$

where, $\boldsymbol{W_E}$ and $\boldsymbol{b_E}$ represent the weight and bias of the encoder network; $f_E()$ denotes the activation function of the network. Contrastingly, the decoder maps the hidden representation back to the output layer for reconstruction through a similar transformation. Given the hidden-layer representation $\boldsymbol{H}$, the reconstructed output $\boldsymbol{X}'$ can be obtained using Eq. 2.

$$\boldsymbol{X}' = f_D(\boldsymbol{W_D} * \boldsymbol{H} + \boldsymbol{b_D}) \tag{2}$$

where, $\boldsymbol{W_D}$ and $\boldsymbol{b_D}$ represent the weight and bias of the decoder network; $f_D()$ is the activation function of the decoder network. In

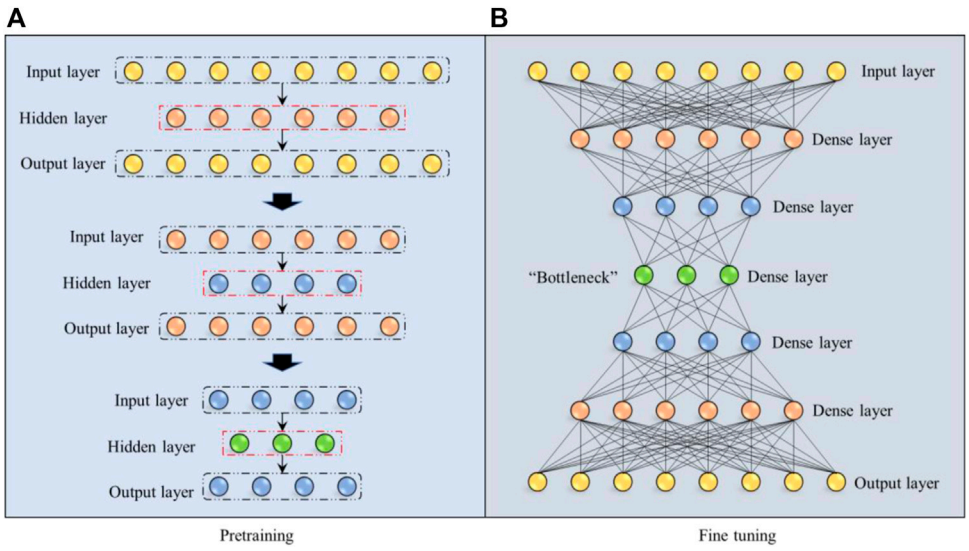

FIGURE 2
Schematic diagram of SAE.

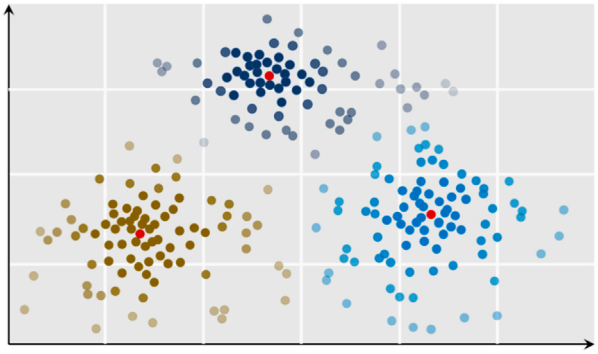

FIGURE 3
Plot depicting an example of the FCM clustering algorithm.

this research, the reconstructed output vector $\boldsymbol{X}'$ always has the same dimensionality as the input vector $\boldsymbol{X}$ while the reconstruction loss can be easily computed by measuring the difference between the two vectors.

The training process of the AE algorithm aimed to reproduce the input data vector in the output layer. Hence, internal hidden nodes can provide compressed information from the original dataset (Khamparia et al., 2020). To ensure high-quality data reconstruction, the values in the hidden nodes can be regarded as new reduced features representing the original vector $\boldsymbol{X}$. Thus, the training of the AE continuously optimizes the parameters $\boldsymbol{\theta} = \{\boldsymbol{W_E}, \boldsymbol{b_E}, \boldsymbol{W_D}, \boldsymbol{b_D}\}$ to pursue high-quality data reconstruction. The parameter $\boldsymbol{\theta}$ above is not a single parameter but a general representation of thousands of parameters within the AE algorithms that includes the weights and biases of numerous neurons along with their connections. The loss function used for training the AE is based on the reconstruction error, which can be expressed as

$$L(\boldsymbol{X}, \boldsymbol{X}') = \frac{1}{n}\sum_{i=1}^{n}\left(x_i - x_i^{'}\right)^2 \tag{3}$$

where, x_i and $x_i^{'}$ denote the ith elements in the input and reconstructed vectors $\boldsymbol{X}$ and $\boldsymbol{X}'$; and $L()$ represents the error computed by the reconstruction. In Eq. 3, the loss function computes the mean-square-error loss which is equivalent to regression loss and it measures the difference between the input vector $\boldsymbol{X}$ and reconstructed vector $\boldsymbol{X}'$. The smaller value of the loss function indicates the higher performance of data reconstruction. Once the values of the loss function converge to a small range, the AE can achieve high-quality data compression and reconstruction.

2.2 SAE and latent representations

An stacked autoencoder (SAE) is considered as an expansion of the traditional AE algorithm. The SAE simply stacks several layers between the input and output layers. This hierarchical structure enables the features to be learned through progressive abstraction levels (Liseune et al., 2020). A schematic of a SAW is shown in Figure 2.

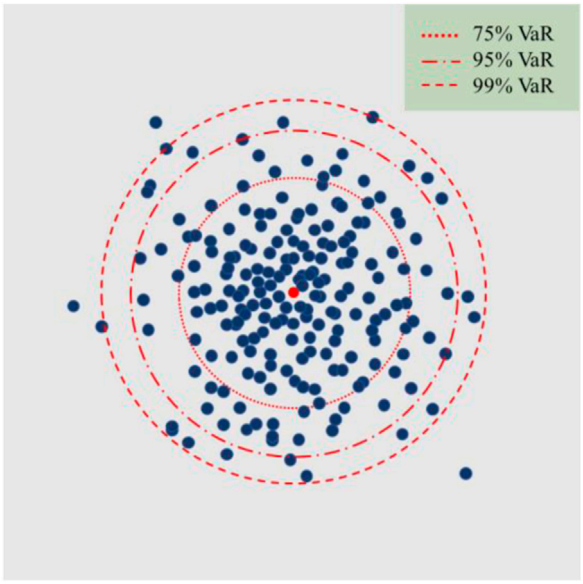

FIGURE 4
Plot illustrating the various confidence levels of a single information granule.

As shown in Figure 2A, the hidden layers within the SAE were pre-trained in a greedy layer-by-layer manner. For example, a typical SAE structure comprises three hidden layers. If the input and output vectors have eight dimensions, the first hidden layer has six dimensions. It can then be formulated as a vanilla AE algorithm to pre-train the first hidden layer. Once the loss function converges to a small range, the pretraining is stopped. Next, a pre-trained hidden layer with six dimensions was used as both the input and output layers for the next pre-training step. The second hidden layer with four dimensions served as the hidden layer in the training step. Here, the same pre-training strategy was adopted as in the first step. In the final pre-training step, the last hidden layer with only three dimensions served as the hidden layer, whereas the pre-trained layer with four dimensions provided by the last step served as both the input and output layers. The majority of the reconstruction loss has been reduced in the pre-training steps while only a limited proportion of the loss has been reduced in the final fine-tuning step. Overall, multiple autoencoders were pre-trained in a bottom-up manner, enabling the encoder to effectively learn the pattern inside the dataset.

As illustrated in Figure 2B, after the pre-training of all hidden layers, all layers were stacked into a hierarchical and symmetric structure. The dense layers are the pre-trained hidden layers, as shown in Figure 2A. Then, back-propagation was applied to fine-tune all SAE network parameters. As the input and output were identical in our study, the fine-tuning was a supervised learning process.

2.3 Prototype selection

The well-trained SAE in this study served as an information compressor for dimension reduction purposes. Using the trained

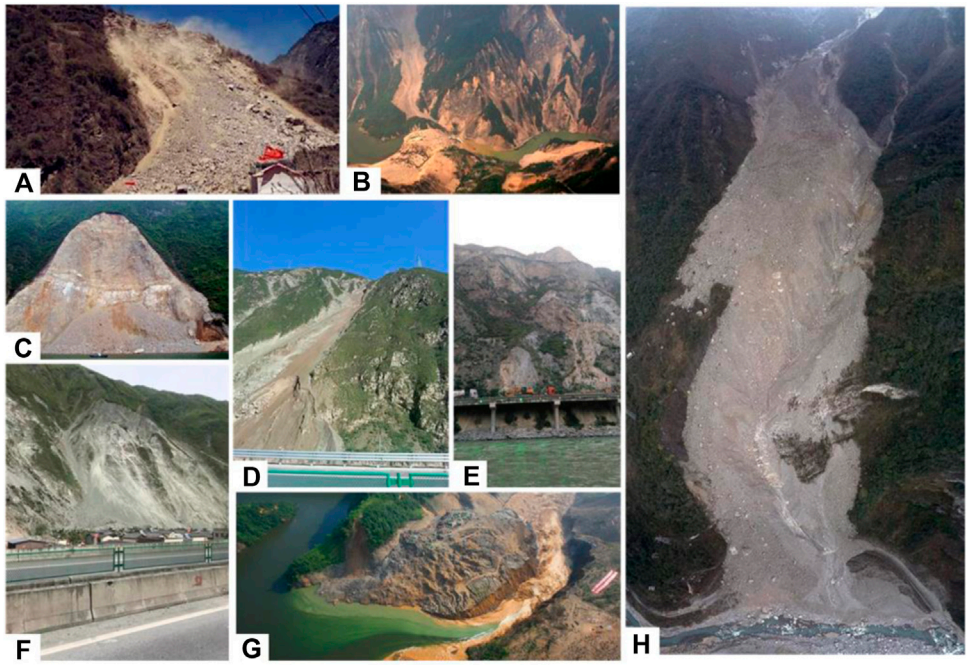

FIGURE 5
Photographs showing the onsite investigation and remote sensing detection of earthquake-induced landslides in Wenchuan County.

TABLE 1 Wenchuan landslides data description.

Name	Unit	Min	Max	Mean	Std	Skewness	Kurtosis
Area	m^2	22.95	43969.79	2097.24	4120.69	5.29	38.33
Elevation	m.a.s.l	2388.00	3448.00	2883.21	241.15	0.03	−0.79
Fault distance	m	2.44	11089.10	2295.83	2107.67	1.09	0.43
Relief amplitude	m	26.00	316.00	164.45	49.57	−0.22	0.29
Runout distance	m	40.94	808546.79	21557.31	63921.32	7.43	70.93
Slide volume	m3	57.99	537129.23	17034.88	44600.79	6.75	59.66
Slope angle	°	3.01	56.05	34.90	9.75	−1.11	1.30
Vertical drop	m	27.87	331912.34	9922.30	27098.63	6.98	63.35

[a]m.a.s.l. means meters above sea level.

TABLE 2 Training strategies of Stacked Autoencoder.

Strategy	Hidden layer	Hidden nodes	Activation function	Loss function	Epoch
I	1	6	ReLU or sigmoid	MSE loss	150
II	3	6-4-6	ReLU or sigmoid	MSE loss	150
III	5	6-4-3-4-6	ReLU or sigmoid	MSE loss	150

SAE structure, higher-level patterns inside the dataset can be effectively compressed into a central latent vector, which preserves important information from the original data space. As illustrated in Figure 2B, the central "Bottleneck" layer is considered the most compressed version of the information from the input data vector. Thus, for every input vector, the values within the "Bottleneck" layer are extracted and utilized to construct information granules in this research.

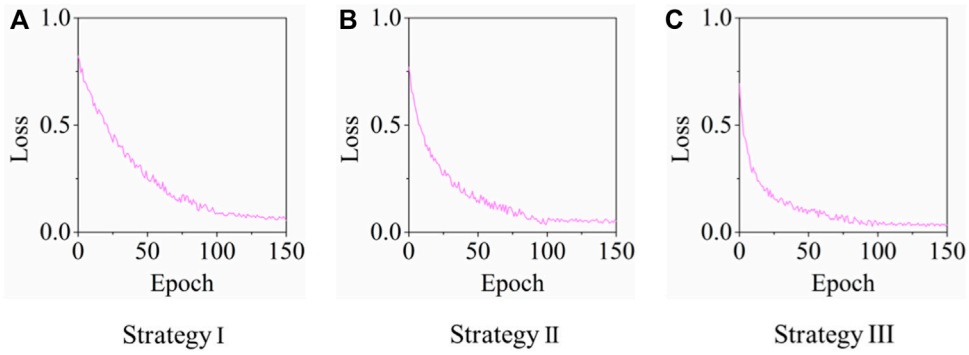

FIGURE 6
Plots showing the loss functions for all training strategies for SAE.

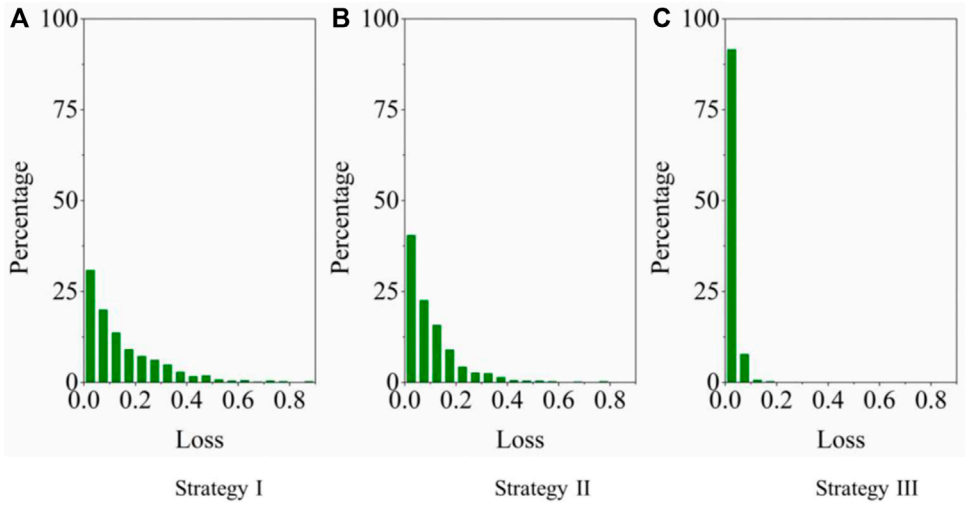

FIGURE 7
Bar charts depicting the distribution of reconstruction MSE error for all training strategies.

In this study, an information granule is defined as a data descriptor of a certain region in the data space according to its size and position (He and Kusiak, 2017; Ouyang et al., 2019a). To localize the granules, the selection of a prototype (data cluster center) is an essential step. An FCM (Ouyang et al., 2019c) algorithm was developed to partition the latent representations of the SAE into several data clusters. The prototype (cluster geometric center) served as a representation of a group of data points within the same constructed granular space. Here, the FCM is selected over the most popular K-mean algorithm is due to the superior capacity of FCM in selecting an actual data point as the prototype while K-mean algorithm is incapable to perform the same task.

For a given dataset $\boldsymbol{H} = \{h_1, h_2, \ldots, h_n\}$ from the central hidden layer of the pre-trained SAE, the FCM partitions n data points into c clusters, where $\boldsymbol{C} = \{C_1, C_2, \ldots, C_c\}$. Based on the similarity scores, the partition matrix $U(\boldsymbol{H})$ can be obtained and expressed in Eq. 4 as follows:

$$U(\boldsymbol{H}) = \begin{bmatrix} \mu_{11} & \cdots & \mu_{1N} \\ \vdots & \ddots & \vdots \\ \mu_{c1} & \cdots & \mu_{cN} \end{bmatrix} \tag{4}$$

where, μ_{ij} denotes the membership degree of data point h_j to cluster C_i. Here, the membership degree μ_{ij} satisfies Eq. 5, 6:

$$\sum_{i=1}^{c} \mu_{ij} = 1, \forall\, j = 1, \ldots, n \tag{5}$$

$$\sum_{i=1}^{c} \sum_{j=1}^{n} \mu_{ij} = n \tag{6}$$

The FCM starts with the determination of the number of clusters, followed by a random selection of the initial cluster centers. Each data point was assigned a membership degree to each cluster. Next, the cluster centers and corresponding membership degrees are updated iteratively by minimizing the objective function. The objective function of the FCM is expressed in Eq. 7:

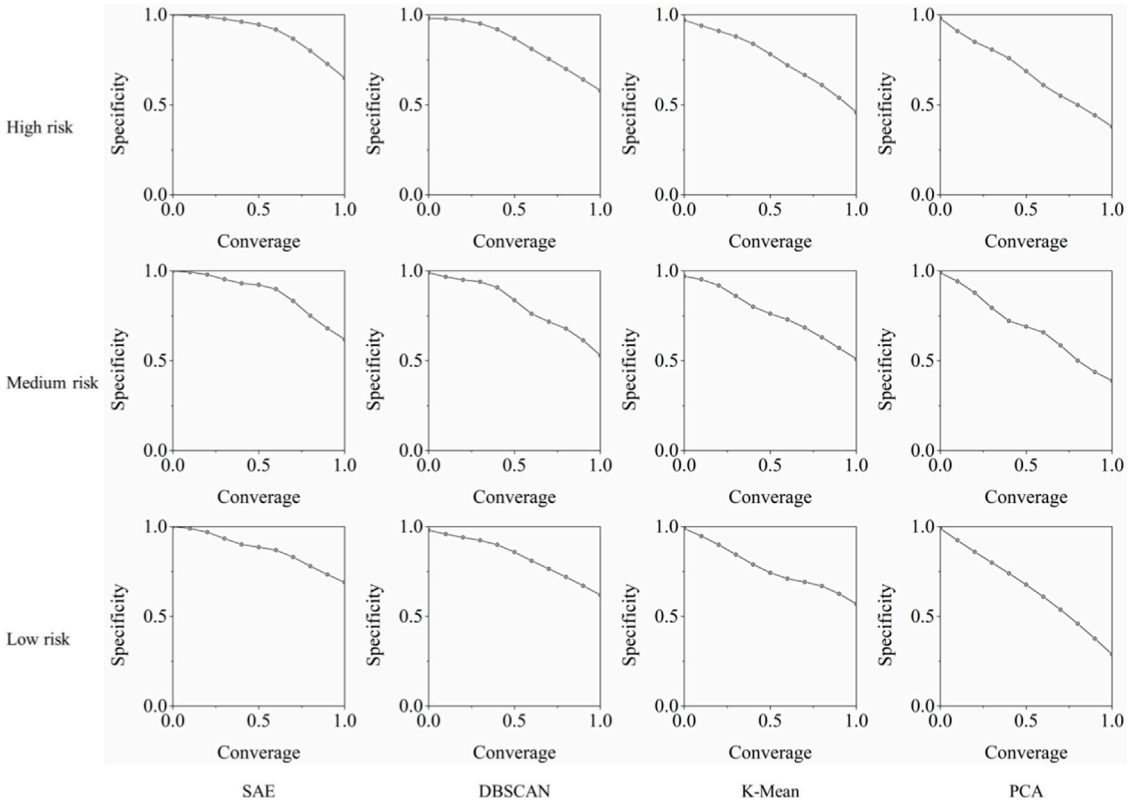

FIGURE 8
Plots showing the comparison of specificity against coverage values against state-of-art approaches.

$$J_c = \sum_{i=1}^{c}\sum_{j=1}^{n}\mu_{ij}^{m}\left\|h_j - v_i\right\|^2 \tag{7}$$

where, h_j is the jth data point, v_i is the ith cluster center, and n denotes the total number of data points in cluster C_i. During the iterations, the μ_{ij}^{m} and v_i are updated using the rules in Eq. 8, 9 respectively:

$$\mu_{ij}^{m} = \frac{1}{\sum_{j=1}^{c}\left(\frac{\left\|h_j - v_i\right\|}{\left\|h_j - v_j\right\|}\right)^{\frac{2}{m-1}}} \tag{8}$$

$$v_i = \frac{\sum_{j=1}^{n}\mu_{ij}^{m}h_j}{\sum_{j=1}^{n}\mu_{ij}^{m}} \tag{9}$$

A visual interpretation of FCM clustering with the three subclusters is shown in Figure 3. This demonstrates an example of a dataset partitioned into three subclusters. The centers of each cluster (red points) were selected as prototypes. Here, the gradient of color shading indicates the value of membership similarity score with respect to the assigned clusters. The brighter color indicates the membership score is higher of a data point while a shallow color indicates lower membership similarity score.

2.4 Optimization of information granule structures

Once the prototypes were selected using the FCM algorithm, it was essential to determine the size of the information granules. According to the general rules of data description methods, a set of information granules is the concentration of numeric prototypes and their membership points, which are formed as data descriptors (Li, 2022b). In this study, we considered generic and simple granule formations based on the radius parameter and selected prototypes. The generic rule-based information granules were depicted as in Eq. 10.

$$R_i\text{: IF } h_k \text{ is in the neighborhood of } v_i\text{,THEN } y_k \text{ should be classified as group } C_i \tag{10}$$

where, h_k is the data point, v_i is the prototype in the corresponding cluster, and y_k is the assigned cluster label for the data point h_k.

Granule formation involves coverage and specificity indices that directly influence the performance of the underlying data description. The formation is based on two randomly selected points: h_i^+ and h_i^- for the upper and lower bound, respectively. Coverage is a reflection of the capacity of an information granule to cover data points between two points, which can be expressed in Eq. 11 and Eq. 12 as follows:

$$\mathrm{cov}\left(h_i^+\right) = \sum_{\left\{h_k > v_i \,\&\&\, h_k < h_i^+\right\}} \mu_{ik} \tag{11}$$

$$\mathrm{cov}\left(h_i^-\right) = \sum_{\left\{h_k < v_i \,\&\&\, h_k > h_i^-\right\}} \mu_{ik} \tag{12}$$

where, μ_{ik} is the membership score of the data point h_k with respect to the ith subcluster; v_i is the computed prototype for the ith sub-

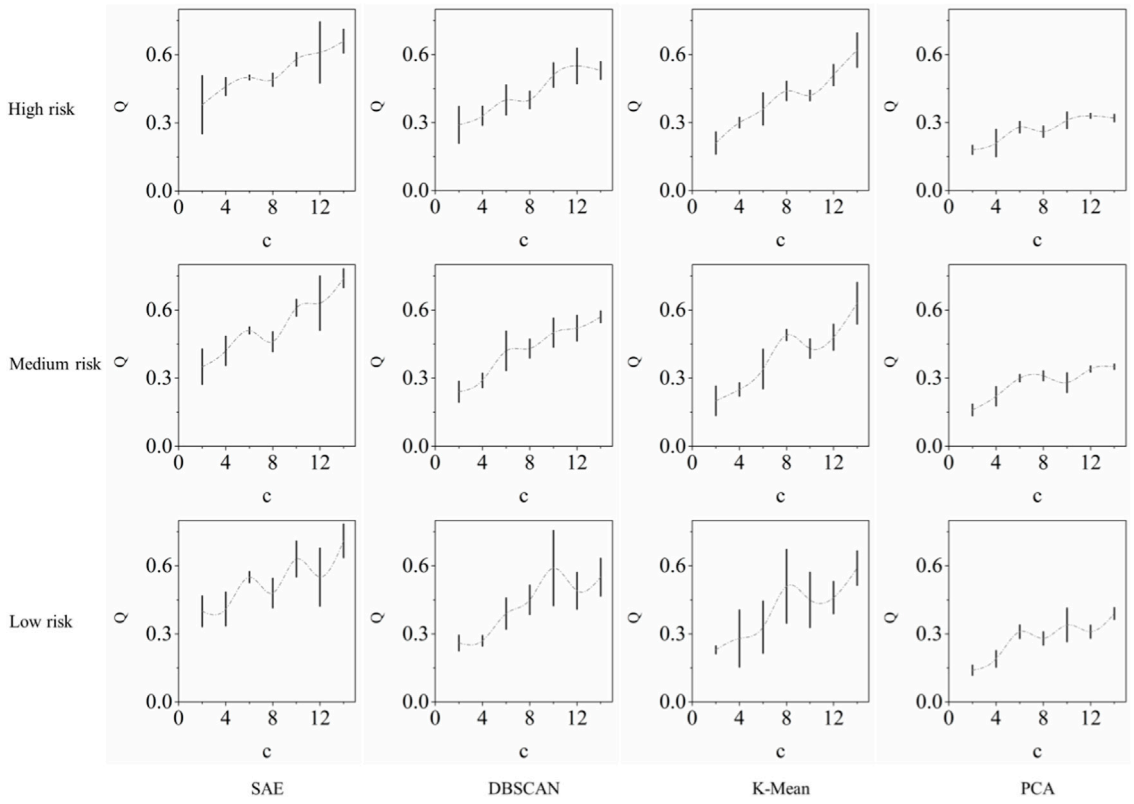

FIGURE 9
Histograms showing the comparison of Q values against state-of-art approaches.

cluster from the FCM algorithm; and h_i^+ and h_i^- are randomly initialized points indicating the upper and lower boundaries presented above, respectively.

Specificity indicates the precision of the constructed information granules. A higher specificity value indicated a smaller granule size. The computation of specificity for the upper and lower bounds is defined in Eq. 13 and Eq. 14, respectively, as follows:

$$\mathrm{sp}\left(h_i^+\right)= 1-\frac{\left\|h_i^+ - v_i\right\|}{\left\|h_{max} - v_i\right\|} \tag{13}$$

$$\mathrm{sp}\left(h_i^-\right)= 1-\frac{\left\|v_i - h_i^-\right\|}{\left\|v_i - h_{min}\right\|} \tag{14}$$

where, $\|.\|$ is the distance measure between the data points; v_i is the computed prototype from the FCM algorithm; h_i^+ and h_i^- are randomly initialized points indicating the upper and lower bounds, respectively; h_{max} and h_{min} are the maximum and minimum points, respectively, encountered within the generated data subclusters for which the information granule is developed.

2.5 Evaluation of information granules

Generally, high-quality information granules are expected to have both high coverage and specificity for describing data (Ouyang et al., 2019b). However, in practice, these two functions are usually in conflict and must be maximized simultaneously. Thus, the product of these two functions was selected to search for the optimal size of the information granules. The product of coverage and specificity is Q and is expressed in Eq. 15 as follows:

$$Q=\int_0^1 \mathrm{cov}\left(h\right)\mathrm{sp}\left(h\right)dh \tag{15}$$

where, h is the data point used to define the granule boundaries. The value of Q must be maximized to obtain the optimal solution for the information granules, and the value of Q needs to be maximized.

Additionally, the representation capacity of the information granules was considered in this study. Considering that granules reflect the structure of the original dataset, the representation capacity can be quantified using a reconstruction criterion. We can reconstruct any data point h_k into $\hat{h}_k$ by Eq. 16.

$$\hat{h}_k = \frac{\sum_{j=1}^n \mu_{ij}^m v_i}{\sum_{j=1}^n \mu_{ij}^m} \tag{16}$$

where, $\hat{h}_k$ is the reconstructed value of h_k; and μ_{ij}^m and v_i can be computed by (8) and (9), respectively. We can then compute the reconstruction error $V\left(c\right)$ using Eq. 17 as follows:

$$V\left(c\right) = \sum_{k=1}^{n}\left\|\hat{h}_k - h_k\right\|^2 \tag{17}$$

where, c is the number of clusters produced by the FCM, and $\|\hat{h}_k - h_k\|^2$ denotes the Euclidean distance between h_k and $\hat{h}_k$. The

TABLE 3 Measurement of information granules for three risk group.

Low risk group									
	SAE		DBSCAN		K-mean		PCA		Student's t-test
	Mean	Std	Mean	Std	Mean	Std	Mean	Std	*p*-value
Coverage	0.61	0.08	0.55	0.21	0.51	0.12	0.58	0.07	0.09
Specificity	0.87	0.1	0.83	0.12	0.77	0.13	0.66	0.22	0.18
Q	0.71	0.14	0.55	0.17	0.59	0.15	0.39	0.05	0.01
V(c)/V(1)	0.07	0.02	0.07	0.03	0.05	0.02	0.04	0.01	0.38
Medium risk group									
	SAE		DBSCAN		K-Mean		PCA		Student's t-test
	Mean	Std	Mean	Std	Mean	Std	Mean	Std	*p*-value
Coverage	0.68	0.11	0.59	0.07	0.52	0.13	0.61	0.12	0.04
Specificity	0.87	0.13	0.81	0.15	0.76	0.15	0.69	0.19	0.06
Q	0.74	0.08	0.57	0.05	0.63	0.18	0.35	0.02	0.01
V(c)/V(1)	0.11	0.05	0.1	0.06	0.08	0.03	0.09	0.04	0.09
High risk group									
	SAE		DBSCAN		K-Mean		PCA		Student's t-test
	Mean	Std	Mean	Std	Mean	Std	Mean	Std	*p*-value
Coverage	0.76	0.14	0.65	0.07	0.6	0.09	0.53	0.11	0.02
Specificity	0.89	0.11	0.83	0.14	0.76	0.16	0.68	0.19	0.14
Q	0.66	0.07	0.53	0.08	0.62	0.15	0.32	0.03	0.02
V(c)/V(1)	0.15	0.04	0.11	0.06	0.08	0.03	0.06	0.04	0.04

smaller the value of $V(c)$, the better the reconstruction capacity of the information granule. In practice, $V(1)$ is typically used as the standard reference to measure the value of $V(c)$ by computing $V(c)/V(1)$.

2.6 Granular boundaries

Information granules provide fuzzy rules to determine the boundaries of the decision-making tasks. However, the interpretability of these rules is vague. Two widely used risk measures namely, VaR and *CVaR* were introduced to interpret the boundaries with respect to all attributes or variables within the original input dataset.

For a certain variable, all data points within the same information granule follow a distribution with a cumulative density function (CDF), $F(X)$. Hence, given a confidence level p, *VaR* and *CVaR* are defined as Eq. 18 and Eq. 19, respectively, (Shi et al., 2021):

$$VaR_p(X) = F_X^{-1}(p) \tag{18}$$

$$CVaR_p(X) = VaR_p(X) + \frac{E[X] - E\left[X \wedge VaR_p(X)\right]}{1-p} \tag{19}$$

where, *VaR* can be conceived as the inverse computation of the CDF with respect to the confidence level p as expressed in Eq. 18, and *CVaR* is the conditional expectation of the distribution when the attributes of the data points exceed the *VaR* threshold. These can be computed for each variable provided in the input dataset to offer interpretable boundaries for the information granules. For example, in a single information granule in 2-dimensional space, various confidence levels for *VaR* are displayed in Figure 4.

3 Field investigation and data collection

In this study, data collected from multiple earthquake-induced landslides in Wenchuan County, Sichuan Province, China, were used to perform a case study analysis using the proposed approach (Carabella et al., 2022). The study area is located in the Longmen Mountains area on the northwest edge of the Sichuan Basin. On 12 May 2008, the Wenchuan earthquake, with a magnitude of 8.0 occurred in the Longmenshan tectonic zone of Sichuan Province (Chigira et al., 2010; Xie et al., 2020). This strong earthquake event in the mountainous region triggered over 3000 landslides and chains of related geohazard events, including rockfalls, debris flows, and unstable slopes (Fan et al., 2019; Li et al., 2022).

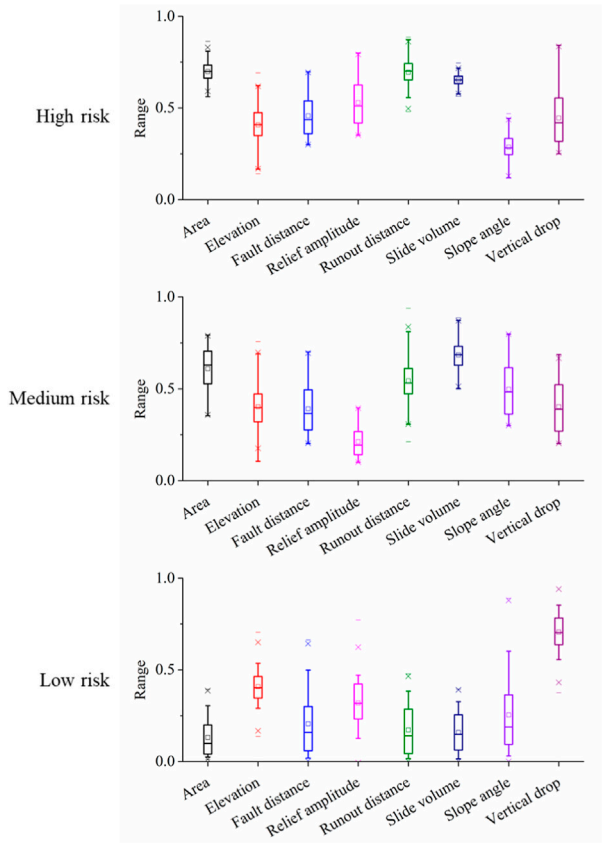

FIGURE 10
Box plots illustrating the interpretation of information granules for all risk groups.

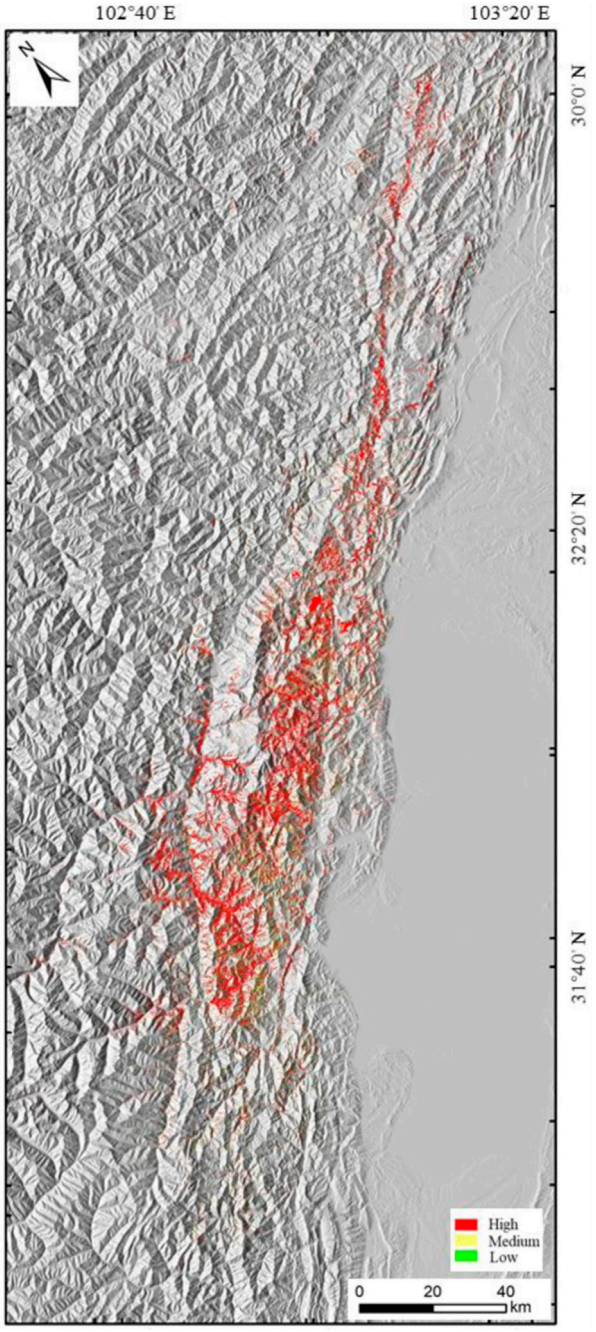

FIGURE 11
Map depicting the geospatial distribution of the earthquake induced landslides in Wenchuan County, China.

This area was selected as our study area because it has the highest seismic intensity (Modified Mercalli Intensity XI) and coseismic landslide density (Chen et al., 2020). The Yingxiu-Beichuan fault crosses the study area and is the leading cause of Wenchuan earthquake event in 2008. The elevation of the study area varies from 760 to 3200 a.s.l. and the topography consists of rugged mountains and deeply incised valleys. Multiple slides and debris flows were discovered along the Mingjiang River Valley, which is a tributary of the Yangtze River, with an average annual discharge of 452 m^3/s. Summer precipitation is the leading factor that triggers post-earthquake slides and debris flows. Typical examples of slides and debris flows are shown in Figure 5.

Since the Wenchuan earthquake, earthquake-stricken regions have been intensively monitored by geologists using remote-sensing techniques combined with field investigations. Remote sensing techniques offer highly precise information for geohazard monitoring and mitigation. Data acquisition, including full coverage and high resolution, was accomplished by multiple groups of geologists in the period between 2008 and 2018. The GIS method was then utilized to integrate the landslide inventory into the spatial dataset to discover the quantitative relationships between landslide activity and triggering factors.

We selected 3000 landslides for our case studies, the majority of which were deep-seated landslides. Based on an on-site investigation, eight geohazard-related geometrical variables of the earthquake-induced landslides are provided in Table 1. These variables are considered critical to fuzzy-rule-based models for geo-risk assessment, according to expert opinions. The statistical properties of each variable are summarized in Table 1.

According to Table 1, eight geomorphology-related variables–slide area, elevation, slope fault distance, relief amplitude, runout distance, slide volume, slope angle, and

TABLE 4 Computed VaR and CVaR for the three risk groups obtained by information granules.

Risk gorup	Variable	Area	Elevation	Fault distance	Relief amplitude	Runout distance	Slide volume	Slope angle	Vertical drop
	Unit	km^2	masl	m	m	km	$10^7\ m^3$	°	km
High	$VaR_{.95}$	5.39	3152.48	106.16	54.60	4.88	8.73	28.90	1.29
	$VaR_{.05}$	4.26	1679.61	48.83	26.52	3.63	7.56	12.52	0.48
	$CVaR_{.95}$	5.62	3334.26	108.37	56.23	5.12	8.89	30.78	1.40
	$CVaR_{.05}$	4.15	1437.23	47.73	26.17	3.38	7.37	10.58	0.47
Medium	$VaR_{.95}$	5.38	3133.84	57.33	26.95	4.51	10.05	53.94	1.13
	$VaR_{.05}$	2.74	1656.30	33.24	8.59	2.31	7.03	22.63	0.40
	$CVaR_{.95}$	5.45	3548.67	106.79	28.08	4.88	10.49	56.25	1.18
	$CVaR_{.05}$	2.61	1437.23	32.61	8.30	2.03	6.74	22.19	0.38
Low	$VaR_{.95}$	2.50	3194.43	86.00	39.78	2.72	4.43	52.43	1.58
	$VaR_{.05}$	0.11	1674.95	1.26	7.81	0.10	0.06	1.19	0.92
	$CVaR_{.95}$	2.64	3390.19	94.51	43.47	2.81	4.71	58.78	1.66
	$CVaR_{.05}$	0.09	1488.51	0.63	3.41	0.08	0.02	0.55	0.85

vertical drop–were measured and included. It also provides a unit of measurement. Additionally, the minimum value, maximum value, mean, and standard deviation were computed as first-order statistical properties. Furthermore, second-order statistical properties such as skewness and kurtosis were computed. Finally, according to expert opinions, three types of labels (high, medium, and low risks) were assigned to all landslide cases in the dataset.

4 Experimental results

4.1 Training of SAE

The proposed data-driven information granule-based approach was applied to the risk assessment of over 3000 landslide case studies in Wenchuan County, Sichuan Province, China. Among which, 2500 cases were utilized for cross-validation, and the remaining 500 cases were used as the independent test dataset. Eight geomorphology-related landslide variables are included in the granule construction dataset. Three training strategies were implemented to achieve high-quality information compression results. The strategies used are summarized in Table 2 below.

In Table 2, the first strategy (Strategy I) contains only one hidden layer with six hidden nodes. This is a typical autoencoder. Both the ReLU and sigmoid functions were tested as the activation functions, and the one with the smallest error was selected. The MSE loss was selected as the loss function, and the Adam optimizer was selected as the optimization algorithm to reduce the loss function. The maximum number of training epochs was 150, and once the loss function converged, early termination was implemented. The second strategy (Strategy II) adopts a similar approach with three symmetric hidden layers. The two outer hidden layers on each side have 6 hidden nodes, and the central "Bottleneck" layer contains only 4 hidden nodes. Layer-by-layer pre-training and fine-tuning of the stacked architecture are both included, as described in Section 2.2 Figure 2. The third training strategy (Strategy III) adopted the same training approach as Strategy II with five hidden layers in total. The central "Bottleneck" hidden layer contains only 3 hidden nodes which aims to further reduce the dimension of the original data vector. The loss functions for the three training strategies during the epochs are shown in Figure 6.

The data reconstruction loss (MSE loss) was also measured for the three training strategies. The error between the input and the reconstructed outputs was measured for the test dataset for performance evaluation. A histogram illustrating the distribution of the MSE loss are provided below in Figure 7. Here, the loss distribution comes from the MSE loss by inputing all validation dataset (the remaining 30%) into the trained SAE algorithm. Thus, the loss distribution in Figure 7 is the validation loss distribution of the SAE algorithm with respect to three different training strategies.

As shown in Figure 7, in comparison, the loss distribution for training strategy III converges close to zero. This indicates that strategy III produces a higher-quality data reconstruction outcome, and useful information is successfully encoded into the central latent layer. We then extracted a central latent vector with less dimensionality to construct robust information granules for landslide risk classification.

4.2 Constructing information-granules

Information granules were constructed using the central latent vector of the pretrained SAE algorithm. The latent

vectors not only reduce dimensionality but also preserve important information in the original input dataset. To validate the superiority of using the SAE latent vector, other state-of-the-art data structures for information granule construction, including density-based spatial clustering of applications with noise (DBSCAN), k-mean clustering, and principal component analysis (PCA), were selected for comparative analysis.

For the predefined three levels of risk by the experts, a global measurement of granular quality was performed. Figure 8 displays the coordinates of various coverage-specificity curves for the test dataset. The area under the coverage-specificity curves directly indicates the quality of the constructed information granules. The proposed approach, using the latent vector of the SAE as the source data structure, had the largest area for the three risk groups. This demonstrates the superior performance of the SAE latent vector as the source data structure to construct information granules.

In Figure 9, we also compute another metric Q with respect to the different numbers of clusters provided by the FCM. The average Q values and 95% confidence intervals were visualized for all possible cluster numbers. It is significant that for all three risk levels, the proposed approach using the latent vector of the SAE as the source data structure has higher Q values, and thus, better granule quality. Additionally, for representation capacity, $V(c)/V(1)$ was computed for the three groups of landslides with different risk levels. All numerical results, including the mean and standard deviation of coverage, specificity, Q, and $V(c)/V(1)$ are summarized in Table 3 below. Pairwise Student's t-tests were also conducted to determine whether there was a significant group difference in measurement metrics between the proposed SAE algorithm and other state-of-the-art algorithms. Here, the *t*-test is an independent sample test which the sample size differs from two sides. If the *p*-value is less than 0.05, it indicates that the corresponding measurement metric of SAE is significantly higher than all others which demonstrates the superiority of using SAE as the data structure to formulate information granules. The *p*-values of the t-tests are listed in Table 3.

4.3 Granular interpretation

Information granules are based on fuzzy rules that lack sufficient explanation for field engineers. To improve the interpretability of the proposed approach, two widely used risk measures, namely, *VaR* and *CVaR* were computed to indicate the boundaries of each variable in the original dataset. Information granules with respect to each variable were visualized using box plots, and are presented in Figure 10. Considering the scale differences across all variables, all box plots used min-max rescaling to ensure that the values were between 0 and 1.

According to Figure 10, the mean, median, 25th–75th, 10th–90th, and 5th–95th percentiles for the distribution in each variable per group are visualized. Here, the information granules denote the interval between $VaR_{.05}$ and $VaR_{.95}$. A significant distinction between the three risk groups existed with respect to area, runout distance, and slide volume. This phenomenon confirms the expert opinion that these three are the top factors in determining landslide risk.

Additionally, the geospatial distribution of the three risk groups was labeled on the map with different colors, as illustrated in Figure 11. These colored points indicate the location and size of the corresponding earthquake-induced landslides in Wenchuan County. Instead of a case-by-case risk assessment, the proposed approach automatically classified the risk of landslide occurrence in the study area.

5 Discussion

The information granules constructed for the three risk groups were computed using the latent vectors of the (SAE) algorithm. The interpretation of the information granules in each risk group has been visualized in Figure 10 with respect to each variable in the provided dataset. To provide meaningful information to field engineers for classifying the risks of applying these information granules, we computed the $CVaR_{.95}/VaR_{.95}$ and $CVaR_{.05}/VaR_{.05}$ for each variable and included them in Table 4.

As listed in Table 4, the computed values indicate the risk boundaries for landslides in each risk group. A new sample can be automatically applied to the explainable rules derived from information granules to obtain the corresponding risk assessment.

6 Conclusion

In this study, a data-driven framework is proposed to assess the risks of earthquake-induced landslides using a semi-supervised learning approach. The development of the proposed framework consists of two phases: training the stacked autoencoder and construction of fuzzy information granules. The stacked autoencoder was trained using field landslide data, following an unsupervised learning approach. The data vector was utilized as both the input and output, and the mean squared error loss was selected as the loss function for all training tasks. The deep patterns within the dataset were effectively compressed into a central latent space, and fuzzy information granules were constructed. The boundaries in the latent space for all risk levels were optimized and obtained.

The development of this framework was compared with that of the different benchmarks in a case study area in Wenchuan County, China. The computational results demonstrate that the pre-trained stacked autoencoder can more effectively compress deep data patterns into a low-dimensional space. A comparative analysis based on the testing dataset demonstrated that the information granules could cover most of the homogenous data points in each subgroup. Additionally, stacked-autoencoder-based information granules offer higher accuracy, robustness, and specificity than other state-of-the-art data structures. The proposed fuzzy information granules based on the latent space of a stacked autoencoder are promising for achieving satisfactory classification performance, especially for earthquake-induced landslide datasets, and can offer valuable suggestions to practicing field geology engineers.

Data availability statement

The original contributions presented in the study are included in the article/Supplementary material, further inquiries can be directed to the corresponding author.

Author contributions

YF: Data curation, Writing–original draft. WY: Writing–original draft, Writing–review and editing. JW: Software, Validation, Writing–original draft. HL: Funding acquisition, Supervision, Writing–review and editing.

Funding

The author(s) declare financial support was received for the research, authorship, and/or publication of this article. This research is supported by Natural Science Foundation of Sichuan Province, China (Grant No. 2023NSFSC0789), and the Open Fund of Sichuan Engineering Research Center for Mechanical Properties and Engineering Technology of Unsaturated Soils (No. SC-FBHT2022-13).

Conflict of interest

The authors declare that the research was conducted in the absence of any commercial or financial relationships that could be construed as a potential conflict of interest.

Publisher's note

All claims expressed in this article are solely those of the authors and do not necessarily represent those of their affiliated organizations, or those of the publisher, the editors and the reviewers. Any product that may be evaluated in this article, or claim that may be made by its manufacturer, is not guaranteed or endorsed by the publisher.

References

Adem, K., Kiliçarslan, S., and Cömert, O. (2019). Classification and diagnosis of cervical cancer with stacked autoencoder and softmax classification. *Expert Syst. Appl.* 115, 557–564. doi:10.1016/j.eswa.2018.08.050

Althuwaynee, O. F., Pradhan, B., Park, H. J., and Lee, J. H. (2014). A novel ensemble decision tree-based CHi-squared Automatic Interaction Detection (CHAID) and multivariate logistic regression models in landslide susceptibility mapping. *Landslides* 11 (6), 1063–1078. doi:10.1007/s10346-014-0466-0

Carabella, C., Cinosi, J., Piattelli, V., Burrato, P., and Miccadei, E. (2022). Earthquake-induced landslides susceptibility evaluation: a case study from the Abruzzo region (Central Italy). *Catena* 208, 105729. doi:10.1016/j.catena.2021.105729

Chen, M., Tang, C., Xiong, J., Shi, Q. Y., Li, N., Gong, L. F., et al. (2020). The long-term evolution of landslide activity near the epicentral area of the 2008 Wenchuan earthquake in China. *Geomorphology* 367, 107317. doi:10.1016/j.geomorph.2020.107317

Chigira, M., Wu, X., Inokuchi, T., and Wang, G. (2010). Landslides induced by the 2008 wenchuan earthquake, sichuan, China. *Geomorphology* 118 (3-4), 225–238. doi:10.1016/j.geomorph.2010.01.003

Chowdhuri, I., Pal, S. C., Janizadeh, S., Saha, A., Ahmadi, K., Chakrabortty, R., et al. (2022). Application of novel deep boosting framework-based earthquake induced landslide hazards prediction approach in Sikkim Himalaya. *Geocarto Int.* 37 (26), 12509–12535. doi:10.1080/10106049.2022.2068675

Cruden, D. M. (1991). A simple definition of a landslide. *Bull. Int. Assoc. Eng. Geology-Bulletin de l'Association Int. de Géologie de l'Ingénieur* 43 (1), 27–29. doi:10.1007/bf02590167

Dai, F. C., Lee, C. F., and Ngai, Y. Y. (2002). Landslide risk assessment and management: an overview. *Eng. Geol.* 64 (1), 65–87. doi:10.1016/s0013-7952(01)00093-x

Fan, X., Scaringi, G., Korup, O., West, A. J., van Westen, C. J., Tanyas, H., et al. (2019). Earthquake-induced chains of geologic hazards: patterns, mechanisms, and impacts. *Rev. Geophys.* 57 (2), 421–503. doi:10.1029/2018rg000626

Gao, G., and Meguid, M. A. (2018a). On the role of sphericity of falling rock clusters—insights from experimental and numerical investigations. *Landslides* 15, 219–232. doi:10.1007/s10346-017-0874-z

Gao, G., and Meguid, M. A. (2018b). Modeling the impact of a falling rock cluster on rigid structures. *Int. J. geomechanics* 18 (2), 1–15. doi:10.1061/(asce)gm.1943-5622.0001045

Gao, G., Meguid, M. A., Chouinard, L. E., and Xu, C. (2020). Insights into the transport and fragmentation characteristics of earthquake-induced rock avalanche: numerical study. *Int. J. Geomechanics* 20 (9), 04020157. doi:10.1061/(asce)gm.1943-5622.0001800

Gao, G., Meguid, M. A., Chouinard, L. E., and Zhan, W. (2021). Dynamic disintegration processes accompanying transport of an earthquake-induced landslide. *Landslides* 18, 909–933. doi:10.1007/s10346-020-01508-1

Gorsevski, P. V., Brown, M. K., Panter, K., Onasch, C. M., Simic, A., and Snyder, J. (2016). Landslide detection and susceptibility mapping using LiDAR and an artificial neural network approach: a case study in the Cuyahoga Valley National Park, Ohio. *Landslides* 13 (3), 467–484. doi:10.1007/s10346-015-0587-0

He, Y., and Kusiak, A. (2017). Performance assessment of wind turbines: data-derived quantitative metrics. *IEEE Trans. Sustain. Energy* 9 (1), 65–73. doi:10.1109/tste.2017.2715061

Huang, F., Yao, C., Liu, W., Li, Y., and Liu, X. (2018). Landslide susceptibility assessment in the Nantian area of China: a comparison of frequency ratio model and support vector machine. *Geomatics, Nat. Hazards Risk* 9 (1), 919–938. doi:10.1080/19475705.2018.1482963

Karakas, G., Nefeslioglu, H. A., Kocaman, S., Buyukdemircioglu, M., Yurur, T., and Gokceoglu, C. (2021). Derivation of earthquake-induced landslide distribution using aerial photogrammetry: the January 24, 2020, Elazig (Turkey) earthquake. *Landslides* 18 (6), 2193–2209. doi:10.1007/s10346-021-01660-2

Kasama, K., Furukawa, Z., and Hu, L. (2021). Practical reliability analysis for earthquake-induced 3D landslide using stochastic response surface method. *Comput. Geotechnics* 137, 104303. doi:10.1016/j.compgeo.2021.104303

Khamparia, A., Saini, G., Pandey, B., Tiwari, S., Gupta, D., and Khanna, A. (2020). KDSAE: chronic kidney disease classification with multimedia data learning using deep stacked autoencoder network. *Multimedia Tools Appl.* 79, 35425–35440. doi:10.1007/s11042-019-07839-z

Li, H. (2022a). SCADA data based wind power interval prediction using LUBE-based deep residual networks. *Front. Energy Res.* 10, 920837. doi:10.3389/fenrg.2022.920837

Li, H. (2022b). Short-Term wind power prediction via spatial temporal analysis and deep residual networks. *Front. Energy Res.* 10, 920407. doi:10.3389/fenrg.2022.920407

Li, H., He, Y., Xu, Q., Deng, j., Li, W., and Wei, Y. (2022). Detection and segmentation of loess landslides via satellite images: a two-phase framework. *Landslides* 19, 673–686. doi:10.1007/s10346-021-01789-0

Li, H., He, Y., Xu, Q., Deng, J., Li, W., Wei, Y., et al. (2023). Sematic segmentation of loess landslides with STAPLE mask and fully connected conditional random field. *Landslides* 20, 367–380. doi:10.1007/s10346-022-01983-8

Liseune, A., Salamone, M., Van den Poel, D., Van Ranst, B., and Hostens, M. (2020). Leveraging latent representations for milk yield prediction and interpolation using deep learning. *Comput. Electron. Agric.* 175, 105600. doi:10.1016/j.compag.2020.105600

Merghadi, A., Yunus, A. P., Dou, J., Whiteley, J., ThaiPham, B., Bui, D. T., et al. (2020). Machine learning methods for landslide susceptibility studies: a comparative overview of algorithm performance. *Earth-Science Rev.* 207, 103225. doi:10.1016/j.earscirev.2020.103225

Ouyang, T., Pedrycz, W., and Pizzi, N. J. (2019b). Record linkage based on a three-way decision with the use of granular descriptors. *Expert Syst. Appl.* 122, 16–26. doi:10.1016/j.eswa.2018.12.038

Ouyang, T., Pedrycz, W., and Pizzi, N. J. (2019c). Rule-based modeling with DBSCAN-based information granules. *IEEE Trans. Cybern.* 51 (7), 3653–3663. doi:10.1109/tcyb.2019.2902603

Ouyang, T., Pedrycz, W., Reyes-Galaviz, O. F., and Pizzi, N. J. (2019a). Granular description of data structures: a two-phase design. *IEEE Trans. Cybern.* 51 (4), 1902–1912. doi:10.1109/tcyb.2018.2887115

Ouyang, T., and Zhang, X. (2022). DBSCAN-based granular descriptors for rule-based modeling. *Soft Comput.* 26 (24), 13249–13262. doi:10.1007/s00500-022-07514-w

Paoletti, M. E., Haut, J. M., Plaza, J., and Plaza, A. (2018). A new deep convolutional neural network for fast hyperspectral image classification. *ISPRS J. photogrammetry remote Sens.* 145, 120–147. doi:10.1016/j.isprsjprs.2017.11.021

Pokharel, B., Alvioli, M., and Lim, S. (2021). Assessment of earthquake-induced landslide inventories and susceptibility maps using slope unit-based logistic regression and geospatial statistics. *Sci. Rep.* 11 (1), 21333. doi:10.1038/s41598-021-00780-y

Rajabi, A. M., Khodaparast, M., and Mohammadi, M. (2022). Earthquake-induced landslide prediction using back-propagation type artificial neural network: case study in northern Iran. *Nat. Hazards* 110 (1), 679–694. doi:10.1007/s11069-021-04963-8

Shi, B., Zeng, T., Tang, C., Zhang, L., Xie, Z., Lv, G., et al. (2021). Landslide risk assessment using granular fuzzy rule-based modeling: a case study on earthquake-triggered landslides. *IEEE Access* 9, 135790–135802. doi:10.1109/access.2021.3116869

Van Westen, C. J., Van Asch, T. W., and Soeters, R. (2006). Landslide hazard and risk zonation—why is it still so difficult? *Bull. Eng. Geol. Environ.* 65 (2), 167–184. doi:10.1007/s10064-005-0023-0

Xie, M., Zhao, W., Ju, N., He, C., Huang, H., and Cui, Q. (2020). Landslide evolution assessment based on InSAR and real-time monitoring of a large reactivated landslide, Wenchuan, China. *Eng. Geol.* 277, 105781. doi:10.1016/j.enggeo.2020.105781

Xu, Q., Li, H., He, Y., Liu, F., and Peng, D. (2019). Comparison of data-driven models of loess landslide runout distance estimation. *Bull. Eng. Geol. Environ.* 78 (2), 1281–1294. doi:10.1007/s10064-017-1176-3

Yi, Y., Zhang, Z., Zhang, W., Jia, H., and Zhang, J. (2020). Landslide susceptibility mapping using multiscale sampling strategy and convolutional neural network: a case study in Jiuzhaigou region. *Catena* 195, 104851. doi:10.1016/j.catena.2020.104851

Zabalza, J., Ren, J., Zheng, J., Zhao, H., Qing, C., Yang, Z., et al. (2016). Novel segmented stacked autoencoder for effective dimensionality reduction and feature extraction in hyperspectral imaging. *Neurocomputing* 185, 1–10. doi:10.1016/j.neucom.2015.11.044

Zhao, W., and Du, S. (2016). Learning multiscale and deep representations for classifying remotely sensed imagery. *ISPRS J. Photogrammetry Remote Sens.* 113, 155–165. doi:10.1016/j.isprsjprs.2016.01.004

Zhou, J., Wei, J., Yang, T., Zhang, P., Liu, F., and Chen, J. (2021a). Seepage channel development in the crown pillar: insights from induced microseismicity. *Int. J. Rock Mech. Min. Sci.* 145, 104851. doi:10.1016/j.ijrmms.2021.104851

Zhou, Q., Xu, Q., Peng, D., Fan, X., Ouyang, C., Zhao, K., et al. (2021b). Quantitative spatial distribution model of site-specific loess landslides on the Heifangtai terrace, China. *Landslides* 18, 1163–1176. doi:10.1007/s10346-020-01551-y

Zhou, Q., Xu, Q., Zeng, P., Zhao, K., and Yuan, S. (2022). Scenario-based quantitative human vulnerability assessment of site-specific landslides using a probabilistic model. *Landslides* 19, 993–1008. doi:10.1007/s10346-021-01827-x

frontiers | Frontiers in Earth Science

TYPE Original Research
PUBLISHED 28 December 2023
DOI 10.3389/feart.2023.1265852

OPEN ACCESS

EDITED BY
Yunhui Zhang,
Southwest Jiaotong University, China

REVIEWED BY
Xun Huang,
Chongqing Normal University, China
Tong Shen,
Henan University of Urban Construction, China
Huiran Gao,
Ministry of Emergency Management, China

*CORRESPONDENCE
Liu Yang,
Yangliu00002023@163.com

RECEIVED 24 July 2023
ACCEPTED 08 November 2023
PUBLISHED 28 December 2023

CITATION
Yang L, Chuan T, Lingfeng G and Jiang X (2023), The evolution of glacial lake and glaciers and their potential impact on glacial debris flow activity in the Palong Zangbu catchment in Southeastern Tibet. *Front. Earth Sci.* 11:1265852. doi: 10.3389/feart.2023.1265852

The evolution of glacial lake and glaciers and their potential impact on glacial debris flow activity in the Palong Zangbu catchment in Southeastern Tibet

Liu Yang[1,2]*, Tang Chuan[1], Gong Lingfeng[3] and Xiong Jiang[4]

[1]State Key Laboratory of Geohazard Prevention and Geoenvironment Protection, Chengdu University of Technology, Chengdu, China, [2]Department of Natural Resources of Sichuan Province, Chengdu, China, [3]Chengdu Geological Survey Center, China Geological Survey, Chengdu, China, [4]Key Laboratory of Mountain Hazards and Earth Surface Processes, Institute of Mountain Hazards and Environment, Chinese Academy of Sciences, Chengdu, China

Due to warm and humid air currents of the Indian Ocean and the southwest monsoon, the Palong Zangbo catchment in southeastern Tibet has developed oceanic glaciers in the valley, and the activity of glacial debris flows has been gradually intensified under neotectonic activity, frequent earthquakes, climate change, and extreme rainfall. In this paper, the topographic and morphological data of the debris flow basin, the dynamic evolution characteristics of glaciers and glacial lakes were analyzed by using multisource long-term series of remote sensing images. Simultaneously, the distribution of moraines and landslide sources were extracted based on satellite image. In addition, climate change in the study area was analysed using temperature and rainfall data from the last 40 years, revealing that the average temperature in the study area from May to October presented a fluctuating tendency as a whole, especially after 2013, when the temperature gradually increased. As these temperature changes led to continuous melting of the glaciers in the study area, the glacier area decreased from 8,300 km^2 in 1988–4,584 km^2 in 2019, which decreased nearly 45%. However, the number and area of glacial lakes in the study area gradually increased under a power-law trend, which further led to a significant increase on the possibility of glacial lake rupture in the study area. Due to the joint effects of earthquakes, glacier melting and glacial lake collapse, the debris flows in the study area were well developed, and a total of 122 debris flows were found with varying channel lengths, areas and material sources. Importantly, the characteristics of the glaciers, glacial lakes and climate change in the study area have indicated that the glaciers have retreated, the number of glacial lakes has increased, and the risk of debris flow in this basin will increase in the future. Therefore, it is necessary to strengthen monitoring and early warnings on floods due to glacial lake collapses and debris flows in the study area to improve the risk management of debris flows and floods and the prevention and mitigation of disasters.

KEYWORDS

glacial debris flow, glacial lake burst, climate change, debris flow activity, remote sensing

1 Introduction

The south eastern region of the Qinghai-Tibet Plateau is a typical alpine canyon area in China with active oceanic glacial activity (Wu et al., 2019). The area is characterised by a fragile ecological and geological environment resulting from high-intensity earthquakes, highland stress, strong tectonic activity and deep river formation, and geological disasters such as rockfalls, landslides, debris flows, ice avalanches and avalanches frequently occurring in this area (Huang et al., 2021). According to the research, there have been 430 watersheds which experienced debris flow in the history of Nyingchi region. The highest frequency of debris flow outbreaks reaches 21 times a year (Chen et al., 2011). In particular, with climate change, the increasing melting glaciers and the glacial lakes outburst have led to frequent glacial debris flow disasters in the southeast of the Qinghai-Tibet Plateau (Liu et al., 2011; Wei et al., 2018; Wang et al., 2014). Among them, the specific debris flows induced by melting snow, glacial lake outbursts, and rainfall along the Palong Zangbo River are extremely developed, which poses great risks and threats to the Sichuan–Tibet Highway, the Sichuan–Tibet Railway and the mountain towns along these routes (Cui et al., 2014; Huang et al., 2021). Therefore, further analysis of the long-term activity characteristics of glacial debris flows in the region is of great significance for disaster prevention and mitigation.

As a fluid coupled with fluids and solids, the formation process of debris flows is the result of the combination of steep terrain, abundant material sources and strong hydrodynamics. The Palong Zangbo Valley passes through the Jiali Fault Zone, where strong tectonic uplift, river bank erosion and glaciation lead to steep mountain slopes in the area (Huang et al., 2021). Particularly, under the action of earthquakes, a large number of rockfalls and landslides in the basin have been triggered (Chigira et al., 2010; Tang et al., 2011). At the same time, strong freeze–thaw cycles have led to the storage of plentiful loose solid material in the watershed of the region, especially with the melting glaciers, which have led to the accumulation of a large amount of moraine in the channel, providing sufficient material sources for the debris flow. Numerous studies have been carried out on the shear failure characteristics and stability of moraine soils (Xie et al., 2019; Fu et al., 2021), which is of great significance on revealing the initiation mechanism of glacial debris flows. However, the sources of materials in the glacial watershed change with the melting of glaciers, resulting in certain differences and dynamics in the outbreak characteristics of glacial debris flows. Studies have shown that the development of glacial debris flows is controlled by factors such as glacier thickness, glacier area, lake area, rainfall intensity, temperature, watershed area, source volume, and longitudinal grade of channels, among which high temperature and rainfall are key factors to glacial debris flow outbreaks (Yan, 2020). In addition, the Palong Zangbo Valley is a highland thermal anomaly area (Huang et al., 2021), which directly leads to the gradual melting of glaciers along the Palong Zangbo River Basin, and abundant moraine provides a sufficient source for the debris flows. With melting glaciers, the areas and water levels of glacial lakes have increased (Li D. et al., 2021), and glacial lakes have the potential to repeatedly burst (Yang et al., 2011a). For example, from 1983 to 1986, there were multiple debris flows from glacial lake outbursts in the Peilong gully, of which debris flows induced by collapsing glacial lakes erupted in 1988 in the Midui gully, a barrage lake was generated from the debris flow in the Guxiang gully in 1975 and 2005, then the Guxiang debris flow erupted due to lake rupture, and the Tianmo debris flow was caused by ice and snow meltwater and rainfall in 2007. Although the above studies about Midui gully, Guxiang gully and Tianmo guly have clearly revealed the initiation mechanism and activity characteristics of glacial debris flows, with the gradual intensification of global warming. Research on the relationship between dynamic laws of glaciers and glacial lakes with the formation of debris flows is remain poorly understood (Medeu et al., 2022; Racoviteanu et al., 2022), which further leads to an insufficient understanding of the long-term activities of glacial debris flows. Therefore, an understanding of the dynamic response process between temperature change and glacial lakes, as well as the dynamic changes in the development status of moraine due to heating, is the basis to analyse the activity of glacial collapse debris flows.

Impacted by the steep terrain, the ground surveys, UAV aerial photography technology and laser scanning are difficult to monitor the glacier changes on a large scale. Numerous previous studies indicated that remote sensing and GIS can effectively monitor the evolution of glaciers and glacial lake in alpine regions by identifying information on glaciers and glacial lakes from satellite images (Shrestha et al., 2016; Bajracharya et al., 2014). For example, many researchers have monitored the long-term dynamics of glaciers using high-definition remote sensing images (Bajracharya et al., 2014). Simultaneously, the long-term evolution of glacial lakes in Boqu in the central Himalayas were also monitored based on satellite images (Chen et al., 2007; Wang et al., 2014; Zhang et al., 2015; Nie et el., 2017; Li D. et al., 2021; Su et al., 2021). However, although changes in glaciers and glacial lakes have been well documented in the previous studies, the influencing factors of the dynamic evolution of glaciers and glacial lakes are not fully understood.

Importantly, with the gradual increase of glacial melting and the water level of moraine lakes, flood events caused by glacial lake ruptures have occurred frequently in recent years (Liu et al., 2014; Riaz et al., 2014). More and more works have documented the chain disaster events induced by changes in glaciers and glacial lakes (Yang et al., 2011b; Cook et al., 2018; Li Y. et al., 2021; Shangguan et al., 2021; Zhang et al., 2021). Obviously, understanding the response relationship between temperature changes to glaciers and glacial lakes and its impact on glacial debris flow activity will provide some guidance for monitoring and providing early warnings on glacial debris flows and preventing risk in the region. This is important for disaster prevention and reduction under climate change. The main purpose of this study is 1) analysis the dynamic evolution of glaciers and glacial lakes; 2) understanding the influence of climate change on evolution of glaciers and glacial lakes evolution; 3) revealed the impact of glacier and glacial lake changes on the activity of glacial debris flow.

1.1 Study area

The study area is located in the section from Ranwu to Thongmai in the Palong Tsangpo Basin, mainly in Bomi, Nyingchi (Figure 1). The study area is 16,021.12 km^2, the highest elevation is 6,650 m a.s.l, the lowest elevation is 2000 m a.s.l, the

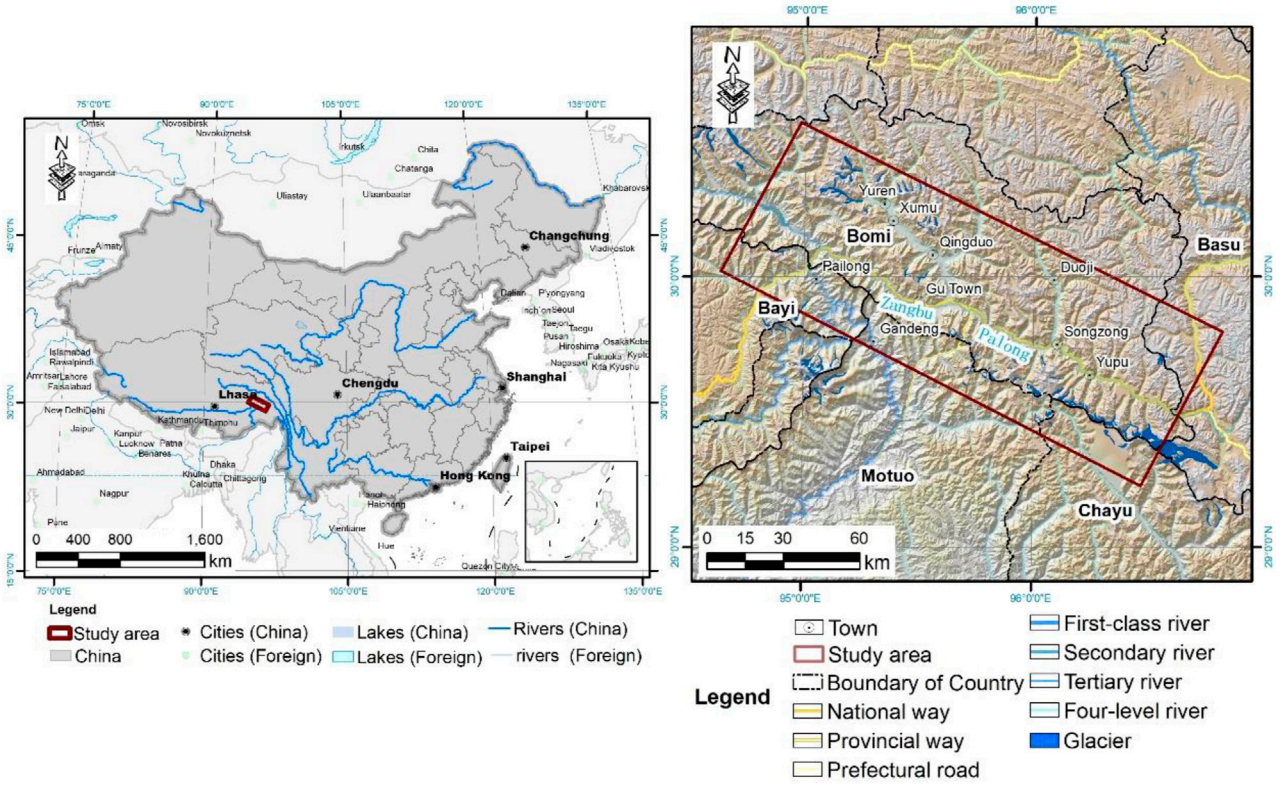

FIGURE 1
Geographical map of the study area.

maximum altitude difference is approximately 4,650 m a.s.l, and a large number of oceanic glacier gullies have developed upstream. Glacial, alpine canyon, and river accumulation landforms are extremely well developed. This area, located on the northern Qinghai-Tibet Plateau, is at the junction of the northern Tibetan and the Himalayan massif and is a typical deep alpine canyon. In addition, the Jiali Fault and the Zamu-Maniwen Fault pass through the study area (He et al., 2005). The geological structure around the study area is extremely complex, and there is frequent seismic activity in the area due to the activity belts of the Namtso-Zhongsha, Jiali-Ranwu and Metuo structures. According to previous researches, there have been as many as 9 strong earthquakes with surface wave magnitude of 6.0 (Ms 6.0) or above in the region in the past 60 years, and approximately 50 earthquakes of Ms 4.7 to Ms 5.9 magnitudes. One of the most representative seismic events was the Ms 8.6 earthquake that occurred in Chayu County on 15 August 1950.

Climatic conditions are the main triggers for geological disasters in the region, and the study area has the monsoon climate of the temperate semi-humid plateau in southeastern Tibet, which is affected by the warm and humid air flow of the Indian Ocean and the southwestern monsoon. The annual average temperature in the study area is 8.5°C, and the lowest temperature is in January, when the average temperature is approximately −0.2°C, while the highest temperature is in July, when the average temperature is approximately 16.4°C. Overall, the highest temperature of the year is 31 °C and the lowest temperature is −20.3°C. The average annual rainfall is approximately 977.1 mm, and the rainfall from March to October accounts for approximately 93.5% of the total annual precipitation.

2 Data and methods

2.1 Sources and data processing

To monitor the dynamic changes in glaciers and glacial lakes in the watershed of the study area over time, this study collected QuickBird, IKONOS, SPOT-5 and Landsat images from 1988 to 2019. Table 1 shows that the QuickBird satellite image resolution is 0.61 m, the SPOT5 image resolution is 2.5 m, and the IKONOS image resolution is 1 m. The multispectral ETM+ and TM image resolutions are 30 m. In addition, ASTER GDEM data measured by the EARTH observation satellite Terra of NASA were collected with a resolution of 30 m.

Subsequently, the collected remote sensing data were processed by band combination, geometric correction, image fusion, image mosaicking and cropping, based in ERDAS 9.2, ENVI 5.0 and ARCGIS 10. Then, compared to the raw data, the geometric accuracy, density, texture and tone information of the processed images were significantly enhanced, improving the interpretation accuracy and quality of the remote sensing images. Finally, the evolution of glacier, glacial lake and their impact on glacial debris flow activity were analysed according to the technical flowchart, as shown in Figure 2.

TABLE 1 The information of data used in this study.

Data	Time	Spectral signature	Resolution
QuickBird	14 November 2001, 25 November 2001, 19 November 2000, 12 February 2013 (Midui catchment)	RGB, NIR	0.61 m–0.72 m (Panchromatic), 2.44 m–2.88 m (Multispectral)
IKONOS	30 April 2006	RGB, NIR	1 m (Panchromatic), 4 m (Multispectral)
SPOT-5	20 November 2001	R、G、NIR and VNIR-SWIR	2.5 m (Panchromatic), 10 m (multispectral)
ETM+	11 November 2002, 4 December 2002	SWIR	30 m (Panchromatic), 120 m (MWIR), 15 m (Panchromatic)
TM	27 October 1988, 9 November 2010, 2 October 2010	SWIR	30 m (Multispectral), 120 m (MWIR)
GF	2019	VNIR	2 m
ASTER GDEM	2009	VNIR-SWIR	30 m
Rainfall and temperature	1980–2020	—	year

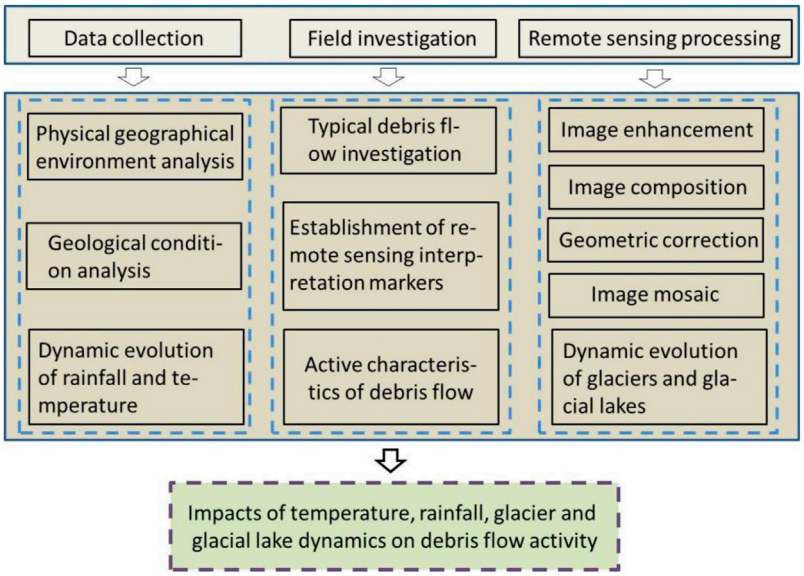

FIGURE 2
Technical flowchart in this study.

2.2 Supervised classification and information extraction

Regional reflection characteristics vary due to different textures, compositions, and shading of materials on the surface; thus, materials are shown in varying shades and shapes in remote-sensing images. Based on these features, a supervised classification method has been adopted to automatically extract the materials. In this region, glaciers in bright white are mainly distributed above the alpine snow line, such as in the ice bucket or inside the ice tongue (Figure 3A), and perennial snow and ice, shown in white and covered by shadows, are mainly distributed below the altitude of the formation glacier, on shady mountain slopes, or in gently sloping areas with low amounts of sunshine; in addition, glacial lakes in dark blue are generally distributed in glaciers and in the lower parts of the perennial snow and ice, and the terrain is relatively gentle (Figure 3B). To fully understand the development characteristics of glacial snow and glacial lakes in the study area, the samples were selected based on the collected TM and ETM+ remote sensing images and the visual interpretation of glaciers, glacial lakes and other geographical features. Then supervised classification, a process of assigning a class value to a set of grid cells in a raster GIS database based on the values of similar grid cells that have been *a priori* classified as representative of a class or group (Abburu and Golla, 2015; Merry et al., 2023), was performed on the ENVI 5.0 platform to automatically identify and extract the glaciers, glacial lakes and snow of three remote sensing images from 1988, 2002 and 2010.

The limitation of using supervised classification for automatic identification and extraction is that it incorrectly combines materials with similar glacier features into the same category as mountain

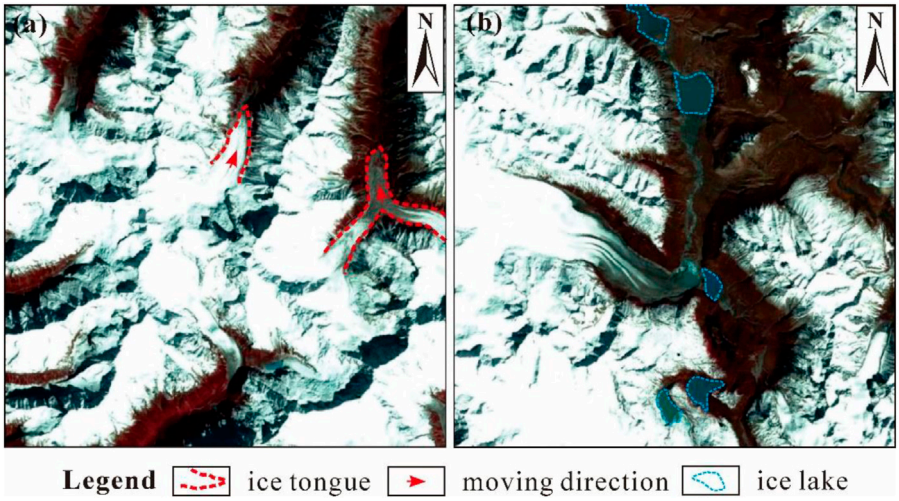

FIGURE 3
Glacier and glacial lake identification markers. **(A)** Glacier, **(B)** Glacial lake.

shadows. Therefore, in this paper, two kinds of remote sensing information of glacial lakes that were extracted by both unsupervised and supervised classification methods were compared and verified in the field, and then sifts and clusters of the remote sensing information were determined by the supervised classification method to remove and synthesise the small classification fragments to obtain reliable and accurate results on the materials and to further reveal the dynamic changes in glaciers and glacial lakes.

In addition, a large number of landslides have developed in the debris flow basin of the study area, and abundant moraine material with melting glaciers has also accumulated in the channel, providing sufficient material for debris flows. Based on field investigation, this study first constructed identification markers of debris materials, moraines, debris flow accumulation fans and other landslides and then combined them with high-definition remote sensing images using the ArcGIS technology platform. A manual, interactive interpretation of moraines was performed on the landslide sources and accumulation fans in the debris flow basin, and the source information of debris flow in the basin was constructed.

2.3 Extraction of historical rainfall and temperature change characteristics

To analyse the effects of dynamic changes such as temperature, rainfall and ground temperature on glaciers and glacial lakes in the study area, the average monthly rainfall and temperature data of the study area from 1988 to 2019 were collected. The data show that in the study region, temperatures higher than 0 °C from May to October were positively correlated with the melting of glacial snow. Therefore, in this paper, the average temperature from May to October each year was considered as the influencing factor of or the reaction temperature to glacial snow melt. Meanwhile, the average monthly rainfall in each year from 1988 to 2019 in the study area was also considered as the influencing factor for interannual glacier and glacial lake dynamics.

Geothermal remote sensing inversion based on the radiation transmission equation is a common method to obtain regional geothermal data. Specifically, by this method, the thermal radiation received by the sensor is inverted into the real ground temperature after correction on the atmospheric radiation, observation angle and amount of radiation on the specific surface (Dash et al., 2002). The split window algorithm is the most common technique for retrieving land surface temperature, in which the Qin algorithm (Qin and Karnieli, 1999) can effectively retrieve the surface temperature corresponding to any cell on the image. The equations are as follows:

$$T_s = A_0 + A_1 T_4 - A_2 T_5 \quad (1)$$

$$A_0 = [66.54067 D_4 (1 - C_5 - D_5) - 62.23928 D_5 (1 - C_4 - D_4)] / (D_5 C_4 - D_4 C_5) \quad (2)$$

$$A_1 = 1 + [0.43059 D_5 (1 - C_4 - D_4)] / (D_5 C_4 - D_4 C_5) \quad (3)$$

$$A_2 = [0.46585 D_4 (1 - C_5 - D_5) + D_4] / (D_5 C_4 - D_4 C_5) \quad (4)$$

$$C_i = \varepsilon_i . T_i(\theta) \quad (5)$$

$$C_i = \varepsilon_i . T_i(\theta) \quad (6)$$

where T_s is the surface temperature; T_4 and T_5 are the brightness temperatures of thermal infrared channels 4 and 5 of the cells, with K as the absolute temperature; ε_i is the specific emissivity in channel i; and $T_i(\theta)$ is the atmospheric transmittance of electromagnetic waves in channel i under the zenith angle θ of the sensor.

3 Analysis results

3.1 Temperature and rainfall dynamics

In glacial areas, temperature is key to the growth and ablation of glacier formation, that is, temperature is a sensitive factor to dynamic changes in glaciers. In this study, the rainfall and temperature monitoring data were collected from a weather station. By analysing the monthly average temperature data over the past

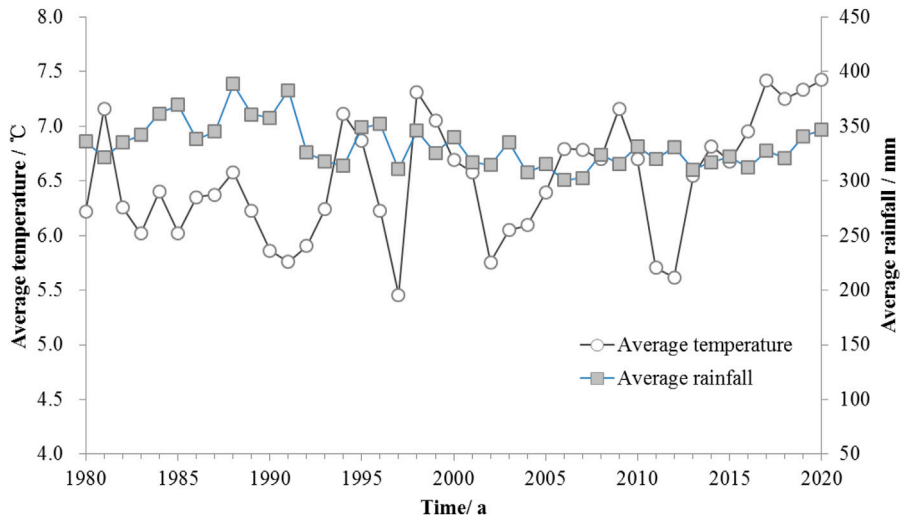

FIGURE 4
Dynamic changes in temperature and rainfall in the study area.

40 years in the Palong Zangbo Valley, it was found that the temperatures from May to October were higher than zero degrees, which was conducive to glacier melting and the water level elevation of glacial lakes. Thus, the average temperature of the above period was analysed to reveal the dynamic changes. In Figure 4, the average temperature variation in the study area in the period ranged from 5.5°C to 7.5°C over the past 40 years. Overall, the temperature in the study area presented a growing increase in the first 4–5 years and then continuously decreased in the following 4–5 years, that is, the pulsed and dynamic temperature change presented in 4–5 years as a cycle. However, the temperature significantly increased from 2012 to 2017 and then tended to rise slowly. This dynamic change in temperature leads to some dynamic differences in the glacier ice and snow cover area and the water level of the glacial lakes in the study area, and it also has an impact on the ground temperature.

In Figure 5A, the geothermal variation ranged from −9°C to 46 °C in the study area in 2002, which was mainly concentrated in the central part of the study area, and the geothermal temperatures in the northwest and southeast regions were relatively high. As the average temperature from May to October in the study area increased from 5.8°C in 2002°C to 6.7°C in 2010, the maximum geothermal temperature in the study area also increased to 53 °C (Figure 5B). As the overall ground temperature increased, the range of low temperature areas decreased. In 2013, the geothermal variation range of the study area was from −12°C to 43°C, and the ground temperature in the northwest region of the study area significantly decreased, while the range of the low temperature in the central zone expanded (Figure 5C). Until 2017, the minimum and maximum ground temperatures were −10°C and 43°C, respectively (Figure 5D). Compared with the previous period, the coverage of the high temperature area increased significantly in 2017, and the low temperature zones were distributed sporadically in the study region. The dynamic differences in time and space between air temperature and ground temperature further led to the dynamic variability of glaciers and glacial lakes in the study area, which was conducive to the development of glacial debris flows.

In addition, the average annual rainfall in the study area from 1980 to 2020 was mostly concentrated between 300 mm and 350 mm and presented pulsed and dynamic changes (Figure 4), but it had slight dynamic differences. However, before 2013, the rainfall and temperature in the study area showed the opposite dynamic trend, that is, the rainfall decreased gradually with increasing temperatures over the years (Figure 4). However, in 2013, the rainfall and temperature in the study area had the same dynamic change trend; that is, the temperature increased with the growing rainfall that year. With rising air and ground temperatures, the glacial meltwater in the study area increased, while increased rainfall led to further increases in runoff in the basin. Therefore, the risk of glacial debris flows and debris flows due to glacial lake collapse in the study area was further increased, and the landslide activity was enhanced.

3.2 Evolution of glaciers and glacial lakes

3.2.1 Dynamic changes in glaciers

The above analysis revealed that the air temperature, ground temperature and rainfall in the study area changed dynamically over time, which exacerbated glacial activity, resulting in dynamic changes in glacial lakes and further affecting the glacial debris flow activity to some extent. To reveals the dynamic differences between glaciers and glacial lakes under the dynamic changes in climatic conditions and ground temperature. The maximum likelihood classifier in the ERDAS platform was used to supervise the classification of glacial lakes. Simultaneously, the distribution maps of glacial lakes in different periods in the study area were obtained after cluster, filtration and removal analysis. In order to enhance the accuracy of the supervised classification results, we conducted visual interpretation and field investigations for verification purposes (Figure 6), and the accuracy of automatic classification results is approximately 97%, indicating that the classification method used in this article is reliable. Figure 8 shows that the glacier coverage area of the study area in

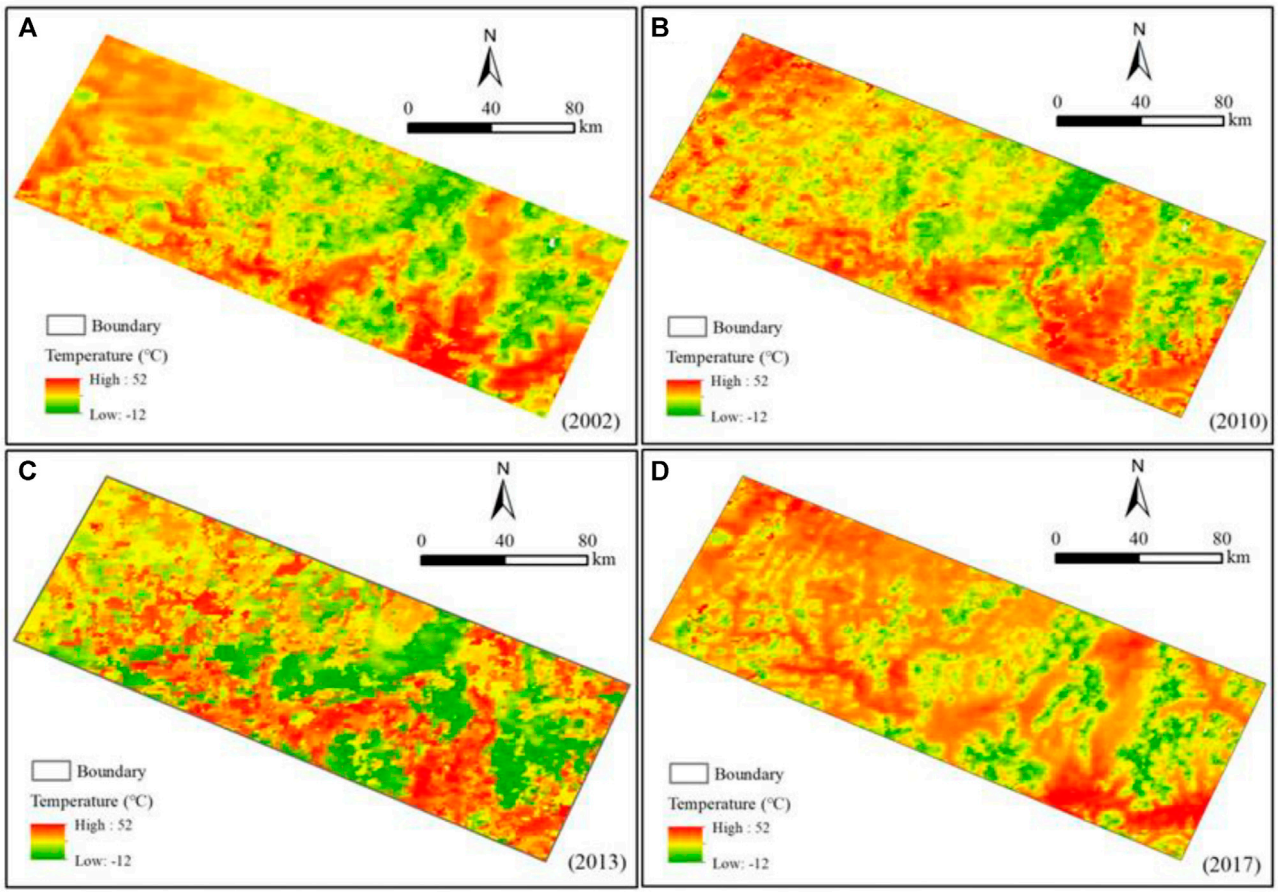

FIGURE 5
Spatiotemporal difference in geothermal temperature in the study area.

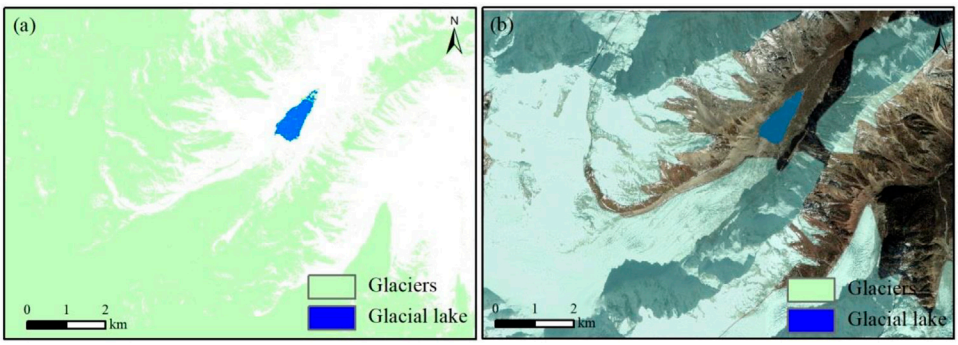

FIGURE 6
Comparison of classification results and translation results. **(A)** Classification results, **(B)** Interpretation.

1988 was approximately 8,300 km^2 and that the glaciers were mainly distributed in the eastern and northern alpine areas of the study area (Figure 7A). In 2002, the average temperature in the study area in the period from May to August was as high as 5.76°C, which led to the continuous melting of glacial snow in the eastern and northeastern of the study area (Figures 7A,B), the glacier area decreased from 8,300 km^2 in 1988–8,284 km^2 in 2002, a decrease of 0.2% compared to that of 1988 (Figure 8). From 2002 to 2010, the temperature of the study area gradually increased overall (Figure 4), resulting in the gradual melting of glaciers in most areas, and the glacier area decreased to approximately 5,276 km^2 (Figure 8), while the geothermal data showed an increasing tendency in the eastern and northeastern of the study area (Figure 5). As a result, the glacier coverage in the northeastern and northeastern of the

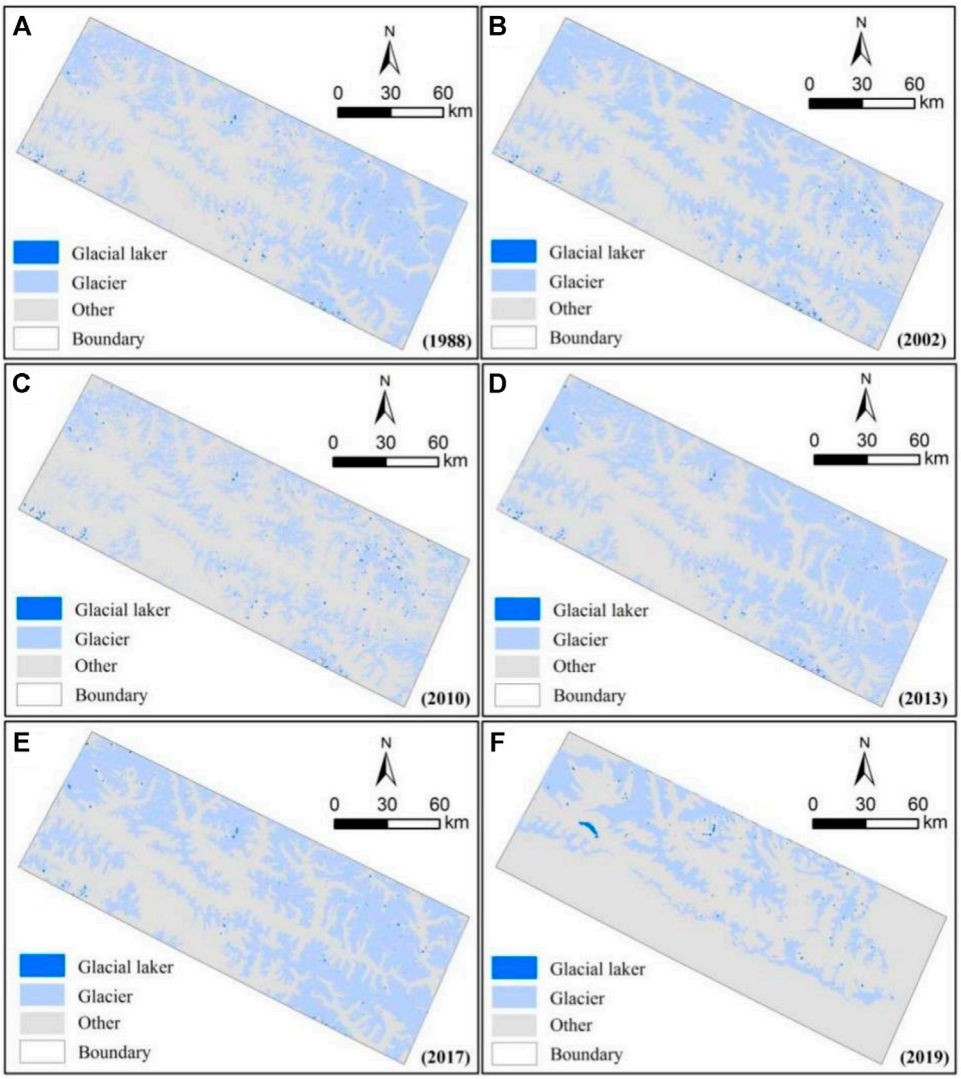

FIGURE 7
Distribution characteristics of glaciers and glacial lakes during 1988–2019. **(A)** 1988, **(B)** 2002, **(C)** 2010, **(D)** 2013, **(E)** 2017, **(F)** 2019.

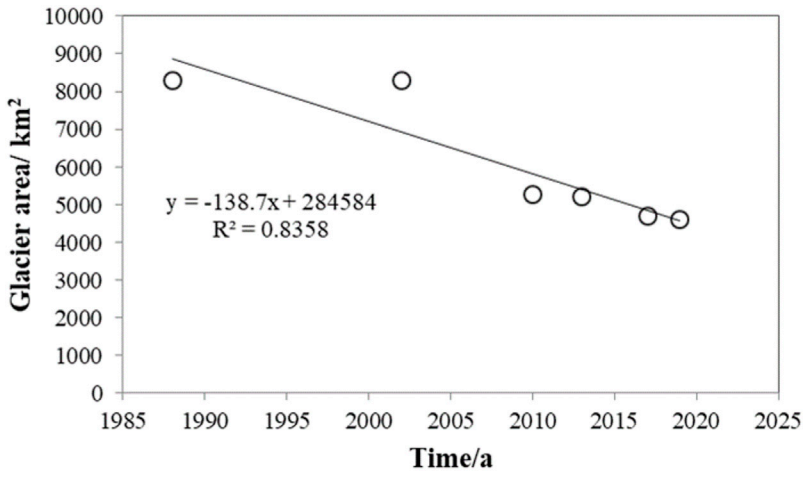

FIGURE 8
The dynamic evolution of glacial area.

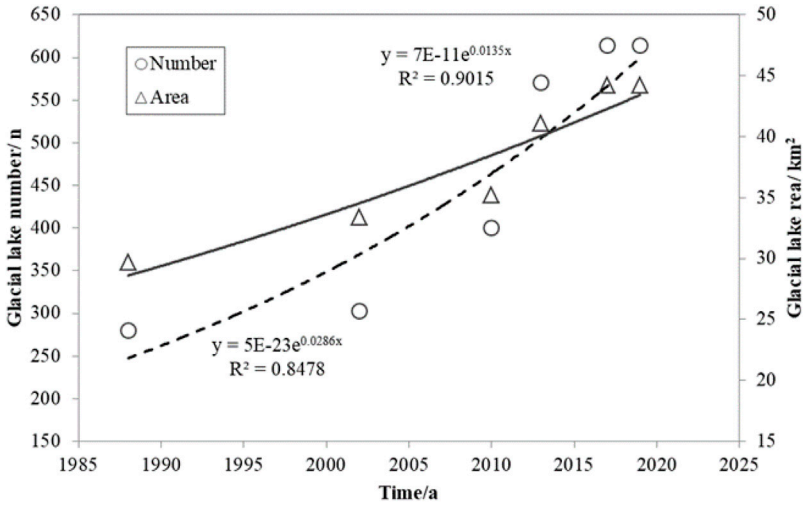

FIGURE 9
The long-term evolution of number and area of glacial lakes.

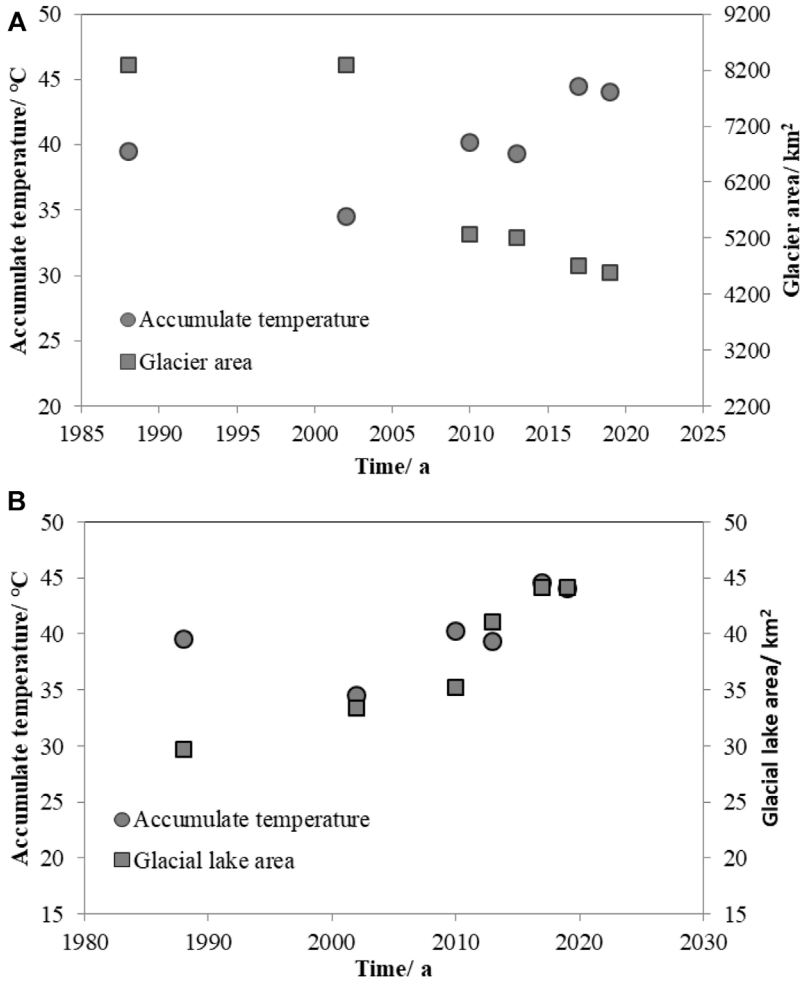

FIGURE 10
Dynamic response of temperature and glaciers and glacial lake. **(A)** The dynamic response relationship between temperature and glacier area, **(B)** The dynamic response relationship between temperature and glacial lake area.

study area decreased significantly from 2002 to 2010 (Figure 7C). From 2010 to 2019, glaciers continued to melt in the southwestern area, and the area decreased from 5,276 km^2 in 2010–4,584 km^2 in 2019 (Figures 7C–F; Figure 8), a reduction of approximately 13%. This suggested that glacier melting has accelerated in this century. Statistics on the glacier area in the past 30 years from 1988 to 2019 showed that as the global temperature has been gradually rising, the glacier snow in the study area has been gradually melting, and the glacier area has linearly decreased accordingly (Figure 8).

3.2.2 Dynamic changes in glacial lakes

The melting of glacial snow will inevitably lead to changes in the number and area of glacial lakes in the study area. To study the dynamic response of glacial lakes to air temperature and glacial snow melting in the study area, based on the results of a supervised classification and combined with ArcGIS statistical software, the number and area of glacial lakes in each time period were statistically analysed (Figure 9). The results concluded that in 1988, there were approximately 280 glacial lakes occupying approximately 30 km^2 in the study area. With the rapid melting of glacial snow, the number and area of glacial lakes in the study area increased slowly from 1988 to 2002, but there was a rapid increase from 2002 to 2017 (Figure 9), which was because since 2002, the average temperature in the study area from May to October has shown a gradually increasing trend overall (Figure 4). As the glacier retreated, some of the original glacier cover areas formed glacial lakes, while the melting of glacial snow cover led to a further increase in the water level of the previously developed glacial lakes, resulting in a rapid increase in the number and area of glacial lakes. From 2017 to 2019, the amount and area of glacial lakes in the study area continued to increase steadily but slowly (Figure 9), which may be because from 2017 to 2019, the average temperature slowly increased in the period from May to October, decelerating the melting of glacier snow. Meanwhile, the higher the altitude is, the lower the temperature is, and the more slowly the glacier melts. Therefore, with the rapid melting of glacial snow in low-altitude areas during the period, the number and area of glacial lakes increased rapidly. However, the glacial snow in high-altitude areas may melt only at higher or extremely high temperatures; therefore, the melting of glacial snow in high-altitude areas may slow down gradually, as did the increase in the number and area of glacial lakes.

However, glacial snow in an ocean valley glacier is strongly affected by the summer monsoon from the Indian Ocean and is characterised by high accumulation and rapid melting. Although slight climate change will cause the glaciers to greatly retreat or advance, the number and area of glacial lakes in the study area presented a power-law increasing trend in general (Figure 9). With the growing area and water level of glacial lakes, the likelihood of glacial lake rupture in the study area will gradually increase, which will further induce glacial lake collapse debris flows.

3.2.3 The impact of temperature evolution on changes in glaciers and glacial lake

Climate change is an important driving factor for the dynamic changes of glaciers and glacial lakes. In order to analyze the response of temperature evolution on changes in glaciers and glacial lake, the average temperature, glaciers area and glacial lake area are used for coupling analysis of their dynamic response relationships. Figure 11A shows an opposite trend between temperature changes and glacier

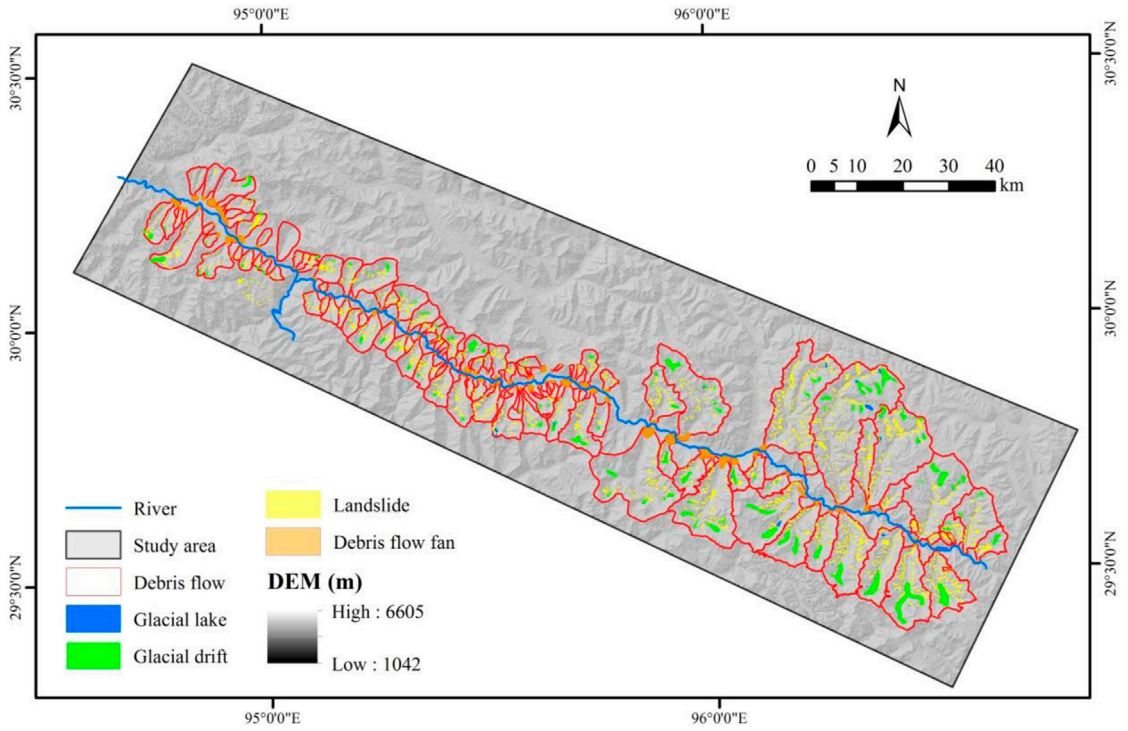

FIGURE 11
Distribution characteristics of glacier debris flows.

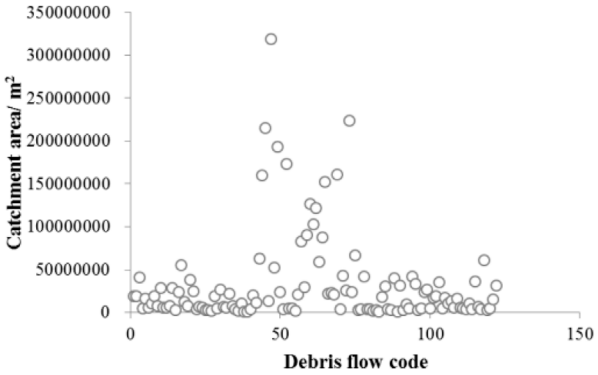

FIGURE 12
Area of the debris flow watershed.

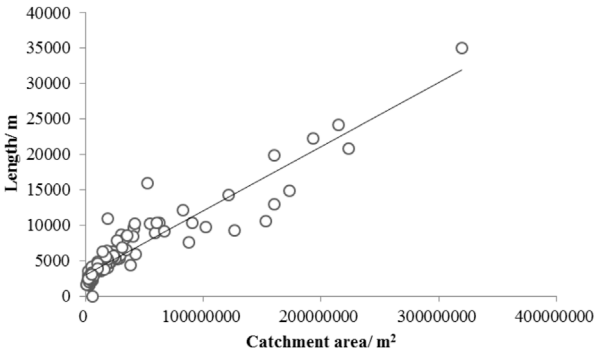

FIGURE 13
Channel length in the debris flow basin.

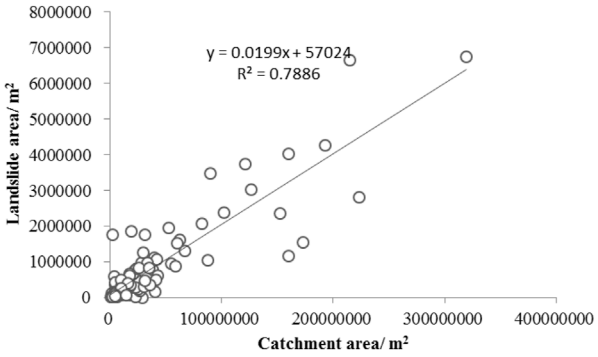

FIGURE 14
Landslides in each basin.

area changes, i.e., the average temperature gradually decreased between 1988 and 2002, but the decrease in temperature leads to a temporarily intensification of the glacier formation process. Therefore, the glaciers area increased slightly during this period. However, the average temperature increased after 2002, this leads to continuous melting of glaciers, and the area of glaciers decreased during this period (Figure 10A).

Inconsistent with the evolution of glacier area, the glacial lake area generally increased between 1988 and 2017. However, as the process of glacier melting intensifies, some glacial lakes experience a process of collapse, and glacier degradation leads to the loss of water supply to glacial lakes. These have led to the disappearance of some glacial lakes in the study area, and the area of glacial lakes has gradually declined after 2017 (Figure 10B).

3.3 Characteristics of debris flow

With climate change glacier snow has melted at an accelerated rate, and glacial debris flows in the Palong Zangbo Valley have become more active. The debris flow visual interpretation of remote sensing images is mainly based on the extraction of the watershed, distribution of loose solid material, erosion characteristics of the channel and the morphological characteristics of the accumulation fan. Remote sensing images combined with field surveys have detected 122 debris flow basins along the Ranwu to Tongmai section of the Palong Zangbo River, including 58 on the right bank and 64 on the left bank (Figure 11). Impacted by the climate change, debris flows frequently break out in these regions, causing serious damage to infrastructure. For example, a catastrophic debris flow in the Midui basin was trigged by the glacier collapse surge in 1988. Field investigation found that the maximum discharge of debris flow is about 1,000 m^3/s. A total of 18 bridges and G318 road were destroyed by this debris flow. In addition, the debris flow widely occurred in Guxiang basin after 1955, and the G318 road frequently destroyed by the Guxiang debris flow.

Additionally, Figure 12 shows that the area of debris flow in the study area varied from 1.24 km^2 to 319.13 km^2, among which debris flows with a drainage area of less than 50 km^2 accounted for 84% of the total and were mainly concentrated in the western part of the study area. With the increase on the watershed area, the channel length also increased (Figure 13). Figure 13 shows that the range of the channel length of the debris flow in the study area was between 1,500 m and 35,000 m. Only 25% of the watersheds had a channel length longer than 7,000 m, and watersheds with longer channel lengths were mainly developed in the southeastern part of the study area. In addition, the area is located in southeastern Tibet, where geological tectonic activity is relatively active. In addition to triggering a large number of coseismic landslides, earthquakes have also formed a large number of damaged mountains. Under the action of rainfall, many shattered mountains gradually became unstable and formed post-earthquake landslides. Therefore, according to the interpretation results of the remote images, landslides are well developed in the study area, but there are significant differences in the development of landslides for watersheds. Figure 14 shows that the landslide coverage area was generally less than 1 km^2 in a watershed area under 25 km^2, but the landslide coverage area increased linearly with the outbreak of large landslides in the basin and the increasing watershed area, which may be because with the increase in the watershed area and the melting of glaciers and snow in the middle and upper reaches of the watershed, the free face is more developed, and at the same time, with the intensification of freeze–thaw cycles and glacier erosion, some slopes become unstable and form landslides. Of course, as the glacier gradually retreats, the released moraine also gradually increases. Figure 15 shows that approximately 70% of the watershed's

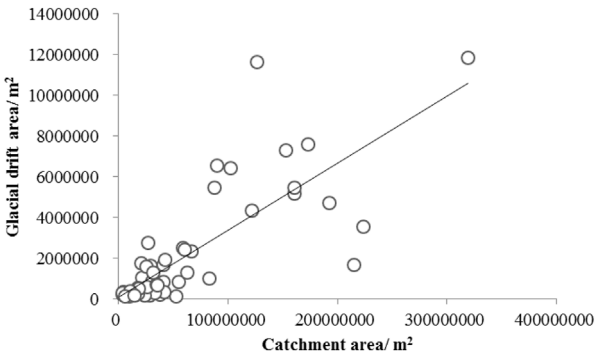

FIGURE 15
Moraines in the debris flow basin.

moraine coverage area was under 2 km^2, but the moraine coverage increased linearly with increasing watershed area. Figure 11 shows that most of the moraine accumulated in the middle and upper reaches of each basin and the moraine was well developed in the debris flow basin in the southeastern part of the study area.

In addition, the interpretation results of highly accurate remote sensing images show that the development areas of moraine and landslides in the debris flow basin were 117.79 km^2 and 84.63 km^2, respectively, accounting for 3% and 2% of the debris flow basin area, respectively. This suggests that although the moraine covers a small area, field investigations have found that the moraine is thicker and more developed than the landslide and is the main component of the glacial debris flow provenance. Meanwhile, Figure 11 reveals that the moraine on the left bank of the Palong Zangbo watershed is well developed, indicating that the glacial activity on the left bank is stronger than that on the right bank. In addition, the rock mass in the study area is fragmented under the action of geological structures such as the Jiali fault. More importantly, the joint plane in the rock mass is continuously infiltrated and freeze–thawed by the combined influence of glacier meltwater and rainfall, resulting in the ice splitting effect and increasing the joint. With the cycle of freezing and thawing, the surface rock mass is completely disintegrated and destroyed, forming fragments and sand grains. These freeze–thawed and weathered detrital materials roll down the slope to the channel to form accumulation cones or ice-water accumulation fans at the foot of the slope after being washed away and transported by the ice and snow meltwater, which provides an abundant source of loose debris for debris flows and constitutes the source of debris flow activities.

It is concluded that with increasing temperature, the melting of glaciers and snow has accelerated, which has led to the increasing moraine in the debris flow basin in the study area. Then, due to the effects of earthquakes and freeze–thaw cycles, the amount of landslide material and weathered debris in the study area

FIGURE 16
Active characteristics of glacier debris flow in the study area. **(A)** Moraines are exposed and transformed to channel, **(B)** Debris flow induced by flash floods, **(C)** Breaked glacial lake of Midui, **(D)** Large amounts of channel material carried by debris flow.

increased, that is, the more abundant the debris flow source was in the study area, the higher the possibility of debris flow.

4 Discussion

Debris flow is one of the important disasters in glacier and seismic disturbance area, but the trend of debris flow activity is not consistent. In earthquake impacted area, sufficient landslide materials with poor consolidation impact the debris flow activity (Tang et al., 2011). Therefore, the richness of materials and rainfall have important impact on debris flow activity in the seismic disturbed area. However, the landslide activity in the seismic impact region gradually decreased over time (Chen et al., 2020), resulting the supply capability of the slope landslide material to the channel weakens (Xiong et al., 2021a). Therefore, the debris flow activity in the earthquake impacted area gradually decayed over time (Xiong et al., 2021b). In consistent with seismic impact area, the average temperature in the study area generally increased from 5.5°C to 7.5°C over the past 40 years (Figure 4). This leads to an overall intensification of the glacier melting process, and the glacier area shows a linear decay trend (Figure 7). Importantly, as the glacier melts, moraines are exposed from the glacier and transferred from the slope to the gully (Figure 16A), which supply sufficient materials for debris flow occurrence, i.e., the melting of glaciers will lead to the increase of moraines, thus providing sufficient material sources for debris flows, which causes the richness of materials for debris flow in our study area is gradually enhanced, this is inconsistent with earthquake impact regions. Subsequently, the strong rainfall induced flash floods to erosion the channel deposits and form debris flow (Figure 16B).

Additionally, as the ample amount of glacial snow melts, the number and area of glacial lakes gradually increased followed a power law in the study area (Figure 9). The melting of glaciers may cause the water level of glacial lakes to increase, enhancing the risk of glacial lake outburst, this can be supported by field investigation and previous studies (Chen et al., 2017; Liu et al.,

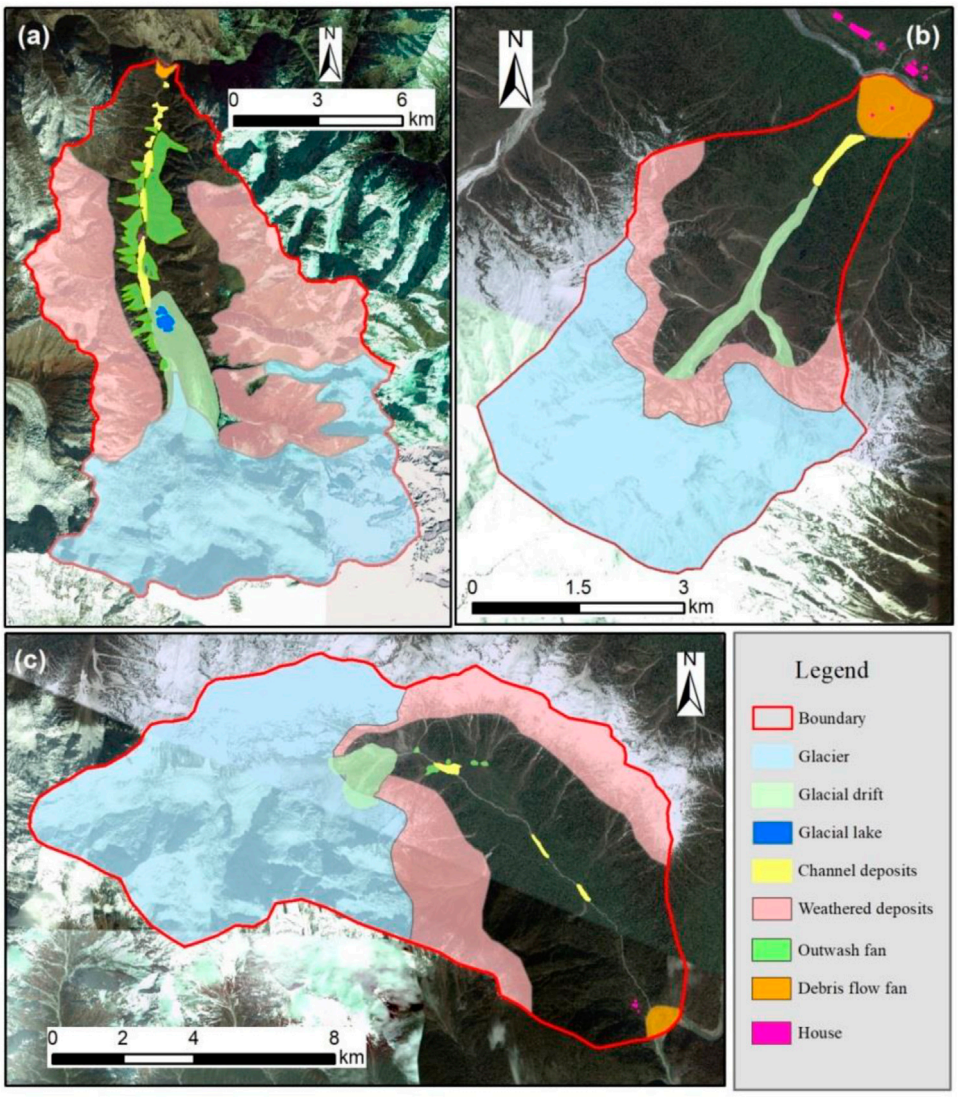

FIGURE 17
Sediment surveys in the **(A)** Midui gully, **(B)** Peilong gully and **(C)** Tianmo gully.

2014). For example, a glacier lake in Midui basin break in 1988 (Figure 16C), and the water level of the glacial lake dropped rapidly by 25 m. Indeed, the flood induced by glacial lake break will carry large amounts of channel material to forms debris flows (Figure 16D). Importantly, the intensification of glacier melting process will lead to the increase of river flow and erosion capacity, and the coupled glacial lake outburst will lead to the increase of hydrodynamic conditions of debris flow. That is, the activity of glacier debris flow is affected by multiple factors and is more complicated than that in earthquake area.

Thus, the activity of glacial debris flow in our study area will increase in the later period, this is not consistent with earthquake impact area. The above conclusion could be verified from field investigations, such as the debris flow first recorded in 1953 in the Guxiang gully, which has been extremely active for the past 20 years and has evolved frequent debris flows since then (Hu et al., 2011). In addition, field surveys have verified that the moraine, weathered sediment, ice water sediment, and channel sediment in the Midui gully (Figure 17A), Peilong gully (Figure 17B) and Tianmo gully (Figure 17C) are well developed. Therefore, the debris flow occurred in these basins in recent years.

5 Conclusion

Glaciers, which are extremely sensitive to climate change, could reflect climate change and play an important role in predicting debris flows in alpine and high-altitude mountains. The Palong Zangbo Valley region in southeastern Qinghai-Tibet is a typical marine glacial area in China in which mountain disasters such as flooding induced by glacial lake outbursts and debris flows occur frequently. Through the collection of temperature and rainfall data in the Bomi area over the past 40 years, it was shown that the annual rainfall in the region did not differ greatly, but the temperature has shown a fluctuating trend with a slow growth, especially in recent years. Additionally, the results of geothermal inversion in the study area revealed that the geothermal temperature varies greatly in different regions. These changes have further accelerated the melting of glacial snow in the southern and southeastern parts of the study area. The glacial area has shown a linear decay trend over time. With the melting of glacial snow, the number and area of glacial lakes in the study area as a whole increased significantly with the power-law trend, the water level of some glacial lakes rapidly rose, and the risk of glacial avalanche increased, as did the possibility of glacial lake collapse. With the melting of glaciers and the collapse of glacial lakes, the debris flow in the area became more active, and glacial debris flows have occurred in channels of varying lengths, basin areas and sources, indicating that the debris flow activity was quite different in the region. More importantly, in recent years, with the combined effects of glacier melting, earthquakes and ice avalanches, the risk of debris flow in the study area has increased. Therefore, to effectively reduce the losses and risk caused by debris flow disasters, it is necessary to strengthen monitoring efforts and early warnings of glacial debris flow in the region.

Data availability statement

The original contributions presented in the study are included in the article/Supplementary material, further inquiries can be directed to the corresponding author.

Author contributions

LY: Conceptualization, Methodology, Writing–original draft. TC: Conceptualization, Data curation, Writing–review and editing. GL: Resources, Writing–review and editing. XJ: Validation, Writing–review and editing.

Funding

The author(s) declare that no financial support was received for the research, authorship, and/or publication of this article.

Conflict of interest

The authors declare that the research was conducted in the absence of any commercial or financial relationships that could be construed as a potential conflict of interest.

Publisher's note

All claims expressed in this article are solely those of the authors and do not necessarily represent those of their affiliated organizations, or those of the publisher, the editors and the reviewers. Any product that may be evaluated in this article, or claim that may be made by its manufacturer, is not guaranteed or endorsed by the publisher.

References

Abburu, S., and Golla, S. B. (2015). Satellite image classification methods and techniques: a review. *Int. J. Comput. Appl.* 119, 20–25. doi:10.5120/21088-3779

Bajracharya, S. R., Maharjan, S. B., and Shrestha, F. (2014). The status and decadal change of glaciers in Bhutan from the 1980s to 2010 based on satellite data. *Ann. Glaciol.* 55 (66), 159–166. doi:10.3189/2014AoG66A125

Chen, H., Cui, P., Chen, X., and Tang, J. (2017). Study on the surge wave induced by glacier avalanches and its effects on dam failure process. *Int. J. Eros. Control Eng.* 10 (1), 9–15. doi:10.13101/ijece.10.9

Chen, M., Tang, C., Xiong, J., Qin, Y. S., Li, N., Gong, L. F., et al. (2020). The long-term evolution of landslide activity near the epicentral area of the 2008 Wenchuan earthquake in China. *Geomorphology* 367, 107317. doi:10.1016/j.geomorph.2020.107317

Chen, N. S., Zhou, H., and Hu, G. (2011). Development rules of debris flow under the influence of climate change in Nyingchi. *Clim. Change Res.* 7 (06), 412–417. (In Chinese). doi:10.1016/B978-0-444-53599-3.10005-8

Chen, X. Q., Cui, P., Li, Y., Yang, Z., and Qi, Y. Q. (2007). Changes in glacial lakes and glaciers of post-1986 in the poiqu River Basin, nyalam, xizang (Tibet). *Geomorphology* 88, 298–311. doi:10.1016/j.geomorph.2006.11.012

Chigira, M., Wu, X., Inokuchi, T., and Wang, G. (2010). Landslides induced by the 2008 wenchuan earthquake, sichuan, China. *Geomorphology* 118, 225–238. doi:10.1016/j.geomorph.2010.01.003

Cook, K. L., Andermann, C., Gimbert, F., Adhikari, B. R., and Hovius, N. (2018). Glacial lake outburst floods as drivers of fluvial erosion in the Himalaya. *Science* 362, 53–57. doi:10.1126/science.aat4981

Cui, P., Chen, R., Xiang, L., and Su, F. (2014). Risk analysis of mountain hazards in Tibetan plateau under global warming. *Clim. Change Res.* 10 (2), 103–109. (In Chinese).

Dash, P., Göttsche, F. M., Olesen, F. S., and Fischer, H. (2002). Land surface temperature and emissivity estimation from passive sensor data: theory and practice-current trends. *Int. J. Remote Sens.* 23 (13), 2563–2594. doi:10.1080/01431160110115041

Fu, Y., Jiang, Y., and Wang, J. (2021). Experimental study on the undrained shear behavior of glacial till in larger-scale triaxial testing. *J. Lanzhou Univ. Nat. Sci.* 57 (2), 200–2006. (In Chinese).

He, Y., Cao, Z., Chen, L., and Chen, Y. (2005). Investigation on site of the2003Southern Bomi MS 5·7 earthquake Tibet. *Earthq. Res. China* 21 (4), 469–474. (In Chinese).

Hu, K. H., Cui, P., You, Y., and Chen, X. Q. (2011). Influence of debris supply on the activity of post-quake debris flows. *Chin. J. Geol. Hazard Control* 22 (1), 1–6. (In Chinese). doi:10.3969/j.issn.1003-8035.2011.01.001

Huang, Y., Meng, X. L., Hu, X., Zhang, L., Wang, Z., Du, S., et al. (2021). Major engineering geological problems and countermeasures along traffic corridor from Ya'an to Nyingchi. *J. Eng. Geol.* 29 (2), 307–325. (In Chinese). doi:10.13544/j.cnki.jeg.2021-0128

Li, D., Shangguan, D. H., Wang, X. Y., Ding, Y. J., Su, P. C., Liu, R. L., et al. (2021). Expansion and hazard risk assessment of glacial lake Jialong Co in the central Himalayas by using an unmanned surface vessel and remote sensing. *Sci. Total Environ.* 784, 147249. doi:10.1016/j.scitotenv.2021.147249

Li, Y., Su, L., Zou, Q., and Wei, X. (2021). Risk assessment of glacial debris flow on alpine highway under climate change: a case study of Aierkuran Gully along Karakoram Highway. *J. Mt. Sci-Engl.* 18 (6), 1458–1475. doi:10.1007/s11629-021-6689-3

Liu, J., Cheng, Z., and Su, P. (2014). The relationship between air temperature fluctuation and glacial lake outburst floods in Tibet, China. *Quatern. Int.* 321, 78–87. doi:10.1016/j.quaint.2013.11.023

Liu, J., Tang, C., Cheng, Z., and Liu, Y. (2011). Impact of temperature on glacier-lake outbursts in Tibet. *J. Jilin Univ. (Earth Sci. Ed.* 41 (4), 1121–1129. (In Chinese). doi:10.3969/j.issn.1671-5888.2011.04.023

Medeu, A. R., Popov, N. V., Blagovechshenskiy, V. P., Askarova, M. A., Medeu, A. A., Ranova, S. U., et al. (2022). Moraine-dammed glacial lakes and threat of glacial debris flows in South-East Kazakhstan. *Earth-Sci. Rev.* 229, 103999. doi:10.1016/j.earscirev.2022.103999

Merry, K., Bettinger, P., Crosby, M., and Boston, K. (2023). *Geographic information system skills for foresters and natural resource managers*. Elsevier, 231–267. doi:10.1016/C2020-0-03530-9

Nie, Y., Sheng, Y., Liu, Q., Liu, L., Liu, S., Zhang, Y., et al. (2017). A regional-scale assessment of Himalayan glacial lake changes using satellite observations from 1990 to 2015. *Remote Sens. Environ.* 189, 1–13. doi:10.1016/j.rse.2016.11.008

Qin, Z., and Karnieli, A. (1999). Progress in the remote sensing of land surface temperature and ground emissivity using NOAA-AVHRR data. *Int. J. Remote Sens.* 20 (12), 2367–2393. doi:10.1080/014311699212074

Racoviteanu, A. E., Nicholsonm, L., Glasserm, N. F., Miles, E., Harrison, S., and Reynolds, J. M. (2022). Debris-covered glacier systems and associated glacial lake outburst flood hazards: challenges and prospects. *J. Geol. Soc. Lond.* 179. doi:10.1144/JGS2021-084

Riaz, S., Ali, A., and Baig, M. N. (2014). Increasing risk of glacial lake outburst floods as a consequence of climate change in the Himalayan region. *Jàmbá J. Disaster Risk Stud.* 6 (1), 1–6. doi:10.4102/jamba.v6i1.110

Shangguan, D., Li, D., Ding, Y., Liu, J., Anjum, M. N., Li, Y., et al. (2021). Determining the events in a glacial disaster chain at Badswat Glacier in the Karakoram Range using remote sensing. *Remote Sens.* 13 (6), 1165. doi:10.3390/RS13061165

Shrestha, F., Uddin, K., Maharjan, S. B., and Bajracharya, S. R. (2016). Application of remote sensing and GIS in environmental monitoring in the Hindu Kush Himalayan region. *Aims Environ. Sci.* 3 (4), 646–662. doi:10.3934/environsci.2016.4.646

Su, P., Liu, J., Li, Y., Liu, W., Wang, Y., Ma, C., et al. (2021). Changes in glacial lakes in the poiqu River Basin in the central Himalayas. *Hydrol. Earth Syst. Sc.* 25, 5879–5903. doi:10.5194/HESS-25-5879-2021

Tang, C., Zhu, J., Qi, X., and Ding, J. (2011). Landslides induced by the Wenchuan earthquake and the subsequent strong rainfall event: a case study in the Beichuan area of China. *Eng. Geol.* 122 (1-2), 22–33. doi:10.1016/j.enggeo.2011.03.013

Wang, W., Xiang, Y., Gao, Y., Lu, A., and Yao, T. (2014). Rapid expansion of glacial lakes caused by climate and glacier retreat in the Central Himalayas. *Hydrol. Process* 29 (6), 859–874. doi:10.1002/hyp.10199

Wei, X., Chen, R., Chen, B., Li, B., and Yang, X. (2018). Control effect of new shallow sill structure on gully erosion of glacial debris flow and its application. *J. Catastrophology* 33 (S1), 40–46. (In Chinese). doi:10.3969/j.issn.1000-811X.2018.Z1.008

Wu, G., Yao, T., Wang, W., Zhao, H., Yang, W., Zhang, G., et al. (2019). Glacial hazards on Tibetan plateau and SurroundingAlpines. *Bull. ChineseAcademy Sci.* 34 (11), 1285–1292. (In Chinese).

Xie, T., Yin, Q., Gao, H., Chen, F., Shen, N., and Lin, D. (2019). Study on early warning model of glacial-rainfall debris flow based on excitation condition and stability of accumulation body. *J. Glaciol. Geocryol.* 41 (4), 884–891. (In Chinese). doi:10.7522/j.issn.1000-0240.2019.0403

Xiong, J., Tang, C., Chen, M., Gong, L., Li, N., Zhang, X., et al. (2021a). Long-term changes in the landslide sediment supply capacity for debris flow occurrence in Wenchuan County, China. *Catena* 203, 105340. doi:10.1016/j.catena.2021.105340

Xiong, J., Tang, C., Chen, M., Zhang, X. Z., Shi, Q. Y., and Gong, L. F. (2021b). Activity characteristics and enlightenment of the debris flow triggered by the rainstorm on 20 August 2019 in Wenchuan County. China. *Bull. Eng. Geol. Environ.* 80 (2), 873–888. doi:10.1007/s10064-020-01981-x

Yan, S. Y. (2020). *Hazard assessment of glacier lake outbursts in the ParlungZangbo basin based on catastrophe progression method*. Beijing: China University of Geosciences. (In Chinese).

Yang, Z., Zhu, Y., and Zou, D. H. (2011a). "Formation conditions and risk evaluation of glacial debris flow disasters along International Karakorum Highway (KKH)," in *5th international conference on debris-flow Hazards mitigation: mechanics, prediction and assessment* (Padua, Italy: Università La Sapienza), 1031–1037.

Yang, Z., Zhu, Y., Zou, D. H., and Liao, L. (2011b). Activity degree evaluation of glacial debris flow along international KARAKORUM Highway (KKH) Based on Fuzzy Theory. *Adv. Mater. Res.* 261, 1167–1171. doi:10.4028/www.scientific.net/AMR.261-263.1167

Zhang, T., Wang, W., Gao, T., and Baosheng, A. (2021). Simulation and assessment of future glacial lake outburst floods in the Poiqu River basin, Central Himalayas. *Water* 13 (10), 1376. doi:10.3390/w13101376

Zhang, X., Liu, S., and Liu, L. (2015). Moraine-dammed glacial lake changes during the recent 40 years in the poiqu River Basin, Himalayas.Sciences in cold and arid regions. *Sci. Cold Arid Regions* 7 (6), 0654–0665. (In Chinese). doi:10.3724/SP.J.1226.2015.00654

frontiers | Frontiers in Environmental Science

TYPE Original Research
PUBLISHED 22 January 2024
DOI 10.3389/fenvs.2023.1336705

OPEN ACCESS

EDITED BY
Yunhui Zhang,
Southwest Jiaotong University, China

REVIEWED BY
Jingwei Guo,
City University of Macau, Macao SAR, China
Hong Liu,
Civil Aviation University of China, China
Wenxin Li,
Hubei University of Arts and Science, China

*CORRESPONDENCE
Li Lu,
lull@cafuc.edu.cn

RECEIVED 11 November 2023
ACCEPTED 26 December 2023
PUBLISHED 22 January 2024

CITATION
Lu L, Lai X, Jiang J and Zhou J (2024), Research on optimization of approach procedures for airports in an alpine environment.
Front. Environ. Sci. 11:1336705.
doi: 10.3389/fenvs.2023.1336705

Research on optimization of approach procedures for airports in an alpine environment

Li Lu*, Xin Lai, Junliang Jiang and Juncheng Zhou

School of Air Traffic Management, Civil Aviation Flight University of China, Guanghan, Sichuan, China

Obstacles in alpine environments pose significant challenges to aircraft safety during terminal operations. Key challenges include constraints from obstacles within the terminal clearance area and the labor-intensive manual calculations of flight procedures. The focal point of concern lies in the design of approach procedures, particularly due to the heightened risk of collisions with obstacles during the descent segment in such terrain. To address these challenges, initially, this paper proposes processing the terrain data and visualizing and extracting the topographic data of the alpine airport by adopting a bi-cubic b-spline interpolation and cellular automatic machine model. Then, the paper proposes improving the A* path algorithm to make sure it can obey the standards of flight procedure design, utilizing the improved A* path algorithm to design approach procedures. As fuel consumption is directly connected with the economy of aviation companies, this research finally suggests employing the fuel consumption evaluation model to select the most efficient approach flight procedures. This research takes a case study of a Yunnan airport and simulates and designs the optimized approach procedures by A* path algorithm and evaluation based on fuel consumption. Results indicate that the parameters of optimized approach procedures align with the regulation of flight procedure design and meet the requirements of real flight operation. Therefore, the core tenant of this research can provide a feasible idea for flight procedures with alpine airports and has the potential to reduce workload and enhance operational efficiency.

KEYWORDS

airports in alpine environment, terrain data processing, approach procedures, improved A* algorithm, fuel consumption evaluation

1 Introduction

When an aircraft is flying over towering mountains, there exists a constant risk of collision with the terrain. The western regions of China are predominantly rounded with mountainous areas, which means that the profile changes of terrain elevation exceed 900 m (3 000 ft) within a distance of 18.5 km (10.0 NM). Despite this, the tourism industry in these regions has always flourished; therefore, it is imperative to develop the aviation transportation in these alpine areas. Currently, the flight procedures of alpine airports confront limitations arising from the extensive reliance on manual design and calculation for obstacle clearance height. Consequently, it is necessary to solve the problem of the presence of numerous obstacles during aircraft departure and arrival in these mountainous terrains, and replace the manual workload with intelligence methods.

The approach segment, as a critical period within the entire flight phase, is considered pivotal due to the numerous potential hazards that aircraft may encounter. When the aircraft descends during the approach segment, the pilot's attention is highly concentrated on the aircraft's landing configuration, aligning with the runway, or descent gradient requirements, and other operational procedures. Because of this, when approaching the complex alpine environment, it is easy for aircraft to collide with the mountain. Therefore, flight procedure design (DOC8168) serves as a primary foundation for airport safety operations. However, the manual calculations are prone to errors and some mistakes, so intelligent approach procedure design has become a focal point for research, especially in situations where terrain is complex (Rahim and Malaek, 2007; Liu et al., 2018).

The authors of this research have done some work in 2022 to optimize approach trajectories (Lu and Liu, 2022); in this paper, they will continue to address the optimization of approach procedures in alpine environments. Drawing upon the standards of Performance-Based Navigation procedures design (ICAO), an algorithmic model serves as the foundation for formulating approach flight procedures in alpine airports. Leveraging MATLAB software facilitates the design and simulation of these procedures, producing approach flight trajectories. Through an evaluation framework that considers fuel consumption, the approach procedures are optimized to offer a dependable solution for enhancing the manual calculation and design of approach flight procedures. This optimization not only contributes to increased safety but also provides valuable ideas for augmenting airspace utilization in alpine terminal areas (Malaek and Kosari, 2007; Lu, 2019).

Based on the former considerations, this research will start with the perspective of secondary improvement of the A* algorithm and conduct simulation research on the approach flight procedures of mountainous airports. The holistic idea of the paper is shown in Figure 1.

2 State of arts

Experts and scholars have conducted extensive research on instrument flight procedures design, using safety assessment and simulation in the early stages. In 2015, Qian Ge adopted the ant colony algorithm to design and improve the departure and arrival procedures of Lanzhou airport, and conducted optimization evaluation, providing a good method for further procedure design (Qian, 2015). In 2017, Zhao Qian conducted an optimization evaluation of the approach segment of the flight procedures based on GIS software (Zhao, 2017). In 2018, scholars such as Chen Shaoqian used the A* algorithm to optimize flight trajectories based on thumbnails (Chen et al., 2019). In 2019, Tang Li and others used an improved ant colony algorithm to simulate unmanned aerial vehicles transporting disaster relief materials in mountainous areas (Tang et al., 2019). The above research has laid an important foundation for the subsequent research of path optimization algorithms to solve civil aviation operation problems.

Scholars both domestically and internationally have conducted significant research on the visualization of three-dimensional terrain. In 2015, scholars such as Plat N combined the Kriging interpolation method with LiDAR to calculate the average elevation values of terrain, thus obtaining more accurate terrain elevation values (Plat et al., 2015). In 2016, Zhao Qian used C language to program ArcGIS software for grid simulation of three-dimensional terrain in the field and combined the advantages of A * and Dijkstra algorithm to explore the optimal trajectory in complex environments (Zhao, 2016). In 2017, scholars such as He Shan used DLG interpolation to simulate three-dimensional terrain, providing a reference for selecting DEM data to simulate three-dimensional elevation terrain (He et al., 2017). In 2018, scholars such as Yuan Wei established a grid terrain elevation map using V parallax, which has important significance for the accurate expression of terrain visualization (Yuan et al., 2018).

Experts in the aviation field have conducted in-depth research on the calculation and evaluation of flight fuel consumption. The calculation of flight fuel consumption not only saves costs for

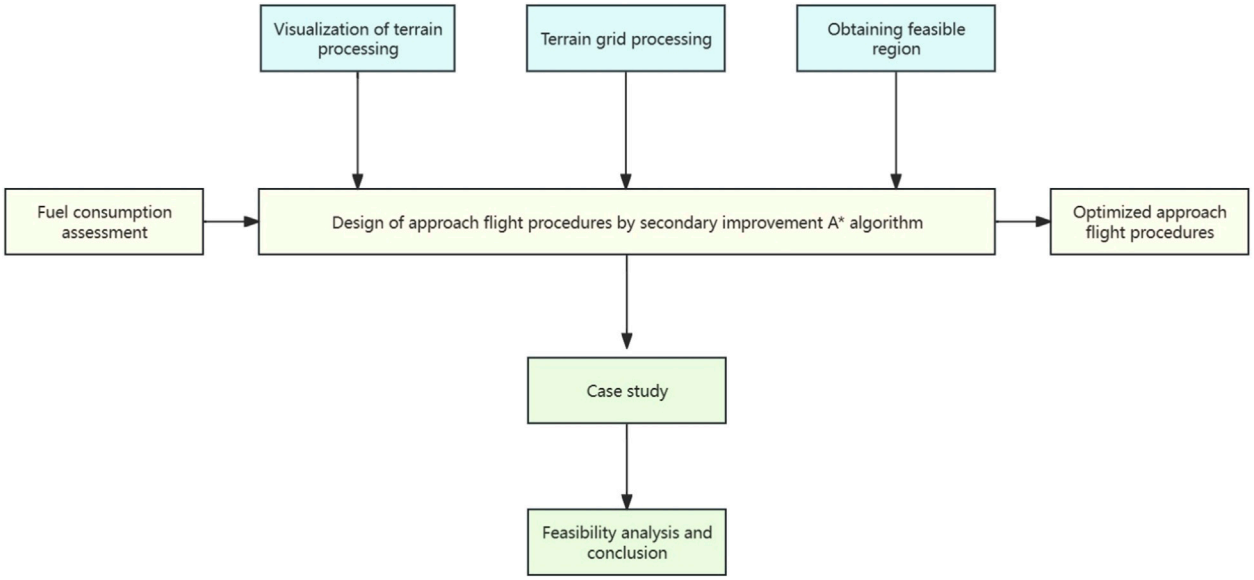

FIGURE 1
Flow chart of the research idea.

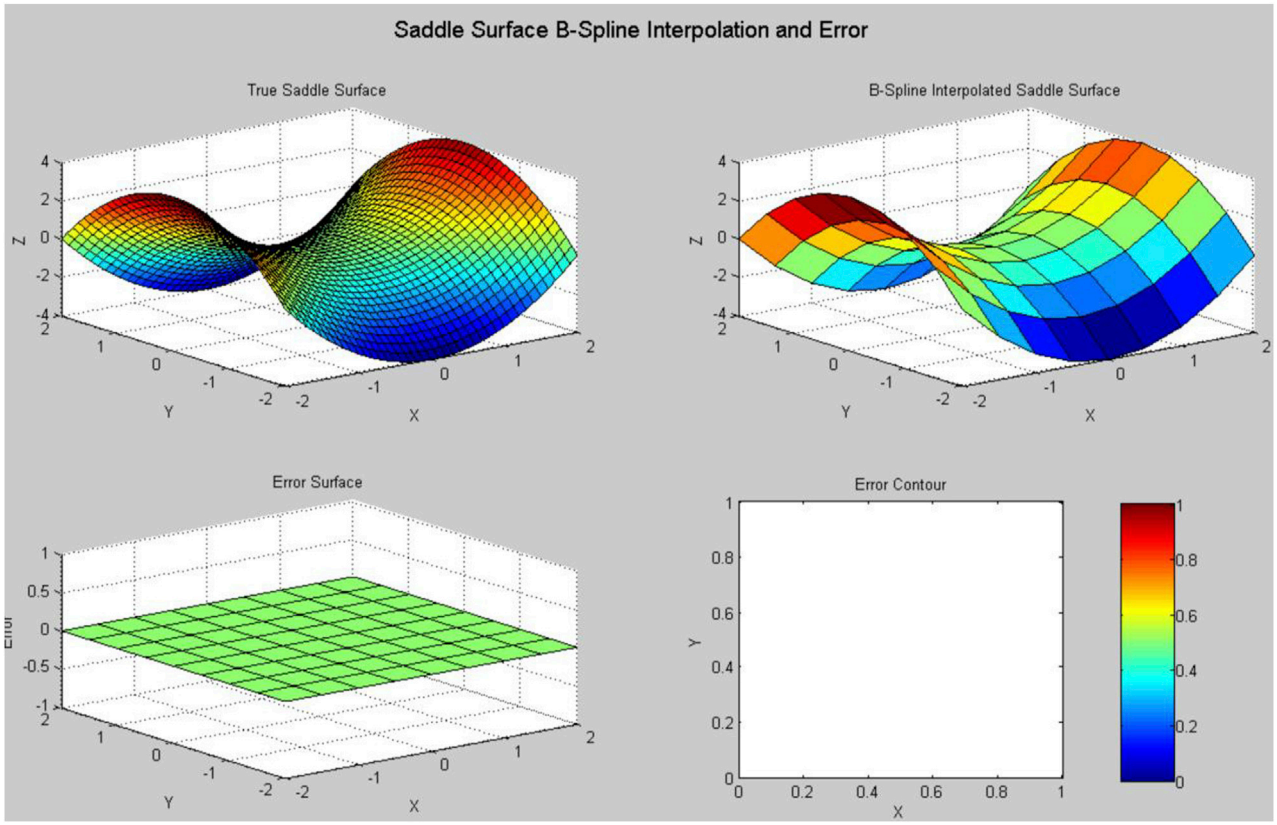

FIGURE 2
The saddle surface simulation.

aviation operators from an economic perspective, but also serves as an important reference for flight trajectory optimization evaluation. In 1982, Bela P. Collins adopted the principle of energy conservation for fuel consumption assessment. This method evaluated and predicted fuel consumption by calculating parameters such as thrust and speed. This method was a cornerstone for subsequent research (Collins, 1982). In 2010, Wang Changkun provided ideas for calculating fuel consumption based on multiple linear regression analysis; results show that this method can correctly obtain the value of fuel consumption (Wang, 2010).

The above research provides important ideas for this research, but more work is needed to design flight procedures with intelligence algorithms, especially approach procedures. This is because, due to the steep terrains around the alpine airports, uncontrollable factors can easily occur, for example, it can result in collision during approach flight. In addition, the difficulty of manual design means the research is urgent.

3 The processing of terrain

3.1 Visualizing of terrain

To design the approach flight procedures for alpine airports, data on the surrounding terrain is needed. It is necessary to acquire the basic information of the airport, such as the magnetic direction of the runway and the clearance conditions of airport. The most important consideration is the surroundings of high natural mountains that can pose a safety hazard to aircraft operation. It is then necessary to execute to visualize the terrain, finally extracting terrain height data (Campos et al., 2016).

In order to visualize the three-dimensional terrain of the airport terminal area, equidistant sampling of the terrain is necessary to further apply the corresponding visualization algorithm. In this research, bi-cubic b-spline interpolation is used, as its simulation difference has lower noise performance, better continuity, and higher smoothness.

Bi-cubic b-spline interpolation is based on b-splines to perform interpolation calculations on any two directions of a spatial surface, resulting in better local deformation and better locality and continuity of the graph. The principle of this method is to calculate pixel values in units of 16 control points, which can be written in a matrix form as shown in Formula 1:

$$s = \begin{bmatrix} s_{11} & s_{12} & s_{13} & s_{14} \\ s_{21} & s_{22} & s_{23} & s_{24} \\ s_{31} & s_{32} & s_{33} & s_{34} \\ s_{41} & s_{42} & s_{43} & s_{43} \end{bmatrix} \quad (1)$$

Firstly, each row of control points is interpolated. The matrix has four columns of row vectors, so four columns of b-spline interpolation curves can be obtained. The expression can be written as a formula, as shown in Formula 2:

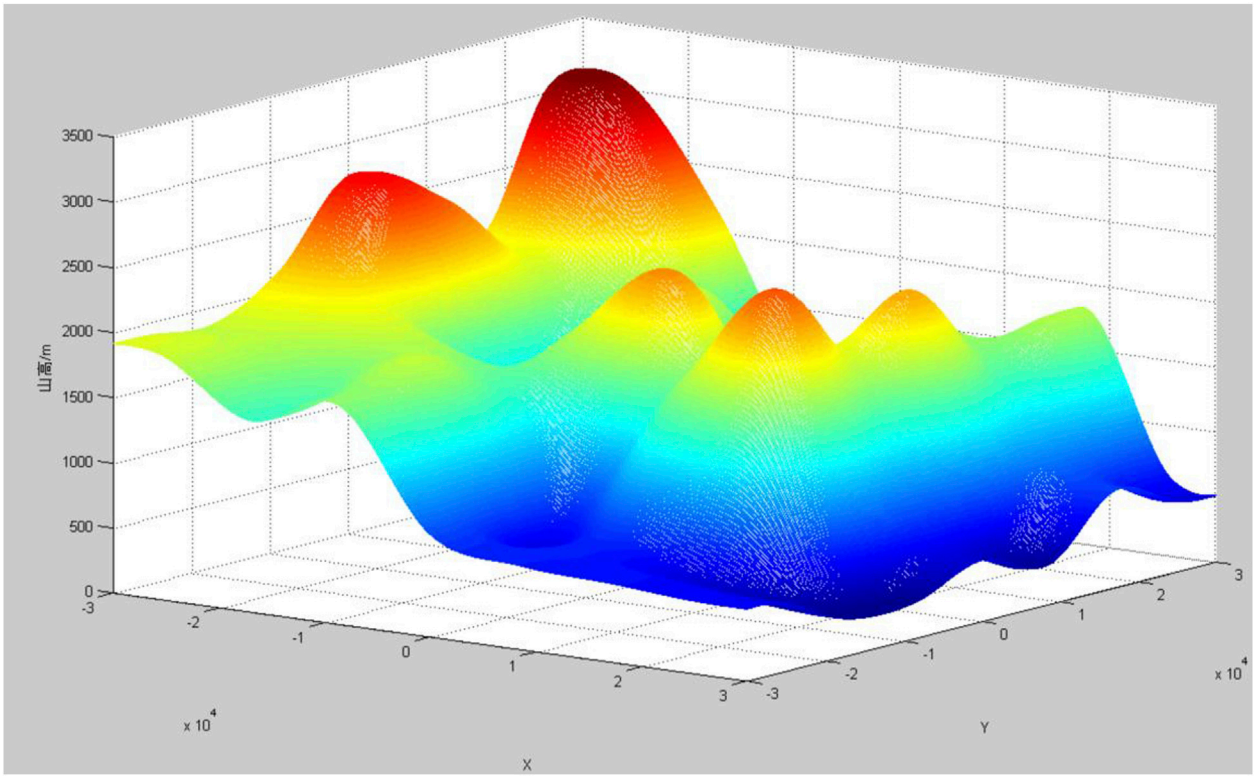

FIGURE 3
Three-dimensional terrain display.

$$f_i(s) = \sum_{j=0}^{3} p_k \times B_{j,3}(s) \times S_{ij}, i = 0, 1, 2, 3 \tag{2}$$

Among them, p_k represents one of the control points $B_{j,3}(s)$ is the b-spline cardinality. The control point matrix has four rows and four columns, and the four-row b-spline interpolation cardinality expression has four forms, as shown in Formula 3, 4; Formula 5, 6:

$$B_0(s) = (1-s)^3/6 \tag{3}$$

$$B_1(s) = (3s^3 - 6s^2 + 4)/6 \tag{4}$$

$$B_2(s) = (-3s^3 + 3s^2 + 3s + 1)/6 \tag{5}$$

$$B_3(s) = s^3/6 \tag{6}$$

Among them, the values of s are between 0 and 1. Since the bi-cubic b-spline interpolation method interpolates in two directions simultaneously, assuming these two directions, it can be written as two directional vectors: and. Therefore, the cubic spline interpolation expression in the direction can be written as a matrix, as shown in Formula 7:

$$\mathbf{P}(\mathbf{u}) = \frac{1}{6}\begin{bmatrix} -1 & 3 & -3 & 1 \\ 3 & -6 & 0 & 4 \\ -3 & 3 & 3 & 3 \\ 1 & 0 & 0 & 0 \end{bmatrix}\begin{bmatrix} u^3 \\ u^2 \\ u \\ 1 \end{bmatrix}\begin{bmatrix} p_0 \\ p_1 \\ p_2 \\ p_3 \end{bmatrix}^T \tag{7}$$

Due to the continuous changes between 0 and 1 after weighting, the values in the other direction v also continuously change between 0 and 1. From the above results, the bicubic b-spline interpolation matrix of the three-dimensional surface can be obtained, as shown in Formula 8:

$$\mathbf{P}(\mathbf{u}) = \frac{1}{6}\mathbf{B}_{3,\mathbf{i}}(\mathbf{v})\begin{bmatrix} p_{00} & p_{01} & p_{02} & p_{03} \\ p_{10} & p_{11} & p_{12} & p_{13} \\ p_{20} & p_{21} & p_{22} & p_{23} \\ p_{30} & p_{31} & p_{32} & p_{33} \end{bmatrix}\mathbf{B}_{\mathbf{j},3}^{\mathbf{T}}(\mathbf{u}) \tag{8}$$

Using the bi-cubic b-spline interpolation method to simulate the saddle surface, as shown in Figure 2, it can be seen that the error accuracy of the saddle surface effect simulated by the bi-cubic b-spline interpolation algorithm reaches 0, with good continuity performance; this method can be used for simulation research on continuous terrain.

The following terrain figure is a visual simulation of mountainous terrain by taking an example. MATLAB is used to simulate the sampling terrain points combined with the bicubic B-spline interpolation method; the three-dimensional terrain and two-dimensional contour map of the mountainous area are shown as Figures 3, 4. It can be seen that the terrain and topography of the mountainous area can be well performed.

3.2 Extraction of terrain data

After presenting the terrain in three-dimensional format, it is necessary to do grid processing of the terrain to extract terrain height and position information, making it more convenient for outputting approach procedures and identifying terrain obstacles. This study uses the Cellular Automatic machine model to process grids. For example, if

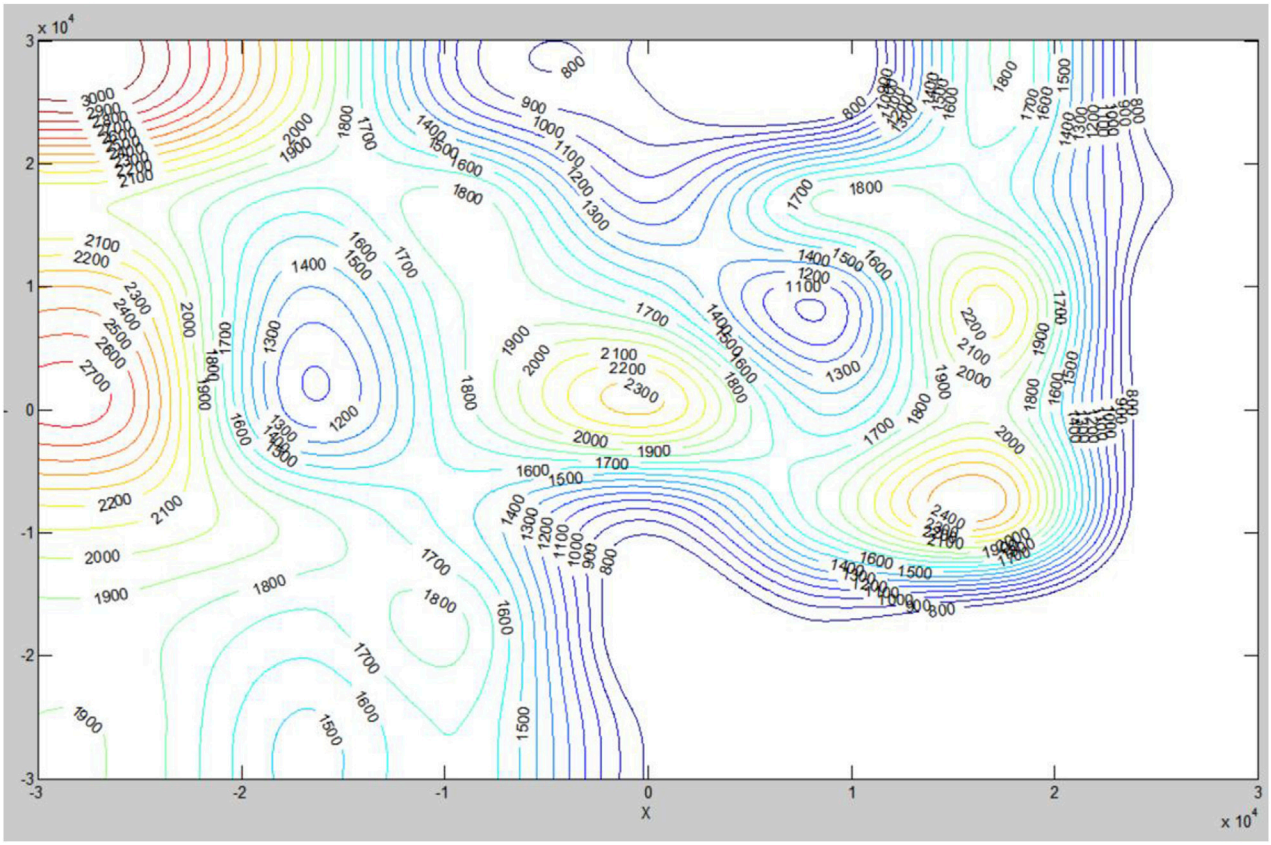

FIGURE 4
Contour map.

TABLE 1 The minimum stabilization distance (maxed changing angle 120°).

Speed (km/h)	>or = 300	>or = 320	>or = 340	>or = 360	>or = 380	>or = 400	>or = 440	>or = 480
MSD (km)	3.2	3.4	3.9	4.3	4.7	5.2	6.3	7.4

the cell is assigned a value of 1, the grid can pass at the next moment, indicating that there are no obstacles at the previous moment. If the cell is assigned a value of 0, the grid is not accessible at the next moment, indicating that there were obstacles at the previous moment.

The more grids the model selects, the more accurate the simulation results will be. When using a cellular automatic machine to process terrain, each grid contains four pieces of information: longitude, latitude, terrain elevation, and traffic status. This research selects three-dimensional Cartesian coordinates: X (longitude), Y (latitude), Z (terrain elevation), and 0–1 (traffic status, 1 means that the obstacles in the grid can pass through at this moment) (Kozmus Trajkovski et al., 2020).

After obtaining the terrain of the airport terminal area, the matrix with terrain elevation Z is shown in Formula 9; n*n means the number of grids (Lee and Shim, 2014).

$$\mathbf{Z} = \begin{bmatrix} h_{11} & h_{12} & \cdots & h_{1n} \\ h_{21} & h_{22} & \cdots & h_{2n} \\ \cdot & \cdot & \cdot & \cdot \\ \cdot & \cdot & \cdot & \cdot \\ h_{n1} & h_{n2} & \cdots & h_{nn} \end{bmatrix} \tag{9}$$

Among them, h represents the terrain elevation information that is contained in every cellular units. The larger the number of grids n, the higher the accuracy.

3.3 The minimum stabilization distance

The design scope of the approach flight procedures involves the whole area of the terminal airport (Chandra et al., 2016). After the terrain is processed to grids, it is necessary to select the relatively low terrain area as a feasible area for setting the waypoint. When the flight segment distance is not less than the minimum stabilization distance (MSD), it is necessary to ensure that the aircraft has sufficient margins to cut into the next scheduled flight segment. Therefore, this study uses MSD as a constraint when selecting a waypoint. If there are two way points on one trajectory, the minimum distance between them is equal to the sum of the MSD of all segments (ICAO, 2014). In general, the MSD of way points in different situations can be obtained by referring to DOC8168, because the turning angle of an aircraft is always less than 120°, so the relationship between the speed of the aircraft and MSD can be shown as in Table 1:

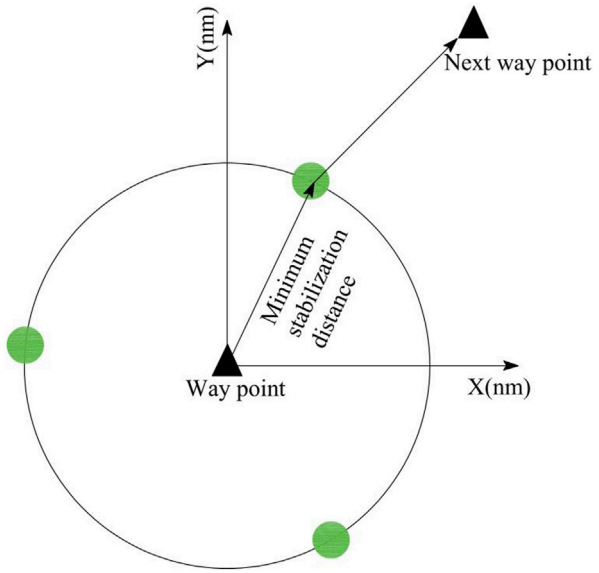

FIGURE 5
MSD used in feasible regions definition.

4 Approach flight procedures design algorithm and optimization evaluation model

4.1 Approach flight procedures design algorithm

The most important element in designing an approach procedure for alpine environments is defining a suitable algorithm or model to do the movement path plan. The movement of an object seems to be very simple, but it is actually very complex. Many scientific researchers have been exploring and improving various path optimization algorithms. In 1959, Dutch computer scientist Dijkstra studied vector path maps and developed the Dijkstra algorithm. Later, heuristic algorithms were added to the A-Star (A*) algorithm to scientifically process the optimal path results based on the Dijkstra algorithm (Hentzen et al., 2018; Dunn and Shultis, 2022).

For static environment path planning, A* and Dijkstra algorithms are usually used; Dijkstra is also used for dealing with partial problems and is suitable for non-direct graphs. Conversely, A* is more suitable for directed graphs and is specifically designed

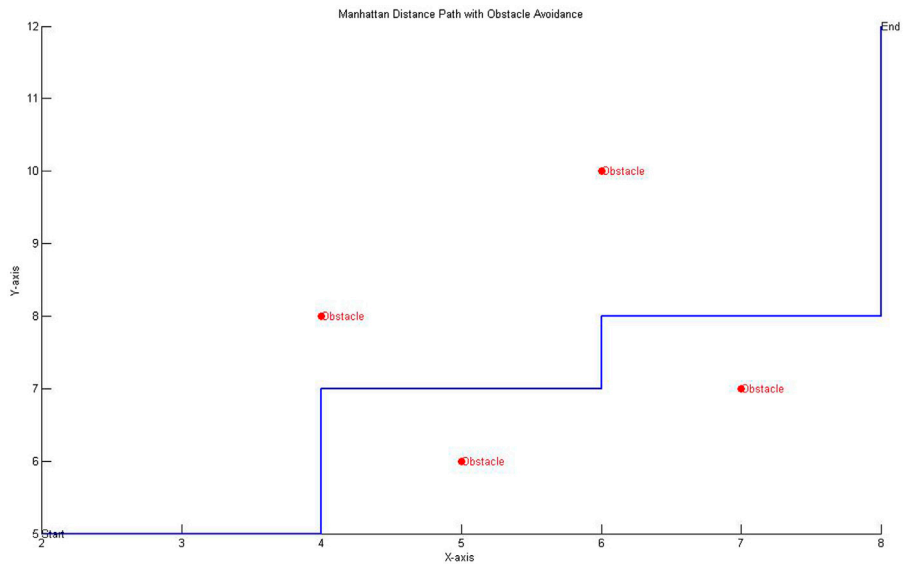

FIGURE 6
Manhattan distance display.

For example, if the flight speed is less than 400 km/h, the MSD at one two way point is 4.7km, so the MSD between the two way points will be double, which is 9.4 km. Therefore, we use a method that draws a circle with the current position as the center and is no less than the MSD as the radius to find a feasible region, when the aircraft is at an airport or a certain waypoint, as shown in Figure 5. Then, a certain altitude is set to limit the terrain obstacles on the circumference, and a relatively low terrain area as a feasible region is selected and marked in green, as in Figure 5. This can allow the selection of the most suitable waypoint within the feasible regions, and the parameters can show the flight procedure design requirements.

for overall path optimization. As for this research, the mountains in alpine environments are a static obstacle, so the design of the approach trajectory should automatically find all the areas of the alpine terrain to define the best result. Therefore, in this research, an improved A* algorithm was selected to solve the background problem mentioned before (González-Arribas et al., 2019).

The classical model of the A* algorithm is to compare various nodes and then add the compared nodes to the path library. The mechanism for finding the path in each step can be seen as a function guide. Based on this, the A* algorithm can be written as Formula 10:

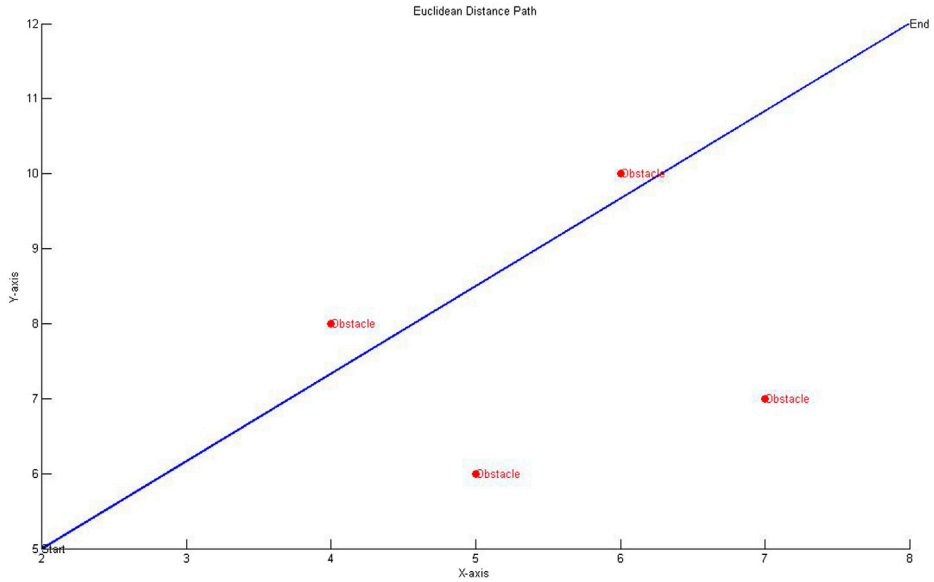

FIGURE 7
Euclidean distance display.

$$F(n) = G(n) + H(n) \tag{10}$$

The relationship between F(n), G(n), and H(n) is not a real additive relationship, as shown in Formula 10. F(n) represents the total path from the starting point to the destination by using the A* algorithm; G(n) is an evaluation function representing the displacement generated from the starting point to the destination, every displacement between grids is 1, and the farther the destination is from the starting point, the larger the displacement is. H(n) represents a heuristic guidance function: if the heuristic function is 0, the A* algorithm is equivalent to the Dijkstra algorithm, and different heuristic functions produce different path algorithm results. The weaker the heuristic function, the more nodes the A* algorithm generates, resulting in a longer operation time. When the number of steps required between the starting and destination points is exactly equal to the heuristic function, the optimal solution is generated, and its function is to preset the direction of the path.

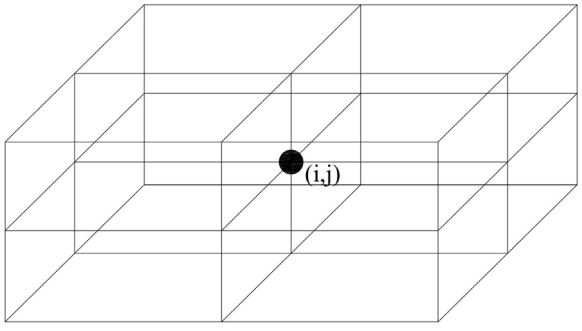

FIGURE 8
Way points of every step.

4.1.1 First improvement of the A* algorithm

The difference between the A* algorithm and other path algorithms is that it contains heuristic functions, which can be divided into various types. The commonly used distances include Manhattan distance and Euclidean distance. These two distances take different paths with obstacles. The following introduction will compare in detail the two heuristic functions andnd make an improvement on the A* algorithm by resetting the heuristic function if necessary (Hongyan et al., 2021).

The Manhattan distance is the default heuristic function of the A* algorithm, which is shown as Formula 11, but its optimization idea is only to find the next point with the shortest step compared to the previous position.

$$F_{\mathrm{Man}}(n) = \sum_{i=1}^{n} \left| (x_i - x_{i-1}) + (y_i - y_{i-1}) \right| \tag{11}$$

Euclidean distance is also a commonly used heuristic function, which is shown as Formula 12, and its optimization idea is to refer to the whole process, which is from the starting point to the final destination, using the Pythagorean theorem as a model to define the shortest distance to reach the destination.

$$F_{Euc}(n) = \sum_{i=1}^{n} \sqrt{(x_i - x_{i-1})^2 + (y_i - y_{i-1})^2} \tag{12}$$

In this part, a simple obstacle avoidance simulation can be conducted using Matlab for these two heuristic functions respectively. Firstly, grid processing to the terrain is carried out to obtain terrain data and set up the obstacles. The next step is to program the A* algorithm; after running, the software can automatically find the shortest path from the starting point to the ending point. The black blocks represent the obstacles and the green block represents the starting point. From the simulation results, it can be seen that the A* algorithm for

TABLE 2 The fuel consumption coefficient.

Fuel consumption coefficient	Reference
C_{f3}	26.805
C_{f4}	45700

If N represents the number of engines installed on a certain type of aircraft, the total fuel consumption of the aircraft from time t_0 to time t_1, according to the BADA, manual, can be expressed as in Formula 16.

Manhattan distance only considers the shortest distance of each step, shown as Figure 6, while the Euclidean distance considers the optimal path of the entire simulation field, shown as Figure 7.

Based on the above analysis, the first improvement of the A* algorithm is to set the heuristic function to Euclidean distance, and select the next way point among the eight 3 dimensional grids around the coordinate field, as shown in Figure 8.

4.1.2 Second improvement of A* algorithm

The A* algorithm needs to meet the DOC8168 operational standards to obtain the optimal path. However, in practical situations, obstacles in mountainous airports pose a threat to flight safety. In order to seek the optimal approach trajectory, the A* algorithm needs to be further improved to meet the obstacle clearance rules of the flight procedure design (Hasegawa et al., 2015).

Each grid contains information on approaching aircraft, such as height, position, gradient, and time. Therefore, the requirement for obstacle avoidance needs to meet two key conditions. The first key condition is that the highest obstacle in each grid will be seen as the controlling obstacle, which will control the minimum flight height of each segment, so the aircraft height will be measured by the controlling obstacle, which can be depicted as Formula 13:

$$H_0 \geq h_{obs} + MOC \tag{13}$$

Here, the minimum obstacle clearance is MOC, H_o represents the height of the aircraft, and h_{obs} represents the height of the controlling obstacle in the grid area.

As to the approach procedure, the flight trajectory still needs to meet the descent gradient, that is, H_{pnext} represents the altitude of the controlling obstacle in the next grid, the current aircraft altitude is H_o, and the distance between two near grids is d. The relationship between them is shown in Formula 14.

$$\frac{H_{P_{nxet}} + MOC - H_0}{d} = Gr \tag{14}$$

The maximum Gr of the approach flight program shall not exceed 8% in the initial approach segment, with an MOC of 300 m and a maximum turning angle of 120°. The maximum Gr of the intermediate approach segment shall not exceed 5.2%, the MOC shall be 150 m, and the maximum turning angle shall not exceed 30°. The maximum Gr of the final approach segment shall not exceed 6.1%, with a MOC of 75 m, consistent with the runway center line (Paveen et al., 2020).

4.2 Fuel consumption evaluation model

The trajectories of approach can be easily obtained using the improved A* algorithm; how to select the most optimized approach procedures will be addressed in this step. The consumption of fuel affects the operating costs of airlines, what's more, the further aircraft fly, the more fuel is consumed, and the higher the risk of delay to the next flight phase. Therefore, using fuel consumption to analyze the feasibility of approach trajectory is the best. This research compares the fuel consumption of different approach procedures as the main evaluation factor. However, fuel consumption is related to various factors, such as flight altitude, speed, different flight segments, and number of engines (Olmstead et al., 2002).

During the aircraft approach process, gravity provides the forward force for the aircraft during the descent period, and the approach segment can be considered as a continuous descent. Referring to the BADA manual (Thomas et al., 2004; Clarke et al., 2006), a function of the fuel flow rate for a single engine per unit time and flight altitude can be shown as in Formula 15:

$$f_{app}(t) = C_{f3} \times \left(1 - \frac{h}{C_{f4}}\right) \tag{15}$$

Among them, C_{f3} and C_{f4} is the fuel consumption coefficient in the descending section (unit: kg/min *N), as shown in Table 2 h represents the standard sea level pressure altitude (in feet) at the current position of the aircraft (Zeh et al., 2020). If N represents the number of engines installed on a certain type of aircraft, the total fuel consumption of the aircraft from time t_0 to time t_1, according to BADA manual, the total fuel consumption of the approach segment can be expressed as Formula 16.

$$Q(t) = \int_{t_0}^{t_1} f(t) \cdot N dt \tag{16}$$

Due to the fact that the fuel flow rate per unit time during the descent segment is related to the altitude of the aircraft, conversion is required. The conversion between time t and altitude h for aircraft can be written as in Formula 17:

$$\begin{cases} dh = -g_r ds \\ \dfrac{ds}{dt} = v_{TAS} \end{cases} \tag{17}$$

Among them, s represents the flight displacement and g_r represents the descent gradient of the aircraft. The relationship between them can be obtained by Formula 18 after transformation.

$$\frac{dh}{dt} = -\frac{1}{g_r} \times v_{TAS} \tag{18}$$

By solving differential Eq. 18, the relationship between aircraft altitude and time can be obtained as shown in Formula 19:

TABLE 3 Equidistant sampling points of the practical terrain (in meters).

Altitude(m) (km)	x = −30 km	x = −20 km	x = −10 km	x = 0 km	x = 10 km	x = 20 km	x = 30 km
y = 30	1400	2084	1216	1346.2	1489.8	1786	1985.8
y = 20	1100	1610	1320	1635.5	1280	1606	1890
y = 10	1450	1780	1310.7	1230	997.3	2198.4	2130
y = 0	1607.1	1201	795.3	863	1507.1	1887.2	2004.1
y = −10	1094.5	1053.2	1189.2	1451.9	1796.4	2398.1	2213.2
y = −20	848.4	1281.3	1782.1	1612.3	1793.2	2403.1	2092.4
y = −30	1602	1516.2	1121.3	781.2	673.2	596.1	539.2

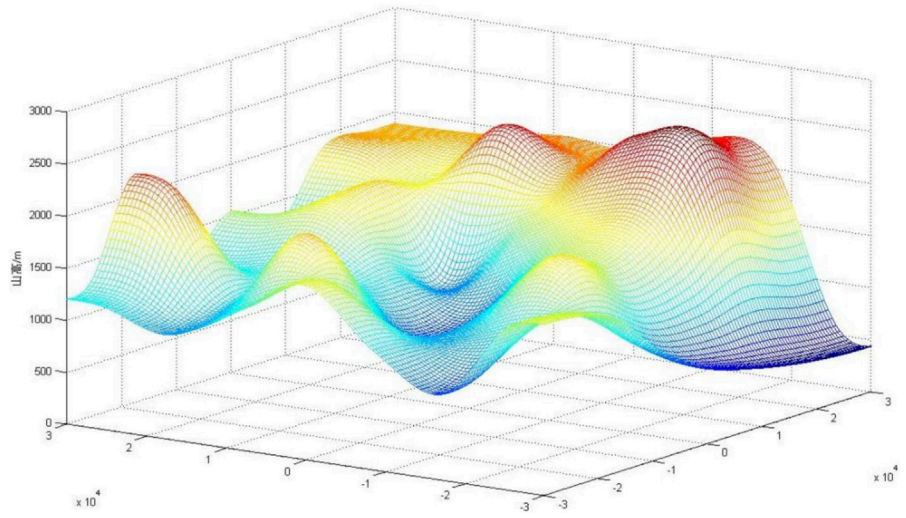

FIGURE 9
Three-dimensional of the practical terrain.

$$h = h_0 - \frac{1}{g_r} \times v_{TAS} \times t \tag{19}$$

Here, H_o represents the initial altitude of the aircraft during the descent segment.

With the transformation, the whole fuel consumption of the approach procedure can be depicted as in Formula 20:

$$Q_{app}(h) = \sum_{k=1}^{n} \int_{h_{ki}}^{h_{kj}} f_{app}(t(h)) \cdot N \cdot \left(-\frac{g_r}{v_{TAS}}\right) dh \tag{20}$$

Through the aforementioned fuel evaluation formulas, the comprehensively optimal approach procedure can be determined, since the formulas are associated with flight distance s, flight altitude h, flight time t, and descent gradient g_r during the conversion process. The evaluation also covers a wide range, demonstrating good feasibility.

5 Case study

This section builds upon established optimization algorithm theories to study practical airport cases, employing MATLAB for the simulation and design of the airport's approach flight procedures.

This research takes one airport in the mountainous area of Yunnan as a case study. The elevation of this airport is 863m, the magnetic direction of the runway is 045° and 225°, and the length and width are 2600 * 45 (m). The airport is located in a valley, surrounded by high mountains 5 km away, with a magnetic direction of 072° relative to the airport reference point. At a distance about 40 km, there are obstacles with elevations of 3000 m, 2326 m, 2229 m, and 1686 m in the area. Therefore, when designing the approach procedures manually, it is difficult to overcome natural mountains. Therefore, this research will adopt intelligence modeling for simulation testing.

For the terrain data of 60 square kilometers around this airport, equidistant sampling points were conducted, as shown in Table 3, where the terrain data have been adjusted and modified.

Firstly, using the bi-cubic b-spline interpolation method for 3D modeling and simulation, the airport coordinate points are (0,0), and the approach points are B and P way points. According to Figures 9, 10, it can be seen that this airport is located in a mountainous terrain similar to a canyon, and the ups and downs

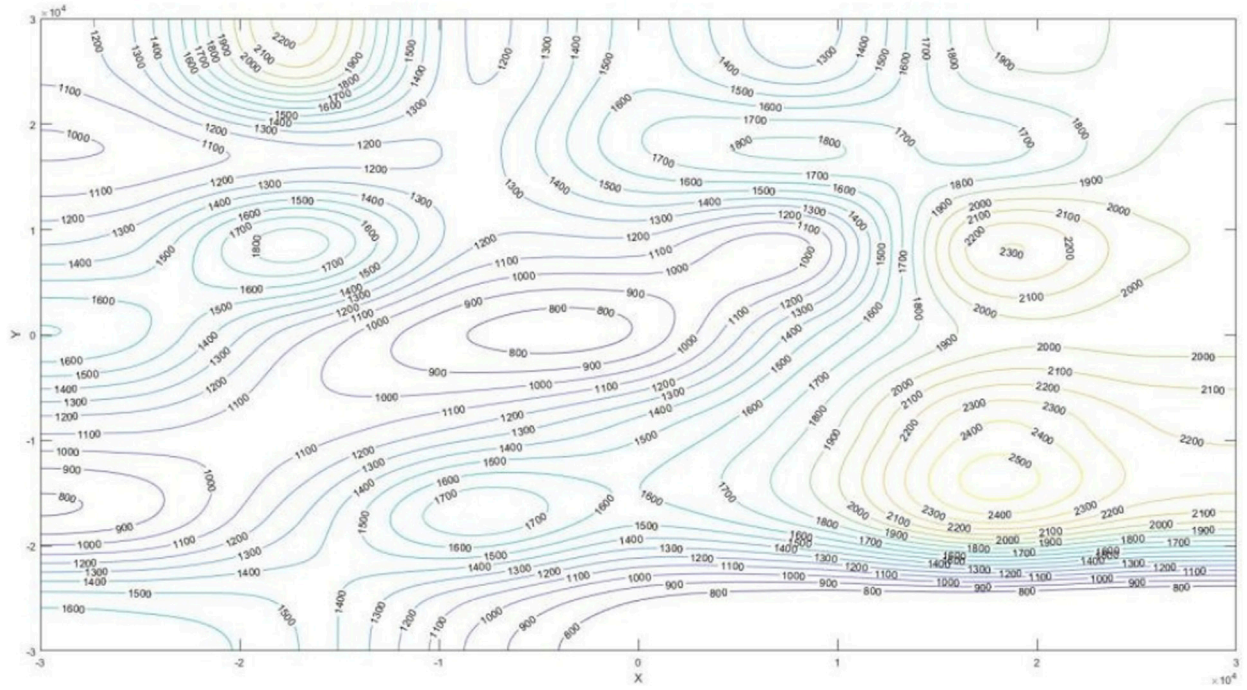

FIGURE 10
Contour map of the practical terrain.

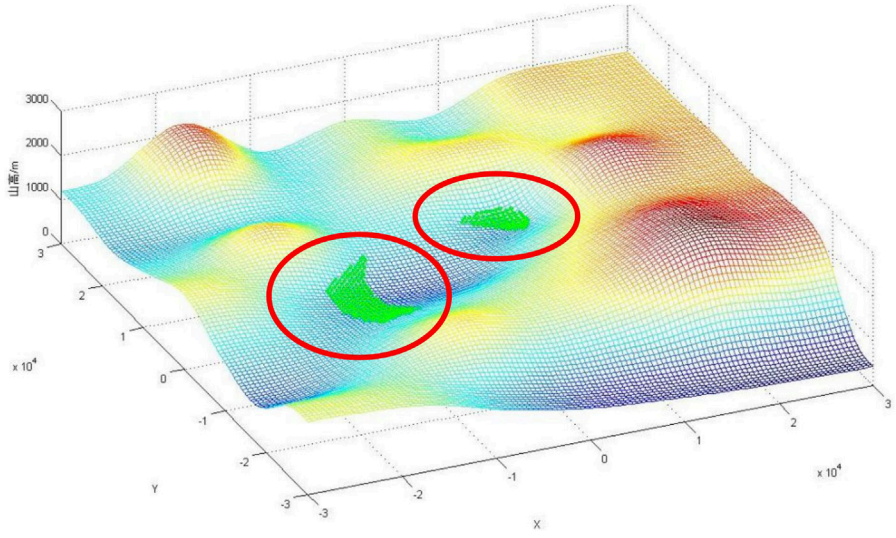

FIGURE 11
The feasible regions near the airport.

of the terrain continually changing can be seen from the simulation map.

Secondly, the cellular automaton model is adopted for grid processing of the terrain. The more grids, the smaller the obstacles will be included in the terrain range, and the higher the calculation accuracy. In this research, the terrain of the airport is divided into grids with an equal distance of 1 km, as shown in Figure 11:

After the terrain of this airport terminal area is grid processed, each grid is assigned information such as terrain height, location, and time, as shown in Figure 11. The green area represents the feasible region.

The design of the approach procedures adopts the twice-improved A* algorithm in this research. Starting from the arrival way points B(1,n) and P(n/2,n/2), n stands for the number of grids within the terminal terrain, so n equals to 120 in this research. The

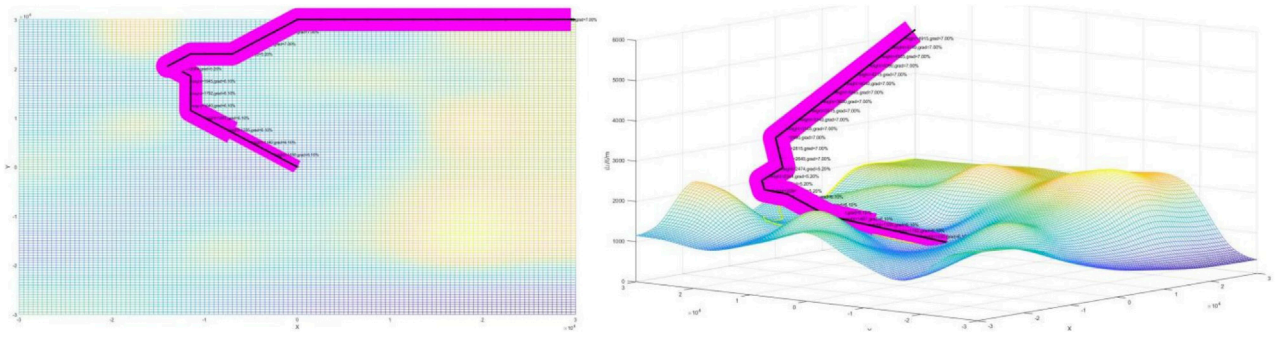

FIGURE 12
Approach procedure A of this airport (left 2D, right 3D).

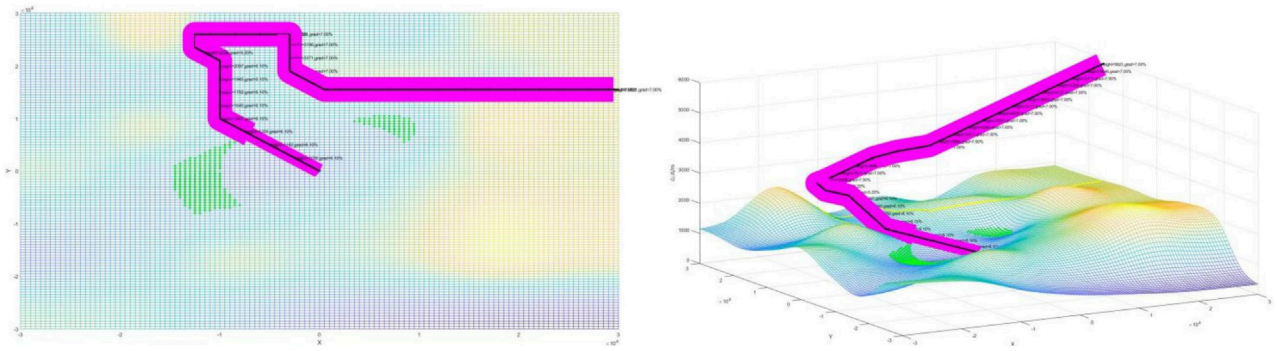

FIGURE 13
Approach procedure B of this airport (left 2D, right 3D).

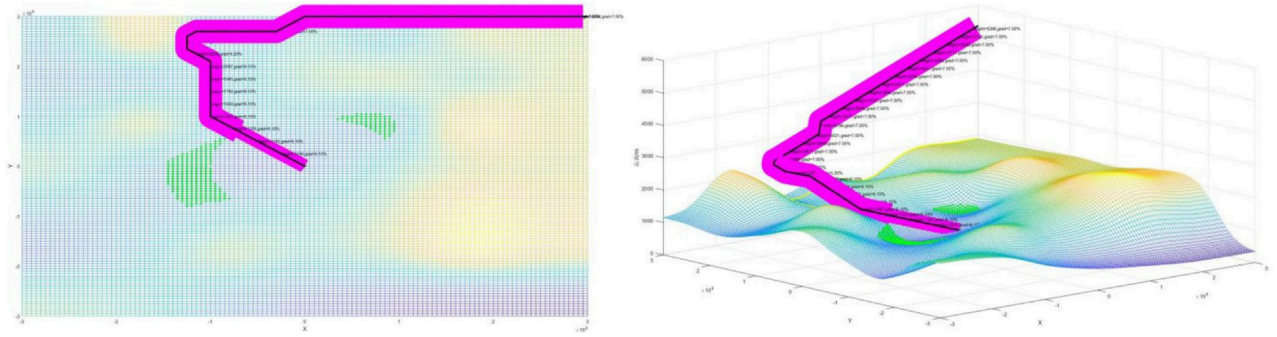

FIGURE 14
Approach procedure C of this airport (left 2D, right 3D).

four procedures are designed as shown in the following Figures 12, 13; Figures 14, 15; among them, procedures A and C's arrival is from way point B, procedures B and D's arrival is from way point P, the gradient of the four procedures in the initial approach segment is 7%, the intermediate approach segment is 5.2%, and the final approach segment is 6.1%. The magenta areas on both sides of the route represent the protected area. If the protected area cannot be displayed completely, it indicates that the obstacle is too high. If the protected area is shaded, this further indicates that the designed procedure is not safe.

It can be observed that four of the approach procedures adhere to the DOC8168 specifications. The gradient in the initial approach segment is less than 8%, and the descent gradient in the final approach segment does not exceed 6.1%. The intermediate approach segment maintains an optimal descent gradient of around 5.2%. The magenta protected areas all avoid obstacles, which, when displayed completely, indicates that the flight procedure can smoothly surpass the obstacles. Next, the fuel consumption calculation method will be applied to optimize and evaluate the four approach procedures.

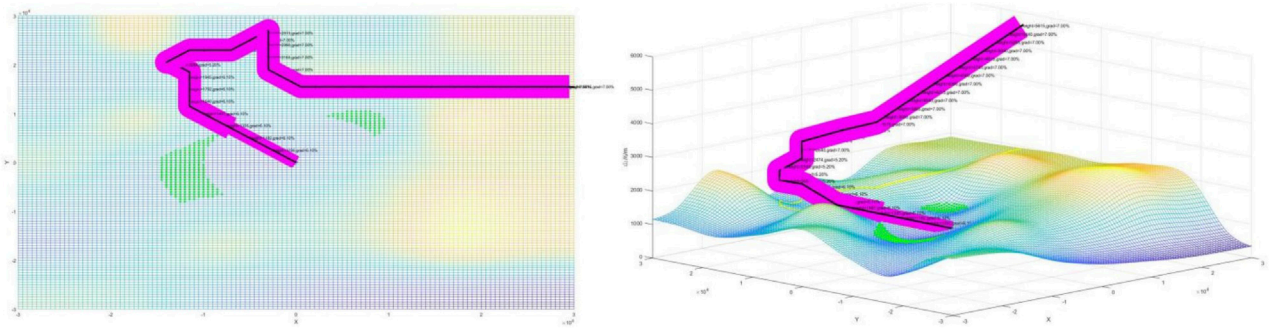

FIGURE 15
Approach procedure D of this airport (left 2D, right 3D).

TABLE 4 The fuel consumption of every simulated approach procedure (unit:kg).

Approach procedure	Segment 1	Segment 2	Segment 3	Segment 4	Total
A	54	52	152	60	318
B	55	94	105	78	332
C	137	105	78	79	399
D	138	63	128	63	392

After completing the design of the approach procedures, this research evaluated the four simulated approach procedures based on the fuel consumption evaluation model. Each approach procedure will be divided into four segments, namely, 1, 2, 3, and 4, representing arrival segment, initial approach segment, intermediate approach segment, and final approach segment, respectively. According to the descent gradient, the total fuel consumption for each segment of the approach was calculated separately. The results are rounded to the nearest whole number and shown in Table 4:

According to Table 4, the fuel consumption of approach procedures A and D is slightly smaller than that of the same approach direction program. Therefore, after optimization and evaluation, approach procedures A and D are appropriate to be retained. This decision can be adopted for the flight procedure designer to have a brief insight to manual design approach procedures for mountainous airports.

6 Conclusion

Flight procedure design is a key technology required for the current development of civil aviation, especially in the approach flight procedure of alpine airports, which have many flight segments and are complex to design for under the presence of dense obstacles. However, based on this challenge, this research used the flight procedures design regulations and standards to form a design idea for trajectory optimization, software programming, and automatically drawing the protected areas. By calculating obstacle clearance to actively avoid obstacles, as we can see from the case study, the result of the approach procedures designed by the improved A* algorithm can strictly obey the regulation of DOC8168, mainly about the turning angle, descent gradient, and the MSD length. With By taking a further step and evaluating fuel consumption, the optimized approach procedures for alpine airports can be intelligently obtained. This removes the difficulties that manually designing approach flight programs, route layouts, protection areas, obstacle clearance calculations and evaluations, gradient optimizations can incur. They are also labor-intensive and inefficient. Ultimately, this research provides a reliable design idea for manually calculating flight procedures. However, in order to make the research results more accurate, the following points need to be further studied: (1) Further use of more accurate digital maps, such as GIS software for in-depth research; and (2Consideration of multiple program evaluation models to comprehensively evaluate the designed approach flight program from multiple aspects and dimensions.

Data availability statement

The datasets presented in this study can be found in online repositories. The names of the repository/repositories and accession number(s) can be found in the article/Supplementary material.

Author contributions

LL: Conceptualization, Data curation, Formal Analysis, Funding acquisition, Investigation, Methodology, Project administration, Resources, Software, Supervision, Validation, Visualization,

Writing–original draft, Writing–review and editing. XL: Data curation, Investigation, Resources, Supervision, Writing–review and editing. JJ: Formal Analysis, Investigation, Writing–review and editing. JZ: Methodology, Resources, Writing–review and editing.

Funding

The author(s) declare financial support was received for the research, authorship, and/or publication of this article. This research is supported by The China Scholarship Council (Grant No. 202108510115) and Research on Feature Extraction and Event Correlation of Aviation Intelligence Information in Big Data Environment (2023 Central University Level Key Projects) (Grant No. ZJ2023-003).

Conflict of interest

The authors declare that the research was conducted in the absence of any commercial or financial relationships that could be construed as a potential conflict of interest.

Publisher's note

References

Campos, I. S. G., Nascimento, E. R., Freitas, G. M., and Chaimowicz, L. (2016). A height estimation approach for terrain following flights from monocular vision. *Sensors* 16 (12), 2071. doi:10.3390/s16122071

Chandra, D. C., and Markunas, R. (2016). "Line pilot perspectives on complexity of terminal instrument flight procedures," in 2016 IEEE/AIAA 35th Digital Avionics Systems Conference (DASC) (IEEE), 1–10.

Chen, S., Dong, G., Tang, T., Zhang, J., Wang, J., Liu, S., et al. (2019). Research on improved A* algorithm for track optimization based on schematic maps. *J. Projectiles. Rockets. Missiles. Guidance* 1–7.

Clarke, J. P., Bennett, D., Elmer, K., Firth, J., Hilb, R., Ho, N., et al. (2006). *Development, design, and flight test evaluation of a continuous descent approach procedure for nighttime operation at Louisville International Airport (No. PARTNER-COE-2005-002)*. Canada: Partnership for Air Transportation Noise and Emissions Reduction.

Collins, B. P. (1982). Estimation of aircraft fuel consumption. *J. Aircr.* 11, 969–975. doi:10.2514/3.44799

Dunn, W. L., and Shultis, J. K. (2022). *Exploring Monte Carlo methods*. Elsevier.

González-Arribas, D., Soler, M., Sanjurjo-Rivo, M., Kamgarpour, M., and Simarro, J. (2019). Robust aircraft trajectory planning under uncertain convective environments with optimal control and rapidly developing thunderstorms. *Aerosp. Sci. Technol.* 89, 445–459. doi:10.1016/j.ast.2019.03.051

Hasegawa, T., Tsuchiya, T., and Mori, R. (2015). Optimization of approach trajectory considering the constraints imposed on flight procedure design. *Procedia Eng.* 99, 259–267. doi:10.1016/j.proeng.2014.12.534

He, S., Wang, C., and Yang, Q. (2017). Determination of suitable grid size for 1: 50000 DLG-based DEM. *J. Mt. Sci.* 35 (04), 572–579.

Hentzen, D., Kamgarpour, M., Soler, M., and González-Arribas, D. (2018). On maximizing safety in stochastic aircraft trajectory planning with uncertain thunderstorm development. *Aerosp. Sci. Technol.* 79, 543–553. doi:10.1016/j.ast.2018.06.006

Hongyan, Y. X., Wei, X., Xinyuan, J., and Ji, X. (2021). A moving path tracking method of the thunderstorm cloud based on the three-dimensional atmospheric electric field apparatus. *J. Sensors* 2021, 1–13. doi:10.1155/2021/8856033

ICAO (2000). *Environmental technical manual on the use of procedures in the noise certification of aircraft*. ICAO.

ICAO (2014). *Procedures for air navigation services — visual and instrument flight procedures*. Canada: International Civil Aviation Organization.

Kozmus Trajkovski, K., Grigillo, D., and Petrovič, D. (2020). Optimization of UAV flight missions in steep terrain. *Remote Sens.* 12 (8), 1293. doi:10.3390/rs12081293

Lee, D., and Shim, D. H. (2014). "Spline-RRT* based optimal path planning of terrain following flights for fixed-wing UAVs," in 2014 11th International Conference on Ubiquitous Robots and Ambient Intelligence (URAI) (IEEE), 257–261.

Liu, Y., Hansen, M., Lovell, D., and Ball, M. O. (2018). "Predicting aircraft trajectory choice–a nominal route approach," in Proc. of the International Conference for Research in Air Transportation.

Lu, Li. (2019). *Optimization and simulation research on flight procedures design for mountainous airports*. Sichuan: Civil Aviation Flight University of China.

Lu, L., and Liu, C. (2022). Research on trajectory planning in thunderstorm weather based on dynamic window algorithm during approach segment. *Sci. Program.* 2022, 1–10. doi:10.1155/2022/7031928

Malaek, S. M., and Kosari, A. R. (2007). Novel minimum time trajectory planning in terrain following flights. *IEEE Trans. Aerosp. Electron. Syst.* 43 (1), 2–12. doi:10.1109/taes.2007.357150

Olmstead, J. R., Fleming, G. G., and Gulding, J. M. (2002). *Integrated noise model (INM) version 6.0 technical manual*. Washington, DC: Federal Aviation Administration Office of Environment and Energy, Paper FAA-AEE-02-01.

Paveen, J., Supatcha, C., Sameer, A., and Daniel, D. (2020). "A distributed metaheuristic approach for complexity reduction in air traffic for strategic 4D trajectory optimization," in 1st conference on Artificial Intelligence and Data Analytics in Air Transportation, Singapore, Feb 2020, 1-9.

Plat, N., Uysal, M., and Toprak, A. S. (2015). An investigation of DEM generation process based on LiDAR data filtering, decimation, and interpolation methods for an urban area. *Measurement* 75, 50–56. doi:10.1016/j.measurement.2015.08.008

Qian, G. (2015). *Research on key technologies for flight procedure optimization design*. Nanjing: Nanjing University of Aeronautics and Astronautics.

Rahim, M., and Malaek, S. M. (2007). "Intelligent operation using terrain following flight in unmanned aerial vehicles," in 2007 IEEE Aerospace Conference (IEEE), 1–8.

Tang, Li, Peng, H., and Zhang, X. (2019). Path planning method for mountainous UAVs based on improved ant colony algorithm. *J. Transp. Syst. Eng. Inf. Technol.* 19 (01), 158–164.

Thomas, C. S., Hume, K. I., and Hooper, P. D. (2004). *Aircraft noise,airport growth and regional development*, 2806. American Institute of Aeronautics and Astronautics, 477–488.

Wang, C. (2010). Research on aircraft cruise stage fuel flow model based on multiple linear regression. *Guide Sci. Technol. Wealth* 2, 15–18.

Yuan, W., Yang, M., Deng, L., Wang, C., and Wang, B. (2018). Rapid construction method of terrain elevation grid map based on V disparity. *J. Shanghai Jiao Tong Univ.* 52 (01), 1–6.

Zeh, T., Judith, R., Richard, A., and Harmut, F. (2020). "Prediction of the propagation of trajectory uncertainty for climbing aircraft," in DASC 2020 IEEE/AIAA 39th Digital Avionics Systems Conference, San Antonio, United Statas, 1–9.

Zhao, Q. (2016). *Research on terrain path planning technology based on geographic information system*. Beijing: The First Institute of China Aerospace Science and Technology Corporation.

Zhao, Q. (2017). *Comprehensive optimization and application of initial approach segments based on GIS*. Guanghan: Civil Aviation Flight University of China.

frontiers | Frontiers in Earth Science

TYPE Original Research
PUBLISHED 25 January 2024
DOI 10.3389/feart.2023.1266559

OPEN ACCESS

EDITED BY
Yunhui Zhang,
Southwest Jiaotong University, China

REVIEWED BY
Huajin Li,
Chengdu University, China
Chang'An Qin,
Beijing University of Civil Engineering and Architecture, China

*CORRESPONDENCE
Meiben Gao,
gaomb@mail.xhu.edu.cn

RECEIVED 25 July 2023
ACCEPTED 08 November 2023
PUBLISHED 25 January 2024

CITATION
Zhang Y, Duan L, Li Y and Gao M (2024), Study on deformation characteristics of underground pipeline corridors and uneven settlement factors of foundations in sandy chalky soil layer.
Front. Earth Sci. 11:1266559.
doi: 10.3389/feart.2023.1266559

Study on deformation characteristics of underground pipeline corridors and uneven settlement factors of foundations in sandy chalky soil layer

Yulong Zhang[1], Lincheng Duan[1], Yuanxiang Li[1] and Meiben Gao[2,3,4,5]*

[1]Shandong Construction Engineering Quality Inspection and Testing Center Co., Ltd., Jinan, Shandong, China, [2]School of Emergency Management, Xihua University, Chengdu, Sichuan, China, [3]Key Laboratory of Landslide Risk Early-warning and Control, Ministry of Emergency Management, Chengdu University of Technology, Chengdu, Sichuan, China, [4]State Key Laboratory of Geohazard Prevention and Geoenvironment Protection, Chengdu University of Technology, Chengdu, Sichuan, China, [5]Key Laboratory of Geohazard Prevention of Hilly Mountains, Ministry of Natural Resources, Fuzhou, Fujian, China

Uneven settlement phenomenon is very easy to occur in the sandy pulverized ground stratum, the underground pipe corridor longitudinal and transverse stiffness difference is obvious, so that it is easy to crack and deformation due to uneven settlement in this type of stratum. This paper carries out research on uneven settlement and cracking and deformation of Qihe tube corridor, analyzes the reasons leading to uneven settlement and the factors affecting the deformation and cracking of the tube corridor, and provides guidance for foundation treatment and tube corridor repair and mixing and reinforcement. It was found that the concrete structure of the corridor itself had exposed reinforcement, pockmarks and holes, and that cracks on the structure of the corridor sprouted and expanded from these defects. Defects and damages on the concrete structure of the pipeline corridor are contributing factors to the deformation and cracking of the members, and the uneven settlement of the foundation is the main initiating factor for the cracking and deformation. The analysis of the numerical simulation results of similar underground pipeline corridors is carried out, and it is found that the simulation results are consistent with the deformation characteristics of the Qihe pipeline corridor, which further supports the conclusions of this paper. The main stratigraphic factors contributing to the inhomogeneous settlement were found to be the water-rich and loose bodies in the lower part of the strata, as revealed by the physical means and the experimental verification boreholes. Localized hydraulic effects such as pumping further accelerate the uneven settlement of the foundation.

KEYWORDS

sandy chalky soil, uneven settlement, underground pipe corridors, rich water bodies, lax bodies, numerical simulation

1 Introduction

Uneven settlement of foundation is the main initiating factor that induces cracking and deformation of the corridor structure, and congenital defects of the corridor structure are factors that promote cracking and deformation. In order to manage and prevent the cracking and deformation of the pipeline corridor, it is necessary to analyze and study the factors that lead to the uneven settlement of the foundation.

Uneven settlement of foundations is one of the main factors leading to damage to building structures, dynamic changes in structural loading conditions and changes in the environment caused by changes in the undercropping of foundations are causing this uneven settlement (Chen and Hanna, 2023; Wu et al., 2022). The degree to which a building is affected by uneven settlement is related to its own characteristics, the greater the stiffness of the building, the poor coordination of deformation, the greater the effect of uneven settlement on it (Chen et al., 2011; Al' Malul and Michail, 2018; Bao et al., 2020; Wang et al., 2022). Therefore, for structures with large stiffness, the uneven settlement of foundations should be strictly controlled, which is not only reflected in general buildings, but also for the uneven settlement of high-speed railroad foundations, which should be paid more attention to (Zhang et al., 2023; Liu and Moore, 2021; Zhang et al., 2021; Shi et al., 2022). When detecting and analyzing the uneven settlement of building foundations, the traditional detection method has the problems of large error and long time (Liu et al., 2020). Uneven settlement of foundations is one of the common engineering quality problems in wetted loess areas, and it was found that changes in settlement area and settlement volume in wetted loess areas have no significant effect on the interlayer displacement ratio (Bao et al., 2020; Xu et al., 2022; Ho and Kuwano, 2021). Underground pipe corridors are not only affected by uneven settlement but also by ground cracks. It was found that with the increase of ground crack settlement, a stress reduction zone near the ground crack appeared at the bottom of the upper plate wall of the tube corridor structure and revealed localized dehollowing phenomena (Deng et al., 2022; Xie et al., 2020; Bian et al., 2017). Diagnosis of inhomogeneous settlement in regional railroad tunnels using spatial correlation of high-density strain measurement points can effectively diagnose the influence range of inhomogeneous settlement (Liang et al., 2023; Hu et al., 2021). After the highway widens the roadbed, under the effect of differential settlement, the old pavement surface layer and the upper base layer are subjected to tensile stress within about 4 cm, and the base layer reaches the destructive strength first. Below 4 cm of old pavement, the sub-base first reaches breaking strength (Shen et al., 2021; Zhou, 2022; Wang et al., 2023). There is a relationship between the water content of foundation soils and uneven settlement, with a higher degree of uneven settlement and a wider range of effects in foundations with high water content (Ngugi Hannah et al., 2021). It was found that the more permeable sand layer and the upper cohesive soil layer have greater cohesion and can effectively reduce differential settlement (Cong et al., 2021). The joints of underground pipeline corridors are the weakest parts and are highly susceptible to the effects of uneven settlement (Liu et al., 2020; Jiang et al., 2020; Xie et al., 2020; Gebremedhn et al., 2019). Rigidly spliced box girder bridges under the influence of uneven settlement, the spliced section will appear the phenomenon of transverse stress peaks, which will lead to concrete cracking and damage (Xu et al., 2023). Settlement monitoring plays a crucial role in preventing geologic risks and disasters, and stochastic differential equations reliably yield short-term settlement predictions (Guo et al., 2023). The monitoring of the gypsum mine hollow area found that the surface deformation was mainly horizontal displacement, and the direction of the horizontal displacement was overall pointing to the hollow area (Xu et al., 2023). The effect of rainfall on wet submerged loess is very significant and can trigger strong inhomogeneous settlement phenomena (Zhao, 2022).

In summary, uneven settlement is closely related to the characteristics of the stratum in which it occurs. In soft and sensitive strata such as chalky sandy soils, loose bodies and water-rich bodies are likely to occur, and loose bodies are susceptible to the influence of groundwater and rainfall. Exploring the causes of uneven settlement of foundation is the key to prevent and manage uneven settlement, this paper carries out research on uneven settlement of Qihe corridor, analyzes the deformation and cracking characteristics of the corridor, explores the factors causing uneven settlement of the corridor, and provides theoretical guidance for the next foundation treatment and the repair and reinforcement of the corridor.

2 Overview of the pipeline corridor project

Jingyi Road comprehensive pipeline corridor project is located in the northwest of Qihe County, Qihe County, West Area, north of Qishun Street, south to Qi Trade Street, a total length of 300 m. For the open excavation construction of the pipe corridor, the foundation holding layer is a pulverized soil layer with a thickness of 0.6–2.7 m.

2.1 Engineering geological conditions

The stratigraphy of the pipeline corridor site is a sandy chalky soil stratum. The groundwater belongs to the hydrogeological zone of the Yellow River alluvial plain, and the lithology of the aquifer is generally dominated by fine and powdery sand and silt, and the aquifer is mostly distributed horizontally in the form of bands and lenses, and vertically in the direction of staggered distribution of the aquifer and the relative waterproof layer. The type of groundwater dynamics is precipitation infiltration evapotranspiration. Groundwater depth ranges from 0.40 to 2.80m, groundwater level elevation is 20.31m, and annual variation of groundwater level is 1.50 m. Figure 1 shows the engineering geologic profile.

2.2 Deformation characteristics of pipe corridor

The pipeline corridor has experienced two heavy rainfalls, the first of which occurred on 9 August 2022, during which pumps were used to pump the water in the pipeline corridor to the river 30 m away from the east side of the corridor in order to lower the

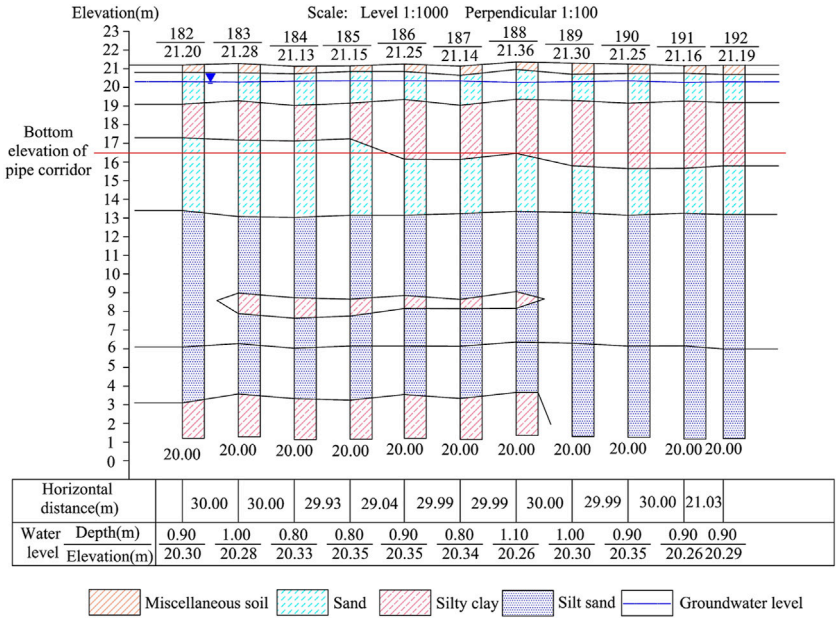

FIGURE 1
Engineering geological profile.

groundwater level of the site and prevent the foundation from settling unevenly. However, on August 16th, the K0+549~K0+579 section of the corridor still had uneven settlement, the corridor tilted to the south in general, and the maximum settlement occurred in the corridor deformation joint K0+579, the maximum settlement of the corridor on the north side of the deformation joint reached 1.2 m, and the maximum settlement of the corridor on the south side reached 0.1 m, and at the same time, the ground around the cracks appeared. The second heavy rainfall occurred in early October 2022, and the pumping work continued until mid-October, during which the subsidence of the pipe corridor on both sides of the deformation joints increased, and the peripheral backfill collapsed, and the maximum subsidence of the pipe corridor on the north side of the deformation joints at K0+579 reached 2.0m, and the maximum subsidence of the pipe corridor on the south side reached 1.1m, while the peripheral backfill collapsed. The status of uneven settlement at the site of the pipe corridor is shown in Figure 1H, the surface subsidence depth of the upper part of the pipe corridor is higher than that of other places, and a large number of longitudinal tensioned downward misalignment cracks appeared on the surface, and the longitudinal cracks were mainly distributed on the two sides of the pipe corridor, which were caused by the significant subsidence around the pipe corridor. There are also a small number of transverse cracks distributed around the pipe gallery. The duration of the first heavy rainfall was 4 h and the cumulative rainfall was 76mm, which is of heavy rainfall level. The duration of the second heavy rainfall was 3 h and the cumulative rainfall was 83mm, which is of heavy rainfall level.

During the pouring process of the pipe corridor structure, due to the small distance between the formwork and the reinforcement and the incomplete vibration of the concrete, the concrete of the pipe corridor structure has defects and damages, which are mainly manifested in the exposed tendons, pockmarks and holes. Figure 2A, B shows the exposed reinforcement, pockmarked surface and hole defects existing in the roof slab of the pipe corridor at K0+552.5 m and K0+556.5 m. This defects and damage left by the concrete casting will promote the subsequent deformation of the concrete construction damage, in the subsequent uneven settlement, these defects at the hidden danger will be amplified, will be the first in these defective parts of the cracking damage, which evolved to the destruction of the concrete structure as a whole. Such defects and damages left due to concrete pouring belong to the congenital influences on the structural deformation of the pipe corridor.

The corridor experienced uneven settlement around the corridor after two heavy rainfall events. Uneven settlement of the foundation leads to unbalanced stress in the corridor structure, and stress concentration occurs at the corridor's variable cross-section due to the change in cross-sectional area, resulting in tension cracks. There are three cracks in the structure of the pipe corridor, the first crack is located in the east and west sides of the outer wall at K0+559m, the source of cracking is located in the concrete surface, and the cracks are radial expansion from the concrete surface. At K0+559 m there are 7 cracks in the west wall with a maximum crack width of 11.5 mm (shown in Figure 2C) and 5 cracks in the east wall with a maximum crack width of 13.3 mm (shown in Figure 2D). The second crack was located on the top slab at K0+566m, with five cracks distributed transversely and the maximum crack width of 1.24 mm (shown in Figure 2E). The third crack was located in the top slab and exterior wall at K0+564m, where a crack penetrated in the top slab causing the concrete to fall off (shown in Figure 2F) and a hole in the waterproofing layer of the exterior wall (shown in Figure 2G). It can be seen that the uneven settlement of the foundation of the corridor makes the

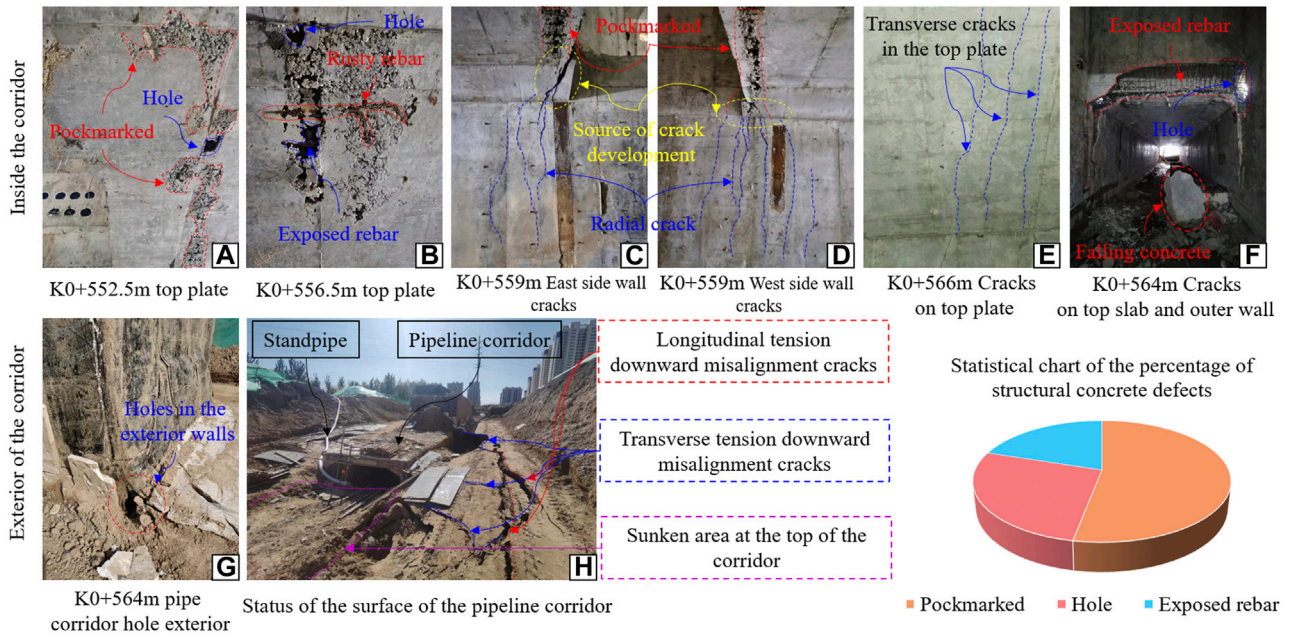

Fig.2 Characteristics of surface settlement and internal concrete cracking damage in pipeline corridors

FIGURE 2
Characteristics of surface settlement and internal concrete craking damage in pipeline corridors.

defects of the concrete structure amplified, and the cracks start to sprout from the concrete defects, and expand through under the action of further uneven settlement, leading to structural cracking and damage.

Analyzing the cracking damage characteristics of the pipeline corridor, it is found that the cracks on the concrete structure are mainly sprouted from the exposed reinforcement and pockmarks at the gestation, and penetrate into each other between the concrete holes, and eventually form macroscopic penetrating cracks. It can be seen that inhomogeneous settlement is the main driving factor leading to cracking damage, and original defects in concrete are the main contributing factors leading to cracking damage in concrete structures.

3 Deformation detection methods for pipe corridors

3.1 High-density resistivity methods

In order to investigate the reasons for the uneven settlement of the foundation of the corridor, the high-density resistivity method was used around the corridor to carry out probing on both sides of the corridor and to investigate the physical characteristics of the foundation soil under the corridor. Six measurement lines were arranged on both sides of the pipeline corridor, the lines were 1.0m, 3.0m and 15.0 m away from the outer wall (the distribution of the lines is shown in Figure 3), the spacing of the measurement points was 1.0 m, and the length of the lines was 60 m, and the dipole-dipole device (the on-site arrangement is shown in Figure 3A). The average ground elevation of the 1.0 m measuring line from the outer wall and the 3.0 m measuring line from the outer wall is 18.4m, and the 25# probing point corresponds to its maximum settlement, while the average ground elevation of the 15.0 m measuring line from the outer wall is about 21.4 m, and the 31# probing point corresponds to its maximum settlement.

The maximum transmitting power of the high-density resistance detector is 9000W, the maximum transmitting voltage is ±1500V, the maximum transmitting current is ±6A, the current accuracy is 0.1%, and the working environment temperature is −20–60°C.

3.2 Multi-channel transient surface wave methods

The detection results of the high-density resistivity method indicate the suspected presence of water-rich and loose bodies in the lower part of the pipe corridor, which were eroded by hydraulic forces, resulting in the formation of cavities that led to the uneven settlement of the upper part of the pipe corridor. Due to the diversity of the subsoil, it is difficult to accurately and reliably reflect the real situation of the subsoil with the results obtained by a single means of detection. In order to improve the reliability of the detection information so that the factors leading to inhomogeneous settlement can be accurately identified, the multi-channel transient surface wave method was used to detect the low-resistance region on the basis of the results of the high-density resistivity method. Along the pipeline corridor along the direction of the arrangement of the east and west 2 lines of measurement, each line arrangement of 24 geophones, channel spacing 1.0m, pile number K0 + 579 excitation, offset distance of 1.0 m, detecting

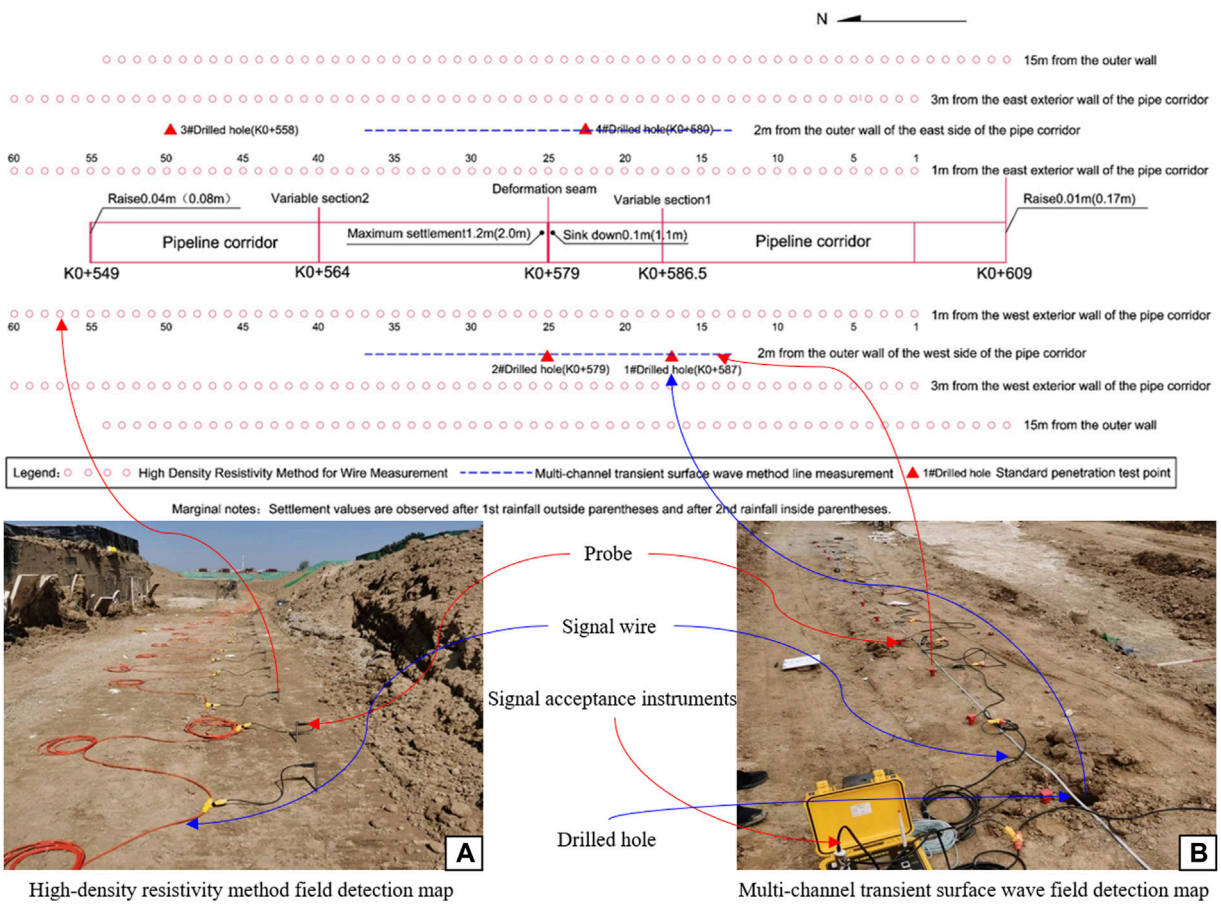

FIGURE 3
Layout of object detection lines and boreholes.

the wave velocity of the soil layer below the top plate of the pipeline corridor in the range of 15.0 m, the layout of the measurement line as shown in Figure 3, the distribution of the field detection points as shown in Figure 3B.

The multi-channel transient surface wave detector has a sampling interval of 4–4000 μs, a sampling resolution of 24AD, a dynamic range of more than 110dB, a channel phase error of less than 0.1 ms, a frequency bandwidth of 0.1–5000Hz, and an operating ambient temperature of −20–55°C.

3.3 Standard penetration probe

The results of both the high-density resistivity method and the multi-channel transient surface wave method indicate a high probability of the presence of water-rich and loose bodies in the lower portion of the corridor, and accurately indicate the depth and extent of the subsurface diseased bodies. In order to further verify the authenticity and reliability of the exploration results, based on the results of the high-density resistivity method and multi-channel transient surface wave, drill holes were drilled to verify the results at three points in the area of the suspected sparsity, with hole 1 located in the west side of the pile No. K0+587, hole 2 located in the west side of the pile No. K0+579, and hole 4 located in the east side of the pile No. K0+580. In the area where no abnormality is found, 3# holes (east side pile No. K0+558) are arranged as comparison holes, which are 2.0 m away from the outer walls on both sides of the pipeline corridor, and the arrangement of the holes is shown in Figure 3.

4 Analysis of deformation detection results of pipeline corridor

4.1 Analysis of the results of the high-density resistivity method

The data collected by the high-density resistivity method were inverted and analyzed, and Figure 4 shows a cloud map of the results of the inversion analysis for the six survey lines. The analysis results based on the cloud map show that: 1) along the pipeline corridor direction, pile number K0+578~K0+586.5 section, there is an obvious low-resistance area below the bottom plate of the pipeline corridor, the resistivity value is ≤8.0 Ω-m, and initially determined to be the distribution of water-rich and sparse bodies, and the distribution range is shown in Table 1. Water-rich body area due to K0 + 609 south side of the pit pumping and other local hydraulic effects, resulting

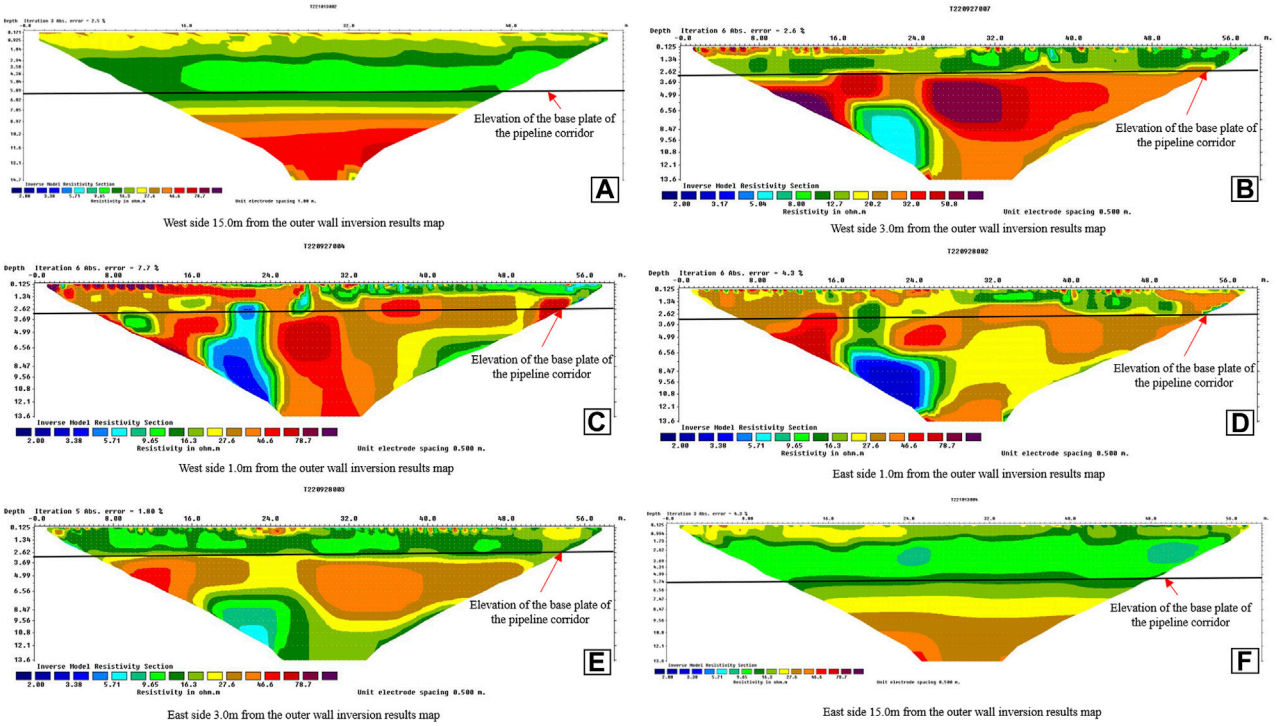

FIGURE 4
Results of the high-density resistivity method.

TABLE 1 Results of the high-density resistivity method.

Line position	Distribution range along the pipeline corridor alignment	Disease body depth distribution range
1.0 m from the outer wall on the west side of the corridor	Pile No. K0+579.5~ K0+585	0.0m–9.0 m below base plate
3.0 m from the outer wall on the west side of the corridor	Pile No. K0+580~ K0+586.5	3.5m–9.0 m below base plate
1.0 m from the outer wall on the east side of the corridor	Pile No. K0+578~ K0+586.5	3.5m–9.5 m below base plate
3.0 m from the outer wall on the east side of the corridor	Pile No. K0+579.5~ K0+585	5.2m–9.5 m below base plate

in the weakening of the soil structure, strength is further reduced, the engineering properties of the soil body deteriorated, endangering the safety of the upper corridor. The hydraulic action triggered by pumping leads to the removal of soil particles from the upper part of the water-rich body, which gradually develops into a cavity and leads to the sinking of the pipe corridor. 2) In the direction of the vertical pipeline corridor axis, it can be seen from Figures 4B–E that the distribution range of the low resistance area is slightly expanded from west to east. As can be seen from Figures 4A, F, the farther away from the centerline of the corridor, the soil below the bottom plate of the corridor as a whole shows that the resistivity of the east side is significantly lower than that of the west side in the same depth range, indicating that the water content of the soil on the east side is significantly higher than that on the west side.

4.2 Analysis of the results of multi-channel transient surface wave method detection

Multi-channel transient surface wave exploration data processing and interpretation are processed by special software, after filtering and de-noising, multi-gun superposition, FK frequency spectrum analysis, frequency dispersion curve extraction, and obtaining V-H velocity depth curves to invert the stratigraphic wave velocity distribution. Figures 5A, B show the depth-velocity curves after data processing, and Figures 5C, D show two-dimensional contour plots of the stratigraphic wave velocity distribution after integrated inversion. Analyzing the change characteristics of the V-H velocity curve, it is found that the wave velocity of the soil layer in the range of 3.0 m below the bottom plate on the east side of the pipeline corridor decreases

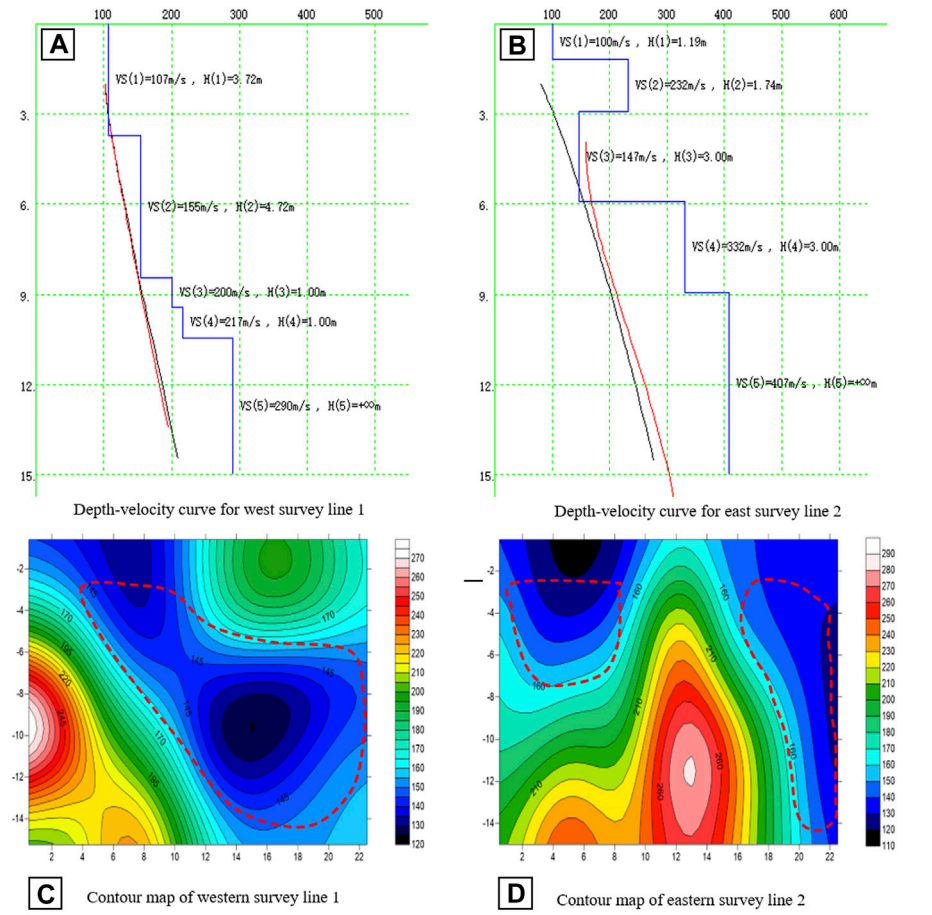

FIGURE 5
Depth-velocity curves *versus* two-dimensional contour plots of stratigraphic wave velocity distributions.

sharply, the shear wave velocity Vs. decreases from 232 m/s to 147 m/s, and the slope of the dispersion curve changes significantly, and the presence of sparsity is suspected in the range of this depth. The wave velocity value of the soil layer in the range of 5.5 m below the bottom plate of the pipeline corridor on the west side is 155 m/s, and the wave velocity value is obviously low, indicating that there is a suspected loose body.

The wave velocity contour map shows that there exists a low wave velocity zone with gradually increasing depth and width in the west side of the pipeline corridor at pile number K0+572~K0+590 (horizontal coordinates 4–22), and the depth range is from 0.0 m below the bottom plate to a maximum depth of 12.0 m (red dashed area in Figure 5C). There are two main low-wave velocity areas on the east side of the pipeline corridor (red dashed area in Figure 5D), one of which is pile number K0+568~K0+577 (horizontal coordinates 0–9), with a depth range of 0.0–5.0 m below the bottom plate of the pipeline corridor. The other one is pile number K0+584~ K0+590 (horizontal coordinates 16–22), and the depth range is 0.0–12.0 m below the bottom plate of the pipe corridor. These two low-wave velocity areas are suspected to be sparsely populated.

Based on the above analysis, it can be seen that the detection results of the multi-channel transient surface wave method also indicate that there is a high probability of the presence of water-rich and loose bodies in the lower portion of the pipeline corridor, which coincides with the results obtained by the high-density resistivity method. The multi-channel transient surface wave test results corroborate with the high-density resistivity method and further refine the extent and depth of the subsurface diseased body, improving the reliability of the detection information.

4.3 Analysis of results of standardized penetration testing

The results of the standard penetration method show that the standard penetration numbers of the holding layer pulverized soil layer in the range of 2.0 m at the bottom of the foundation of 1#, 2# and 4# verification holes are smaller than those of the corresponding soil layer of 3# comparison holes. The standard penetration number of the silt layer in the depth range of 3.5m–6.5 m below the base of 1#, 2# and 4# verification holes is less than the standard penetration number of the corresponding soil layer of 3# comparison holes. It can be seen that both the chalk and silt layers in the area of the suspected sparsity are more sparse

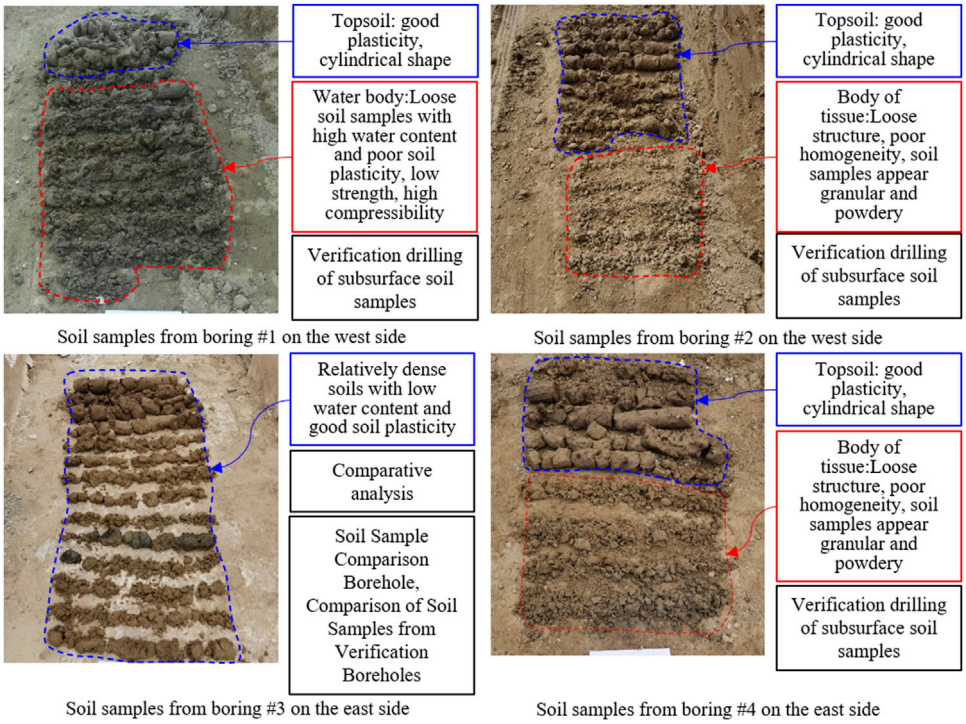

FIGURE 6
Photographs of soil samples from verification and comparison borings.

TABLE 2 Standardized penetration test number results.

Soil layer name	Standard depth of Penetration/m)	Number of hammer blows corrected for rod length/N′ (hit)			
		3# drilled hole/(Contrasting holes)	1# drilled hole	2# drilled hole	4# drilled hole
Sand	3.15–3.45	9.7	1.9	2.9	7.8
	4.65–4.95	11.0	2.8	8.3	2.8
Silty clay interlayer	5.15–5.45	—	—	—	2.7
Silt sand	6.15–6.45	13.5	12.5	13.5	—
	6.65–6.95	—	—	—	3.5
	7.65–7.95	15.0	11.3	12.9	—
	8.15–8.45	—	—	—	12.9
	9.15–9.45	16.0	12.6	13.4	—
	10.65–10.95	15.4	—	17.0	—
	12.15–12.45	15.8	—	15.0	—
	14.15–14.45	16.2	—	—	—

than the other areas where no anomalies were found. Figure 6A, B, D show sample soils from verification holes 1#, 2#, and 4#, respectively, and Figure 6C shows sample soils from comparison hole 3#. Based on the analysis of the soil samples taken from each of the boreholes in Figure 6, the samples from verification boreholes 1#, 2# and 4# have loose soil and high water content, while the sample from comparison borehole 3 has relatively dense soil and low water content. Figure 6 shows photographs of soil samples from the four borings at the site, and Table 2 shows the results of the standard penetration tests.

TABLE 3 Comparative analysis results.

Detection method	Line position/Drill position	Distribution range along the pipeline corridor alignment	Disease body depth distribution range
High-density resistivity method	1.0 m from the outer wall on the west side of the corridor	K0+579.5~ K0+585	0.0m–9.0 m below base plate
	3.0 m from the outer wall on the west side of the corridor	K0+580~ K0+586.5	3.5m–9.0 m below base plate
	1.0 m from the outer wall on the east side of the corridor	K0+578~ K0+586.5	3.5m–9.5 m below base plate
	3.0 m from the outer wall on the east side of the corridor	K0+579.5~ K0+585	5.2m–9.5 m below base plate
Multi-channel transient surface wave method	2.0 m from the outer wall on the west side of the corridor	K0+572~ K0+590	0.0m–12.0 m below base plate
	2.0 m from the outer wall on the east side of the pipe corridor	K0+568~ K0+577	0.0m–5.0 m below base plate
	2.0 m from the outer wall on the east side of the pipe corridor	K0+584~ K0+590	0.0m–12.0 m below base plate
Standard penetration probe	Drill hole #1	K0+587	0.0m–6.5 m below base plate
	Drill hole #2	K0+579	0.0m–6.5 m below base plate
	Drill hole #3	K0+580	0.0m–5.5 m below base plate

4.4 Comparative analysis

Table 3 shows the results of the comparative analysis of the two physical means and the standard penetration probing method. Comparing and analyzing the detection results of high-density resistivity method and transient surface wave method, there are suspected water-rich and loose bodies in the soil layer below the bottom plate of the section of pile number K0+572~K0+590 on the west side of the pipeline corridor. There are suspected water-rich and loose bodies in the soil layer below the bottom plate of the section of pile number K0+568~K0+590 on the east side of the pipeline corridor. The distribution of spars in the depth range of 1#, 2# and 4# verification holes is basically consistent with the inversion results of the two physical exploration methods. It can be determined that there are water-rich and loose bodies in the lower part of the corridor, and the strong rainfall makes the water content of the loose bodies increase, and the hydraulic effect triggered by pumping leads to the hollowing out of the loose bodies and the formation of cavities, which triggers the upper corridor to undergo inhomogeneous settlement.

5 Analysis and discussion of the chain of causes of pipeline corridor damage

5.1 Causal chain analysis

Based on the results of the above analysis, it is shown that there are two reasons for the cracking and damage of the pipe corridor. One reason is the defects of concrete elements caused by poor vibration and curing during concrete placement, which lay hidden dangers for subsequent cracking and damage of concrete structures. Another reason is the uneven settlement of the foundation of the pipe corridor. The overlying soil layer of the corridor is thin, and the possibility of structural deformation and cracking of the corridor due to the loading of the overlying soil layer is small, so this is not considered as one of the causes of cracking and damage of the corridor. Figure 7 shows the network diagram of the chain relationship between the causes of damage to the pipe corridor.

Uneven foundation settlement is the main driver of cracking and deformation of concrete structures. Due to the uneven force applied to the concrete structure as a result of the uneven settlement, stress concentration occurs at the variable cross section of the pipe corridor structure and at the concrete defects, and initial cracks start to breed in these places. With the further development of the uneven settlement of the foundation, the cracks on the concrete structure gradually expand and develop, cracks and holes in the concrete structure and pockmarked surface connected to each other through, and eventually formed through the cracks, the structure of the corridor subsequently cracking damage. It can be seen that the uneven settlement of the foundation of the corridor is the main driving factor leading to the deformation and damage of the corridor, which provides the driving force for the cracks on the structure of the corridor to sprout and expand. Defects on concrete members are promoters of deformation cracking, and under the action of uneven settlement, the defects on concrete members are activated, and cracks begin to gestate and sprout at the defects.

Uneven settlement of the foundation becomes the main driving factor for the cracking and deformation of the pipe corridor structure, and the factors leading to the uneven settlement of the foundation are the fundamental factors for the cracking and damage of the pipe corridor. By means of physical exploration to explore the reasons for the uneven settlement of the foundation of the pipe corridor, the results show that the pipe corridor pile number K0+568 ~ K0+590 section of the bottom plate below the depth range of 0.0 m–12.0 m, the foundation holding layer is suspected to exist in

FIGURE 7
Network diagram of chain relationship between causes of cracking and damage in pipe corridors.

the water-rich body, sparse body, at the same time in the pile number K0+564, K0 + 566, K0 + 559, the pipe corridor due to the uneven settlement of the foundation to produce serious damage. In order to further verify the reliability of the results of the physical exploration, three verification holes and one comparison hole were excavated within the uneven settlement range of the pipeline corridor, and the distribution of loose bodies within the depth range of the 1#, 2# and 4# verification holes exposed basically coincided with the results of the inversion of the two physical exploration methods. By analyzing the results of physical exploration and verification of soil extraction, it was found that the main reasons leading to the uneven settlement of the foundation are the following 3 points.

(1) Several spars and water-rich bodies exist in the depth range of 0–12.0 m below the base plate of the pipeline corridor in this section. Loose bodies are characterized by loose structure and poor homogeneity, and water-rich bodies are characterized by high water content, low strength and high compressibility. Heavy rainfall led to a sudden increase in the water content of the soil around the corridor, the strength of the loose body was significantly reduced by rainwater soaking, the water content of the water-rich body further increased, the strength of the further reduction of its compression at the same time increased. Due to the uneven distribution of loose and water-rich bodies below the subgrade of the corridor, this leads to an uneven settlement of the soil layer below the subgrade. This is the stratigraphic condition in which uneven settlement occurs in the pipeline corridor.
(2) The pumping of water after heavy rainfall caused a rapid decline in the water table, the effective stress of the foundation soil below the base plate of the corridor increased, soil compression occurred, and further contributed to the uneven settlement of the foundation, which is also an important causative factor for the aggravation of the uneven settlement of the foundation.
(3) The pumping operation also triggered localized hydraulic action, and such underground diseased bodies as loose bodies and water-rich bodies were weakened by localized hydraulic action, the soil structure was weakened, the strength was reduced, and the bearing capacity of foundations was decreased. The hydraulic action takes away the soil particles within the loose body and water-rich body, leading to the development of the loose body and water-rich body into a cavity and accelerating the rate of settlement.
(4) The cross-section area of the pipe corridor structure is changing, and under the effect of uneven settlement, the junction of the cross-section change will have a significant stress concentration phenomenon, which will lead to the cracking damage of the pipe corridor structure.

Combined with the analysis of the actual situation on the site, the first time after the rain pumping caused uneven settlement, K0 + 579 position deformation joints staggered, the corridor substrate soil extrusion, surging into the interior of the corridor. The second pumping location at K0+579 deformation seam caused the loss of powdered soil in the holding layer of the base of the pipe corridor, destroying the soil structure of the base and increasing the sinking of the pipe corridor at both ends of the deformation seam.

5.2 Discussion

This paper investigates the cracking and damage characteristics and uneven settlement factors of Qihe pipe corridor. The results of the study show that there are self-factors and external factors in the cracking damage of the pipe corridor, and the self-factors are the self

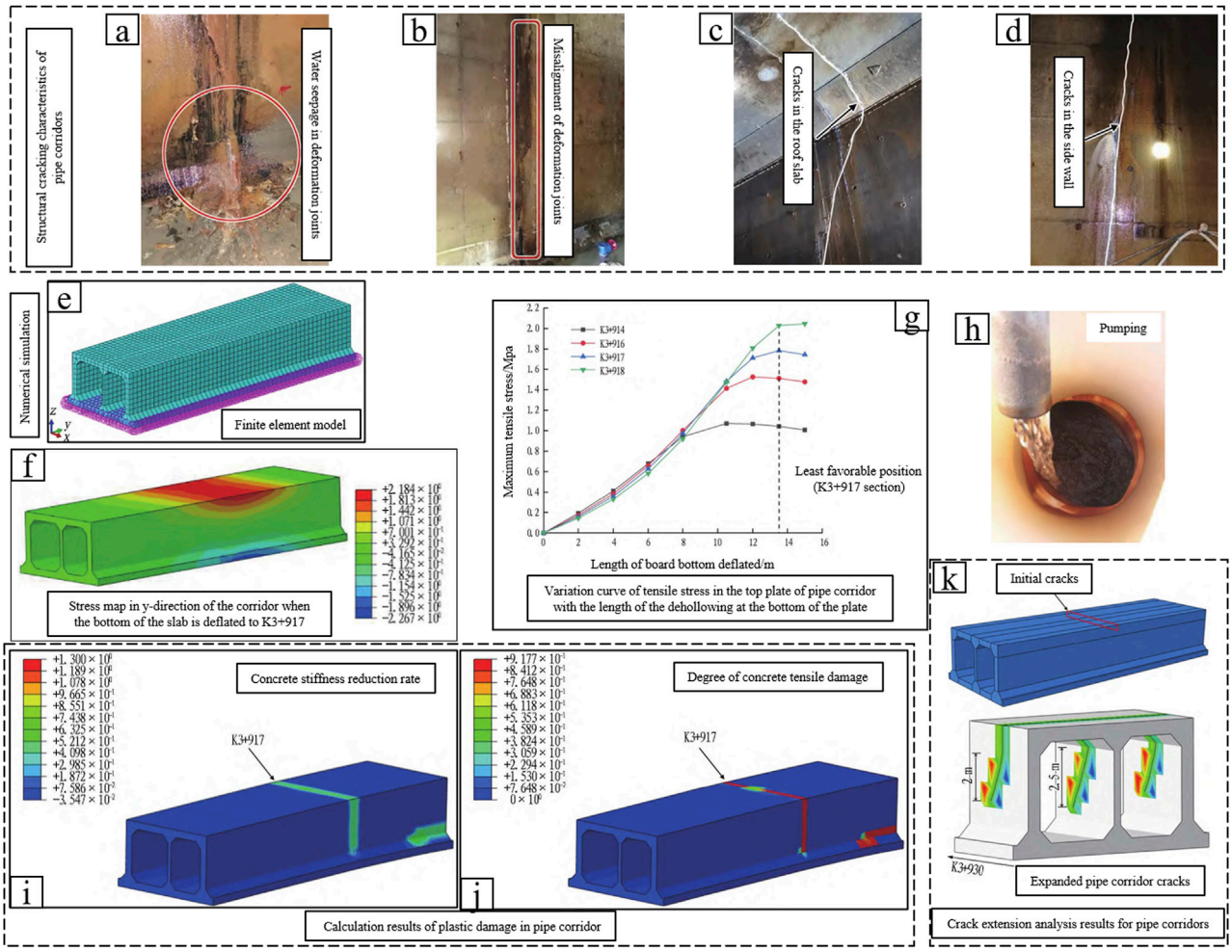

FIGURE 8
Uneven settlement cracking characteristics and Numerical Simulation Analysis of Comprehensive Pipe Corridor in Fuzhou Southeast Expressway (Zhao et al., 2021).

defects such as pockmarks, holes, exposed tendons and other defects caused by the lack of compactness of vibration and poor maintenance during the pouring of concrete. The external factor is the uneven settlement of the foundation of the pipe corridor. There are four reasons for the uneven settlement of the foundation of the pipe corridor: 1) the loose and water-rich bodies distributed in the foundation of the pipe corridor. 2) Heavy rainfall causes a sudden increase in the water content of water-rich and loose bodies in foundations, which reduces strength and increases compressibility. 3) Pumping causes the water table to fall, the effective stress on the foundation soil increases, and the soil is compressed, thus promoting increased uneven settlement. 4) Pumping causes localized hydraulic action, and soil particles in loose and water-rich bodies are carried away under hydraulic action, thus developing into cavities.

In the study of the uneven settlement factors of the foundation of the pipeline corridor, it was found that the localized hydraulic action caused by pumping carried away the soil particles in the loose and water-rich bodies, resulting in uneven settlement of the foundation. The main cause of cracking and damage in pipe corridors is the uneven settlement of the foundation. These two results coincide with the findings of Yang Zhao (Zhao et al., 2021). Yang Zhao analyzed the cracks triggered by the uneven settlement of the comprehensive pipeline corridor of Fuzhou Southeast Expressway and its causes, and used numerical simulation methods to analyze the plastic damage area and crack expansion process of the corridor (shown in Figure 8). Figures 8A, B show water seepage in the deformation joints and misalignment of the deformation joints, respectively, and Figures 8C, D show cracks in the top slab and cracks in the sidewalls; Figure 8E shows the finite element model of the corridor, Figure 8F shows the Y-direction stress cloud diagram of the corridor, Figure 8G shows the curve of variation of the tensile stress of the top slab of the corridor with the length of dehiscence at the bottom of the slab, and Figure 8H shows the on-site drainage from the precipitation wells; Figure 8I shows the rate of decrease in the stiffness of the concrete, Figure 8J shows the degree of tensile damage of the concrete, and Figure 8K shows the results of the analysis of crack extension in the corridor. It was found that the main cause of cracking in integrated pipe corridors is uneven settlement of foundations. The pumped water carries a large number of fine sand particles, and the soil on the outside of the pit is partially hollowed out, leading to uneven settlement and misalignment of the deformation joints in the later stage

of the pipe corridor. This is the root cause of cracking in large mileage sections of pipe corridors. Numerical simulation results show that tensile stresses will occur locally in the top slab of the pipe corridor in the event of dehiscence at the bottom of the slab. Near the K3+917 location in the middle of the corridor, the concrete in the top slab and side walls showed a decrease in stiffness and tensile damage zones, indicating that the concrete had cracked. The cracks in the pipe corridor will expand from the top plate to the side wall and center wall, and the crack expansion pattern is more consistent with the actual crack pattern in the field. The uneven settlement of the comprehensive pipeline corridor of Fuzhou Southeast Expressway studied by Yang Zhao is basically consistent with the object of this paper in terms of engineering geological conditions, cross-section shape of the pipeline corridor, pumping operation, and deformation mode of cracking, and the conclusions drawn are also in line with each other. Uneven settlement is the main cause of pipeline corridor cracking, pumping-induced hydraulic action to take away the fine sand particles in the foundation soil, resulting in hollowing out of the soil and dehollowing at the bottom of the slab. The research results obtained by Yang Zhao further support the conclusions of this paper, and his numerical simulation results are also consistent with the cracking of the Qihe pipe corridor, so that the numerical simulation results in Yang Zhao's paper can well reflect the plastic damage region and the crack extension process of the pipe corridor studied in this paper.

The object of the study is the cracking damage caused by uneven settlement of underground structures in soft ground. Physical exploration methods and standard penetration detection methods are used to reveal the causes of uneven settlement, and numerical simulation methods are used to analyze the cracking process of underground pipe corridors subjected to uneven settlement, and the results of the study provide guidance for the prevention and control of uneven settlement of underground structures. This paper investigates the effect of uneven settlement on the cracking damage of underground pipeline corridors in sandy chalky soil stratum, reveals the main reasons for triggering uneven settlement, and provides guidance for the repair and prevention of underground pipeline corridors. The results of the study are primarily for diseased bodies in foundations, and when foundations without diseased bodies are encountered, the results of this analysis will be unguided. Underground engineering geological conditions are complex and variable, the object studied in this paper is the cracking damage characteristics of underground pipeline corridors triggered by inhomogeneous settlement in soft ground, the research object is relatively single, unable to reflect the deformation characteristics of underground structures under various engineering geological conditions in a holistic and comprehensive manner. Subsequent studies should continue to characterize foundation settlement under different geological conditions and the deformation and damage characteristics of underground structures, so as to provide more comprehensive guiding information for the construction of underground structures and disaster prevention and control.

6 Conclusion

In this paper, the deformation and cracking caused by inhomogeneous settlement of Qihe tube corridor is studied, and the deformation characteristics of the corridor and the reasons for the occurrence of inhomogeneous settlement are analyzed, and the following conclusions are drawn.

(1) The concrete of the pipe corridor structure has exposed reinforcement, pockmarks and holes, and the subsequent deformation cracks start to develop and further expand from these defects and damages. Defects and damages on concrete elements are contributing factors for deformation and cracking of pipe corridors, and uneven settlement is the main initiating factor for deformation and cracking of pipe corridors. The research results are of guiding significance for the prevention and control of cracking damage in underground pipeline corridors.
(2) The detection of high-density resistivity method shows that along the length direction of the pipe corridor, the section of pile number K0+578~K0+586.5, there is an obvious low-resistance area below the bottom plate of the pipe corridor, with a resistivity value of ≤8.0Ω-m, which is suspected to be the distribution of water-rich and sparse bodies. The results of the multi-channel transient surface wave method of detection are in agreement with the high-density resistivity method.
(3) Through the standard penetration detection, it was found that the distribution of spars in the depth range of 1#, 2# and 4# verification holes was basically consistent with the inversion results of the two physical exploration methods.
(4) Stratigraphic factors that lead to uneven foundation settlement are water-rich and loose bodies in the lower part of the strata, and localized hydraulic effects, such as pumping, are catalysts for accelerating uneven foundation settlement.
(5) The research results reveal the triggering factors of uneven settlement of sandy chalky soil and the intrinsic and extrinsic causes of structural damage of underground pipeline corridors, and the results provide technical guidance for disaster prevention and control in similar projects.

Data availability statement

The original contributions presented in the study are included in the article/Supplementary material, further inquiries can be directed to the corresponding author.

Author contributions

YZ: Writing–original draft, Data curation. LD: Formal Analysis, Writing–original draft. YL: Conceptualization, Writing–original draft. MG: Funding acquisition, Writing–review and editing.

Funding

The author(s) declare that financial support was received for the research, authorship, and/or publication of this article. This work was supported in part by the Opening fund of State Key Laboratory of Geohazard Prevention and Geoenvironment Protection (Chengdu University of Technology) (No. SKLGP 2022K014), the Opening Foundation of Key Laboratory of Landslide Risk Early-

warning and Control, Ministry of Emergency Management (Chengdu University of Technology) (No. KLLREC 2022K003), the Opening Foundation of Key Laboratory of Geohazard Prevention of Hilly Mountains, Ministry of Natural Resources (Fujian Key Laboratory of Geohazard Prevention) (Grant No. FJKLGH 2022K005), and the Humanities and Social Sciences Research Project of Ministry of Education (No. 23YJCZH051).

Conflict of interest

Authors YZ, LD, and YL were employed by Shandong Construction Engineering Quality Inspection and Testing Center Co., Ltd.

The remaining authors declare that the research was conducted in the absence of any commercial or financial relationships that could be construed as a potential conflict of interest.

Publisher's note

All claims expressed in this article are solely those of the authors and do not necessarily represent those of their affiliated organizations, or those of the publisher, the editors and the reviewers. Any product that may be evaluated in this article, or claim that may be made by its manufacturer, is not guaranteed or endorsed by the publisher.

References

Al' Malul, R., and Michail, G. (2018). The reliability of multistory buildings with the effect of non-uniform settlements of foundation. *E3S Web Conf.* 33, 02040. doi:10.1051/e3sconf/20183302040

Bao, C., Xu, F. Z., Chen., G., Ma, X. T., and Lim, K. (2020). Seismic response analysis of frame structure with uneven settlement of foundation. *Phys. Chem. Earth(prepublish)* 120, 102928. doi:10.1016/j.pce.2020.102928

Bian, H., Zhang, X., and Shao, J. (2017). A coupled elastoplastic and visco-plastic damage model for hard clay and its application for the underground gallery excavation. *Undergr. Space* 1, 60–72. doi:10.1016/j.undsp.2017.03.002

Chen, W., and Hanna, A. (2023). Experimental investigation on structural response of multi-story buildings subjected to differential settlement of its foundations. *Int. J. Struct. Integr.* 14 (2), 204–228. doi:10.1108/IJSI-09-2022-0115

ChenChuanXin, D. L. R., Liu, R. X., and Li, D. K. (2011). Analysis of the effect of super-structure's stiffness on foundation's uneven settlement. *Adv. Mater. Res.* 374-377, 1690–1693. doi:10.4028/WWW.SCIENTIFIC.NET/AMR.374-377.1690

Cong, S., Tang, L., Ling, X., Geng, L., and Lu, J. (2021). Numerical analysis of liquefaction-induced differential settlement of shallow foundations on an island slope. *Soil Dyn. Earthq. Eng.* 140, 106453. doi:10.1016/j.soildyn.2020.106453

Deng, B., Pan, L., Xin, L., Jiang, T., and Zhi, B. (2022). Mechanical behavior of underground pipe gallery structure considering ground fissure. *J. Mt. Sci.* 19 (2), 547–562. doi:10.1007/S11629-021-6867-3

Feng, X., Li, H., Chen., B., and Zhou, J. (2020). Numerical investigations into the failure mode of buried prestressed concrete cylinder pipes under differential settlement. *Eng. Fail. Anal.* 111, 104492. doi:10.1016/j.engfailanal.2020.104492

Gebremedhn, Z., Qiao, G., and Li, J. (2019). The influence of differential settlement analysis for the single and multi-combined longitudinal precast box culvert. *J. Civ. Environ. Eng.* 2019, 2.

Guo, W., Song, M., Teng, L., Liao, X., Pei, N., and Chen, X. (2023). Stochastic differential equation modeling of time-series mining induced ground subsidence. *Front. Earth Sci.* 10, 1026895. doi:10.3389/FEART.2022.1026895

Ho, H. M., and Kuwano, J. (2021). Confined-reinforced earth with various geogrid lengths in reducing differential settlement. *Geosynth. Int.* 28, 560–573. doi:10.1680/JGEIN.21.00021

Hu, L., Xu, Q., and Liu, Y. (2021). Method for diagnosing the uneven settlement of a rail transit tunnel based on the spatial correlation of high-density strain measurement points. *Sustainability* 16, 9245. doi:10.3390/SU13169245

Jiang, J., Dong, B., Ding, Z., Gang, W., Zhang, H., and Liao, J. (2020). Dynamic analysis of metro train-monolithic bed track system under tunnel differential settlement. *Shock Vib.* 2020, 1–12. doi:10.1155/2020/5632180

Liang, X., Qiu, Z., Yang, L., Dong, Y., and Zhou, X. (2023). Rigid spliced box girder bridge under the action of foundation settlement difference analysis of mechanical behavior of splice section. *J. Phys. Conf. Ser.* 1, 12093. doi:10.1088/1742-6596/2468/1/012093

Liu, H., and Moore, A. (2021). The detection method for uneven settlement of foundation in the area of industrial waste miscellaneous filling. *Int. J. Environ. Technol. Manag.* 24 (3-4), 135. doi:10.1504/IJETM.2021.116805

Liu, P., Chen, J., Chen, Y., Yang, J., and Tang, Q. (2020). Mechanical model for joints of immersed tunnel considering the influence of joint differential settlement. *Int. J. Geosynth. Ground Eng.* 6 (4), 57. doi:10.1007/s40891-020-00241-y

Ngugi Hannah, N., Shitote Stanley, M., and Ambassah Nathaniel., (2021). Effect of variation in moisture content on soil deformation and differential settlement of frame structures in nairobi area and its environs. *Open Constr. Build. Technol. J.* 15, 106–128. doi:10.2174/1874836802115010106

Shen, Q., Lu, Y., Yang, Y., and Guanxu, L. (2021). Research on mechanical response of pavement structure to differential settlement of subgrade on highway widening. *Adv. Mater. Sci. Eng.* 2021, 1–11. doi:10.1155/2021/4445185

Shi, L., He, J., Huang, Z., Sun, H., and Yuan, Z. (2022). Numerical investigations on influences of tunnel differential settlement on saturated poroelastic ground vibrations and lining forces induced by metro train. *Soil Dyn. Earthq. Eng.* 156, 107202. doi:10.1016/J.SOILDYN.2022.107202

Wang, B., Liu, Z., and Yuan, S. (2022). Behavior of large shaft sinking headframe subjected to uneven foundation settlement. *Front. Earth Sci.* 10, 941126. doi:10.3389/FEART.2022.941126

Wang, T., Bui, P., Luo, Q., Liu, K., and Zhang, L. (2023). Three-dimensional physical modeling of load transfer in basal reinforced embankments under differential settlement. *Geotext. Geomembranes* 51 (2), 330–341. doi:10.1016/J.GEOTEXMEM.2022.12.001

Wu, H., Zhai, K., Fang, H., Wang, F., Xiang, Y., and Li, B. (2022). Bell-and-spigot joints mechanical properties study of PCCP under the uneven settlement of foundation: simulation and full-scale test. *Structures* 43, 1692–1703. doi:10.1016/J.ISTRUC.2022.07.060

Xie, J., Huang, N., Feng, J., and Zhang, G. (2020). Study on deformation of shallow buried underground pipe gallery. *IOP Conf. Ser. Mater. Sci. Eng.* 741, 012058. doi:10.1088/1757-899x/741/1/012058

Xu, F., Bao, C., Ma, X., Zhang, Y., Kar, S. L., Zhang, Y., et al. (2022). Shaking table test on seismic response of a planar irregular structure with differential settlements of foundation. *Structures* 46, 988–999. doi:10.1016/J.ISTRUC.2022.10.090

Xu, Z., Xu, W., Zhu, Z., and Zhao, J. (2023). Research on monitoring and stability evaluation of ground subsidence in gypsum mine goaf. *Front. Environ. Sci.* 10, 1097874. doi:10.3389/FENVS.2022.1097874

Zhang, J., Zhao, M., and Chang, S. (2021). Early warning limits for uneven settlement of metro tunnels based on vehicle–track interaction simulations. *J. Civ. Struct. Health Monit.* 11 (2), 507–520. doi:10.1007/S13349-020-00465-6

Zhang, K., Zhang, X., and Zhou, S. (2023). Analysis on dynamic behavior of 400 km/h high-speed train system under differential settlement of subgrade. *Eng. Struct.* 278, 115521. doi:10.1016/J.ENGSTRUCT.2022.115521

Zhao, B. (2022). *Study on the influence of uneven settlement andrainfallinfiltration of loess filling foundation onpile-raftfoundation*. Chang'an University.

Zhao, Y., Li, Y., and Yang, R. (2021). Analysis on cracks of cast-in-place utility tunnel induced by uneven settlement: a case study of utility tunnel of Fuzhou Southeast freeway. *Tunn. Constr.* 41 (12), 2098.

Zhou, L. (2022). Research on differential settlement monitoring of highway expansion based on BIM technology. *Int. J. Crit. Infrastructures* 18 (4), 1. doi:10.1504/IJCIS.2022.10038008

frontiers | Frontiers in Environmental Science

TYPE Brief Research Report
PUBLISHED 05 February 2024
DOI 10.3389/fenvs.2024.1343903

OPEN ACCESS

EDITED BY
Lei Xia,
KU Leuven, Belgium

REVIEWED BY
Jin Wu,
Beijing University of Technology, China
Hongji Wang,
Southwestern University of Finance and Economics, China
Liting Hao,
Beijing University of Civil Engineering and Architecture, China

*CORRESPONDENCE
Zhongyuan Xu,
zyxu@swjtu.edu.cn

RECEIVED 24 November 2023
ACCEPTED 19 January 2024
PUBLISHED 05 February 2024

CITATION
Xu X, Zhu M, Zhou L, Ma M, Heng J, Lu L, Qu W and Xu Z (2024), The impact of slope and rainfall on the contaminant transport from mountainous groundwater to the lowland surface water.
Front. Environ. Sci. 12:1343903.
doi: 10.3389/fenvs.2024.1343903

The impact of slope and rainfall on the contaminant transport from mountainous groundwater to the lowland surface water

Xiaojun Xu[1], Ming Zhu[1], Ling Zhou[1], Mingxia Ma[1], Jingmei Heng[1], Li Lu[1], Weiyi Qu[1] and Zhongyuan Xu[2]*

[1]Sichuan Communication Surveying and Design Institute Co., Ltd., Chengdu, China, [2]Faculty of Geosciences and Environmental Engineering, Southwest Jiaotong University, Chengdu, China

The surface water and groundwater in the mountainous area are vulnerable to contamination from the mining and transportation construction in Sichuan Province, China. Pollutants produced by anthropogenic activities transport within the groundwater from mountains to rivers on the plain, transferring contamination to the surface water. This study investigates the process of groundwater flow and contaminant transport from mountains to the lowlands based on synthetic numerical models. Two key factors are considered: precipitation and the slope of the mountain. Based on the real situation in Sichuan Province, four rainfall recharge rates are defined as 600, 800, 1,000, and 1,200 mm/yr, and five slope angles are considered: 20°, 25°, 30°, 35°, and 40°. The simulation results reveal that the groundwater level and solute transport are strongly influenced by the precipitation amounts and slope angles. The mountains with lower slopes maintain a relatively higher groundwater level under steady-state rainfall conditions; for example, groundwater levels decrease from 340 m to 300 m as slope angles increase at a 1,200 mm/yr precipitation level. Contaminant transport from the source in the mountain to the surface river is faster with increasing precipitations and decreasing slope angles. The model with 20° slope angle and 1,200 mm/yr precipitation exhibits the fastest solute migration, with the contaminant arrival time of 65 years. Furthermore, the models with 35° and 40° slope angles at a 600 mm/yr precipitation level show the slow transport speed with the contaminant arrival time of more than 75 years. In addition, higher precipitation may lead to more contaminant transport to the river. The analysis and findings of this study offer valuable insights into groundwater protection at the boundaries of mountains and plains.

KEYWORDS

mountain–plain area, groundwater contamination, river pollution, solute transport, MODFLOW simulation

1 Introduction

The water resource is the valuable natural resource for human survival in the world. Surface water and groundwater are the primary constitutions of water resources on earth. Due to intensive anthropogenic activities including industrial, construction, agricultural, and sewage processes, the quality of surface water and groundwater is deteriorated

(Paladino et al., 2018; Su et al., 2018). Accordingly, the quality of surface water and groundwater has been the focus of attention for water resource management (Li, 2020; Nasim et al., 2020).

So far, the hydrochemical monitoring of surface water and groundwater has been carried out for improving groundwater management in the world (Yin et al., 2021). Plenty of hydrochemical data provide a robust support for water quality evaluation in the spatial and temporal scale. Various water quality indices (e.g., the WQI and EWQI) have been used to evaluate the quality of surface water and groundwater (Amiri et al., 2014; Lapworth et al., 2017; Zhai et al., 2017). Hence, the spatial and temporal characteristics of the quality of surface water and groundwater have been clarified properly. However, the interaction between surface water and groundwater affecting water quality has remained unclear, failing to explain the dynamic evolution in the spatial and temporal scale.

The interaction between surface water and groundwater can be analyzed using the approaches of hydrochemistry, isotopy, and numerical simulation (Raiber et al., 2019; Marti et al., 2023; Wang et al., 2023). Hydrochemistry and D-O stable isotopes were used to reveal the hydrological relationship between surface water and groundwater in the Notwane River Catchment, Southeast Botswana (Modie et al., 2022). Multiple isotopic tracers (δD-H_2O, $\delta^{18}O$–H_2O, $\delta^{15}N$–NO_3^-, and $\delta^{18}O$–NO_3^-) indicated that shallow groundwater is contaminated with organic fertilizers and subsequently transferred to surface water (Le et al., 2023). The SWAT + gwflow model was constructed to investigate the long-term groundwater–surface water interactions in the Scheldt Basin (Liberoff and Poca, 2023).

Substantial amounts of population are living in basin areas in the world due to the advantages of warm climate and gentle terrain. The Sichuan Basin in southwestern China is the typically large-scale basin within more than 100 million people. The quality of surface water and groundwater has been investigated for decades. However, previous studies mostly focused on the hydrochemical and isotopic information of surface water and groundwater in the basin area (Zhang et al., 2020; Zhang et al., 2021a; Zhang et al., 2021b). Seldom studies investigate the dynamic interaction and transport processes between surface water and groundwater at the boundaries of plains and mountains. It is known that the contamination would be transferred between surface water and groundwater (Xu et al., 2022). Among those pollutions, the contamination produced by the mining projects and tunnel constructions in the mountainous area is a serious environmental problem (Tomiyama and Igarashi, 2022). The water system is interrupted by excavation, and the unpredicted groundwater flow may pollute the fresh groundwater in mining sites and surface water system in the plain (Wu et al., 2018), especially the transport of heavy metal in the wastewater (Santana et al., 2020). The recent investigation pointed out that mountainous water system in Sichuan Province is heavily contaminated by the regional mining and tunneling industry (Sun et al., 2023). Hence, a hydrological model of large-scale catchment from the basin margin to basin center is built in this study. Afterward, the dynamic interaction between surface water and groundwater is simulated under different conditions of climate precipitation and terrain slope. Finally, the contamination in surface water and groundwater can be evaluated under different conditions. The achievements of this study would significantly contribute to evaluating the quality of surface water and groundwater in the catchment of the Sichuan Basin.

2 Methods

To investigate the issue of groundwater contamination from mountains to lowland rivers, a 2D numerical model is constructed in this study. The groundwater flow is steady-state since our model is synthetic to represent the general situation. Flow is simulated using MODFLOW (Harbaugh, 2005) with the Darcy equation (Eq. 1), and the solute transport is simulated in MT3DMS (Zheng and Wang, 1999) to depict advection and dispersion (Eq. 2).

$$\frac{\partial}{\partial x}\left[K\frac{\partial H}{\partial x}\right]+\frac{\partial}{\partial z}\left[K\frac{\partial H}{\partial z}\right]+w=0, \tag{1}$$

where K is the value of hydraulic conductivity [LT^{-1}]; H is the hydraulic head [L]; and w is the volumetric flux per unit volume representing sources and/or sinks of water [T^{-1}].

$$\frac{\partial}{\partial x_i}\left(\theta D_{ij}\frac{\partial C}{\partial x_j}\right)-\frac{\partial}{\partial x_i}\left(\theta v_i C\right)+q_s C_s=\frac{\partial(\theta C)}{\partial t}, \tag{2}$$

where θ is the porosity of porous media [dimensionless]; v_i is the seepage velocity [LT^{-1}]; C is the solute concentration [dimensionless]; C_s is the solute concentration of water entering from sources or flowing out from sinks [dimensionless]; D_{ij} is the hydrodynamic dispersion coefficient tensor [L^2T^{-1}]; and q_s is the volumetric flow rate per unit volume of aquifer representing the fluid source (positive) and sink (negative) [T^{-1}].

2.1 Model setup and boundary conditions

The framework of this synthetic model is based on the general conditions of mountainous area around the Chengdu Plain in Sichuan Province, China. The total length of the model is 1,700 m, with the left side representing the mountainous area at a height of 500 m and the right side representing the plain area with dimensions of 200 m in length and 150 m in height (Figure 1A). The entire domain is discretized into numerous cells, with each cell measuring 10 m × 10 m in size.

The model was defined as an unconfined aquifer, with the left and right boundaries designated as no-flow boundaries, representing the water divide between the mountain and the river, respectively. The bottom also serves as a no-flow boundary, indicating the presence of impermeable rock beneath the model. The top is an active boundary, receiving the rainfall recharge at rates of 600, 800, 1,000, and 1,200 mm/year with an infiltration rate of 0.4. These settings are based on the precipitation data around the Chengdu Plain (Liu and Xu, 2016).

Furthermore, based on the slope inclination around Chengdu, we consider five slope angles at the interaction of mountainous area and lowlands, ranging from 20° to 40° (Figure 1B). Different slope angles may change the water infiltration rate since steep slopes bring more water flow on the surface. Although this is not considered in this synthetic study, we hope to investigate the effect of slopes on the groundwater flow. Additionally, we assume the lithology of the model as porous media, setting the hydraulic conductivity and porosity at 0.1 m/

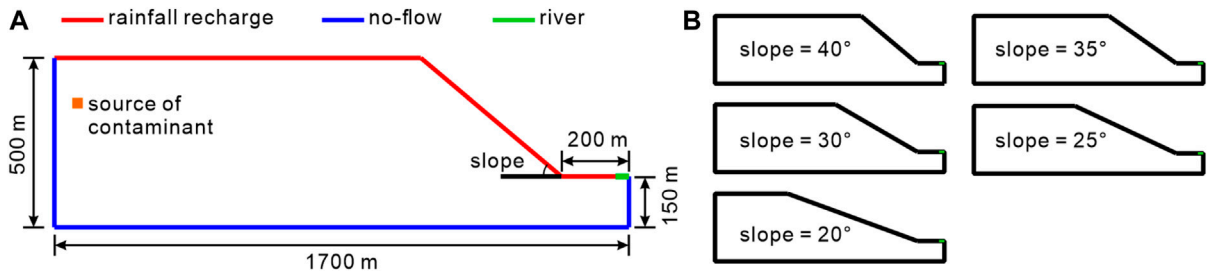

FIGURE 1
Model setup: **(A)** model domain and boundary conditions; **(B)** models with different slope angles.

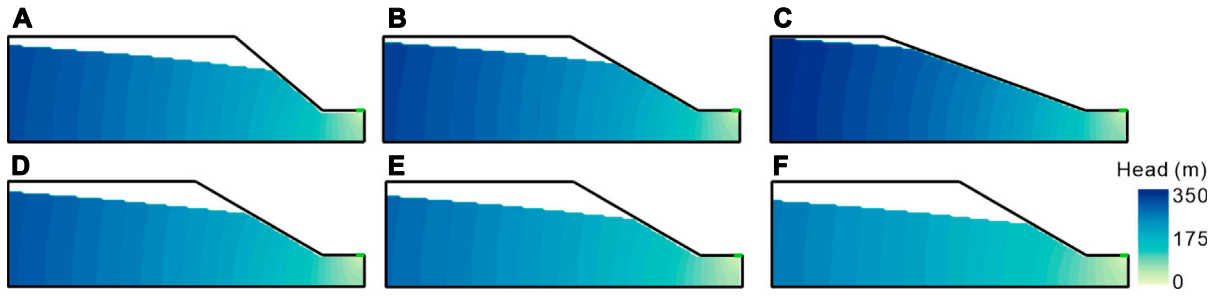

FIGURE 2
Examples of head distribution with different slope angles and precipitation levels: **(A)** slope angle is 40° and precipitation is 1200 mm/yr; **(B)** slope angle is 30° and precipitation is 1200 mm/yr; **(C)** slope angle is 20° and precipitation is 1200 mm/yr; **(D)** slope angle is 30° and precipitation is 1000 mm/yr; **(E)** slope angle is 30° and precipitation is 800 mm/yr; **(F)** slope angle is 30° and precipitation is 600 mm/yr. For the head distribution of all models, see Supplementary Figure S1.

d and 0.2, respectively. Dispersity in porous media is set at 10 m, with a horizontal transverse ratio of 0.1 and a vertical transverse ratio of 0.01. A contaminant source is defined near the left boundary at the concentration of 1.0 (dimensionless), representing contamination produced by anthropogenic activities in the mountain area.

2.2 Solute transport assessment

To assess river contamination, we use two evaluation metrics to delineate solute transport from the mountainous area to the river: contaminant arrival time and the total mass of contamination over a 20-year period. Contaminant arrival time denotes the moment when the contaminant (concentration ≥0.01) first reaches the river from the beginning of the simulation, providing a measure of the solute transport speed from the mountainous region to the river. The total mass of contamination over a 20-year period represents the cumulative mass of solute flowing into the river in the 2 decades following the contaminant arrival time. For each scenario involving varying precipitation and slope angles, both metrics are derived from simulation results to quantify the vulnerability of the river to mountainous contamination.

3 Results and discussion

This study aims to investigate the effect of slope and precipitation on the transport of contaminants from the mountainous area to lowland river. Figure 3 illustrates examples of simulation results for steady-state groundwater levels. At a precipitation level of 1200 mm/yr, the highest groundwater head level is approximately 300 m for the 40° slope angle, 320 m for the 30° slope angle, and 340 m for the 20° slope angle (Figures 2A–C). It indicates that the groundwater head level increases with a steeper slope angle. On the other hand, the precipitation also controls the groundwater level, in which the groundwater head increases with precipitation from 600 mm/yr to 1,000 mm/yr (Figures 2D–F). Hence, it can be inferred that groundwater head levels possessed a positive relationship with precipitation while a negative relationship with the slope angle.

The process of solute transport was simulated from the mountainous area to the river based on the steady-state flow field (Figure 3). Figure 4 presents the arrival time and total contaminant mass to the river for each simulation case. The arrival time analysis reveals that pollutants take approximately 70 years to reach the river. Specifically, the case of 20° slope angle at a 1,200 mm/yr rainfall recharge rate exhibits the earliest arrival time at ~65 years. In contrast, the case of 35° and 40° slope angles at a 600 mm/yr rainfall recharge rate show the slowest solute transport with the arrival time at ~75 years. Arrival time decreases with increasing precipitation, indicating that higher rainfall recharge rates promote the speed of solute transport. Furthermore, it increases with slope angles, highlighting that the gentler slopes are more conducive to contaminant transport. On the other hand, the total mass of pollutants discharged into the river is greatly influenced by the

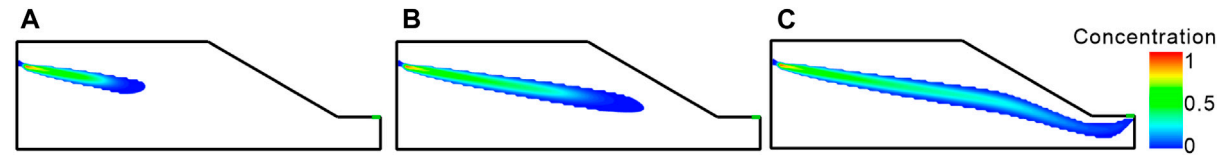

FIGURE 3
Example of solute transport with time (slope angle is 30° and precipitation is 1000 mm/yr): **(A)** 25 years; **(B)** 50 years; **(C)** 75 years. Other plots of contaminant transport are shown in Supplementary Figures S2–6.

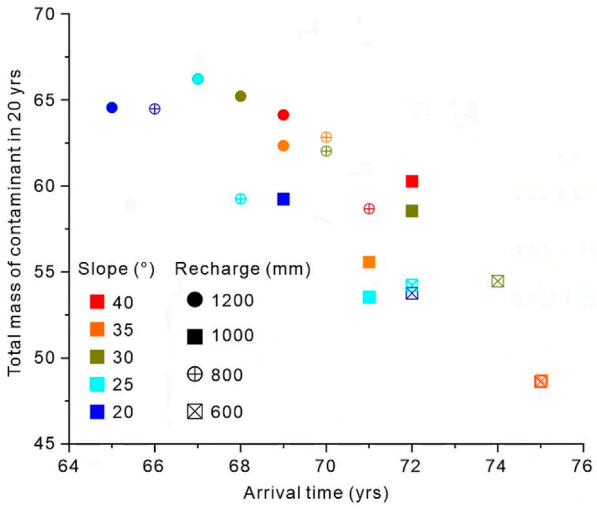

FIGURE 4
Total mass of contaminants in 20 years and arrival time of each case.

precipitation. The mass of contaminants discharged into the river increases from 45 to 67 with the increasing rainfall recharge rate over a 20-year period. However, the relationship between total mass and slope angle is less apparent, suggesting that slope angles have a limited impact on the mass of contaminants transported into the river.

The findings of this study indicate the importance of evaluating contaminant transport between the mountainous area and basin plain, suggesting that a comprehensive analysis with multiple factors are needed in studying the contamination interaction between groundwater and surface water. In addition, the protection of groundwater resources in the mining sites and tunnels should be stressed as the contaminants possibly transport with groundwater from mountains to the surface water in the basin. Engineers should pay more attention to the groundwater flow system and water–rock interaction around the mining sites and tunnels, as well as techniques of water drainage and pollutant deposition in the underground engineering.

4 Conclusion

This study conducts simulations to analyze contaminant transport from the mountainous area to the lowland river. The investigation considers multiple cases with varying precipitation and slope angles along the gradient from the mountain to the plain, with a focus on calculating the total mass and arrival time of contamination. The simulation results reveal that both groundwater level and solute transport are influenced by precipitation and slope angles. The main findings are listed below:

(1) The general groundwater head demonstrates an increase with higher precipitation and a decrease with steeper slope angles, ranging from 300–340 m.
(2) The arrival time of contaminants from the mountain to the river exhibits a decrease with higher precipitation and an increase with steeper slope angles, with the minimum arrival time of approximately 65 years and the maximum arrival time of more than 75 years.
(3) The total mass of contaminants discharging into the river in 20 years shows an increase with precipitation. Although the trend is less clear with slope angles, slope angles have an unclear impact on the mass of contaminants transported into the river.

Data availability statement

The original contributions presented in the study are included in the article/Supplementary Material; further inquiries can be directed to the corresponding author.

Author contributions

XX: investigation, methodology, and writing–original draft. MZ: funding acquisition, project administration, validation, and writing–original draft. LZ: data curation, formal analysis, investigation, and writing–original draft. MM: methodology, software, and writing–original draft. JH: investigation, methodology, and writing–original draft. LL: formal analysis and writing–original draft. WQ: software and writing–original draft. ZX: conceptualization, validation, and writing–review and editing.

Funding

The author(s) declare that financial support was received for the research, authorship, and/or publication of this article. This work

was supported by the National Natural Science Foundation of China (No. 42207074), Natural Science Foundation of Sichuan Province (No. 2023NSFSC0788), and Sichuan Transportation Science and Technology Program (2023-B-15).

Conflict of interest

Authors XX, MZ, LZ, MM, JH, LL, and WQ were employed by Sichuan Communication Surveying and Design Institute Co., Ltd.

The remaining author declares that the research was conducted in the absence of any commercial or financial relationships that could be construed as a potential conflict of interest.

Publisher's note

Supplementary material

The Supplementary Material for this article can be found online at: https://www.frontiersin.org/articles/10.3389/fenvs.2024.1343903/full#supplementary-material

References

Harbaugh, A. W. (2005). *MODFLOW-2005, the US Geological Survey modular ground-water model: the ground-water flow process*. US Geological Survey Scientific Investigations Report, 253.

Lapworth, D. J., Krishan, G., MacDonald, A. M., and Rao, M. S. (2017). Groundwater quality in the alluvial aquifer system of northwest India: new evidence of the extent of anthropogenic and geogenic contamination. *Sci. Total Environ.* 599-600, 1433–1444. doi:10.1016/j.scitotenv.2017.04.223

Le, F., Li, R., Ruan, X., and Liu, C. (2023). Isotopic tracing of nitrogen source and interaction between surface water and groundwater of a small valley plain in the Zhangxi watershed. *Appl. Geochem.* 151, 105615. doi:10.1016/j.apgeochem.2023.105615

Li, P. (2020). To make the water safer. *Expo. Health* 12, 337–342. doi:10.1007/s12403-020-00370-9

Liberoff, A. L., and Poca, M. (2023). Groundwater-surface water interactions in a semi-arid irrigated agricultural valley: a hydrometric and tracer-aided approach. *Sci. Total Environ.* 903, 166625. doi:10.1016/j.scitotenv.2023.166625

Liu, L., and Xu, Z. (2016). Regionalization of precipitation and the spatiotemporal distribution of extreme precipitation in southwestern China. *Nat. Hazards* 80, 1195–1211. doi:10.1007/s11069-015-2018-x

Marti, E., Leray, S., Villela, D., Maringue, J., Yáñez, G., Salazar, E., et al. (2023). Unravelling geological controls on groundwater flow and surface water-groundwater interaction in mountain systems: a multi-disciplinary approach. *J. Hydrology* 623, 129786. doi:10.1016/j.jhydrol.2023.129786

Modie, L. T., Kenabatho, P. K., Stephens, M., and Mosekiemang, T. (2022). Investigating groundwater and surface water interactions using stable isotopes and hydrochemistry in the Notwane River Catchment, South East Botswana. *J. Hydrology Regional Stud.* 40, 101014. doi:10.1016/j.ejrh.2022.101014

Nasim, S., Helfand, S., and Dinar, A. (2020). Groundwater management under heterogeneous land tenure arrangements. *Resour. Energy Econ.* 62, 101203. doi:10.1016/j.reseneeco.2020.101203

Paladino, O., Seyedsalehi, M., and Massabò, M. (2018). Probabilistic risk assessment of nitrate groundwater contamination from greenhouses in Albenga plain (Liguria, Italy) using lysimeters. *Sci. Total Environ.* 634, 427–438. doi:10.1016/j.scitotenv.2018.03.320

Raiber, M., Lewis, S., Cendón, D. I., Cui, T., Cox, M. E., Gilfedder, M., et al. (2019). Significance of the connection between bedrock, alluvium and streams: a spatial and temporal hydrogeological and hydrogeochemical assessment from Queensland, Australia. *J. Hydrology* 569, 666–684. doi:10.1016/j.jhydrol.2018.12.020

Santana, C. S., Olivares, D. M. M., Silva, V. H. C., Luzardo, F. H. M., Velasco, F. G., and de Jesus, R. M. (2020). Assessment of water resources pollution associated with mining activity in a semi-arid region. *J. Environ. Manag.* 273, 111148. doi:10.1016/j.jenvman.2020.111148

Su, H., Kang, W., Xu, Y., and Wang, J. (2018). Assessing groundwater quality and health risks of nitrogen pollution in the shenfu mining area of shaanxi Province, northwest China. *Expo. Health* 10, 77–97. doi:10.1007/s12403-017-0247-9

Sun, H., Hu, X., Yang, X., Wang, H., and Cheng, J. (2023). Estimating water pollution and economic cost embodied in the mining industry: an interprovincial analysis in China. *Resour. Policy* 86 (B), 104284. doi:10.1016/j.resourpol.2023.104284

Tomiyama, S., and Igarashi, T. (2022). The potential threat of mine drainage to groundwater resources. *Curr. Opin. Environ. Sci. Health* 27, 100347. doi:10.1016/j.coesh.2022.100347

Wang, W., Chen, Y., Wang, W., Zhu, C., Chen, Y., Liu, X., et al. (2023). Water quality and interaction between groundwater and surface water impacted by agricultural activities in an oasis-desert region. *J. Hydrology* 617, 128937. doi:10.1016/j.jhydrol.2022.128937

Wu, Q., Dong, S., Li, B., and Zhou, W. (2018). "Mine water inrush," in *Encyclopedia of sustainability science and technology*. Editor R. A. Meyers (New York: Springer).

Xu, Z., Hariharan, J., Passalacqua, P., Steel, E., Chadwick, A., Paola, C., et al. (2022). Effects of geologic setting on contaminant transport in deltaic aquifers. *Water Resour. Res.* 58, e2022WR031943. doi:10.1029/2022wr031943

Yin, Z., Luo, Q., Wu, J., Xu, S., and Wu, J. (2021). Identification of the long-term variations of groundwater and their governing factors based on hydrochemical and isotopic data in a river basin. *J. Hydrology* 592, 125604. doi:10.1016/j.jhydrol.2020.125604

Zhai, Y., Zhao, X., Teng, Y., Li, X., Zhang, J., Wu, J., et al. (2017). Groundwater nitrate pollution and human health risk assessment by using HHRA model in an agricultural area, NE China. *Ecotoxicol. Environ. Saf.* 137, 130–142. doi:10.1016/j.ecoenv.2016.11.010

Zhang, H., Xu, Y., Cheng, S., Li, Q., and Yu, H. (2020). Application of the dual-isotope approach and Bayesian isotope mixing model to identify nitrate in groundwater of a multiple land-use area in Chengdu Plain, China. *Sci. Total Environ.* 717, 137134. doi:10.1016/j.scitotenv.2020.137134

Zhang, Y., Dai, Y., Wang, Y., Huang, X., Xiao, Y., and Pei, Q. (2021a). Hydrochemistry, quality and potential health risk appraisal of nitrate enriched groundwater in the Nanchong area, southwestern China. *Sci. Total Environ.* 784, 147186. doi:10.1016/j.scitotenv.2021.147186

Zhang, Y., He, Z., Tian, H., Huang, X., Zhang, Z., Liu, Y., et al. (2021b). Hydrochemistry appraisal, quality assessment and health risk evaluation of shallow groundwater in the Mianyang area of Sichuan Basin, southwestern China. *Environ. Earth Sci.* 80, 576. doi:10.1007/s12665-021-09894-y

Zheng, C., and Wang, P. P. (1999). *MT3DMS: a modular three-dimensional multispecies transport model for simulation of advection, dispersion, and chemical reactions of contaminants in groundwater systems; documentation and user's guide, DTIC Document*.

frontiers | Frontiers in Environmental Science

TYPE Brief Research Report
PUBLISHED 20 February 2024
DOI 10.3389/fenvs.2024.1298327

OPEN ACCESS

EDITED BY
Yihuai Zhang,
University of Glasgow, United Kingdom

REVIEWED BY
Jakub Nalepa,
Silesian University of Technology, Poland
Sartajvir Singh,
Chandigarh University, India
Mohammed Oludare Idrees,
University of Abuja, Nigeria

*CORRESPONDENCE
Wen Zhang,
3463287@qq.com

RECEIVED 21 September 2023
ACCEPTED 29 January 2024
PUBLISHED 20 February 2024

CITATION
Xia W, Zhang W and Wu S (2024), Classification algorithm for land use in the giant panda habitat of Jiajinshan based on spatial case-based reasoning.
Front. Environ. Sci. 12:1298327.
doi: 10.3389/fenvs.2024.1298327

Classification algorithm for land use in the giant panda habitat of Jiajinshan based on spatial case-based reasoning

Wanlu Xia[1], Wen Zhang[2,3]* and Sen Wu[4]

[1]School of Ecology and Nature Conservation, Beijing Forestry University, Beijing, China, [2]Institute of Exploration Technology, Chinese Academy of Geological Sciences, Chengdu, China, [3]Technology Innovation Center for Risk Prevention and Mitigation of Geohazard, Ministry of Natural Resources, Chengdu, China, [4]Sichuan Institute of Geological Engineering Investigation Group Co. Ltd, Chengdu, China

Jiajin Mountain, where the giant pandas reside, is an essential nature reserve in China. To comprehend the land use classification of the habitat, this article proposes a remote sensing interpretation algorithm based on spatial case reasoning, known as spatial case-based reasoning (SCBR). The algorithm incorporates specific spatial factors into its framework and does not require an extensive amount of domain knowledge and eliminates the need for a complex model training process, making it capable of completing land use classification in the study area. SCBR comprises a spatial case expression model and a spatial case similarity reasoning model. The paper conducted comparative experiments between the proposed algorithm and support vector machine (SVM), U-Net, vision transformer (ViT), and Trans-Unet, and the results demonstrate that spatial case-based reasoning produces superior classification outcomes. The land use classification experiment based on spatial case-based reasoning at the Jiajinshan giant panda habitat produced satisfactory experimental results. In the comparative experiments, the overall accuracy of SCBR classification reached 95%, and the Kappa coefficient reached 90%. The paper further analyzed the changes in land use classification from 2018 to 2022, and the average accuracy consistently exceeds 80%. We discovered that the ecological environment in the region where the giant pandas reside has experienced significant improvement, particularly in forest protection and restoration. This study provides a theoretical basis for the ecological environment protection of the area.

KEYWORDS

remote sensing image segmentation, land use, case-based reasoning, spatial features, machine learning, Jiajinshan giant panda habitat

1 Introduction

As one of China's nature reserves, the Jiajinshan Giant Panda Reserve is an important part of China's giant panda habitat network. It is also a World Heritage Site, a national-level nature reserve, a national key scenic area, and a key biodiversity area. The Chinese government attaches great importance to the conservation of ecological resources in the Jiajinshan giant panda habitat. It has already implemented a series of policies, such as establishing national-level nature reserves; strengthening, monitoring, and management of

the habitat; and controlling environmental damages caused by human activities. Land use classification refers to the classification, division, and statistics of land within a certain area to understand the types, distribution, and area of land use in that region, which provides important information about land use types, distribution, and area. It also provides basic data support for rational land resource utilization, environmental protection, and sustainable development. It has important scientific and practical value (Xu et al., 2022; Zhang et al., 2022). Therefore, conducting land use classification for the Jiajinshan giant panda habitat is crucial for its scientific protection and sustainable development.

At present, land use classification based on remote sensing imagery is a commonly used method (Castelluccio et al., 2017). In particular, it involves a process of using satellite or aerial image data obtained using remote sensing technology to classify and identify land cover through digital image processing and classification algorithms. Common classification methods include supervised classification (Shi et al., 2012; Rwanga and Ndambuki, 2017), unsupervised classification (Riese et al., 2019; Zhang et al., 2021), and semi-supervised classification (Dalsasso et al., 2021; Xia et al., 2022). Among these, supervised classification in the field of land use classification of remote sensing images has always been an active research area. Its development trajectory has gradually transitioned from traditional methods to machine learning, and then to deep learning, while emphasizing technological innovations such as multisource data fusion and semi-supervised learning. In traditional methods, land use classification mainly relied on manually designed features, such as texture, color, and shape. The classification methods used included minimum distance classification (Haapanen et al., 2004), support vector machine (SVM; Ustuner et al., 2015), and decision trees (Pham et al., 2022). These methods achieved success to a certain extent, but the classification performance for complex land cover categories and high-dimensional data was relatively poor. With the rise of machine learning, artificial intelligence methods have gradually replaced traditional methods. Significant achievements have been made in land use classification using structures such as convolutional neural networks (CNN; Liu et al., 2022) and transformers (Kaselimi et al., 2022). Simultaneously, various improved deep learning architectures, such as U-Net (Wang et al., 2022) and ResNet (Wang et al., 2023), have emerged to address different land use classification problems. These network structures perform well in handling different scales and complexities of land cover categories. However, machine learning-based methods have obvious drawbacks, such as requiring extensive training based on a large number of annotated samples for an extended period and being prone to overfitting. This makes AI-based methods still have considerable room for improvement. Table 1 lists the strengths and weaknesses of some recent algorithms.

Case-based reasoning (CBR) (Schank and Abelson, 1977; Aamodt and Plaza, 1994), as an artificial intelligence method for solving complex problems, has been widely researched and applied. Its basic idea can be summarized as follows: for the given case (or new problems), CBR can search for similar cases in a historical case bank and reuse the solutions of those similar cases in the given case. If the solution through direct reuse is deemed impractical, modifications to the case solution are made based on domain knowledge or alternative approaches, resulting in the ultimate resolution. Furthermore, the typical cases with direct or revised

TABLE 1 Advantages and disadvantages of various algorithms for remote sensing land use classification.

Algorithm	Year	Advantages	Disadvantages
Minimum distance	—	Simple and easy to understand	Sensitive to outliers, not suitable for complex classes
Support vector machine (Burges, 1998)	1998	Handles high-dimensional data well, strong generalization	High computational complexity, insensitive to large-scale and imbalanced data
Decision tree (Quinlan, 1986)	1986	Easy to interpret and captures nonlinear relationships	Sensitive to noise, prone to overfitting
Random forest (Breiman, 2001)	2001	Good performance on high-dimensional data, mitigates overfitting	Long training times and relatively lower interpretability
k-nearest neighbors	—	Simple and easy to implement	Sensitive to noise and outliers and requires tuning of k
Principal component analysis (Hotelling, 1933)	1933	Effective dimensionality reduction and retains main information	Ignores some details that may contain important information
Convolutional neural network (Krizhevsky et al., 2012)	2012	Learns complex feature representations and suitable for large high-dimensional data	Requires a large amount of labeled data, high computational resources
U-Net (Ronneberger et al., 2015)	2015	Suitable for semantic segmentation tasks and preserves high-resolution information	May not perform as well as other methods for small objects and requires substantial data for training
ResNet (He et al., 2016)	2016	Addresses the vanishing gradient problem and suitable for deep learning tasks	Long training times and requires substantial computational resources
Multi-source data fusion	—	Improves classification accuracy and enhances robustness	Challenges in handling data inconsistency during fusion and complex fusion algorithms
Temporal information fusion	—	Captures temporal variations and enhances classification accuracy	Higher demands on data acquisition, storage, and research on handling temporal information
Semi-supervised learning	—	Reduces labeling costs and improves model performance	Requires certain levels of model generalization and robustness
Transfer learning (Pan and Yang, 2009)	2009	Adapts to new environments and reduces dependency on extensive labeled data	Careful selection of models and transfer strategies is necessary

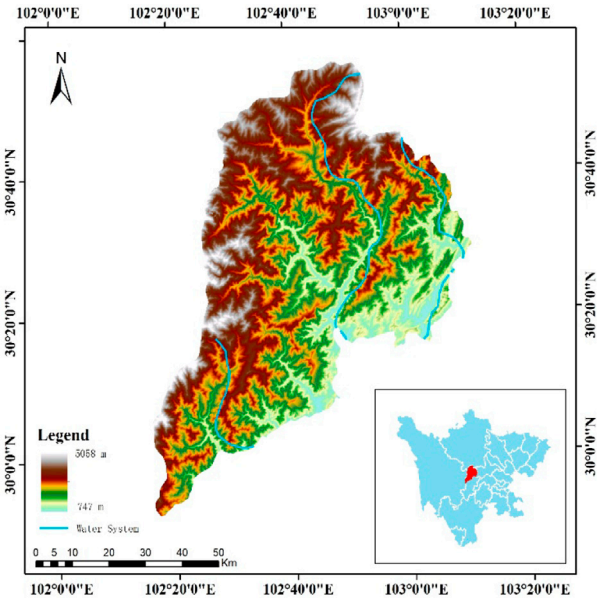

FIGURE 1
Topographic map and location of the study area.

solutions are added to the case bank to expand its contents. CBR does not require precise domain models but rather uses historical case knowledge to deduce solutions for new cases. It has significant advantages in solving complex and uncertain problems, especially in domains where specialized knowledge is abstract and difficult to generalize and express.

In recent years, CBR has been widely researched and applied in various fields, such as environmental science (Bajo et al., 2010; Lee et al., 2014; Mounce et al., 2016; Caro et al., 2017), urban development (Li and Liu, 2006; Liu et al., 2014; Yu and Li, 2018), land use (Shi and Zhu, 2004; Du et al., 2010), geological engineering (Fyson and Toll, 2008; Dou et al., 2015), mineral resource evaluation (Chen et al., 2010), oil and gas engineering (Skalle and Aamodt, 2004; Popa and Wood, 2011; Shokouhi et al., 2014; Mazhari et al., 2018), and oil and gas resource evaluation (Chen et al., 2010; Chen et al., 2014), and has achieved good results. However, from the current research, there are still relatively few attempts to use CBR for land use classification. In the aforementioned studies, the reasoning models mainly employs the classical attribute similarity reasoning, with less emphasis on spatial similarity reasoning based on spatial features. The few studies that have explored spatial similarity reasoning are focused on specific domain problems. While spatial features of different research objects vary from different domains to problems, and because of the different features, the spatial similarity reasoning methods tend to be different. Therefore, for land-use classification, in addition to the attribute features, it is meaningful to explore the spatial features and construct corresponding integrated reasoning models to enhance the effectiveness and accuracy of land use classification in the Jiajinshan giant panda habitat.

Therefore, this paper proposes a land use remote sensing interpretation algorithm based on spatial case-based reasoning (S-CBR). In particular, it comprises the construction of a spatial case expression model and a spatial case similarity reasoning model. Based on this, comparative experiments were conducted with ablative analysis and land use classification experiments in the Jiajinshan giant panda habitat. Further discussions analyze the changes in land use classification from 2018 to 2022 over a 5-year period. This provides decision support for relevant departments in protection planning, rational resource utilization, monitoring of land use changes, and even scientific research and education in the region.

The remaining structure of the article is as follows: Section 2 provides a detailed introduction to the study area; Section 3 elaborates on the proposed spatial case reasoning algorithm; Section 4 expounds on the experimental results of the algorithm and related discussions; and Section 5 provides the conclusion of this paper.

2 Study area

The Jiajinshan giant panda habitat is located in the Jiajin Mountain region at the junction of Wenchuan County, Li County, and Songpan County in Aba Tibetan and Qiang Autonomous Prefecture, Sichuan Province, China (Figure 1). It includes the Jiajinshan Nature Reserve, Shapinggou Nature Reserve in Barkam County, Ma'anshan Nature Reserve in

TABLE 2 Data types and their acquisition sources.

Category	Processing result	Source
Topography	Slope	Google Earth Engine (https://developers.google.com/earth-engine)
	Aspect	
	Isoheight	
Meteorology	Isotherm	Google Earth Engine (https://developers.google.com/earth-engine)
	Isohyet	
	Iso-evaporation lines	
Hydrological	Water network distribution	OpenStreeMap (https://www.openstreetmap.org/)
Imagery	Sentinel-2 satellite remote sensing data	Google Earth Engine (https://developers.google.com/earth-engine)
	MODIS NDVI MODIS NDWI time series data	

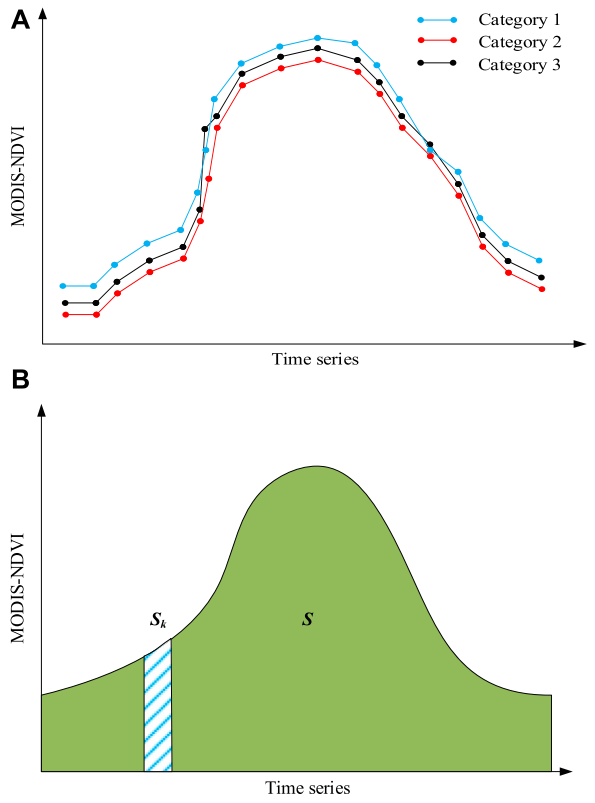

FIGURE 2
MODIS NDVI time series curve. **(A)** Different land use types tend to have different time series curves. **(B)** Different land use types tend to have different peak areas.

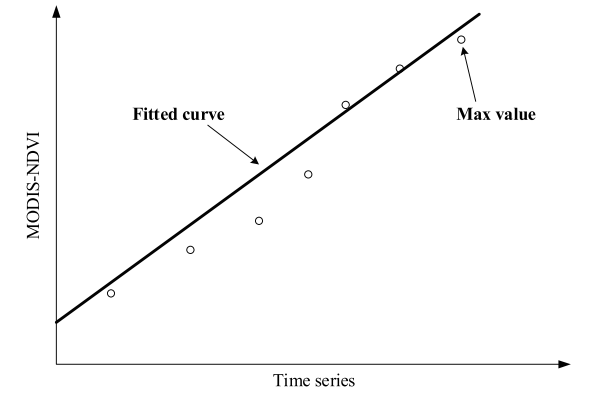

FIGURE 3
MODIS NDVI growth rate fitting curve. Different land use types tend to have different growth rate fitting curves.

Xiaojin County, and Baishuigou Nature Reserve in Wenchuan County. It has an alpine sub-frigid humid climate, with an annual average temperature ranging from −2°C to 12°C. The region receives abundant rainfall, with an annual precipitation of approximately 800–1,200 mm, mainly concentrated from May to October. Due to high altitude, the climate in the Jiajinshan giant panda habitat changes dramatically, with large temperature differences between day and night, and the temperature at night can drop to below −20°C. The Jiajinshan giant panda habitat is located in the mountain area with complex terrain, numerous rivers, and a forest coverage rate of over 70%. The region has undulating topography, with mountain peaks over 3,000 m, and the highest peak exceeding 5,000 m. The area is crisscrossed by many rivers, including the Barkam River, Qingyi River, Songpan River, and Dadu River. These rivers have abundant water resources and are mostly tributaries of the Yangtze River. Due to its unique geographical location and climatic conditions, the Jiajinshan giant panda habitat possesses rich natural resources, including many rare wildlife and plants. Endangered species such as giant pandas, golden monkeys, and snow leopards live and reproduce here. Therefore, research on land classification in this area is of great significance to the protection of China's ecological environment and biodiversity.

TABLE 3 Allocation of weights for each feature.

Feature name	Sub-feature	Value	
Attribute feature	Spectral	0.384	0.24
	NDVI	0.253	
	Temperature	0.161	
	Precipitation	0.086	
	Evaporation	0.013	
	Slope	0.086	
	Aspect	0.017	
Spatial feature	Isoheight	0.097	0.52
	Isotherm	0.236	
	Isohyet	0.186	
	Isothyme	0.481	
	Peak area	0.5	
Auxiliary feature	Coupling value of growth rate	0.5	0.24

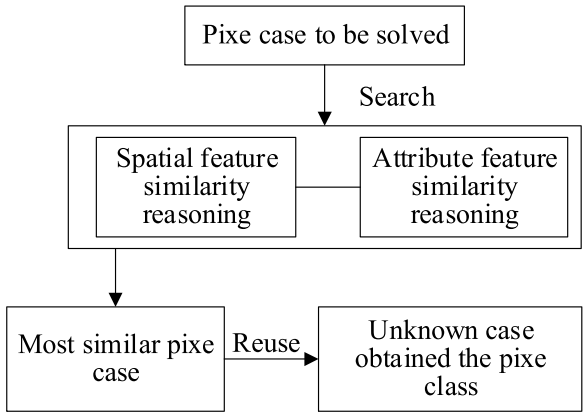

FIGURE 4
Spatial case-based reasoning process.

TABLE 4 Results of the ablation experiment.

Class	O-CBR			A-CBR			S-CBR		
	Recall	Precision	F1	Recall	Precision	F1	Recall	Precision	F1
Water bodies	0.6702	0.6299	0.6078	0.7424	0.7488	0.7274	0.8540	0.8441	0.8532
Forests	0.6517	0.7012	0.7028	0.7484	0.7134	0.7494	0.8756	0.8091	0.8522
Grasslands	0.6567	0.6864	0.6062	0.7530	0.7467	0.7686	0.8369	0.8440	0.8904
Wetlands	0.7296	0.5538	0.6144	0.7372	0.7706	0.7367	0.8391	0.8526	0.8713
Cultivated lands	0.6580	0.6480	0.6141	0.7879	0.7407	0.7608	0.8092	0.8445	0.8420
Shrub lands	0.6692	0.6621	0.7228	0.7534	0.7669	0.7336	0.8548	0.8518	0.8253
Building lands	0.5928	0.6839	0.6757	0.7697	0.7402	0.7840	0.8541	0.8794	0.8637
Bare lands	0.6221	0.6650	0.6766	0.7479	0.7741	0.7602	0.8911	0.8391	0.8584
Snowfields	0.6131	0.6154	0.6078	0.7118	0.7538	0.7317	0.8315	0.8742	0.8227
Clouds	0.6366	0.6543	0.6718	0.7484	0.7447	0.7477	0.8537	0.8612	0.8211

TABLE 5 Results of the comparative experiments in 2020. Bolded entries indicate the optimal results.

Class name	SVM	U-Net	ViT	Trans-Unet	S-CBR
Water bodies	0.92	0.93	0.92	0.93	**0.96**
Forests	0.82	0.85	0.84	0.86	**0.89**
Grasslands	0.77	0.75	0.82	0.84	**0.93**
Wetlands	0.80	0.83	0.87	0.91	**0.95**
Cultivated lands	0.83	0.89	0.84	**0.92**	0.88
Shrub lands	0.82	0.88	0.85	0.91	**0.94**
Building lands	0.81	0.89	0.86	0.92	**0.93**
Bare lands	0.80	0.89	0.83	0.91	**0.95**
Snowfields	0.80	0.87	0.83	0.91	**0.94**
Clouds	0.84	0.88	0.84	0.92	**0.93**
AA	0.76	0.79	0.82	0.83	**0.84**
OA	0.81	0.85	0.89	0.92	**0.95**
Kappa	0.85	0.87	0.86	0.88	**0.90**

3 Research methods

3.1 Data acquisition and processing

In this paper, multi-sources and multi-temporal data were used as the basis for land use classification in the Jiajinshan giant panda habitat. All the data were obtained from Google Earth Engine and OpenStreetMap, more specifically, including Sentinel-2 satellite remote sensing data, MODIS normalized difference vegetation index (NDVI), MODIS NDWI time series data, digital elevation model (DEM) data, and hydrological and meteorological data. The specific data contents are given in Table 2.

The multiple-source data have various formats, and usually, the resolution and coordinate systems are inconsistent, making them difficult to use directly. To accurately and correctly identify land use types, tools such as ArcMap and ENVI were used to process the raw data. For DEM, hydrological and meteorological data, basic elements such as slope, aspect, isoheight, distribution of water network, isotherm, isohyet, and isothyme, and other calculations were performed. Additionally, the size of the grid cells will greatly affect the calculation amount and precision of the model. Considering the calculation amount after dividing the cells and whether the attributes of the grid cells can effectively reflect the real features of the area and in combination with the available resolution of multi-source and multi-temporal data, the research proposed to use a regular grid cell at a size of 30 m × 30 m as the minimum unit for land use classification, regarding each cell as homogeneity.

3.2 Construction of a spatial case expression model

In case reasoning, each grid cell represents a case, where cases with known land use categories are called known cases, and cases that are unknown and awaiting classification are called unknown cases. Unlike traditional case reasoning, which only uses attribute features to construct case expression models, the proposed spatial case reasoning model in this paper adopts an integrated approach that incorporates attribute features, spatial features, and auxiliary features in the construction of spatial case expression models.

3.2.1 Attribute features

Attribute features are extracted from multiple data sources, including topography and imagery data. The Sentinel-2 satellite imagery comprises 13 bands ranging from 440 nm to 2,090 nm. The spectral information can reflect land cover types and biological growth from different perspectives, providing an important basis for land use classification. MODIS NDVI data contain NDVI values for each grid cell during 23 periods within a year. They directly reflect the changes in surface vegetation and water resources during different periods of the year, making a strong factor for identifying land use types. Additionally, factors such as

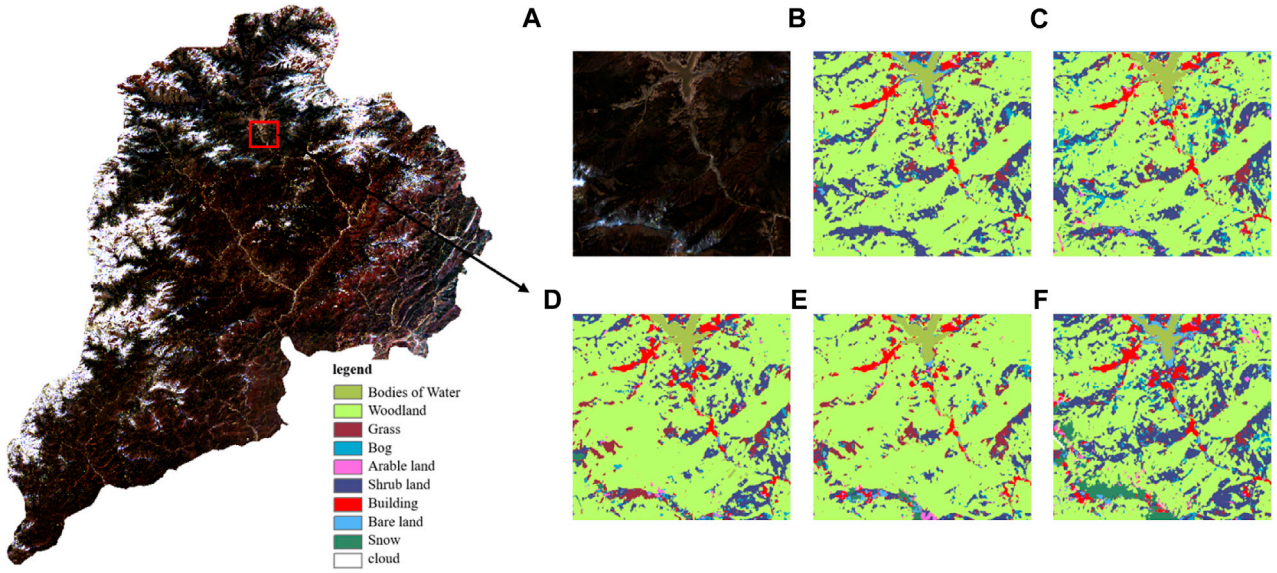

FIGURE 5
Results of comparative experiments on land use classification in the study area using different methods. Subfigures include **(A)** image; **(B)** SVM; **(C)** U-Net; **(E)** Trans-Unet; and **(F)** S-CBR.

temperature, precipitation, evaporation, slope, and aspect indirectly affect land cover, local climate, and biological distribution, and thus, they are also essential reference factors for land classification. In summary, each case in the study comprises 19 factors, including Sentinel-2 spectral imagery, MODIS NDVI, temperature, precipitation, evaporation, slope, and aspect as its attribute features.

3.2.2 Spatial features

Spatial features are derived from topographic data, meteorological data, and hydrological data. After fully considering the spatial features of various land types, spatial metric relationships were selected as spatial features.

Spatial metric relationships quantify the distance between two geographic units. First, isolines with appropriate intervals are obtained for the four basic data of elevation, temperature, precipitation, and evaporation. For any grid cell within the study area, the distances from the center of each grid cell to the isolines of elevation, temperature, precipitation, evaporation, and the distance to the water network are calculated as the spatial metric relationship features of the case.

3.2.3 Auxiliary features

Auxiliary features are designed to supplement case features and enrich the feature factors of case features. Auxiliary features are further derived from attribute features or spatial features, and often have special meanings for case features, so they are not repetitions of the aforementioned features. The auxiliary features in this study are obtained from MODIS NDVI time series data and consist of the peak area (S) and coupling value of the growth rate.

Generally, different land use types exhibit different MODIS NDVI time series curves, as shown in Figure 2A. The peak area (S) and coupling value of the growth rate are designed to reflect this feature. The peak area represents the area enclosed by the time curve and the x-axis, which is composed of trapezoids formed by discrete data, as shown in Figure 2B.

The formula is as follows:

$$S = \sum_{k=1}^{n-1} \frac{y_k - y_{k+1}}{2} \Delta x. \tag{1}$$

In Eq. 1, S represents the peak area; n represents the number of time series; y_k represents the NDVI value of the kth time series; and Δx represents the time interval, which is set as 1 in the study.

The coupling value of the growth rate is composed of the slope of the fitted curve during the growth phase of the MODIS NDVI time series curve and the maximum value of the fitted curve (Figure 3). This is because different land use types had different growth rates during the growth phase of the MODIS NDVI time series curve, and they also have different peak values (Figure 2A). The coupling value of the growth rate is calculated as follows:

$$E = \beta + \max_{NDVI}. \tag{2}$$

In Eq. 2, β represents the slope of the fitted curve, which is obtained through the least squares method. max_{NDVI} represents the maximum value of the fitted curve.

In summary, the spatial case expression model can be expressed as follows:

$$\begin{aligned} C = (&a_1, a_2, ..., a_k; d_{11}, d_{12}, ..., d_{1m}, \\ &d_{21}, d_{22}, ..., d_{2m}, d_{q1}, d_{q1}, ..., d_{qm}, \\ &...S, E, R). \end{aligned} \tag{3}$$

In Eq. 3, a_k represents the attribute feature value; k represents the number of basic parameters; d_{qm} represents the distance value from the case to the mth isoline of the qth basic data; S represents the feature value of the peak area of the case; E represents the coupling

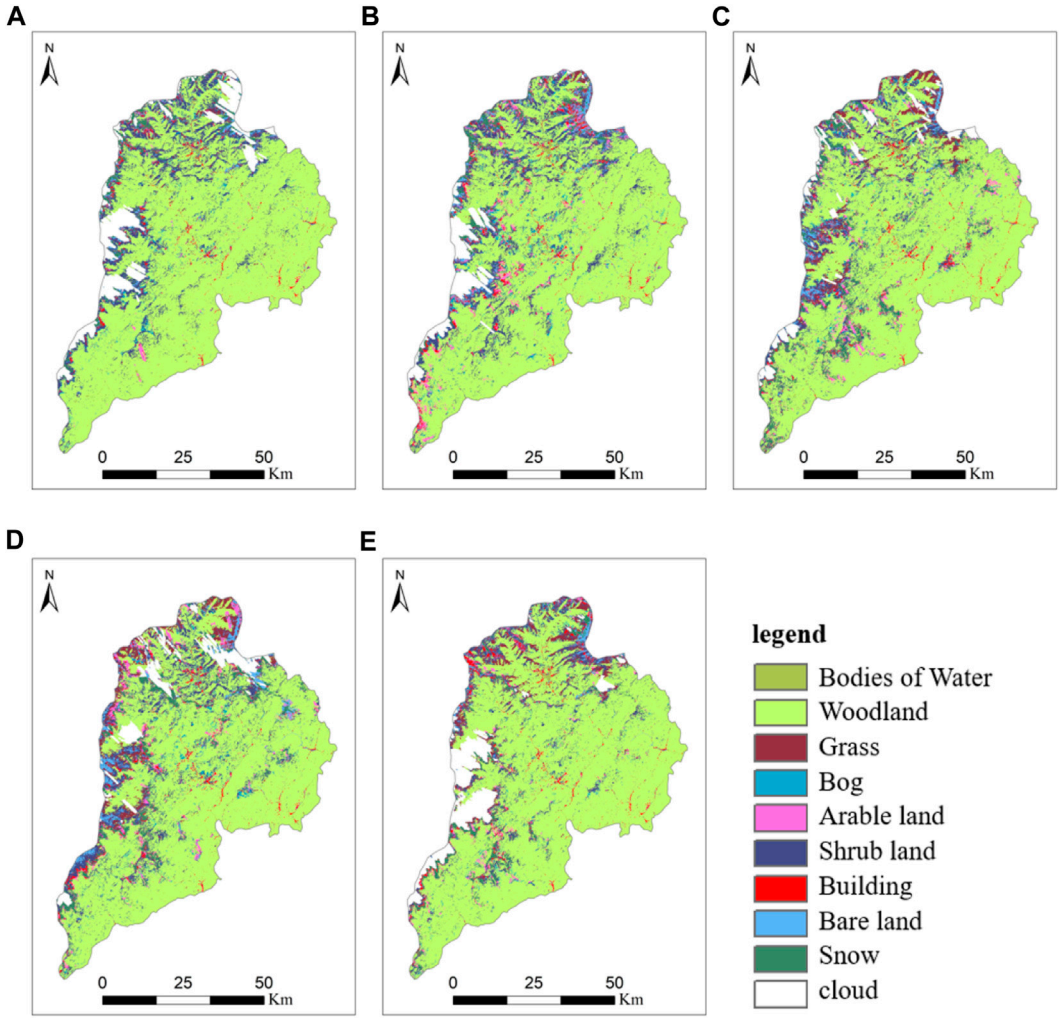

FIGURE 6
Land use classification results: **(A–E)** represent the land use classification results from 2018 to 2022, respectively.

TABLE 6 Total precision of land use classification by year.

Year	2018	2019	2020	2021	2022
Precision	0.8166	0.8219	0.8437	0.8316	0.8521

value of growth rate feature value; and R represents the land use category of the case. For unknown cases, the value of R is left blank.

3.3 Construction of a spatial case similarity reasoning model

The spatial case similarity reasoning model consists of two parts: attribute similarity reasoning model and spatial similarity reasoning model.

The similarity reasoning formula of attribute features and auxiliary features is as follows:

$$S_a = \frac{\sum_{i=1}^{n} \frac{v_i^h}{v_i^u} w_i}{\sum_{i=1}^{n} w_i} \quad If \frac{v_i^h}{v_i^u} > 1, \frac{v_i^h}{v_i^u} = \frac{v_i^u}{v_i^h}. \tag{4}$$

In Eq. 4, i represents a feature item corresponding to an attribute feature; n represents the total number of attribute features; v_i^h represents the ith attribute feature value of the known-layer case; v_i^u represents the ith attribute feature value of the unknown case; w_i represents the weight of the ith attribute feature; and S_a represents the attribute feature similarity between the known and unknown cases.

The similarity reasoning formula of spatial metric relationship is as follows:

$$S_d = \frac{\sum_{j=1}^{n} \frac{d_j^h}{d_j^u} w_j^x}{\sum_{j=1}^{n} w_j^x} \quad If \frac{d_j^h}{d_j^u} > 1, \frac{d_j^h}{d_j^u} = \frac{d_j^u}{d_j^h}. \tag{5}$$

TABLE 7 Evaluation of land use classification indicators by category (2018–2022).

Year	Categories								
	Water bodies	Forests	Grasslands	Wetlands	Cultivated lands	Shrub lands	Building lands	Bare lands	Snowfields
2018	0.8401	0.8028	0.7954	0.8110	0.7954	0.8110	0.8167	0.8012	0.8164
2019	0.8440	0.8229	0.7990	0.7989	0.7996	0.8290	0.8374	0.8189	0.8304
2020	0.8548	0.8414	0.8278	0.8069	0.8529	0.8124	0.8268	0.8176	0.8294
2021	0.8534	0.8281	0.8136	0.8276	0.8413	0.8460	0.8431	0.8442	0.8627
2022	0.8633	0.8457	0.8471	0.8522	0.8608	0.8431	0.8572	0.8370	0.8436

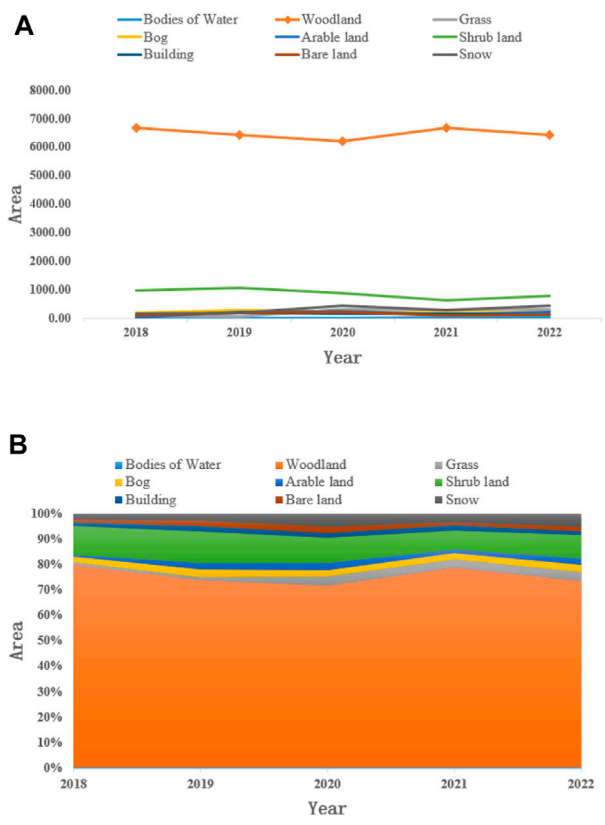

FIGURE 7
Changes in the land use types of the Jiajinshan giant panda habitat. **(A)** Changes in the proportion of land use categories in the habitat of giant pandas in Jiajin Mountain. **(B)** Changes in the land use types and areas of the Jiajinshan giant panda habitat.

In Eq. 5, j represents the index of spatial metric relationships; n represents the total number of items; d_j^h represents the feature value of jth spatial metric relationship of the known case; d_j^u represents the feature value of the jth spatial metric relation of the unknown case; w_j^x represents the weight of the corresponding metric relationship feature; and S_d represents the spatial metric relationship similarity value between the known and unknown cases.

The integrated reasoning formula of spatial similarity and attribute similarity is as follows:

$$S = \frac{S_s W_s + S_a W_a}{W_s + W_a}. \tag{6}$$

In Eq. 6, W_s and W_a represent the weights of spatial similarity reasoning and attribute similarity reasoning, respectively. S_s and S_a represent the similarity values of spatial and attribute similarity, respectively. S represents the similarity of the integrated inference of spatial similarity and attributes similarity integrated reasoning.

3.4 Model evaluation metrics

In the context of spatial inference models for remote sensing image analysis, the quality of inference results needs to be measured using appropriate accuracy evaluation metrics. This paper adopts two accuracy evaluation metrics: accuracy, commonly referred to as accuracy or correctness, and evaluation metrics, such as recall, precision, and F-measure.

The accuracy or correctness metric is the most widely used accuracy evaluation measure. It is generally expressed as the ratio of the number of correctly classified samples to the total number of samples in the validation set, as shown in Eq. 7:

$$a = \frac{c}{n}. \tag{7}$$

In the formula, c represents the number of correctly classified samples, n represents the total number of validation samples, and a represents accuracy.

The evaluation metrics of recall, precision, and F-measure are derived from the fields of machine learning and statistics. Compared to simple accuracy or correctness metrics, these indicators provide a more effective and detailed assessment of the results of model classification. For a specific class to be predicted, this class is referred to as the positive class, while the rest are considered negative classes. True positives (TPs) represent the number of samples in the validation set where the true class is positive and the predicted result is also positive. False positives (FPs) represent the number of samples in the validation set where the true class is negative, but the predicted result is positive. False negatives (FNs) represent the number of samples in the validation set where the true class is positive, but the predicted result is negative. True negatives (TNs) represent the number of samples in the validation set where the true class is negative, and the predicted class is also negative.

Thus, the calculation for recall is given by Eq. 8:

$$R = \frac{TP}{TP + FN}. \tag{8}$$

It calculates the proportion of all correctly classified samples to all samples that should have been predicted as positive class.

The calculation for precision is given by Eq. 9:

$$P = \frac{TP}{TP + FP}. \tag{9}$$

It calculates the proportion of all correctly classified samples to all samples predicted as positive class.

Precision and recall are interrelated; ideally, the higher both values are, the better the classification performance. However, in general, when precision is high, recall tends to be low and *vice versa*. If both are low, the classification performance is considered poor. Therefore, when both high precision and high recall are desired, the F-measure metric can be used to measure the trade-off between them. Its calculation is shown in Eq. 10:

$$F = \frac{(\alpha^2 + 1)PR}{\alpha^2 (P + R)}. \tag{10}$$

In the formula, P represents the precision value, R represents the recall value, and when the parameter $\alpha = 1$, F-measure is commonly referred to as the F1 evaluation metric, expressed as in Eq. 11

$$F1 = \frac{2PR}{P + R}. \tag{11}$$

In addition, in the comparative experiments, we employed overall accuracy (OA), average accuracy (AA), and Cohen's kappa coefficient to measure the overall effectiveness of different methods. OA is a straightforward evaluation metric representing the proportion of correctly classified samples to the total number of samples. AA calculates the average accuracy of each class in a multi-class classification problem, balancing the sample distribution across different classes. Kappa is a measure of consistency that considers random classification, addressing the issue of imbalanced sample distribution affecting OA.

3.5 Experimental design

According to the aforementioned research methods, this study employs Python as the programming language for algorithm development. Remote sensing imagery and meteorological, hydrological, and topographic data from 2018 to 2022 were collected in the Jiajinshan giant panda habitat. In addition, the land use of the study area was classified for each year, including 10 categories: water bodies, forests, grasslands, wetlands, cultivated lands, shrub lands, building lands, bare lands, snowfields, and clouds. In the experimental project, multiple remote sensing images of each year were mosaicked with a median composition method. Through visual interpretation, regions were uniformly selected as the case bank, while the remaining regions were taken as unknown cases. In the case bank, 30% of the cases were randomly chosen as test cases to evaluate the effectiveness of the model.

Before conducting the spatial case reasoning of strata, it is necessary to determine the internal and mutual weights of attribute features, spatial features, and auxiliary features. The weights of each factor can be determined as follows: first, case reasoning was performed with individual feature sub-items to obtain the classification precision based solely on that feature sub-item. After performing case reasoning on all feature sub-items, the importance ranking of all feature sub-items can be obtained. Then, the analytic hierarchy process (AHP) is used to determine the specific weights of each feature sub-item, as shown in Table 3. The specific process of case-based reasoning used in the experiment is shown in Figure 4.

4 Results and discussion

4.1 Ablation experiment

To verify the effectiveness of spatial features in the model, we conducted three sets of controlled experiments based on the dataset of 2020. These experiments include the ordinary case-based reasoning (O-CBR) model with only attribute features, case-based reasoning (A-CBR) model combining attribute and auxiliary features, and spatial feature-integrated case-based reasoning model. The experimental results are shown in Table 4.

Among the three CBR methods, the S-CBR method, which incorporates spatial features, achieved the best performance, while the O-CBR method, only using attribute features, had the worst performance. The A-CBR method, which combines attribute and auxiliary features, achieved moderate classification results. This indicates that auxiliary features and spatial features play an important role in remote sensing image segmentation, especially in land use classification. It also proves that exploring features with spatial significance is one of the approaches to applying general artificial intelligence methods to land use classification of remote sensing images.

4.2 Comparison experiments

To validate the advancement of the proposed algorithm, we conducted comparative experiments based on imagery from the study area in 2020. The selected algorithms for experimentation range from traditional statistical learning algorithms to advanced machine learning algorithms, including SVM (Burges, 1998), U-Net (Ronneberger et al., 2015), vision transformer (ViT) (Dosovitskiy et al., 2020), and Trans-Unet (Chen et al., 2021). Among these, support vector machine represents traditional statistical learning algorithms, U-Net is a convolutional neural network-based algorithm, ViT utilizes the transformer structure, and Trans-Unet combines the CNN and transformer. In the comparative experiments, we fine-tuned the hyperparameters for some methods. In particular, for the SVM, we used cross-validation to set the regularization parameter (C), gamma parameter, and degree of the polynomial kernel. The kernel function chosen was the default radial basis function (RBF) kernel. In practical implementation, we used GridSearchCV from scikit-learn to carry out this process. For several other deep learning methods, we conducted comparative experiments by referring to the optimal parameters mentioned in their respective papers.

Table 5 presents the results of the comparative experiments. It can be observed that the proposed S-CBR algorithm exhibits optimal experimental results for the majority of categories, although its performance is less satisfactory for a few categories. In terms of overall accuracy, S-CBR demonstrates the best results. This indicates that the proposed algorithm has advantages in experimental accuracy and is relatively straightforward in its algorithmic principles.

Figure 5 illustrates the results of the comparative experiments, and it aligns with the findings given in Table 5.

4.3 Experimental results and discussion of spatial case-based reasoning

The results of an ablation experiment show that S-CBR achieves the best land use classification performance of the Jiajinshan giant panda habitat. Therefore, we chose the S-CBR method to classify the land use of the Jiajinshan giant panda habitat based on remote sensing images from 2018 to 2022. The classification results are shown in Figure 6 and Table 6.

The results of the evaluation indicators given in Table 7 show that the classification precision of land use in the Jiajinshan giant panda habitat, based on spatial case-based reasoning, is above 80% for various categories. The precision is higher for water bodies and snowfields while lower for grasslands, wetlands, and cultivated lands (Table 7).

This may be because water bodies and snowfields have more distinctive spectral features and are greatly influenced by topographic images, which play a significant role in the classification process. On the other hand, the spectral features of cultivated lands, grasslands, and wetlands are relatively similar, and from a spatial perspective, their distribution patterns are not closely related to climate and topographic factors. Hence, their classification results perform worse. From the perspective of a 5-year span, the precision of classification results in 2022 is the highest, while it is the lowest in 2018. This is because the satellite imagery in 2022 had the lowest cloud coverage, so the image quality is the best, while the opposite was true for 2018. This indicates that image quality can affect the characterization degree of image spectral features on land objects, thus affecting the quality of classification results.

4.4 Analysis of changes in land use types

Figures 7A, B show the land use changes in the Jiajinshan giant panda habitat from 2018 to 2022. Over the past 5 years, the forest land has been the dominant land use type, with its proportion decreasing first and then increasing. The trend in grassland area changes is similar to the forest land, but its proportion has been increasing year by year. The area of the cultivated land reached its peak in 2020, and since then, it decreased to some extent. The aforementioned changes in land use types reflect that the ecological environment of the giant panda habitat area in Jiajinshan has been improved, especially in forest protection and restoration.

5 Conclusion

In order to understand the land use classification of the Jiajinshan giant panda habitat, this paper proposes a land use remote sensing interpretation algorithm based on spatial case-based reasoning, including the construction of a spatial case expression model and a spatial case similarity reasoning model. On this basis, comparative experiments were conducted through ablation analysis, and the results showed that the spatial feature-integrated case-based reasoning model (S-CBR) achieved better classification results. Then, using S-CBR as the representative algorithm, land use classification experiments were carried out in the Jiajinshan giant panda habitat. The experimental results showed that S-CBR had better performance in land use classification. This paper further analyzed the land use classification changes from 2018 to 2022 over a 5-year period, and the results can provide a theoretical basis for the ecological environment protection in this region.

Data availability statement

The raw data supporting the conclusion of this article will be made available by the authors, without undue reservation.

Author contributions

WX: data curation, investigation, methodology, and writing–original draft. WZ: data curation, investigation, supervision, writing–original draft, and writing–review and editing. SW: methodology, supervision, validation, and writing–review and editing.

Funding

The author(s) declare that no financial support was received for the research, authorship, and/or publication of this article.

Conflict of interest

Author WZ was employed by Sichuan Institute of Geological Engineering Investigation Group Co. Ltd.

The remaining authors declare that the research was conducted in the absence of any commercial or financial relationships that could be construed as a potential conflict of interest.

Publisher's note

References

Aamodt, A., and Plaza, E. (1994). Case-based reasoning: foundational issues, methodological variations, and system approaches. *Artif. Intell. Commun.* 7 (1), 39–59. doi:10.3233/aic-1994-7104

Bajo, J., De Paz, J. F., Rodriguez, S., and González, A. (2010). Multi-agent system to monitor oceanic environments. *Computer-Aided Eng.* 17 (2), 131–144. doi:10.3233/ica-2010-0332

Breiman, L. (2001). Random forests. *Mach. Learn.* 45, 5–32. doi:10.1023/a:1010933404324

Burges, C. J. C. (1998). A tutorial on support vector machines for pattern recognition. *Data Min. Knowl. Discov.* 2 (2), 121–167. doi:10.1023/a:1009715923555

Caro, F. D., Vaccaro, A., and Villacci, D. (2017). Spatial and temporal wind power forecasting by case-based reasoning using big-data. *Energies* 10 (2), 1–14. doi:10.3390/en10020252

Castelluccio, M., Poggi, G., Sansone, C., and Verdoliva, L.(2017). Land use classification in remote sensing images by convolutional neural networks. arXiv preprint arXiv:1508.00092.

Chen, J., He, B., and Cui, Y. (2010). "Case-based reasoning and GIS approach to regional metallogenic prediction," in International Conference on Geoinformatics, 1–4.

Chen, J., Lu, Y., Yu, Q., Luo, X., Adeli, E., Wang, Y., et al. (2021). Transunet: Transformers make strong encoders for medical image segmentation. arXiv preprint arXiv:2102.04306.

Chen, J., Wang, W., and Li, J. W. (2014). Case-based reasoning with GIS to oil-gas reservoir comprehensive mapping. *Adv. Mater. Res.* 1073-1076, 2010–2014. doi:10.4028/www.scientific.net/amr.1073-1076.2010

Dalsasso, E., Denis, L., and Tupin, F. (2021). SAR2SAR: a semi-supervised despeckling algorithm for SAR images. *IEEE J. Sel. Top. Appl. Earth Observations Remote Sens.* 14, 4321–4329. doi:10.1109/jstars.2021.3071864

Dosovitskiy, A., Beyer, L., Kolesnikov, A., Weissenborn, D., Zhai, X., Unterthiner, T., et al. (2020). *An image is worth 16x16 words: Transformers for image recognition at scale*. arXiv preprint arXiv:2010.11929.

Dou, J., Chang, K., Chen, S., Yunus, A., Liu, J. K., Xia, H., et al. (2015). Automatic case-based reasoning approach for landslide detection: integration of object-oriented image analysis and a genetic algorithm. *Remote Sens.* 7 (4), 4318–4342. doi:10.3390/rs70404318

Du, Y., Wen, W., Cao, F., and Ji, M. (2010). A case-based reasoning approach for land use change prediction. *Expert Syst. Appl.* 37 (8), 5745–5750. doi:10.1016/j.eswa.2010.02.035

Fyson, M., and Toll, D. G. (2008). Case-based system for slope design. *Comput. Geotechnics* 35 (3), 468–478. doi:10.1016/j.compgeo.2007.06.007

Haapanen, R., Ek, A. R., Bauer, M. E., and Finley, A. O. (2004). Delineation of forest/nonforest land use classes using nearest neighbor methods. *Remote Sens. Environ.* 89 (3), 265–271. doi:10.1016/j.rse.2003.10.002

He, K., Zhang, X., Ren, S., and Sun, J. (2016). "Deep residual learning for image recognition," in Proceedings of the IEEE conference on computer vision and pattern recognition, 770–778.

Hotelling, H. (1933). Analysis of a complex of statistical variables into principal components. *J. Educ. Psychol.* 24 (6), 417–441. doi:10.1037/h0071325

Kaselimi, M., Voulodimos, A., Daskalopoulos, I., Doulamis, N., and Doulamis, A. (2022). A vision transformer model for convolution-free multilabel classification of satellite imagery in deforestation monitoring. *IEEE Trans. Neural Netw. Learn. Syst.* 34, 3299–3307. doi:10.1109/tnnls.2022.3144791

Krizhevsky, A., Sutskever, I., and Hinton, G. E. (2012). Imagenet classification with deep convolutional neural networks. *Adv. neural Inf. Process. Syst.* 25. doi:10.1145/3065386

Lee, M., Koo, C., Hong, T., and Park, H. S. (2014). Framework for the mapping of the monthly average daily solar radiation using an advanced case-based reasoning and a geostatistical technique. *Environ. Sci. Technol.* 48 (8), 4604–4612. doi:10.1021/es405293u

Li, X., and Liu, X. (2006). An extended cellular automaton using case-based reasoning for simulating urban development in a large complex region. *Int. J. Geogr. Inf. Sci.* 20 (10), 1109–1136. doi:10.1080/13658810600816870

Liu, X., Ma, L., Li, X., Ai, B., Li, S., and He, Z. (2014). Simulating urban growth by integrating landscape expansion index LEI and cellular automata. *Int. J. Geogr. Inf. Sci.* 28 (1), 148–163. doi:10.1080/13658816.2013.831097

Liu, Z. Q., Tang, P., Zhang, W., and Zhang, Z. (2022). CNN-enhanced heterogeneous graph convolutional network: inferring land use from land cover with a case study of park segmentation. *Remote Sens.* 14 (19), 5027. doi:10.3390/rs14195027

Mazhari, S. M., Memarian, H., and Tokhmechi, B. (2018). A hybrid learning automata and case-based reasoning for fractured zone detection using petrophysical logs. *Arabian J. Geosciences* 11 (19), 577. doi:10.1007/s12517-018-3934-3

Mounce, S. R., Mounce, R., and Boxall, J. B. (2016). Case-based reasoning to support decision making for managing drinking water quality events in distribution systems. *Urban Water J.* 13 (7), 727–738. doi:10.1080/1573062x.2015.1036082

Pan, S. J., and Yang, Q. (2009). A survey on transfer learning. *IEEE Trans. Knowl. data Eng.* 22 (10), 1345–1359. doi:10.1109/tkde.2009.191

Pham, Q. B., Chandra Pal, S., Chakrabortty, R., Saha, A., Janizadeh, S., Ahmadi, K., et al. (2022). Predicting landslide susceptibility based on decision tree machine learning models under climate and land use changes. *Geocarto Int.* 37 (25), 7881–7907. doi:10.1080/10106049.2021.1986579

Popa, A., and Wood, W. (2011). Application of case-based reasoning for well fracturing planning and execution. *J. Nat. Gas Sci. Eng.* 3 (6), 687–696. doi:10.1016/j.jngse.2011.07.013

Quinlan, J. R. (1986). Induction of decision trees. *Mach. Learn.* 1, 81–106. doi:10.1007/bf00116251

Riese, F. M., Keller, S., and Hinz, S. (2019). Supervised and semi-supervised self-organizing maps for regression and classification focusing on hyperspectral data. *Remote Sens.* 12 (1), 7. doi:10.3390/rs12010007

Ronneberger, O., Fischer, P., and Brox, T. (2015). "U-net: convolutional networks for biomedical image segmentation," in Proceedings, Part III 18 Medical Image Computing and Computer-Assisted Intervention–MICCAI 2015: 18th International Conference, Munich, Germany, October 5-9, 2015 (Springer International Publishing), 234–241.

Rwanga, S. S., and Ndambuki, J. M. (2017). Accuracy assessment of land use/land cover classification using remote sensing and GIS. *Int. J. Geosciences* 8 (4), 611–622. doi:10.4236/ijg.2017.84033

Schank, R. C., and Abelson, R. P. (1977). *Scripts, plans, goals, and understanding: an inquiry into human knowledge structures*. Oxford, UK: Lawrence Erlbaum.

Shi, X., Zhu, A., Burt, J. E., Qi, F., and Simonson, D. (2004). A case-based reasoning approach to fuzzy soil mapping. *Soil Sci. Soc. Am. J.* 68 (3), 885–894. doi:10.2136/sssaj2004.8850

Shi, Z., Ma, Y., Wang, Y., Ma, Z. W., Huang, Q., and Huang, Y. Y. (2012). Review on the classification methods of land use/cover based on remote sensing image. *Chin. Agric. Sci. Bull.* 28 (12), 273–278. doi:10.12677/AG.2020.106047

Shokouhi, S. V., Skalle, P., and Aamodt, A. (2014). An overview of case-based reasoning applications in drilling engineering. *Artif. Intell. Rev.* 41 (3), 317–329. doi:10.1007/s10462-011-9310-2

Skalle, P., and Aamodt, A. (2004). Knowledge-based decision support in oil well drilling. *Int. Conf. Intelligent Inf. Process.*, 443–455. doi:10.5555/1139563.1139627

Ustuner, M., Sanli, F. B., and Dixon, B. (2015). Application of support vector machines for landuse classification using high-resolution rapideye images: a sensitivity analysis. *Eur. J. Remote Sens.* 48 (1), 403–422. doi:10.5721/eujrs20154823

Wang, C., Chen, T., and Plaza, A. (2023). MFE-ResNet: a new extraction framework for land cover characterization in mining areas. *Future Gener. Comput. Syst.* 145, 550–562. doi:10.1016/j.future.2023.04.001

Wang, J., Hadjikakou, M., Hewitt, R. J., and Bryan, B. A. (2022). Simulating large-scale urban land-use patterns and dynamics using the U-Net deep learning architecture. *Comput. Environ. Urban Syst.* 97, 101855. doi:10.1016/j.compenvurbsys.2022.101855

Xia, Y., Li, J. Y., and Guo, D. E. (2022). Semi-supervised remote sensing image scene classification based on GAN. *Acta Photonica Sin.* 51 (3), 0310003. doi:10.3788/gzxb20225103.0310003

Xu, Y., Zhou, B., Jin, S., Xie, X., Chen, Z., Hu, S., et al. (2022). A framework for urban land use classification by integrating the spatial context of points of interest and graph convolutional neural network method. *Comput. Environ. Urban Syst.* 95, 101807. doi:10.1016/j.compenvurbsys.2022.101807

Yu, F., and Li, X. (2018). Improving emergency response to cascading disasters: applying case-based reasoning towards urban critical infrastructure. *Int. J. Disaster Risk Reduct.* 30, 244–256. doi:10.1016/j.ijdrr.2018.04.012

Zhang, C., Li, F., Li, J., Xing, J., Yang, J., Guo, J., et al. (2022). Recognition of land use on open-pit coal mining area based on DeepLab v3+ and GF-2 high-resolution images. *Coal Geol. Explor.* 50, 94–103.

Zhang, W., Tang, P., Corpetti, T., and Zhao, L. (2021). WTS: a Weakly towards strongly supervised learning framework for remote sensing land cover classification using segmentation models. *Remote Sens.* 13 (3), 394. doi:10.3390/rs13030394

frontiers | Frontiers in Environmental Science

TYPE Original Research
PUBLISHED 05 April 2024
DOI 10.3389/fenvs.2024.1335574

OPEN ACCESS

EDITED BY
Yunhui Zhang,
Southwest Jiaotong University, China

REVIEWED BY
Anoop Kumar Shukla,
Manipal Academy of Higher Education, India
Chun Zhu,
Hohai University, China

*CORRESPONDENCE
Hong Liang,
lianghong@mail.cgs.gov.cn

RECEIVED 09 November 2023
ACCEPTED 18 March 2024
PUBLISHED 05 April 2024

CITATION
Zhou F, Liang H, Lyu T, Li M, Zhang J, Wang B and Hao M (2024), Data driven assessment of rock mass quality in red-bed hilly area: a case study of Guang'an city, SW China.
Front. Environ. Sci. 12:1335574.
doi: 10.3389/fenvs.2024.1335574

Data driven assessment of rock mass quality in red-bed hilly area: a case study of Guang'an city, SW China

Fang Zhou[1], Hong Liang[1]*, Tao Lyu[1], Minghui Li[1], Jianlong Zhang[1], Baodi Wang[2] and Ming Hao[3]

[1]Department of Geological Information, Chengdu Center, China Geological Survey (Geosciences Innovation Center of Southwest China), Chengdu, China, [2]Department of Fundamental Geological, China Aero Geophysical Survey and Remote Sensing Center for Nature Resources, Beijing, China, [3]Department of Geological Information, Application Center of Geological Survey, Chengdu, China

The evaluation of geological suitability for urban underground space (UUS) development is an indispensable prerequisite for its optimal utilization. As the actual carrier of underground facilities, the evaluation of rock mass quality plays a crucial role in assessing geological suitability. However, it is notable that the evaluation of rock mass quality has regrettably remained somewhat marginalized within the broader framework of the geological suitability assessment in recent years. The selection of pertinent indicators for the evaluation of rock mass quality inherently presents an appreciable degree of subjectivity. Predominantly subjective evaluation methods continue to dominate the field, while the application of objective algorithms, such as unsupervised clustering, remains in its nascent stage. Furthermore, there is a lack of comprehensive investigations into distinct combinations of attributes. This limitation confines the broader applicability of the evaluation outcomes in the context of urban underground space. Within this study, we meticulously amassed rock core test data from over 40 boreholes of engineering geological significance within the urban planning ambit of Guang'An City. Utilizing the K-means unsupervised clustering algorithm and the Principal Component Analysis (PCA) algorithm. We successfully conducted an unsupervised clustering procedure with nine distinct physical and mechanical attributes. This yielded an aggregation into five discernible clusters. Building upon the derived clustering outcomes, a stratification of rock mass quality was effectuated into three distinct tiers: Level 1 (characterized by pure sandstone), Level 2 (primarily dominated by sandstone), and Level 3 (denoting fair conditions predominantly influenced by mudstone). This structured stratification facilitates a relatively objective and comprehensive evaluation of rock mass quality within the context of the red-bed hilly terrain. In the course of this analytical trajectory, we conducted a dissection of the clustering efficacy. For strongly correlated attributes, we propose a preliminary dimensionality reduction procedure prior to the clustering endeavor. Moreover, we recommend intervals of 10 m for the stratified evaluation in red bed hilly urban terrains.

KEYWORDS

quality assessment of rock mass, K-means, urban underground space, red-bed hilly areas, objective assessment

1 Introduction

Since the commencement of the 21st century, concomitant with the swift proliferation of the Chinese economy, a substantial surge in population influx has gravitated toward urban locales, thereby engendering an accentuated escalation in the urbanization quotient. In order to address the issues arising from the population-density imbalance, alleviate the problems associated with large cities, and achieve sustainable future development, the concept of "subterranean development" has emerged as an important direction and trend in the development of large to mega-cities worldwide (Pan and Jin, 2006; Peng and Peng, 2012; Qu et al., 2015; Qian, 2019; Lapenna and Chambers, 2020; Zhang et al., 2021b; Ge et al., 2021).

Urban Underground Space (UUS) represents an idiosyncratic spatial reservoir subject to profound transformation throughout its developmental trajectory. In contrast to surface domains, the ramifications of UUS advancement, epitomized by entities like subway systems, inherently harbor precise and exclusive functionalities. Once deployed, such infrastructures stand impervious to facile dismantlement or modification. Therefore, prior to the development and utilization of UUS, a thorough assessment of the geological suitability of the underground conditions is essential (Andriamamonjisoa and Hubert, 2019; Hu et al., 2019; Zhu et al., 2020; Tao et al., 2021). Furthermore, the underground geological conditions, represented by the subsurface rock and soil formations, play a crucial role as the actual carriers of underground facilities. They have a significant influence on the development of Urban Underground Space (UUS) (Peng et al., 2019; Zhu et al., 2021; Tang et al., 2022). Hence, the appraisal of rock mass quality assumes an eminent stance within the overarching framework of a comprehensive UUS evaluative paradigm.

The evaluation of rock mass quality, akin to the assessment of Urban Underground Space (UUS), encompasses two primary dimensions: the selection of evaluation attributes/indicators and the discernment of suitable mathematical models. Previous studies have shown that rock mass quality is primarily influenced by lithological composition, physical properties, and mechanical attributes (El et al., 2010; Zhou et al., 2019). Therefore, in the evaluation process, it is common to consider attributes such as bearing capacity, lithology, or selected mechanical experimental properties as evaluation criteria (Zhang et al., 2020; Wu et al., 2021; Tong et al., 2022; Wang et al., 2022; Li et al., 2023; Zhao et al., 2023). Nonetheless, it is noteworthy that existing scholarship alludes to the absence of a standardized corpus of criteria governing attribute selection, and the imperative of the chosen attributes has not been comprehensively interrogated within this context (Tan et al., 2021). Hence, it is imperative to investigate the interrelationships among evaluation indicators to choose an appropriate type and quantity of indicators for the evaluation endeavors.

In the evaluation of rock and soil quality, an array of semi-quantitative mathematical models frequently finds application, encompassing methodologies such as the Analytic Hierarchy Process (AHP) and the Most Unfavorable Grade Method (MUGM) (Xiong et al., 2006; Wang, 2013; Yuan, 2020; Li et al., 2021; Tian et al., 2021), Fuzzy Comprehensive Evaluation (Zhou B. et al., 2022; Zhao et al., 2022) and combination of the above method (Wu, 2021; Tong et al., 2022). Although these methodologies incorporate expert knowledge, their outcomes are conspicuously shaped by subjective elements, consequently engendering challenges in terms of result reproducibility. On the contrary, unsupervised clustering algorithms, characterized by a diminished susceptibility to subjective influences, have the capacity to yield relatively objective evaluation outcomes. Wang et al. (2022) and Li (2020) employ Fuzzy C-mean clustering algorithm to evaluate geological suitability; Du et al. (2022) adopted spectral clustering in Jiaozhou Bay stability evaluation. These studies have pioneered the application of clustering methods in the suitability assessment of subterranean spaces. However, extant scholarship reveals a paucity of research delving into comparative analyses of clustering outcomes across distinct attributes. Moreover, the formulation of definitive guidelines for the curation of evaluation criteria remains an unexplored terrain within this domain.

This study incorporates classical unsupervised learning (K-means) and dimensionality reduction algorithms (PCA) into the assessment of rock-soil mass quality in Guang'an City. Through clustering physical and mechanical attributes from over 40 boreholes of engineering geological, it evaluates the effectiveness of various attribute combinations. Additionally, a detailed analysis of the clustering results is performed. Providing a foundation for the future utilization of underground spaces in the red-bed hilly areas and offering insights into the transition from empirical and expert-driven suitability assessments to data-driven methodologies. In a broader spectrum, this inquiry furnishes illuminating insights germane to the structuring of a comprehensive evaluation indicator framework, extending its relevance to the expanse of diverse urban subterranean locales.

2 Geological setting

The study area is situated at the confluence of Chongqing municipality and Sichuan province in the southwestern region of China (Figure 1) (Zhang et al., 2021a). It serves as a pioneering demonstration zone for the advancement of China's western regions and the establishment of the Chengdu-Chongqing economic sphere. A further facet of its distinctiveness lies in its characteristic as a prolific milieu characterized by the pervasive juxtaposition of red sandstone-mudstone amalgams. The study area encapsulates a dyadic delineation of natural terrains, delineated as the Sichuan red bed hilly belt and the lower elevation sector of the Huaying Mountain terrain. It is noteworthy that these domains are situated within the precincts of the Upper Yangtze platform, concurrently aligning with the Central Sichuan depression, as delineated in the scholarly oeuvre authored by Wei et al. (2017).

The region exhibits a prevalence of tectonically inactive fractures, with seismic activity of relatively low magnitude primarily observed in the eastern sector (Zhou et al., 2022; Zhou et al., 2023). Within Guang'An, a total of eight distinct geological strata can be identified, namely the Cambrian, Ordovician, Silurian, Carboniferous, Permian, Triassic, Jurassic, and Quaternary. The initial six strata are predominantly present in the mountainous terrain, while the remaining exposed strata in the red soil hilly area

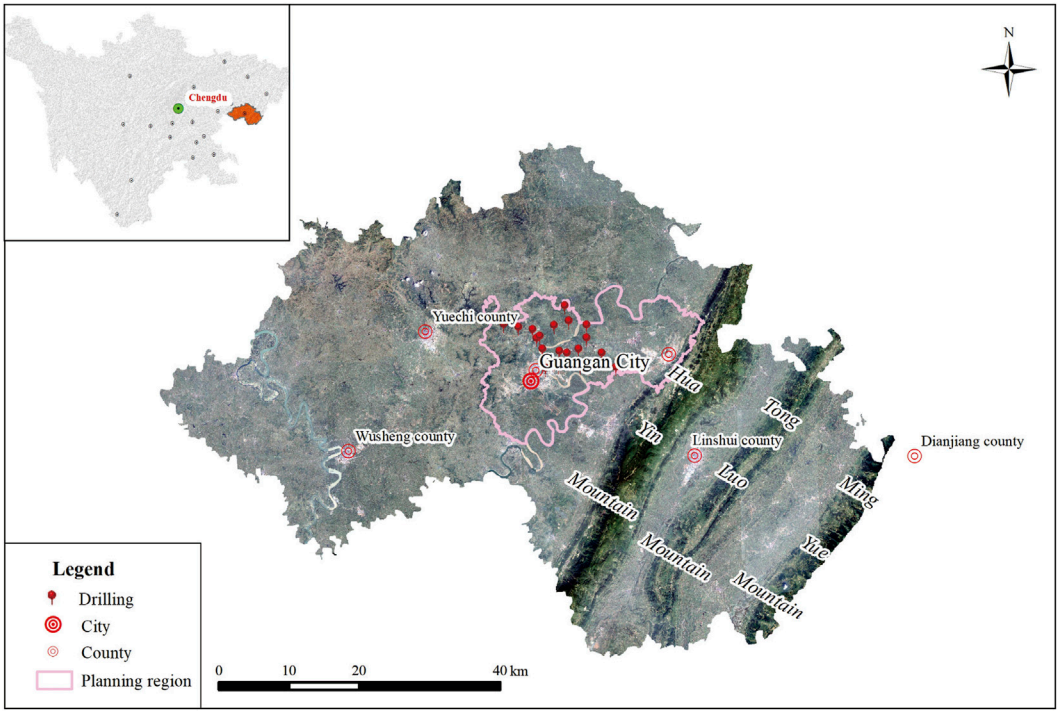

FIGURE 1
Location of study area and distribution of wells.

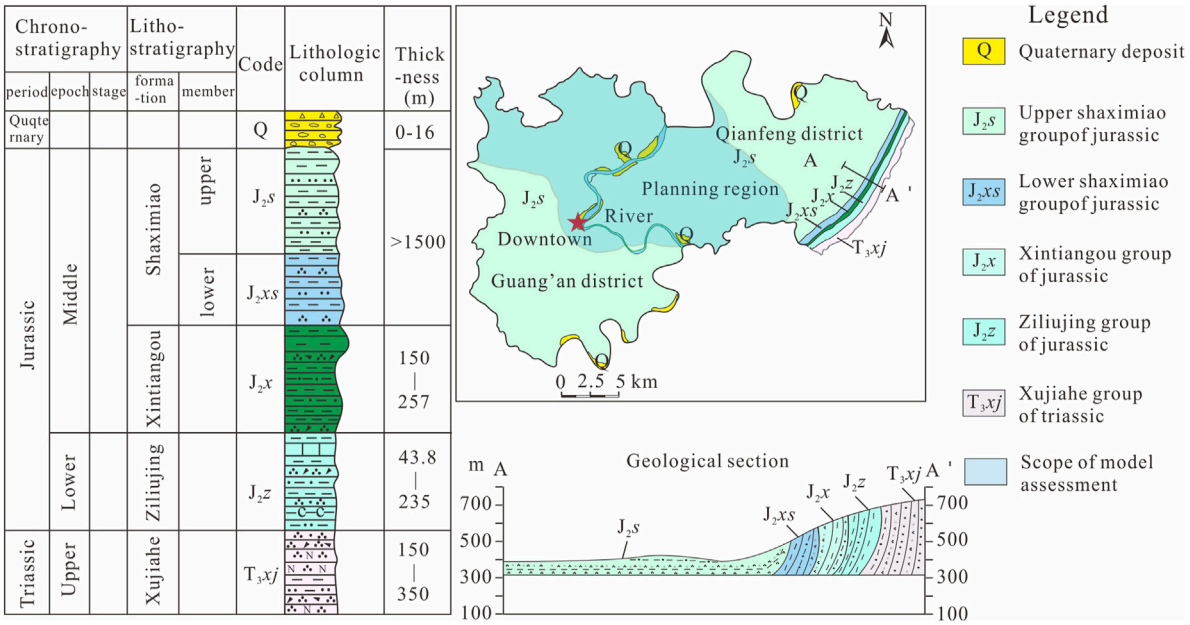

FIGURE 2
Simplify geological map of study area [modified after (Zhou et al., 2022)].

exhibit gentle dip angles ranging from 1 to 5°. The Jurassic Shaximiao Formation (J_2s), which is extensively distributed with a thickness of 400–500 m, displays varying degrees of weathering, ranging from moderate to severe (Zhou et al., 2022). Moreover, approximately 80% of the entire outcrop consists of interlayered and lenticular sand and mudstone (Figure 2).

3 Methodology

3.1 Theory review of k-means

K-means, a prominent exemplar within the spectrum of unsupervised machine learning algorithms, traces its origins to an incipient proposition by Stuart (1982), wherein its conceptualization was envisioned as a mechanism to effectuate signal quantization within the realm of telecommunications. It is of pertinence to highlight that its subsequent rediscovery and consequential propagation within the scientific milieu can be attributed to E. W. Forgy, who independently rekindled the algorithm's conceptual essence in the year 1965.

The fundamental tenet underpinning the K-means algorithm entails the partitioning of a bestowed dataset into a set of K clusters, with K signifying a predetermined numeric value. This partitioning is actualized through the imperative of minimizing the cumulative sum of squared distances, spanning the interrelation between individual data points and their corresponding cluster centroids. The algorithm embarks upon an iterative expedition, which commences with the assignment of each data point to its nearest centroid, subsequently culminating in the recalibration of these centroids, predicated on the arithmetic mean encapsulated within the assortment of data points ascribed to each specific centroid. This iterative voyage persists until such time that the centroids evince nominal displacement, indicative of a state of relative stasis, or alternately, upon the exhaustion of a predetermined threshold pertaining to the maximum number of iterative cycles. Concretely, the algorithm adheres to the following sequential series of steps:

1. Initially, assign the data center vector with an appropriate value based on the data characteristics (assuming an initial setting of K = 3, representing three distinct types) (Eq. 1). In the case of non-numeric data within the dataset, utilize the one-hot encoding technique to initialize the category indicator variable R, ensuring that all data instances are categorized as type 1 (Eq. 2).

$$\boldsymbol{u_k} = \begin{bmatrix} u_{k0} \\ u_{k1} \\ u_{k2} \end{bmatrix} \tag{1}$$

$$R = \begin{bmatrix} r_{00} & r_{01} & r_{02} \\ r_{10} & r_{11} & r_{12} \\ \vdots & \vdots & \vdots \\ r_{N-1,0} & r_{N-1,1} & r_{N-1,2} \end{bmatrix} = \begin{bmatrix} 1 & 0 & 0 \\ 1 & 0 & 0 \\ \vdots & \vdots & \vdots \\ 1 & 0 & 0 \end{bmatrix} \tag{2}$$

Where K is the number of quasi-clustering clusters of the dataset, u_k is the center vector of the cluster, and 0 in u_{k0} indicates the first dimension (attribute).

2. Update data cluster type R in dataset according to the nearest square Euclidean distance between u_k and data (Eqs 3, 4).

$$\|\boldsymbol{x_n} - \boldsymbol{u_k}\|^2 = (x_{n0} - u_{k0})^2 + (x_{n1} - u_{k1})^2 + \ldots + (x_{n,m} - u_{k,m})^2 \tag{3}$$

$$R = \begin{bmatrix} 1 & 0 & 0 \\ 0 & 0 & 1 \\ \vdots & \vdots & \vdots \\ 0 & 1 & 0 \end{bmatrix} \tag{4}$$

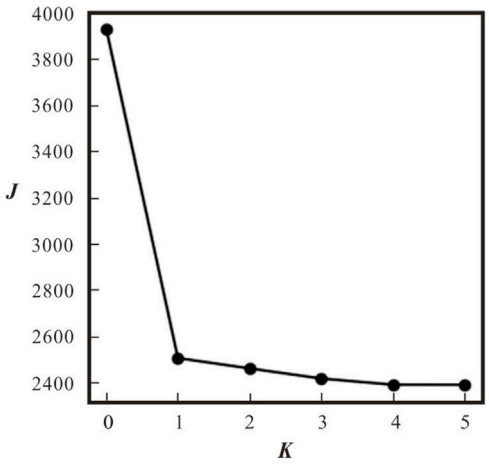

FIGURE 3
Demonstration of loss function (J) calculation results (also known as elbow chart).

Where $\boldsymbol{x_n}$ are dataset matrix, m is the dimensionality of the data (the number of datasets attributes).

3. Update u_k according to R which makes the center of all data points for each cluster is the new u_k (Eq. 5).

$$\boldsymbol{u_k} = \frac{1}{N_k} \sum_{clusterk} \boldsymbol{x_n} \tag{5}$$

4. Repeat steps 2 and 3 until the values of R and u_k no longer change.
5. Calculate the loss function J for evaluating the clustering results using the provided loss measure illustrated in Figure 3 (Eq. 6). This involves computing the sum of the squared Euclidean distances between each data point and its corresponding cluster center u_k.

$$J = \sum_{cluster\,0} \|\boldsymbol{x_n} - \boldsymbol{u_0}\|^2 + \sum_{cluster\,1} \|\boldsymbol{x_n} - \boldsymbol{u_1}\|^2 + \sum_{cluster\,2} \|\boldsymbol{x_n} - \boldsymbol{u_2}\|^2 \tag{6}$$

3.2 Description of cluster dataset

The dataset emanates from engineering geological drilling endeavors undertaken within the chronological span of 2019–2021, encapsulated within the tapestry of the urban planning expanse. A cumulative tally of 29 boreholes stands completed, although their distribution within the study area is characterized by an asymmetric dispersion, prominently accentuated by a concentration bias towards the western terrain, with a meager representation on the eastern facet. The altitudinal and profundity metrics span the spectrum from 409 to 236 m and 120.4 to 50 m, correspondingly. The boreholes were meticulously executed in a vertical trajectory, thereby accommodating comprehensive coring along the entire well section. Notably, the coring extents oscillate within the bounds of 0.3–0.7 m, as delineated in Figure 4. Every distinct section within this vertical continuum

FIGURE 4
Coring samples in the study area **(A)**: upper section, **(B)** bottom section).

manifests as a distinctive datum within the comprehensive dataset. Predicated upon the coring findings in tandem with the geological contextual milieu, the lithological spectrum was systematically categorized into five distinct strata, namely clay, sandstone, mudstone, shaly sandstone, and sandy mudstone. The suite of mechanical experiments concomitant with the coring processes were seamlessly orchestrated by two duly accredited entities, situated within Sichuan and Chongqing correspondingly. Notably, the ambit of mechanical experimentation encompassed tensile strength and shear strength assessments, undertook by the southern construction engineering testing corporation in Chongqing, while the remaining array of attribute experiments were adroitly executed under the aegis of the geological engineering exploration institute corporation in Sichuan. Pertinently, in instances where particular attribute assessments were repeated on a single coring specimen, an average value was judiciously computed to bestow attribute modeling consistency. The comprehensive dataset amalgamates an aggregate of 442 data points, each imbued with an assortment of 9 distinct attributes. The summative statistical portrait of this clustered dataset is comprehensively documented within Table 1.

3.3 K-means cluster

3.3.1 Dataset scaling

As delineated in Tables 1, 2, the nine attributes exhibit conspicuous disparities in scales or magnitudes. This discrepancy can potentially hinder the performance of machine learning algorithms. To address this issue, two distinct feature scaling methodologies emerge as viable remedies: min-max scaling and standard scaling. Min-max scaling transforms the values to a range of 0–1 in the scaled dataset. In contrast, standard scaling does not rescale the values to a specific range like min-max scaling but is less susceptible to the influence of outliers or anomalous data. This characteristic is particularly advantageous when working with large datasets. Therefore, for this study, we have selected the standard scaling method to rescale the datasets (Formula 7).

$$X\_scale = (X\text{-}\bar{X}) / var \tag{7}$$

Where X_scale signifies the scaled dataset, X corresponds to the original dataset, $\bar{X}$ represents the mean value, and "*var*" denotes the variance.

3.3.2 Methods for determining the optimal value of K

The K-means algorithm mandates the *a priori* definition of K for clustering. This value bears substantial significance, exerting considerable impact on the resultant clusters. The discernment of an apt K value assumes paramount importance, given its pivotal role in shaping the ensuing cluster architecture. A misjudged selection of K can culminate in suboptimal clustering outcomes, thereby failing to effectively discern the sought-after cluster delineation. Consequently, the judicious determination of the optimal K value emerges as a pivotal factor in the pursuit of attaining robust clustering results.

For datasets encompassing merely two or three attributes, the determination of the suitable K value, or rather the cluster count, can be gleaned through discerning visual insights from intuitive plots. However, when the attribute count surpasses four, a mathematical methodology assumes precedence in the quest for selecting the appropriate K value. In this context, the inertia (sum squared errors, SSE, formula 8) and silhouette coefficient stand as prominent mathematical instruments employed in the quest to ascertain the optimal K. The inertia, meticulously formulated by Eq. (8), emerges as a statistical metric affording quantification to the extent of variability or dispersion inherently housed within a dataset. It embodies the sum of squared discrepancies between each data point and the mean manifestation of the dataset. In the evaluation of clustering efficacy, should the ascertained K value fall short of the optimal K, an augmentation of K will be mirrored by a pronounced elevation in inter-class aggregation, thereby engendering a commensurate diminution in the inertia value. Once the K value aligns with the optimal quotient, the inertia value stabilizes, exhibiting insubstantial oscillation upon further K escalation. It follows, therefore, that the trajectory of the inertia value plot typically conforms to an "elbow" configuration, and the value at the juncture of this bend is conventionally regarded as the optimal K.

$$\mathrm{SSE} = \sum (X - \bar{X})^2 \tag{8}$$

TABLE 1 Statistics summary of the cluster dataset.

Statistics project	Density (g/cm^3)	Water content (%)	Porosity (%)	Compressive strength (MPa)	Tensile strength (MPa)	Deformation modulus (MPa)	Elastic modulus (MPa)	Poisson ratio (None)	Soften coefficient (None)
Count	442	442	442	442	442	442	442	442	442
mean	2.54	3.61	9.64	16.18	1.37	3103.49	3239.49	0.31	0.37
STD	0.05	0.75	1.67	14.21	0.84	1865.06	1926.69	0.06	0.16
Min	2.44	1.36	4.13	1.03	0.20	420.66	469.53	0.17	0.12
25%	2.50	3.40	9.19	4.93	0.61	1342.14	1403.01	0.27	0.23
50%	2.53	3.83	10.14	11.26	1.22	2664.58	2808.19	0.31	0.33
75%	2.59	4.10	10.75	23.68	1.99	4591.23	4787.69	0.37	0.48
Max	2.65	5.00	12.52	64.13	3.34	7663.39	7878.93	0.42	0.74

TABLE 2 The average sector of each cluster.

Cluster	Average depth (m)	Density (g/cm^3)	Water content (%)	Por (%)	CS (MPa)	Tensile strength (MPa)	Deformation modulus (MPa)	Elastic modulus (MPa)	Poisson ratio (None)	Soften coefficient (None)
0	33.60	2.51	3.82	10.16	18.21	1.79	4082.49	4276.91	0.28	0.41
1	21.25	2.48	4.26	11.08	5.87	0.72	1612.26	1704.99	0.35	0.25
4	41.91	2.51	3.75	9.72	38.35	2.60	5838.12	6052.65	0.23	0.61
2	45.72	2.59	3.65	9.84	5.42	0.61	1443.36	1511.18	0.36	0.24
3	33.71	2.62	1.89	5.84	26.43	1.85	4170.14	4336.31	0.27	0.49

10.3389/fenvs.2024.1335574

However, it should be noted that the inertia method entails a rather coarse estimation for determining the optimal K value. An alternative avenue encompasses the computation of the silhouette coefficient (SC, Eq. 9) across diverse K values. The silhouette coefficient delineates the degree of similitude between a data object and its affiliated cluster as juxtaposed against alternative clusters. Its quantitative manifestation embodies the amalgamation of clustering compactness and inter-cluster separation. This metric, residing within a range spanning from +1 to −1, holds profound explanatory power. A SC value of +1 attests to the coherence of a data point with its corresponding cluster while also highlighting its incongruity with adjacent clusters. In contradistinction, a SC value of 0 bespeaks the proximate alignment of data points with the inter-cluster boundaries. Conversely, a SC value of −1 conveys the misclassification of a data point within an erroneous cluster context.

$$s(i) = (b(i)\text{-}a(i))/\max(a(i), b(i)) \quad (9)$$

Where *s(i)* represents the value of the i-th data point, *a(i)* denotes the average dissimilarity value between i and all data points within its own cluster, *b(i)* signifies the average dissimilarity value between i and all data points within the nearest neighboring cluster, and max (*a(i)*, *b(i)*) conveys the pinnacle of dissimilarity observed between i and any other data point.

To ensure the judicious choice of a clustering outcome, we will employ both the inertia and silhouette coefficient methods. This dual approach seeks to procure a reinforced validation of the optimal K value, thus augmenting the thoroughness of our clustering analysis while elevating its overall reliability.

The dataset underwent clustering using the Python programming language, facilitated by the Scikit-Learn library within the Spyder coding platform. The initialization of dataset centroids was accomplished through the k-means++ algorithm, introduced by David and Sergei (2007). The clustering procedure retained the default parameter settings for all other aspects of the process.

3.4 Principle component analysis (PCA)

Principal Component Analysis (PCA) stands as a widely embraced statistical technique catering to dimensionality reduction and data exploration purposes. It functions as a means to transmute high-dimensional datasets into lower-dimensional renditions, all the while preserving fundamental information. PCA achieves this through the identification of principal components, which are linear amalgamations of the original variables. The fundamental underpinning of PCA lies in discerning the directions, known as principal components, along which data showcases its most pronounced variability. The customary steps associated with PCA encompass the following: ①Computation of the covariance matrix; ②Computation of eigenvectors and eigenvalues; ③Selection of principal components; ④Data projection. For a more comprehensive exposition, the exhaustive inquiry undertaken by Shlens (2014) is recommended as a reference.

4 Results and discussion

4.1 Feature selection

Considering the intrinsic characteristics of the experimental data attributes, a bifurcation into two principal categories is discerned: physical properties and mechanical properties. The former encapsulates density, porosity, and water content, while the latter encompasses compressive strength, tensile strength, deformation modulus, elastic modulus, Poisson's ratio, and softening coefficient. The selection of features for subsequent clustering endeavors is fundamentally anchored in the computation of correlation coefficients between these distinctive attributes (Figures 5, 6).

On the whole, individual mechanical and physical properties manifest a planar distribution concerning depth. The correlation coefficient values span from −0.37 to −0.12 and from 0.2 to 0.29, indicating a lack of pronounced correlation yet revealing distinct zonations. Among these attributes, density can be dichotomized into two classes based on a threshold of 2.55 g/cm3 (refer to Figure 5). The left side is predominantly characterized by sandstone and shaly sandstone, while the right side is predominantly occupied by mudstone and sandy mudstone. This suggests that despite their lithological similarities, these formations exhibit marked divergences in their physical attributes. The categorization of water content, porosity, and mechanical parameters proves to be relatively intricate. Noteworthy is the significant differentiation observed within the mudstone category, particularly between mudstone and sandy mudstone. Additionally, several outliers are evident within the sandstone category, resulting in a classification that intersects between 3 and 4 categories.

Substantial positive or negative correlations are discernible among the mechanical attributes, with correlation coefficient values spanning from −0.86 to −0.97 and 0.86 to 0.99. The demarcation between sandstone and mudstone is distinguishable, although it lacks precise definition (refer to Figure 5). In broad terms, the categorization can be roughly delineated into three classes: ①predominantly consisting of mudstone; ②displaying a mixed composition of shaly sandstone and sandy mudstone; ③primarily composed of sandstone.

The correlation coefficients among the physical parameters manifest noteworthy disparities. The correlation coefficients between density-porosity and density-water content are relatively alike, spanning from −0.64 to −0.67, whereas the correlation coefficient between porosity and water content approaches 1. The correlation coefficient plot within the realm of physical properties exhibits a relatively well-defined boundary, signifying substantial stratification. It can be broadly categorized into 3–4 classes (refer to Figure 5).

In the realm of supervised learning, it is typically advantageous to opt for parameters that demonstrate a strong correlation with the target data, especially for predictive tasks (Yu and Liu, 2003). Conversely, within the domain of unsupervised clustering learning, employing attributes with high correlations for clustering can substantially elevate the influence of correlated features and obscure inherent clusters, particularly in the presence of noisy data (Parsons et al., 2004).

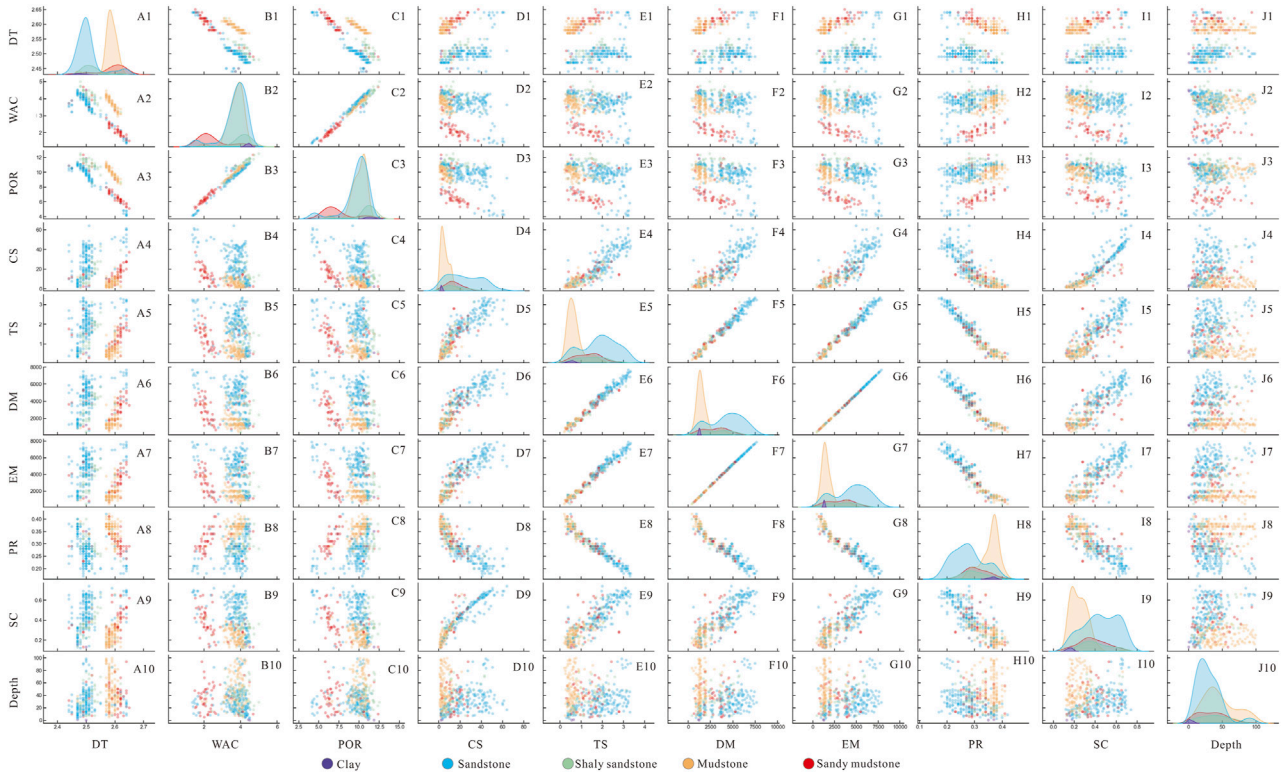

FIGURE 5
The scatter matrix of the 9 attributes. DT-density; WAC-water content; POR-porosity; CS-compressive strength; TS-tensile strength; DM-deformation modulus; EM-elastic modulus; PR-poisson ratio; SC- soften coefficient; Lithos-lithology.

To validate these concepts, we conducted unsupervised clustering using six mechanical attributes. To compare the clustering results of strongly correlated attributes across different values of K (ranging from 2 to 15), we generated an elbow plot and computed the silhouette coefficient values. The clustering results are depicted in Figure 7. Initially, as K increases, the inertia values exhibit a relatively smooth and insignificant variation, lacking a distinct inflection point. This observation suggests that there may not be a definitive optimal value of K. However, the silhouette coefficient consistently decreases as K increases, indicating that with the expansion of K, the boundaries between different clusters tend to blur, resulting in a gradual decline in clustering performance. Consequently, the optimal value of K likely falls within the range of 2–4.

Therefore, we generated parallel coordinate clustering plots for K = 2, 3, and 4 to visually elucidate the actual clustering results (Figure 8). The observations drawn from these plots indicate that, as K increases, the clusters tend to retain approximate parallelism. Specifically, the softening coefficient, which exhibits the lowest correlation coefficient with other mechanical attributes, demonstrates noticeable intersections when K = 4. In contrast, the remaining attributes do not manifest distinct intersections as K increases. This discovery suggests that the choice of K has minimal impact on the clustering results for strongly correlated attributes, posing a challenge in ascertaining an optimal K value. Consequently, it is recommended to consider data merging or dimensionality reduction for strongly correlated attributes before embarking on clustering, as this approach effectively mitigates computational complexity and conserves processing time.

In light of these findings, this study incorporates PCA (Principal Component Analysis) as a dimensionality reduction technique to amalgamate porosity and water content into a singular attribute, while condensing the six mechanical parameters into two attributes. Following this transformation, a new dataset is created, and subspace clustering is subsequently conducted upon it.

4.2 Optimal K

The new dataset is also assessed using inertia and silhouette coefficient plots to ascertain the optimal K value. In the elbow plot, the inertia values span from 300 to 2000, with the point of inflection occurring between 4 and 7, signifying that the optimal K value falls within the range of 4–7 (Figure 9). The silhouette coefficient plot suggests that the ideal range for the optimal K value is between 3 and 7 (Figure 10). Upon closer inspection of the silhouette coefficient plot, when K is set to 6 or 7, clusters with silhouette coefficients near the red line (the average value) indicate blurred boundaries between different clusters. However, when K is set to 4 or 5, the silhouette coefficients for the clusters significantly surpass the average value, indicating strong clustering performance. All things considered, in light of similar conditions, the silhouette coefficient for K = 5 outperforms that for K = 4. Consequently, K = 5 is chosen as the optimal number of clusters for this clustering analysis. This result slightly deviates from the

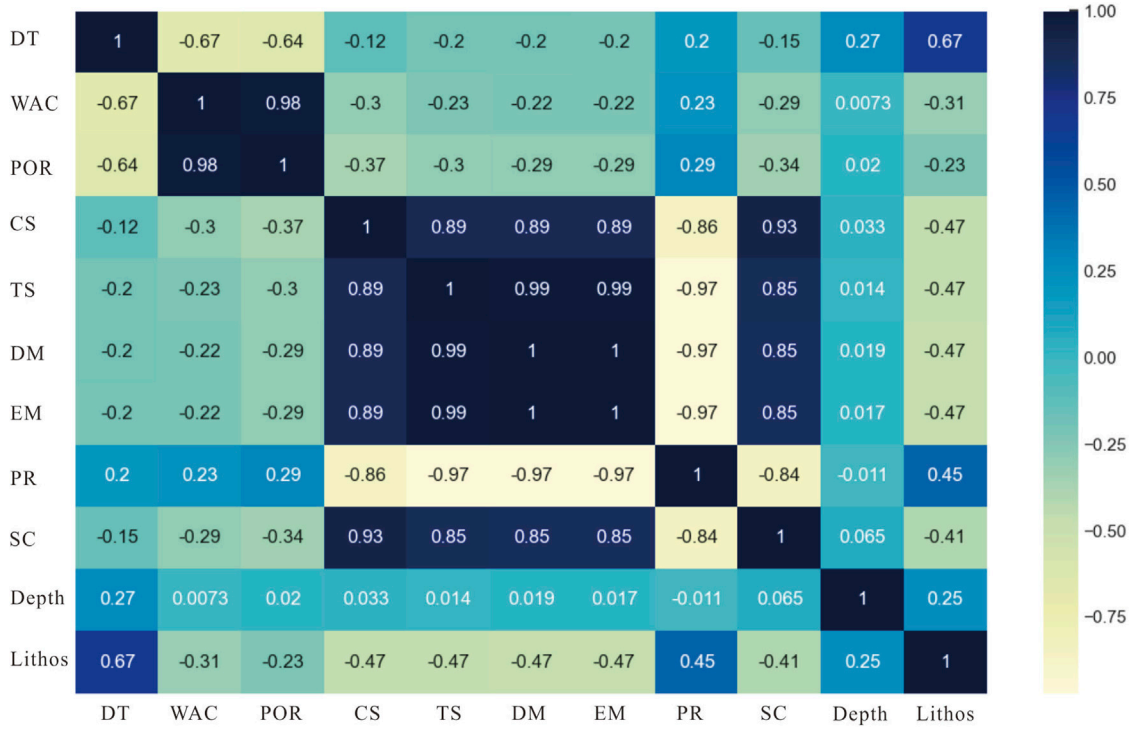

FIGURE 6
Correlation coefficients values of the nine attributes.

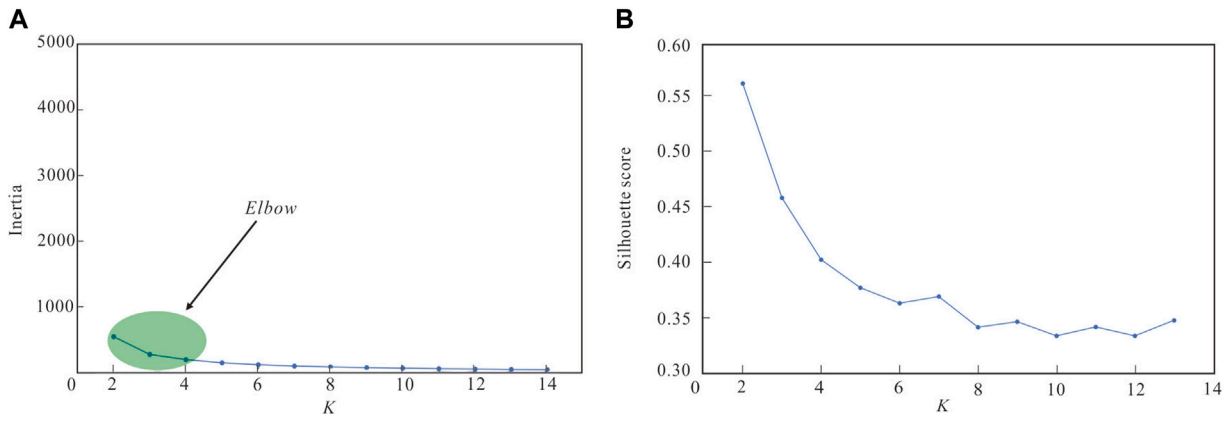

FIGURE 7
Elbow **(A)** and silhouette coefficient **(B)** plots.

suggestion of 2–4 clusters in the correlation coefficient plot, underscoring that the optimal number of clusters in multi-attribute clustering, as determined through data analysis, may exhibit slight variations from the outcomes depicted in intuitive charts and graphs.

4.3 Cluster results

From the clustering outcomes (Figures 11, 12), each cluster demonstrates a predominant rock type, constituting more than 50% of the total data points. Specifically, Cluster 0 (comprising 102 data points), Cluster 1 (consisting of 70 data points), and Cluster 4 (encompassing 72 data points) predominantly consist of sandstone, with no substantial disparities in their overall quantities. In Cluster 4, sandstone constitutes over 93% of the data points, while the remaining 7% are also primarily sandstone. Clusters 0 and 1 both exhibit a composition of over 80% sandstone and shaly sandstone data points, suggesting significant variations in the properties and attributes of sandstone. On the other hand, Cluster 2 (comprising 148 data points) and Cluster 3 (comprising 50 data points) are

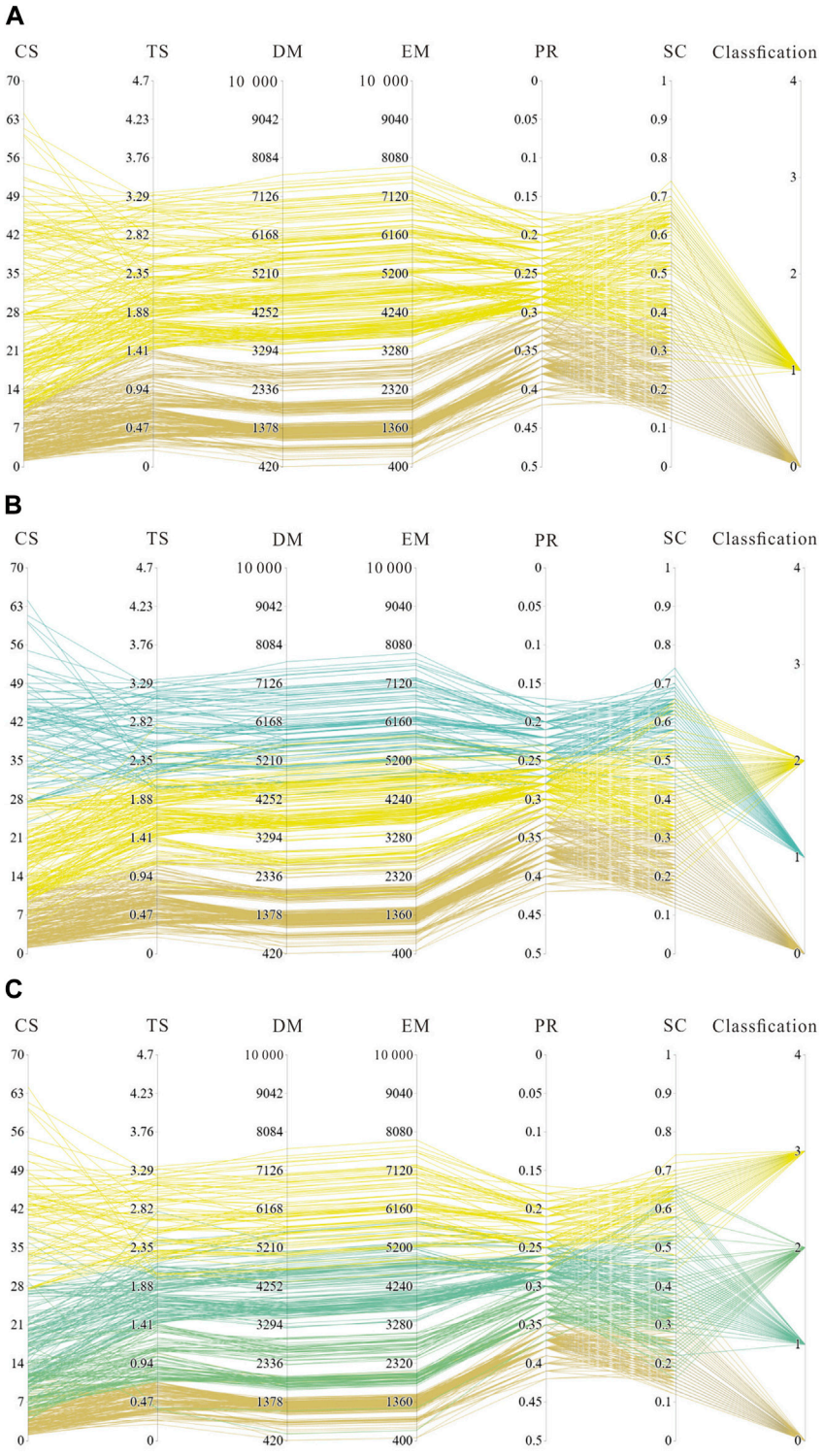

FIGURE 8
Different K **(A)**: K = 2, **(B)** K = 3, **(C)** K = 4) values for parallel parameters.

predominantly composed of mudstone. Cluster 2, in particular, contains over 88% mudstone data points, representing over 95% of the total mudstone category. In Cluster 3, silty mudstone accounts for over 60% of the data points. However, in terms of quantity, Cluster 3 is considerably smaller than Cluster 2, implying that mudstone may not exhibit as substantial variations in properties as sandstone.

Through the computation of mean vectors for the identified clusters (Clusters 0, 1, and 4), it becomes evident that there is no significant disparity in rock density among them. Nevertheless, both

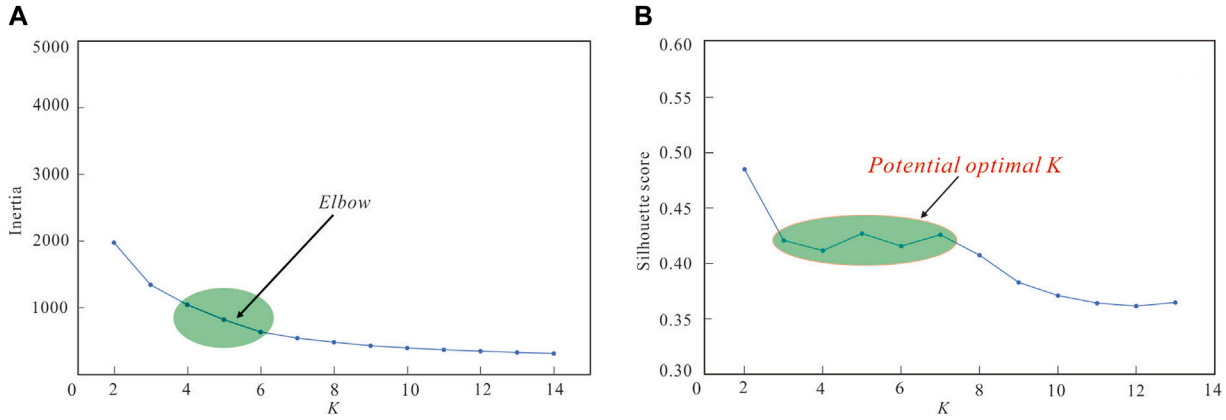

FIGURE 9
Elbow **(A)** and silhouette coefficient **(B)** plots.

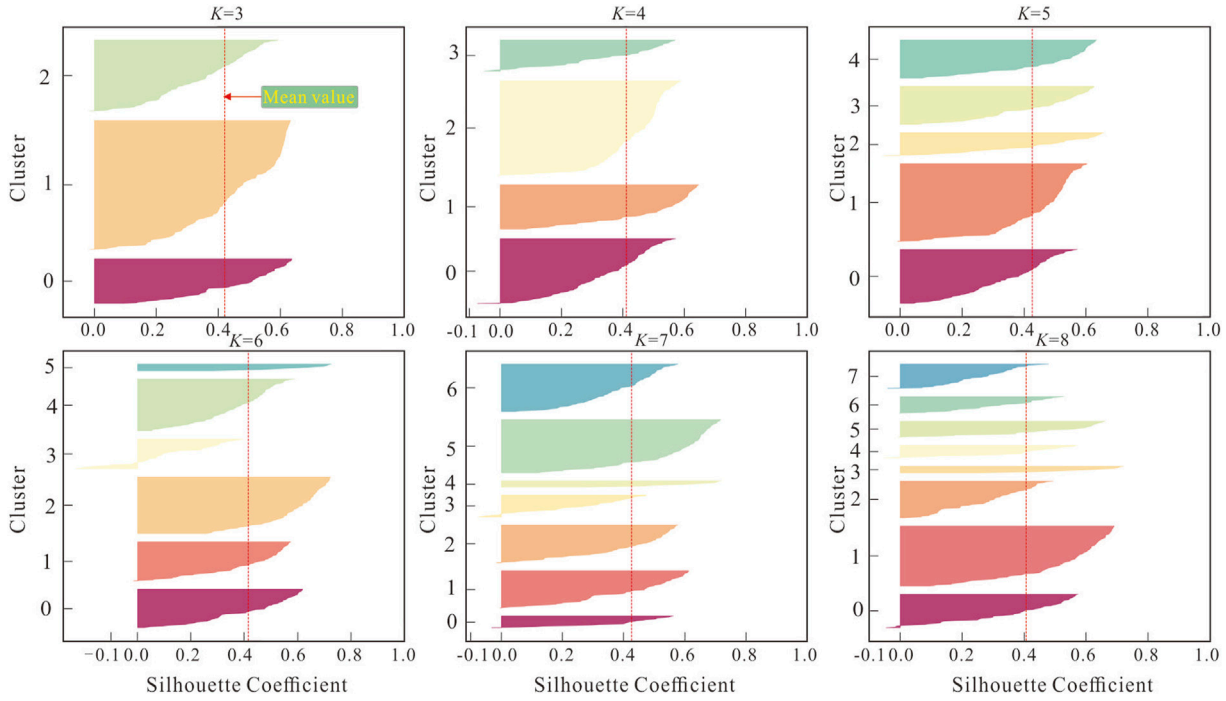

FIGURE 10
Silhouette coefficient plots.

porosity and water content exhibit a discernible trend with depth. Porosity gradually decreases from shallow to deep, following the order of Cluster 1 (11.08%, 21.25 m) < Cluster 0 (10.16%, 33.6 m) < Cluster 4 (9.27%, 41.91 m). Similarly, water content also decreases in the same sequence: Cluster 1 (11.08%) < Cluster 0 (10.16%) < Cluster 4 (9.72%). In parallel, physical parameters (e.g., CS) increase following this order: Cluster 1 (5.87 MPa) < Cluster 0 (18.21 MPa) < Cluster 4 (38.35 MPa).

Based on these observations, we deduce that the primary factor contributing to the differentiation in sandstone properties is the compaction effect. This effect results in reduced porosity, increased rock densification, and consequent alterations in their mechanical parameters. Furthermore, this discovery indirectly validates that clustering algorithms can effectively perform the role of conventional stratigraphic evaluation by identifying property variations within the same rock type at different depths.

On the other hand, there exists a depth discrepancy of 12.1 m and 8.3 m between Clusters 0, 1, and 4, with an average interval of 10.2 m (Table 2). Based on this observation, for urban areas situated in the red bed hilly region, when employing a traditional stratigraphic assessment of rock mass quality, we recommend utilizing a depth interval of 10 m for stratification. Clusters 2 and

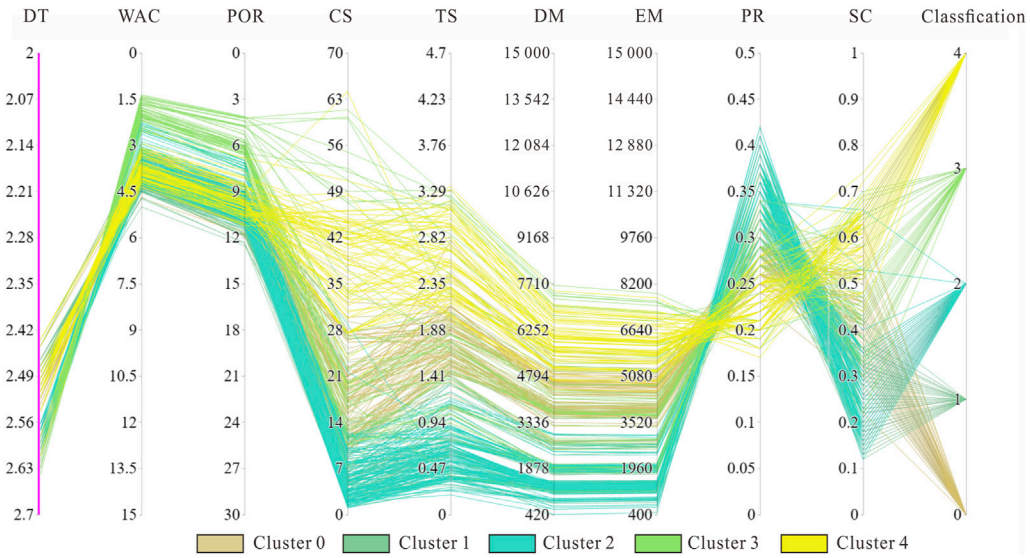

FIGURE 11
Parallel coordinate plot of cluster results, including all attributes (before PCA).

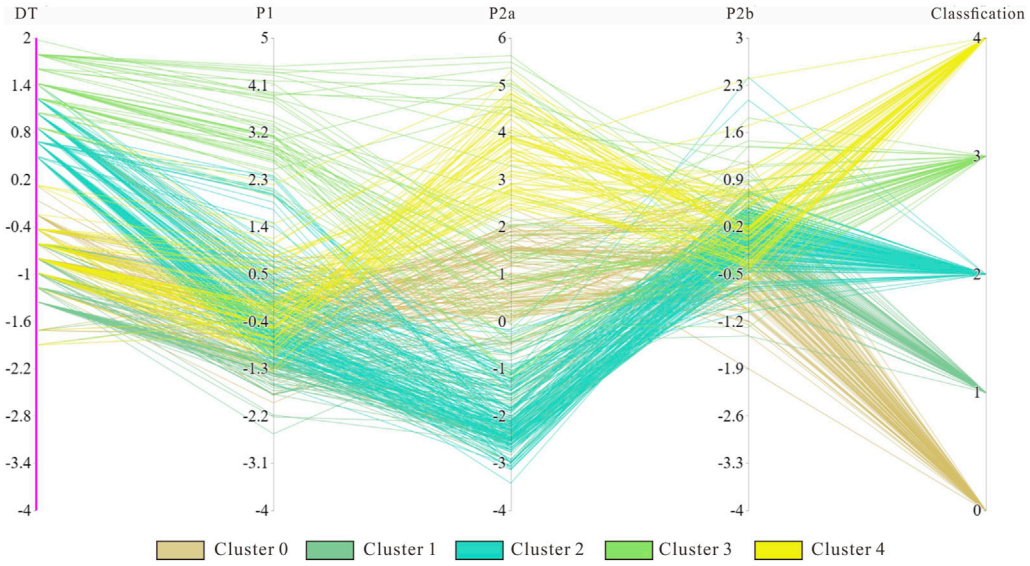

FIGURE 12
Parallel coordinate plot of cluster results (dataset after PCA).

3 also exhibit depth-related trends; however, owing to a substantial shift in their predominant lithology, transitioning from fine-grained sandy mudstone to mudstone, they are not directly comparable.

4.4 Assessment of rock mass

Based on the average vectors of the five clustering results, excluding cluster 3, there is minimal disparity in the physical parameters among the various lithological clusters. Consequently, this study primarily stratifies the rock mass based on the mechanical properties derived from the clustering outcomes. Cluster 4, characterized by pure sandstone, manifests the highest compressive strength, tensile strength, and deformation modulus, positioning it as the category with relatively superior rock mass quality within the study area. Clusters 1 and 2, possessing comparable overall physical and mechanical parameters but the lowest compressive strength, are categorized as having relatively inferior quality within the study area. Clusters 0 and 3, due to significant lithological distinctions leading to substantial variations

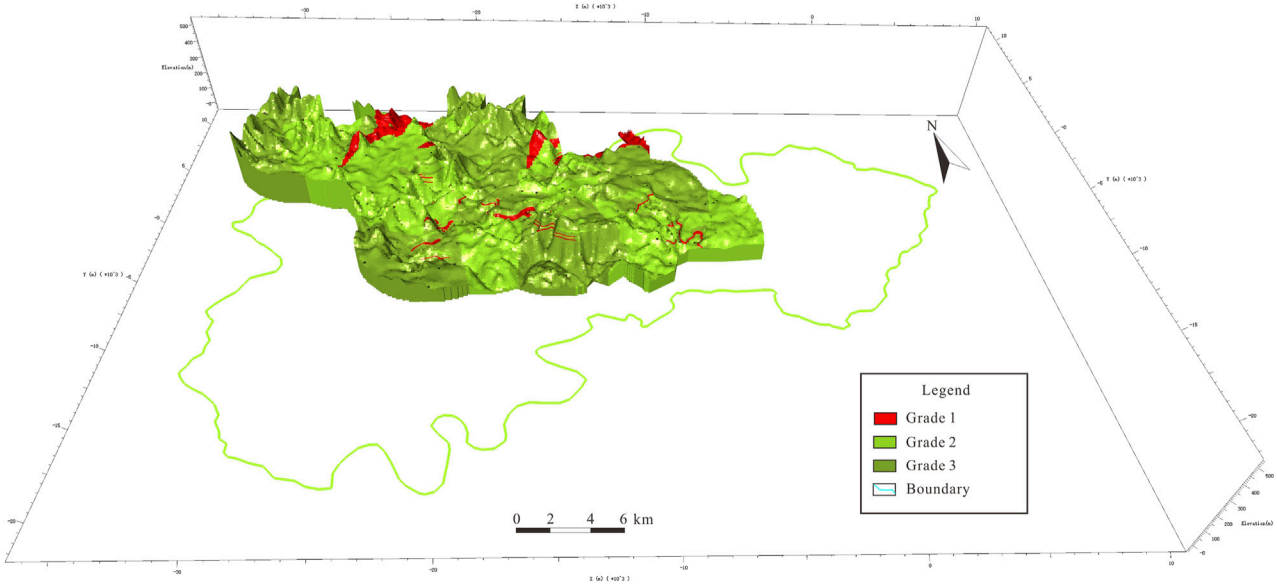

FIGURE 13
3D model of assessment results using kriging interpolation.

in physical parameters, exhibit minor deviations in the mean values of the mechanical parameters, and are classified as intermediate categories in terms of rock mass quality. Consequently, grounded in the clustering results, the rock mass quality in the study area is stratified into three levels: cluster 4 (optimal, grade 1) → clusters 0 and 3 (relatively good, grade 2) → clusters 1 and 2 (ordinary, grade 3).

Furthermore, cluster 1 is predominantly characterized by sandstone, whereas cluster 2 is primarily composed of mudstone. Despite substantial distinctions in lithology and depth between these two clusters, their values for the nine attributes exhibit relatively minor fluctuations. This implies that in the red bed hilly region, there might not be a substantial correlation between rock mass quality and either depth or lithology. This suggests that the conventional stratified approach may not be imperative for rock mass quality assessment in this context.

Based on the clustering outcomes, we constructed a three-dimensional geological model of the study area for in-depth exploration. Utilizing indicator kriging interpolation, we obtained a grade distribution model for the rock mass quality assessment of the study area (Figure 13). However, due to data concentration in the central region, the kriging interpolation results were limited to this area, leaving peripheral zones with sparse interpolated data. The model indicates that Grade 1 represents 6.4%, Grade 2 comprises 50.8%, and Grade 3 constitutes 42.8% of the total. Grade 1 displays a scattered distribution, primarily concentrated in the northern part of the study area, while Grade 2 and 3 exhibit an interactive distribution covering a significant portion of the area. In summary, the rock mass quality across the entire study area generally falls within the relatively good to ordinary range. Considering other assessment factors, this dataset serves as essential reference information for the comprehensive evaluation of underground space suitability in this region.

5 Conclusion

The current investigation applied an unsupervised clustering algorithm, K-means, coupled with PCA dimensionality reduction, to appraise the geotechnical quality of a representative urban zone within the red-bed hilly region. This strategy proficiently alleviated the impact of subjective variables on the evaluation outcomes, consequently attaining a heightened level of objectivity in the assessment. The particular conclusions are delineated as follows:

1. The engineering geological drilling core test data from Guang'an City were categorized into five clusters, and the geotechnical quality was stratified into three levels. Cluster 4 signifies the highest quality (Level 1), primarily consisting of pure sandstone, while clusters 0 and 3 denote a relatively favorable quality (Level 2) characterized by the prevalence of sandstone. Conversely, clusters 1 and 2 signify the lowest quality (Level 3), predominantly comprised of mudstone. The classification order is as follows: Cluster 4 (optimal, grade 1) → Clusters 0 and 3 (relatively good, grade 2) → Clusters 1 and 2 (ordinary, grade 3). And the entire study area generally falls within the relatively good to ordinary range.
2. The clustering results suggest that there is relatively minor variation in the physical properties among distinct clusters, whereas there is substantial variation in the mechanical properties. Consequently, it is advisable to consider compressive strength and the softening coefficient as representative physical properties indicators for assessing rock mass quality.
3. Within the red-bed hilly regions, there appears to be no notable correlation between rock mass quality and depth. Therefore, it is recommended to evaluate the underground space rock mass as a unified entity. Nonetheless, for those employing the

classical stratified evaluation method, a stratification interval of 10 m is suggested.

Data availability statement

The data that support the conclusion of this study are available from corresponding author upon reasonable request. Due to privacy concerns, certain restrictions may apply to the availability of these data.

Author contributions

FZ: Conceptualization, Writing–original draft. HL: Formal Analysis, Methodology, Writing–review and editing. TL: Data curation, Writing–review and editing. ML: Data curation, Writing–review and editing. JZ: Supervision, Writing–review and editing. BW: Investigation, Writing–review and editing. MH: Writing–review and editing.

Funding

The author(s) declare financial support was received for the research, authorship, and/or publication of this article. This work was financially supported by the China Geological Survey projects "Shale gas investigation and evaluation in key basins" (DD20221661); "China-ASEAN geo-information big data platform construction" (DD20230577).

Acknowledgments

We gratefully acknowledge architecture archives of Guang'an city for providing the resources and support. And we also would like to express our gratitude for contents revised suggestions from reviews and editor.

Conflict of interest

The authors declare that the research was conducted in the absence of any commercial or financial relationships that could be construed as a potential conflict of interest.

Publisher's note

References

Andriamamonjisoa, S. N., and Hubert, F. A. (2019). Combining geology, geomorphology and geotechnical data for a safer urban extension: application to the antananarivo capital city (Madagascar). *J Afr. Earth Sci.* 151, 417–437. doi:10.1016/j.jafrearsci.2018.12.003

David, A., and Sergei, V. (2007). K-means++: the advantages of careful seeding. in *Proc of the 18th annu ACM-SIAM symp on discrete algorithms*, 1027–1035.

Du, X., Sun, Y. F., Dong, J., Wang, Q., Song, Y. P., Su, Z. M., et al. (2022). Assessment and subdivision of environmental suitability for submarine engineering in the jiaozhou bay by unsupervised machine learning. *Oceanol. limnologia sinica* 53 (4), 972–980. doi:10.11693/hyhz20210900206

El, M. M., Dlala, M., and Chenini, I. (2010). Urban geological mapping: geotechnical data analysis for rational development planning. *Eng. Geol.* 116 (1-2), 129–138. doi:10.1016/j.enggeo.2010.08.002

Forgy, E. W. (1965). Cluster analysis of multivariate data: efficiency vs interpretability of classifications. *Biometrics* 21, 768–780.

Ge, W. Y., Wang, R., Zhang, Q., Xing, H. X., and Zhou, J. (2021). Conception of comprehensive utilization evaluation of urban underground space resources. *Geol. Bull. China* 40 (10), 1601–1608. doi:10.12097/j.issn.1671-2552.2021.10.001

Hu, Z. P., Peng, J. B., Zhang, F., Wang, R., and Chen, N. N. (2019). The critical issues and creative concepts in the development of urban underground space. *Earth Sci. Front.* 26 (3), 76–84. doi:10.13745/J.esf.2019.03.009

Lapenna, V., Chambers, J., Shi, B., Lienhart, W., and Zhu, H. H. (2020). Preface to the special issue on "Frontiers and applications of geological engineering and geophysical monitoring technologies in urban areas". *Eng. Geol.* 268, 105508. doi:10.1016/j.enggeo.2020.105508

Li, P. Y., Han, H. D., Wang, D. H., and Wang, C. S. (2021). Current situation and development trends of suitability evaluation of urban underground space resources. *Sediment Geol. Tethyan Geol.* 41 (1), 121–128. doi:10.19826/j.cnki.1009-3850.2020.11004

Li, S., Hong, Z. L., Xue, X. P., Liu, X. F., and Shi, W. (2023). Comprehensive evaluation of the underground space resources in Xianyang city. *Sci. Rep.* 13, 17348. doi:10.1038/s41598-023-44657-8

Li, X. (2020). *Evaluation of the suitability for urban underground space resources development using GIS*. Dalian: Dalian University of Technology. [dissertation/master's thesis].

Pan, M., and Jin, J. J. (2006). Urban geology and prospects of its development. *Urban Geol.* 1 (1), 5–9. doi:10.3969/j.issn.1007-1903.2006.01.003

Parsons, L., Haque, E., and Liu, H. (2004). Subspace clustering for high dimensional data: a review. *ACM SIGKDD Explor Newsl.* 6 (1), 90–105. doi:10.1145/1007730.1007731

Peng, F. L., Qiao, Y. K., Cheng, G. H., and Zhu, H. H. (2019). Current situation and exsiting problems of and coping strategies for urban underground space planning in China. *Earth Sci. Front.* 26 (3), 57–68. doi:10.13745/j.esf.sf.2019.5.23

Peng, J. W., and Peng, F. L. (2012). Utilization of deep underground space in Japan and its enlightenment for Chinese city. *Chin J Undergr Sp Eng.* 8 (S1), 1341–1343. doi:10.3969/j.issn.1673-0836.2012.z1.002

Qian, Q. H. (2019). Scientific use of the urban underground space to construction the harmonious livable and beautiful city. *Hazard Control Tunn Undergr Eng* 1 (1), 1–7.

Qu, H. G., Pan, M., Liu, X. Q., and Yu, C. L. (2015). Urban 3D geological modeling and its application to urbanization. *Geol. Bull. China* 34 (7), 1350–1358. doi:10.3969/j.issn.1671-2552.2015.07.013

Shlens, J. (2014). *A tutorial on principal component analysis*. San Diego La Jolla: University of California. http://www.snl.salk.edu/~shlens/pca.pdf/ (Accessed April 3, 2014).

Stuart, P. L. (1982). Least squares quantization in PCM. *IEEE Trans. Inf. Theory* 28, 129–137. doi:10.1109/tit.1982.1056489

Tan, F., Wang, J., Jiao, Y. Y., and Ma, B. C. (2021). Current situation and development of urban underground space suitability evaluation. *Earth Sci.* 46 (5), 1896–1908. doi:10.3799/dqkx.2020.155

Tang, X., Gong, X. L., Xu, S. G., Zhang, Q. Q., Guo, H., and Deng, F. L. (2022). Development and utilization of urban underground space resources and geological survey countermeasures in southern Jiangsu metropolitan area. *Geol. Rev.* 68 (2), 593–605. doi:10.16509/j.georeview.2021.12.125

Tao, Z., Zhu, C., He, M. C., and Murat, K. (2021). A physical modeling-based study on the control mechanisms of Negative Poisson's ratio anchor cable on the stratified toppling deformation of anti-inclined slopes. *Int. J. Rock Mech. Min.* 138, 104632. doi:10.1016/j.ijrmms.2021.104632

Tian, C., Su, J. W., Ni, H. Y., and Wang, R. (2021). Progress and prospect of urban underground space resources evaluation. *East China Geol.* 42 (2), 147–156. doi:10.16788/j.hddz.32-1865/P.2021.02.003

Tong, D. F., Tan, F., Ma, B. C., Jiao, Y. Y., and Wang, J. (2022). A suitability evaluation method of urban underground space based on rough set theory and conditional entropy: a case study in wuhan changjiang new town. *Appl. Sci.* 12 (3), 1347. doi:10.3390/app12031347

Wang, B. (2013). *Exploration and practice of the development and utilization of urban underground space*. Beijing: China university of Geosciences.

Wang, M. L., Wang, H. X., Feng, Y., He, Y. Z., Han, Z., and Zhang, B. (2022). Investigating urban underground space suitability evaluation using fuzzy c-mean clustering algorithm-a case study of huancui district, Weihai city. *Appl. Sci.* 12 (23), 12113. doi:10.3390/app122312113

Wei, X. J., Fu, B., Deng, X. L., and Wang, Z. L. (2017). The risk evaluation on geological hazards assessment in Guang'an urban overall plan areas. *J Changchun Inst Technol Nat Sci Ed.* 18 (2), 110–116. doi:10.3969/j.issn.1009-8984.2017.02.026

Wu, X. Z. (2021). Study on assessment of urban underground space resources in Wuhu City. *Chin J Undergr Sp Eng.* 17 (1), 9–18.

Xiong, J. X., Ni, S. J., Zhang, C. J., Ding, J., and Wei, L. W. (2006). The design and implementation of the GIS software for risk assessment of urban geo-environments. *Sediment Geol. Tethyan Geol.* 26 (2), 106–109. doi:10.3969/j.issn.1009-3850.2006.02.021

Yu, L., and Liu, H. (2003). Feature selection for high-dimensional data: a fast correlation-based filter solution. Machine Learning. *Proc Twent Int. Conf.* 2, 856–863.

Yuan, X. R. (2020). *Research on evaluation of geological environment suitability of urban underground Facilities*. Beijing: Beijing University of Civil Engineering and Architecture.

Zhang, X. B., Wang, C. S., Fan, J., Wang, H. J., and Li, H. L. (2020). Optimizing the analytic hierarchy process through a suitability evaluation of underground space development in tonghu district, Huizhou city. *Energies* 13 (3), 742. doi:10.3390/en13030742

Zhang, Y. H., Dai, Y. S., Wang, Y., Huang, X., Xiao, Y., and Pei, Q. M. (2021a). Hydrochemistry, quality and potential health risk appraisal of nitrate enriched groundwater in the Nanchong area, Southwestern China. *Sci. Total Environ.* 784, 147186. doi:10.1016/J.Scitotenv.2021.147186

Zhang, Y. H., He, Z. H., Tian, H. H., Huang, X., Zhang, Z. X., Liu, Y., et al. (2021b). Hydrochemistry appraisal, quality assessment and health risk evaluation of shallow groundwater in the mianyang area of sichuan basin, Southwestern China. *Environ. Earth Sci.* 80 (17), 576–592. doi:10.1007/S12665-021-09894-Y

Zhao, S. C., Xu, B., Li, X. J., Zhang, W. B., and Liu, B. L. (2022). 3D evaluation of suitability of underground space development in core areas of mountainous cities. *J Tongji Univ. Sci.* 50 (1), 70–78. doi:10.11908/j.issn.0253-374x.20489

Zhao, Y. T., Liu, H. H., Qu, W. L., Luan, P. Y., and Sun, J. (2023). Research on geological safety evaluation index systems and methods for assessing underground space in coastal bedrock cities based on a back-propagation neural network comprehensive evaluation–analytic hierarchy process (BPCE-AHP). *Sustainability* 15 (10), 8055. doi:10.3390/su15108055

Zhou, B., Gui, Y. B., Xie, X. Y., Li, W. S., and Li, Q. (2022a). A measurable evaluation method of visual comfort in underground space by intelligent sorting and classification algorithms. *Undergr. Sp.* 7 (3), 453–464. doi:10.1016/j.undsp.2021.10.004

Zhou, D. K., Li, X. Z., Wang, Q., Wang, R., Wang, T. D., Gu, Q., et al. (2019). GIS-based urban underground space resources evaluation toward three-dimensional land planning: a case study in Nantong, China. *Tunn Undergr Sp Technol* 84, 1–10. doi:10.1016/j.tust.2018.10.017

Zhou, F., Li, M. H., Huang, C. J., Liang, H., Liu, Y. J., Zhang, J. L., et al. (2022b). Lithology-based 3d modeling of urban geological attributes and their engineering application: a case study of Guang'an city, SW China. *Front. Earth Sci* 10, 918285. doi:10.3389/feart.2022.918285

Zhou, F., Li, M. H., Huang, C. J., Liu, Y. J., Zhang, J. L., Wang, B. D., et al. (2023). Modeling of urban geological attributes based on conditional simulation: a case study of Guang'an City. *Sediment Geol. Tethyan* 43 (4), 844–855. doi:10.19826/j.cnki.1009-3850.2022.06002

Zhu, C., He, M. C., Murat, K., Cui, X. B., and Tao, Z. G. (2020). Investigating toppling failure mechanism of anti-dip layered slope due to excavation by physical modelling. *Rock Mech. Rock Eng.* 53 (11), 5029–5050. doi:10.1007/s00603-020-02207-y

Zhu, C., He, M. C., Murat, K., Zhang, X. H., and Tao, Z. G. (2021). Numerical simulations of the failure process of anaclinal slope physical model and control mechanism of negative Poisson's ratio cable. *Bull. Eng. Geol. Environ.* 80, 3365–3380. doi:10.1007/s10064-021-02148-y

frontiers | Frontiers in Environmental Science

TYPE Original Research
PUBLISHED 05 April 2024
DOI 10.3389/fenvs.2024.1338016

OPEN ACCESS

EDITED BY
Yunhui Zhang,
Southwest Jiaotong University, China

REVIEWED BY
Yubing Liu,
China University of Mining and Technology, China
Xiaoping Zhou,
Chongqing University, China

*CORRESPONDENCE
Nengpan Ju,
jnp@cdut.edu.cn

RECEIVED 14 November 2023
ACCEPTED 18 March 2024
PUBLISHED 05 April 2024

CITATION
Zhou X, Ju N, Cai J, He C, Wang J, Wang H and Liu R (2024), Damage creep model of viscoelastic rock based on fractional derivative and experimental verification.
Front. Environ. Sci. 12:1338016.
doi: 10.3389/fenvs.2024.1338016

Damage creep model of viscoelastic rock based on fractional derivative and experimental verification

Xin Zhou[1], Nengpan Ju[1]*, Junchao Cai[2], Chaoyang He[1], Jue Wang[3], Hao Wang[1] and Ruiting Liu[1]

[1]State Key Laboratory of Geohazard Prevention and Geoenvironment Protection, Chengdu University of Technology, Chengdu, Sichuan, China, [2]School of Civil Engineering, Henan University of Science and Technology, Luoyang, China, [3]Changjiang Geotechnical Engineering Co., Ltd., Wuhan, Hubei, China

Exploring the creep law of sandstone provides a theoretical basis for evaluating the long-term stability of geotechnical engineering projects in red beds. Based on a conventional triaxial test of sandstone, a progressive loading triaxial creep test is conducted. The deformation characteristics and laws of each sample in different deformation stages are summarized, and the laws relating steady creep rate, stress and time are analyzed. On this basis, a nonlinear viscoelastic–plastic creep model based on fractional derivative theory and damage theory is established. According to the nonlinear fitting results, the parameter sensitivities are analyzed. The results verify the rationality of the model; this model has a good fitting effect for each creep deformation stage, especially for the accelerated creep stage. The constitutive relationship of the model is simple, clear and easily applicable. The research results provide a reference for studying the long-term stability of geotechnical engineering projects.

KEYWORDS

sandstone, creep test, rock damage, fractional class derivative, accelerated creep

1 Introduction

Rocks are divisible into soft and hard rocks according to their strength characteristics. Soft rock is the most widely distributed rock type, and it is most closely related to human engineering activities (Liu et al., 2023). Soft rock has low strength and shows great rheological properties (Sun, 2007), severely affecting the long-term safety performance of the project. The creep behavior of rock is directly related to the long-term stability of rock slopes and rock engineering activities; additionally, this behavior is an important basis for evaluating the long-term stability of the rock (Yang et al., 2014; Deng et al., 2016; Wang et al., 2018a). Creep is a key mechanical behavior of rock, and it is an important foundation for studying the long-term stability of rock engineering projects (Xu et al., 2004; Chang et al., 2015; Wang et al., 2018a). There are significant differences in the mechanical properties of rocks under different saturated conditions. Sandstone is one of the main rock types in the China red bed area, and it is one of the most extensive strata in the China branch. This kind of stratum is considered prone to landslides (Li et al., 2004), and many red bed landslides (Tang et al., 2015; Hu et al., 2017; Zhang et al., 2018) have developed in the Yangtze River basin. Wang et al. (Wang et al., 2017) found that the strength of sandstone in a saturated state is 40% higher than that under dry conditions. Song et al. (Song et al., 2015)

conducted triaxial creep tests on carbonaceous slate and found that under the same stress conditions, the strain value of saturated rock is much larger than that of dry rock.

Many researchers have explored a suitable rock rheological model to describe creep characteristics (Jiang et al., 2018). To date, the commonly used creep models include Maxwell, Kelvin, and Burgers. These models have clear physical definitions and intuitive concepts; however, they must combine more components to meet the experience requirements (Li and Chao, 2014; Luo et al., 2018). This kind of model is generally composed of several mechanical elements in different manners, such as Hooke's spring body and Newton's damping body. Based on traditional component models, many scholars have established optimized constitutive models by introducing new theories and methods, such as damage mechanics and fractional derivatives. According to Wang's concepts of damage and damage acceleration, a constitutive equation (Wang, 2004) is proposed that describes the whole process creep curve of rock. Yang et al. conducted creep tests and theoretical research on the creep characteristics of frozen sand (Yang et al., 2010). Zhou et al. replaced the Newton body in a traditional Xiyuan model with an Abel body and established a new time-based fractional derivative creep constitutive model (Zhou et al., 2018). Wang et al. established the Xiyuan creep constitutive model (Wang et al., 2018b) based on the damage mechanism through creep tests of granite at different temperatures. Zhou et al. used the fractional derivative viscoelastic Kelvin model to describe the creep characteristics of different soft soils and achieved remarkable results (Zhu et al., 2017). Hou et al. suggested that in the nonlinear rheological process of rock, there is a nonlinear functional relationship between the viscosity coefficient and the rheological time and stress level (Hou et al., 2018). Zhou et al. introduced a fractional derivative to describe its constitutive characteristics (Zhou et al., 2018) in salt rock creep tests. Wu improved the Maxwell creep model by introducing a variable fractional derivative (Wu et al., 2015).

In summary, studying rock creep characteristics and constitutive models remain important research topics. Based on a triaxial creep test of sandstone, with the advantages of the fractional derivative creep model and damage theory, a new creep constitutive model is proposed with the characteristics of a simple structure and clear physical parameter definitions. By fitting the test results, the parameters of the creep model are determined. In addition, the triaxial creep law of sandstone is systematically analyzed in this paper; the deformation characteristics of each stage of the rock creep test curve and the relationship between the strain rate and stress level are discussed. This creep model accurately describes the creep characteristics of different stress conditions and creep deformation stages throughout the process and provides an important basis for research in the field of rock creep.

2 Triaxial creep test of rock

2.1 Preparation of rock samples and test instruments

Sandstone is processed into a standard cylinder sample with a diameter of 50 mm and a height of 100 mm according to International Society for Rock Mechanics and Rock Engineering (ISRM) standards (Zhang and Zhou, 2020). As shown in Figures 1, 2, deviations in diameter and height should be controlled within 0.3 mm, and the deviations of both ends should be controlled within 0.05 mm to minimize the end effects. The method of graded loading is adopted to load the sandstone test. First, a triaxial creep test is conducted to confirm the conventional triaxial compressive strength of rock. According to the failure strengths of sandstone under different confining pressures, the conventional triaxial strength obtained is multiplied by an empirical coefficient of 0.8 as the predicted long-term strength. Then, the predicted long-term strength is divided into several grades, and the creep test is conducted through graded loading. The computer control system is used to collect the time and strain data during the test. Before the test, the samples are wrapped with preservative film and held at a constant temperature of 22°C to prevent the influences of air temperature and humidity changes on the samples.

The test device is a ysj-01-00 rock triaxial creep testing machine, as shown in Figure 1. The system is used for conventional triaxial tests, triaxial rheological tests and uniaxial compression tests. The instrument is controlled by a computer and powered by electricity, gas and liquid. The instrument controls the confining pressure, axial load and axial displacement. The confining pressures are 0–3 30 MPa, and the axial loads are 0–11,000 kN. The accuracies of confining pressure and axial load are 0.5% F.S.

2.2 Creep test procedure

To improve the test efficiency, a load mode of step loading was adopted. The strength of the sample was comprehensively determined according to the results of the conventional triaxial test. The loading curve and stress characteristics are shown in Figure 3. The sample numbers were B-1, B-2 and B-3, and the confining pressure values were 5 MPa, 10 MPa and 15 MPa, respectively. The specific test steps were as follows:

(1) The prepared samples were wrapped with preservative film to prevent water loss. The samples were removed when the test began. When removing the fresh-keeping film, shaking was avoided.
(2) The sample was removed and the preservative film was removed; additionally, the sample was placed in a heat shrinkable sleeve and the upper loading end and the lower loading end of the test device were inserted into the heat shrinkable sleeve. The sample was placed vertically on a horizontal table top after contacting the loading end, and then the loading end was slowly adjusted to make a contact surface from two better contacts and alignments.
(3) A high-power hot air blower was used to blow out hot air from bottom to top, and the hot air shrink tube gradually shrunk. During the blowing process, the blower was screwed and the sample did not move. The shrinkage of each heat shrinkable tube should be reduced as much as possible to place all parts under uniform stress. This method could effectively reduce the error caused by the later loading test.
(4) The initial loading sample was loaded into the middle of the base of the confining pressure cylinder, and then the lower

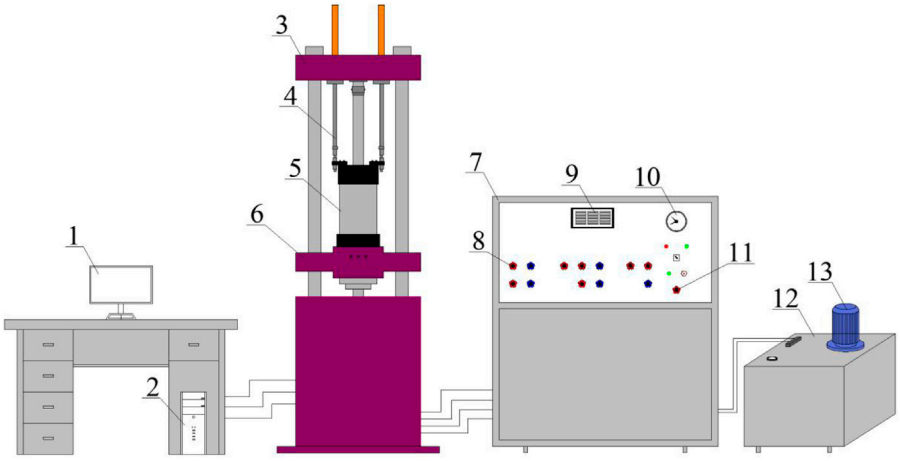

1-color data display 2-Data collection host 3-Texting machine 4-Confining cylinder lifting device 5- Confining pressure cylinder 6- Axial displacement console 7-Control box 8- Hydraulic manual control device 9- Equipment control 10- Hydraulic indicator 11-Eemergency stop push button 12- Hhydraulic fluid chamber 13-Pressurizer motor

FIGURE 1
Load testing system.

FIGURE 2
Experimental setup of the long-term creep test.

loading end was rotated to optimize the contact surface between the lower loading end and the base. After adjusting the position and installation, the upper loading end was manually controlled to move down slowly to preload the sample. The load value was preset as 0.1 According to the preset value of confining pressure, a computer was used to control the loading of confining pressure.

(5) The axial load control mode was adjusted to the load mode with a loading speed of 0.1 MPa/s, and then the axial load value was preset. The control mode was adjusted from manual mode to computer automatic control, and the load recording time interval was 1 min. Furthermore, the axial load was slowly loaded to the preset value and remained constant.

(6) After the axial strain of each stage of loading was basically stable, the computer was controlled to conduct the next stage of loading, and the loading time of each stage was not less than 72 h. The specimens were subjected to progressive cyclic loading until failure.

2.3 Test results and analysis

The test curve is obtained by the triaxial compression creep test, as shown in Figure 4. The B1 sample lasts 480 h, the B2 sample lasts

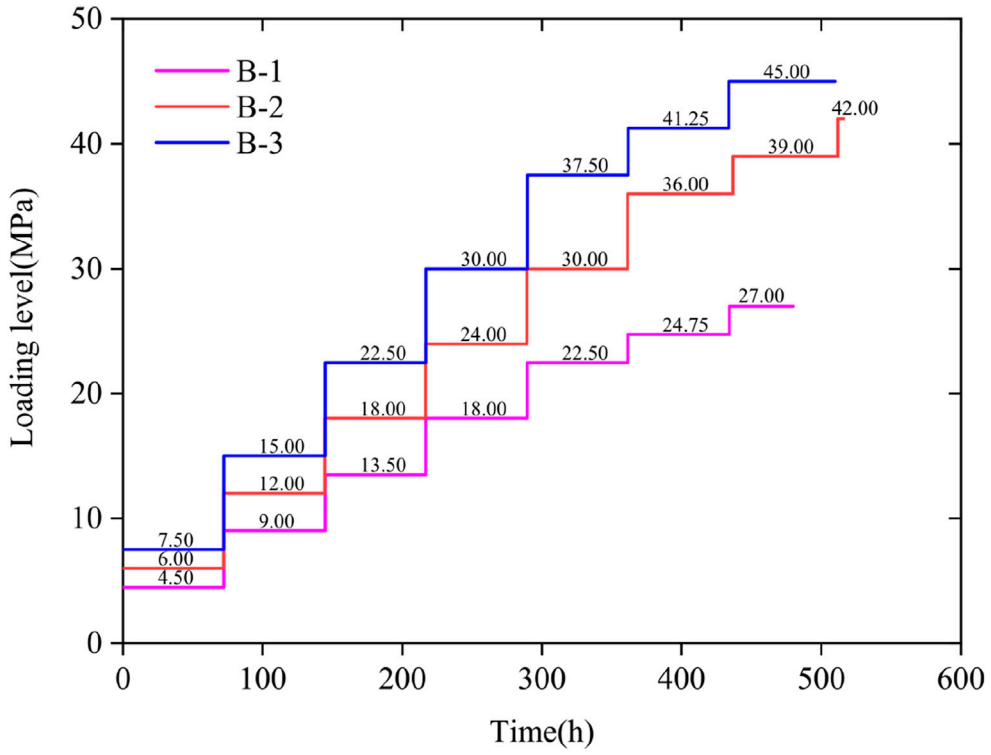

FIGURE 3
Loading levels and duration at all levels in creep tests.

557 h, and the B3 sample lasts 510 h, totaling 1,547 h. The curve shows that the sample has undergone the stages of instantaneous elastic deformation, initial deceleration creep, constant velocity creep and accelerated creep. Due to the different confining pressures and axial loads of the different specimens, the deformation characteristics of the test curves are different. In addition to the last stage of loading, the creep curves of the other stages only include three stages: the instantaneous elastic deformation stage, initial deceleration creep stage and constant velocity creep stage. Only the last stage of accelerated creep occurs. The appearance of accelerated creep indicates that the microfracture process in rock is accelerated irreversibly until the specimen is destroyed.

Figure 5 shows a statistical relationship between the steady-state creep rate and the load. The figure shows that with the increase in the load, the steady-state creep rate tends to increase nonlinearly. However, at the last stage of loading, the steady-state creep rate increases rapidly; this turning point is a sign that the specimen is about to enter the accelerated failure stage (Fairhurst and Hudson, 1999; Jian-Zhi et al., 2023). When the confining pressure is 5 MPa, the steady creep rate is 1.075×10^{-4}/h. When the confining pressure is 10 MPa, the steady creep rate is 1.078×10^{-4}/h. When the confining pressure is 15 MPa, the steady creep rate is 1.347×10^{-4}/h, and the values of the steady creep rate are on the same order of magnitude. The evolution law of the steady creep rate with time is represented by a rational number function. Through further analyses and treatments of the test, the creep rate of each specimen under the last stage of loading is obtained, as shown in Figure 6. The results show that the creep rate of the B-1 sample is 0.0113/h, that of the B-2 sample is 0.651/h, and that of the B-3 sample is 0.148/h. There are no obvious correlations between the rates, but they exceed the steady-state creep rate of each sample under the previous loading level. The results show that the deformation rate of the last loading curve of each sample decreases sharply in the early stage, remains stable in the middle stage, and increases sharply in the later stage. This phenomenon occurs because the expansion and penetration characteristics of internal cracks in the rock are near the failure degree of the specimen. The creep rate of the last stage is expressed by a power function with an absolute value function.

According to an analysis of the whole process creep curve and the change characteristics of the creep rate, the deformation of each creep stage is counted, as shown in Figures 7–9. Figure 7 shows the statistics of the instantaneous deformation of each sample under different confining pressures under various loading conditions. The evolution law of deformation is characterized by an exponential function. The figure shows that with the increase in the loading series, the instantaneous deformation decreases gradually, the amplitude of reduction in the early stage is larger, and the reduction range in the later stage gradually decreases and tends to a fixed value. This phenomenon occurs because the internal cracks gradually close in the initial stage of loading; with the increase in load, the cracks cannot be further closed. Therefore, the reduction range of instantaneous deformation decreases gradually. Additionally, the instantaneous deformation of each sample during the first stage loading is much larger than that of other loading stages. This phenomenon occurs because during sampling, sample preparation and loading, the microcracks in the rock mass are greatly affected by the

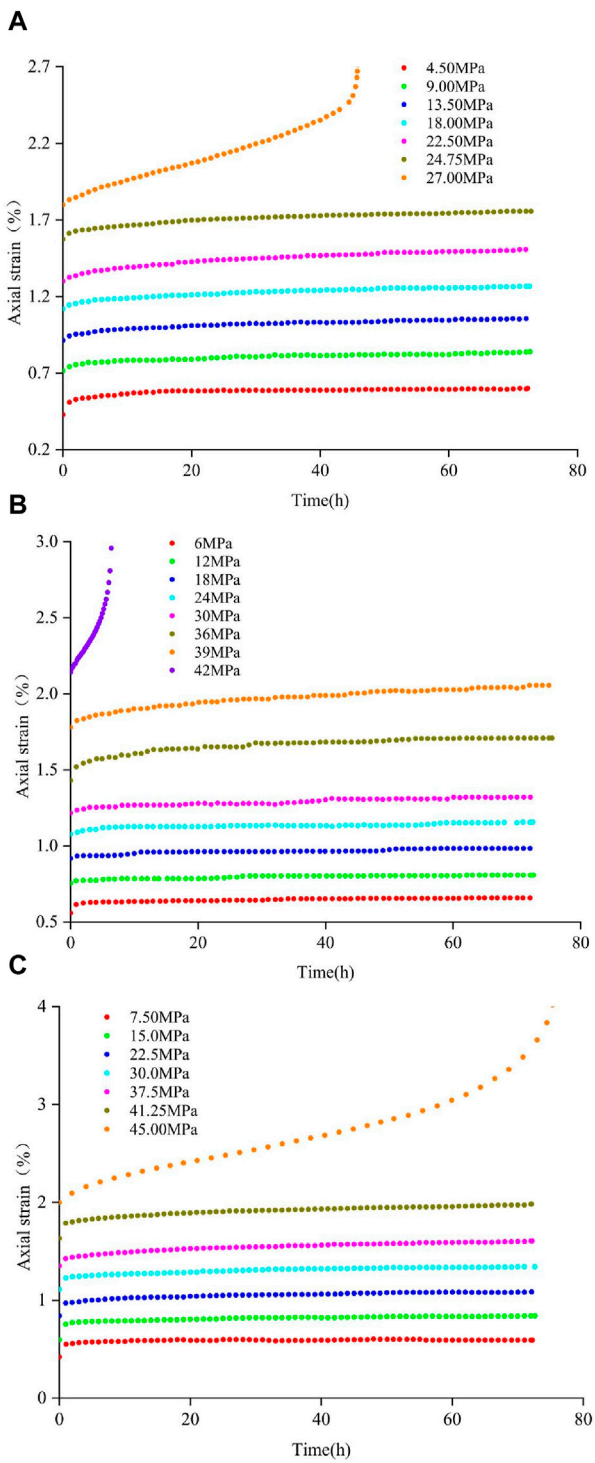

FIGURE 4
Relationship curves of axial strain with time for sandstone under different confining pressures. **(A)** σ3 = 5 MPa, **(B)** σ3 = 10 MPa, **(C)** σ3 = 15 MPa.

disturbance; thus, the strain presents the characteristics of maximum value in the first loading.

Figure 8 shows the statistics of the strain in the decay creep stage of each sample under different confining pressure conditions. The strain in the decay creep stage decreases first and then increases. At this stage, the closure of microcracks in the rock is greater than that in the rock; the closure value of the microcracks in the early stage of loading is larger than that in the rock. Furthermore, due to the lower load, there are fewer internal cracks. With increasing load, the closing amount of microcracks gradually decreases; the number of microcracks increases gradually. The macroscopic behavior is that the strain first decreases and then increases until it reaches a relative equilibrium state. Furthermore, the specimen enters the steady-state creep stage. The evolution law of deformation is characterized by a cubic function.

The results show that under the condition of constant loading, the deformation amplitude of each stage increases gradually with increasing total deformation under different loading conditions. However, in the later stage, the strain increases sharply. The evolution law of deformation is characterized by a cubic function.

3 Typical creep characteristics and basic assumptions

Studying the creep mechanisms and characteristics of rocks are the basis for understanding the long-term stability of geotechnical engineering activities. As far as rock materials are concerned, many scholars have performed much research on the long-term time effect of rock deformation. Despite the results from the uniaxial compression, triaxial compression and shear tests, it is observed that the creep curve of rock in the whole process has typical zoning characteristics. Generally, the creep deformation characteristics of rock materials are divided into four typical stages, as shown in Figure 10A: (i) the instantaneous elastic deformation stage; (ii) the initial deceleration creep stage; (iii) the intermediate constant velocity creep stage; and (iv) the late accelerated creep stage. Additionally, according to the strain rate and strain curve characteristics of rocks, rock creep is divisible into a deceleration zone, constant velocity zone and acceleration zone, as shown in Figure 10B. Unfortunately, the creep rate in the constant velocity zone is not constant; however, the variation range is relatively small, and the duration of this stage is longer than the time–strain curve throughout the process. Therefore, these phenomena need to be divided into one stage separately.

(i) Instantaneous elastic deformation stage: the deformation in this stage is only related to the stress level, not time; the deformation in this stage is elastic deformation. The deformation at this stage mainly depends on the stress level σ_0 and the elastic modulus E_0. This stage is included in the deceleration zone.

(ii) Initial deceleration creep stage: the strain rate in this stage gradually decreases with time and gradually tends to a constant value. The stress curve is convex at this stage. This stage is included in the deceleration zone.

(iii) Intermediate constant velocity creep stage: the overall change in the strain rate in this stage is small. From the microrate, the variable speed in this stage is first negative and then positive, but the overall absolute value is low. At this stage, the generation of new microcracks in the rock mass and the closure of old microcracks reach a relatively balanced state. Furthermore, the applied stress level is insufficent for

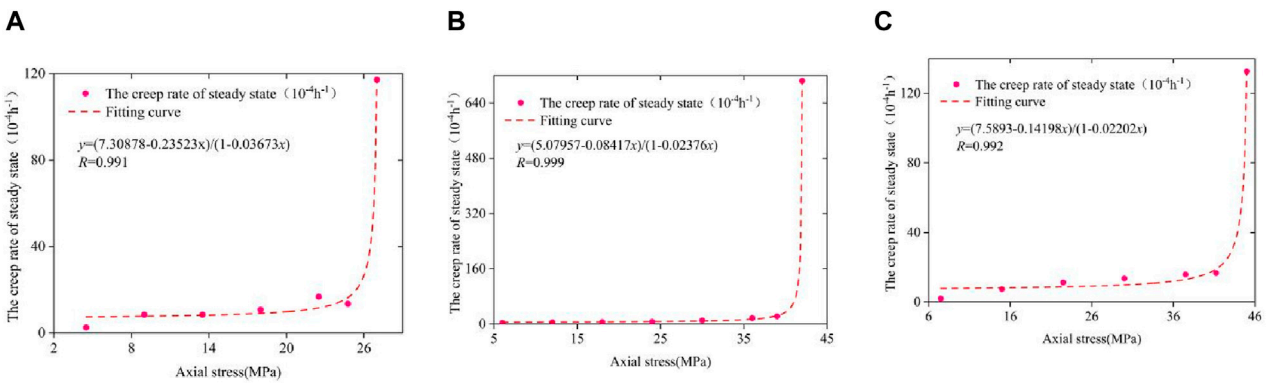

FIGURE 5
Steady-state creep rates under stress loading at all levels. **(A)** σ3 = 5 MPa, **(B)** σ3 = 10 MPa, **(C)** σ3 = 15 MPa.

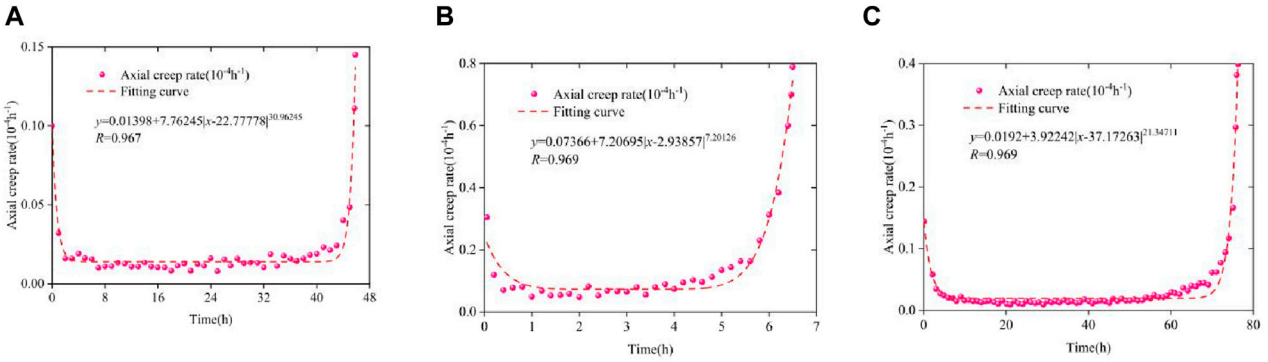

FIGURE 6
Long-term creep rate vs. last stage loading. **(A)** σ3 = 5 MPa, **(B)** σ3 = 10 MPa, **(C)** σ3 = 15 MPa.

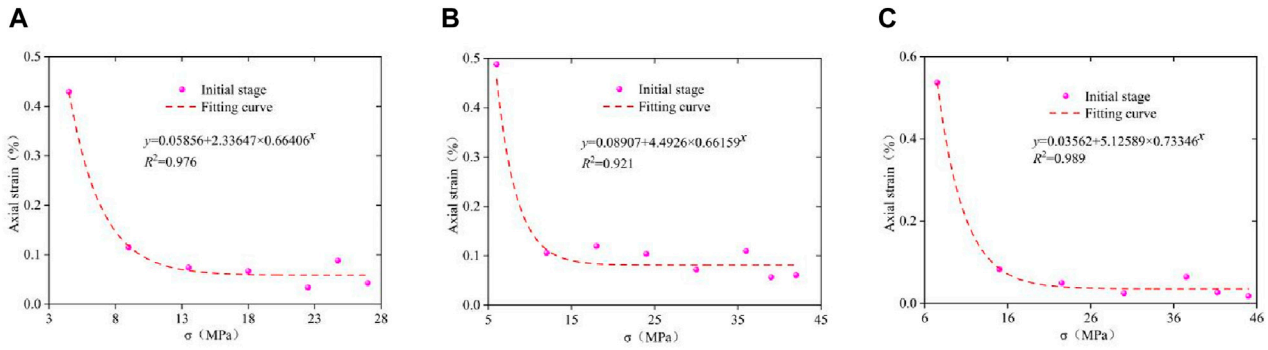

FIGURE 7
Strain statistics in the instantaneous deformation stage. **(A)** σ3 = 5 MPa, **(B)** σ3 = 10 MPa, **(C)** σ3 = 15 MPa.

breaking the above equilibrium state, and the macroscopic deformation rate is relatively stable. The constant velocity zone mainly refers to this deformation stage.

(iv) Late accelerated creep stage: in this stage, the strain rate gradually increases with time and finally tends to infinity, at which time the specimen is destroyed. The acceleration zone mainly refers to the deformation stage. Note that, according to the research of many scholars, the deformation characteristics of different lithologies at this stage are obviously different. Generally, a rock mass with high strength presents the characteristics of brittle failure (Jianchao et al., 2022), and the curve exhibits an obvious

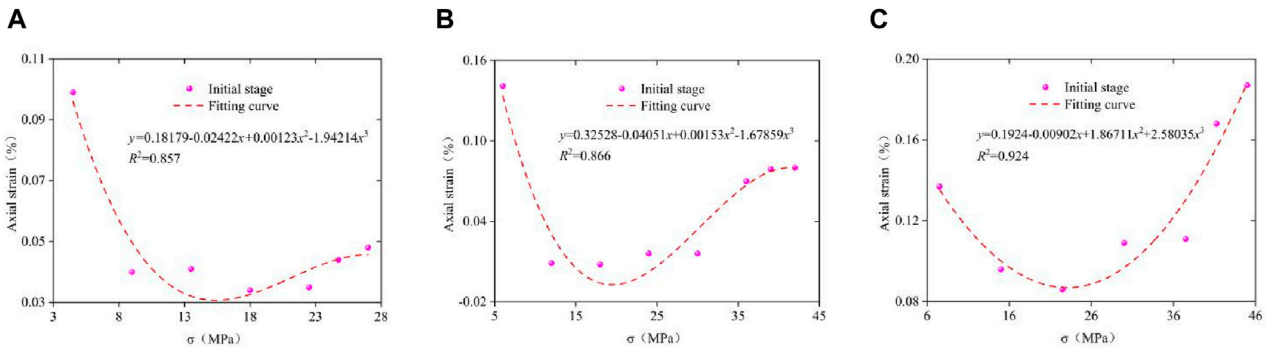

FIGURE 8
Strain statistics in the decaying creep stage. **(A)** σ3 = 5 MPa, **(B)** σ3 = 10 MPa, **(C)** σ3 = 15 MPa.

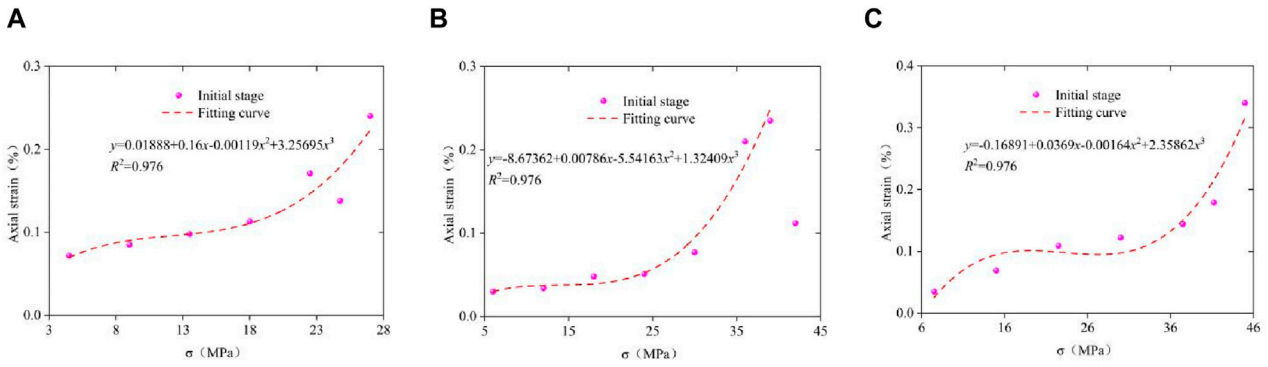

FIGURE 9
Strain statistics in the constant creep stage. **(A)** σ3 = 5 MPa, **(B)** σ3 = 10 MPa, **(C)** σ3 = 15 MPa.

sharp turning point. When the intensity of lithology is low, the curve shows the characteristics of flexible failure; additionally, the curve shows the morphological characteristics of a first-out arc.

4 Viscoelastic–plastic creep model

4.1 Establishment of a viscoelastic–plastic creep model

To better describe the creep characteristics of rocks, the Abel clay pot based on a fractional derivative and the nonlinear damage damping element based on damage theory are connected in series to construct a new creep constitutive model, as shown in Figure 11. This model effectively describes the creep characteristics of sandstone. Total strain $\varepsilon(t)$ is expressed by Eq. (1):

$$\begin{cases} \varepsilon(t) = \varepsilon_e + \varepsilon_{ve}, & \sigma < \sigma_s \\ \varepsilon(t) = \varepsilon_e + \varepsilon_{ve} + \varepsilon_{vp}, & \sigma \geq \sigma_s \end{cases} \tag{1}$$

In the creep test, there is instantaneous deformation with extreme time during initial loading. The deformation ε_0 is mainly determined by the load size and has nothing to do with time; thus, elastic elements are used to represent the elastic deformation at this stage, as shown in Eq. (2):

$$\varepsilon_e = \frac{\sigma_0}{E_0} \tag{2}$$

Because of its inherent characteristics, the fractional differential equations better describe the characteristics of nonlinear curves; additionally, the equation has been widely used in research on material rheology in recent years (Papoulia et al., 2010; Mainardi and Spada, 2011; Sapora et al., 2016). Fractional calculus describes derivatives and integrals of any order, and there are many definitions. Operators of fractional integrals mainly include Riemann–Liouville (R–L) fractional differential operator theory (Miller and Ross, 1993) and the Caputo operator. In this paper, Riemann–Liouville fractional differential theory is mainly adopted.

The R–L fractional derivative is one of many definitions developed based on integer differential equations. This definition is as follows: f is $(0, +\infty)$. The upper segment is continuous and in $(0, +\infty)$. Integrable on any finite subinterval of $\mathrm{Re}(\beta) > 0$, $t > 0$, the following is true:

$${}_0D_t^{-\beta} f(t) = \frac{d^{-\beta} f(t)}{dt^{-\beta}} = \frac{1}{\Gamma(\beta)} \int_0^t (t-\tau)^{\beta-1} f(\tau) d\tau \tag{3}$$

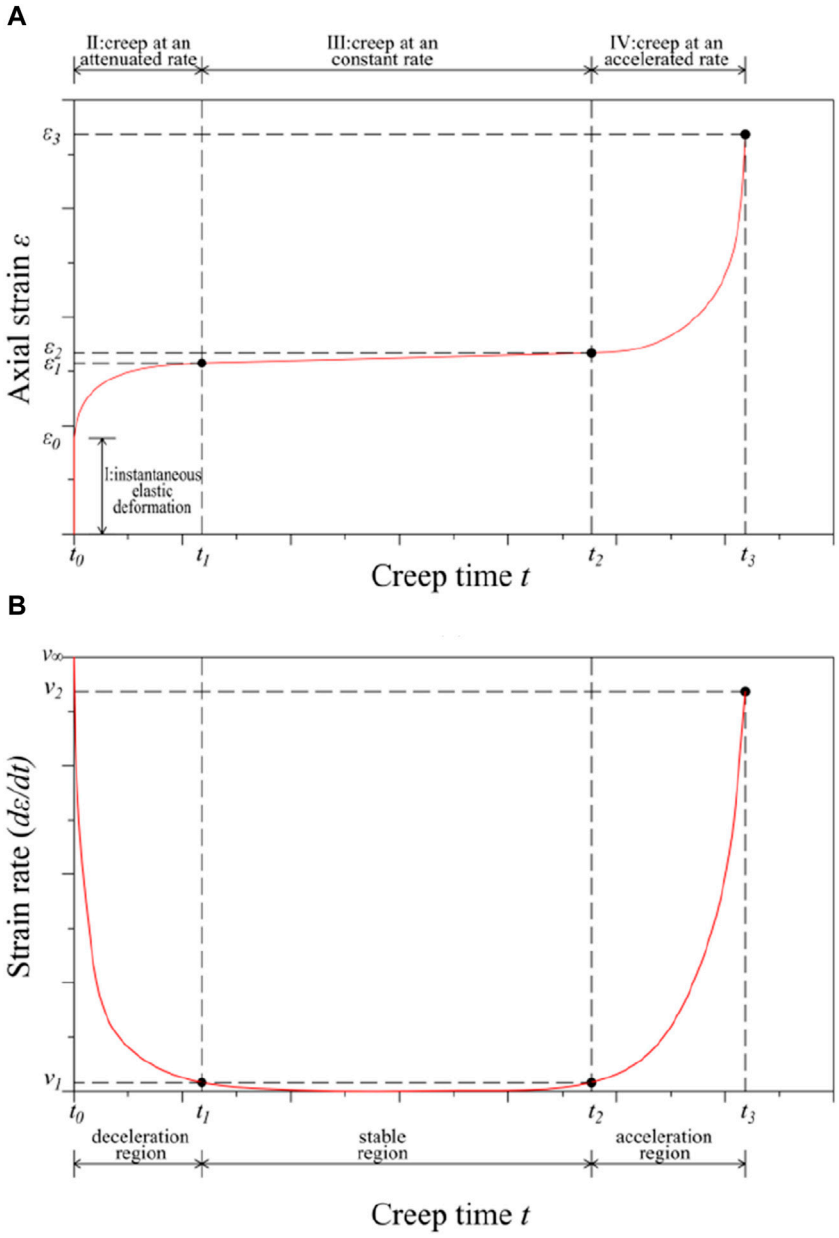

FIGURE 10
Complete creep curves of rock specimens under multiple stress levels. **(A)**: Typical time-strain curve. **(B)**: Typical time-strain rate curve.

$\Gamma(\beta)$ is the gamma function, which is defined as follows:

$$\Gamma(\beta) = \int_0^{\infty} t^{\beta-1} e^{-t} dt \tag{4}$$

Abel clay pots represent the rheological properties of geotechnical materials between ideal rheological bodies and ideal rigid bodies. The Abel clay pot stress–strain relationship is as Eq. (5):

$$\sigma(t) = \eta \frac{d^{\beta}\varepsilon(t)}{dt^{\beta}} \quad (0 < \beta < 1) \tag{5}$$

In studying the creep constitutive models of geotechnical materials, it is considered that $\sigma(t)$. As a constant value, the creep constitutive equation of the Abel clay pot is obtained by using R–L fractional differential operator theory at this time as follows (Kiryakova and Al-Saqabi, 1999; Zhou et al., 2011):

$$\varepsilon_{ve} = \frac{\sigma_0}{\eta} \frac{t^{\beta}}{\Gamma(1+\beta)} \quad (0 < \beta < 1) \tag{6}$$

The creep rate of the kettle is adhered to by taking the derivative of Eq. 6, as shown in Eq. (7):

$$\dot{\varepsilon_a}(t) = \frac{\sigma_0}{\eta} \frac{\beta t^{(\beta-1)}}{\Gamma(1+\beta)} dt \quad (0 < \beta < 1) \tag{7}$$

where E_0 represents the elastic modulus of rock and σ_0 is the initial loading stress. After instantaneous elastic deformation, the stress

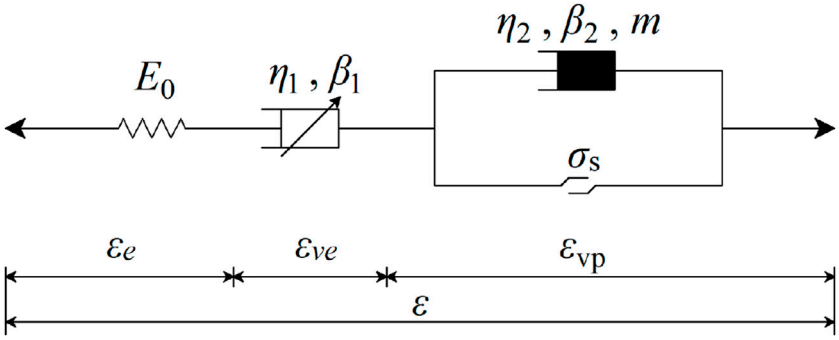

FIGURE 11
Creep constitutive model.

remains unchanged, and the rock shows viscoelasticity. The viscoelastic deformation stage after instantaneous elastic deformation includes the attenuation creep stage and the stable creep stage. The strain in this stage is represented by the Abel viscous pot element, as shown in Figure 11. The creep constitutive equation is expressed as follows:

$$\varepsilon(t) = \frac{\sigma_0}{E_0} + \frac{\sigma_0}{\eta_1}\frac{t^{\beta_1}}{\Gamma(\beta_1+1)} \quad (\sigma_0 \le \sigma_S) \tag{8}$$

It is not enough to use elastic elements and Abel clay pot elements to express rock after entering the accelerated creep stage. Zhou et al. (Zhou et al., 2013) established a salt rock rheological model based on fractional derivative and found that the model accurately describes the rheological test curve of salt rock. Subsequently, the researchers proposed the variable coefficient Abel damper. The viscosity coefficient of rock is not constant in the rheological process. Therefore, for crack evolution and damage accumulation on a fine scale, only the effect of load action time is considered; the damage variable D is introduced to describe the deterioration of the viscosity coefficient. The damage variable D can be expressed by Eq. (9).

$$\eta^{\gamma} = \eta^{\gamma}(D) = \eta^{\gamma}(1-D) \tag{9}$$

In Equation (3) (4), D assumes that the damage during rock rheology evolves into a negative exponential function, which is described as Eq. 10 follows:

$$D = 1 - e^{-\alpha t} \tag{10}$$

where α is the coefficient related to the properties of the rock mass. The variation in rock damage variables with loading time based on the Weibull random distribution is described as follows:

$$D = 1 - e^{-\beta t^m} \tag{11}$$

where β and m are parameters representing the mechanical properties of the materials.

According to the strain equivalence principle (Lemaitre, 1996) proposed by Lemaitre, the strain of damaged material under full stress is equal to that of undamaged materials under effective stress. Cauchy stress is changed to effective stress $\tilde{\sigma}$ to obtain the following Eq. 12:

$$\tilde{\sigma} = \frac{\sigma}{1-D} \tag{12}$$

By introducing the damage variable D into the damping element, the constitutive equation of the nonlinear damage damping element is obtained as follows:

$$\varepsilon = \frac{\tilde{\sigma}}{\eta_2} = \frac{\sigma}{\eta_2(1-D)} \tag{13}$$

Combining the constitutive Eq. 13 of the nonlinear damage damping element with the rock damage variable in Eq. 11yields the following Eq. 14:

$$\varepsilon_{vp} = \frac{\sigma_0 - \sigma_s}{\eta_2 e^{-\beta t^m}} = \frac{\sigma_0 - \sigma_s}{\eta_2} e^{\beta t^m} \tag{14}$$

As shown in Figure 11, the total strain of unstable creep of rock is obtained by connecting all parts of creep in series:

$$\varepsilon(t) = \frac{\sigma_0}{E_0} + \frac{\sigma_0}{\eta_1}\frac{t^{\beta_1}}{\Gamma(\beta_1+1)} + \frac{\sigma_0 - \sigma_s}{\eta_2} e^{\beta_2 t^m} \quad (\sigma_0 > \sigma_S) \tag{15}$$

In summary, the creep constitutive Eq. 16 can be obtained from Eq. Eq. 8 and Eq. 15:

$$\varepsilon(t) = \begin{cases} \dfrac{\sigma_0}{E_0} + \dfrac{\sigma_0}{\eta_1}\dfrac{t^{\beta_1}}{\Gamma(\beta_1+1)} & (\sigma_0 \le \sigma_S) \\ \dfrac{\sigma_0}{E_0} + \dfrac{\sigma_0}{\eta_1}\dfrac{t^{\beta_1}}{\Gamma(\beta_1+1)} + \dfrac{\sigma_0 - \sigma_s}{\eta_2} e^{\beta_2 t^m} & (\sigma_0 > \sigma_S) \end{cases} \tag{16}$$

4.2 Model validation

A triaxial creep test of sandstone is conducted; based on the creep test data, the test results under different confining pressures are fitted and analyzed to verify the accuracy and rationality of the model. First, the elastic modulus is determined according to the initial strain and deviator stress in the elastic deformation stage E_0. Then, the Levenberg–Marquardt algorithm is used to fit the experimental curve nonlinearly. The model fitting parameters of this model are shown in Tables 1–3.

The nonlinear viscoelastic–plastic creep model proposed in this paper describes the nonlinear creep characteristics of rock masses, especially the irregular nonlinear damage creep in the

TABLE 1 Simulation parameters of the nonlinear creep damage constitutive model for sample B-1.

Loading level (MPa)	E_0 (GPa)	η_1 (GPa·h)	β_1	η_2 (GPa·h)	β_2	m	R^2
4.50	10.490	47.564	0.127				0.952
9.00	12.587	308.960	0.305				0.980
13.50	14.770	437.807	0.331				0.991
18.00	16.071	669.656	0.373				0.994
22.50	17.294	716.639	0.415				0.992
24.75	15.556	652.780	0.345				0.993
27.00	10.490	1,569.309	0.923	2.368	4.356	0.678	0.995

TABLE 2 Simulation parameters of the nonlinear creep damage constitutive model for sample B-2.

Loading level (MPa)	E_0 (GPa)	η_1 (GPa·h)	β_1	η_2 (GPa·h)	β_2	m	R^2
6.0	12.295	37.477	0.074				0.986
12.0	15.686	343.116	0.261				0.978
18.0	19.397	960.011	0.245				0.973
24.0	22.059	669.656	0.373				0.994
30.0	24.450	2,757.239	0.478				0.997
36.0	25.175	375.322	0.234				0.989
39.0	21.910	978.07611	0.419				0.996
42.0	19.617	623.533	0.921	773.898	5.594×10^{-4}	4.728	0.995

TABLE 3 Simulation parameters of the nonlinear creep damage constitutive model for sample B-3.

Loading level (MPa)	E_0 (GPa)	η_1 (GPa·h)	β_1	η_2 (GPa·h)	β_2	m	R^2
7.50	17.857	54.601	0.050				0.986
15.00	22.222	203.684	0.170				0.988
22.50	25.281	313.872	0.215				0.992
30.00	27.027	315.307	0.190				0.986
37.50	27.778	588.911	0.298				0.998
41.25	25.276	321.080	0.207				0.997
45.00	22.534	1,201.026	0.766	171.063	3.631×10^{-9}	4.781	0.994

accelerated creep stage. The creep model is easily used for engineering tests and numerical simulations and effectively predicts and evaluates the long-term stability characteristics of geotechnical engineering projects. All samples show accelerated creep deformation in the last loading stage until the samples are deformed and destroyed. The creep curves of each sample are selected for model verification and fitting, and the fitting results are shown in Figure 12. The correlation coefficient is selected as the evaluation index. The fitting results show that the correlation coefficients are all near 1, proving that the constitutive model has a good fitting effect and effectively describes the nonlinear characteristics of curves.

5 Parameter sensitivity analysis and discussion

The strain of this model formula depends on six parameters: E_0, M, β_1, β_2, $\eta1$ and η_2. Considering the deformation curve of the last stage of the specimen under an axial load of 45 MPa when the confining pressure is 15 MPa, parameter sensitivity analysis is conducted. Specifically, certain parameters are set to 70%, 85%, 100%, 115% and 130%, and the remaining parameters remain unchanged. As shown in Figure 13, three parameters—E_0, $\beta1$ and η_1—mainly correspond to the deformation characteristics of the strain curve in the instantaneous deformation stage, attenuation

10.3389/fenvs.2024.1338016

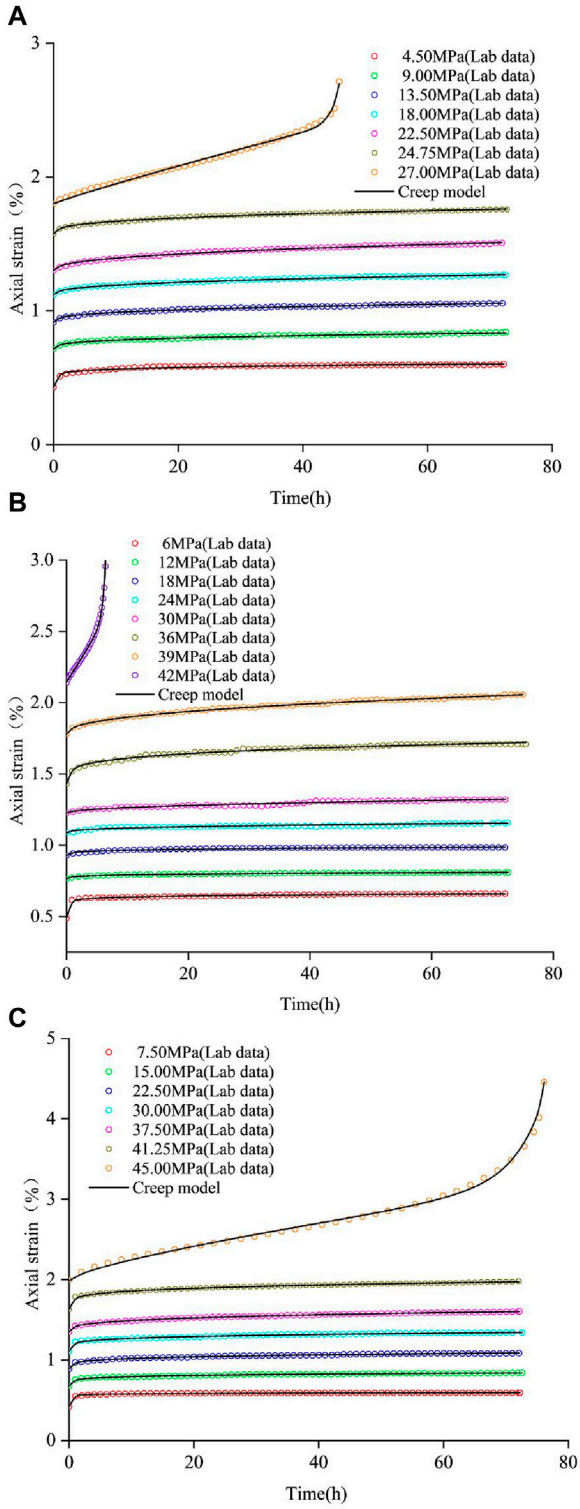

FIGURE 12
Experimental data and fitting curves by the creep model. **(A)** σ3 = 5 MPa, **(B)** σ3 = 10 MPa, **(C)** σ3 = 15 MPa.

creep stage and steady creep stage. Figure 13A shows that E_0 mainly controls the instantaneous elastic deformation stage and mainly determines the amount of elastic strain; however, it has no influence on the decay creep, steady creep and accelerated creep stages. The magnitude of E_0 is negatively correlated with the strain. WhenE_0 increases, the curve moves downward; while when E_0 decreases, the curve moves upward. Figure 13C and Figure 13E show that β_1 and η_1 are the stages that mainly affect the attenuation creep and steady creep characteristics; their values are not affected in the instantaneous deformation stage. Then, different deformation characteristics appear with curves of β_1 and η_1, which are negatively correlated with the deformation rate in the steady creep stage. The larger η_1 is, the smaller the steady creep rate, and the larger the deformation value in the decay creep stage. Figure 13 shows that m, β_2 and η_2 jointly determine the deformation at the accelerated creep stage. Figures 13B, F shows that the larger the value of m is, the earlier the creep curve specimen enters the accelerated creep stage; additionally, the larger the value of m is, the higher the curve strain rate. Figures 13D, F show that β_2 is generally positively correlated with the deformation rate in the accelerated creep stage, and η_2 is generally negatively correlated with the deformation rate in the accelerated creep stage; these parameters determine the slope characteristics in the accelerated creep stage. Therefore, through the different changes in parameters, the curve presents different deformation characteristics and has a high fitting degree in various deformation stages, and the results are more reliable.

The experimental curve obtained in this paper has obvious characteristics of flexible failure, and the final failure of the sample requires a long process. The rheological characteristics are obviously different from those of high-strength hard rock. The creep curve has relatively obvious deformation stages, which are clearly divisible into instantaneous deformation, attenuation creep, constant velocity creep and accelerated creep. The creep model proposed in this paper has a good fitting degree to the experimental data; it is proven to be a model that describes the creep characteristics of rocks well. According to the fitting results, the order of the fractional derivative is always at a minimum when different samples are loaded in the first stage; the order is close to one when the samples are loaded in the last stage. This trend shows that with increasing load, rock elasticity gradually decreases; however, the viscosity gradually increases. In the accelerated creep stage, the accumulation of rock rheological damage and crack propagation are the main influencing factors leading to deformation and failure, which are closely related to the damage characteristics of materials. In this paper, a damage analysis of rock is introduced into the analysis of the constitutive model, providing some reference for the rheological study of rock. Although the introduction of damage theory has promoted the development of research in the field of rock rheology, the rheological research on the accelerated failure stage of rock still needs systematic and in-depth discussion.

6 Conclusion

Through triaxial creep experiments of sandstone, rock deformation characteristics and mechanisms are studied. By combining fractional derivative theory and damage theory, a new creep constitutive model is established that effectively captures and describes the deformation characteristics of each stage of creep. The conclusions are as follows:

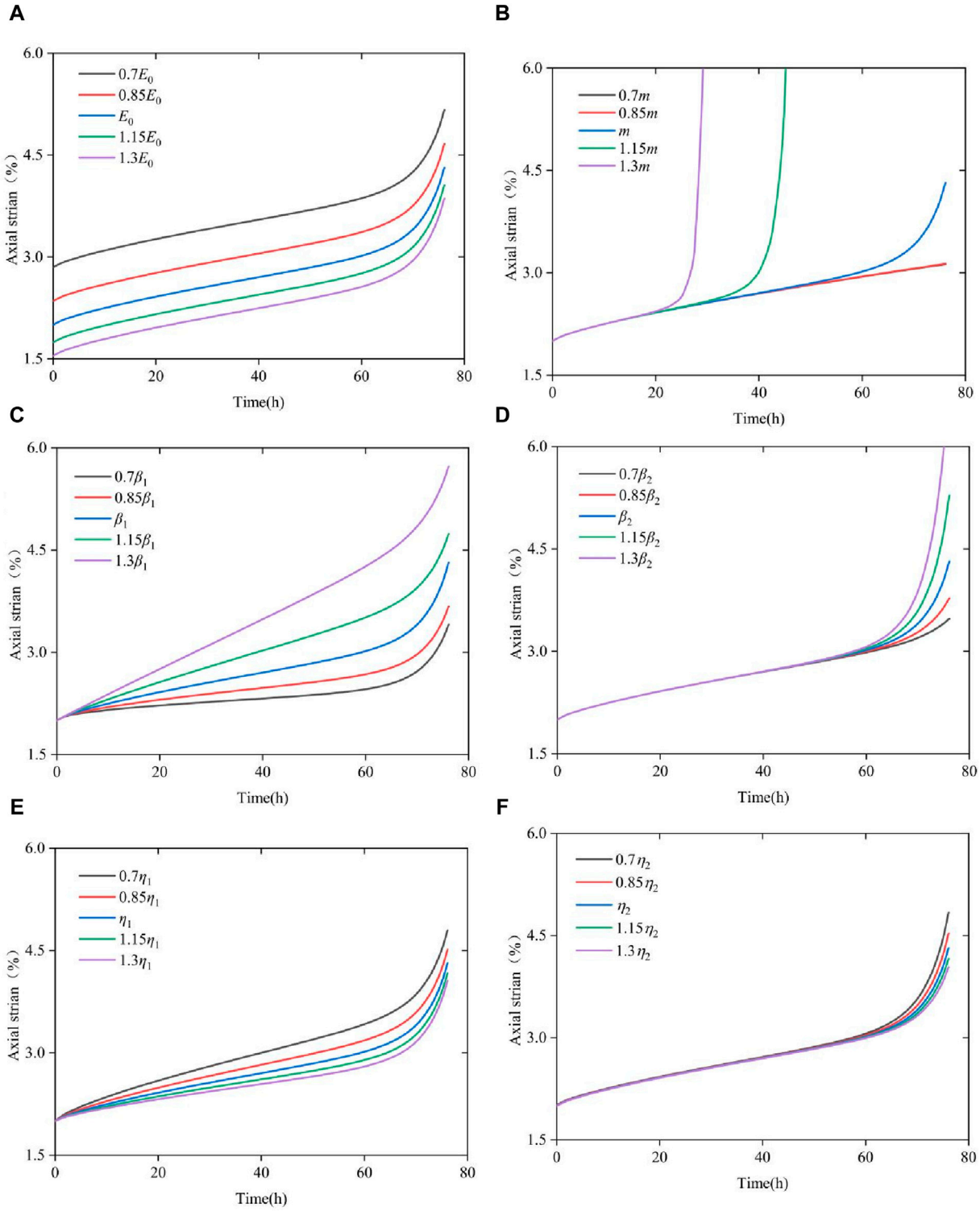

FIGURE 13
Effects of each parameter on the creep response. **(A)** E0, **(B)** m, **(C)** β1, **(D)** β2, **(E)** η1, **(F)** η2.

(1) The unified creep model has a simple structure, and the parameters can be determined conveniently; this model describes the deformation characteristics of different creep stages, including instantaneous deformation, attenuation creep, constant velocity creep and accelerated creep. It is proven that the rheological model based on fractional derivative theory and damage theory is reasonable and practical.

(2) According to an analysis of the test curve, the deformation characteristics and rates in different stages of the creep curve

are obtained; the causes and mechanisms of these phenomena are analyzed and summarized. During loading, the elastic deformation of rock gradually decreases, while the viscoplastic deformation gradually increases. Damage theory effectively describes the creep accelerated failure deformation stage of a rock mass.

(3) According to the test results, the nonlinear creep parameters under different creep stress conditions are obtained, and the accuracy of the creep model is verified. The fitting curve is in good agreement with a test curve. It is proven that the model describes the creep curve of rock throughout the process, especially the creep curve in the accelerated creep stage. A sensitivity analysis of model parameters is conducted by a quantitative evaluation method for verifying the rationality of the model.

Data availability statement

The original contributions presented in the study are included in the article/Supplementary Material, further inquiries can be directed to the corresponding author.

Author contributions

XZ: Conceptualization, Investigation, Writing–original draft, Writing–review and editing. NJ: Conceptualization, Funding acquisition, Resources, Supervision, Writing–review and editing. JC: Data curation, Validation, Writing–review and editing. CH: Funding acquisition, Resources, Writing–review and editing. JW: Investigation, Writing–review and editing. HW: Data curation, Investigation, Writing–review and editing. RL: Data curation, Investigation, Writing–review and editing.

Funding

The author(s) declare that financial support was received for the research, authorship, and/or publication of this article. This work was supported by Sichuan Provincial Natural Science Foundation (2023NSFSC0263), State Key Laboratory of Geohazard Prevention and Geoenvironment Protection Independent Research Project (SKLGP2020Z006), State Key Laboratory of Geohazard Prevention and Geoenvironment Protection (Chengdu University of Technology, SKLGP2022K004), Sichuan Science and Technology Program (NO:2022YFG0183).

Acknowledgments

The authors are also grateful to the referees for their useful comments and careful review of the manuscript.

Conflict of interest

Author JW was employed by Changjiang Geotechnical Engineering Co., Ltd.

The remaining authors declare that the research was conducted in the absence of any commercial or financial relationships that could be construed as a potential conflict of interest.

Publisher's note

References

Chang, K. T., Ge, L., and Lin, H. H. (2015). Slope creep behavior: observations and simulations. *Environ. Earth Sci.* 73 (1), 275–287. doi:10.1007/s12665-014-3423-2

Deng, H. F., Zhou, M. L., Li, J. L., Sun, X., and Huang, Y. (2016). Creep degradation mechanism by water-rock interaction in the red-layer soft rock. *Arab. J. Geosci.* 9 (12), 601–612. doi:10.1007/s12517-016-2604-6

Fairhurst, C. E., and Hudson, J. A. (1999). Draft ISRM suggested method for the complete stress-strain curve for intact rock in uniaxial compression. *Int. J. Rock Mech. Min. Sci.* 36 (3), 279–289. doi:10.1016/S0148-9062(99)00006-6

Hou, R., Zhang, K., Tao, J., Xue, X., and Chen, Y. (2018). A nonlinear creep damage coupled model for rock considering the effect of initial damage. *Rock Mech. Rock Eng.* 52, 1275–1285. doi:10.1007/s00603-018-1626-7

Hu, X., Tan, F., Tang, H., Zhang, G., Su, A., Xu, C., et al. (2017). In-situ monitoring platform and preliminary analysis of monitoring data of Majiagou landslide with stabilizing piles. *Eng. Geol.* 228, 323–336. doi:10.1016/j.enggeo.2017.09.001

Jianchao, W., Guoqing, C., Yafeng, C., and Serati, M. (2022). Interrelation analysis method of acoustic emission for failure prediction of brittle failure based on vibration mechanics. *Bull. Eng. Geol. Environ.* 81 (6), 247. doi:10.1007/s10064-022-02752-6

Jiang, P., Pan, P. Z., and Zhao, S. K. (2018). Coupled creep constitutive model of rock viscoelasticplastic damage based on strain energy and its application. *J. Coal Mine* 43 (11), 2967–2979.

Jian-Zhi, Z., Wen-Tao, W., and Xiao-Ping, Z. (2023). On the predictability of localization instabilities of quasibrittle materials from accelerating rates of acoustic emission. *Eng. Fract. Mech.* 289, 109455. doi:10.1016/j.engfracmech.2023.109455

Kiryakova, V., and Al-Saqabi, B. (1999). Explicit solutions to hyper-Bessel integral equations of second kind. *Comput. Math. Appl.* 37 (1), 75–86. doi:10.1016/s0898-1221(98)00243-0

Lemaitre, J. (1996). *A course on damage mechanics*. Berlin, Germany: Springer.

Li, R. D., and Chao, L. J. (2014). Nonlinear rheological constitutive model of soft soil based on fractional derivative. *J. Appl. Found. Eng. Sci.* 22 (5), 856–864.

Li, S. D., Li, X., Zhang, X. N., et al. (2004). Sedimentation characteristics of the Jurassic sliding-prone stratum in the three gorges reservoir area and their influence on physical and mechanical properties of rock. *J. Eng. Geol.* 12 (4), 385–389.

Liu, Y., Wang, E., Li, M., Song, Z., Zhang, L., and Zhao, D. (2023). Mechanical response and gas flow characteristics of pre-drilled coal subjected to true triaxial stresses. *Gas Sci. Eng.* 111, 204927. doi:10.1016/j.jgsce.2023.204927

Luo, Z., Li, J. L., Jiang, Q., Zhang, Y., Huang, Y., Assefa, E., et al. (2018). Effect of the water-rock interaction on the creep mechanical properties of the sandstone rock. *Period Polytech. Civ. Eng.* 62 (2), 451–461. doi:10.3311/ppci.11788

Mainardi, F., and Spada, G. (2011). Creep, relaxation and viscosity properties for basic fractional models in rheology. *Eur. Phys. J. Spec. Top.* 193 (1), 133–160. doi:10.1140/epjst/e2011-01387-1

Miller, K. S., and Ross, B. (1993). *An introduction to the fractional calculus and fractional differential equations*. Hoboken, NJ, USA: Wiley.

Papoulia, K. D., Panoskaltsis, V. P., Kurup, N. V., and Korovajchuk, I. (2010). Rheological representation of fractional order viscoelastic material models. *Rheol. Acta* 49 (4), 381–400. doi:10.1007/s00397-010-0436-y

Sapora, A., Cornetti, P., Carpinteri, A., Baglieri, O., and Santagata, E. (2016). The use of fractional calculus to model the experimental creep-recovery behavior of modified bituminous binders. *Mater Struct.* 49 (1–2), 45–55. doi:10.1617/s11527-014-0473-6

Song, Y., Lei, S., Zou, C., et al. (2015). Study on creep characteristics of carbonaceous slates under dry and saturated states. *Chin. J. Undergr. Space Eng.* 11 (3), 619–664.

Sun, J. (2007). Some advances in rheological mechanics of rock and its engineering applications. *Chin. J. Rock Mech. Eng.* (06), 1081–1106.

Tang, H., Li, C., Hu, X., Su, A., Wang, L., Wu, Y., et al. (2015). Evolution characteristics of the Huangtupo landslide based on *in situ* tunneling and monitoring. *Landslides* 12 (3), 511–521. doi:10.1007/s10346-014-0500-2

Wang, G. J. (2004). A new constitutive creep-damage model for salt rock and its characteristics. *Int. J. Rock Mech.Min. Sci.* 41, 61–67. doi:10.1016/j.ijrmms.2004.03.020

Wang, H., Yang, T., Liu, H., et al. (2017). Mechanical properties and energy evolution of dry and saturated sandstones under cyclic loading. *Rock Soil Mech.* 38 (6), 1600–1608.

Wang, X., Huang, Q., Lian, B., Liu, N., and Zhang, J. (2018b). Modified Nishihara rheological model considering the effect of thermal-mechanical coupling and its experimental verification. *Adv. Mater Sci. Eng.* 2018, 1–9. doi:10.1155/2018/4947561

Wang, X., Yin, Y., Wang, J., Lian, B., Qiu, H., and Gu, T. (2018a). A nonstationary parameter model for the sandstone creep tests. *landslides* 15 (7), 1377–1389. doi:10.1007/s10346-018-0961-9

Wu, F., Liu, J. F., and Wang, J. (2015). An improved Maxwell creep model for rock based on variable-order fractional derivatives. *Environ. Earth Sci.* 73 (11), 6965–6971. doi:10.1007/s12665-015-4137-9

Xu, P., Yang, T. Q., and Zhou, H. M. (2004). Study of the creep characterictics and long-term stability of rock masses in the high slopes of the three gorges ship lock, China. *Int. J. Rock Mech. Min. Sci.* 41 (3), 405. doi:10.1016/j.ijrmms.2003.12.002

Yang, T., Xu, T., Liu, H., Zhang, C., Wang, S., Rui, Y., et al. (2014). Rheological characteristics of weak rock mass and effects on the long-term stability of slopes. *Rock Mech. Rock Eng.* 47 (6), 2253–2263. doi:10.1007/s00603-013-0527-z

Yang, Y. G., Lai, Y. M., and Chang, X. X. (2010). Experimental and theoretical studies on the creep behavior of warm ice-rich frozen sand. *Cold Reg. Sci. Technol.* 63 (1-2), 61–67. doi:10.1016/j.coldregions.2010.04.011

Zhang, J., and Zhou, X. (2020). Forecasting catastrophic rupture in brittle rocks using precursory AE time series. *J. Geophys. Res. Solid Earth* 125 (8). doi:10.1029/2019jb019276

Zhang, Y., Hu, X., Tannant, D. D., Zhang, G., and Tan, F. (2018). Field monitoring and deformation characteristics of a landslide with piles in the Three Gorges Reservoir area. *Landslides* 15 (3), 581–592. doi:10.1007/s10346-018-0945-9

Zhou, H. W., Liu, D., Lei, G., Xue, D., and Zhao, Y. (2018). The creep-damage model of salt rock based on fractional derivative. *Energies* 11 (9), 2349. doi:10.3390/en11092349

Zhou, H. W., Wang, C. P., Han, B. B., and Duan, Z. Q. (2011). A creep constitutive model for salt rock based on fractional derivatives. *Int. J. Rock Mech. Min. Sci.* 48 (1), 116–121. doi:10.1016/j.ijrmms.2010.11.004

Zhou, H. W., Wang, C. P., Mishnaevsky, L., Duan, Z. Q., and Ding, J. Y. (2013). A fractional derivative approach to full creep regions in salt rock. *Mech. Time-Dependent Mater* 17 (3), 413–425. doi:10.1007/s11043-012-9193-x

Zhu, H. H., Zhang, C. C., Mei, G. X., Shi, B., and Gao, L. (2017). Prediction of one-dimensional compression behavior of Nansha clay using fractional derivatives. *Mar. Georesour Geotechnol.* 35 (5), 688–697. doi:10.1080/1064119x.2016.1217958

frontiers | Frontiers in Earth Science

TYPE Original Research
PUBLISHED 19 June 2024
DOI 10.3389/feart.2024.1339169

OPEN ACCESS

EDITED BY
Yihuai Zhang,
University of Glasgow, United Kingdom

REVIEWED BY
Chun Zhu,
Hohai University, China
Yifei Gong,
Beijing University of Technology, China

*CORRESPONDENCE
Junping Wang,
280076123@qq.com
Qi Guoqing,
dr.guoqingqi@163.com

RECEIVED 05 December 2023
ACCEPTED 20 May 2024
PUBLISHED 19 June 2024

CITATION
Cai J, Wang J, Li Z, Kong Y, Zhang L and Qi G (2024), Study on deformation characteristics of toppling failure of anti-dip rock slopes under different soft and hard rock conditions. *Front. Earth Sci.* 12:1339169. doi: 10.3389/feart.2024.1339169

Study on deformation characteristics of toppling failure of anti-dip rock slopes under different soft and hard rock conditions

Junchao Cai[1,2], Junping Wang[1]*, Zhen Li[3], Yanli Kong[4], Liang Zhang[1] and Guoqing Qi[2]*

[1]School of Civil Engineering and Architecture, Henan University of Science and Technology, Luoyang, China, [2]International Scientific and Technological Cooperation Base for Geological Disaster Prevention of Zhejiang Province, Shaoxing University, Shaoxing, China, [3]Henan Communications Investment Construction Group Co Ltd, Zhengzhou, China, [4]Huanghe Science and Technology College, Zhengzhou, China

For the widespread exposure of toppling deformation phenomena in anti-dip engineering slopes such as hydropower, transportation, and mining, especially deep-seated toppling, these large-scale deep-seated toppling deformations reaching depths of hundreds of meters have become significant geotechnical engineering problems that restrict large-scale engineering construction and require urgent solutions. There are significant differences in the failure characteristics and mechanisms of anti-dip rock slopes under different soft and hard rock conditions. This study, starting from the failure characteristics and mechanisms under different soft and hard conditions of rocks, summarizes two types of toppling deformation: ductile bending deep toppling (DBDT) and brittle fracture shallow toppling (BFST). The UDEC method is used to preliminarily explore the threshold of rock mechanical parameters for these two types of toppling, with 80 MPa (UCS, uniaxial compressive strength) mechanical parameters serving as the preliminary threshold. The results indicate that hard rock undergoes BFST, whereas soft rock undergoes DBDT. The rock mechanical parameters of 100 MPa (UCS) and 20 MPa (UCS) were selected to study the evolution process and mechanism of DBDT and BFST deformations, respectively. Numerical simulation results have innovatively revealed the mechanical behavior characteristics between rock layers during the process of toppling deformation. Because toppling deformation mainly originates from interlayer displacement deformation and intra-layer tensile deformation of rock layers, the interlayer mechanical characteristics are of great significance for understanding the mechanism of toppling deformation. This research can provide a theoretical basis for the stability assessment and development utilization of anti-dip rock slopes and toppled slopes.

KEYWORDS

toppling failure, soft and hard rock conditions, deformation characteristics, anti-dip layered rock slope, evolution mechanism

1 Introduction

Toppling failure occurs in layered or quasi-layered rock masses, which trend parallel to the slope surface, with bending deformation toward the free face. As a typical slope failure mode, this occurs in an increasing number of engineering constructions, such as hydropower, transportation, and mining (Cruden and Hu, 1994; Tamrakar et al., 2002; Goodman, 2013; Hungr et al., 2014; Liu et al., 2016; Huang et al., 2017; Ning et al., 2019; Sardana et al., 2019; Zhu et al., 2020; Zhao et al., 2021; Jensen et al., 2024). The representative examples of toppling slopes include the left bank slope of the Jinping first-level Hydropower Station, the Yinshuigou slope of the Xiaowan Hydropower Station, the right dam shoulder slope of the Huangdeng Hydropower Station, the dam front slope of the Miaowei Hydropower Station, the dam front slope of the Gushui Hydropower Station, the Guobu bank slope of the Laxiwa Hydropower Station, the Cardinal River Coal Mine slope in Alberta, and the open-pit mine slope in Jinchuan.

The large-scale toppling deformation of rock masses with a depth of hundreds of meters has become a major geotechnical engineering problem that restricts the construction of large-scale projects and needs to be solved urgently. Once instability and failure occur, it can pose a threat to the safety of people's lives and property, bringing about significant disasters to the development of the country (Xia et al., 2019; Tu et al., 2020; Zhao et al., 2021).

There are currently two mainstream classification methods for toppling failure. One of them is the Goodman and Bray (GB) method classification. Goodman and Bray (1976), through extensive case studies and by considering differences in the failure characteristics of toppling deformation, categorized toppling into two major types: primary toppling and secondary toppling. Primary toppling is further divided into three categories based on the deformation and failure modes of rock layers: flexural toppling, block toppling, and block-flexural toppling. Heok and Bray (1981) categorized secondary toppling deformation into five types based on the deformation location and mechanical mode of rock layers: sliding-head toppling, plastic flow toppling, sliding-toe toppling, tension-crack toppling, and sliding-base toppling. In actual practice, toppling slopes often involve a combination of two or more types of failure modes. Many scholars have conducted in-depth research and analysis on its influencing factors, deformation and failure mechanisms, and occurrence conditions. They mostly use a single numerical simulation method or incorporate on-site survey, monitoring, and model experiments. (Wang et al., 1992; Huang et al., 1994; Han and Wang, 1999; Huang, 2007; Huang, 2011; Huang et al., 2017; Cai et al., 2023; Guo et al., 2023; Zhang et al., 2024; Zheng et al., 2024).

Another classification of toppling deformation is summarized by Huang et al. (1994; 2007; 2012; 2017), who have analyzed numerous toppling cases. They classify toppling deformation into three categories from the perspective of genetic mechanisms and evolutionary processes: shallow toppling (brittle fracture toppling), deep toppling (ductile bending toppling), and complex toppling deformation (Figure 1). The brittle fracture shallow toppling (BFST) primarily corresponds to the block toppling and block-flexural toppling of the GB classification. The ductile bending deep toppling (DBDT) mainly corresponds to flexural toppling. Complex toppling mainly corresponds to secondary toppling. Nichol et al. (2002) also mentioned two types of toppling modes: brittle fracture toppling and ductile bending toppling.

As key controlling factors influencing the development of toppling deformation, in addition to the spatial relationship between the rock layer orientation and slope surface, the rock soft and hard conditions are also crucial factors influencing the development of toppling slopes. Complex toppling is primarily influenced by the rock mass structural characteristics of the slope. The BFST and DBDT are significantly influenced by the soft and hard conditions of the rock.

The DBDT primarily occurs in geological formations dominated by soft rocks, including layers with certain thicknesses of hard rocks or interlayers (Figure 1A). It is widely distributed in "flexible" metamorphic rock formations, such as interbedded formations of metamorphic sandstone and slate, carbonaceous slate, phyllite, and other similar formations, as well as interbedded formations of gneiss and schist (Huang et al., 2017; Cai, 2020). Such rock masses are generally characterized by their soft nature behavior, low strength, thin individual layers, steeply dipping slopes, or nearly vertical orientations. They experience bending, creeping, and time-dependent deformation under the influence of sustained gravitational moments. This deformation is characterized by long-term bending toppling with minimal fracturing and exhibits a "flexible" deformation pattern.

The BFST primarily occurs in hard rock formations, such as carbonate rock formations and platy or blocky igneous rock formations subjected to jointing and fracturing (such as thin to moderately thick limestone, sandstone, and densely jointed granite). The essence of deformation in these formations is the "brittle" fracturing of hard rock layers or the "rigid" structural rotation along the bending fracture planes. Due to the brittle characteristics of these rock masses, even slight "bending" deformation can lead to fracture, resulting in a clear bending fracture surface (Figure 1B).

Based on the summary of a large number of case studies and starting from the soft and hard conditions of rocks, this study summarizes two types of toppling deformation: DBDT and BFST. Using the UDEC numerical simulation method, it preliminarily explores the rock mechanical parameter threshold values for these two types of toppling. Based on this, the study investigates the deformation evolution and mechanisms of DBDT and BFST.

2 Geological setting of toppling failure

The failure characteristics of DBDT and BFST are described through case studies.

2.1 Brittle fracture shallow toppling (BFST)

As a typical toppling case, the Guobu bank slope of the Laxiwa Hydropower Station is used to illustrate the basic characteristics of BFST. The bank slope comprises ditches and ridges. The lithology of the slope rock mass mainly contains granites, which were formed in the Indosinian Period.

The Guobu bank slope at the Laxiwa Hydropower Station reveals a large-scale BFST. The reason for this is the intense unloading effect on blocky granite due to the down-cutting of the valley.

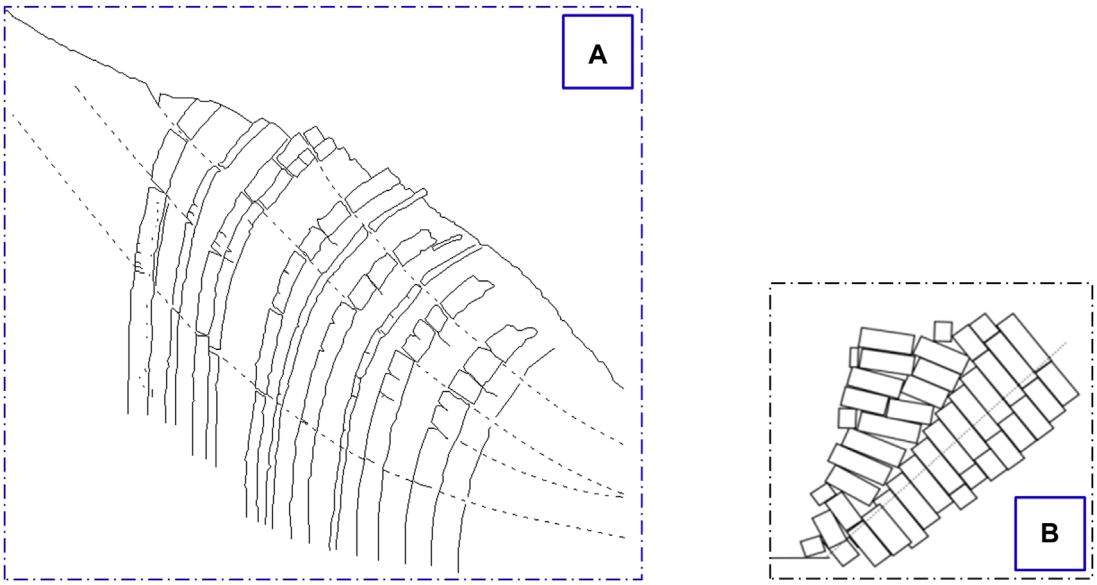

FIGURE 1
Schematic diagram of toppling model. **(A)** ductile bending deep toppling model; **(B)** brittle fracture shallow toppling modl.

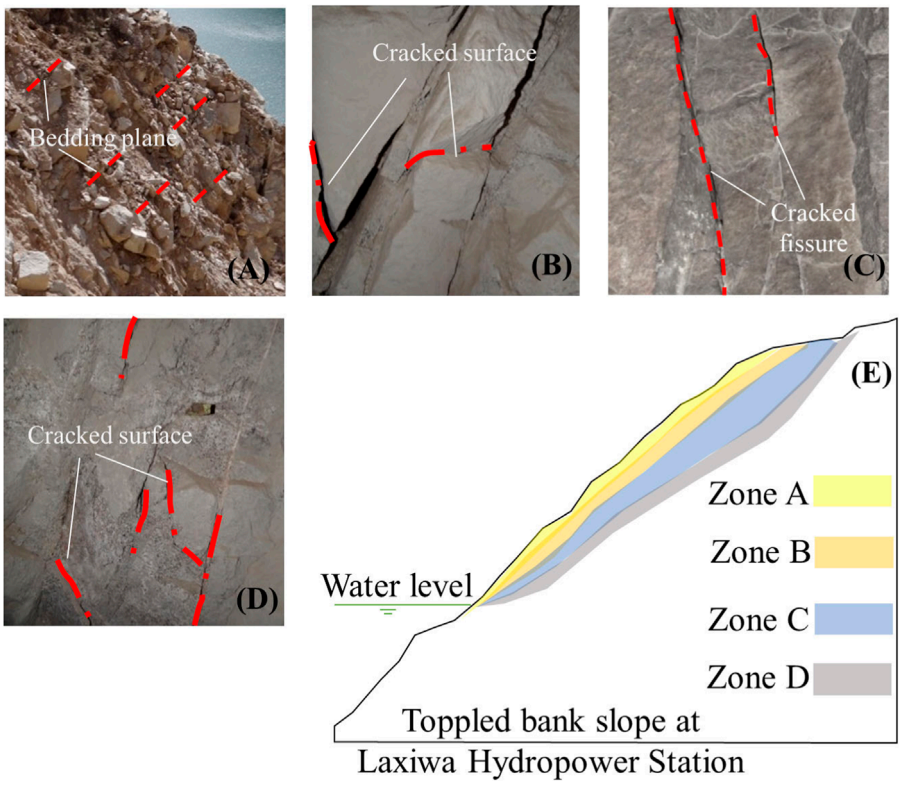

FIGURE 2
Rock mass of toppling zones of bank slope at Laxiwa Hydropower Station. **(A)** Zone A rock mass; **(B)** zone B rock mass; **(C)** zone C rock mass; **(D)** zone D rock mass; **(E)** toppled bank slope section at Laxiwa Hydropower Station.

This leads to the dense development of steep unloading fractures parallel slope surface, effectively transforming the blocky rock mass into a “plate-like” structure, resulting in the occurrence of toppling deformation. According to the observed characteristics of toppling deformation and structure, the toppling rock masses can be divided into intensified strong toppling (zone A), strong toppling (zone B),

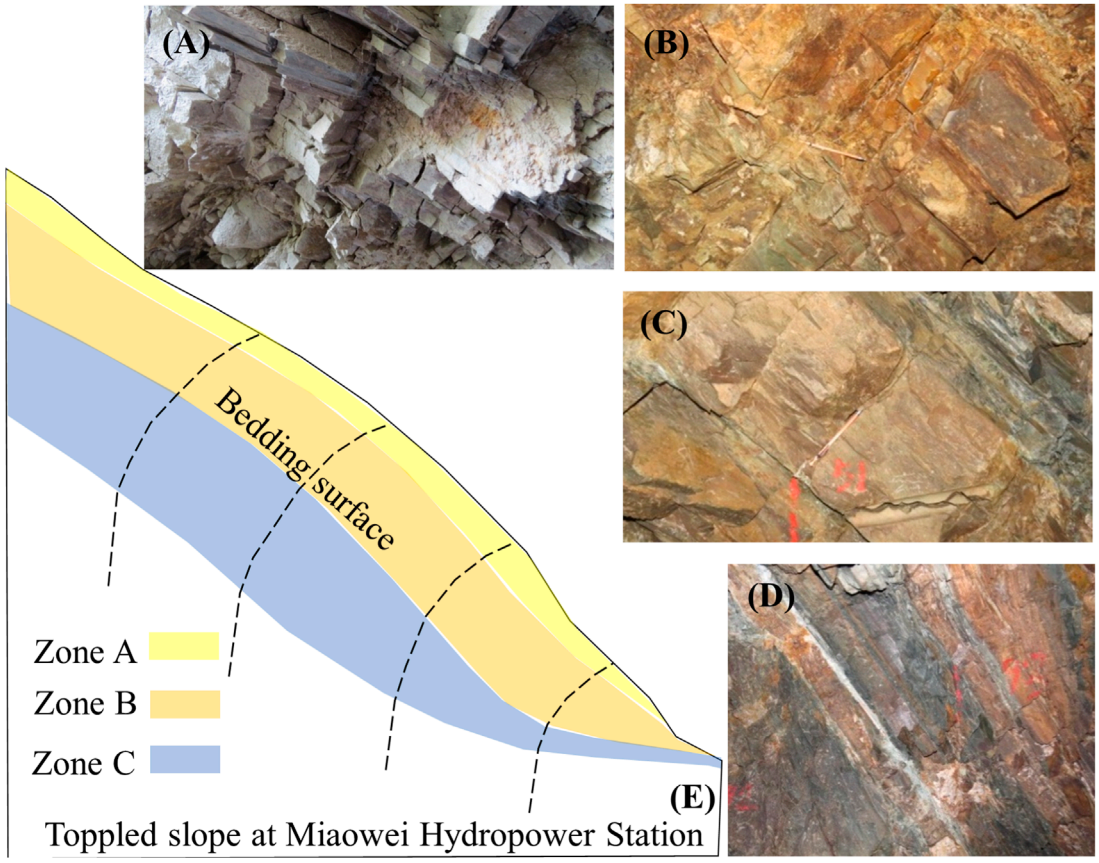

FIGURE 3
Rock mass of toppling zones of the slope in front of the dam at Miaowei Hydropower Station. **(A)** Zone A rock mass; **(B)** zone B upper rock mass; **(C)** zone B lower rock mass; **(D)** zone C rock mass; **(E)** toppled front slope of the dam section at Miaowei Hydropower Station.

weak toppling (zone C), and loose-tensile fracture rock mass (zone D) (Figure 2). The zoning characteristics of the rock mass in the toppled slope are described as follows (Cai et al., 2019):

Zone A—intensified strong toppling zone: the plate-like granite rock mass undergoes intense "cantilever beam"-type toppling and breaking, forming a tension-shear fracturing zone outside the gently inclined slope. The shallow fractured rock mass near the slope surface undergoes gravity overturning along the toppling fracture surface (zone) inclined toward the outside of the slope. This situation mainly occurs in the protruding part of the terrain where the three sides of that face free face (Figure 2A).

This type of rock mass exhibits intense toppling fracture. It generally has embedded fragmentation and blocky structures with some local fragmented structures, and it is in a state of intense unloading and relaxation. The prominent feature of this deformation and fracturing is that unlike the situation where a toppled angle greater than 50° is usually required for whole breaking and fracturing to occur in plate-like metamorphic rock mass, the plate-like granite rock mass begins to experience fracturing at a toppled angle exceeding 18°, with overall breaking and fracturing occurring at around 35°. In zone A, rock masses after toppling and fracturing experience partial collapse and destabilization. Most of them remain in a "stacked" shape on the shallow surface of the slope, typically in a state of blocky fractures or disintegration. This situation often leads to shallow stability issues of the toppled slope.

Zone B—strong toppling zone: toppling deformation results in tension cracks between granite rock slabs, resulting in wide tension cracks. The rock slabs are partially fractured and broken, and the variation of toppled angle generally ranges from 10° to 15°. The rock mass undergoes tensile and relaxation deformation, and the bedding plane generally undergoes relatively strong tensile deformation, with an overall blocky structure and locally embedded fragmented structure. The rock mass is generally under overall strong unloading and local weak unloading, with relatively poor integrity (Figure 2B).

Zone C—weak toppling zone: the toppled angle of the granite rock slabs in this zone is very small, less than 5°, or almost non-existent. There are only tensional fractures occurring between rock slabs, and within rock slabs, there are localized minor tensile fractures (fractures within the rock slabs become visible when the toppled angle reaches 5°). The rock mass is generally in a weak unloading state of tensional fracture, with a blocky structure, and it exhibits relatively good overall integrity. This type of deformation represents a weaker degree of toppling deformation and generally occurs in the deeper parts of the deformed rock mass, which is a relatively stable part within the slope (Figure 2C).

Zone D—relaxation with tensional fractures: this zone represents an elastic relaxation area in the deeper parts of the slope, resulting from the outward toppling effect. No significant toppling is observed; only localized relaxation and tensional

TABLE 1 Typical cases of toppled slopes and their rock mass mechanical parameters.

Disaster point	Deformation features	Main lithology	UCS MP	Deformation modulus MPa	Poisson's ratio
Jiefang Gou slope at Jinping Hydropower Station	DBDT	Metamorphic sandstone, slate, and carbonaceous slate	51/12.5	2,100	0.16/0.24
Hydrological station landslide at the Jinping Hydropower Station	DBDT	Metamorphic sandstone, slate, and carbonaceous slate	51/12.5	2,100	0.16/0.24
Xingguang Group III bank slope at Xiluodu Hydropower Station	BFST	Marl limestone, muddy fine sandstone, and sandy shale	78	900	0.3
Dam site toppled slope at Miaowei Hydropower Station	DBDT	Slate and schist with metamorphic sandstone	63/3.2	1,050	0.28
Guobu bank Slope at Laxiwa Hydropower Station	BFST	Granite cut by joints	100	1,500/10,000	0.23
Double-sided toppled slope	DBDT	Quartz schist	18	1,600	0.28
Toppling slope at Longtan Hydropower Station	DBDT	Sandstone and slate	60/130	1,500	0.27
Toppled lope at Gushui Hydropower Station	DBDT	Metamorphic sandstone, slate, and limestone	15/130	1,580	0.2/0.25

UCS: uniaxial compressive strength; DBDT: ductile bending deep toppling; BFST: brittle fracture shallow toppling.

TABLE 2 Mechanical parameters of rock mass.

Scheme	FA01	FA02	FA03	FA04	FA05	FA06
UCS(MPa)	10	20	40	60	80	100
Gravity (kg/m3)	2,700	2,700	2,700	2,700	2,700	2,700
GSI	62	62	62	62	62	62
Bulk modulus K(Pa)	4.2e9	5.9e9	8.4e9	10.3e9	11.9e9	13.0e9
Shear modulus G (Pa)	2.5e9	3.6e9	5.0e9	6.2e9	7.1e9	8.0e9
Internal friction angle φ(°)	33	38	44	47	49	51
Cohesion c (Pa)	1.7e5	2.3e5	3.3e5	4.2e5	5.0e5	5.9e5
Tensile strength (Pa)	3.0e4	4.0e4	6.0e4	8.0e4	1.0e5	1.2e5
Dilation angle (°)	2	2	2	2	2	2

UCS: uniaxial compressive strength.

fractures along joint surfaces are seen. The rock mass exhibits a blocky-whole structure and is essentially in its original state. This phenomenon is one of the characteristics of the plate-like fractured granite rock mass, which shows its prominent elastic properties (Figure 2D).

2.2 Ductile bending deep toppling (DBDT)

The slope in front of the dam at the Miaowei Hydropower Station is a typical soft and hard interbedded structure slope, primarily composed of metamorphic rocks. Using the slope in front

TABLE 3 Mechanical parameters of the structural plane.

Structural plane	Normal stiffness jkn	Shear stiffness jks	Cohesion c (Pa)	Internal friction angle (°)	Dilation angle (°)	Tensile strength (Pa)
joint1	5e10	3e10	0	30	0	0

TABLE 4 Elastic modulus and Poisson's ratio parameters of rock mass.

Scheme	FA01	FA02	FA03	FA04	FA05	FA06
Bulk modulus K(Pa)	4.2e9	5.9e9	8.4e9	10.3e9	11.9e9	13.0e9
Shear modulus G(Pa)	2.5e9	3.6e9	5.0e9	6.2e9	7.1e9	8.0e9
Elastic modulus E(Pa)	6.3e9	9.0e9	12.5e9	15.5e9	17.8e9	20.0e9
Poisson's ratio μ	0.25	0.25	0.25	0.25	0.25	0.25

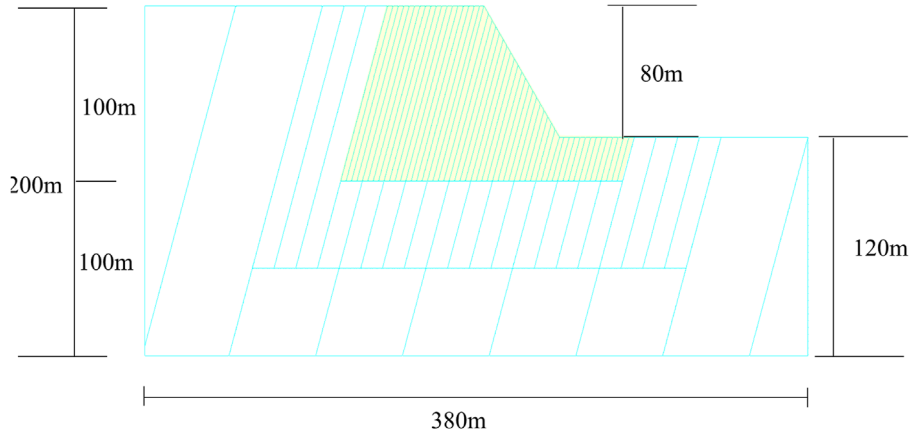

FIGURE 4
Experimental design model.

of the dam as an example, the basic characteristics of the DBDT are explained.

The exposed bedrock in this slope is the third sub-rock group (J_2h^{2-3}) in the upper section of the Jurassic Huakai Left Formation. The rock types mainly include slate, phyllite, schist, and metamorphic quartz sandstone, with alternating soft and hard rock conditions. Due to significant tectonic activity, the structural orientation of the rock layers varies considerably in space, and the overall trend of the normal bedding planes is with a dip angle of 80°–85°. Due to factors such as slope terrain and rock mass structure, the slope in front of the dam experiences strong toppling deformation (Figure 3).

(1) Zone A—toppling and collapse zone

When the rock layers topple and rotate significantly, the rock mass undergoes intense fracturing and breaking, forming a tensile fracture zone steep dip outside the slope. There is significant internal rock tensile fracture, strong relaxation, and clear evidence of overhangs, with cracks filled with gravel, angular fragments, and rock debris. For those with severe deformation, the rock mass above the fracture zone is almost separated from the underlying bedrock, and local gravitational fall displacement occurs. This type of fracture is extremely intense toppling deformation and occurs in the shallow surface of the rock mass undergoing toppling deformation (Figure 3A).

(2) Zone B—strong toppling zone

This zone can be further divided into two subsections, upper and lower, based on the intensity of toppling and the different fracturing mechanisms.

Zone B upper-toppling and dislocation zone (Figure 3B).

When the rock layers experience significant toppling, in addition to intense tensile fracturing within the layers, shear deformation (tensile-shear) occurs along gentle dip outer joints of the slope, exhibiting significant development of cutting shear layer. This type of

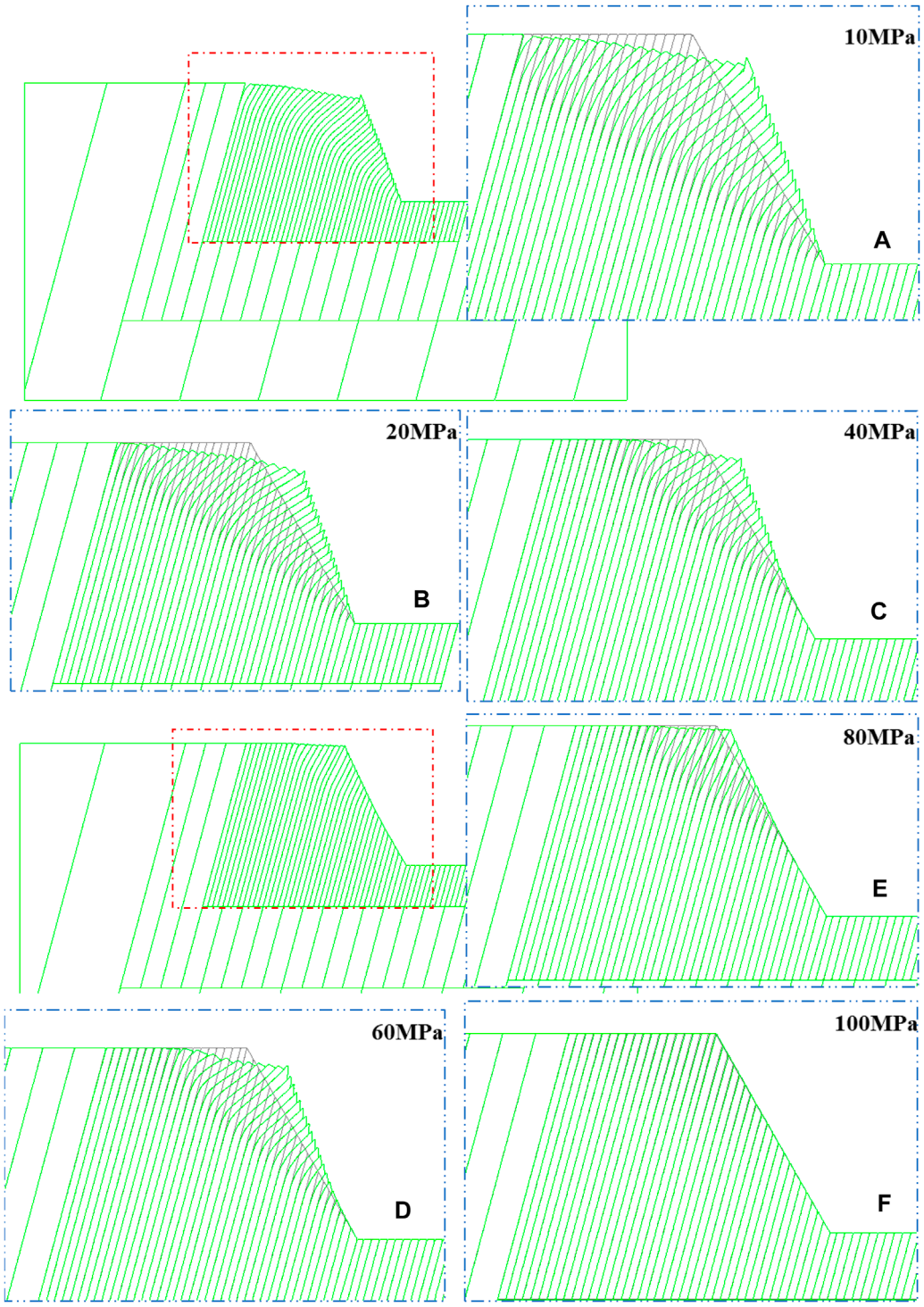

FIGURE 5
Model overlay effect images of different rock mechanics parameters. **(A)** FA01, 10 MPa; **(B)** FA02, 20 MPa; **(C)** FA03, 40 MPa; **(D)** FA04, 60 MPa; **(E)** FA05, 80 MPa; **(F)** FA06, 100 MPa.

deformation and fracturing belongs to the upper section of intense toppling and occurs in the middle part of the rock mass undergoing toppling deformation.

Zone B lower-toppling and tensile zone (Figure 3C).

With an increasing toppled angle of the rock layers, vertical bedding tensile fracturing begins to develop within the layers or along existing structural planes. This type of tensile fracturing generally occurs in the hard rock layers between two softer rock layers, representing a situation with a relatively strong toppling

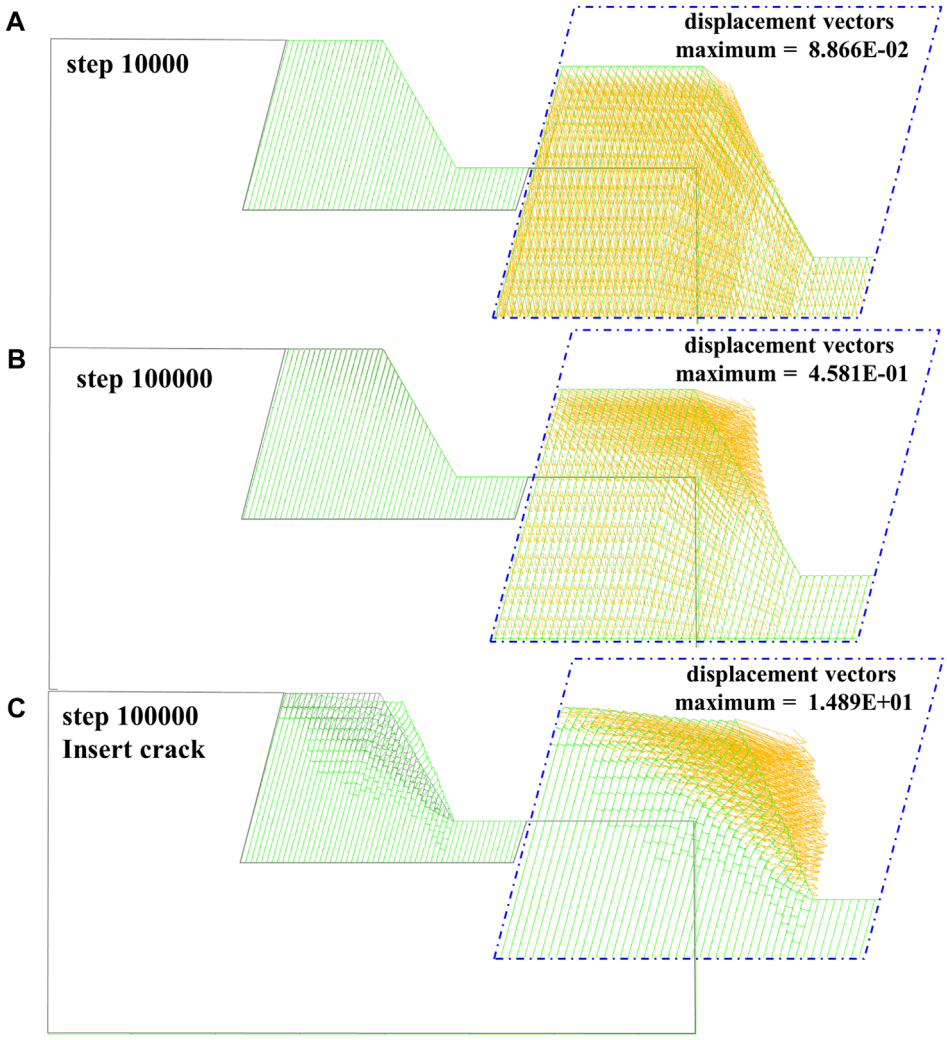

FIGURE 6
BFST displacement vectors evolution process. **(A)** Original model 10,000 steps; **(B)** original model 100,000 steps; **(C)** inserted cracks model 10,000 steps.

deformation. Spatially, it occurs in the deeper parts of the toppled slope.

(3) Zone C—weak toppling deformation zone

In this zone, the toppled angle of rock layers is relatively small, which is generally less than 10°. The layered rock masses experience shear sliding along interlayer or relatively weak rock zones. There are no significant fractures within the layers, and only minimal tensile fractures occur within the harder rock layers. This type of situation represents a weak toppling deformation and is typically found in the deeper parts of the slope (Figure 3D).

It is worth noting that the interface between zones B and C is also where the rock layers exhibit the higher curvature of bending toppling. It is the location where rock layer fracturing is most likely to occur. Therefore, the bottom surface of zone C and the top surface of zone B serve as potential sliding surfaces for deep-seated sliding associated with toppling deformation (Figure 3E).

3 Typical toppling cases

From the existing research works, it is evident that the mechanical properties of the toppled rock mass are closely related to the development characteristics of its toppling deformation. Starting from the soft and hard conditions of rocks, we can summarize the relationship between the characteristics of toppling deformation and the rock mass's mechanical parameters through typical cases. Table 1 presents the selected typical examples of toppled slopes and their rock mass mechanical parameters.

According to the standard for engineering classification of rock mass (Ministry of Construction of the People's Republic of China, 2014), the uniaxial compressive strength (UCS) value is used to differentiate between hard and soft rock for the classification of engineering rock masses. If the UCS is greater than 30 MPa, it is classified as hard rock, and if it is less than 30 MPa, it is classified as soft rock. However, the soft and hard characteristics of toppling rock masses are different from those of engineering rock masses.

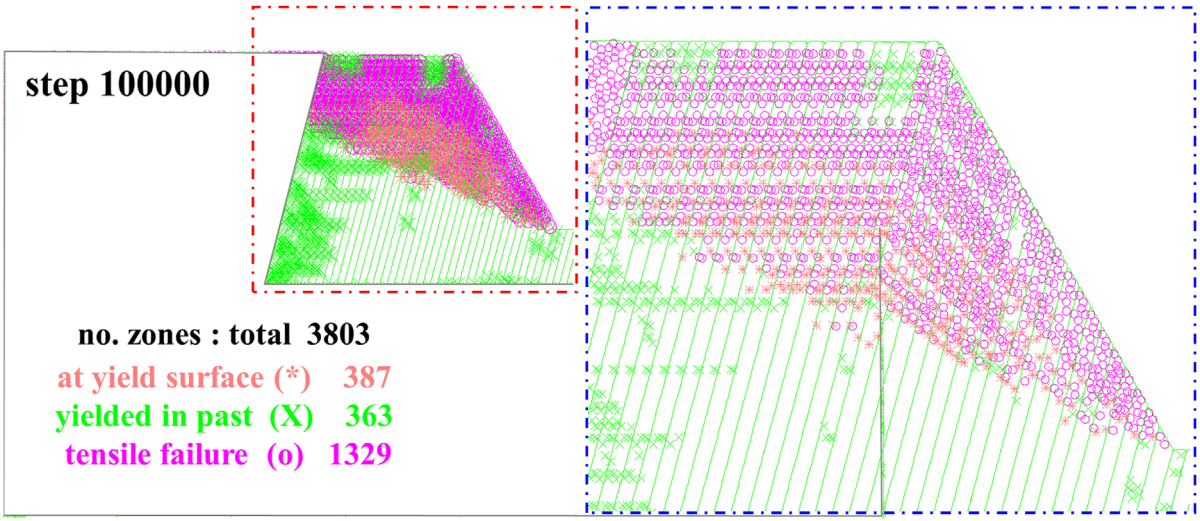

FIGURE 7
Plastic zone distribution of the original model at 100,000 steps.

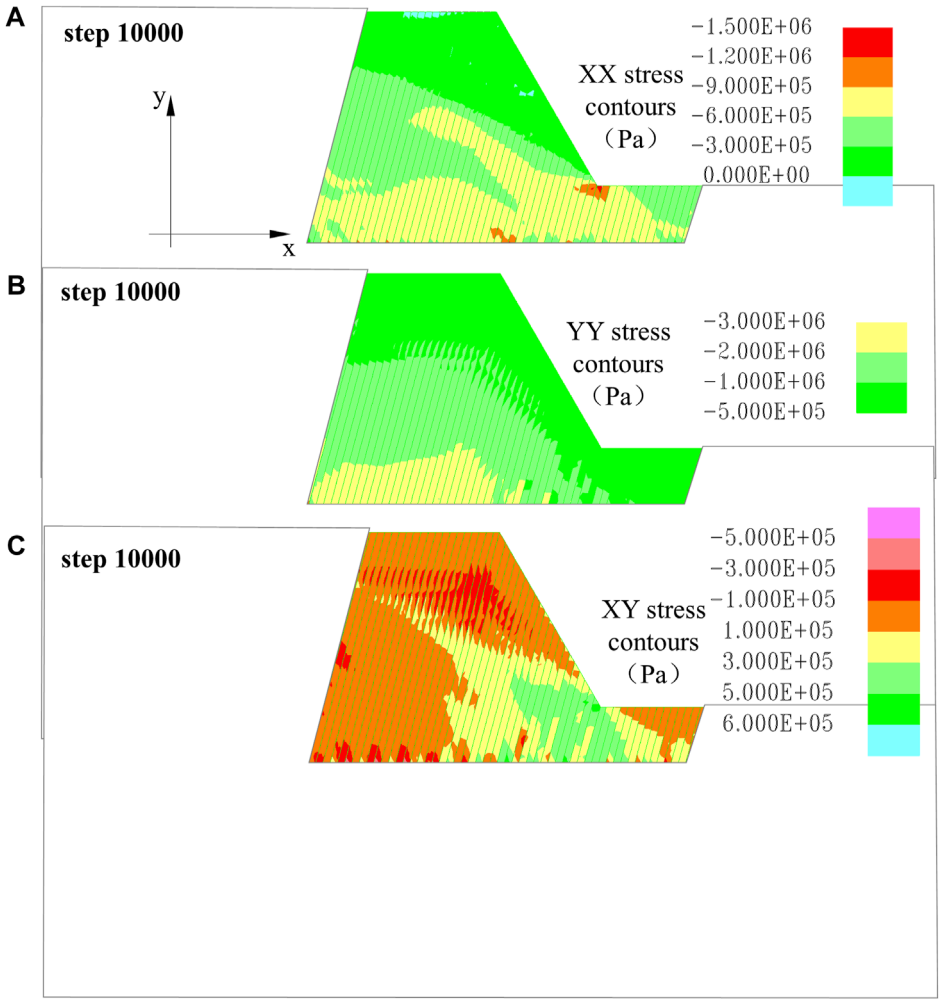

FIGURE 8
Stress characteristics of the original model evolution process. **(A)** XX stress contour 10,000 steps; **(B)** YY stress contour 10,000 steps; **(C)** XY stress contour 10,000 steps.

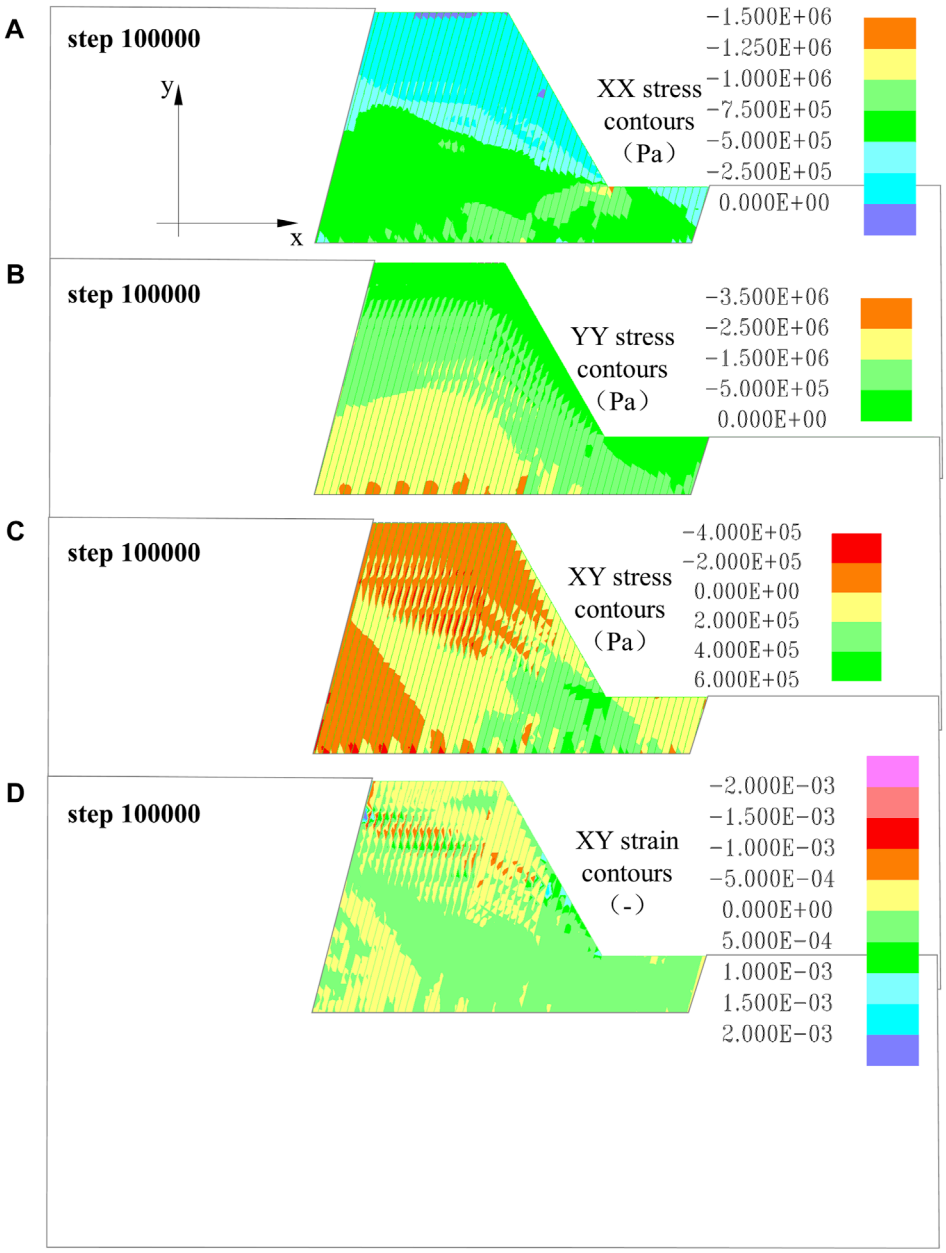

FIGURE 9
Stress characteristics of the original model evolution process. **(A)** XX stress contour 100,000 steps; **(B)** YY stress contour 100,000 steps; **(C)** XY stress contour 100,000 steps; **(D)** XY strain contour 100,000 steps.

4 Mechanical parameter threshold for toppling soft and hard rocks

4.1 Model parameters

The classification of soft and hard rock in toppling rock masses is different from the classification of general engineering rock masses (Table 1). Table 1 provides statistics of rock mechanics parameters for typical toppled rock mass cases, demonstrating significant differences in mechanical parameters (saturated uniaxial compressive strength, elastic modulus, and Poisson's ratio) between toppled rock masses and general rock masses. Hard rock typically exhibits characteristics of breaking and fracturing, whereas soft or relatively soft rock generally shows "flexible" features, involving ductile deformation, and experiences ductile bending toppling.

This section adopts the discrete element method (UDEC) to establish a numerical simulation model to investigate the mechanical parameter thresholds between BFST hard rock and DBDT soft rock. The discrete element method is highly effective for analyzing toppling deformations in layered and blocky rock masses.

The numerical model will provide a detailed representation of the development and evolution of toppling deformations, including the law of interlayer dislocation and movement and the development of interlayer stresses. The model parameters are chosen with

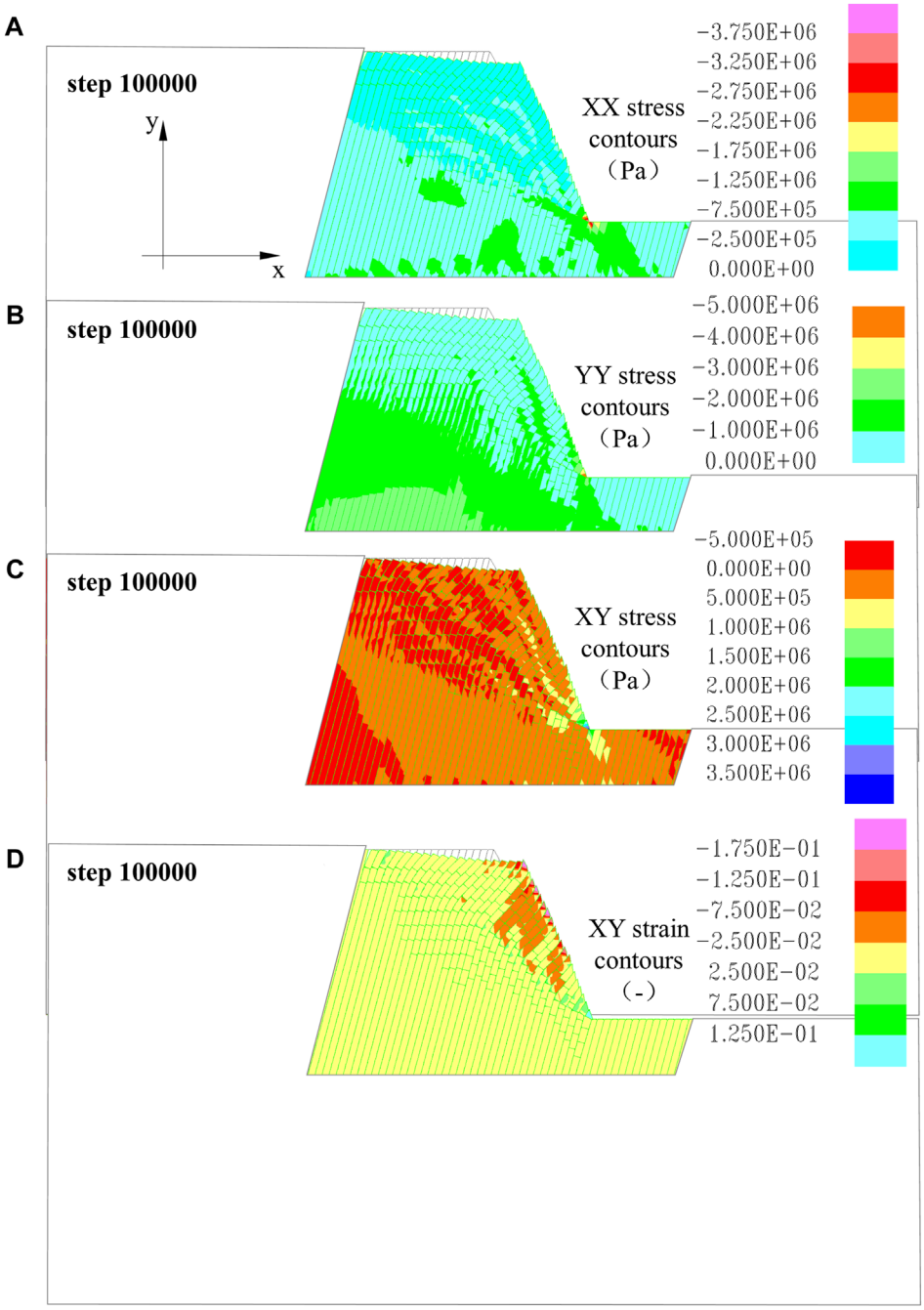

FIGURE 10
Stress characteristics of the inserted crack model evolution process. **(A)** XX stress contour 100,000 steps; **(B)** YY stress contour 100,000 steps; **(C)** XY stress contour 100,000 steps; **(D)** XY strain contour 100,000 steps.

reference to the research parameters of Nichol et al. (2002) to analyze the effects of toppling deformations for different UCS rock mechanical parameter sets. Considering that toppling deformations commonly occur in rock masses with blocky or massive structures, it is assumed to select a block structured rock mass with a rock mass strength index (GSI=62). The UCS values selected for the numerical model are 10, 20, 40, 60, 80, and 100 MPa, representing a range of rock mechanical parameters for the threshold analysis. The parameters used in the models are shown in Tables 2–4.

4.2 Numerical model

The experimental model in this study takes into account the influence of boundary effects on the study area. The simplified model has dimensions of 380 m (horizontal direction) × 200 m (horizontal direction) and includes a single set of bedding planes. The rock layers have a dip angle of 75°, and within the main study area, the spacing between them is 3 m. From the surface of the slope toward the interior of

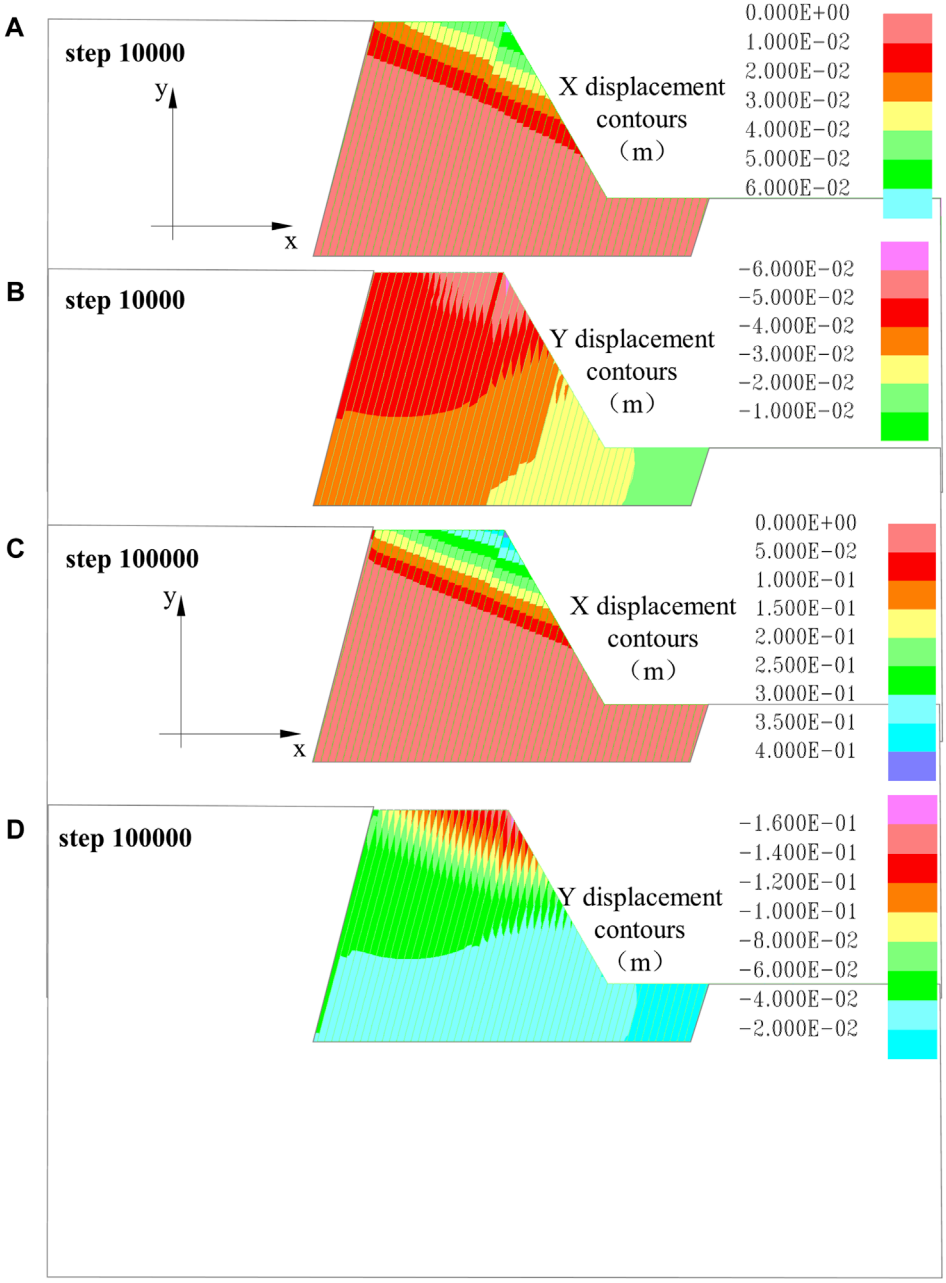

FIGURE 11
Displacement characteristics of the original model evolution process. **(A)** XX displacement contour 10,000 steps; **(B)** YY displacement contour 10,000 steps; **(C)** XX displacement contour 100,000 steps; **(D)** YY displacement contour 100,000 steps.

the slope, the spacing gradually increases to 3 m, 12 m, and 48 m. The main research area has a slope height of 80 m. The numerical model created for this study is shown in Figure 4. The boundary conditions of the model are set with velocity constraints on the left and right boundaries (X-direction) and the bottom boundary (Y-direction), whereas the slope surface is considered a free face. The model's rock materials adopt an elastic–plastic model with the Mohr–Coulomb yield condition, and the stress field in the model only considers the effects of gravity.

4.3 Mechanical parameters threshold

The model was computed to obtain its toppling failure process. The same steps of iterations were set (100,000). The final failure patterns for different schemes were overlaid with the original model, as shown in Figure 5.

The comparative analysis of overlay effect images for different schemes with varying rock mechanics parameters reveals the following. In the images (Figure 5), the left corner shows the final failure state of the model, while the right corner displays enlarged

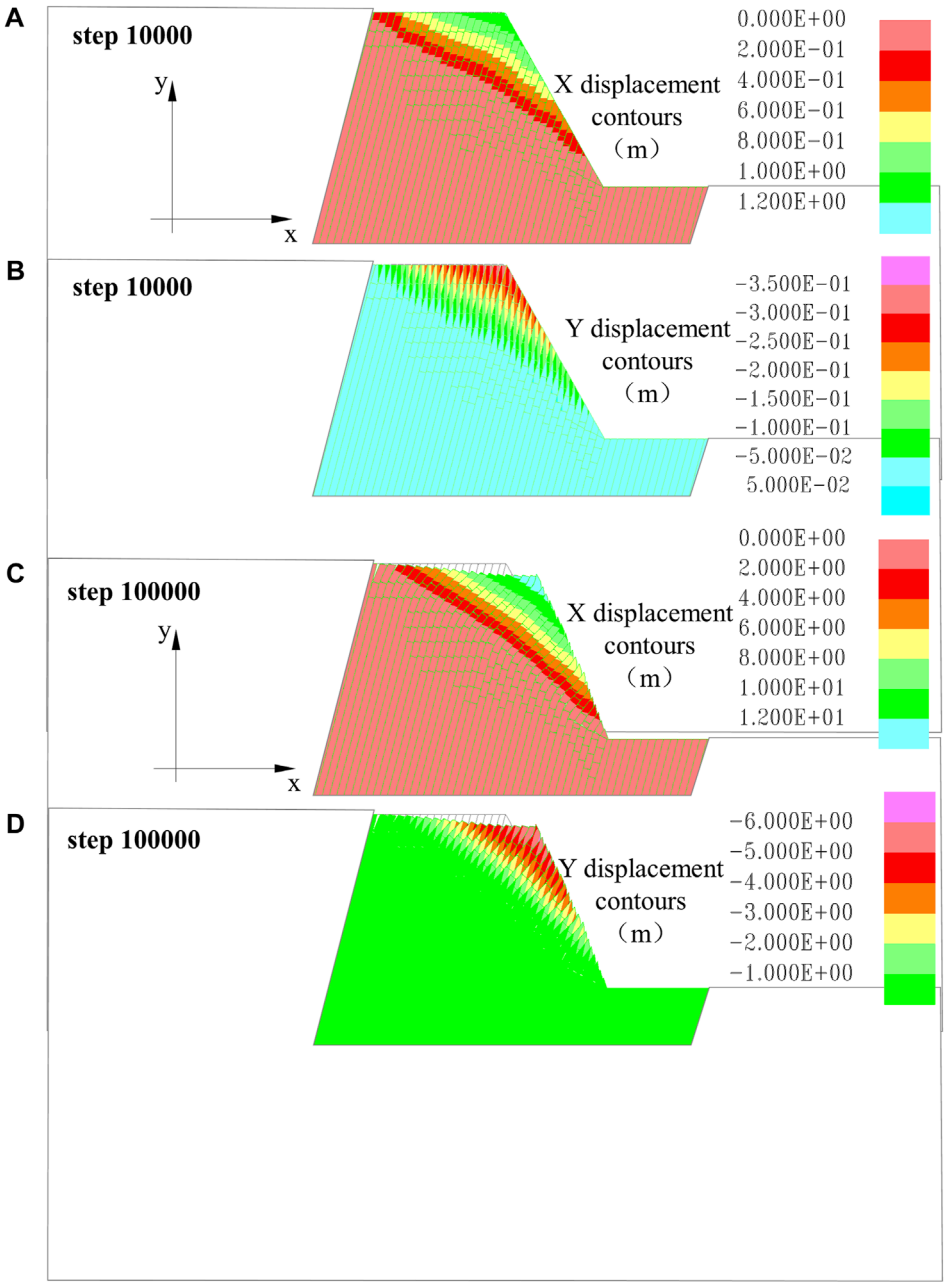

FIGURE 12
Displacement characteristics of the inserted crack model evolution process. **(A)** XX displacement contour 10,000 steps; **(B)** YY displacement contour 10,000 steps; **(C)** XX displacement contour 100,000 steps; **(D)** YY displacement contour 100,000 steps.

overlay images of the models before calculation and after failure. The black lines represent the model before calculation, and the green lines represent the final failure state after 100,000 steps.

From Figure 5, it is evident that within a UCS range of 10 MPa–80 MPa, significant bending toppling deformations occur near the crest of the model. As UCS increases, the extent of the toppling deformation and the magnitude of deformation decrease gradually. Specifically, when UCS is 80 MPa, the bending toppling deformations are minimal and not significant. When UCS is 100 MPa, as seen in the local magnification of the deformation overlay images, the deformation values are minimal, and there are no apparent toppling and bending phenomena.

Based on the analysis of the overlay effect images, it can be concluded that the range of rock mechanics parameters corresponding to bending toppling deformations in the model lies within the range of 80 MPa–100 MPa for UCS. The Poisson's ratio of the rock is assumed to be 0.25, and the range of values for tensile strength and elastic modulus are 0.01 MPa–0.12 MPa and 17.8 MPa–20.0 MPa, respectively. It is reasonable to preliminarily assume that the rock mechanics parameters with UCS = 80 MPa

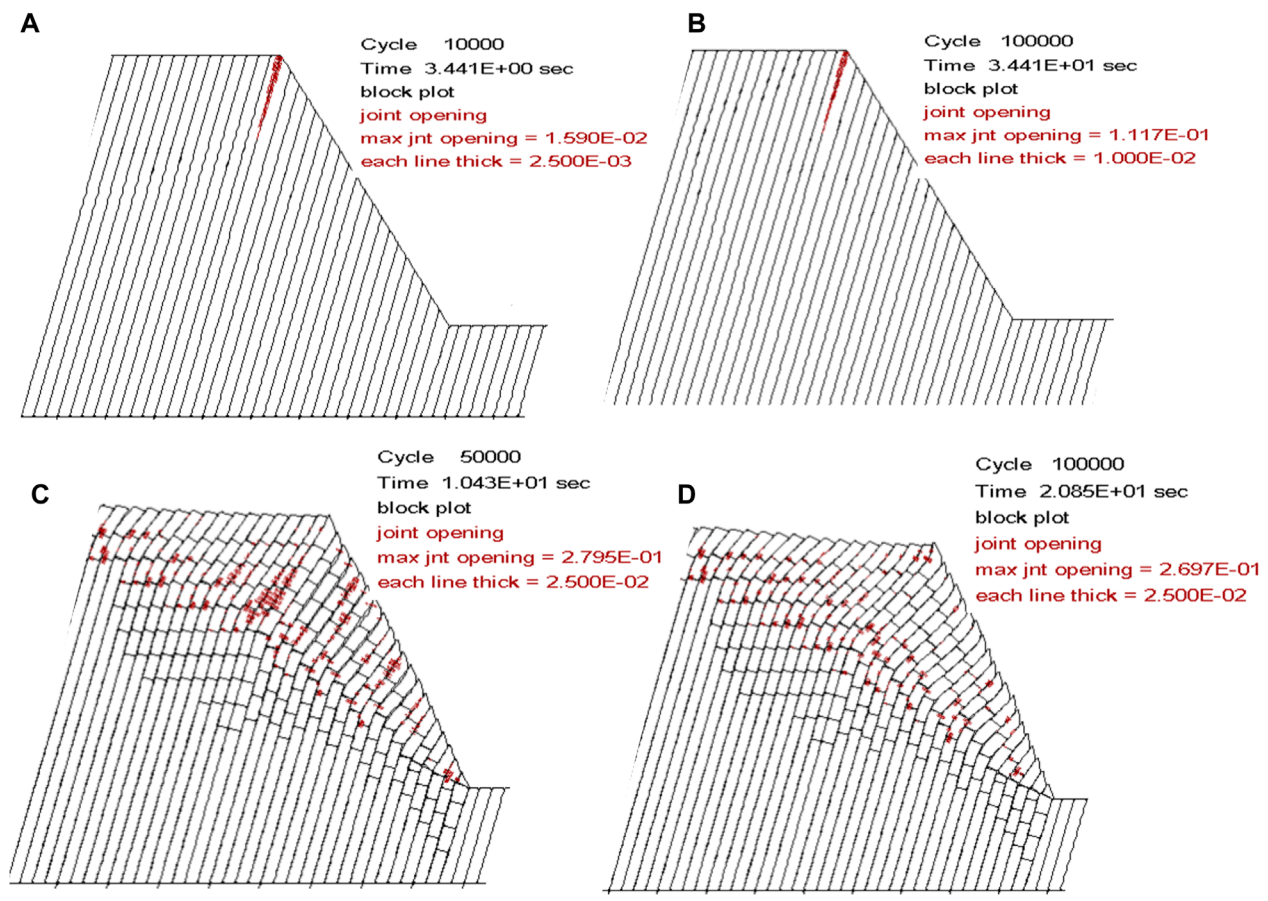

FIGURE 13
Distribution and variation of structural plane openings. Each red line in the figure has a width equal to "each line thick," where the overall width represents the cumulative opening of multiple lines, and this width signifies the opening of the structural planes. **(A)** Original model 10,000 steps; **(B)** original model 100,000 steps; **(C)** inserted crack model 50,000 steps; **(D)** inserted crack model 100,000 steps.

serve as the threshold values that separate soft rock with ductile bending deformations from hard rock with brittle fractures. These threshold values are as follows: tensile strength of 0.01 MPa, Poisson's ratio of 0.25, and elastic modulus of 17.8 MPa.

As the parametric study through numerical simulations is not comprehensive enough and lacks depth, further calibration is needed through extensive investigations of field cases to confirm whether 80 MPa is indeed the critical threshold for ductile bending toppling deformations. However, for trend analysis in numerical simulations, this threshold can be considered a preliminary reference value for rock mechanics parameters, subject to further validation by additional research.

5 Evolution analyses of BFST and DBDT

5.1 Brittle fracturing shallow toppling (BFST)

For the BFST, the rock mechanical parameters are chosen with UCS = 100 MPa.

The experimental design considered that the UDEC calculation process cannot simulate block self-fracture breaking. We determine bending fracture based on the plastic zone of tension failure, and a verification model for rock tensile failure was chosen to reveal the tensile fracture process in brittle fracturing toppling failure (Cai et al., 2020).

The approach for brittle fracturing toppling failure is to insert a stepped fracture plane based on the depth of toppling fracture. The depth of fracture is determined according to the mechanical analysis (Cai et al. 2022). To analyze the mechanical behavior characteristics throughout the development of toppling deformation, multiple levels of fracture depths are inserted, mainly to capture tensile failure in the plastic zone of the model.

5.1.1 BFST displacement vector evolution

After calculating 100,000 steps for the BFST model, there were no significant macroscopic flexible toppling deformations or signs of failure. On examining the distribution of the plastic zone, it is apparent that the rock layers have experienced tensile failure. As the UDEC software itself cannot simulate block self-fracture breaking, and to account for the rock's tensile fracture, fractures are inserted to represent the occurrence of tensile fractures in the model.

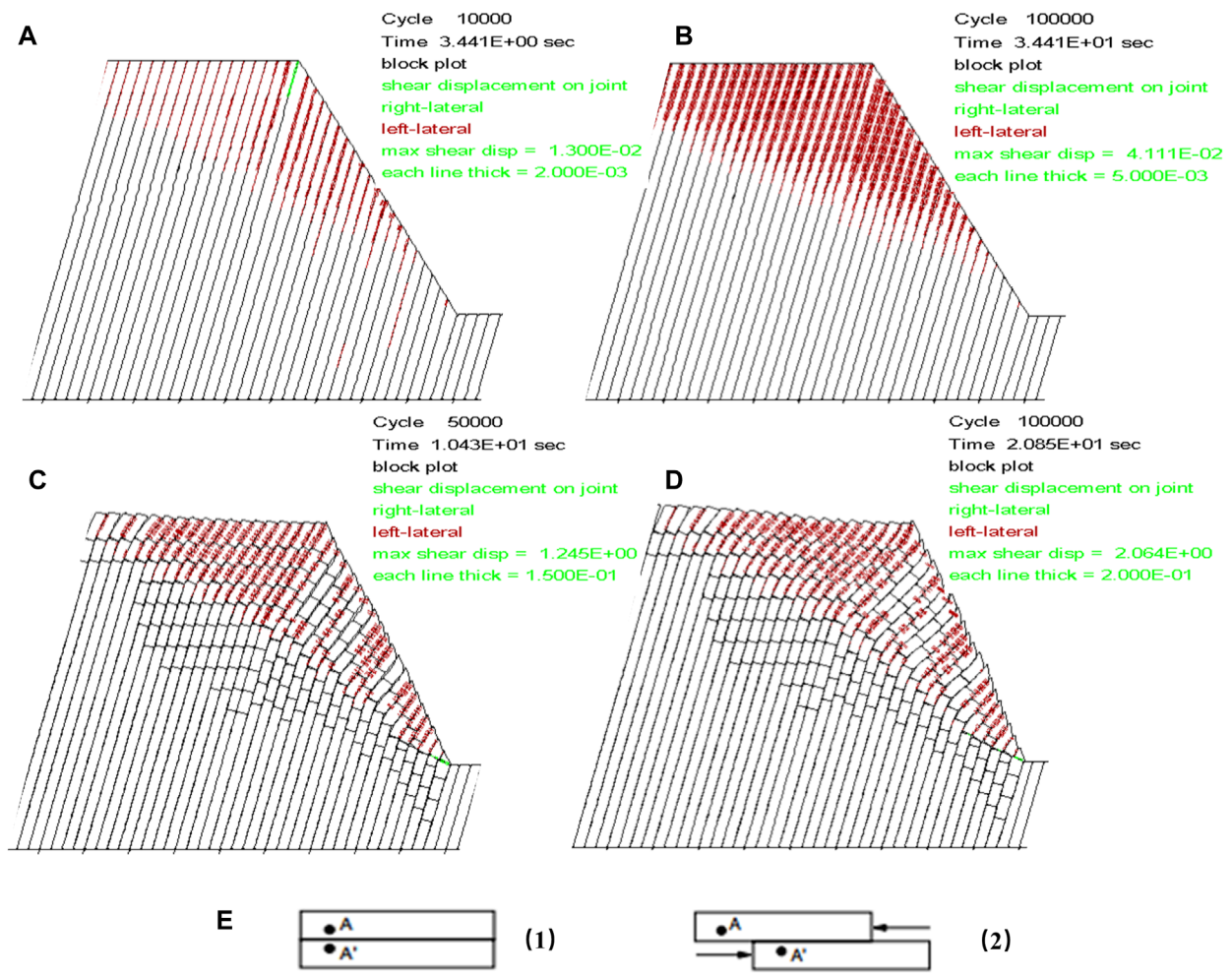

FIGURE 14
Distribution and variation of shear displacement on structural planes. Each red line has a width equal to "each line thick," where the overall width represents the cumulative width of multiple lines, and this width signifies the value of shear displacement of the structural planes. **(A)** Original model 10,000 steps; **(B)** original model 100,000 steps; **(C)** inserted crack model 50,000 steps; **(D)** inserted crack model 100,000 steps; **(E)** definition of shear displacement direction, two points A and A′, before separation (1), after separation (2); left lateral shear displacement is the left side of A at the original corresponding point after separation.

The depths of these inserted fractures represent multiple levels of toppling fracture depths.

In the model's slope foot, based on studies of toppling fracture surfaces (Aydan and Kawamoto, 1992), a straight line inclined at an angle of 12° to the plane of the rock layers was chosen as the base sliding surface for the lower sliding area of the slope. This line intersects with the model's toppling fracture depth. The specific deformation and failure evolution process is described as follows.

The original model underwent 100,000 steps without showing significant macroscopic flexural deformation or signs of failure. However, the displacement vectors during the computation process indicated the toppling deformation of the rock layers, with the horizontal component being significantly greater than the vertical component. The vector's direction corresponds to the direction of the toppling deformation. With an increase in the number of iterative steps, the values of the displacement vectors gradually increased, changing from 0.08866 m at 10,000 steps to 0.4581 m at 100,000 steps, with the horizontal displacement component increment being larger than the vertical component increment. Figure 6 shows the overlay images of the initial model (in gray) and the certain step model (in green), and a clear comparison of the rock slab deformation before and after also highlights its toppling deformation characteristics.

When the iteration reached 100,000 steps, the plastic zone was primarily characterized by tension failure. Those yielded in past elements during the model stress adjustment process were not considered for the current slope failure. These elements on the yield surface or undergoing tension failure is similar in shape to the calculated fracture depth of a single rock slab in the rock layer, approximately in a stepped shape, as illustrated in Figure 7.

Based on the distribution characteristics of the plastic zone after 100,000 steps and the toppling fracture depth (Cai et al., 2022), a new calculation model was constructed by inserting cracks (fracture surfaces). The newly toppled fractured model was then recalculated, and each level of fracture depth at this time was simplified as the first fracture depth.

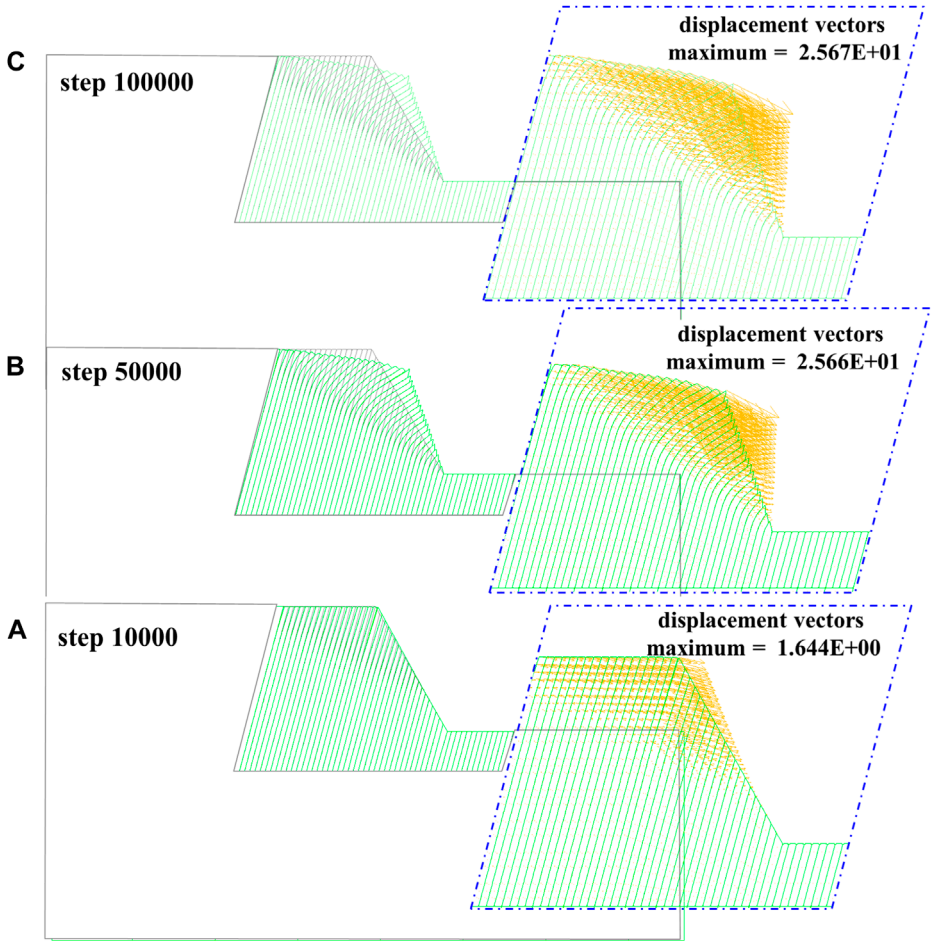

FIGURE 15
DBDT displacement vectors evolution process. **(A)** Original model 10,000 steps; **(B)** original model 50,000 steps; **(C)** original model 100,000 steps.

Figure 6C indicates that the maximum displacement vector of the new model after 100,000 steps is 14.89 m, and the maximum displacement vector occurs at the top corner of the slope, with the toppling deformation being most prominent. At this point, the failure baseline mainly occurs at the interface of the same level fracture depth within the slope.

5.1.2 Stress and deformation characteristics evolution

The results of the BFST original model are shown in Figure 8 to Figure 9.

Figure 8 displays stress distribution after 10,000 iterations, and the Y-direction stress conforms to the typical layer-wise distribution. The X-direction stress contour shows the presence of localized compressive stress at the slope foot, with an area of tensile stress concentration at the slope crest. The XY shear stress contour reveals a concentration of shear stress in a certain depth range at the slope foot, with the maximum shear stress value being 6×10^5Pa.

When the iteration increases to 100,000 steps (Figure 9), the Y-direction stress shows compressive stress concentration in individual layers at the bottom of the study area, as a result of stress adjustments. The numerical values of compressive stress concentration at the slope foot in the X-direction stress contour have increased from 1.2×10^6 Pa to 1.5×10^6Pa, and the scale of tensile stress concentration at the slope crest has also expanded. The range of shear stress concentration at the slope crest in the XY shear stress has increased. Figure 9 indicates that, at this point, the model exhibits relatively small shear strains with an irregular distribution, and there is no apparent potential surface for instability or failure.

After inserting cracks into the newly created model, the stress–strain characteristics of 100,000 steps are as shown in Figure 10. At this point, the rock mass exhibits significant toppling deformation along the toppled fracture surfaces.

Figure 10 illustrates the X-direction stress, with compressive stress increasing to 3.75×10^6Pa at the slope foot. Y-direction stress experiences an increase in compressive stress within the toppled slope along the same level fracture surfaces, with stress values rising to $1–2\times10^6$Pa. XY shear stress, centered at the slope foot, forms multiple bands of concentrated shear stress along the same-level fracture surfaces, with shear stress values increasing to 3.5×10^6Pa. Figure 10 indicates that shear strain mainly occurs within the rock blocks at the slope foot and within the range of the second-level fracture depth. These results suggest that the implantation cracks of the newly created model result in significant toppling deformation and stress concentration related to the toppled fractured surfaces.

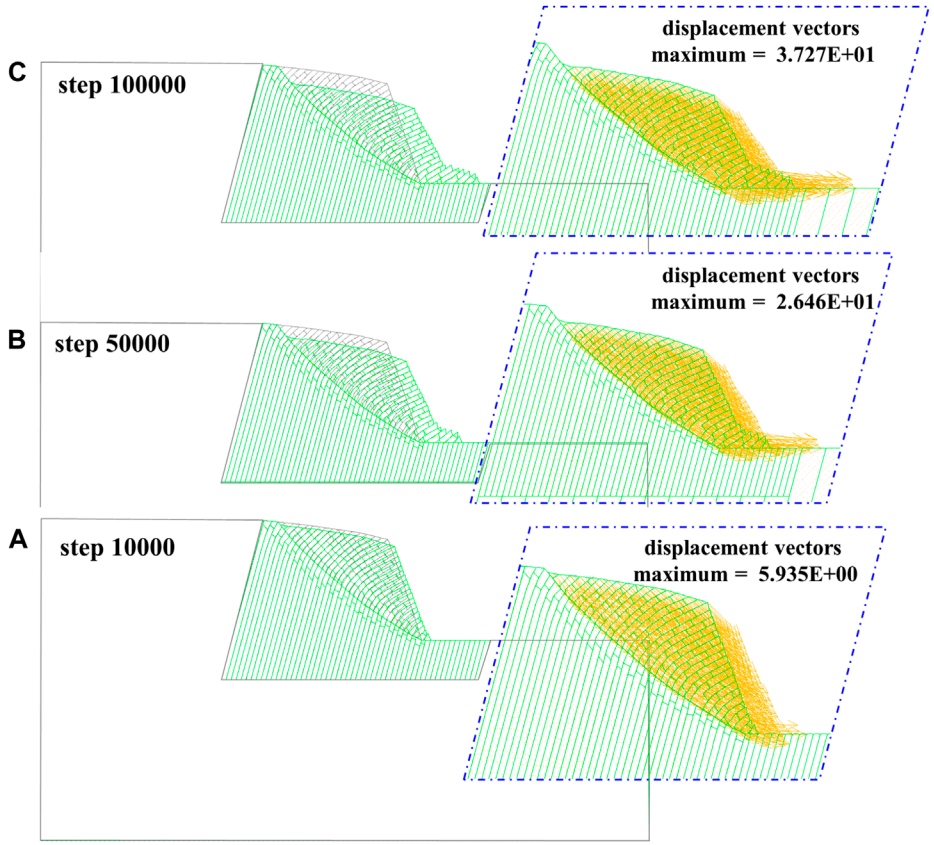

FIGURE 16
DBDT displacement vectors evolution process. **(A)** Inserted cracks model 10,000 steps; **(B)** inserted cracks 50,000 steps; **(C)** inserted cracks model 100,000 steps.

After 100,000 iterations of the original model, the model overlay images show that there was no significant deformation. The specific displacement results can be seen in Figure 11. As the steps increase, both the maximum displacements in the *X* and *Y* directions slightly increase. At 10,000 steps, the maximum displacements were 0.06 m in the X-direction and 0.06 m in the Y-direction. However, at 100,000 steps, the maximum displacement increased to 0.4 m in the X-direction and 0.16 m in the Y-direction, with the X-direction displacement being greater than the Y-direction displacement change. Overall, the extent of deformation development did not change significantly.

After inserting cracks and reconstructing the model, the overlay image results of the newly created model reveal that significant toppling deformation and failure occur after 100,000 iterations (Figure 12). The results of the iterative calculations indicate that as the steps increase, both the maximum displacements in the *X*and *Y*directions increase. At 10,000 steps, the maximum displacements were 1.2 m in the X-direction and 0.35 m in the Y-direction. However, at 100,000 steps, the maximum displacements increased to 12.0 m in the X-direction and 6.0 m in the Y-direction. It is evident that the X-direction displacement change is greater than that in the Y-direction, indicating the characteristics of toppling deformation. Additionally, the range of deformation and failure continuously expands.

5.1.3 Characteristics of interlayer stress and displacement

When the tensile and shear stress acting on the structural planes exceed their strength, the cracks begin to open. Once the opening exceeds a certain limit, it becomes impossible to obtain information about further opening changes and the stress distribution on the structural planes. The magnitude of the opening obtained in the model is directly proportional to the forces acting on the structural planes within the model. The opening of the structural planes can reflect the stress distribution on the rock layer's structural planes.

From Figure 13, each red line in the figure has a width equal to "each line thick" shown in the figure. The overall width represents the cumulative opening of multiple lines, and this width signifies the opening of the structural planes. During the development of toppling deformation, the maximum opening of the structural planes in the original model was 0.0159 m at 10,000 steps and 0.1117 m at 100,000 steps, respectively. After inserting the cracks, the maximum opening of the structural planes was 0.2795 m at 50,000 steps and 0.2697 m at 100,000 steps, respectively.

The structural plane opening of the original model initially occurred at the front edge of the slope, and the deformation in the original model was not significant. The opening values were relatively small, with a maximum of 0.1117 m, and there was no extension of the opening of the structural plane.

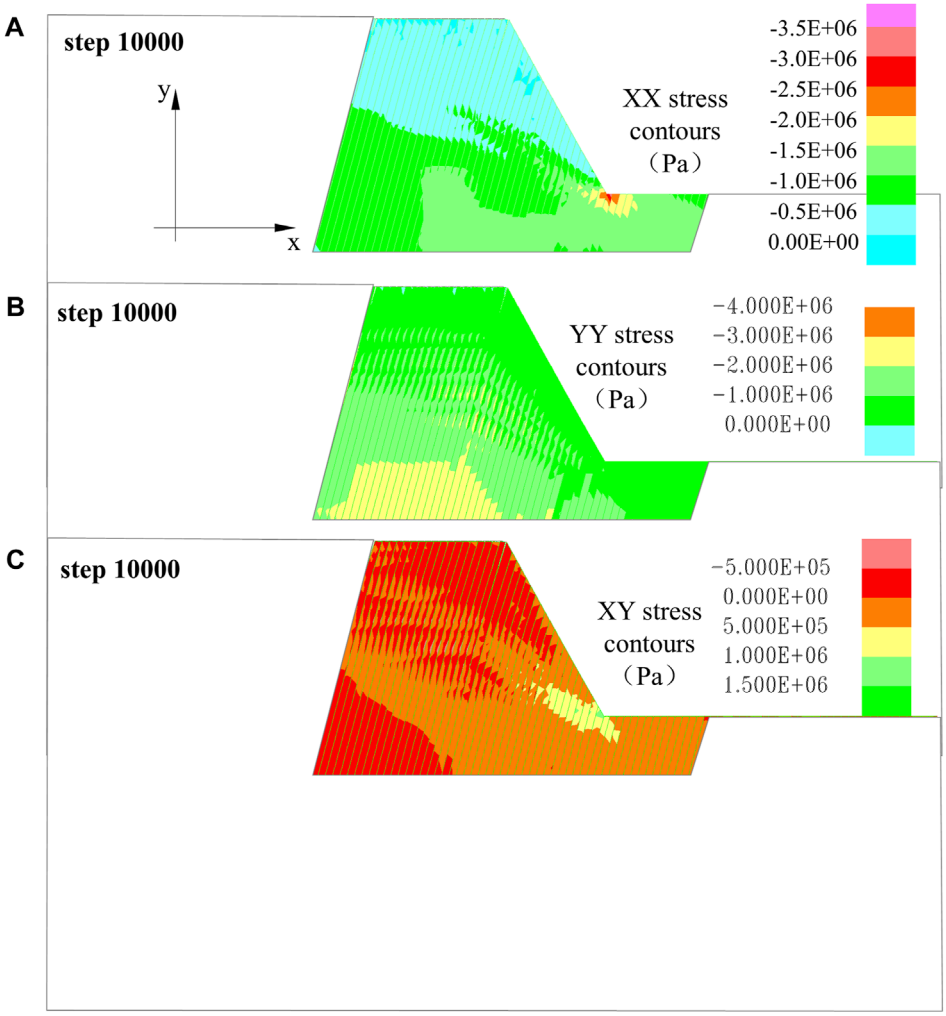

FIGURE 17
Stress characteristics of the original model evolution process. **(A)** XX stress contour 10,000 steps; **(B)** YY stress contour 10,000 steps; **(C)** XY stress contour 10,000 steps.

The structural plane opening of the inserted cracks model was larger, and the opening phenomenon is significant. Additionally, the pre-existing opening of the structural planes extended into the deeper slope. The opening of the structural planes often occurred near the root of the toppled fracture surfaces. The main reason was the rotational deformation of rock blocks after the fracture, which resulted in non-coordinated deformation between the blocks, leading to the formation of open spaces near the fracture surfaces and in triangular areas above the fracture surfaces. As the toppling deformation continued, some of the local openings closed.

The toppling deformation originates from the interlayer shear displacement, and the development of interlayer shear displacement can reflect the displacement characteristics of toppling deformation. From Figure 14, it is evident that each red line has a width equal to "each line thick," as shown in the figure. The overall width represents the cumulative width of multiple lines, and this width signifies the value of shear displacement of the structural planes.

During the development of toppling deformation, the maximum shear displacement of the structural planes was 0.013 m at 10,000 steps and 0.0411 m at 100,000 steps in the original model. The maximum shear displacement of the structural planes was 1.245 m at 50,000 steps and 2.064 m at 100,000 steps in the inserted cracks model.

Overall, the original model exhibited insignificant shear deformation, with relatively small maximum shear displacement values, reaching a maximum of 0.0411 m. There is no significant extension of shear displacement along the structural planes. The shear displacement of the structural planes was larger, and shear dislocation was more pronounced in the inserted cracks model.

5.2 Ductile bending deep toppling (DBDT)

For the DBDT, the rock mechanical parameters are chosen with UCS = 20 MPa. The DBDT takes into account the development characteristics of the plastic zone, the distribution law of shear strain, and the curvature of rock slabs comprehensively. Different bending curvature values are selected to insert cracks instead of potential bending fracture surfaces to reconstruct the model for the toppling failure process analysis.

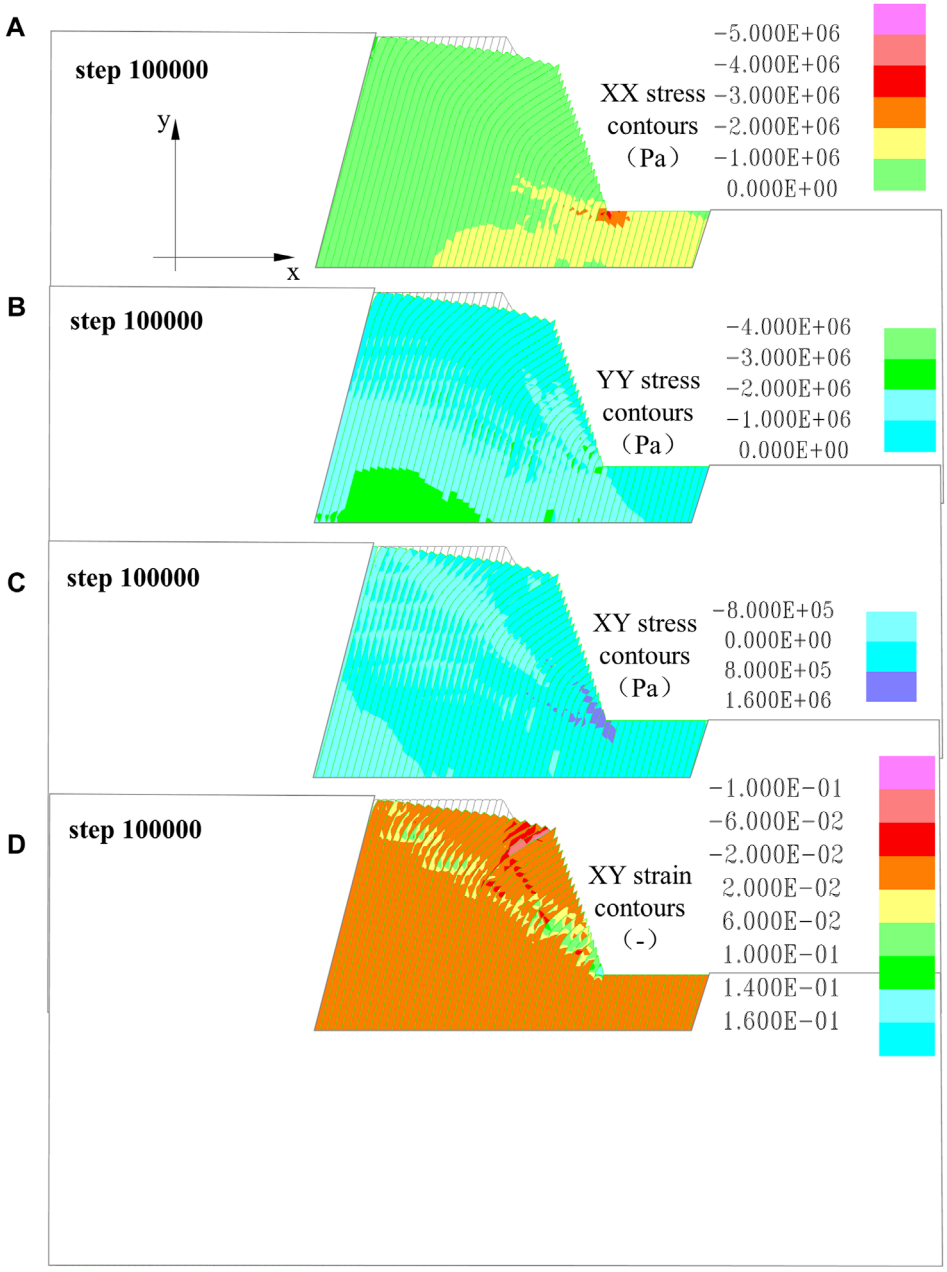

FIGURE 18
Stress characteristics of the original model evolution process. **(A)** XX stress contour 100,000 steps; **(B)** YY stress contour 100,000 steps; **(C)** XY stress contour 100,000 steps; **(D)** XY strain contour 100,000 steps.

5.2.1 DBDT displacement vector evolution

After calculating 100,000 steps, significant macroscopic flexible deformation becomes apparent, and the rock layers exhibit notable tensile failure. The multiple fracture depths for toppling are expressed through the depth of inserted cracks. Simultaneously, considering the maximum tensile strain characteristics, the deformation trace lines of maximum curvature experience complex tensile and compressive stresses and the deformation failure is severe. These areas serve as toppling bending surfaces and are most likely to evolve into potential sliding surfaces after long-term geological periods. Field investigations suggest that flexible toppling deformation leading to instability and failure typically occurs at moderate to relatively deep levels along the curvature surfaces.

The specific evolution of deformation failure is described as follows.

Figure 15 illustrates the displacement vectors of the original model during the calculation process. The direction of the vectors corresponds to the toppling direction. As the number of steps increases, the values of the maximum displacement vectors gradually increase. The maximum displacement at 10,000 steps is 1.644 m, at 50,000 steps, it is 25.66 m, and at 100,000 steps, it is 25.67 m. Additionally, the increment in the horizontal displacement

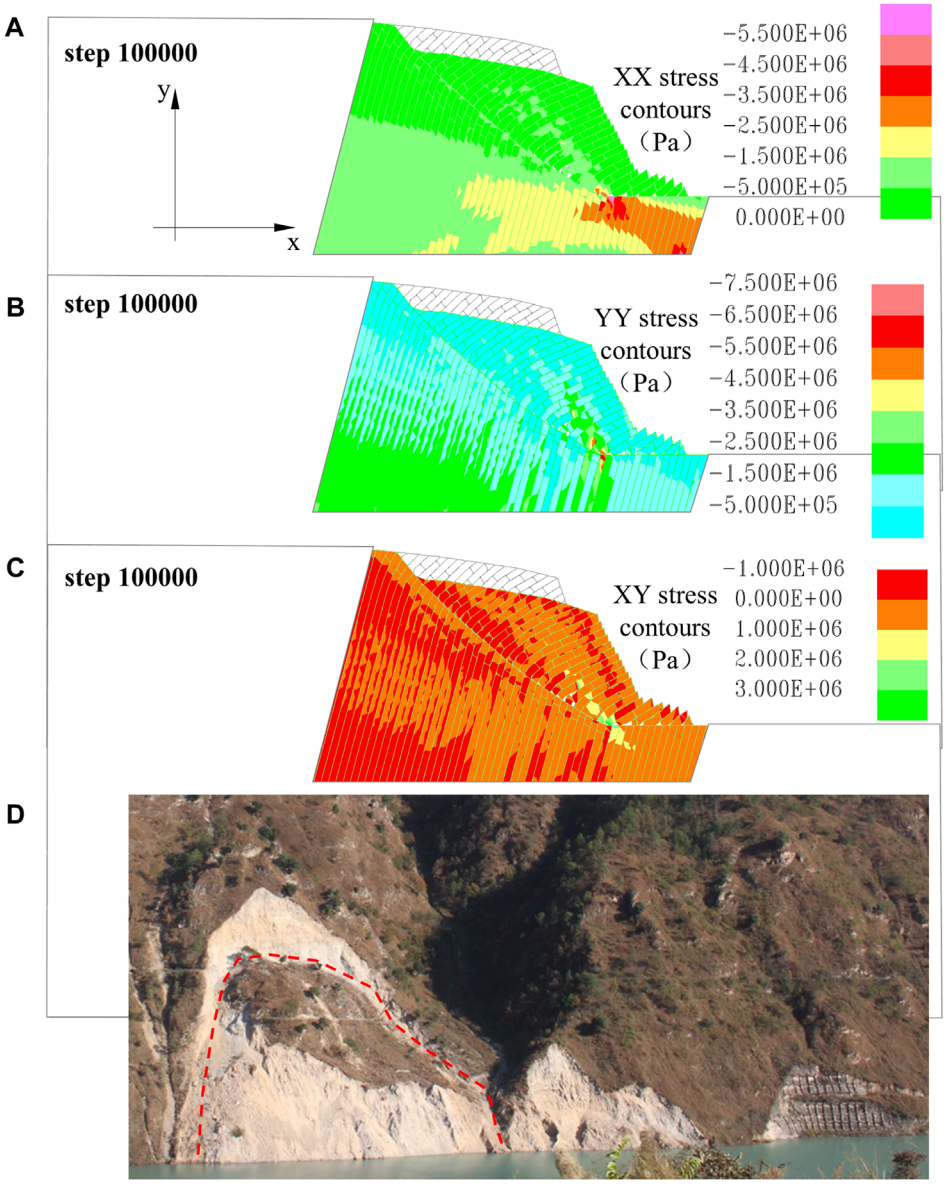

FIGURE 19
Stress characteristics of the inserted crack model evolution process. **(A)** XX stress contour 100,000 steps; **(B)** YY stress contour 100,000 steps; **(C)** XY stress contour 100,000 steps; **(D)** accumulation rock mass of toppled bank slopes at Miaowei Hydropower Station.

component is larger than that of the vertical displacement component.

At this point, the deformation displacement also tends to stabilize, and it can be considered to have entered the creep stage. Due to the software's own limitations, the rock blocks will not undergo further fracture. It is assumed that the final failure of the slope will occur along the curved fracture surfaces along the fracture surfaces with approximately equal curvature, and the deepest maximum curvature trace line is inserted as the potential sliding surface.

Figure 16 shows the deformation characteristics of the inserted cracks model during the entire process of 100,000 iterations. The calculation results indicate that as the number of steps increases, the value of the maximum displacement vector gradually increases. The toppling rock slabs begin to slide and become unstable along the inserted potential sliding surface. The maximum displacement at 10,000 steps is 5.935 m, at 50,000 steps it is 26.46 m, and at 100,000 steps, it is 37.27 m. At this point, the maximum deformation displacement occurs at the slope foot.

5.2.2 Stress and deformation characteristics evolution

The results of the original models for the DBDT can be seen in Figure 17 and Figure 18. Figure 17 shows the stress distribution at 10,000 steps, and the stress distribution in the Y-direction conforms to the typical layer-wise distribution. The X-direction stress distribution indicates a concentration of compressive stress in the slope foot, with a maximum X-direction stress value of

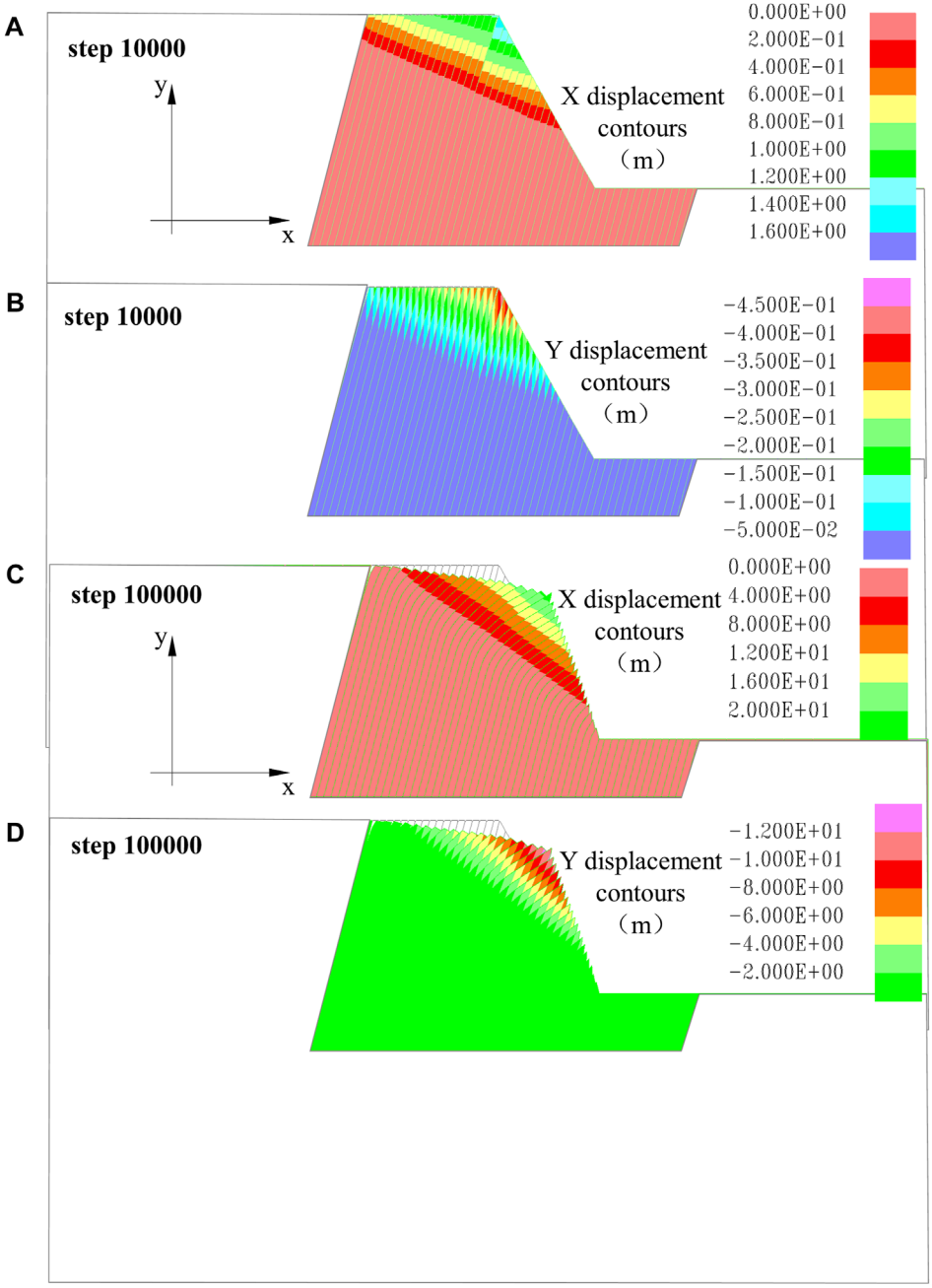

FIGURE 20
Displacement characteristics of the original model evolution process. **(A)** XX displacement contour 10,000 steps; **(B)** YY displacement contour 10,000 steps; **(C)** XX displacement contour 100,000 steps; **(D)** YY displacement contour 100,000 steps.

3×10^6 Pa. The shear stress distribution in the XY plane shows a concentration of shear stress in the slope foot, with a maximum shear stress of 1.5×10^6 Pa. When it reaches 100,000 steps, the X-direction stress distribution in the slope foot exhibits a higher concentration, increasing from 3.0×10^6 Pa to 4.0×10^6 Pa.

Figure 18 indicates that the shear strain in the model at 100,000 iterations is nearly continuous, with a likely potential surface for instability and failure that extend along the curvature equivalent points from near the front edge of the slope to the slope crest.

After 100,000 iterations, the rock mass of the inserted cracks model exhibits significant sliding deformation along the trace lines of the curvature equidistant points and the bending surfaces (Figure 19).

The compressive stress in the X-direction at the slope foot increases to 5.5×10^6 Pa. In the Y-direction, the compressive stress in the X-direction near the slope foot experiences an increase along the fracture surfaces, with stress values increasing to $6.5–7.5\times10^6$ Pa. Shear stress in the XY plane is centered at the slope foot, forming localized bands of concentrated shear stress along the same level

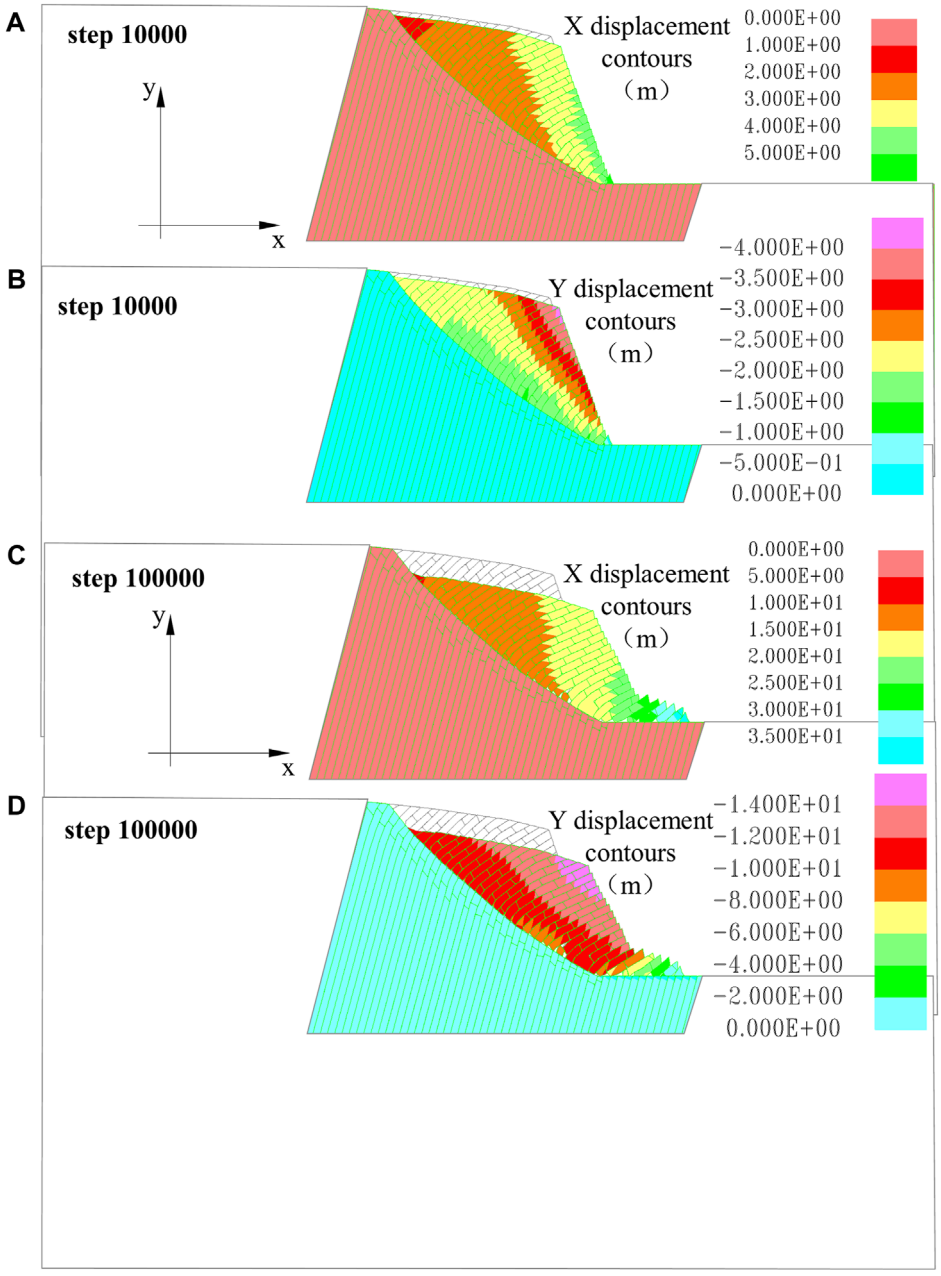

FIGURE 21
Displacement characteristics of the inserted crack model evolution process. **(A)** XX displacement contour 10,000 steps; **(B)** YY displacement contour 10,000 steps; **(C)** XX displacement contour 100,000 steps; **(D)** YY displacement contour 100,000 steps.

fracture surfaces, with shear stress values increasing to 3.0×10^6 Pa. The structural effect of the toppled rock mass controls the non-collapse discretization of the accumulation rock mass, as shown in Figure 19C.

The support conditions of the slope foot control the deformation and failure of the toppling slope. If the support of the slope foot is lost, the toppling slope will experience instability and failure along the potential sliding surface with the maximum shear strain zone. On the other hand, when the support conditions at the foot of the slope are intact, the toppling slope experience enters a temporary stable stage until the support conditions of the slope foot are lost (Figure 19D).

As the steps of the original model increase, the maximum displacements in both the X-direction and Y-direction increase (Figure 20). At 10,000 steps, the X-direction displacement is 0.06 m and the Y-direction displacement is also 0.06 m. At 100,000 steps, the X-direction displacement is 0.4 m and the Y-direction displacement is 0.16 m. The displacement in the X-direction is greater than the change in the Y-direction. Overall, the extent of deformation development did not change significantly.

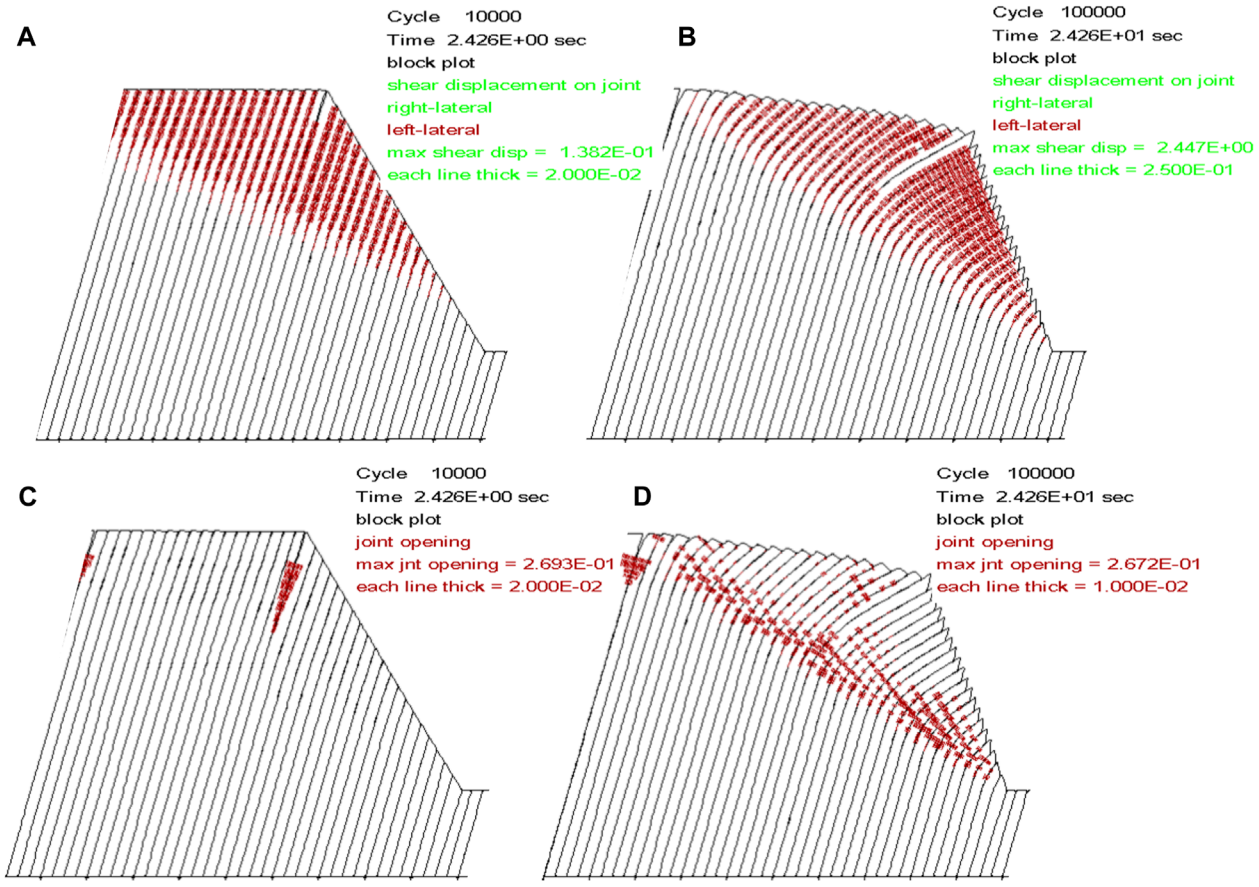

FIGURE 22
Distribution and variation of structural plane opening and shear displacement on structural planes. Each red line in the figures **(A)** and **(B)** has a width equal to "each line thick," where the overall width represents the cumulative opening of multiple lines, and this width signifies the opening of the structural planes. Each red line in the figures **(C)** and **(D)** has a width equal to "each line thick," where the overall width represents the cumulative width of multiple lines, and this width signifies the value of shear displacement of the structural planes. **(A)** Original model 10,000 steps; **(B)** original model 100,000 steps; **(C)** inserted crack model 50,000 steps; **(D)** the inserted crack model 100,000 steps.

After reconstructing the model, the calculation results indicate that as the steps of the inserted model increase, the maximum displacements in both the X-direction and Y-direction also increase (Figure 21). At 10,000 steps, the X-direction displacement is 5.0 m, and the Y-direction displacement is 4.0 m. At 100,000 steps, the X-direction displacement is 35.0 m, and the Y-direction displacement is 14.0 m. It is evident that in the initial stage of deformation, the maximum displacement occurs at the slope crest, and then the maximum deformation displacement occurs at the slope foot. The deformation development at the slope foot further intensifies the toppling deformation of the toppled rock mass.

5.2.3 Characteristics of interlayer stress and displacement

From Figures 22A,B, it can be observed that the red lines in the figure, with each line having a width equivalent to "each line thick," represent the cumulative width of multiple lines, signifying the opening degree of the structural planes.

During the development of toppling deformation, the maximum opening of these structural planes is recorded as 0.2693 m at 10,000 steps and 0.2672 m at 100,000 steps. The structural planes opening of the original model initially occurs at the front edge of the slope, and the original model exhibits a significant toppling deformation effect with relatively large structural planes openings. The existing structural planes opening continue to develop deeper into the model. Structural planes openings mainly occur near the portions with significant curvature and bending in the layers. This is primarily due to the occurrence of detachment of layers as a result of the interlayer bending. At this point, anti-slope scarps are visible at the slope crest and the slope surface, and some of the local openings close with the toppling deformation continuing.

The toppling deformation originates from the interlayer shear displacement, and the development of interlayer shear displacement can reflect the displacement characteristics of toppling deformation. From Figures 22C,D, it is evident that each red line has a width equal to "each line thick," as shown in the figure. The overall width represents the cumulative width of multiple lines, and this width signifies the value of shear displacement of the structural planes. During the development of toppling deformation, the maximum shear displacement of the structural planes is recorded as 0.1382 m at 10,000 steps and 2.447 m at 100,000 steps in the original model. Overall, the original model exhibits significant shear deformation with relatively large shear displacement of the structural planes, and shear dislocation was more pronounced in the original model.

5.3 Discussion of toppling failure

Generally, hard rock masses typically develop into shallow toppling, primarily characterized by stability issues at shallow depths of toppled slope. Most studies are focused on addressing these concerns of shallow toppling stability. However, rock masses dominated by soft rocks exhibit greater depths of toppling deformation, and once overall instability and failure occur, the engineering hazards are significant (Alejano et al., 2018; Zheng et al., 2018).

The rock mass mainly composed of soft rock undergoes bending and toppling deformation, resulting in certain interlayer openings at the maximum bending position, while other parts exhibit interlayer closures. In contrast, formations dominated by hard rock undergo BFST, with significant rock fragmentation and overhead state at the toppling fracture surface.

Ductile bending toppling deformations in formations dominated by soft rock require a relatively long evolutionary process, whereas brittle fracture toppling in formations dominated by hard rock tends to be sudden. This study is in agreement with the works of research workers namely, Huang et al. (2017) and Huang. (2007). These characteristics also indicate the primary features and mechanisms of toppling deformations under different rock hardness conditions.

6 Conclusion

Using the UDEC numerical simulation method, we can conclude that the range of rock mechanics parameters correspond to bending toppling deformations within the range of 80 MPa–100 MPa. This 80 MPa can be considered a preliminary reference threshold for two types of toppling; this threshold can be considered a preliminary reference value for rock mechanics parameters of ductile bending deep toppling.

Based on the summary of a large number of case studies, we summarize two types of toppling deformation: DBDT and BFST. The Guobu bank slope at the Laxiwa Hydropower Station reveals a large-scale BFST of blocky granite. The toppling rock masses are divided into intensified strong toppling (zone A), strong toppling (zone B), weak toppling (zone C), and loose-tensile fracture rock mass (zone D) based on the characteristics of toppling deformation and structure. The dam front slope at the Miaowei Hydropower Station is a typical DBDT case with alternating soft and hard rock conditions. The toppling rock masses are divided into toppling and collapse (zone A), strong toppling (zone B), and weak toppling (zone C).

Using the UDEC numerical simulation method, the development process and characteristics of DBDT and BFST were revealed from the displacement vector, overall displacement stress characteristics, interlayer stress, and displacement characteristics, which are in good agreement with the field investigation results.

Data availability statement

The original contributions presented in the study are included in the article/supplementary material; further inquiries can be directed to the corresponding authors.

Author contributions

JC: conceptualization, investigation, methodology, software, validation, writing–original draft, and writing–review and editing. JW: conceptualization, methodology, software, supervision, validation, and writing–review and editing. ZL: investigation, methodology, software, validation, and writing–original draft. YK: formal analysis, investigation, methodology, validation, and writing–original draft. LZ: investigation, methodology, validation, and writing–original draft. GQ: conceptualization, investigation, methodology, supervision, validation, and writing–review and editing.

Funding

The author(s) declare that financial support was received for the research, authorship, and/or publication of this article. The study is financially supported by the International Scientific and Technological Cooperation Base for Geological Disaster Prevention of Zhejiang Province (IBGDP-2022-04), the National Natural Science Foundation of China (42107169), the Scientific and Technological Project in Henan Province (222102210298), the Opening fund of State Key Laboratory of Geohazard Prevention and Geoenvironment Protection (Chengdu University of Technology, SKLGP 2022K004), and the Opening fund of Key Laboratory of Geological Hazards on Three Gorges Reservoir Area (China Three Gorges University), Ministry of Education (2022KDZ01).

Acknowledgments

The authors appreciate the linguistic assistance provided by AJE during the preparation of this manuscript. The authors specially thank the expert comments from the reviewers and editors for improving the manuscript.

Conflict of interest

Author LZ was employed by the Henan Communications Investment Construction Group Co., Ltd.

The remaining authors declare that the research was conducted in the absence of any commercial or financial relationships that could be construed as a potential conflict of interest.

Publisher's note

References

Alejano, L. R., Alonso, C. S., Rey, I. P., Arzúa, J., Alonso, E., González, J., et al. (2018). Block toppling stability in the case of rock blocks with rounded edges. *Eng. Geol.* 234, 192–203. doi:10.1016/j.enggeo.2018.01.010

Aydan, O., and Kawamoto, T. (1992). The stability of slopes and underground openings against flexural toppling and their stabilisation. *Rock Mech. Rock Eng.* 25, 143–165. doi:10.1007/BF01019709

Cai, J. C. (2020). *Research on mechanical behavior and stability of anti-dip rock slope in the whole process of flexible flexural toppling*. Chengdu, China: Chengdu University of Technology.

Cai, J. C., Ju, N. P., Huang, R. Q., Zheng, D., Zhao, W. h., Li, L. q., et al. (2019). Mechanism of toppling and deformation in hard rock slope: a case of bank slope of Hydropower Station, Qinghai Province, China. *J. Mt. Sci.* 16, 924–934. doi:10.1007/s11629-018-5096-x

Cai, J. C., Lu, S. Q., Li, K., Wu, Z., Zhao, R., and Wang, J. (2023). Mechanical mechanism of rock mass slabbing aggravating toppling failure. *J. Mt. Sci.* 10, 1103249. doi:10.3389/fevo.2022.1103249

Cai, J. C., Zheng, D., Ju, N. P., Huang, R. q., and Zhao, W. h. (2022). Boundary effect of toppling failure based on three-dimensional mechanical model. *J. Mt. Sci.* 19 (11), 3314–3322. doi:10.1007/s11629-022-7337-2

Cruden, D. M., and Hu, X. Q. (1994). Topples on underdip slopes in the highwood pass, Alberta, Canada. *Q. J. Eng. Geol. Hydrogeology* 27, 57–68. doi:10.1144/GSL.QJEGH.1994.027.P1.08

Goodman, R. E. (2013). "Toppling- A fundamental failure mode in discontinuous materials Description and analysis," in 2013 Congress on Stability and Performance of Slopes and Embankments III, Geo-Congress 2013, San Diego, United States, 2348–2378.

Goodman, R. E., and Bray, J. W. (1976). "Toppling of rock slopes," in *Rock engineering for foundations & slopes* (Reston, Virginia, United States: ASCE), 201–234.

Guo, H., Yan, C. Z., Zhang, G. H., Xu, R., Wang, T., and Jiao, Y. Y. (2024). Mechanical analysis of toppling failure using FDEM: a case study for soft-hard interbedded anti-dip rock slope. *Comput. Geotechnics* 165, 105883. doi:10.1016/j.compgeo.2023.105883

Han, B. C., and Wang, S. J. (1999). Mechanism for toppling deformation of slope and analysis of influencing factors on it. *J. Eng. Geol.* 7 (3), 213–217. doi:10.3969/j.issn.1004-9665.1999.03.004

Hoek, E., and Bray, J. W. (1981). *Rock slope engineering*. London, UK: Institution of Mining and Metallurgy.

Huang, R. Q. (2007). Large-scale Landslides and their sliding mechanisms in China since the 20th Century. *Chin. J. Rock Mech. Eng.* 26 (32), 433–454. doi:10.3321/j.issn:1000-6915.2007.03.001

Huang, R. Q., and Li, W. L. (2011). Formation, distribution and risk control of landslides in China. *J. Rock Mech. Geotechnical Eng.* 3 (2), 97–116. doi:10.3724/sp.j.1235.2011.00097

Huang, R. Q., Li, Y. S., and Yan, M. (2017). The implication and evaluation of toppling failure in Engineering geology practice. *J. Eng. Geol.* 25 (05), 1165–1181. doi:10.13544/j.cnki.jeg.2017.05.001

Huang, R. Q., Wang, Z. R., and Xu, Q. (1994). *A study of failure rules of anti-dip strata slopes Advance of Engineering Geology*. Naeem Muhammad, Pakistan: Chengdu:Southwest Jiaotong University Press, 47–51.

Hungr, O., Leroueil, S., and Picarelli, L. (2014). The Varnes classification of landslide types, an update. *Landslides* 11 (2), 167–194. doi:10.1007/s10346-013-0436-y

Jensen, E. K., Moore, J. R., Geimer, P. R., and Finnegan, R. (2024). Combined ambient vibration and surface displacement measurements for improved progressive failure monitoring at a toppling rock slab in Utah, USA. *Front. Earth Sci.* 12, 1364653. doi:10.3389/feart.2024.1364653

Liu, M., Liu, F. Z., Huang, R. Q., and Pei, X. j. (2016). Deep-seated large-scale toppling failure in metamorphic rocks: a case study of the Erguxi slope in southwest China. *J. Mt. Sci.* 13, 2094–2110. doi:10.1007/s11629-015-3803-4

Ministry of Construction of the People's Republic of China (2014). *GB50218T-2014 Standard for engineering classification of rock mass*. Beijing: China Construction Industry Press.

Nichol, S. L., Hungr, O., and Evans, S. G. (2002). Large-scale brittle and ductile toppling of rock slopes. *Can. Geotechnical J.* 39 (4), 773–788. doi:10.1139/t02-027

Ning, Y. B., Zhang, G. C., Tang, H. M., Shen, W., and Shen, P. (2019). Process analysis of toppling failure on anti-dip rock slopes under seismic load in southwest China. *Rock Mech. Rock Eng.* 52, 4439–4455. doi:10.1007/s00603-019-01855-z

Sardana, S., Verma, A. K., Verma, R., and Singh, T. N. (2019). Rock slope stability along road cut of Kulikawn to Saikhamakawn of Aizawl, Mizoram, India. *Nat. Hazards* 99, 753–767. doi:10.1007/s11069-019-03772-4

Tamrakar, N. K., Yokota, S., and Osaka, O. (2002). A toppled structure with sliding in the Siwalik Hills, midwestern Nepal. *Eng. Geol.* 64, 339–350. doi:10.1016/S0013-7952(01)00095-3

Tu, G. X., Deng, H., Shang, Q., Zhang, Y., and Luo, X. (2020). Deep-seated large-scale toppling failure: a case study of the lancang slope in southwest China. *Rock Mech. Rock Eng.* 53, 3417–3432. doi:10.1007/s00603-020-02132-0

Wang, S. J., Xiao, Y., and Du, Y. L. (1992). The Mechanism of bending creep of bedded rockmass in the slope on the left bank of Longtan dam site in Hongshui River, Guangxi, China. *Chin. J. Geol.* (S1), 342–352.

Xia, M., Ren, G. M., Li, T. B., Cai, M., Yang, T. J., and Wan, Z. L. (2019). Complex rock slope deformation at Laxiwa Hydropower Station, China: background, characterization, and mechanism. *Bull. Eng. Geol. Environ.* 78, 3323–3336. doi:10.1007/s10064-018-1371-x

Zhang, B. C., Tang, H. M., Fang, K., Ding, B., and Gong, Q. (2024). Experimental study on deformation and failure characteristics of interbedded anti-inclined rock slopes induced by rainfall. *Rock Mech. Rock Eng.* 57, 2933–2960. doi:10.1007/s00603-023-03633-4

Zhao, W. H., Zhang, C. Q., and Ju, N. P. (2021). Identification and zonation of deep-seated toppling deformation in a metamorphic rock slope. *Bull. Eng. Geol. Environ.* 80, 1981–1997. doi:10.1007/s10064-020-02027-y

Zheng, Y., Chen, C. X., Liu, T. T., Zhang, H., Xia, K., and Liu, F. (2018). Study on the mechanisms of flexural toppling failure in anti-inclined rock slopes using numerical and limit equilibrium models. *Eng. Geol.* 237, 116–128. doi:10.1016/j.enggeo.2018.02.006

Zheng, Y., Wu, R. F., Yan, C. Z., Wang, R., and Ma, B. (2024). Numerical study on flexural toppling failure of rock slopes using the finite discrete element method. *Bull. Eng. Geol. Environ.* 83, 111. doi:10.1007/s10064-024-03589-x

Zhu, C., He, M. C., Karakus, M., Cui, X., and Tao, Z. (2020). Investigating toppling failure mechanism of anti-dip layered slope due to excavation by physical modelling. *Rock Mech. Rock Eng.* 53 (11), 5029–5050. doi:10.1007/s00603-020-02207-y

Frontiers in
Environmental Science

Explores the anthropogenic impact on our natural world

An innovative journal that advances knowledge of the natural world and its intersections with human society. It supports the formulation of policies that lead to a more inhabitable and sustainable world.

Discover the latest Research Topics

See more →

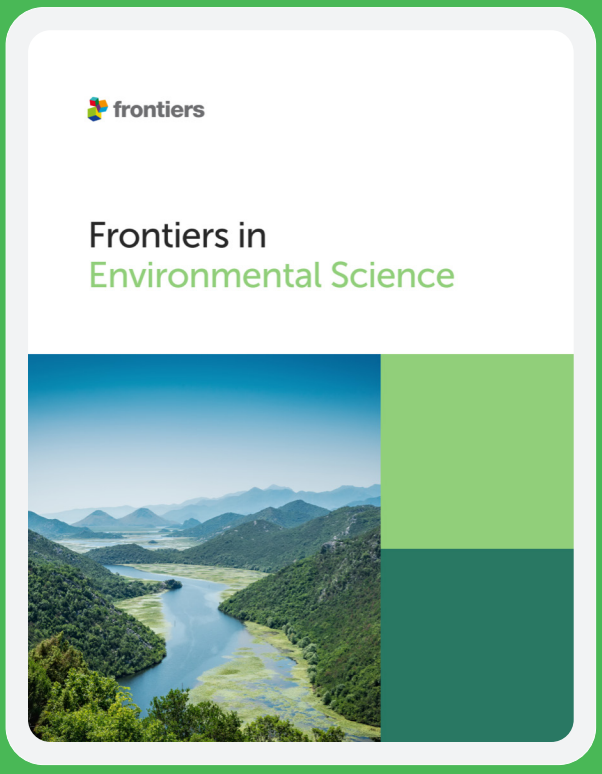

Frontiers

Avenue du Tribunal-Fédéral 34
1005 Lausanne, Switzerland
frontiersin.org

Contact us

+41 (0)21 510 17 00
frontiersin.org/about/contact